Fabrication, characterization and modeling of microcrystalline silicon-carbon alloys thin films

Sofia Gaiaschi

▶ **To cite this version:**

Sofia Gaiaschi. Fabrication, characterization and modeling of microcrystalline silicon-carbon alloys thin films. Materials Science [cond-mat.mtrl-sci]. Université Paris Sud - Paris XI, 2014. English. ⟨NNT : 2014PA112412⟩. ⟨tel-01127211⟩

HAL Id: tel-01127211

https://theses.hal.science/tel-01127211v1

Submitted on 7 Mar 2015

HAL is a multi-disciplinary open access archive for the deposit and dissemination of scientific research documents, whether they are published or not. The documents may come from teaching and research institutions in France or abroad, or from public or private research centers.

L'archive ouverte pluridisciplinaire **HAL**, est destinée au dépôt et à la diffusion de documents scientifiques de niveau recherche, publiés ou non, émanant des établissements d'enseignement et de recherche français ou étrangers, des laboratoires publics ou privés.

HAL Authorization

UNIVERSITÉ PARIS-SUD

ECOLE DOCTORALE : Sciences et Technologie de l'Information, des Técommunications et des Systèmes

Laboratoire de Génie Electrique de Paris (Supélec)
Laboratoire de Physique des Interfaces et Couches Minces (Ecole Polytechnique)

DISCIPLINE : Physique

THÈSE DE DOCTORAT

Soutenue le 10/12/2014

par

Sofia GAIASCHI

Fabrication, caractérisation et modélisation de couches minces d'alliages silicium-carbone microcristallins

Directeurs de thèse :	Marie-Estelle GUEUNIER-FARRET	Maître de conférence (Université de Paris Sud)
	Erik V. JOHNSON	Chargé de recherche (CNRS)
Composition du jury :		
Rapporteurs :	Matthieu DESPEISSE	Chargé de recherche (CSEM)
	Kacem ZELLAMA	Professeur (Université d'Amiens)
Examinateurs :	Frédéric ANIEL	Professeur (Université de Paris Sud)
	Christophe LONGEAUD	Directeur de recherche (CNRS)
	Aleš PORUBA	Professeur (Academy of Science of the Czech Republic)
Membre invité :	Patrick CHAPON	Ingénieur (HORIBA Jobin-Yvon)

To my mum and Giulio

"Je n'ai pas compris le mode d'emploi

Je n'ai pas appris à faire sans toi

[..] sans toi je sais plus qui je suis

J'ai oublié

sans toi je sais plus qui je suis"

—Babylon Circus

Did I remember to keep your beer as full as mine
Did I remember to say cheers
Did I at least try to make sure everybody had a good time
Had the best time
[...] Did I do it right

— Alkaline Trio

ACKNOWLEDGEMENTS

A PhD thesis is the result of three years of hard work and during this period one can feel very lonely. However, thanks to the (direct and indirect) support of many people, it is possible to survive and thrive in graduate school.

I sincerely thank both my advisors, Marie Gueunier-Farret and Erik Johnson. This thesis has proved to be very ambitious, but they have always tried to find the best way to keep me focused and to teach me that it's always possible to find (and also appreciate) the silver lining, even in the darkest moments (100 happy days!).

I thank Jean-Paul Kleider for having given me the chance to spend an additional year in LGEP as a teaching assistant. This will be another exciting experience!

I thank Christophe Longeaud and Pavel Bulkin for all the fruitful discussions, the caustic humor and for having always found the time to answer to my (many) questions. I thank Pavel and Tatiana also for having accepted the challenge to educate me to the "love of wine" and for having opened the doors of their beautiful house to numerous dinners.

I thank Giovanni Mannino for having accepted to collaborate with us, and having let Rosa work with me despite the difficulty of this task.

I thank Patrick Chapon for giving me access to the HORIBA's facilities whenever I needed.

A special mention goes to Rosa, not only for the numerous and endless work-related discussions but, above all, for always being there as a Friend. She's definitely one of the best people I've ever met and she has taught me a great deal of how to be a researcher and a woman. Supportive and encouraging, I know I will always be able to count on her (I hope she knows she can always count on me ♥). See you soon in Sicily...mhmmm...pasta di mandorle....

I thank all LGEP and LPICM colleagues, in particular Thomas, Federico (you must be counted twice, but stop jumping from one lab to the other!) and Martina, who never gave up on me, despite my laziness. I must thank also Romain and Ismael, for always coming to my rescue when the AR-CAM was involved. I specially thank Linh, Nancy, Selin (see you soon in London!!), Soumyadeep, Prabal and Dennis for their kindness and their friendship. I wish you all the best of luck. You definitely deserve it.

This PhD has brought me quite far from home. Nevertheless, I must admit that some things have not changed thanks to Vale, Franca, Matty and Cami! Some of them have now moved, but it is nice to know that there's a little piece of Bicocca everywhere in the world.

There are some old friends that have managed to always be there to support me, despite the distance. Thank you Eusy, Margina, Pale, Kia, Pit, Andre, Mattia, Giovanna, Noemi and Marzio.

I must thank also Giumba, for being always available when a good concert was coming up, and Julien and Isa for being themselves.

I thank my brother and his beautiful family for supporting me, despite the doubts and the expectations.

I especially thank my father for the love and support and for always having been there for me.

I thank my mum for being who she was, and I think that she would be proud of the person I have become. I miss you.

Last (but not least) I thank Giulio for having always believed in me and for having been by my side, no matter what. See you soon.

Paris, january 8, 2015 S. G.

ABSTRACT

Despite continuous effort, thin-film silicon multi-junction solar cells are still limited by the light-induced degradation of hydrogenated amorphous silicon (a-Si:H) or the amorphous silicon-germanium (a-SiGe:H) they employ. This technology could benefit from the ease with which multi-band gap photovoltaic devices can be assembled. Therefore, materials that are stable under light soaking and have an electronic band gap between that of hydrogenated microcrystalline silicon (μc-Si:H, 1.1 eV) and that of a-Si:H (1.7 eV) are needed.

This doctoral work was done in the framework of the French national project CANASTA. One of the goals of this project was to develop a new class of materials satisfying all these requirements, by alloying carbon and silicon. Indeed, hydrogenated microcrystalline silicon-carbon alloys (μc-$Si_{1-x}C_x$:H) thin films are a promising candidate for expanding the toolbox of useful materials for thin-film photovoltaics. The interest in these alloys lies in the possibility of varying their average band gap by changing the amount of carbon in the composition.

In this work it is shown that deposition conditions have a strong influence on both microstructural properties and carbon incorporation, resulting in a variety of transport and defect-related properties. The main disadvantage of this kind of materials is the absence of a stable sub-stoichiometric crystalline phase (i.e. no parallel for silicon-rich SiGe is expected). In fact, when grown by standard Radio Frequency Plasma Enhanced Chemical Vapor Deposition (RF-PECVD), these materials are composed of submicron-size silicon crystallites embedded in an amorphous silicon-carbon (a-$Si_{1-x}C_x$) matrix. While the presence of the crystallites assures a higher conductivity, compared to a-$Si_{1-x}C_x$:H, the carbon incorporation leads to an average energy gap larger than that of microcrystalline silicon.

In the first part of this work, different deposition strategies have been investigated, to achieve the widest range of freedom in processing conditions and to learn the most about the specific physical processes required to produce a high quality material. Material properties were extensively characterized both on the structural side and also from an electrical point of view, in order to establish a correlation between the effect of the deposition parameters on the microstructural, transport and defect-related properties.

In the end, a few sets of photovoltaic devices using these alloys as active layers were made. Still, very modest conversion efficiencies have been obtained (around 3.5 %) but these are the first ever results concerning the application of such a new class of materials as the active layer in thin-film solar cells. However, it was shown that it is possible to obtain variations in the open circuit voltage by varying the amount of carbon incorporated in the alloys. This is an important result showing that a process parameter other than silane dilution can be used to control this device parameter.

RÉSUMÉ

INTRODUCTION

Les besoins énergétiques de la société contemporaine augmentent sans cesse, et s'accroissent encore plus fortement depuis la montée en puissance de certains pays en voie de développement, notamment en Asie et en Amérique du Sud. Pour pouvoir répondre à cette demande en énergie, il sera indispensable dans le futur d'en augmenter la production en utilisant les ressources naturelles le plus efficacement possible via le développement de nouvelles technologies. En outre, de nouvelles habitudes de consommation devront être prises afin d'utiliser l'énergie produite de manière responsable. Néanmoins, une seule forme d'énergie ne sera pas suffisante pour satisfaire les besoins de la population mondiale. Les énergie renouvelables sont alors des candidats prometteurs puisqu'elles peuvent être développées aussi bien sous forme de centrales étant intégrées aux réseaux nationaux que pour des productions locales.

Parmi les différents types d'énergies renouvelables, l'énergie solaire photovoltaïque (PV) est de plus en plus intéressante. Même si les efforts continus de la communauté scientifique et sur le plan industriel ont conduit à une augmentation importante des rendements de conversion dans les différentes filières PV, les cellules solaires à base de silicium mono- (ou multi-) cristallin dominent toujours le marché ($\sim$ 80 % du marché). Néanmoins, la filière couches minces (tellure de cadmium, chalcogénures et silicium amorphe - a-Si :H) a une part de marché importante (> 10 %) dans la mesure où elle reste compétitive en termes de coût de production par rapport au silicium cristallin, en permettant la fabrication de cellules sur de grandes surfaces et sur des substrats bon marché.

Les rendements stabilisés de la filière a-Si :H restent toutefois limités ($\sim$ 13 %), car ce matériau souffre de la détérioration de ses propriétés après exposition prolongée sous lumière (effet de vieillissement communément appelé effet Staebler- Wronski). Pour s'affranchir de cette limitation, plusieurs pistes sont envisagées et plus particulièrement la fabrication de cellules solaires micromorphes qui sont composées d'une cellule avant à base de silicium amorphe hydrogéné (*top cell*) et d'une cellule arrière à base de silicium microcristallin (*bottom cell*). L'avantage vient de la possibilité de combiner des matériaux avec des gap énergétiques différents, permettant d'assurer une plus grande absorption du spectre solaire. Différents types de cellules multi-jonctions peuvent être réalisées, mais dès lors que l'une des cellules est constituée de a-Si :H ou de l'un de ces alliages (silicium-germanium a-SiGe :H, par exemple), se pose le problème du vieillissement sous lumière. Les recherches s'orientent donc vers la réalisation de cellules avant à base de matériaux qui ont un gap optique compris entre celui du silicium microcristallin (μc-Si :H - 1.1 eV) et celui du a-Si :H (1.7 eV.) et qui ne souffrent pas du vieillissement. Dans ce contexte a été développé le projet CANASTA, financé par l'agence nationale de la recherche.

CANASTA est l'acronyme de **C***arbon* **A***lloyed* **NA***nocrystalline* **S***ilicon* **TA***ndem*. Un des objectifs de ce projet, dans le cadre duquel a été réalisée cette thèse, était de développer une nouvelle classe de matériaux microcristallins

à base de silicium et de carbone, satisfaisant les conditions listées précédemment. Les alliages silicium-carbone microcristallins (µc-$Si_{1-x}C_x$:H) sont en effet des candidats prometteurs pour la croissance des matériaux utiles à la filière photovoltaïque en couches minces. L'un des intérêts de ces alliages est que leur gap optique peut être facilement modifié en changeant la quantité de carbone incorporé.

La nature exploratoire de cette partie du projet a exigé une étude systématique de l'effet de différents paramètres de dépôts sur les propriétés structurales et électriques des alliages silicium-carbone déposés afin de déterminer les conditions les plus adaptées pour leur exploitation comme couches actives dans des dispositifs photovoltaïques. Différentes techniques de dépôt plasma ont ainsi été utilisées : la technique standard *"RF-PECVD"* (pour Radio Frequency - Plasma Enhanced Chemical Vapour Deposition) à 13.56 MHz et la TVW-PECVD (Tailored Voltage Waveform-PECVD), développée récemment au sein des laboratoires LPICM et LPP de l'École Polytechnique. La technique RF-PECVD a permis de confirmer la possibilité de déposer ce type d'alliages, dans la mesure où c'est une technique de dépôt standard et bien maîtrisée. La technique TVW a notamment permis d'étudier le rôle du bombardement ionique lors de la croissance de ces matériaux et l'effet de ce paramètre sur l'incorporation du carbone. Le projet CANASTA envisageait également l'utilisation de la technique plasma MDECR-PECVD (Matrix Distributed Electron Cyclotron Resonance - PECVD), afin d'utiliser une source plasma à haute densité permettant d'obtenir une plus grande vitesse de dépôt. Malheureusement, les premiers essais avec cette technique n'ont pas permis de développer de manière efficace ces alliages sans changer complètement le système d'approvisionnement des gaz du réacteur, compte tenu de la forte sensibilité de ce matériau aux conditions de dépôt.

La Figure 1 présent l'ensemble des paramètres de dépôts étudiés, mettant en évidence les différentes combinaisons retenues pour une meilleure compréhension de l'effet de ces paramètres sur les propriétés structurales et électriques des alliages.

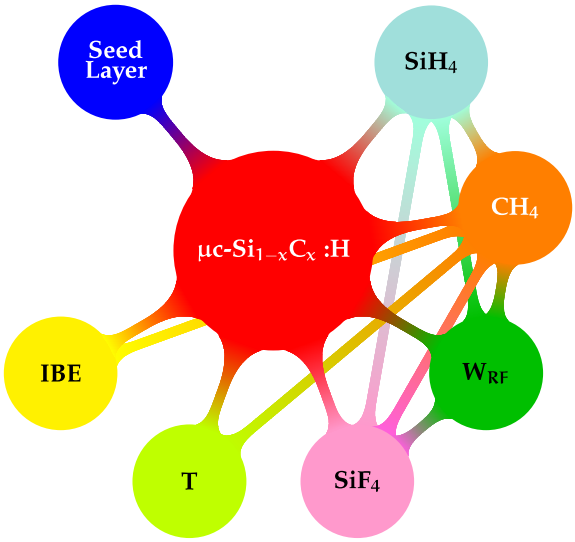

FIGURE 1. – Carte heuristique représentant les différents paramètres de dépôt étudiés (flux de SiH_4, CH_4 et SiF_4, puissance RF - W_{RF}, température - T et bombardement ionique - IBE) et leurs sous-liens.

PROPRIÉTÉS STRUCTURALES DES MATÉRIAUX

Dans la première partie du manuscrit, les propriétés structurales des échantillons obtenus par RF-PECVD et TVW-PECVD ont été caractérisées à l'aide de nombreuses techniques. Des mesures d'ellipsométrie ont permis de distinguer rapidement la structure amorphe ou microcristalline des échantillons, et d'identifier les conditions qui amènent à la transition de phase microcristallin-amorphe. Elles ont été complétées par des analyses de spectroscopie Raman et de diffraction de rayons X à incidence rasante (GIXRD) afin d'évaluer le degré de cristallinité et la nature de la phase cristalline. La plus grande difficulté liée à ce type de matériaux est l'absence d'une phase microcristalline sous-stoechiométrique stable (il n'y a pas de correspondance avec le SiGe cristallin, riche en germanium). En effet, compte tenu du diagramme de phase silicium-carbone, le seul composé stable est le carbure de silicium. Tous les alliages avec un taux de carbone inférieur à la stoechiométrie sont métastables, compte tenu du bas taux de solubilité du carbone dans le silicium ($\sim 3 \times 10^{17}$ atomes cm^{-3} au point de fusion). Ce type de composé stable peut être déposé uniquement audessous du seuil critique et par des techniques de dépôts qui utilisent des conditions très loin de l'équilibre thermodynamique, permettant une stabilisation cinétique des phases métastables, comme l'*épitaxie par jet moléculaire* (Molecular beam epitaxy). Les techniques PECVD conduisent à l'obtention de matériaux bi-phase composés de cristallites de silicium ($< \mu m$) dans une matrice de silicium-carbone amorphe (a-$Si_{1-x}C_x$:H), dont la stoechiométrie est variable.

Toutes les techniques de caractérisation structurales ont mis en évidence l'absence de forme cristalline de carbure de silicium ou de carbone. Néanmoins, la présence de carbone dans les couches minces a été vérifiée par des mesures de spectroscopie infrarouge à transformée de Fourier (FTIR) qui ont révélé que le carbone est préférentiellement lié au silicium. Pour la détermination du niveau de carbone incorporé dans les échantillons, une nouvelle technique d'analyse, la spectroscopie optique de décharge luminescente radiofréquence (radio frequency glow discharge optical emission spectroscopy) a été utilisée, grâce à une collaboration avec HORIBA Jobin-Yvon. Cette technique permet la détermination directe de tous les éléments présents dans la couche étudiée, sans besoin d'ultra-vide. Elle utilise une décharge luminescente à basse pression qui permet à la fois de pulvériser une zone représentative de l'échantillon à analyser et de générer une lumière caractéristique. L'échantillon est utilisé comme cathode pour pouvoir établir une décharge plasma d'argon. Les ions du plasma sont accélérés vers la cathode et ont suffisamment d'énergie pour effectuer l'érosion cathodique de la couche. Les espèces pulvérisées sont transférées dans le plasma où elles sont excitées et ionisée. Leur désexcitation cause l'émission de lumière, c'est-à-dire de photons caractéristiques du matériau. Cette lumière est recueille par un spectromètre optique en permettant la détermination de la composition élémentaire du matériau. Le taux de carbone incorporé dans le matériau (R_C) a été défini comme le rapport entre l'intensité de la ligne correspondante à l'émission du carbone, divisé par l'intensité relative à l'émission du silicium. Un étalonnage est nécessaire pour obtenir des informations quantitatives sur la composition des échantillon analysés. Dans ce travail, la calibration a été faite en divisant le rapport carbone-silicium des échantillons, par le même rapport mesuré pour du carbure de silicium cristallin stoechiométrique.

Pour nos échantillons, la croissance microcristalline a été amorcée par le dépôt préalable d'une couche de silicium microcristallin, appelée *"seed layer"* (Gaiaschi, Ruggeri, Johnson et al., 2014). Sans cette couche, la croissance conduit systématiquement à des échantillons complètement amorphes (pour des épaisseurs au tour de 50 nm). Pour mieux comprendre son effet, une série d'échantillons a été déposée en faisant varier le temps de dépôt de cette couche entre 0 et 16 minutes. Dès l'ajout de la *"seed layer"* s'effectue une transition de phase mise en évidence par les techniques de caractérisation standard (ellipsométrie et spectroscopie Raman), mais aussi par la technique de microscopie à force atomique (AFM).

Comme montré sur la Figure 2, l'utilisation d'une couche *"seed layer"* permet de passer d'un matériau caractérisé par une surface plate (rugosité de surface de 0.5 nm) à un alliage marqué par la présence de protubérances dispersées dans des zones plates, qui conduisent à une augmentation de la rugosité de surface (8 nm). Ces protubérances correspondent à des agrégats

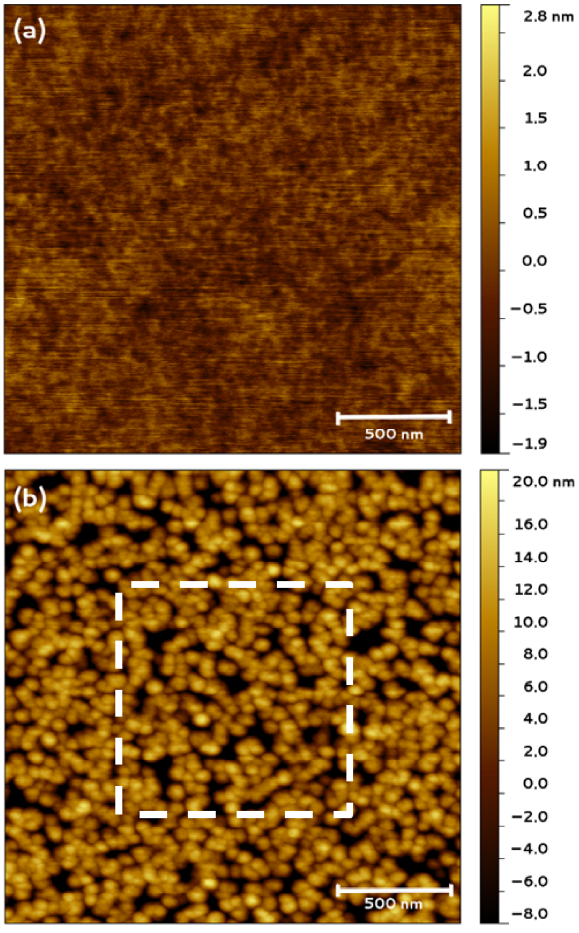

Figure 2. – Images AFM images d'échantillons déposés (a) sans couche *"seed layer"*et (b) avec une couche *"seed layer"* de quatre minutes. L'augmentation de la rugosité de surface est mise en évidence par les différentes échelles. Dans la Figure (b) les tâches noires correspondent à des zones amorphes entre les agrégats microcristallins et la ligne blanche hachée correspond à une zone étudiée avec un plus grand grossissement.

(que l'on peut appeler grains) composés de cristallites de taille nanométrique et qui s'allongent dans la direction de la croissance.

Des analyses de microscopie en transmission (TEM) ont été réalisées dans le cadre d'une collaboration avec le laboratoire CNR-IMM de Catania (Italie), afin d'étudier l'effet de la variation du temps de dépôt de la *"seed layer"* et de comprendre la nature de ces agrégats. Une correspondance entre les mesures AFM et les analyses TEM a été établie, mettant en évidence les même formes et rugosités locales (Figure 3).

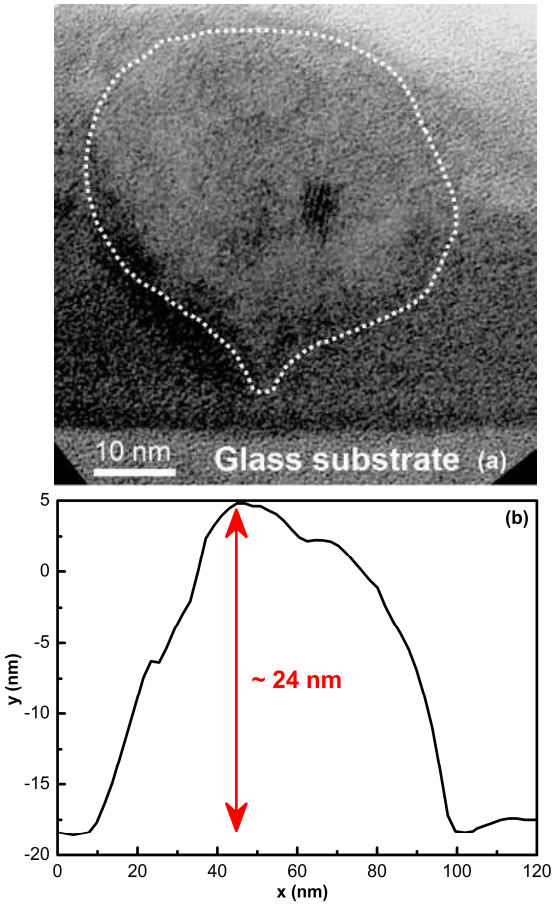

FIGURE 3. – (a) Image TEM en section transversale d'un échantillon déposé avec une couche *"seed layer"* (dépôt de 8 minutes) et (b) profil AFM obtenu pour un seul grain isolé. Les lignes pointillées en Figure (a) indiquent la présence d'un cristal de silicium dans la matrice.

Les protubérances correspondent effectivement à des grains de silicium cristallin dispersés dans une matrice amorphe. Des analyses TEM avec un filtre en énergie ont montré que la matrice enrobant les grains est composée de silicium et de carbone (Figure 4). En outre, l'utilisation de cette *"seed layer"* permet de réduire la région d'incubation à une épaisseur de 5-10 nm à l'interface entre le substrat et la couche. Cette couche d'incubation, typique pour la croissance de matériaux à base de silicium microcristallin, est caractérisée par une structure amorphe. Sachant que l'introduction de gaz à base de carbone dans une décharge plasma amène à l'amorphisation du matériau déposé (à cause de la distorsion des liaisons dans le réseau cristallin), on peut s'attendre à que le début de la croissance cristalline soit retardé (voire inexistant si le taux de carbone est trop élevé) dans le cas où l'on n'utilise pas de *"seed layer"*.

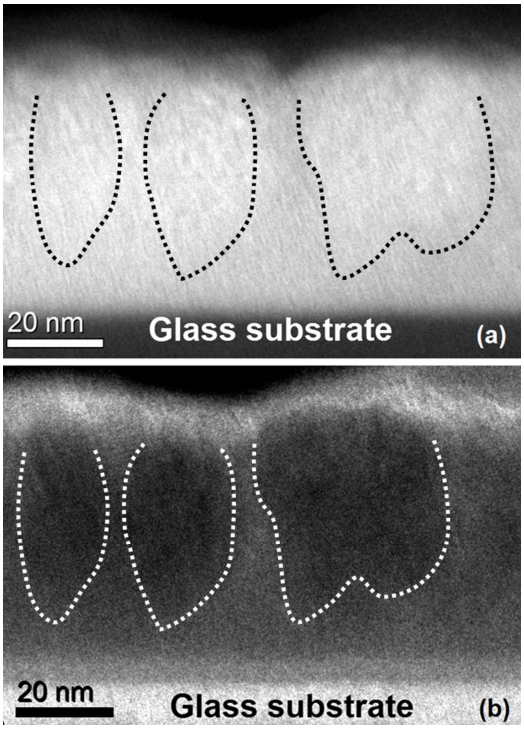

FIGURE 4. – Images plasmoniques d'un échantillon déposé avec une couche *"seed layer"* de 16 minutes. Les images ont été obtenus en centrant la fenêtre en énergie à (a) 16 eV et (b) 24 eV.

Mais, finalement, à quoi correspond cette couche *"seed layer"* ? Afin de l'étudier, une telle couche a été déposée sur un substrat de type "Corning glass". À partir de mesures AFM effectuées sur le verre (Figure 5), la présence de structures rondes dispersées dans une croissance avec une rugosité de 0.36 nm est observée. Sachant que les conditions utilisées pour la croissance de la couche *"seed layer"* sont celles typiquement utilisées au laboratoire pour obtenir des couche de silicium microcristallin (de 15 nm d'épaisseur, pour des temps de dépôt plus longs), on peut supposer que la croissance observée en Figure 5 correspond aux premières étapes d'une croissance microcristalline.

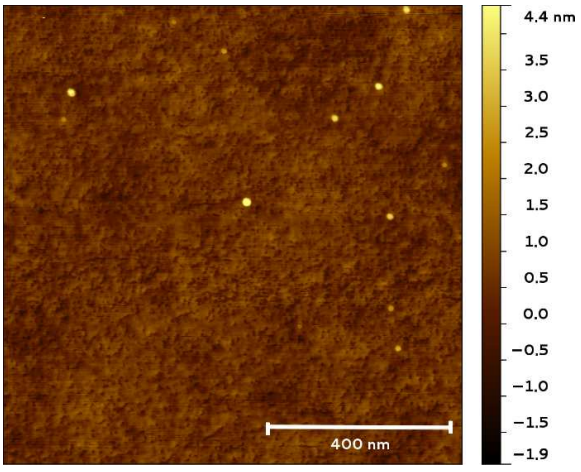

FIGURE 5. – Image AFM d'une couche *"seed layer"* déposée pendent 10 minutes sur un substrat de type "Corning glass".

L'influence des différents paramètres de dépôt (flux de silane, flux de méthane, puissance RF, flux de SiF_4, température du substrat) sur les propriétés structurales et électriques des couches, et plus particulièrement sur la transition de la phase microcristalline à la phase amorphe, a été étudiée en détails.

L'augmentation du flux de silane à puissance RF constante conduit à un plus grand nombre de radicaux SiH_x qui arrivent à la surface du substrat. Ainsi, le flux de silane a-t-il une influence non seulement sur la vitesse de dépôt mais également sur la fraction cristalline de l'alliage déposé, comme montré sur la Figure 6.

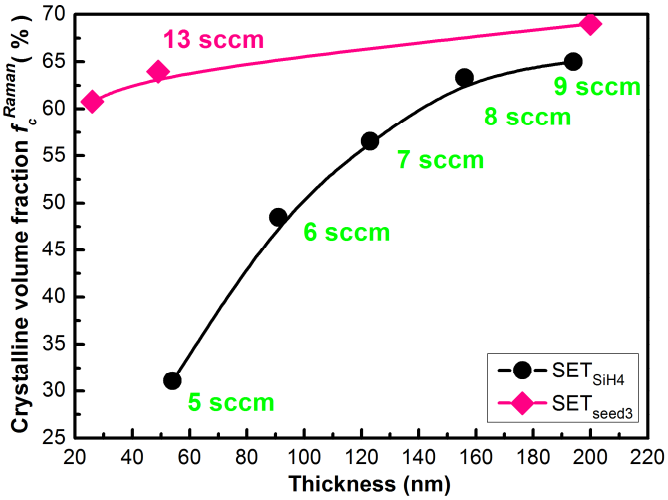

FIGURE 6. – Évolution de la fraction cristalline pour des échantillons déposés en variant le flux de SiH_4 (●) et pour des échantillons déposés en variant le temps de dépôt (◆). Les valeurs correspondant au flux de SiH_4 utilisé sont notées en vert pour la série en SiH_4 et en rose pour la série en épaisseur.

En utilisant certaines techniques de caractérisation, comme la spectroscopie Raman, la spectroscopie infra-rouge, ou la RF-GD-OES, il est possible de montrer que la variation indépendante de paramètres de dépôt tel que le flux de méthane, la puissance RF ou le flux de SiF_4, amène à des matériaux avec un taux de carbone incorporé plus bas et donc une fraction cristalline plus élevée.

Sur la Figure 7, l'évolution du rapport carbone-silicium total R_C est présentée en fonction du flux de méthane, pour certaines séries d'échantillons. Il apparaît que le taux de carbone incorporé dans les couches peut être contrôlé de façon similaire, en utilisant différents paramètres de dépôt. Certains paramètres agissent uniquement sur la quantité de molécules de méthane dissociées (comme le flux de méthane et la puissance RF), autres s'appuient sur l'introduction d'un deuxième mécanisme de décapage de la phase amorphe (comme l'introduction de SiF_4 dans la phase gazeuse). La ligne rouge hachée met en évidence le seuil correspondant à la transition microcristallin-amorphe. Quel que soit le paramètre de dépôt modifié, tous les alliages deviennent amorphes pour des rapport $R_C > 0.1$.

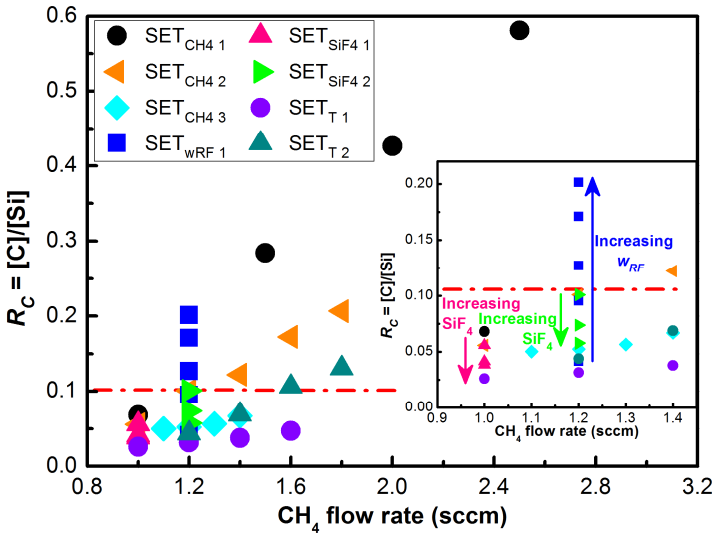

FIGURE 7. – Évolution du rapport carbone-silicium total R_C, en fonction du flux de méthane, pour certaines séries d'échantillons analysés. La ligne rouge hachée met en évidence la transition microcristallin-amorphe.

À partir des spectres Raman il a été possible de déterminer la fraction cristalline des alliages f_c^{Raman}. En Figure 8 l'évolution de ce paramètre est présentée en fonction de R_C, en connectant directement l'amorphisation des matériaux à l'incorporation de carbone. Comme mentionné précédemment, la variation indépendante de différents paramètres de dépôt peut être responsable de la diminution de la fraction cristalline dans l'alliage.

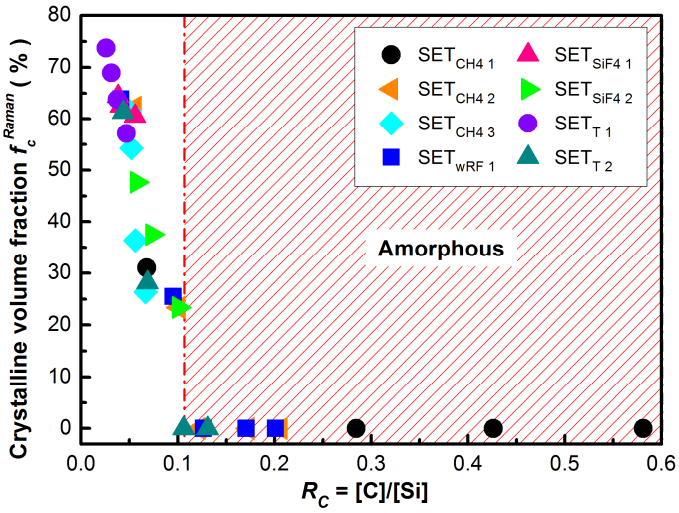

FIGURE 8. – Évolution de la fraction cristalline f_c^{Raman} en fonction du rapport carbone-silicium total R_C.

En réalité la variation de la puissance RF n'a pas seulement un effet sur la chimie du plasma, mais aussi sur le bombardement ionique à la surface de la couche qui est déposée. La variation de ce paramètre peut être en elle même néfaste pour la croissance microcristalline. En effet, des techniques de caractérisation sensibles à la microstructure des alliages (comme la diffraction des rayons X ou les analyses TEM) ont mis en évidence l'impact de la puissance RF sur la taille moyenne des cristallites (Figure 9). Deux tendances peuvent être soulignées, montrant que la taille moyenne des cris-

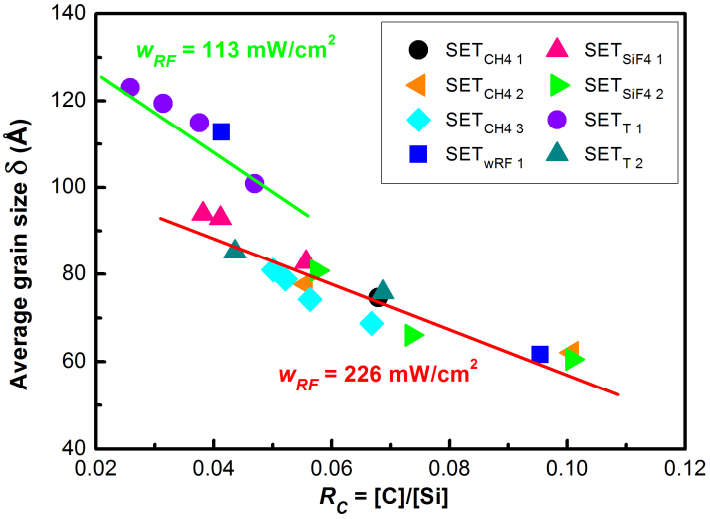

FIGURE 9. – Évolution de la taille moyenne des cristallites δ, en fonction du rapport carbone-silicium total R_C. Les lignes verte et rouge mettent respectivement en évidence l'existence d'un régime de *"basse puissance"* et d'un régime de *"haute puissance"*.

tallites est contrôlée au maximum par la puissance RF utilisée pendant le dépôt.

Ces résultats sont en bon accord avec les analyses TEM qui montrent qu'une plus basse puissance RF amène à échantillons caractérisés par des structures colonnaires plus ordonnées.

Dans un premier temps, les dépôts ont été réalisés en utilisant une température de substrat de 285° C, qui est la température la plus élevée possible au sein du réacteur RF-PECVD. Notre objectif était de déposer du carbure de silicium microcristallin (déposé typiquement à 300° C, mais par dépôt chimique en phase vapeur, activé par filament chaud (Hot Wire Chemical Vapor Deposition). L'utilisation d'une température aussi élevée est néanmoins un inconvénient majeur pour la fabrication de dispositifs photovoltaïques. Nous avons donc réalisé des dépôts à plus basse température(175° C), dans la mesure où le dépôt de photodiodes à cette température est bien maîtrisé. Deux séries d'échantillons ont été déposées à 175° C en faisant varier la puissance RF et le flux de méthane afin d'étudier la transition de phase à cette température de substrat (GAIASCHI, GUEUNIER-FARRET et al., 2014). Les résultats obtenus sont très comparables à ceux observés pour les séries d'échantillons similaires déposés à 285° C. En particulier, la diminution de la température n'a pas d'effet notoire sur les propriétés structurales des alliages. Ainsi, il est préférable de réaliser des dépôts à 175° C afin de concevoir les dispositifs photovoltaïques à base de ces matériaux plus aisément.

Croissance par TVW-PECVD

Enfin, nous avons étudié l'effet du bombardement ionique à la surface du substrat (tout-en gardant la même puissance de dépôt et donc la même chimie plasma) à l'aide de la technique de dépôt TVW-PECVD. Dans le cas des dépôts par RF-PECVD, la puissance RF de dépôt contrôle le bombardement ionique et le taux de dissociation des gaz précurseurs alors que ces

paramètres sont décorrélés dans le cas des dépôts par TVW-PECVD. Cette technique utilise en effet des formes d'ondes non-sinusoïdales pour produire un effet d'asymétrie électrique dans le réacteur plasma. Ces formes d'ondes sont obtenues par une superposition cohérente d'une fréquence fondamentale (f) et des ses harmoniques (f + 2f + 3f + . . .). Elles sont caractérisées par un temps de montée ou de descente très court par rapport aux formes d'onde sinusoïdales. Leur fréquence doit être suffisante pour exciter le plasma, donc la fréquence fondamentale varie entre 3 et 30 MHz. Dans ce travail, deux formes d'onde ont été utilisées, nommées *pics* et *vallées*. Pour les obtenir, toutes les harmoniques qui les composent ont leur phase (définie par rapport à la phase de la fréquence fondamentale) fixé à 0 (*pics*) ou à π (*vallées*). Le bombardement ionique à la surface du substrat peut être diminué dans le cas des "pics" et augmenté dans le cas de "vallées". Malgré une pression assez élevée (310 Pa) lors des dépôts, un effet de la variation des formes d'onde a été observé. Les matériaux déposés utilisant les formes d'onde *vallées* (haut bombardement ionique) sont caractérisés par un taux de carbone incorporé plus élevé et irrégulier. En outre, des mesures AFM ont montré la présence de cratères de $\sim$ 50 nm de diamètre et aussi épais que la couche (Figure 10).

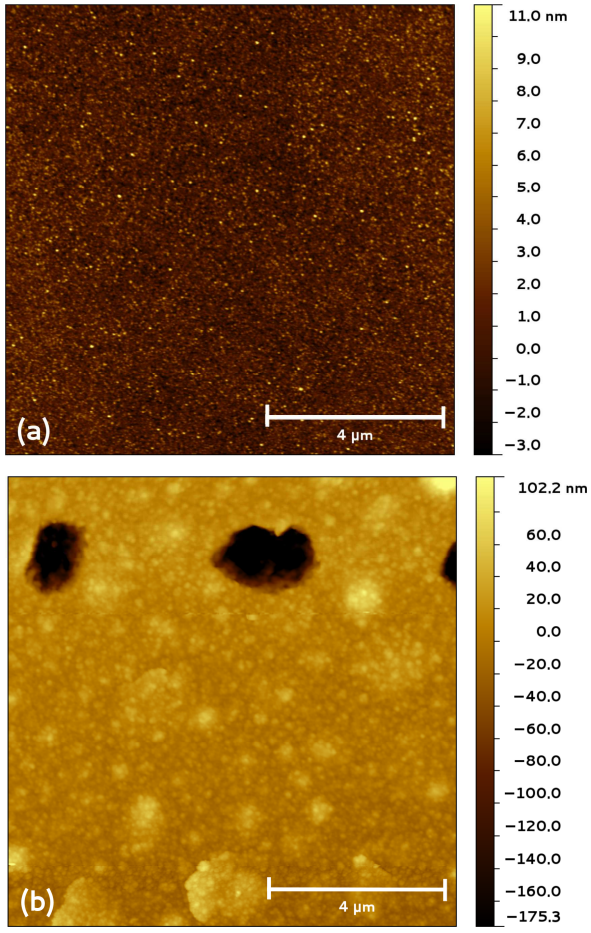

FIGURE 10. – Images AFM d'échantillons déposés utilisant des formes d'onde (a) "pics" et (b) "vallées". Les deux échantillons ont été déposés avec un flux de CH_4 = 1.2 sccm.

Ces cratères sont assimilables à des "écailles" d'échantillons qui ont pelé à cause du stress induit dans la couche. L'utilisation de formes d'onde *pic* (bas bombardement ionique) conduit a des échantillons avec des propriétés structurales peu affectées par la variation du flux de méthane. Ces alliages présentent tous des valeurs similaires de fraction cristalline, de taille de cristallites et de taux de carbone incorporé, montrant donc que le bombardement ionique a un effet sur le mécanisme d'incorporation de carbone, qui doit être étudié davantage.

Modèle de croissance

L'ensemble des caractérisations structurales effectuées sur les différentes séries d'échantillons à permis de développer un modèle de croissance de ce type d'alliages bi-phase (Gaiaschi, Ruggeri, Gueunier-Farret et al., 2014). À partir d'analyses TEM effectuées sur des échantillons épais d'environ 250 nm, il a été montré que la croissance de ces alliages présente une structure en V comparable à celle du silicium microcristallin (Figure 11).

Le carbone, qui ne peut pas être incorporé dans la phase cristalline, est piégé aux joints de grains, formant des couches de tissu amorphe qui s'interconnectent et limitent la croissance des grains cristallins. Nous avons démontré que l'incorporation de carbone ne se produit jamais dans des phases cris-

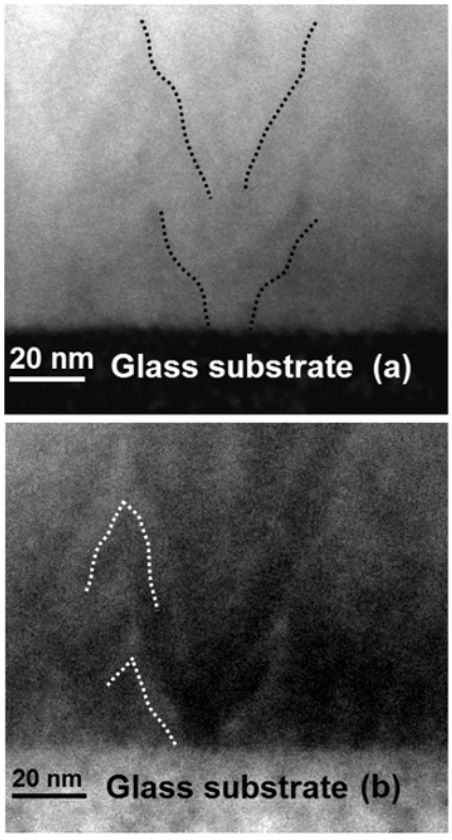

Figure 11. – Images plasmoniques d'alliages µc-$Si_{1-x}C_x$:H déposés avec un flux de méthane de 1.2 sccm, acquises avec différentes énergies plasmoniques : (a) 17 eV, correspondent au Si bluk et (b) 24 eV, correspondant au a-$Si_{1-x}C_x$. Les lignes hachées soulignent des zones avec changement de contraste, selon l'excitation plasmonique choisie.

tallines sous-stoechiométriques que ce soit pour des grands cristaux (µm), ou pour des cristallites de taille nanométrique. Le carbone ne peut être incorporé que dans la phase amorphe, qui enrobe les cristallites. D'autre part, on peut supposer que le flux de radicaux lors du dépôt est homogène sur toute la surface du matériau et que cristallites et phase amorphe "voient arriver" le même flux. Ainsi, comment le carbone peut-il interagir avec la surface de la couche en croissance ? Vu que l'instabilité des phases sous-stoechiométriques dépend de la formation de cristaux tridimensionnels, on peut supposer que le carbone reste incorporé dans les premières couches monoatomiques des régions cristallines avant d'être éliminé. Le point fondamental du modèle développé est donc le suivant : même à la surface des zones cristallines, le carbone est incorporé dans les couches monoatomiques surfaciques, dans des formes sous-stoechiométriques (Figure 12).

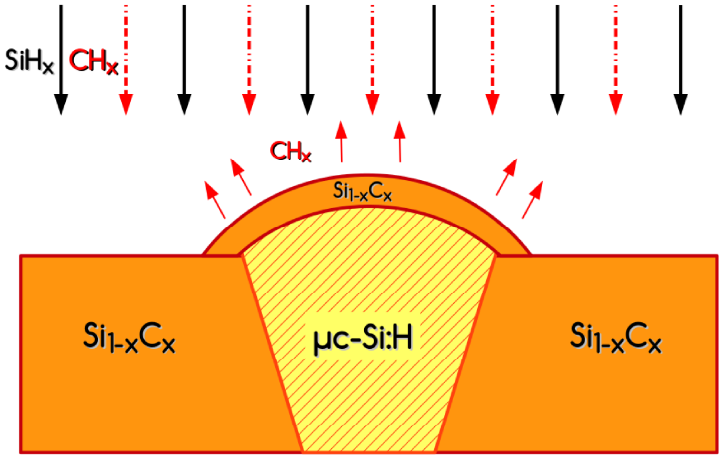

FIGURE 12. – Schéma du modèle proposé dans cette thèse pour l'incorporation de carbone dans la croissance d'alliages µc-$Si_{1-x}C_x$:H. Les cônes hachés correspondent à la croissance colonnaire des cristaux de µc-Si :H, tandis que les volumes pleins correspondent à la matrice a-$Si_{1-x}C_x$:H.

L'élimination du carbone de ces zones cause le retard de la croissance cristalline, tandis que les régions amorphes continuent de croître vu qu'elles peuvent exister dans des phase sous-stoechiométriques. A l'aide de ce modèle, nous avons pu expliquer l'effet du flux du méthane et de la puissance RF sur la croissance de nos alliages. En outre, l'introduction de quelques sccm (0.5-1) de SiF_4 dans le plasma, qui, d'après la littérature, est responsable d'une diminution de l'oxygène incorporé dans la couche de µc-Si :H et d'une plus haute fraction cristalline, induit l'existence d'un deuxième mécanisme de décapage. Les atomes de silicium et de carbone sont décapés à la fois par l'hydrogène (le carbone étant décapé plus rapidement) et par les atomes de fluor (qui décapent le silicium plus rapidement). Les flux d'hydrogène et de méthane étant fixes, le décapage contrôlé par l'hydrogène est constant et l'introduction des atomes de fluor (par la dissociation de SiF_4 dans le plasma) entraîne un décapage supplémentaire des zones amorphes(de préférence), conduisant à une plus haute fraction cristalline. Ce phénomène semble être dépendant de la phase du matériau de départ (déposé sans SiF_4). Si l'échantillon de départ a une haute fraction cristalline (> 50 %), l'ajout de SiF_4 n'est pas significatif (variations faibles de carbone et de cristallinité) ; en revanche, si l'échantillon déposé sans SiF_4 est au seuil de la transition de phase (fraction cristalline autour de 25 %), l'ajout de SiF_4 dans le plasma permet de doubler la fraction cristalline.

Dans une deuxième partie du manuscrit, les propriétés optiques, de transport et liées aux défauts électriquement actifs ont été étudiées pour plusieurs échantillons.

Pour les alliages à phase mixte comme les alliages μc-$Si_{1-x}C_x$:H la définition de gap d'énergie n'est pas évidente. Nous avons donc utilisé deux définitions de gap optique : le gap de Tauc (E_g) obtenu en effectuant le "fit" des spectres d'ellipsométrie, et le gap iso-énergétique (E_{04}), défini comme l'énergie à laquelle le coefficient d'absorption α est égal à 1×10^4 cm^{-1}. L'application du modèle de Tauc pour les matériaux bi-phase est discutable, on peut néanmoins considérer $E_g$comme un gap moyen déterminé par la contribution des deux phases simultanément. Ces deux définitions de "gap optique" peuvent être considérées comme les limites inférieure et supérieure du gap d'énergie, indiquant qualitativement le degré de transparence des couches. Une variation du gap de nos alliages aura une influence sur les performances des cellules photovoltaïques à base de ces alliages. En effet, comme observé dur la Figure 13, la variation de E_g et de E_{04} en fonction des différents paramètres de dépôts semble ne pas dépendre de la microstructure des alliages, mais seulement du taux de carbone incorporé. Ainsi, une corrélation entre le taux de carbone incorporé et la tension de circuit ouvert des cellules à pu être établie.

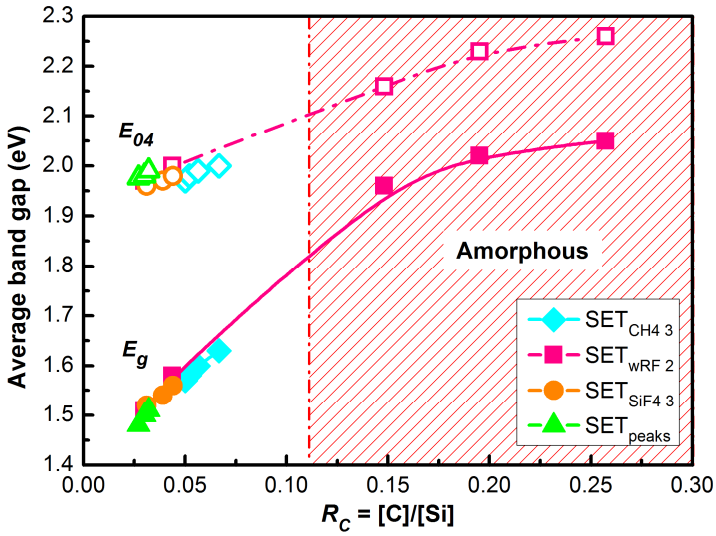

FIGURE 13. – Évolution de E_g et E_{04} (symboles fermés et ouverts, respectivement), pour les échantillons des séries SET_{CH_43} (◆), $SET_{w_{RF}2}$ (■), SET_{SiF_43} (●) and SET_{peaks} (▲), en fonction du rapport R_C.

Pour toutes les séries étudiées, si les échantillons sont microcristallins, l'augmentation de carbone entraîne une augmentation de E_g qui n'est pas reflétée par une augmentation de E_{04} (qui reste stable autour de 2 eV). Une fois que la transition de phase s'est produite, les deux gap optiques augmentent de façon similaire. Ce comportement peut être expliqué si on tient compte du fait que le gap E_{04} est la valeur moyenne du gap iso-énergétique de la phase cristalline (E_{04c}) et de celui de la phase amorphe (E_{04a}), pondérée respectivement par leurs fractions. En augmentant le rapport carbone-silicium (et donc en diminuant la fraction cristalline) pour que le gap E_{04} reste stable il est nécessaire que E_{04a} diminue. E_{04a} peut décroître avec la

fraction cristalline seulement si le rapport carbone-silicium dans la phase amorphe (R_{amorph}) diminue en augmentant cette phase. Ce résultat peut sembler contradictoire. Néanmoins, en considérant hydrogène et oxygène comme des quantités petites, par rapport à celles de silicium et carbone, le rapport carbone-silicium contenu dans la seule phase amorphe à pu être déterminé. A partir de cette analyse il a été montré que, en effet, à plus hautes fractions cristallines on obtient les valeurs les plus élevés de R_{amorph}.

Les mesures du courant d'obscurité et du photo-courant en fonction de la température permettent d'évaluer simplement la qualité électronique des matériaux. Ces mesures ont été effectuées entre 450 K et 110 K. L'évolution du courant d'obscurité en fonction de la température apporte des informations importantes sur les mécanismes de transport dans le matériau. Dans le cas des matériaux à phase mixte, la conductivité électrique dans une large plage de températures peut impliquer plusieurs mécanismes qui ne dépendent pas seulement de la microstructure des échantillons, mais aussi de la nature chimique des différentes phases. Des études antérieures sur des alliages μc-$Si_{1-x}C_x$:H (Demichelis et al., 1994) ont montré l'existence de trois régions distinctes dans les courbes de conductivité en fonction de la température, attribuées à différents mécanismes de transport :

1. dans le régime de *haute température* (450-200 K), le mécanisme de transport dominant dépend de la phase cristalline. Pour les échantillons ayant une haute fraction cristalline la conduction se fait par percolation à travers les région très conductrices. Pour les échantillons avec une basse fraction cristalline, le mécanisme de transport principal est le "hopping" entre îlots cristallins voisins, dispersés dans la matrice amorphe, et l'émission thermoionique des zones cristallines aux zones amorphes.

2. dans le régime de *température moyenne* (200-90 K), le chemin de conduction préférentiel est le "hopping" dans les queues de bande. L'élargissement des queues de bande provient du désordre induit par la présence des deux phases, de la fluctuation de la taille des grains et le variation de la stoechiométrie du tissu amorphe.

3. dans le régime de *basse température* (90-50 K), le mécanisme de conduction est le "hopping" entre les états localisés du gap de mobilité.

L'impact des différents paramètres de dépôt sur les propriétés de transport a été étudié à l'aide des mesures de conductivité à l'obscurité, de photo-conductivité à température ambiante et de la détermination de la photo-réponse Φ, définie comme le rapport entre la photo-conductivité et la conductivité d'obscurité. La détermination de l'énergie d'activation et du préfacteur de la conductivité d'obscurité complètent ces résultats.

La Figure 14 montre que la diminution de la fraction cristalline liée à l'augmentation du taux de carbone incorporé, se traduit par une détérioration soit de la conductivité à l'obscurité, soit de la photo-conductivité. Ceci conduit à une augmentation de la photo-réponse qui atteint des valeurs proches de 10^4 pour des alliages complètement amorphes. A fraction cristalline équivalente($\sim$ 60 %), la diminution de la puissance RF entraîne une augmentation importante de Φ (environ multipliée par 5 pour des dépôts réalisés avec une puissance RF de 113 mW/cm^2). L'ajout de SiF_4, permettant d'augmenter la fraction cristalline, est accompagné par une détérioration des propriétés de transport, sans doute liée à une augmentation des défauts dans le matériau.

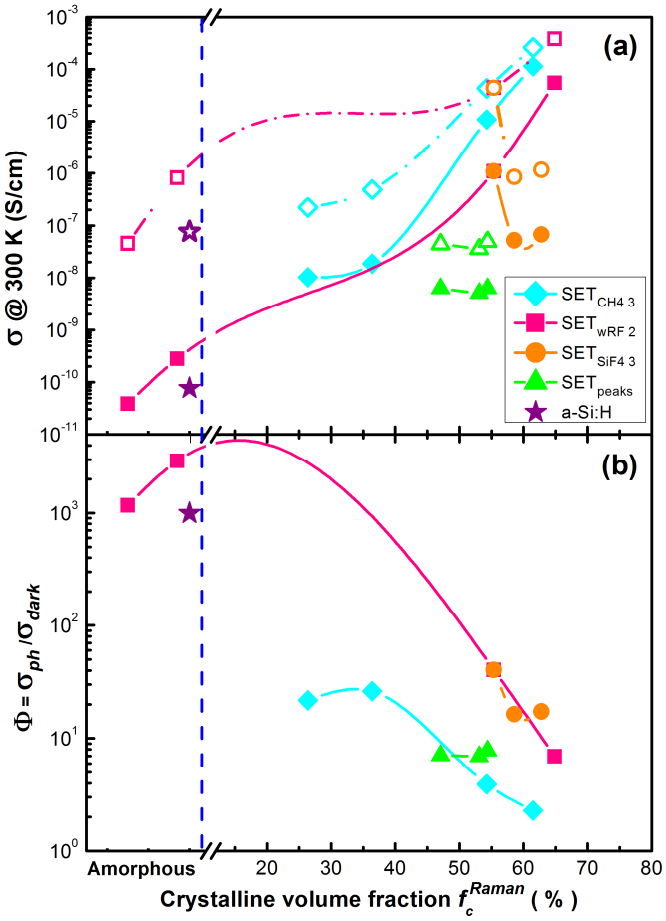

FIGURE 14. – Évolution (a) de la photo-conductivité (symboles ouverts) et de la conductivité d'obscurité (symboles fermés) à température ambiante et (b) de la photo-réponse Φ pour les séries d'échantillons SET_{CH_43} (◆), $SET_{w_{RF}2}$ (■), SET_{SiF_43} (●) et SET_{peaks} (▲), en fonction de la fraction cristalline f_c^{Raman}. Les résultats sont comparés à ceux obtenus pour du a-Si :H de qualité photovoltaïque, déposé par RF-PECVD standard (★).

Enfin, les alliages déposés par TVW-PECVD avec les formes d'onde *pic*, montrent des résultats de mesures électriques qui sont en accord avec les propriétés structurales. La variation du flux de méthane, dans des conditions de faible bombardement ionique, n'est pas suffisante pour induire des modifications majeures au sein des échantillons qui, même du point de vue électrique, ont des propriétés très comparables. De plus, ces alliages sont caractérisés par des valeurs de conductivité d'obscurité et de photo-conductivité nettement plus faibles que les alliages déposés par RF-PECVD.

Les valeurs d'énergie d'activation et du préfacteur de la conductivité à l'obscurité déterminées dans le régime de hautes températures, sont comparables à celles trouvées dans la littérature (Figure 15). L'énergie d'activation varie entre 0.1 eV et 0.6 eV selon le degré de cristallinité (0.1 eV étant la valeur pour les alliages les plus cristallins). En outre, pour une même fraction cristalline, les alliages déposés à basse puissance RF ont des valeurs d'énergie d'activation environ 65 % plus élevées que pour les alliages déposés à haute puissance. Si l'on considère que l'énergie d'activation donne la position du niveau de Fermi à 0 K par rapport au bord de la bande de conduction, et compte tenu des valeurs de gap mesurées, ces alliages ont

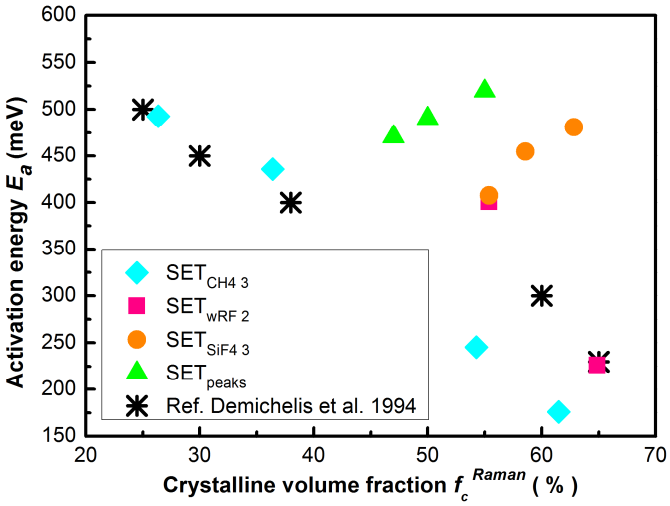

FIGURE 15. – Évolution de l'énergie d'activation E_a pour les échantillons des séries SET_{CH_43} (◆), SET_{wRF2} (■), SET_{SiF_43} (●) et SET_{peaks} (▲), en fonction de la fraction cristalline f_c^{Raman}. Les résultats obtenus dans cette thèse sont comparés à ceux présentés dans DEMICHELIS et al., 1994 (✳).

un comportement de type dopé. Nous ne savons pas encore expliquer ce comportement mais il est possible qu'il soit lié à l'existence de défauts à l'interface entre les microcristaux et la matrice amorphe qui immobiliseraient le niveau de Fermi proche du bord de la bande de conduction.

Nous avons également mesuré la longueur de diffusion des porteurs minoritaires de nos alliages à l'aide de la technique Steady-State Photocarrier Grating (Figure 16). Ces mesures sont délicates à interpréter car nos matériaux présentent une structure qui n'est pas homogène avec, pour les alliages microcristallins, un axe de croissance perpendiculaire à la surface.

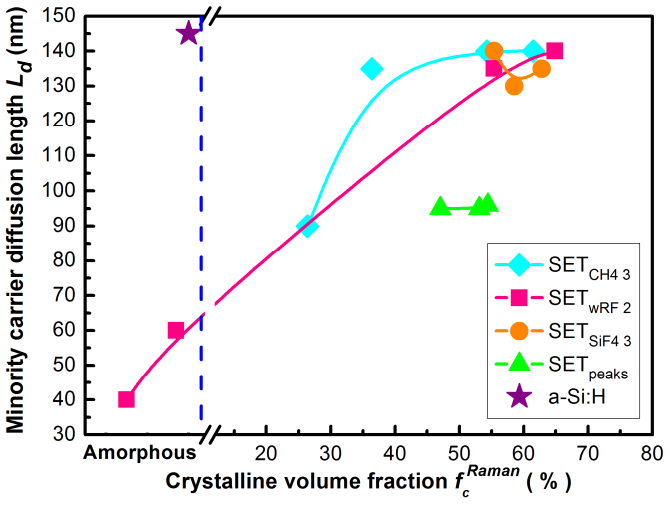

FIGURE 16. – Évolution de la longueur de diffusion des porteurs minoritaires L_d pour les échantillons des séries SET_{CH_43} (◆), SET_{wRF2} (■), SET_{SiF_43} (●) et SET_{peaks} (▲), en fonction de la fraction cristalline f_c^{Raman}. Les résultats sont comparés à ceux obtenus pour du a-Si :H de qualité photovoltaïque, déposé par RF-PECVD standard (★).

Par conséquent, les propriétés de transport mesurées en configuration coplanaire peuvent être différentes de celles mesurées en configuration transverse. Nous obtenons des longueurs de diffusion de l'ordre de 135 nm pour des alliages avec des fractions cristallines supérieures à 40 %, indépendamment de la puissance RF utilisée lors du dépôt. Cette valeur peut être comparée à la longueur de diffusion des porteurs minoritaires du silicium amorphe (a-Si :H) qui peut être comprise entre 140 et 200 nm. Les échantillons déposé par TVW-PECVD avec les formes d'onde *pics* sont caractérisés par des valeurs de longueur de diffusion autour de 90 nm et qui correspondent aux valeurs obtenues pour les alliages avec une fraction cristalline de 25 %.

Les propriétés liées aux défauts électriquement actifs on été étudiées à l'aide de la technique du photo-courant modulé en régime de haute fréquence (MPC-HF). Le principe de cette technique consiste à éclairer un échantillon à l'aide d'une lumière monochromatique modulée. Le flux lumineux incident est donc composé d'une partie continue F_{DC} et d'une partie alternative F_{AC}. Par conséquent, le photo-courant mesuré est aussi composé d'une partie continue et d'une partie alternative déphasée de φ par rapport à la lumière d'excitation. Cette différence de phase est liée à l'interaction des porteurs générés par la lumière avec les états localisés de la bande interdite. Dans le régime de haute fréquence, les porteurs sont piégés dans des états qui ont une probabilité d'émission plus grande que celle de capture. Ainsi, une position énergétique dans le gap est sondée quand ces états pièges possèdent un temps de re-émission des porteurs piégés qui coïncide avec la période de la lumière d'excitation. Ces états créent le déphasage entre le photo-courant et la lumière excitatrice en introduisant un retard dans la réponse en photocourant. Dans ce régime de fréquence, ce sont le temps de réponse des pièges et la température qui déterminent la position énergétique des pièges par rapport au bord de la bande de conduction (pour les électrons) et de valence (pour les trous). Par conséquent, en variant la température (typiquement entre 110 et 450 K) et la fréquence (typiquement entre 12 Hz et 40 kHz) de la lumière d'excitation, on effectue une spectroscopie en sondant les différent états du gap et en obtenant des informations sur la densité d'états (DOS) dans une région du gap du matériau étudié. Pour nos alliages, comme pour a-Si :H, pour lesquels les électrons sont les porteurs majoritaires, nous obtenons une représentation de la DOS au-dessus du niveau de Fermi.

La forme de cette DOS est donnée par l'enveloppe supérieure obtenue à partir de la superposition des données reconstruites à différentes températures et différentes fréquences. Cette technique est sensible au rapport Nc/μ (MPC-DOS), où N est la densité d'états, c le coefficient de capture et μ la mobilité dans les états étendus. Il est possible de démontrer que la MPC-DOS dépend seulement de quantités mesurables expérimentalement. Le seul paramètre pour lequel il est nécessaire de faire une hypothèse est le coefficient de capture c, qui détermine l'échelle des énergie. Le choix des valeurs raisonnables de c est déterminé par la qualité de l'enveloppe. Pour une valeur de c correcte, les courbes à différentes températures se superposent correctement. La mesure de la MPC-DOS n'a pas pu être faite pour les échantillons avec une énergie d'activation inférieur à 200 meV.

La densité d'états du a-Si :H est caractérisée par la présence d'une queue de bande de conduction et d'une queue de bande de valence de type exponentiel et de défauts profonds dans le gap de type gaussien. L'allure de la MPC-DOS de nos alliages dépend de la fraction cristalline (Figure 17). Pour les alliages à forte fraction cristalline, la MPC-DOS est donnée par

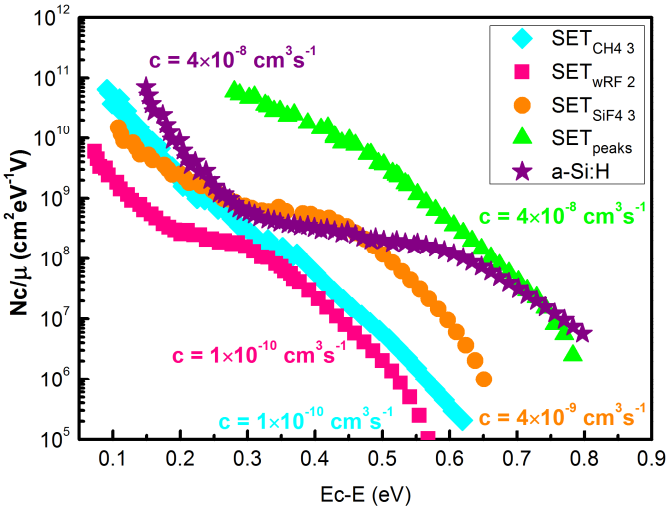

FIGURE 17. – MPC-DOS (rapport Nc/μ) pour les échantillons des séries SET_{CH_43} (◆ - CH_4 = 1.2 sccm), SET_{wRF2} (■ - CH_4 = 1.4 sccm), SET_{SiF_43} (● - SiF_4 = 1 sccm) et SET_{peaks} (▲ - CH_4 = 1.2 sccm), ayant des fractions cristallines similaires ($f_c^{Raman} \approx$ 55-60 %). Ces courbes MPC-DOS sont comparées à celle obtenue pour du a-Si :H de qualité photovoltaïque, déposé par RF-PECVD standard (★).

une large queue de bande et les défauts profonds n'apparaissent pas clairement. Pour les alliages à faible fraction cristalline, on observe une queue de bande moins large et l'apparition de défauts profonds. L'amorphisation des alliages avec l'augmentation du carbone incorporé est accompagnée par la hausse des défauts profonds et donc par une MPC-DOS plus importante. D'autre part, il est particulièrement difficile d'attribuer les défauts du matériau à la présence de carbone ou à la croissance microcristalline (qui est elle-même défectueuse) et des travaux de simulation pourraient aider dans l'interprétation de ces résultats.

Enfin, l'effet du vieillissement (effet Staebler Wronski) a été étudié sur certaines couches. En général, le terme "microcristallin" est synonyme de stabilité sous éclairement. Cependant si le matériau est caractérisé par une fraction amorphe importante, il sera sensible à l'effet de vieillissement, au même titre que le silicium amorphe. Des études antérieures ont montré que le silicium microcristallin donnant les meilleures performances photovoltaïques est déposé au seuil entre phase amorphe et phase microcristalline. Dès lors que les alliages μc-$Si_{1-x}C_x$:H sont composés pour la majorité de silicium microcristallin, on pourrait s'attendre à une tendance identique. L'effet du vieillissement a ainsi été étudié pour 3 alliages μc-$Si_{1-x}C_x$:H : deux échantillons avec une fraction cristalline au dessus du 50 % (déposé à basse puissance et déposé avec l'ajoute de SiF_4) et le dernier avec une fraction cristalline de 25 % (Figure 18). La possibilité de guérir les défauts créés a été étudiée avec des recuit thermique à haute température. La cinétique de vieillissement, qui est étudiée en mesurant l'évolution du photo-courant (normalisé par sa valeur dans l'état avant le vieillissement) à été comparée à celle du silicium amorphe. Il est évident que tandis que la dégradation du a-Si :H commence dès que l'échantillon est sous lumière, ce processus de vieillissement est beaucoup plus lent sur nos alliages. L'interprétation de ce phénomène est encore en phase d'étude.

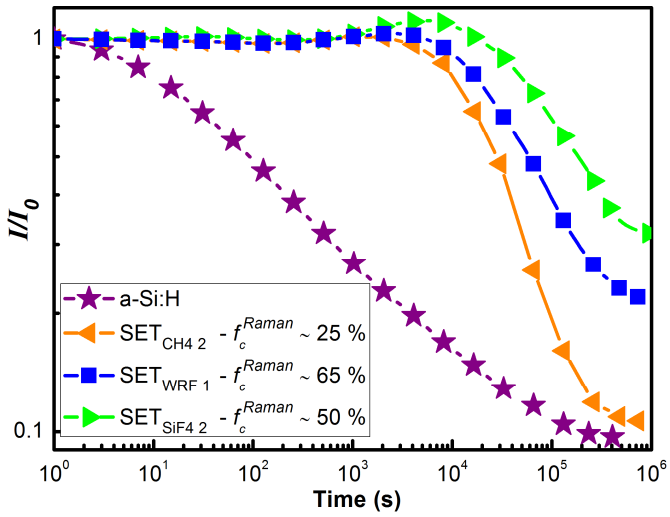

FIGURE 18. – Évolution du photo-courant normalisé, en fonction du temps de vieillissement, pour les échantillons des séries $SET_{CH_4 2}$ (◀), $SET_{w_{RF}1}$ (■) et $SET_{SiF_4 2}$ (▶). Leur cinétique de vieillissement est comparé à celle obtenue pour du a-Si :H de qualité photovoltaïque, déposé par RF-PECVD standard (★).

L'effet du vieillissement sur les propriétés de transport et liées aux défauts électriquement actifs à été étudié. Tous les échantillons montrent une dégradation de la conductivité à l'obscurité et de la photo-conductivité et une augmentation de la DOS (avec élargissement de la queue de bande de conduction et augmentation des défauts profonds). Ces propriétés ne sont pas restaurées après un recuit thermique à haute température.

PROPRIÉTÉ DES DISPOSITIFS PHOTOVOLTAÏQUES

Dans la dernière partie du manuscrit, la possibilité d'incorporer les alliages µc-$Si_{1-x}C_x$:H comme couches actives dans des dispositifs photovoltaïques a été étudiée. Les premiers tests ont été faits avec les alliages déposés à 285° C. Compte tenu de cette haute température, nous avons réalisé des dispositifs n-i-p, la couche p étant la plus sensible à la température de dépôt. Les cellules ont été déposées sur de l'oxyde de zinc dopé aluminium (ZnO :Al) texturé pour le contact arrière et d'une couche d'oxyde d'indium-étain (ITO) pour le contact avant. Les couches dopées sont du silicium microcristallin dopé. Aucune optimisation particulière n'a été effectuée, l'objectif principal étant de valider l'utilisation de ces alliages µc-$Si_{1-x}C_x$:H comme couches actives dans des dispositifs photovoltaïques.

Un de nos résultats importants est que la variation du taux de carbone incorporé dans la couche active conduit à une variation du courant de saturation à l'obscurité (Figure 19). En outre, pour des fractions cristallines similaires, la variation de la puissance RF à 113 mW/cm^2 amène à des valeurs du courant de saturation à l'obscurité d'un ordre de grandeur plus bas par rapport à ceux obtenus pour des diodes déposées à 226 mW/cm^2.

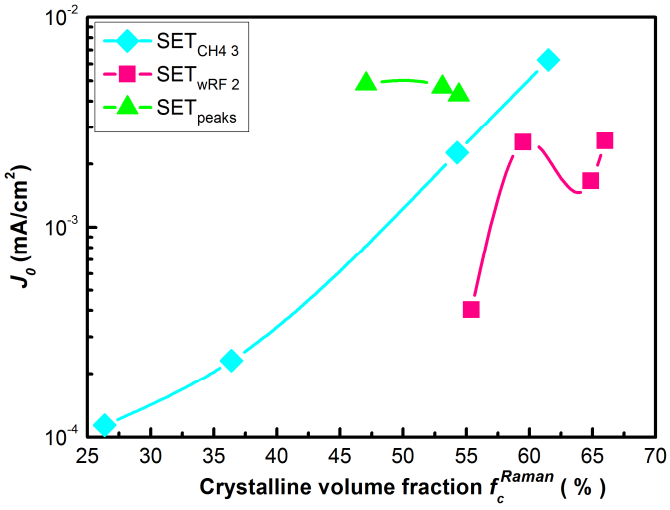

FIGURE 19. – Évolution de J_0 en fonction de la fraction cristalline f_c^{Raman} pour les diodes n-i-p des séries SET_{CH_43} (RF-PECVD à 226 mW/cm^2 - ◆), SET_{wRF2} (RF-PECVD à 113 mW/cm^2 - ■) et SET_{peaks} (TVW-PECVD utilisant les formes d'ondes "pics" - ▲).

Les mesures J(V) sous éclairement ont montré que la variation de carbone dans la couche cristalline a un effet sur la tension de circuit ouvert (V_{oc}). Nous obtenons cependant des valeurs de V_{oc} assez basses ($\sim$ 300 mV pour fractions cristallines de 60 %) par rapport aux dispositifs à base de silicium microcristallin. Ces valeurs peuvent être limitées à cause de l'utilisation de couches dopées à base de silicium microcristallin, mais aussi par des effets parasites comme les résistances en séries et les résistance de shunt. Néanmoins, les propriétés des dispositifs reflètent bien les propriétés des matériaux. Les cellules à base des couches µc-$Si_{1-x}C_x$:H déposées à plus haute puissance RF présentent des valeurs du courant de court-circuit très faibles ($\sim$ 4-6 mA/cm^2). En effet, pour qu'un dispositif soit performant, il est nécessaire que plusieurs propriétés du matériau soient suffisamment bonnes simultanément (énergie d'activation assez grande, longueur de diffusion des porteurs minoritaires supérieure à 100 nm, photo-réponse assez élevée et DOS basse) et nos caractérisations électriques et structurales on mis en évidence que la voie la plus prometteuse pour obtenir un matériau avec cet ensemble de propriétés est le dépôt à basse puissance RF.

En utilisant une puissance RF de 113 mW/cm^2, nous avons obtenu des dispositifs avec les meilleures performances, notamment au niveau du courant de court-circuit. En effet, pour valeurs de V_{oc} similaires (300 mV) on passe de 6 mA/cm^2 (puissance RF de 226 mW/cm^2) à 10 mA/cm^2 (puissance RF de 113 mW/cm^2). D'autre part, l'absence de réflecteur arrière et le fait que les dispositifs soient très minces ($\sim$ 250 nm), limitent le photocourant généré. Enfin, des mesures de réponse spectrale ont montré que l'absorption principale du spectre solaire se situe aux faibles longueurs d'onde (autour de 400 nm) ce qui est particulièrement encourageant pour l'utilisation de ces cellules comme cellule avant de structures de type tandem.

L'utilisation d'une haute température de substrat empêche la réalisation de structures plus performantes et l'exploitation de notre savoir-faire. Nous avons donc effectué en fin de projet des dépôts de diodes à 175° C. Nous avons réalisé des dispositifs de type p-i-n en utilisant du ZnO :Al comme contact en face avant et de l'ITO-argent comme contact et réflecteur arrière,

les couches dopées étant du silicium microcristallin dopé p et du silicium amorphe dopé n.

Comme pour les diodes précédentes, les mesures $J(V)$à l'obscurité et sous éclairement ont montré qu'il était possible de faire varier la tension de circuit ouvert en variant le taux de carbone incorporé. Nous avons obtenu de meilleures performances que pour les cellules déposées à haute température avec, pour des fractions cristallines de la couche active autour de 60 %, des valeurs de V_{oc} de l'ordre de 400 mV (à comparer à 300 mV pour les cellules déposées à haute température).

Bien que présentant encore des performances modestes, nous sommes convaincus que les dispositifs PV à base d'alliages μc-$Si_{1-x}C_x$:H ont une large marge de progression. Notre étude exploratoire, particulièrement poussée pour la compréhension de la croissance et des propriétés de ces alliages, nous laisse penser que ce matériau peut sérieusement devenir une alternative intéressante, par rapport à des technologies plus compliquées et coûteuses comme les nanocristaux de silicium dans des matrices SiOx ou SiC, réalisés par recuit thermique.

CONTENTS

LIST OF SYMBOLS AND ACRONYMS xxxv
Symbols xxxv
Acronyms xxxvii

INTRODUCTION xxxix

I Background and Fundamentals 1

1 AMORPHOUS AND MICROCRYSTALLINE SILICON AND THEIR ALLOYING WITH CARBON 3
1.1 Introduction 3
1.2 Amorphous silicon 4
1.2.1 Band structure: Bandtails, Band edges, and Band Gaps 4
1.2.2 Growth mechanism 6
1.2.3 Light-induced degradation 7
1.3 Microcrystalline silicon 7
1.3.1 Structural properties 7
1.3.2 Growth mechanism 9
1.3.3 Band structure 9
1.3.4 Electronic transport 9
1.3.5 Light-induced degradation 11
1.4 Silicon-carbon alloys 11
1.4.1 Physico-chemical introduction to a-$Si_{1-x}C_x$:H alloys 12
1.4.2 Growth mechanism of a-Si1-xCx:H alloys from a SiH4-CH4 gas mixture 13
1.4.3 Network structure and properties 14
1.4.4 Microcrystalline alloys 15

2 FUNDAMENTALS 17
2.1 Introduction 17
2.2 Deposition techniques 17
2.2.1 Radio Frequency Plasma Enhanced Chemical Vapor Deposition 18
2.2.2 Tailored Voltage Waveform Chemical Vapor Deposition 19
2.2.3 The ARCAM reactor 21
2.3 Material characterization techniques 22
2.3.1 Structural characterizations 22
2.3.2 Electrical characterizations 40
2.4 Device characterization techniques 51
2.4.1 Characterization methods 51

II Material study 55

3 STRUCTURAL PROPERTIES AND GROWTH MECHANISMS 57
3.1 Introduction 57
3.2 Role of the seed layer 59

3.2.1 Seed layer deposition time 59
3.2.2 Thickness series 66
3.2.3 Role of the substrate 69
3.2.4 What is the seed layer? 71
3.3 Growth of μc-$Si_{1-x}C_x$:H alloys by standard RF-PECVD 73
3.3.1 Effect of SiH_4 73
3.3.2 Effect of CH_4 75
3.3.3 Effect of RF-power 82
3.3.4 Effect of SiF_4 90
3.3.5 Effect of substrate temperature 99
3.3.6 Summary 103
3.4 Growth of μc-$Si_{1-x}C_x$:H alloys by TVW-PECVD 107
3.4.1 Introduction 107
3.4.2 Effect of CH_4 107
3.5 Growth model 113

4 OPTO-ELECTRONIC PROPERTIES 117
4.1 Introduction 117
4.2 Band gap 117
4.3 Transport properties 122
4.3.1 Room temperature dark and photo conductivity and activation energy 122
4.3.2 Minority carrier diffusion length 131
4.3.3 Summary 132
4.4 Defect-related properties 138
4.4.1 Summary 143
4.5 Light-Soaking and annealing 144
4.5.1 Light-soaking kinetics 145
4.5.2 Evolution of transport properties 146
4.5.3 Evolution of defect-related properties 147
4.6 The Meyer-Neldel Rule 149

III Device study 153

5 DEVICE PROPERTIES 155
5.1 Introduction 155
5.1.1 The structure 156
5.1.2 The Transparent Conductive Oxide: Front and Back contacts 157
5.1.3 The doped layers 157
5.1.4 The devices 158
5.2 Dark J(V) characteristics 160
5.2.1 n-i-p devices at 285° C 160
5.2.2 p-i-n devices at 175° C 162
5.3 Light J(V) characteristics 165
5.3.1 n-i-p devices at 285° C 165
5.3.2 p-i-n devices at 175° C 168
5.4 External Quantum Efficiency 171
5.4.1 n-i-p devices at 285° C 171
5.4.2 p-i-n devices at 175° C 173
5.5 Summary 179

Conclusions 185

Appendices 191

A MDECR-PECVD 193
A.1 Introduction 193
A.2 Fundamentals 193
A.2.1 Matrix Distributed Electron Cyclotron Resonance Chemical Vapor Deposition 193
A.2.2 The ATOS reactor 194
A.3 μc-$Si_{1-x}C_x$:H alloys 195
A.3.1 Determination of uc-Si:H growth conditions 196
A.3.2 Role of the seed layer 198
A.3.3 Hydrogenated microcrystalline silicon carbon alloys 199

BIBLIOGRAPHY 203

LIST OF PRESENTATIONS & POSTERS 215
Oral presentations 215
Posters 215

LIST OF PUBLICATIONS 217

LIST OF SYMBOLS AND ACRONYMS

SYMBOLS

α	Absorption coefficient	cm^{-1}
A_{X-Y}	Inverse cross section of the X — Y bond	cm^{-2}
c	Capture coefficient	cm^3s^{-1}
δ	Average grain size, determined using the Scherrer approach	Å
$<\epsilon_i>$	Imaginary part of the pseudo-dielectric function	
E_{04}	Iso-absorption band gap (from UV/VIS transmission modeling)	eV
E_a	Activation energy of the dark conductivity	eV
E_c	Conduction band edge	
E_g	Average optical band gap (from ellipsometry fitting)	eV
E_{MNR}	Meyer-Neldel energy	eV
f_c^{Raman}	Crystalline volume fraction	%
FF	Fill Factor	%
J_0	Dark saturation current	mA
J_{sc}	Short-circuit current	mA
L	Thickness of the layer	nm
L_d	Minority carrier diffusion length	nm
N_{X-Y}	Density of X — Y bonds	cm^{-3}
$\frac{Nc}{\mu}$	Modulated PhotoCurrent-density of states (MPC-DOS)	$cm^2eV^{-1}V$
Φ	Photo-response	
ρ_{RMS}	Root-mean-square roughness	nm
R_{amorph}	Carbon-silicon ratio for the amorphous phase	
R_C	Total carbon-silicon ratio	
σ_{00}	Dark conductivity prefactor	S/cm
σ_{dark}	Dark conductivity	S/cm
σ_{MNR}	Meyer-Neldel conductivity prefactor	S/cm
σ_{ph}	Photo conductivity	S/cm
θ_i	Incident angle for grazing incidence X-ray diffraction measurements	°
V_{oc}	Open-circuit voltage	mV
w_{RF}	RF-power density	mW/cm^2
ω	Wavenumber	cm^{-1}
η	Efficiency	%

ACRONYMS

A	Annealed state
AD	As deposited state
AFM	Atomic Force Microscopy
a-Si:H	Hydrogenated amorphous silicon
a-$Si_{1-x}C_x$:H	Hydrogenated amorphous silicon-carbon alloys
EFTEM	Energy Filtered Transmission Electron Micorscopy
EQE	External quantum efficiency
FTIR	Fourier Transform Infrared spectroscopy
HAADF-STEM	High Angle Annular Dark Field Scanning Transmission Electron Microscopy
IBE	Ion Bombardment Energy
ITO	Indium Tin Oxide
LS	Light soaked state
MDECR	Matrix Distributed Electron Cyclotron Resonance
µc-Si:H	Hydrogenated microcrystalline silicon
µc-$Si_{1-x}C_x$:H	Hydrogenated microcrystalline silicon-carbon alloys
µc-SiO_x:H	Hydrogenated microcrystalline silicon oxide
PECVD	Plasma Enhanced Chemical Vapor Deposition
RF	Radio Frequency
SAADF-STEM	Small Angle Annular Dark Field Scanning Transmission Electron Microscopy
TCO	Transparent conductive oxide
TVW	Tailored Voltage Waveforms

Hey man of science with your perfect rules of measure,
Can you improve this place with the data that you gather?
[..]I want to conquer the world

— Bad Religion

Ex falso sequitur quodlibet
$\{\phi, \neg\phi\} \vdash \psi$

— Principle of Explosion

INTRODUCTION

The energetic needs of the modern society continue growing and in the last years a significant increase has been observed due to the driving energy demand of some developing countries, namely in South America and Asia. However, a predominant aspect of modern life should include a more drastic energy-awareness education of the developed countries population, in order to efficiently reshape the modern society's compulsive needs. It is necessary to acknowledge that the world is changing at a staggering rate (as highlighted by the world electricity demand in Figure Intro.1), and to allow to all populations the same privileges requires drastic measures especially in the more developed countries.

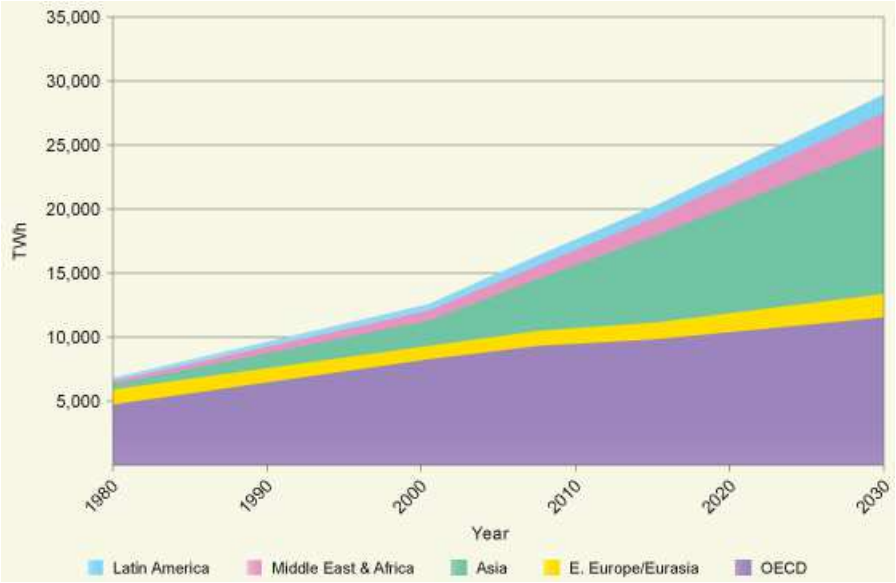

Figure Intro.1.: World electricity demand per region. **OECD = Organization for Economic Co-operation & Development** includes Australia, Austria, Belgium, Canada, Chile, the Czech Republic, Estonia, Denmark, Finland, France, Germany, Greece, Hungary, Iceland, Ireland, Italy, Japan, Korea, Luxembourg, Mexico, the Netherlands, New Zealand, Norway, Poland, Portugal, Spain, Sweden, the Slovak Republic, Slovenia, Switzerland, Turkey, the United Kingdom and the United States (IEA, World Energy Outlook 2009).

According to the International Energy Agency (IEA), the world energy demand will expand at an average rate of increase of 1.6 % per year, between now and 2030, with oil and coal still accounting for most of the energy production (Figure Intro.2). But what will happen when fossil fuels will start running low? A strong contribution from nuclear power plants and natural gas has started since the 1980, due to the necessity of the governments to face the oil crisis (1973 and 1979). More recently, additional measures have been taken in order to reduce the greenhouse gases and the interest in *renewable energies* has risen. All these options can be summarized in the concept of "Energy Sustainability".

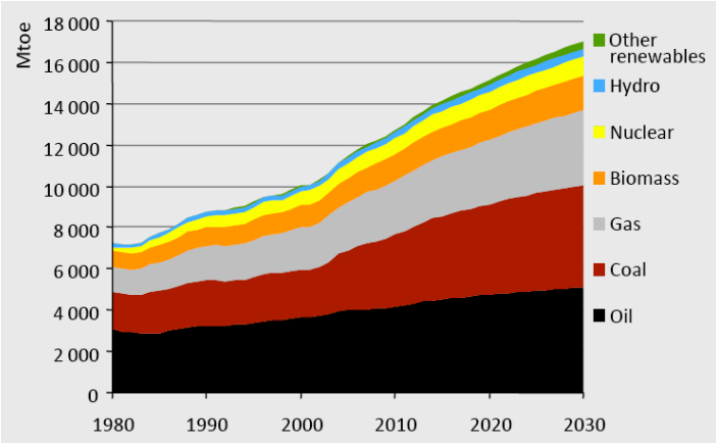

Figure Intro.2.: Energy demand in Million Tonnes of Oil Equivalent (1 Mtoe = 11.63 TWh) (IEA, World Energy Outlook 2008).

Actually, energy sustainability involves the search of the balance between a growing economy, the need for environmental protection and social responsibilities. The goal is to provide an improved quality of life for current and future generations: fulfilling the needs of the present without compromising the world of the future.

To meet the energy demand over the next century it will be required not just to produce more electricity (developing countries will keep on increasing their energy consumption, the number of electrical equipments owned per family will keep on growing and more public means such as trains, electric cars and trams will increasingly transit), but also to produce it much more efficiently. New technologies and new cultural habits will be required in order to learn how to use less energy to power everything and to produce more with less consumption of resources. Public research and industries are (and will keep on) working side-by-side to improve and modernizing smart grids in order to reduce energy waste. However, it is also important to remember that one source will not be sufficient and that different ones will need to be efficiently integrated in order to exploit ones quality when (and where) the others have only flaws. Moreover, even though nuclear energy may have appeared as an attractive alternative in the past, the accident at the Fukushima nuclear power plant in Japan (2011), lead many countries to put on hold many projects concerning the construction of new nuclear power plants or even to schedule the progressive closure of their power stations in the years to come (Breidthardt, 2011). In addition, a part from the safety issues, it must be remembered that this source of energy suffers from several disadvantages such as the fact that uranium is, as fossil fuels, in limited amount and nuclear wastes are difficult to handle. Besides, it cannot

be adapted to every country as it cannot be implemented in rural situations. In this context, a decentralized production would make more sense.

In that regard, renewable energy sources are diverse, from solar, tidal and wave energy to hydro, geothermal and biomass-based power generation, and most of them can provide a decentralized production. Among these, solar energy conversion has the advantage of being possibly implemented in both centralized (plants) and decentralized (roofs, etc) production centers.

Concerning photovoltaic energy (conversion of sun light into electricity), its production capacity continues an amazing expansion, with an average yearly growth of 50 % between 2001 and 2008. Moreover, the declining PV prices will continue to power an international market surge, with annual installations doubling by 2020 (Figure Intro.3). In addition, this price decline has made solar PV appealing also to developing nations and an entire new class of homeowners and businesses.

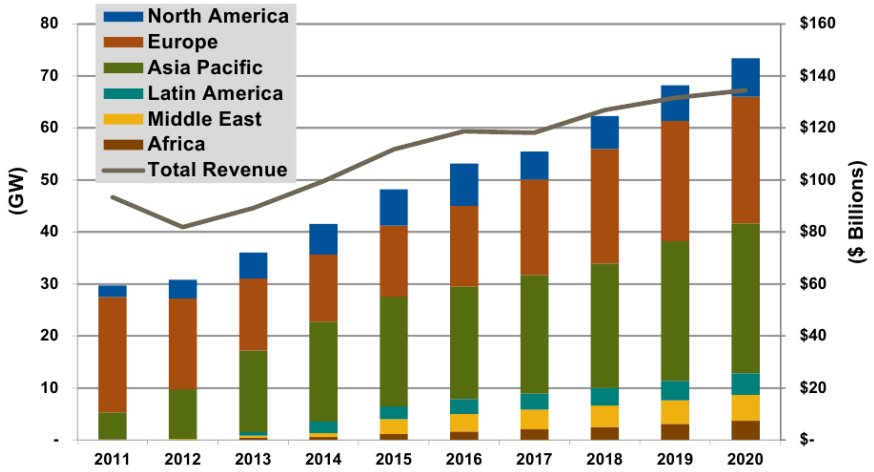

Figure Intro.3.: Annual solar PV installed capacity and revenue per region. World markets 2011 - 2020 (predicted for the 2013 - 2020 period - Navigant research).

Despite the continuous efforts in the optimization of the efficiency of the different solar cell technologies, the PV market remains controlled by technologies based on mono- and multicrystalline silicon wafer solar cells (the so-called *"first generation"* of solar cells). Nevertheless, large a-Si:H modules are extremely attractive, compared to "traditional" wafer-based ones, due for example to their substantial potential of cost reduction. Indeed, in silicon thin-film technology, only a very thin layer of silicon is used ($\sim$ 1 μm thick, against the hundreds of micrometers needed for wafer-based technologies). Moreover, the active layers are usually deposited on cheap substrates like glass, but also stainless steel and plastics can be used. In addition, the fabrication energy required is far less than wafer-based technologies. Thus, the energy payback time of thin film silicon modules is reduced. Finally, when compared to other CIGS or CdTe technologies, silicon thin-films have the key advantage of using a raw material that is non-toxic and widely abundant.

The main disadvantage of a-Si:H thin film PV modules is that they present relatively lower stable conversion efficiencies ($10 - 13$ %, NREL - National center for photovoltaics, 2013), due to the fact that amorphous silicon exhibits light-induced degradation, which means that the exposure to the sun light creates dangling bonds that act as recombination centers and lead to

a deterioration of solar cell performance. However, a-Si:H can be combined with μc-Si:H to form so-called "micromorph" tandem solar cells. This technology was first developed at IMT in Neuchâtel (Meier et al., 1994; Keppner et al., 1997), but has now been transfered to large-scale PV modules (Yamamoto et al., 2002; Noda et al., 2003).

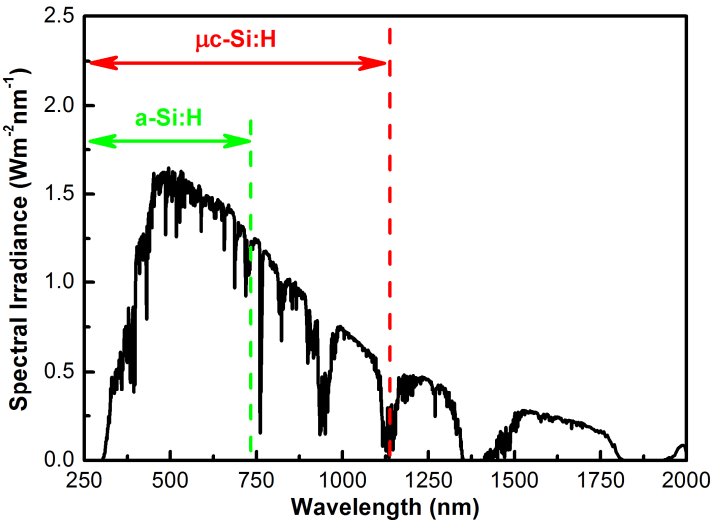

Figure Intro.4.: Spectral distribution of the AM 1.5 solar spectrum incident on the Earth's surface. The dashed lines indicate the spectral ranges of the absorption of a-Si:H (green) and μc-Si:H (red), respectively.

A micromorph solar cell consists of the combination of a "top" a-Si:H cell (where light enters first) and a "bottom" μc-Si:H cell. This technology takes advantage of the fact that compared to a-Si:H, μc-Si:H absorbs light coming from a broader spectral range (see Figure Intro.4). Therefore, the combination of these materials leads to the exploitation of a larger part of the solar spectrum (compared to a single-junction solar cell) and an improved cell's sunlight to electrical energy conversion efficiency can be expected. The ease with which multi-band gap PV devices can be assembled, has also led to the development of multi-junction solar cells made up of the stack of cells using multiple semiconductor materials having different band gaps (J. Yang et al., 1997; Cao et al., 2013; Kim et al., 2013). However, the choice of the materials to be used in each sub-cell is determined by the requirements for lattice-matching (apart when employing a-Si:H), current-matching, and high performance opto-electronic properties.

One of the problems with this technology is that the stabilized efficiency of micromorph devices is advancing lower than expected and technologies such as CdTe are currently growing to be the single largest thin film technology by production volume. Despite gradual and incremental improvements in thin film silicon technology, the micromorph module design continues to be limited by two major factors: (i) the metastable light-induced degradation of a-Si:H, and (ii) the slow deposition rate of μc-Si:H.

It is in this context that the national French project CANASTA finds its origins.

CANASTA is an acronym that stands for **C**arbon **A**lloyed **NA**nocrystalline **S**ilicon **TA**ndem (Figure Intro.5).

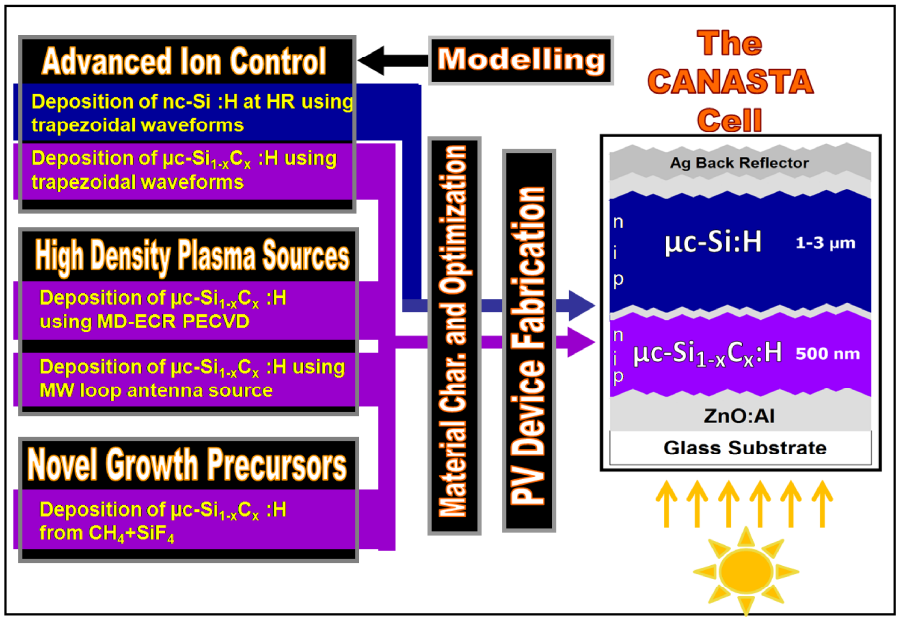

Figure Intro.5.: The CANASTA road map.

The aim of this project, which was a collaboration of the LPICM, LPP and LGEP laboratories, was to address the limiting factors of the micromorph technology. The route through which these goals had to be achieved involved:

- the removal of the primary barrier to stable thin-film silicon-based tandem cells by the elimination of the troublesome a-Si:H and its replacement with hydrogenated microcrystalline silicon-carbon alloys (µc-$Si_{1-x}C_x$:H);
- the deposition of high-quality hydrogenated microcrystalline silicon at a high deposition rate.

The purpose of this doctoral work, which happens to be also one of the most challenging goals of this project, was to obtain an absorber layer quality hydrogenated microcrystalline silicon-carbon material (µc-$Si_{1-x}C_x$:H) at low temperatures ($< 300°$ C). This challenge has been addressed using not only standard deposition techniques, but also novel technologies. To achieve the widest range of freedom in processing conditions, different deposition strategies have been investigated, to learn the most about the specific physical processes required to produce a high quality material. Frankly, this goal of the CANASTA project was very ambitious, however stable wide band-gap materials would be universally useful.

The current state of the art regarding sub-stoichiometric crystalline silicon-carbon alloys, deposited by means of plasma enhanced chemical vapor deposition, is limited and their development required an exploratory approach. Most of this work involved the investigation of the possible correlation between deposition parameters and structural and opto-electronic properties

of the deposited materials (Gaiaschi, Ruggeri, Gueunier-Farret, et al., 2014). The role of the addition of a seed layer was the starting point of this study, in order to avoid the complete amorphization of thin ($\sim$ 50 nm) films (Gaiaschi, Ruggeri, Johnson, et al., 2014). First tests of their possible applicability to devices were conducted, highlighting the key role of substrate temperature not really for the structural quality of the alloys (Gaiaschi, Gueunier-Farret, et al., 2014), but mostly for the possibility of fully benefit from the LPICM know-how in device design. The conclusions and the experiments leading to the identification of some promising paths for the development of μc-$Si_{1-x}C_x$:H alloys are presented in the following chapters, stressing especially the sensitivity of these materials to the deposition conditions. This thesis is therefore structured as follows:

- Part I: Background and Fundamentals
  - Chapter 1: fundamentals about the μc-Si:H, a-Si:H and their alloying with carbon are given.
  - Chapter 2: experimental details for the deposition of microcrystalline and amorphous silicon-carbon alloys are described, giving first details on the deposition tools and then, on the characterization methods (structural and electrical) for materials and devices.
- Part II: Material Study
  - Chapter 3: results concerning the studies of structural properties of μc-$Si_{1-x}C_x$:H alloys are presented, paying particular attention to the effect of the different deposition parameters.
  - Chapter 4: results concerning the studies of transport and defect-related properties of silicon-carbon alloys are presented.
- Part III: Device Study
  - Chapter 5: fundamentals about device structure and results concerning the behavior of microcrystalline silicon-carbon alloys when introduced in working devices are given.

Part I.

Background and Fundamentals

1 AMORPHOUS AND MICROCRYSTALLINE SILICON AND THEIR ALLOYING WITH CARBON

1.1 INTRODUCTION

For over two decades hydrogenated amorphous silicon (a-Si:H) has been a promising candidate as an absorber layer for thin film solar cells, going as far as achieving mass-production on a 100 MW scale. Since the first a-Si:H solar cell was reported by Carlson and Wronski in 1976 with an efficiency of 2.4 % (Carlson et al., 1976), great improvements have been made and nowadays a-Si:H single junction solar cells show stable efficiencies above 10 %, with the latest record at 10.7 % (Benagli et al., 2009). At the present time, a-Si:H is also efficiently used in other kind of technologies, such as **"micromorph"** and **multi-junction** solar cells. The former are made by coupling a thin a-Si:H top cell and a thicker hydrogenated microcrystalline silicon (μc-Si:H) bottom cell (world record stable efficiency has reached 11.6 % - Green et al., 2014), while the latter are made by coupling multiple devices fabricated with different semiconductor materials and allowing the absorbance of a broader range of wavelengths (efficiency $\sim$ 13.4 % for a-Si:H/nc-Si:H/nc-Si:H devices - Ahn et al., 2012). Nevertheless, the light-induced degradation of the a-Si:H cell, known as the *Staebler-Wronski effect* (see section 1.2.3), is still a limiting factor for the efficiency of these kind of devices. In this respect, materials that are stable under light soaking and have an electronic band gap between that of μc-Si:H (1.1 eV) and that of a-Si:H (1.7 eV) are needed, as they could be a breakthrough for this kind of technologies. In the search for a material satisfying all these requirements, hydrogenated microcrystalline silicon-carbon alloys (μc-$Si_{1-x}C_x$:H) thin films become a very attractive new class of materials (Demichelis, Giorgis, et al., 1995) as their average band gap can be tuned by changing the amount of carbon in the alloy composition (see Figure 1.1).

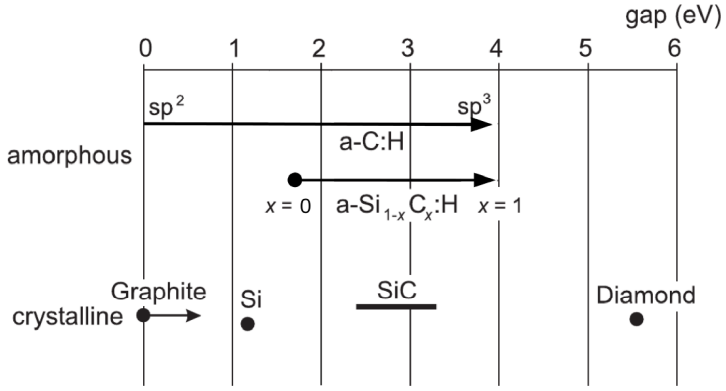

Figure 1.1.: Reported band gaps of different amorphous and crystalline materials containing carbon and/or silicon (Ledoux et al., 2001).

Actually, several factors limit the usefulness of carbon. Carbon has, in fact, a very low solubility in silicon and, depending on the deposition conditions, can form undesirable silicon carbide (SiC) precipitates or degrade the properties of the deposited films. Therefore, a short review on a-Si:H, μc-Si:H and their possible alloying with this element has to be presented, in order to define the key aspects of an exploratory research aiming at using this element as a possible way to expand the toolbox of useful materials for thin-film photovoltaics.

1.2 AMORPHOUS SILICON

1.2.1 Band structure: Bandtails, Band edges, and Band Gaps

In a crystalline silicon wafer (c-Si) each atom is connected to four others by covalent bonds forming a tetrahedron. In this kind of material the crystal lattice is continuous and therefore a long-range order is observed (Figure 1.2(a)). On the other hand, in an amorphous network, such as the one of a-Si:H, a well-ordered structure is missing and atoms are bonded to each other in a random way (disorder). Bond lengths and angles can vary and some atoms may present unsaturated bonds, the so-called *dangling bonds* (DB), which can be saturated with the incorporation of hydrogen (see Figure 1.2(b)).

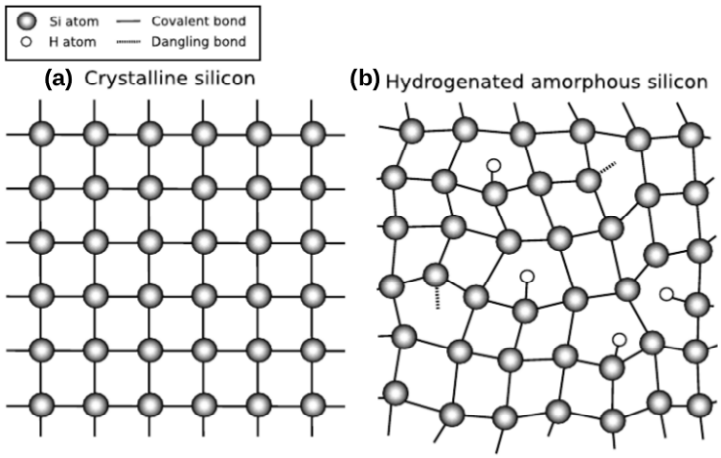

Figure 1.2.: (a) Crystalline silicon and (b) a-Si:H structures (Pieters, 2008).

The disorder in a-Si:H induces a different band structure, compared to crystalline silicon. A crystalline semiconductor is, in fact, characterized by a forbidden band gap between the valence band (VB) and the conduction band (CB), which arises from the periodicity of the lattice and in general lacks of electronic states. If some states are present, they are due to coordination defects or interstitial atoms, which are characterized by a discrete distribution. On the other hand, the peculiar structure of a-Si:H leads to a significant density of states in the forbidden gap. The presence of such defects finds its origin in two mechanisms:

- *localized wave-functions at both sides of a band*: the lack of order in the material causes a broadening of VB and CB, leading to the so-called "band tails", which have an exponential distribution in energy and where localized energy states exist (Overhof, 1998);

- *localized electronic states near the center of the band gap*: defects, such as dangling bonds or lattice vacancies, give rise to these additional localized states.

A schematic representation of the a-Si:H density of states (DOS) is presented in Figure 1.3, where the extended states in the VB and CB, the VB and CB tails and the states originating from dangling bonds are shown. Due to the localized nature of band tail states and of states arising from structural defects, the mobility of electrons and holes at these states is much lower as compared to the non-localized states in the valence and conduction band, where the carriers are considered free. The energy separating localized and non-localized states is called *mobility edge* (in Figure 1.3 are indicated as E_v and E_c for the VB and the CB, respectively), whereas the energy difference between E_v and E_c is the so-called *mobility gap* (Mott, 1987).

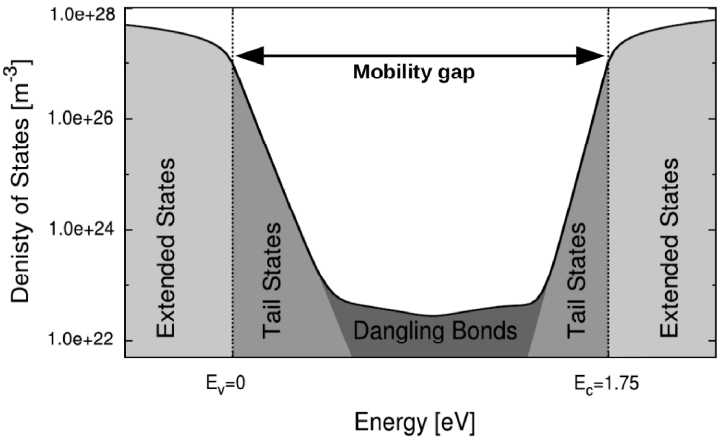

Figure 1.3.: Schematic representation of the density of states in a-Si:H (Pieters, 2008). A typical value of the mobility gap in a-Si:H is 1.75 eV.

Due to the lack of long range order in a-Si:H the crystal momentum is not a proper quantum number. As a result, this material acts like a direct semiconductor (Jackson et al., 1985). Moreover, its disordered nature brings into question the existence of a defined energy band gap (Schiff et al., 2011). Unfortunately, for noncrystalline semiconductors there is no single, conclusively established procedure for locating the band-edges within the DOS. The band gap is thus difficult to determine without some ambiguity. Since amorphous silicon-based materials with varying band gaps are used in solar cells, it is nonetheless very important to establish conventional procedures for comparing band gaps.

As the energy separation of localized and non-localized states is sharp, electronic transport in a-Si:H is dominated by the carriers in the states just below E_v and just above E_c. Therefore for electronic transport the mobility gap can be considered as the amorphous equivalent of the band gap. On the other hand, the absorption spectrum is often used to determine the "optical band gap" of amorphous semiconductors. As the most filled electron states available for optical absorption are in the VB and the most empty electron states are located in the CB, the optical band gap can be considered as a measure of the distance between the extended states in the VB and CB. Several definitions exist for this kind of band gap. The most common approach

is to consider the *Tauc band gap* E_T, which is derived from the plot of the absorption coefficient according to the following expression

$$\alpha(h\nu) = \left(\frac{A}{h\nu}\right) \cdot (h\nu - E_T)^2. \tag{1.1}$$

where $\alpha(h\nu)$ is the optical absorption coefficient, h is Planck's constant, ν the photon frequency and A a proportionality constant (Wooten, 1972). For a-Si:H, the typical value of E_T obtained using this approach, is $\sim$ 1.75 eV. Finally, it is also common to define the *iso-absorption band gap* E_{04}, which corresponds to the photon-energy for which the absorption coefficient equals 10^4 cm^{-1}.

1.2.2 Growth mechanism

When grown by plasma enhanced chemical vapor deposition at low pressure, the main precursor for the growth of a-Si:H is thought to be SiH_3, due to its no reactivity with silane (SiH_4). In Figure 1.4 the surface reaction model developed by Matsuda et al. is presented (Matsuda et al., 2003). When a SiH_3 radical reaches the hydrogen-terminated film-growing surface, it starts to diffuse and it can abstract surface hydrogen, forming SiH_4. A Si-dangling bond is left on the surface and a second surface-diffusing SiH_3 radical can diffuse to this dangling bond forming a Si-Si bond.

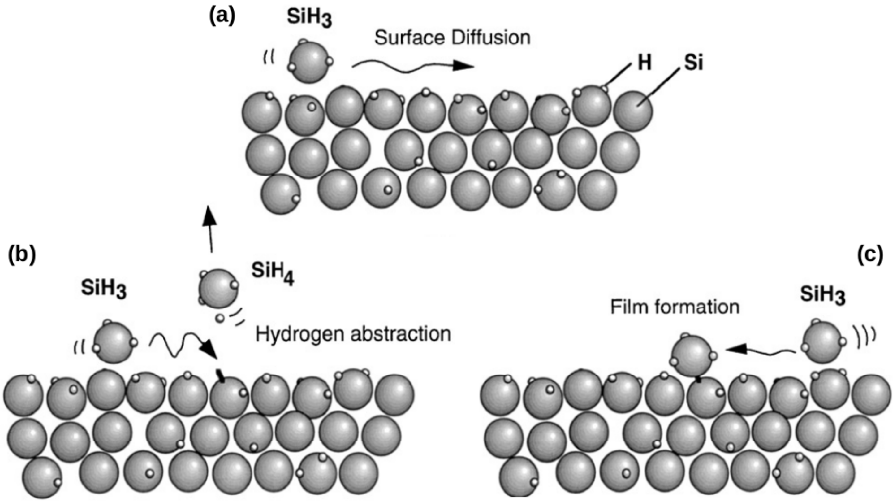

Figure 1.4.: Growth of amorphous silicon. (a) SiH_3 radicals diffuse over the hydrogen-terminated surface and (b) can abstract a hydrogen atom from a Si-atom, forming SiH_4 which does not contribute to the film growth. (c) A second SiH_3 radical may diffuse to the Si-dangling bond left on the Si-atom, forming Si-Si bonds and enabling the film growth (Matsuda et al., 2003).

This surface reaction model can successfully explain the relation between the dangling bonds density in the resulting a-Si:H and the substrate temperature during film growth if one considers that the density of defects in the resulting film is determined by the density of defects of the film-growing surface. In fact, one can assume that with the film growth the surface at one instant becomes a part of bulk at the following instant.

1.2.3 Light-induced degradation

In common amorphous silicon the concentration of dangling bonds is in the order of 10^{19} cm^{-3}, making this material of no use for solar application. In fact, the disorder induces the presence of recombination centers that severely reduce the carrier lifetime and pin the Fermi level so that the material cannot be doped either n- or p-type. When in 1969 Chittick et al. first deposited hydrogenated amorphous silicon (which includes about 10 at% hydrogen), they were able to decrease the unsaturated Si dangling bonds concentration to $10^{15} - 10^{16}$ cm^{-3} (Chittick et al., 1969). The reduction of the defect density made this new a-Si:H material suitable for doping, alloying with different elements and junction device fabrication (Chopra et al., 2004).

Actually, the main problem limiting the application of a-Si:H in single junction solar cells, was reported by Staebler and Wronski in 1977 (Staebler et al., 1977). They demonstrated that under illumination the conductivity of a-Si:H degrades but can be totally (or sometimes only partially) restored by annealing at high temperatures ($\sim$ 150° C) for several hours. This reversible degradation, known as the *Staebler-Wronski effect*, is ascribed to the light-induced creation of additional metastable defects, which are generally accepted as additional dangling bonds, created by the breaking of weak or strained Si-Si bonds and acting like recombination centers in the material.

Nowadays, the major concern of the scientific community is to be able to develop materials having the lowest possible density of defects, or to make devices able to minimize such phenomenon. In order to partially tackle the light-induced degradation of a-Si:H devices, two approaches have been explored so far:

1. *reduction of the a-Si:H layer thickness*. In this case, photogenerated carriers need to move only a short distance before reaching the electrode. However, thinning down the a-Si:H layer thickness also results in lower light absorption and thus optical confinement techniques, employing diffusely reflecting front and back contacts, are required to increase effective layer thickness in order to absorb the photons;

2. *suitable deposition conditions to obtain materials having less defect density and more stable performance against light degradation*. These materials, such as **polymorphous silicon**, deposited using conditions at the limit of powder formation (Longeaud, Kleider, et al., 1998), or **protocrystalline silicon**, deposited on the verge of microcrystalline silicon deposition (Guha et al., 1999), are characterized by the existence of very small silicon crystallites dispersed in amorphous matrix.

1.3 MICROCRYSTALLINE SILICON

1.3.1 Structural properties

Hydrogenated microcrystalline silicon is characterized by complex structural properties which are translated into complex transport properties. Indeed, it can be considered as a mixed phase material consisting of varying amounts of c-Si nano-crystallites, a-Si:H and grain boundaries.

Figure 1.5 shows a schematic representation of typical compositions and structures found in this material. Usually, a μc-Si:H layer shows inhomo-

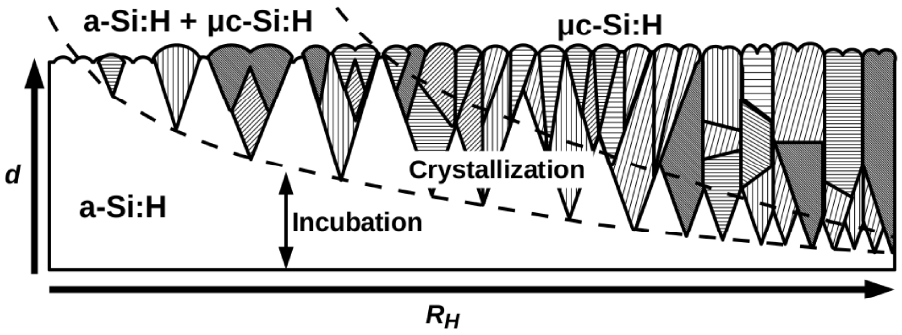

Figure 1.5.: Schematic representation of the growth of µc-Si:H films prepared as a function of hydrogen dilution R_H. The dashed lines identify the amorphous-to-(mixed-phase) and the (mixed-phase)-to-microcrystalline transitions (Collins et al., 2003).

geneity in the growth direction and presents three characteristic phases, the thickness and composition of which strongly depend on the deposition conditions (Vallat-Sauvain et al., 2000) and the substrate used (Bailat et al., 2002). Indeed, in Figure 1.5 one can clearly distinguish an a-Si:H *incubation phase*, a *crystallization phase* (which is a mixed phase of a-Si:H and µc-Si:H) and a *phase with a saturated crystalline fraction* (Collins et al., 2003). The hydrogen dilution $R_H = [H_2]/[SiH_4]$ is used as the abscissa of the phase diagram since it exerts the greatest control over the phase of the film. From left to right the composition changes from amorphous (low R_H) to highly microcrystalline (high R_H). The amorphous-to-(mixed-phase) transition boundary exhibits a negative slope as a function of R_H in the d versus R_H plane, where d designates the layer thickness (Koh et al., 1998). This is inferred from the observation of the nucleation of Si microcrystallites from within the growing a-Si:H phase, after a critical phase-transition thickness (the incubation layer) that decreases with increasing R_H. During the following crystallization phase, columnar agglomerates of crystallites are formed. The diameter of these columns increases with film thickness at the expense of the a-Si:H fraction, resulting in the typical conical shape (Kočka et al., 2004). It is noteworthy that the structure inside the columns is not monocrystalline, but it consists of coherent regions with a diameter of $4 - 20$ nm that are separated from each other by stacking faults and twin boundaries (Houben, Luysberg, Hapke, et al., 1998). Moreover, the columns themselves are not only separated by disordered material, but also by crack-like voids that may extend from the surface deep into the film and allow for in-diffusion of atmospheric gases along the column boundaries. Transmission electron microscopy (Luysberg et al., 1997; Houben, Luysberg, Hapke, et al., 1998), infrared spectroscopy (Tzolov et al., 1997; Houben, Luysberg, and Carius, 2003), and hydrogen effusion (Beyer, 2003) studies have shown that highly crystalline materials often exhibit a pronounced porosity. When cells are grown on rough substrates, "cracks" can appear in the µc-Si:H layers, having a detrimental effect on the fill factor and open-circuit voltage of the photovoltaic devices (Smets et al., 2008). These cracks are zone of porous material with nanovoid size below 70 nm and not lack of material. They permit the incorporation of oxygen (post-oxidation) and are responsible for bad electrical performance of the devices (Python et al., 2010).

1.3.2 Growth mechanism

Hydrogenated microcrystalline silicon is an attractive material for thin-film silicon solar cells. In comparison to a-Si:H, μc-Si:H is more stable to light exposure and has a lower band gap. For its growth several models have been proposed, having all in common the key-role played by atomic hydrogen (Matsuda, 1999).

SURFACE DIFFUSION MODEL This model suggests that the high hydrogen dilution used for the growth of μc-Si:H can induce a sufficient flux density of atomic hydrogen able to create a full surface coverage by bonded hydrogen, also producing local heating through hydrogen-recombination reactions on the film-growing surface (Vepřek and Mareček, 1968). These two events enhance the surface diffusion length of adsorbed SiH_3 radicals, which can find energetically favorable sites, leading to a formation of atomically flat surfaces.

ETCHING MODEL This model was proposed based on the experimental fact that film growth rate is reduced by an increase of hydrogen dilution (Tsai et al., 1989). The general idea is that an atomic hydrogen provided on the film-growing surface breaks weak, stressed, or angulated Si-Si bonds in the amorphous tissue, leading to a removal of a Si atom. A new precursor can then insert at this site, forming a stable Si-Si bond.

CHEMICAL ANNEALING MODEL This model, which is similar to the previous one, was initially proposed in order to explain the experimental observation of crystal formation during hydrogen plasma treatment in *layer-by-layer* depositions (alternating sequence of amorphous film growth and hydrogen plasma treatment). According to this model, crystallization occurs under the assumption that hydrogen atoms permeate into the sub-surface region where a flexible crystalline network develops if sufficient hydrogen is present and the abstraction of Si-atoms is negligible (Nakamura et al., 1995).

1.3.3 Band structure

The lack of translational symmetry in μc-Si:H leads to some major consequences for the electronic properties of the material. As for a-Si:H, the disorder leads to a different DOS, compared to c-Si. However, as the electronic structure is mostly determined by the short range order, the overall electronic properties are very similar compared to the equivalent crystal. Nevertheless, the lack of long range order (grain boundaries and amorphous phase are predominant features in the μc-Si:H structure) causes potential fluctuations which are responsible for the abrupt band edges found in crystalline semiconductors to be replaced by broadened tail states, extending into the forbidden gap. Moreover, the deviation from the ideal network structure also results in electronic states deep within the gap (dangling bonds).

1.3.4 Electronic transport

The presence of grain boundaries, a-Si:H tissue and crystalline grains, which are sources of defects in the material, has a strong impact on the quality of transport properties on multiple scales: subnanometric (atomic com-

position and local arrangement), nanometric (crystalline grains and their boundaries) and submicron (large grain aggregates or columns). In addition, the evolution of the material structure with its growth, adds complexity to the prediction of macroscopic transport properties.

In 2003 Hattori et al. performed a detailed investigation of photocarrier transport and localized states in undoped μc-Si:H, using the modulated photocurrent technique (see section 2.3.2). As expected, they showed that the photocarrier MPC-derived drift mobility varies systematically with the crystalline grain size, the volume fraction, as well as the transport direction. They showed that in the coplanar electrode configuration, the measured drift mobility increases with the crystalline volume fraction, while a lower mobility is observed for smaller grains. On the other hand, measurements performed in the "sandwich" arrangement, revealed that the drift mobility in the direction perpendicular to the substrate is one order of magnitude higher than parallel to the substrate (Hattori et al., 2003).

Much work has been carried out to investigate the electrical transport properties of μc-Si:H, taking into account its inhomogeneity in both directions (perpendicular and parallel to the substrate) and several transport mechanisms have been developed.

BARRIER LIMITED TRANSPORT Originally developed by Seto to model transport in polycrystalline silicon, it proposes that the transport properties are mainly determined by defect states located at the grain boundaries (Seto, 1975). According to this model, charge carriers can be trapped at grain boundaries giving rise to potential barriers that limit their mobility. To overcome these barriers, thermionic emission is needed. Temperature dependent measurements, performed by Hourd et al. in a small temperature range, seemed to prove this model showing the characteristic temperature activated mobility expected for barrier limited transport (Hourd et al., 1991). On the other hand, extending the conductivity measurements over a wider range of temperatures showed that μc-Si:H does not exhibit a single activated transport behavior (Carius et al., 1997). Moreover, there are indications that the grain boundaries between the crystallites do not form potential barriers. In fact, when studying μc-Si:H transport properties analyzing the temperature dependent dark conductivity, Ruff et al. realized that for their "intrinsic" μc-Si:H samples it was impossible for grain boundaries *between the crystallites* to form potential barriers, as this would require a large number of trapped electrons (Ruff et al., 1998). However, they proposed that the boundaries between the whole columns act as potential barriers. Lately this model has been extended to include tunneling effects in order to describe the Hall mobility in n-type μc-Si:H (Weis et al., 2002).

MULTIPLE-TRAPPING IN BAND TAILS The existence of broad tail states extending into the gap suggests that these states might play an important role in the transport mechanism. The multiple-trapping model considers that charge carriers have a fixed mobility in extended states and are immobile when trapped in localized states. In order to contribute to transport, they first need to be thermally excited above the mobility edge. The temperature dependency of the drift mobility and the dispersive transport properties of μc-Si:H are then explained by the dynamics of trapping of charge carriers on localized states and the thermal emission of charge carriers from the localized states.

HOPPING In a hopping system, developed by Scher and Montroll (Scher et al., 1975), the transport is based on hopping and tunneling of the charge carriers between states. Hopping in an exponential band-tail can be applied to describe the transport behavior of μc-Si:H in the low temperature region (Fuhs et al., 2000; Ambrosone, U. Coscia, Cassinese, et al., 2007).

1.3.5 Light-induced degradation

Since the discovery of the *Staebler-Wronski effect*, a wide effort is being undertaken to obtain more stable materials, especially for photovoltaic applications. The interest for μc-Si:H lies in the absence of light-induced degradation (Kleider, Longeaud, Brüggemann, et al., 2001; Shah, Meier, et al., 2003). However, it has been shown that the term "μc-Si:H" covers a large variety of different materials, presenting different microstructures, crystallites sizes and crystalline volume fractions. Therefore, it should not be ruled out that certain types of hydrogenated microcrystalline silicon layers may suffer from light-induced degradation.

Indeed, in 1986 Liu et al. showed that in μc-Si:H the light-induced degradation decreases and approaches zero with increasing grain size (Liu et al., 1986). They explained such behavior by considering μc-Si:H to be a two-phase material in which the microcrystalline grains are surrounded by the amorphous matrix, and assuming that with increasing grain size, the amorphous fraction is decreasing, leading to a lower light-induced degradation. Similarly, Meillaud et al. have demonstrated that the crystalline volume fraction has an impact on the stability of photovoltaic devices. The lower the crystallinity of the cells the stronger is the light-induced degradation (Meillaud et al., 2005). They showed that cells of medium crystallinity show approximately a 10 % reversible relative efficiency loss after 1000 hours of light soaking. Moreover, using the Fourier Transform Photocurrent Spectroscopy technique they investigated the evolution of the defect-related absorption spectra, before and after degradation. For two cells having an i-layers with a crystallinity of 10 % and of 80 %, they observed that defect-related absorption before and after light-induced degradation depends on the crystalline volume fraction. While for the first one, the defect-related absorption was increased by a factor of more than 20 after light-soaking, for the second one it was only increased by a factor 2.

1.4 SILICON–CARBON ALLOYS

The main disadvantage that has to be faced when trying to alloy silicon and carbon, is the fact that stoichiometric crystalline silicon carbide (c-SiC) is the only stable compound in the Si-C equilibrium system (Osten, 2000). For these elements no parallel with silicon-rich SiGe ($Si_{1-x}Ge_x$), which crystallize over the whole range of compositions, can be expected.

Stoichiometric c-SiC can be found in nature only in meteorites. Thus, it cannot be mined, but must be manufactured with elaborate furnace techniques. In its polycrystalline forms, SiC has long been a well proven material in high-temperature, high-strength and abrasion resistant applications like ceramics, but as a semiconductor it is a more recent discovery (Janz, 2006). Its amorphous counterpart is currently being applied in several domains, such as in solar cells, for anti-reflection coatings (Klyui et al., 2002) and window layers (Chang et al., 2011), and in microelectronics (El Khakani et al.,

1994). Depending on the deposition parameters, such as silicon-carbon ratio in the gas phase, the stoichiometry of the material can be varied, obtaining a wide variety of amorphous silicon-carbon alloys (a-$Si_{1-x}C_x$:H).

When Spear and LeComber demonstrated the possibility of doping a-Si:H (Spear and LeComber, 1976), they drew increasing interest on amorphous tetrahedral semiconductors. As it has already been said, due to its low solubility ($\sim 3 \times 10^{17}$ atoms cm^{-3} at the melting point) the incorporation of carbon into silicon is difficult. Nevertheless, the variation of the optical gap of a-$Si_{1-x}C_x$:H alloys, obtained by increasing the carbon concentration, is desirable for many device strategies and has been one of the main appeals of these alloys.

1.4.1 Physico-chemical introduction to a-$Si_{1-x}C_x$:H alloys

First of all it can be stated that amorphous tetrahedral alloys are more disordered than amorphous silicon, since chemical inhomogeneity is added to the inherent structural one. Indeed, if the coordination geometries of two atoms are different, the structural disorder will be enhanced and this is especially the case for increasing difference in bond lengths (see Table 1.1).

Table 1.1.: SiC relevant bonds and bond lengths (Bullot et al., 1987).

Bond	Length (Å)	Bond	Length (Å)
C — C	1.54	C = C	1.33
C — H (sp^3)	1.09	C = C (graphite)	1.42
C — Si	1.87	C ≡ C	1.21
Si — Si (in c-Si)	2.35	Si — H	1.48

In order to describe the a-$Si_{1-x}C_x$:H network, one could use the network models developed for amorphous silicon. On the other hand, the ratio of the covalent radii $r_C/r_{Si} = 0.66$ (see Table 1.2) clarifies that these network models are not suitable. In fact, a-$Si_{1-x}C_x$:H networks are expected to be much more disordered, but it is however difficult to predict the evolution of the disorder as a function of x.

Table 1.2.: Covalent radii and electronegativity of the atoms appearing in the SiC network (Bullot et al., 1987).

Atom	radius (Å)	Electronegativity
C	0.77	2.50
Si	1.17	1.74
H	0.28	2.20

If one considers a statistical distribution of atoms in the alloy, there will always be some homonuclear bonding between majority atoms. Since C — C bonds are thermodynamically more stable than Si — Si and Si — C bonds, it is probable to find C — C bonds already in a material with $x = 0.5$. At higher carbon concentrations carbon clusters may be formed and are expected to contain graphitic configurations. In Figure 1.6 an illustration of the microstructure of a-$Si_{1-x}C_x$:H alloys is given.

Finally, if both a-Si:H and a-C:H exhibit some local order, an a-$Si_{1-x}C_x$:H alloy will be more and more disordered for increasing values of x. If one considers a continuous random network, there must be a maximum disor-

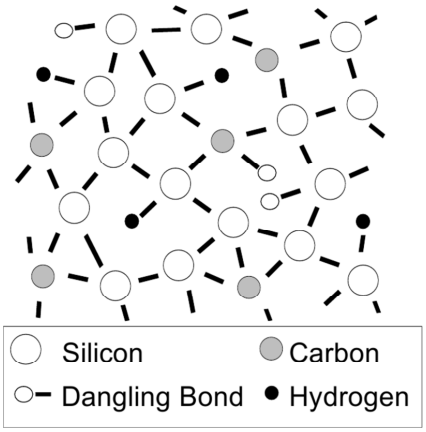

Figure 1.6.: Scheme of the microstructure of pure amorphous silicon-carbon alloys (Kirner, 2013).

der somewhere between pure a-Si:H and pure a-C:H. Since the stability of $Si-Si$ and $C-C$ bonds are different, this maximum has not to be expected for $x = 0.5$. On the other hand, carbon clustering may induce some highly ordered domains, but in this case the continuous random network configuration is invalid. At the same time, it is noteworthy that $C-H$ bonds are much more stable than $Si-H$ bonds, therefore in a-$Si_{1-x}C_x$:H alloys this should have consequences on the hydrogen distribution in the films, expecting carbon atoms to be more hydrogenated than silicon atoms. Nevertheless, due to the different electronegativities of silicon and carbon (Table 1.2), $Si-H$ bonds are strengthened if the silicon atom is carbon-backbonded. In turn, $C-H$ bonds are weakened if a silicon atom is bonded to the carbon atom.

1.4.2 Growth mechanism of a-$Si_{1-x}C_x$:H alloys from a SiH_4-CH_4 gas mixture

The plasma chemistry of low pressure radio frequency (RF) discharges in SiH_4 is very complex and the addition of carbon-based precursors increases its complexity. Catherine at al. have performed the most comprehensive study of RF discharges in silane-hydrocarbon mixtures using an inductively coupled reactor and diluting the mixture with helium, which behaves as an inert gas not participating to the plasma chemistry (Catherine and Turban, 1979; Catherine, Turban, and Grolleau, 1981).

Assuming that the activation of a simple molecule is a "first-order" process, a rate constant K_1 can be defined as

$$K_1 = K_a < n_e >, \tag{1.2}$$

where $<n_e>$ is the mean electron density in the plasma and K_a the activation constant. Turban et al. have estimated the following values for K_a (Turban et al., 1979)

$$\begin{array}{lcll} K_a(SiH_4) & \approx & 5 \times 10^{-9} & cm^3 s^{-1} \\ K_a(CH_4) & \approx & 4 \times 10^{-10} & cm^3 s^{-1} \end{array} \tag{1.3}$$

Thus, SiH_4 is decomposed faster than CH_4. Moreover, with their investigations, Catherine et al. demonstrated that the primary decomposition products of SiH_4 and CH_4 are the neutral radicals SiH_2, SiH_3, CH_3 and

CH_2 (Catherine, Turban, and Grolleau, 1981). Species like SiH, CH, Si and C are also formed, but seem to be negligible when considering the following rate constant ratios (Bullot et al., 1987):

$$\begin{aligned} K(SiH_3)/K(SiH_2) &\approx 0.75 \\ K(Si)/K(SiH_2) &\approx 0.05 \\ K(SiH)/K(SiH_2) &\approx 0.1 \end{aligned} \tag{1.4}$$

Rate constants for electron impact ionization of SiH_4 and CH_4 are lower than for dissociation. The main ionic species among the primary decomposition products are listed in Table 1.3. They can further react in the gas phase or at the surface. A detailed analysis of the gas phase chemistry in these systems is presented in Catherine, Turban, and Grolleau, 1981.

Table 1.3.: Main primary products of CH_4 and SiH_4 electron impact fragmentation (Bullot et al., 1987).

Gas	Radical	Positive ions
CH_4	CH_3, CH_2, CH	CH_4^+, CH_3^+, CH_2^+, CH^+
SiH_4	SiH_3, SiH_2, SiH	SiH_3^+, SiH_2^+, SiH^+

The deposition of the films is mainly due to neutral radicals which are adsorbed at the surface where they can either react or desorb. According to Catherine et al. surface rearrangements are preponderant for bond formation. Finally, the ion bombardment of the growing-film surface may also have an influence on the film structure.

1.4.3 Network structure and properties

The best way to study the network structure and therefore the chemical order in a-$Si_{1-x}C_x$:H alloys is by performing vibrational spectroscopy studies. In 1980 Lee presented a detailed x-ray photoemission and Auger study of a-$Si_{1-x}C_x$:H alloys (Lee, 1980). He showed that Si atoms are bonded to C and the percentage increases slightly with increasing x. Therefore, for *low carbon concentrations* the Si network is only slightly disturbed by the replacement of a small number of Si by C and H as would be the case for dilute alloys. He also showed that for nearly stoichiometric films Si — C bonds are predominant, but the presence of homonuclear bonds (Si — Si and C — C) indicates a strong topological disorder.

Optical gaps in a-$Si_{1-x}C_x$:H range between 1.8 eV and 4.0 eV, whereas the refractive index at infinite wavelength may vary between 3.7 and 1.8. Such a wide variety of optical properties has been the driving force motivating increasing interest in a-$Si_{1-x}C_x$:H alloys (Bullot et al., 1987).

The knowledge of the evolution of the DOS with carbon concentration in a-$Si_{1-x}C_x$:H alloys is essential for understanding the origin and nature of defects and the electronic transport properties of such a complex class of materials. In the early 1990s, several studies were performed investigating the DOS at the Fermi level by space charge limited current (SCLC) measurements (Schmidt et al., 1985) and were in agreement with photothermal deflection spectroscopy (PDS) and electron spin resonance (ESR) results (Morimoto et al., 1982; Boulitrop et al., 1985; Alvarez et al., 1992), proving an increase of the DOS with the carbon fraction. Experimental SCLC results led the authors to the definition of a model of defect creation by "pairing of defects precursors". They assumed that some of the incorporated carbon

atoms lead to distorted coordinations which by themselves do not induce localized states in the gap. On the other hand, when two sites of distorted coordination are close enough, the relaxation of the structural strain by the surrounding network is no longer possible and some structural defects are created, which introduce localized states in the gap. The interpretation of the ESR measurements is complicated by the fact that while in a-Si:H the only paramagnetic states are the silicon DB, when carbon is incorporated it can be bonded in sp^3 and sp^2 configurations, leading to C sp^3 DB, C isolated sp^2 DB or odd sp^2 C clusters (Giorgis et al., 2001). However, experimental results showed that in a-$Si_{1-x}C_x$:H alloys the Landé factor g shifts from $g = 2.0055$ (in Si-rich a-$Si_{1-x}C_x$:H alloys) to $g = 2.003$ (in C-rich a-$Si_{1-x}C_x$:H alloys), due to defect topology and to atoms surrounding the paramagnetic defects, suggesting the existence of both types of deep states defects in the material (Bullot et al., 1987).

The most challenging thing about these alloys concerns the fact that all these properties strongly depend on the deposition conditions and the deposition techniques. Therefore, a more detailed analysis of vibrational, optical and electrical properties of a-$Si_{1-x}C_x$:H alloys will be discussed in chapter 3 and 4, comparing amorphous and microcrystalline materials.

1.4.4 Microcrystalline alloys

Since stoichiometric c-SiC is the only stable compound, any alloy with a smaller carbon concentration is thermodynamically metastable. Such alloy layers can be achieved, below critical thickness, only by kinetically dominated growth methods like molecular beam epitaxy (Powell et al., 1993; Osten, 1996) or special kinds of chemical vapor deposition, e.g. rapid thermal chemical vapor deposition (Regolini et al., 1993; Stewart, 2004). These methods generally work far away from thermodynamic equilibrium conditions allowing a kinetic stabilization of metastable phases.

As shown in Figure 1.7, when grown by standard RF-PECVD, hydrogenated microcrystalline silicon carbon alloys are composed of submicron-size silicon crystallites embedded in an a-$Si_{1-x}C_x$:H matrix (Demichelis et al., 1992a; Itoh et al., 2001).

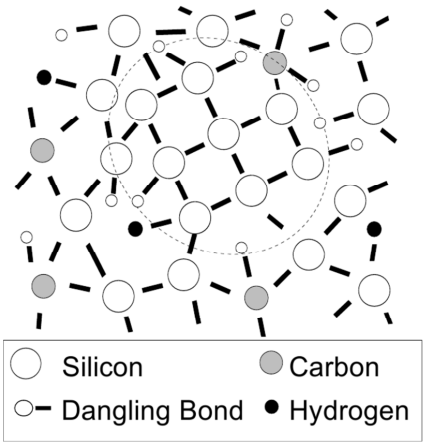

Figure 1.7.: Scheme of the microstructure of hydrogenated microcrystalline silicon-carbon alloys. The dashed line identifies a crystalline region (Kirner, 2013).

While the presence of the crystallites assures a higher conductivity, compared to standard a-$Si_{1-x}C_x$:H (Dasgupta et al., 1999), the carbon incorporation leads to an energy gap larger than that of microcrystalline silicon (Demichelis et al., 1992b; U. Coscia, Ambrosone, Lettieri, Maddalena, Rigato, et al., 2005) This complex nature not only motivates a more detailed study on the growth mechanisms, but also on the role of the carbon incorporation on the final structure of the alloy. In this respect, the influence of deposition techniques and parameters has to be extensively studied in order to define the most promising conditions for the growth of this new class of alloys and their successful application in photovoltaic devices.

In the following chapters the experimental results concerning the fabrication and characterization of μc-$Si_{1-x}C_x$:H alloys will be presented. The goal of this doctoral work is to define deposition conditions leading to μc-$Si_{1-x}C_x$:H alloys with structural and opto-electronic properties ideal for the integration of these alloys as wide-band gap material in PV devices.

2 FUNDAMENTALS

2.1 INTRODUCTION

The goals of this doctoral work has been to develop a new stable photovoltaic device-quality microcrystalline material in thin-film form, composed of an alloy of silicon and carbon, and deposited by plasma enhanced chemical vapor deposition (PECVD) at glass-compatible temperatures. Hydrogenated microcrystalline silicon-carbon alloys are in fact very attractive materials since by varying the carbon content in the alloy composition it is possible to tune the energy gap (Demichelis, Giorgis, et al., 1995). In this work, this new class of alloys was deposited using standard radio frequency (RF-) PECVD at 13.56 MHz and tailored voltage waveform (TVW-) PECVD. Attempts at growing these materials using the Matrix Distributed Electron Cyclotron Resonance (MDECR-) PECVD highlighted the sensitivity of this material system to the deposition conditions (namely the CH_4 percentage in the gas phase). As only preliminary results were obtained applying this deposition technique, a brief theoretical discussion and some results are presented in appendix A, paying particular attention to the reasons that made this deposition technique unsuitable for the growth of these alloys.

For the efficient development of this new mixed-phase material, it has been necessary to understand:

- the keys to growth in each of the systems;
- the influence of the addition of a carbon-based precursor on the growth and the structural and electrical quality of the materials;
- the most promising deposition conditions for optimal opto-electronic performance of these alloys.

Thus, μc-$Si_{1-x}C_x$:H materials had to be tested through a battery of complementary characterization techniques to investigate the effect of the different deposition parameters and techniques on the structural and electrical properties (chapter 3 and 4). In the final phase of this project, the most promising materials were incorporated into cell structures (chapter 5).

2.2 DEPOSITION TECHNIQUES

One of the main questions of the CANASTA project involved the *possibility of using alternative PECVD technologies to produce photovoltaic-quality a-$Si_{1-x}C_x$:H and μc-$Si_{1-x}C_x$:H*. For this reason two main aspects concerning the deposition of these materials were investigated:

1. the possible application of a well-developed deposition technique such as *standard radio frequency plasma enhanced chemical vapor deposition* (RF-PECVD) to the growth of these alloys;

2. the role of the variation of ion bombardment energy independently of power using the *Tailored Voltage Waveforms PECVD* (TVW-PECD) deposition technique;

In the following sections, a brief description of the general principles of the two deposition techniques will be given, even though a more comprehensive study of plasma processes was beyond the scope of this work. More detailed analyses can be found in textbooks such as the ones by Lieberman or Franz (Lieberman et al., 2005; Franz, 2009).

In general, PECVD is a thin film deposition method based on the dissociation of gas molecules by electron impact in an electrical discharge. The dissociation of the precursors and the surface reactions of the ionized species are both controlled by the plasma.

2.2.1 Radio Frequency Plasma Enhanced Chemical Vapor Deposition

Figure 2.1 illustrates the setup of the RF-PECVD system that was used in this work. Two parallel electrodes plates are located in a vacuum chamber that can reach base pressures $\sim 10^{-5}$ Pa. The RF-power, which enables PECVD deposition also on insulating substrates and is commonly used at a frequency of 13.56 MHz, is supplied at one electrode, the so called "powered electrode", while the substrate-holder serves also as the grounded electrode.

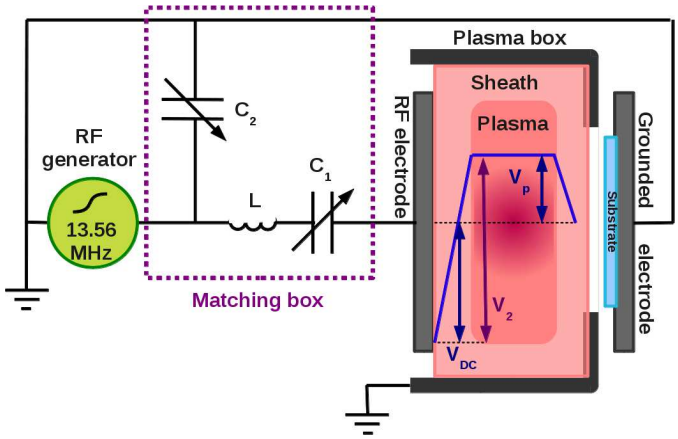

Figure 2.1.: Schematic representation of a RF-PECVD capacitively coupled reactor and of the potential distribution in the RF discharge.

The power produced by the RF-generator is capacitively coupled to the powered electrode via a matching box, which consists in an inductive coil (L) and two variable capacitors (C_1 and C_2). The capacitances are automatically adjusted such that the impedance of the plasma matches the impedance of the RF generator (50 Ω). This configuration, called *L-matching network*, consists mainly of a blocking capacitor connected in series to the plasma, facilitating the built-up of the self-bias on the RF electrode (the so called V_{DC}).

When the plasma is ignited, the different mobility of electrons and ions causes a potential distribution such as the one represented in Figure 2.1 to arise. In fact, the customary excitation frequency of 13.56 MHz is lower than the electrons plasma frequency, but greater than the ions one. Therefore, due to their inertia, ions cannot follow the oscillations of the time-dependent electric field, leading to the polarization of the RF electrode to the V_{DC}. Regions with very low electron density, called *sheath*, are formed between

the electrodes and the plasma and the potential drop from the plasma to the sheath is called *plasma potential* (V_p).

In a parallel plate reactor, the sheaths are assumed to play the role of a capacitance between two electrodes. For a fixed charge, the area of the electrodes mainly determines the capacitance and the potential drop. In many practical reactors, the grounded electrode usually has a much larger area compared to the RF one. In such reactors the dependence of the voltage ratio across the sheaths on the area ratio, can be written as:

$$\frac{V_1}{V_2} = \left(\frac{A_2}{A_1}\right)^s \tag{2.1}$$

where V_1 and V_2 are the average potentials, A_1 and A_2 are the areas of the grounded and RF electrode, respectively and s is an experimentally-determined parameter. This means that in asymmetric discharges most of the applied voltage is distributed across the sheath in front of the smaller electrode, resulting in a geometrical DC self-bias effect, whereas in symmetric discharges, such as the industrial reactors for which the difference in areas is much smaller, the voltage distribution is symmetric.

2.2.2 Tailored Voltage Waveform Chemical Vapor Deposition

The need for high rates deposition involves managing the fact that the high injected RF-powers needed for gas dissociation lead to an increased mean ion bombardment energy (IBE) and thus to a degradation of the deposited film quality. This means that for high-quality thin films production, a limitation of the process rate exists.

So far, two ways to overcome such problem have been implemented: either increasing process pressure or increasing excitation frequencies to very high frequencies (typically ranging from 27 MHz to 300 MHz). Actually, both strategies present disadvantages such as powder formation or non-uniformity, respectively. In a conventional reactor, it is therefore not possible to independently adjust the RF-power and the IBE.

On the other hand, an additional degree of flexibility can be obtained by providing more than one frequency of excitation of the capacitive plasma. If for example two separate power supplies are employed, one at the standard 13.56 MHz and the second one at 100 kHz, the higher frequency will control the plasma density while the lower one will influence the IBE. However:

1. in symmetric discharges the effect on sheaths in front of both electrodes will still be the same;
2. two RF generators are required;
3. IBE can only be increased. No control on low IBE can be achieved;
4. the substrate must be floating.

Recently, Heil et al. demonstrated that a new DC self-bias effect can be generated using an asymmetric excitation voltage, instead of different electrodes geometry (Heil et al., 2008; Czarnetzki et al., 2009). This effect, known as the *electrical asymmetry effect* (EAE), is based on the application of a RF waveform, containing an even harmonic of the fundamental. Then in this way, the two sheaths are not electrically symmetric. Moreover, as ions in the plasma have a large mass and inertia in comparison with the electrons, the energy that the ions gain in the plasma sheath is heavily dependent upon

the period averaged electric field in the sheath. Therefore, by adjusting the DC self-bias, the energy of the ions striking a substrate can be adjusted.

An additional alternative is the use of the *tailored voltage waveforms* (TVWs), comprising multiple synchronized harmonics. TVWs are non-sinusoidal waveforms made of the coherent superposition of a fundamental frequency and its harmonics (f + 2f +3f + ..). Therefore, as they contain more harmonics, an even stronger EAE can be expected.

The TVWs take the form of either positive pulses (maximizing the negative self-bias), or negative pulses (maximizing the positive self-bias). They are usually called as "*peaks*" and "*valleys*", respectively. Since any periodic waveform can be decomposed into a Fourier series, the peaks and valleys voltage waveforms can be expressed as:

$$V(t) = \sum_{k=1}^{n} V_k \cos(k\omega t + \theta_k), \tag{2.2}$$

where V_k is the voltage amplitude of an individual harmonic, n the total number of harmonics, ω the angular frequency and θ_K the phase shift of an individual harmonic. While a "*peaks*" waveform is obtained by setting the phases θ_k to zero for all harmonics, a "*valleys*" one is obtained by setting all θ_k to π. Moreover, the amplitude of the harmonics is set according to equation 2.3 which gives a constant peak-to-peak voltage, V_{pp} independent of the number of harmonics, n (Delattre et al., 2013).

$$V_k = V_{pp} \frac{2(n-k+1)}{(1+n)^2}. \tag{2.3}$$

In Figure 2.2 examples of such waveforms for specific values of θ_k are shown.

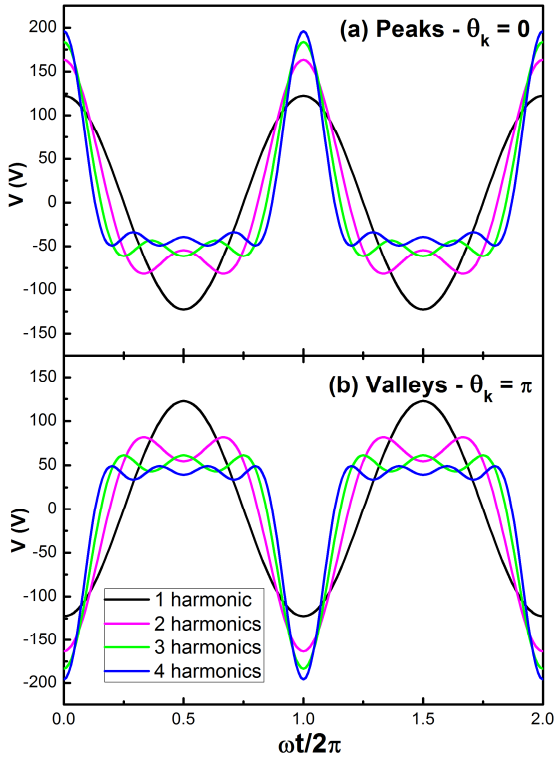

Figure 2.2.: Sine waveform (1 harmonic) and TVW (a) peaks and (b) valleys with 2-4 harmonics.

In this work a fixed fundamental frequency of 10 MHz was used and the TVW waveforms were made by adding 3 harmonics at frequencies 20, 30 and 40 MHz, respectively. An arbitrary function generator (AFG, Tektronix 3150) was used to produce the input signal which is amplified by a broad band class A amplifier (Prana AP32GN310, 0.1-200 MHz, 1 kW). The amplifier is directly connected to the reactor (i.e. with no match box) through a cable via a capacitor which blocks any DC current. The voltage waveforms were monitored by a high voltage probe (Tektronix P5100) at the voltage feedthrough entering the reactor and corrected in Fourier space using an algorithm similar to that of Patterson et al., 2007.

Waveforms shown in Figure 2.2 are those applied to the reactor, before a blocking capacitor, and therefore have a DC value of zero. When the plasma is lit, a V_{DC} will be established due to the asymmetry of the reactor and the DC value will become non-zero. No matching network was used and as the reactor (even with the plasma ignited) displays a large capacitive impedance, more than 90 % of the output power of the amplifier is reflected.

2.2.3 The ARCAM reactor

In this work, standard RF-PECVD and TVW-PECVD depositions were performed in the ARCAM reactor, shown in Figure 2.3.

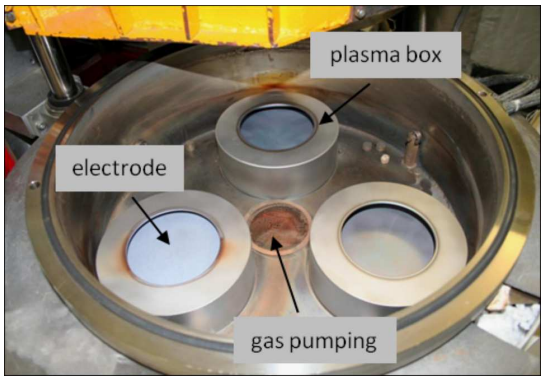

Figure 2.3.: Photo of the inside of the vessel of the ARCAM reactor.

This system consists of a single isothermal vacuum vessel containing three independent plasma chambers (Roca i Cabarrocas, Chévrier, et al., 1991). Such a multi-chamber reactor allows the minimization of the cross contamination when p-i-n (or n-i-p) solar cells are deposited. In fact, as the silane plasma is a very reactive environment, both deposition and removal of a material take place, causing the sputtering of this same material on the reactor walls. Therefore, when working in a mono-chamber system, cross contamination between the different layers constituting the device can happen. In the ARCAM reactor, each plasma chamber consists of a powered-electrode surrounded by a grounded cylinder called *plasma box*. By changing the powered-electrode it is possible to vary the inter-electrode distance, enabling the control of the symmetry of the discharge or the gas residence time. The powered-electrode terminals with the plasma boxes are located at the bottom of the reactor vessel, together with the pumping port and the gas inlets. The whole system can be described as an oven-like structure as all the walls, electrodes and substrate-holders are kept at the same temperature using three thermo-coax wires, while a protecting thermal isolation on the outside minimizes thermal losses. The presence of a rotating plate that

handles six substrate-holders allows multiple samples production without breaking vacuum.

2.3 MATERIAL CHARACTERIZATION TECHNIQUES

In order to be able to predict the behavior and the potential of a material, when applied to a photovoltaic device, an extensive study of both its structural and electrical properties is necessary, especially when it is fundamental to establish a possible correlation between these aspects and the deposition parameters.

Materials were deposited simultaneously on two different substrates: <100> float zone crystalline silicon (FZ c-Si) for infrared (IR) measurements, and Corning "Eagle" glass for all the other characterization methods that will be explained in the following.

2.3.1 Structural characterizations

Radio Frequency Glow Discharge Optical Emission Spectroscopy

The elemental composition of the obtained alloys, with particular interest in the depth profiles of carbon and silicon, was determined by Radio Frequency Glow Discharge Optical Emission Spectroscopy (RF-GD-OES) using a HORIBA Jobin-Yvon GD-Profiler 2. This spectrochemical approach allows direct determination of major and trace elements having high depth resolution, fast sputtering rate, multi-elemental capability and low limits of detection (Pisonero et al., 2006; Sanchez et al., 2010).

The development and application of glow discharge devices for chemical analysis began as early as 1930s and 1940s (McNally et al., 1947). However they did not become a major focus of research until the 1960s and 1970s. Research interest has obviously grown since that time and has been mainly directed toward the development of glow discharge sources, the study of the physical characteristics of the glow discharge and, most of all, the possibility of using glow discharge spectroscopic techniques for several analytical applications (Winchester et al., 2004).

Despite its first major use being in the steel industry as a fast bulk analysis of conducting materials (Grimm, 1967), nowadays GD-OES has become a widely used technique for rapid depth profile analysis of surfaces, thin films and coatings. Moreover, in recent years it has gained further interest with the introduction of the *radio frequency glow discharge*. This technique can, in fact, be applied also to non-conductive materials as a radio frequency field is providing the power to sustain the plasma. Direct current and RF show very similar performance, in both depth resolution and sensitivity, when applied to electrically conducting materials. However, non-conducting materials can be analyzed only with RF-powered discharges (Nelis and Pallosi, 2006).

In general, a glow discharge is a plasma sustained between two electrodes that are immersed within a reduced pressure, inert gas environment. In a HORIBA Jobin-Yvon GD-Profiler 2 the sample, which serves as the negatively charged electrode, is mounted on an O-ring, outside of the plasma chamber (the anode being a grounded copper tube), making sample placement fast and simple (Figure 2.4). Once the sample is set, the chamber is pumped continuously using a mechanical pump. Common discharge-support gas pressures are in the range 100-1500 Pa and argon is the usual

discharge-support gas. By supplying a RF-power to the sample, it is possible to create a plasma in the tubular anode, the inner diameter of which (commonly 4 mm, but possibly ranging from 2 to 8 mm) defines the analysis spot size, as the plasma is restricted to this area. When the discharge gas breaks down electrically, forming electrons and positively charged ions, the latter are accelerated towards the sample by the electric field (step (1) in Figure 2.4) and the ion bombardment of the surface of the sample causes the erosion of the material (sputtering). When entering the gas phase environment of the glow discharge, the sputtered atoms are excited by collisions with high energy electrons, metastable argon atoms and ions (step (2) in Figure 2.4). De-excitation of the excited species causes the emission of photons characteristic of the material, which are collected using an optical spectrometer (step (3) in Figure 2.4). As the sample is continuously sputtered, the collected light reflects the temporal evolution of the sputtered species (Nelis and Payling, 2003; Winchester et al., 2004).

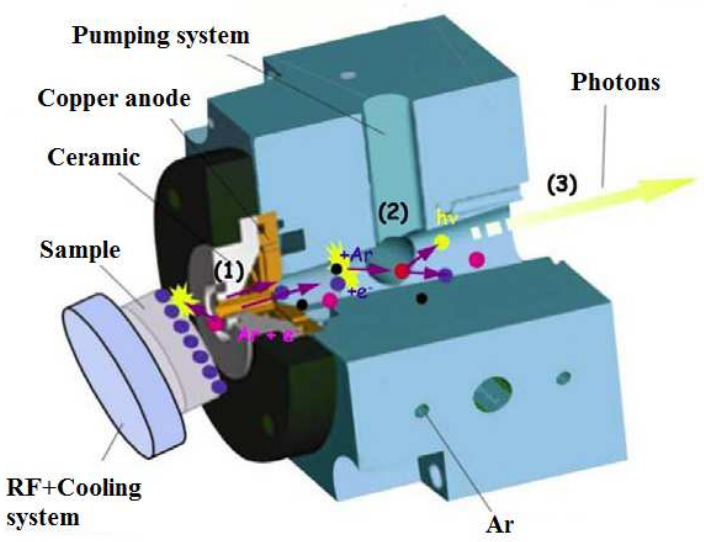

Figure 2.4.: Schematic representation of the sample holder and the plasma chamber in a HORIBA Jobin-Yvon GD-Profiler 2 (HORIBA Jobin Yvon).

In Figure 2.5 a schematic representation of a HORIBA Jobin-Yvon GD-Profiler 2 is given. The light emitted from the plasma is brought to the spectrometer entrance by a transfer optic system made of one or several lenses (Figure 2.6). The main optical component of the GD-Profiler 2 is the polychromator, although an additional monochromator can be available.

The optical configuration of the polychromator, as represented in Figure 2.7, is the Paschen Runge mounting, with a concave grating (with 2400 lines/mm) placed on the focal curve (the Rowland circle) together with entrance and exit slits. The exit slits are engraved on a metal strip (the optical mask), which is marked in red in the figure. These slits can be changed according to the user's needs. The spectral range covered by the grating of the polychromator goes from the VUV to the visible range ($120 - 600$ nm). When elements emitting in the red are required (such as K, F and Li), the zero order is used in order to mount a second polychromator equipped with a dedicated grating designed for the IR region. This is called "flat field" and is made of a parabolic shaped grating (with 1200 lines/mm) focusing on a plane and not on a circle.

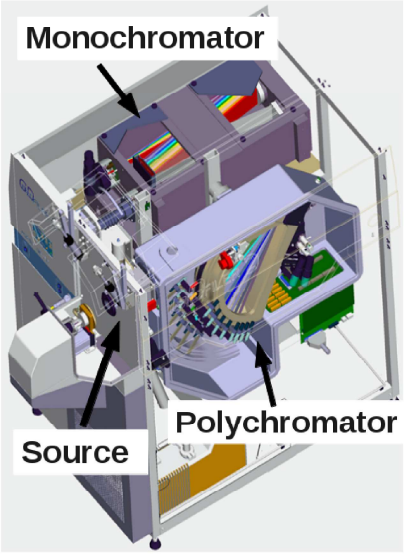

Figure 2.5.: Schematics of a HORIBA Jobin-Yvon GD-Profiler 2 (HORIBA Jobin Yvon).

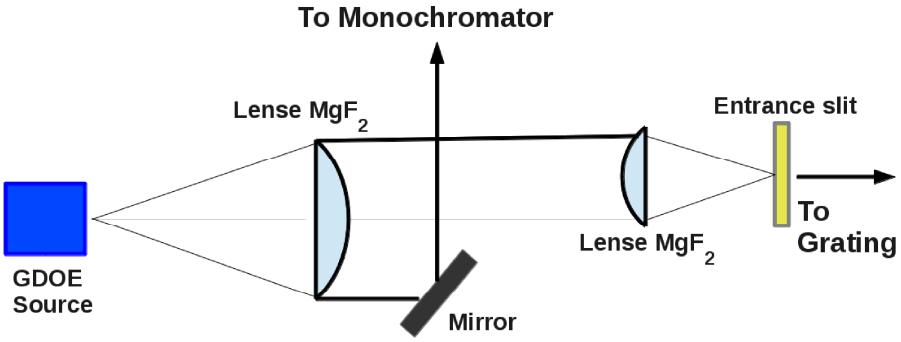

Figure 2.6.: Optical interface block diagram (HORIBA Jobin Yvon).

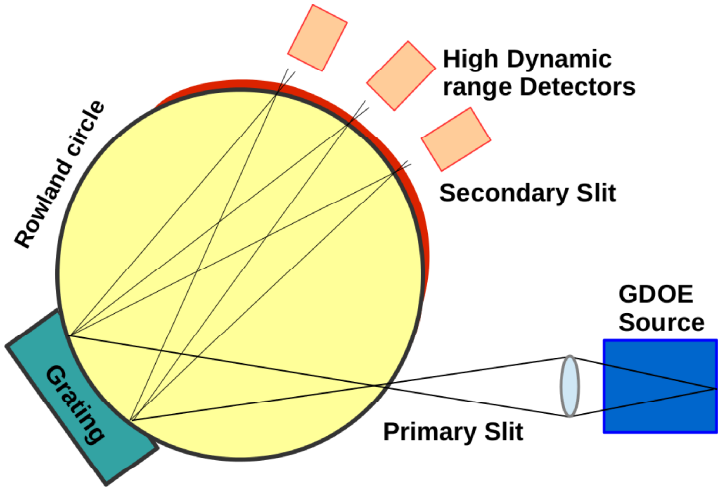

Figure 2.7.: Schematics of the spectrometer with the concave grating, the identification of the Rowland circle and the position of the High Dynamic range Detectors for the measurements of individual spectral lines (HORIBA Jobin Yvon).

The measurement of the individual lines is done using the **High Dynamic range Detectors** (HDD), for which HORIBA Jobin-Yvon holds a patent. The analytical specificity of the glow discharge technique is its capability to measure in depth profile multi-layered samples for which an element could be a trace ($\sim$ ppm) in one layer but become a major one in the one after. The dynamic range of the detector should therefore be very large, covering from the ppm to the 100 %. Moreover, as the technique provides an ultra-fast sputtering, the response of the detectors should also be ultra-fast, leaving no time for low signals integration. The HDD can respond to these challenges. In fact, when normal photomultiplier tubes (PMTs), which operate at a constant voltage (400-1000 V), are applied, the dynamic range of the glow discharge is limited. For each spectral line, depending on the intensity of the signal, the voltage value of the PMT is set, but the variation of the concentration from one layer to the other cannot be efficiently recorded. HDDs are PMTs with an automatic adjustment capability of their supplied voltage. In this way, a true dynamic range on all lines is guaranteed and no pre-adjustment of the instrument has to be done for unknown samples.

It must also be remembered that RF-GD-OES is a comparative technique. When quantitative information is needed, the concentration of the different elements can be inferred from the intensity of the characteristic spectral lines (arbitrary units) through calibration against known reference materials. Obviously such calibration is not universal. It is not the instrument that is calibrated, but a certain method dedicated and adapted to a specific kind of materials.

To study the evolution of the carbon incorporation in μc-$Si_{1-x}C_x$:H with the variation of the deposition parameters, it was decided to define the total carbon-to-silicon ratio in the sample as R_C = [C]/[Si], where [C] and [Si] are respectively the line intensities for carbon and silicon, as measured from the sputtering profile (an example is given in Figure 2.8). This quantity is then calibrated by measuring this ratio in a reference monocrystalline silicon carbide sample.

Finally, RF-GD-OES is not the only technique capable of depth profiling. Some of its main competitors are secondary ion mass spectrometry (SIMS)

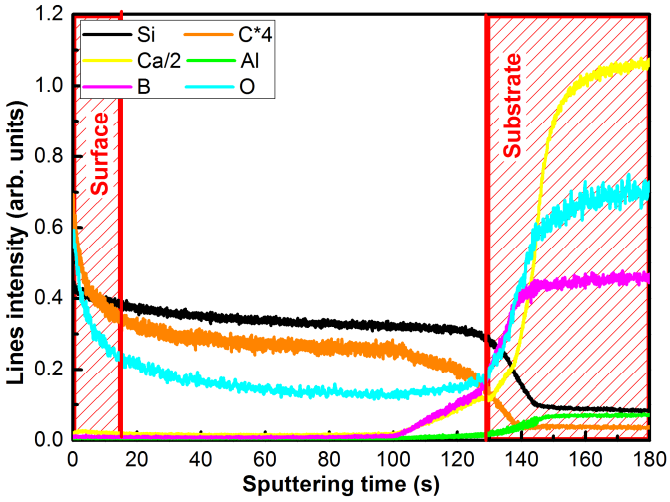

Figure 2.8.: Sputtering profile (lines intensity vs. sputtering time) obtained for a μc-$Si_{1-x}C_x$:H sample. Surface and substrate interfaces are highlighted with red lines.

and X-ray photo-electron spectroscopy (XPS). In Table 2.1 the main characteristics of these techniques are summarized and compared (Escobar Galindo et al., 2009). All of these methods are destructive techniques that use the sputtering of the surface of the material to provide the elemental distribution as a function of the erosion time. But while XPS and SIMS rely on the high energy bombardment (2-5 keV) of the sample, using an ion gun in high vacuum ($< 10^{-5}$ Pa), the RF-GD-OES technique, as it has been previously explained, uses a reduced pressure plasma and ions that are attracted to the sample with energies of ~ 50 eV. Moreover, both XPS and SIMS suffer from preferential sputtering artifacts which for the first technique derive from the analysis of the residual surface composition and for the latter from the flux composition of sputtered ions. Another important characteristic is the maximum depths of analysis. While for XPS this parameter is restricted to the sub-μm range, thus limiting the study of thicker layers, SIMS and RF-GD-OES are capable of analyzing depths of several μm with nm resolution although without chemical information. Thus, it is clear that no surface-analysis technique stands out and that the choice of a technique depends on several factors (e.g., the system to be studied, the accuracy to be achieved, and the experimental time required).

Table 2.1.: Comparative summary of the main characteristics of different surface-analysis techniques (Escobar Galindo et al., 2009).

	SIMS	**XPS**	**RF-GD-OES**
Excitation probe	Ions	Photons (XR)	Ions
Emission (detection)	Ions (m/e)	Electrons	Photons (λ)
Sputtering	Ion beam (< 10 keV)	Ion beam (< 10 keV)	RF < 50 eV
Crater Effect	Yes	No	Yes
Max. Depth Analysis (μm)	5	0.1	> 100
Depth Resolution	$0.5 - 2.5$	$0.5 - 2.5$	1
Lateral Resolution	10	10^2	10^6
Chemistry Information	Yes	Yes	No
Detection Limit (ppm)	$10^{-1} - 10$	10^3	1
Elemental Range	All	$Z > 2$	All
Calibration Method	Complex	Easy	Complex
Crater Diameter (mm)	< 1	< 1	4
Vacuum (mbar)	10^{-10}	10^{-10}	10^{-2}
Acquisition Time	Slow (hours)	Slow	Very fast (seconds)

Fourier Transform Infrared Spectroscopy

RF-GD-OES is a useful technique for the quantification of the total carbon incorporated in the alloys. One of its disadvantages is that no information of the chemical composition, and thus of the chemical order in the alloy (i.e. bonds), can be obtained. This complementary information can be supplied by Fourier Transform Infrared Spectroscopy (FTIR). This technique can be used to study the local chemical environment of the interested atomic species and can give both qualitative and quantitative information after deconvolution of the absorption spectra. For these measurements layers are deposited on a highly resistive (10000-20000 Ω) FZ c-Si wafer, the reason being the need of an IR transparent substrate. The absorption of the substrate is removed using a bare FZ c-Si wafer as a reference.

Spectra were acquired in the 400-4000 cm^{-1} range, using a Fourier transform infrared spectrometer Brüker Equinox 55. In Figure 2.9 an example of FTIR absorption spectrum of an a-$Si_{1-x}C_x$:H sample is presented. Two main absorption bands can be observed. The first one, in the 500-1000

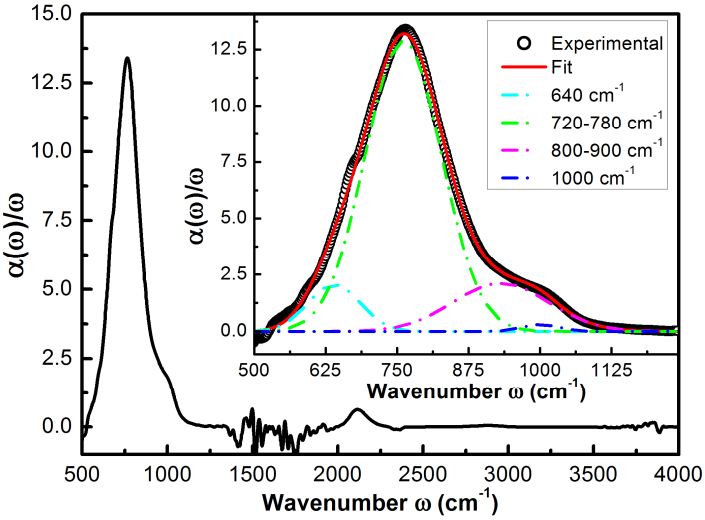

Figure 2.9.: IR absorption spectrum for an a-$Si_{1-x}C_x$:H sample. In the inset, the deconvolution of the first absorption region is shown. The experimental points are represented by black open circles, the fit of the data by a straight red line and the deconvoluted absorption bands by dashed-dotted lines.

cm^{-1} range, can be considered as the superposition of four different bands (Wieder et al., 1979):

- 640 cm^{-1}, the Si — H *wagging mode*;
- 720-780 cm^{-1}, the Si — C *stretching mode*;
- 800-900 cm^{-1}, the Si — H *bending mode*;
- 1000 cm^{-1}, the C — H *wagging mode*;

while the second one, in the 2000-2100 cm^{-1} range, is due to the superposition of two bands (Cardona, 1983):

- 2000 cm^{-1}, the Si — H *stretching mode*;
- 2090 cm^{-1}, the $Si-H_2$ *stretching mode*.

The other two absorption regions at 1500-2000 cm^{-1} and 3500-4000 cm^{-1} are due to the absorption of residual atmospheric water in the measurement system and can be ignored. It is noteworthy that the band due to C — H stretching modes, that should be located at 2800-3000 cm^{-1}, cannot be observed for the samples discussed in this work. Such virtual absence, in the low carbon content range, should not be over-interpreted since the absorption strength of C — H bonds is very low if carbon is bonded to silicon (Wieder et al., 1979; Bullot et al., 1987).

The Si-C and the Si-H bond concentration (N_{Si-C} and N_{Si-H}, respectively) can be calculated from the integrated area of the deconvoluted band at 780 cm^{-1} and 2000 cm^{-1}, respectively, using the following relation

$$N_{X-Y} = A_{X-Y} \cdot \int \frac{\alpha(\omega)}{\omega} d\omega \tag{2.4}$$

where A_{X-Y} is the inverse cross-section for the X — Y bond and the integration is done over the deconvoluted peak, after the subtraction of a baseline.

The value of the inverse cross section is specific of the bond and has been taken as $A_{Si-C} = 2.13 \times 10^{19}$ cm^{-2} (Basa et al., 1990; U. Coscia, Ambrosone, Lettieri, Maddalena, Rava, et al., 2003) and $A_{Si-H} = 1.4 \times 10^{20}$ cm^{-2} (Fang et al., 1980). In the inset in Figure 2.9 an example of deconvolution of the first absorption region is shown.

Spectroscopic Ellipsometry

Once the amount of carbon incorporated in the alloy is determined, the influence of the alloying with this element can be studied looking also at the evolution of the optical band gap. A way to determine this parameter is by spectroscopic ellipsometry, which is a sensitive non-destructive technique that provides information about the optical properties of a material.

The main principle of this technique, relies on the measurement of the change in the polarization state experienced by linearly polarized light after reflection on the sample. Measurements were performed using a UVISEL spectroscopic ellipsometer from HORIBA Jobin-Yvon in the 1-4.7 eV spectral range.

The measured dielectric function, called the *pseudo-dielectric function* $<\epsilon>$, contains information about the film and its substrate, as the signal measured by ellipsometry is a combination of contribution from different parts of the sample. For low photon energies the penetration depth can be larger than the actual thickness of the sample, thus interference fringes appear. These are due to the interaction between the beam reflected at the film surface and that reflected at the substrate-film interface. With increasing photon energy, the film becomes opaque and no influence of the reflection at the substrate can be observed.

In Figure 2.10 the imaginary part of the pseudo-dielectric function $<\epsilon_i>$ of an a-$Si_{1-x}C_x$:H sample, co-deposited on Corning "Eagle" glass and FZ c-Si, is shown. It can be seen that the low energy part of the spectra depends only on the type of substrate. The different amplitude of the interference fringes is linked to the difference in the refractive index of the substrate and the layer, being higher in the case of the deposition done on Corning "Eagle" glass.

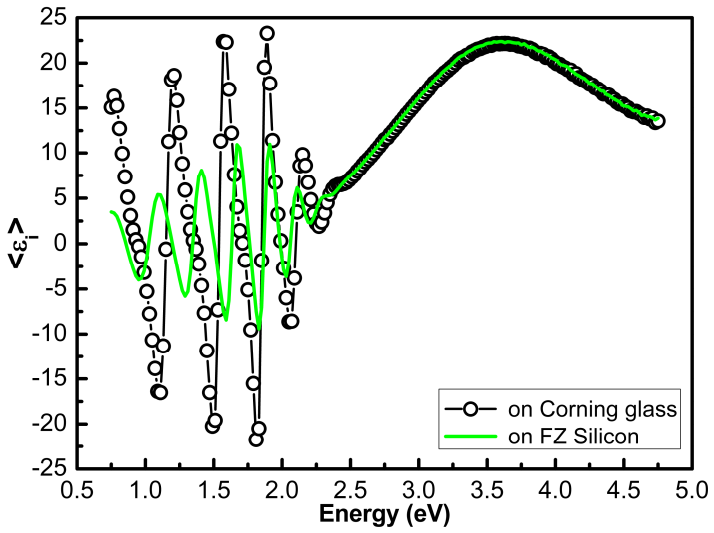

Figure 2.10.: Imaginary part of the pseudo-dielectric function $<\epsilon_i>$ of the same material deposited on Corning glass (O) and Float Zone silicon (—).

Inferring the optical properties of the studied film from $<\epsilon>$ is one of the major challenge in ellipsometry. This is done by comparing the experimental data with the pseudo-dielectric function calculated based on a specific model of the sample structure. For this analysis, in this work it was decided to use a simple model including the substrate, the main layer and the roughness. In Figure 2.11 an example of such modeling is given. A two Tauc-Lorentz (Jellison et al., 1996) dispersion formula for microcrystalline layers and a single Tauc-Lorentz dispersion formula for the amorphous ones were used to parameterize the dielectric function $\epsilon(E) = \epsilon_r(E) + i \cdot \epsilon_i$ as a function of the photon energy E, where $\epsilon_r(E)$ and $\epsilon_i(E)$ are the real and imaginary parts respectively. From the fitting of the experimental results, an estimation of the optical band gap and of the thickness of the layers was obtained.

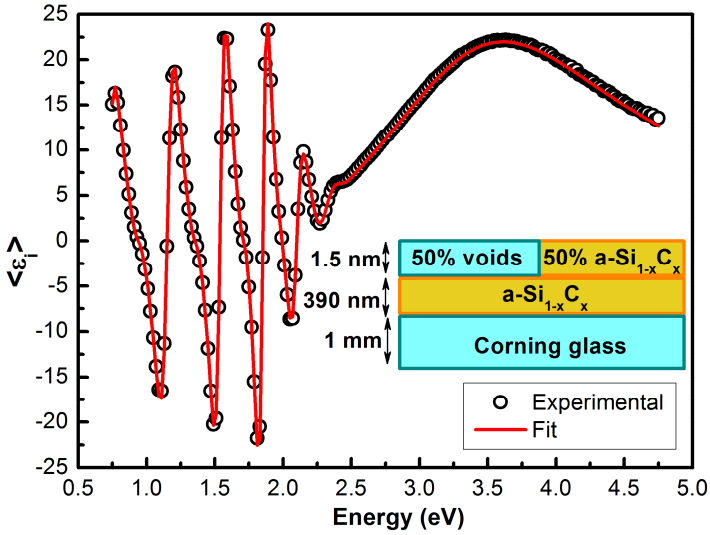

Figure 2.11.: Example of modeling. The resulting fit (—) of a measured ellipsometric spectrum (○) of a-$Si_{1-x}C_x$:H on glass. In the inset, the model used to fit the experimental data, made of a single layer plus roughness, is shown. The thicknesses reported are the results of the modeling procedure.

UV-VIS Transmission

To determine the band gap of a material it is also possible to perform transmission measurements in the ultraviolet-visible spectral region. In this work these measurements were done at room temperature using a PerkinElmer Lambda 950 UV/VIS Spectrometer and a Corning "Eagle" substrate as a reference. In this configuration the light is incident on the sample and the transmission is collected as a function of the wavelength (measurements are performed in the 250-2500 nm range). Experimental data were then treated with the software *Diplot*, that was developed by Dr. Erwin Lotter. This software is using a model to reproduce optical transmission measurements and calculate the absorption coefficient, varying several parameters such as the thickness of the layer, the Urbach energy, the optical band gap...The variation of these parameters is continued until the convergence between the experimental data and the calculated curve is reached for both transmission and absorption spectra. In Figure 2.12 an example of the transmission and absorption spectra obtained using the Diplot software is given. Spectra in (b) are calculated from the spectra in (a).

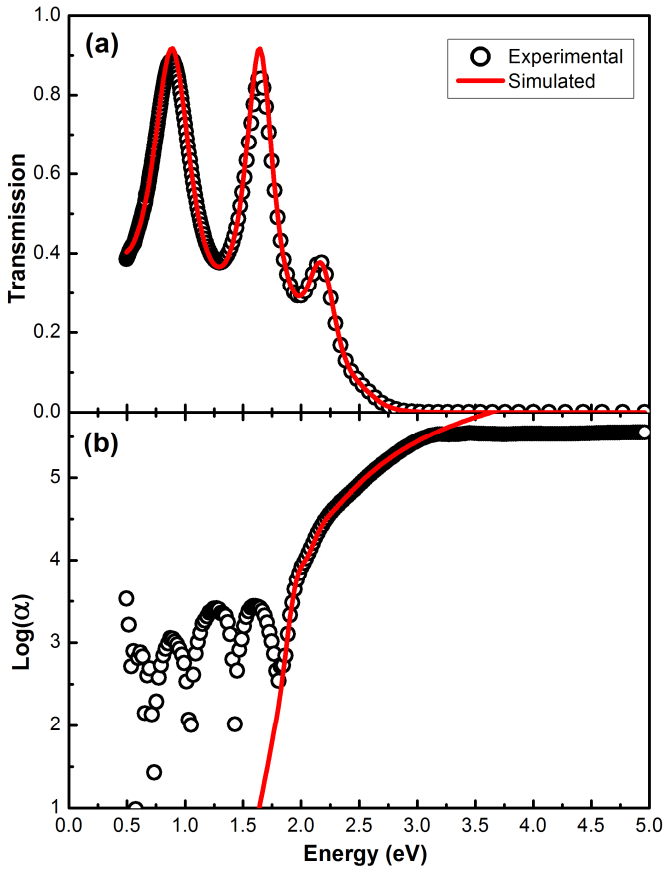

Figure 2.12.: (a) Transmission and (b) absorption spectra of a μc-$Si_{1-x}C_x$:H sample, obtained from transmission measurements and fitting with Diplot. In both figures O correspond to the experimental data and the red continuous line to the modeling.

Atomic Force Microscopy

Atomic force microscopy (AFM) is a technique to obtain images and other information (conductivity, variation in the chemical nature, etc..) of a sample, at the nano-scale. An AFM works by scanning a very sharp (end radius $\sim$ 10 nm) probe along the sample surface, carefully maintaining the force between the probe and the surface at a set, low level (see Figure 2.13). Usually, the probe is formed by a silicon cantilever with a sharp integrated tip. When the tip is brought into proximity of the sample, forces between the tip and the surface of the sample lead to a deflection of the cantilever. Such vertical bending is detected using a laser focused on the back of the cantilever and reflected onto a photodetector (*optical lever*). The probe is then moved over the sample by a scanner, typically a piezoelectric element, which can make extremely precise movements. The combination of the sharp tip, the very sensitive optical lever and the highly precise movements of the scanner, combined with the careful control of probe-sample forces, allow the extremely high resolution (nanometer) of the AFM.

For this work, measurements were done in air, using a Dimension 5000 AFM by Digital Instruments Inc., operated in tapping mode. In this mode an additional piezoelectric element is used to oscillate the cantilever at its resonant frequency. When the oscillating probe approaches the sample surface, the oscillation changes due to the interaction between the probe and

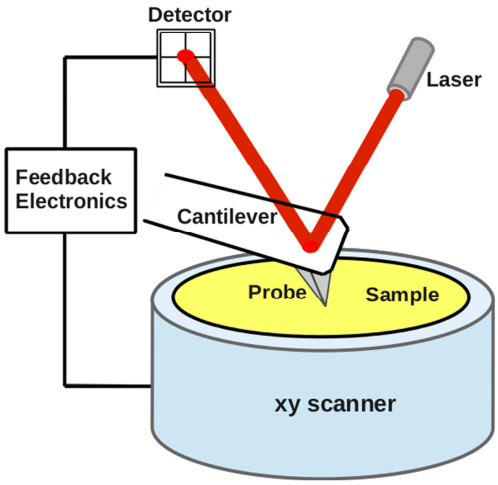

Figure 2.13.: Schematic representation of an AFM operation.

the force field from the sample. The effect is a damping of the cantilever oscillation, which leads to a reduction in the frequency and amplitude of the oscillation, monitored by the optical lever. The scanner adjusts the z height via the feedback loop to maintain the probe at a fixed distance from the sample. The primary reason for using this oscillating mode, is to take advantage of the signal-to-noise benefits associated with modulated signals. Moreover, the use of the tapping mode lessens the damage done to the surface and the tip, as it prevents the cantilever dragging across the surface (Eaton et al., 2010).

Raman Spectroscopy

Raman spectroscopy is probably the most widely used technique to estimate the crystalline volume fraction of a microcrystalline silicon-based sample. It relies on the inelastic scattering, or *Raman scattering*, of monochromatic light with the sample in order to provide information about the chemical environment of the atoms. Like FTIR, this is a vibrational spectroscopy based on the vibrating dipole formed by bonded atoms. The main difference between these two techniques lies in the nature of the molecular transitions taking place. For a transition to be "Raman-active" there must be a change in the polarizability of the molecule during the vibration. On the other hand, for an "IR-active" transition, the molecule must undergo dipole momentum change during vibration. For molecules with a center of symmetry, these two phenomena are mutually exclusive. In this case, vibrations that are symmetric (anti-symmetric) with respect to the center of symmetry, are Raman-active but IR-inactive (IR-active but Raman-inactive).

When the sample is illuminated with a laser beam, usually from a laser in the visible, near infrared, or near ultraviolet range, most of the incident light is scattered elastically by Rayleigh scattering (the incident and the scattered light have the same wavenumber). Only a small fraction is scattered at a shifted wavelength, due to the absorption or emission of a phonon (Stokes and Anti-Stokes processes). The shift in energy gives information about the vibrational modes in the analyzed system. The light from the illuminated spot is collected with a lens and sent through a monochromator. Wavelengths close to the laser line (due to the elastic Rayleigh scattering) are filtered out, while the rest of the collected light is dispersed onto a detector.

In a perfect crystal, because of its periodicity and translation symmetry, only certain phonon transitions are allowed. Thus, Raman scattering can only appear at specific wavenumbers. On the other hand, in amorphous materials this translation symmetry is lost and selection rules for allowed and forbidden phonon transitions are relaxed. Therefore, no discrete lines appear, but the Raman spectra are characterized by broad bands.

To analyze a-$Si_{1-x}C_x$:H and μc-$Si_{1-x}C_x$:H alloys, Raman spectra were obtained in the 250-1000 cm^{-1} range using a LABRAM Aramis system, Confocal Raman Microscope by HORIBA Jobin-Yvon, equipped with 473 nm, 532 and 633 nm lasers. The unpolarized incident beam is focused on the sample and the backscattered light is analyzed by a monochromator with a Charge Coupled Detector (CCD). The different wavelengths can be used to probe the samples at different depths. To be able to compare different samples, the set-up conditions to obtain the spectra, such as magnification, filters and integration time, were kept constant for each set of samples.

As it has been said, Raman spectroscopy is probably the most commonly used technique to determine the crystalline volume fraction (f_c^{Raman}) in a sample. The main disadvantage is that there are many ways to estimate this parameter. The first method would be to fit the experimental data with several Gaussian peaks, corresponding to the different vibrational modes, after the subtraction of a baseline (Vepřek, Sarott, et al., 1987; Viera et al., 2001). Another method consists in subtracting a typical amorphous spectrum and to consider that the remaining area represents the crystalline fraction (Smit et al., 2003). In this work, instead of subtracting a scaled amorphous spectrum, the deconvolution of the spectra in the 250-600 cm^{-1} range was performed in the following way. First the Raman spectrum of an amorphous sample deposited in similar conditions was fitted with three Gaussians, to determine the position and the full width at half maximum of the longitudinal acoustical, longitudinal optical and transversal optical mode of the amorphous phase. Then the Raman spectra of microcrystalline samples were fitted fixing these parameters and adding two additional components for the grain boundaries and the c-Si. Therefore, a total of five Raman-active modes were used to perform the deconvolution of the spectra:

- 310 cm^{-1}, *Longitudinal Acoustic* (LA) mode in a-Si:H;
- 450 cm^{-1}, *Longitudinal Optical* (LO) mode in a-Si:H;
- 480 cm^{-1}, *Transversal Optical* (TO) mode in a-Si:H;
- 510 cm^{-1}, corresponding to grain boundaries or the hexagonal phase induce by the presence of twin boundaries and stacking faults;
- 520 cm^{-1}, *Transversal Optical* mode in c-Si.

An example of such a deconvolution is given in Figure 2.14. Actually, it cannot be neglected that the peaks can be fitted using Gaussian or Lorentzian functions (Iqbal et al., 1981). Bustarret et al. proposed that while Gaussians are more suitable for small grain sizes, an asymetrical Lorentzian peak would be more appropriate in case of crystallites with an average size larger than $\sim$ 13 nm (Bustarret et al., 1988).

The crystalline volume fraction f_c^{Raman} is always defined from the integrated scattered intensities. The simplest way to define this quantity is to

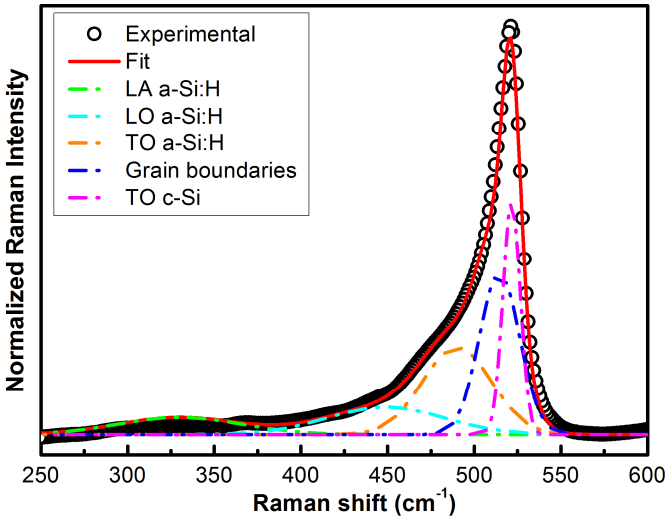

Figure 2.14.: Common deconvolution of the Raman spectrum of a μc-$Si_{1-x}C_x$:H sample. The experimental points are represented by black open circles, the fit of the data by a straight red line and the deconvoluted Gaussian bands by dashed-dotted lines.

consider only contribution from the crystalline and the amorphous components, leading to:

$$f_c^{Raman} = \frac{I_{520}}{I_{480}}, \tag{2.5}$$

where I_{480} and I_{520} are the areas of the deconvoluted peaks at 480 cm^{-1} and 520 cm^{-1} (Mishima et al., 1982). However, a more appropriate definition (still considering only contributions from the crystalline and amorphous fractions), can be given as:

$$f_c^{Raman} = \frac{I_{520}}{y \cdot I_{480} + I_{520}}, \tag{2.6}$$

where y is the Raman emission cross-section ratio (Tsu et al., 1982; Okada et al., 1985). Commonly y is taken equal to 1, but it has been actually reported that this parameter varies as a function of the crystallite size and laser wavelength (Bustarret et al., 1988). This means that an additional technique should be used to estimate the crystallite size. At the same time, it must be remembered that small sized crystallites and grain boundaries are responsible for the breakdown of the wavenumber selection rule, thus the intermediate peak at 510 cm^{-1} should be taken into account when calculating f_c^{Raman} (Wakagi et al., 1993; Kaneko et al., 1994; Johnson, Kherani, et al., 2006), leading to

$$f_c^{Raman} = \frac{I_{510} + I_{520}}{y \cdot I_{480} + I_{510} + I_{520}} \tag{2.7}$$

where I_{480}, I_{510} and I_{520} are the integrated intensities of the bands centered at 480 cm^{-1}, 510 cm^{-1} and 520 cm^{-1}, respectively. In this work it has been chosen to estimate the crystalline volume fraction using the expression in Equation 2.7, taking $y = 1$.

Finally, as the power density of the laser used to perform the Raman measurements is very intense ($\sim 10^6$ W/cm^2 when using a 100x objective) it is possible that the local heating is inducing the crystallization of the

amorphous fraction. To avoid this effect, neutral density filters are applied to reduce the transmitted power. First a high neutral density filter is used to ensure that no shift towards lower wavenumbers or crystallization is taking place. Then, the power of the laser is increased by changing the neutral density filter until a phase change is observed. Finally, the measurement is performed in the center of the sample, using the appropriate neutral density filter to reduce the incident power. Usually, a ND 3 filter was the most appropriate one, reducing the incident power density by a factor of 1000.

X-Ray Diffraction

X-ray diffraction (XRD) is a technique that can give information about both the macroscopic and microscopic structures in the layer. In fact, it can be used to:

- identify the crystallographic phases present in the analyzed material, which are indicated by the presence of the diffraction peaks;
- estimate the crystalline fraction of the layer;
- estimate the crystallites size;
- evaluate stress from the displacement of the diffraction peaks, corresponding to a variation in the inter-plane distances.

The possible appearance of the diffraction peaks at an angle θ is described by the *Bragg law*:

$$2d \sin\theta = n\lambda \tag{2.8}$$

where d is the inter-planes distance and λ the X-ray wavelength. This law states that if the atomic planes have a constant distance d, then it exists an angle θ between these planes and the X-rays for which the path length difference of the scattered X-rays is equal to a multiple integer n of their wavelength.

For the analysis of thin films, for which the penetration depth in the standard Bragg-Brentano configuration would exceed the layer thickness by far, grazing incidence X-ray diffraction (GIXRD) measurements are more advantageous. In this configuration the primary beam enters the sample at very small angles of incidence (θ_i), causing the path traveled by the X-rays to increase significantly (Birkholz, 2006).

In this work, measurements were performed using a D8Discover Brüker-AXS diffractometer. The X-rays were generated by electrons accelerated in a 40 kV field and bombarding a copper anode (Cu_{K_α}). To perform the measurements in the GIXRD configuration, the use of a parabolic mirror (the so-called *Göbel mirror*) was required to convert the divergent radiation emitted from the source into a parallel beam (see Figure 2.15). On the primary side (the source side), divergent slits of small opening angles are used to reduce the X-rays footprint; in this way, it is possible to avoid the illumination of the substrate holder, which could lead to the occurrence of unexpected Bragg reflections. Finally, on the detector side, a Soller slit is added in order to reduce the axial divergence, as depicted in Figure 2.16.

The different measurement geometry has important consequences for the orientation of the scattering vector. In the symmetric $\theta/2\theta$ configuration (standard Bragg-Brentano) the scattering vector is always parallel to the surface normal. Therefore, the crystallographic lattice planes causing a diffraction peak are all oriented in parallel to the substrate plane. On the other

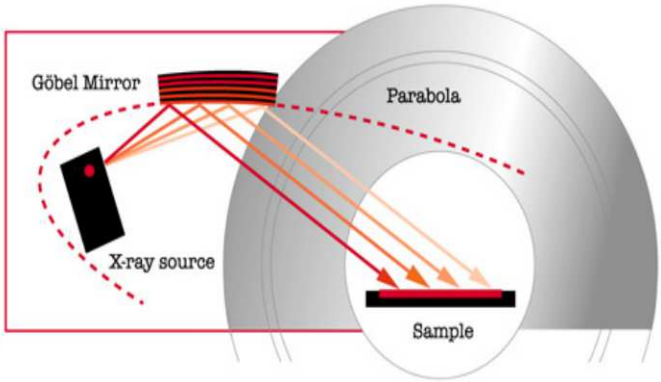

Figure 2.15.: Representation of the adjustment of the X-rays to the focus of the parabola of the Göbel mirror, resulting in a reflected parallel beam (Birkholz, 2006).

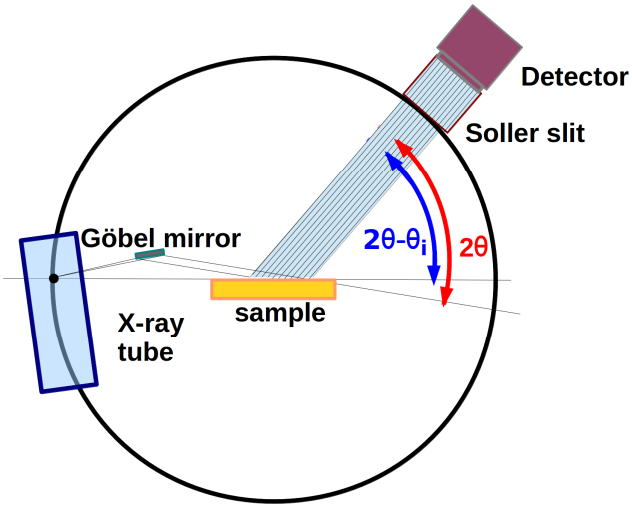

Figure 2.16.: Diffractometer configuration for GIXRD measurements. The plane of the figure is the scattering plane.

hand, in the grazing incidence configuration, the scattering vector is neither parallel to the surface normal nor its orientation remains constant, but it changes in the course of the measurement (from the start position close to the surface normal, towards an end position ever closer to the incoming beam). This means that in the GIXRD configuration the diffraction peaks are caused by lattice planes that are neither parallel to the substrate surface nor to each other. In the case of randomly oriented thin films, a comparable pattern will be measured in both the Bragg-Brentano and grazing-incidence configuration. However, if some texture is present, the GIXRD will identify such existence, but it will not be sufficient to identify which is the preferential orientation. Indeed, to infer such information, the different tilt of the crystalline domains with respect to the substrate surface, should be considered.

In Figure 2.17 the penetration depth of the X-rays in silicon is shown as a function of the incident angle θ_i on a semi-log scale. The critical angle θ_c ($\sim 0.22^\circ$ in silicon) is the angle for which total reflection occurs. When varying θ_i in the proximity of θ_c, the sample is probed at depth that can vary by several orders of magnitude, whereas for higher incident angles

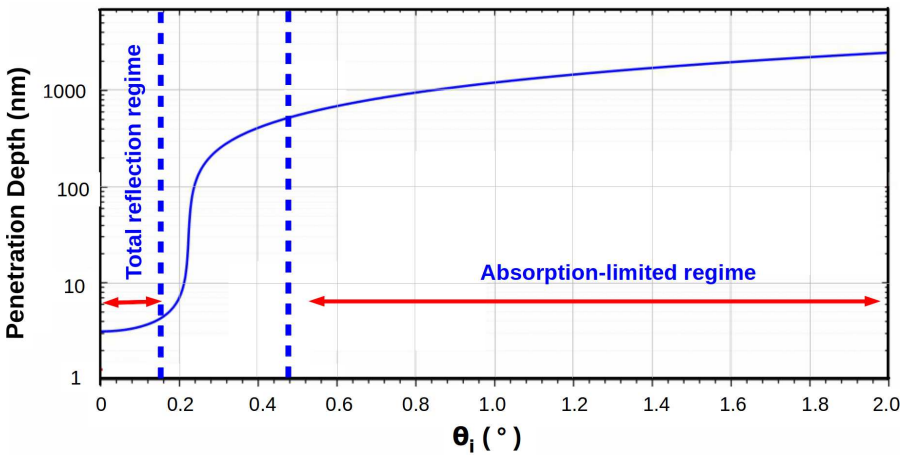

Figure 2.17.: X-rays penetration depth as a function of the incident angle θ_i in silicon. The dashed lines delimit the three different regimes.

the change in penetration depth is far less pronounced. Therefore, being the thickness of the layers known, it is crucial to chose the correct incident angle to limit X-rays penetration deep into the substrate.

Due to the finite size of the crystallites in the direction perpendicular to the diffracting planes, the interferences at the angles close to those satisfying the Bragg condition will not be completely destructive and the peaks will have a certain width, which can be related to the crystallites size. Thus, it is also possible to determine the average size δ of the crystallites using the *Scherrer formula*

$$\delta = \frac{K\lambda}{w \cos\theta_B}, \tag{2.9}$$

where K is a factor depending on the crystallites shape and orientation, λ is the X-rays wavelength in Angströms, w is the full width at half maximum of the peak in radians and θ_B is the Bragg angle. Typical values of K vary from 0.85 to 0.99. For unknown shapes and distribution of crystallites, it is often chosen to set $K = 1$, which introduces a 20 % error in δ at most (Godet et al., 1987). For this analysis it has been chosen to set $K = 1$.

Finally, from the intensity of the diffraction peaks it is possible to determine if the layer is textured. Once again, it must be pointed out that GIXRD will highlight the existence of a texture, but it will not be sufficient to determine the preferential orientation. In a 2θ scan from 20° to 65°, the Bragg reflections of the cubic silicon crystalline phase are located at 28.44°, 47.3° and 56.12°, corresponding respectively to the (111), (220) and (311) diffraction planes. It is often observed also the reflection from the hexagonal phase at $\sim 27^\circ$, which will be discussed in details in section 3.3.3. To appraise the existence of a texture, the integrated intensities ratio of the (220) and the (111) is compared to the powder standard of cubic silicon. Depending on the growth conditions, microcrystalline silicon may exhibit a random orientation, which means that the crystal growth appears in all possible directions with the same probability. Moreover, in a polycrystalline growth, each grain usually has a different orientation from the adjacent one (Houben, Luysberg, and Carius, 2003). In these conditions, the observed intensity ratios of the cubic reflections are consistent with those of the powder standard cubic silicon, which are (111) : (220) : (311) = 1 : 0.55 : 0.3, according to the American Standard for Testing Materials (ASTM) card number 27-1402 (Schicho et al., 2012).

Transmission Electron Microscopy

The most powerful tool to study the structural properties of materials is transmission electron microscopy (TEM). With this technique, a direct observation of the material structure obtained through different deposition processes can be obtained. However, several drawbacks can be found, such as the difficult and time consuming preparation of the samples, along with its destructive nature, the high cost of the apparatus and its operation, all of which made quite unsuitable the systematic study of the samples. Nevertheless, for few selected alloys the investigation of the effect of the deposition parameters on the microstructural properties has been performed.

In TEM analyses, the transmission of a focused electron beam is used to form images of a sample in an analogous way as a light microscope. However, as electrons are used rather than light to illuminate the sample, a significantly higher resolution can be achieved than light-based imaging techniques (Williams et al., 2009).

A transmission electron microscope is constituted of a vacuum system in which the electrons travel, an electron emission source for generation of the electron beam, two or three condenser lenses to focus such beam on the sample, an objective lens to form the diffraction in the back focal plane and the image of the sample in the image plane and some intermediate lenses to magnify the image or the diffraction pattern on the screen (projective system). In Figure 2.18 a simplified representation of the beam path leading to the first intermediate image in the image plane of the objective lens is given. Electrons, which come from the condenser system of the TEM, are scattered by the sample, situated in the object plane of the objective lens. Those scattered in the same direction are focused in the back focal plane, and, as a result, a diffraction pattern is formed. Those coming from the same point of the object are focused in the image plane.

The TEM has two standard imaging modes: *bright field* (BF) and *dark field* (DF). A schematic representation of both modes is given in Figure 2.19. In the BF mode (Figure 2.19 (a)), an aperture (in red in the figure) is placed in the back focal plane of the objective lens allowing only the direct beam to

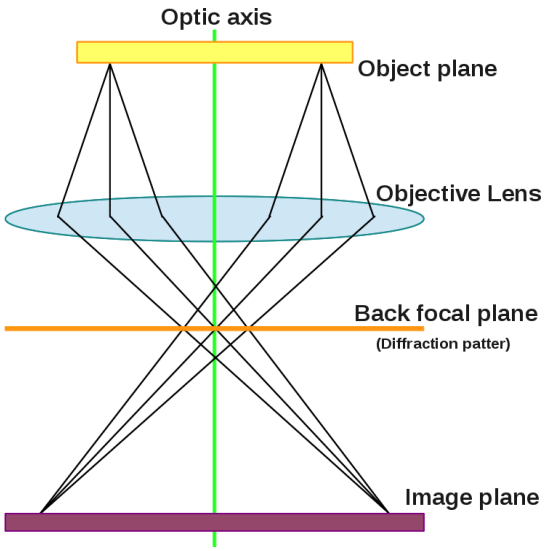

Figure 2.18.: Simplified representation of the beam path leading to the first intermediate image in the image plane of the objective lens.

pass. In this case, the image results from a weakening of the direct beam by its interaction with the sample. Therefore, mass-thickness and diffraction contrast contribute to image formation: thick areas, areas in which heavy atoms are enriched and crystalline areas appear with dark contrast. On the other hand, in the DF mode (Figure 2.19 (b)), the image is formed with electrons scattered in a specific direction, usually as a result of diffraction from a particular atomic plane or planes. In fact, while the direct beam is blocked, one or more diffracted beams are allowed to pass the objective aperture. Since diffracted beams have strongly interacted with the specimen, very useful information is present in DF images, e.g., about the presence of crystalline areas, planar defects, stacking faults or particle size.

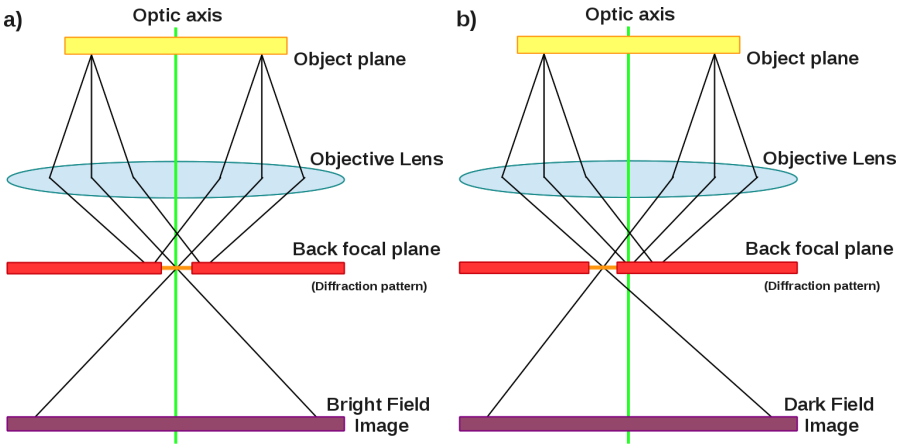

Figure 2.19.: Schematic representation of the beam path leading to (a) an image in the BF mode and (b) an image in the DF mode.

Actually, there are more complex ways to operate a TEM in order to infer additional informations about the analyzed sample. In this respect, *energy filtering* is a valuable tool for materials characterization. It can be applied for several reasons, such as increase the contrast in the TEM images or generate elemental distribution maps. The first is called *zero-loss filtering* and consists in using only the zero-loss beam to omit all inelastically scattered electrons and achieve a reduction of noise. The latter is called *electron spectroscopic imaging* and uses electrons with a well-defined energy loss (ionization edge) to obtain chemical information about the analyzed sample.

Thus, in energy filtered TEM (EFTEM) mode, images are obtained by collecting electrons that have lost a characteristic amount of energy when interacting with the sample. To select the desired plasmonic energy, a Gatan Imaging Filter (GIF) is mounted below the column of a TEM. This energy filter consists of two main parts:

1. a magnetic prism, which is used to create a curved magnetic field where electrons with different energies are dispersed. Consequently, an electron energy loss (EEL) spectrum is obtained;

2. an optical column, in which a slit located at the dispersion plane is used to select an energy range. Electrons of the selected energy pass through the lenses of the optical system producing an energy-filtered image at the end of the GIF.

Therefore, EFTEM concerns selecting a range of energy-losses from an EEL spectrum and turning them back into an image. High intensity in this image corresponds to regions generating high signals in that energy range.

By selecting energies corresponding to characteristic element signals and removing the background, it is possible to obtain element distribution images or maps (Iacona et al., 2004; Ruggeri et al., 2012).

Another type of TEM is the scanning transmission electron microscope (STEM). In this kind of microscope, a tiny, convergent electron beam is scanned over a defined area of the sample. At each spot, the generated signal is simultaneously recorded by selected detectors, building up an image. Furthermore, such a convergent beam is used to gain a highly localized signal from the specimen in analytical TEM (e.g., EDXS, EELS), and thus the combination of STEM with analytical methods is a main application in practical work.

Three types of detectors are used to obtain STEM images (see Figure 2.20)

1. *BF detector*, which is placed at the same site as the aperture in BF-TEM and detects the intensity in the direct beam from a point on the specimen;

2. *annular dark field (ADF) detector* (also known as small angle annular dark field - SAADF), which is a disk with a hole in its center where the BF detector is installed. The ADF detector uses scattered electrons for image formation, similar to the DF mode in TEM. The measured contrast mainly results from electrons diffracted in crystalline areas but is superimposed by incoherent Rutherford scattering;

3. *high angle annular dark field (HAADF) detector*, which is also a disk with a hole, but their diameter is much larger than in the ADF detector. Thus, it detects electrons that are scattered to higher angles and almost only incoherent Rutherford scattering contributes to the image. Thereby, Z contrast is achieved (Pennycook, 1989).

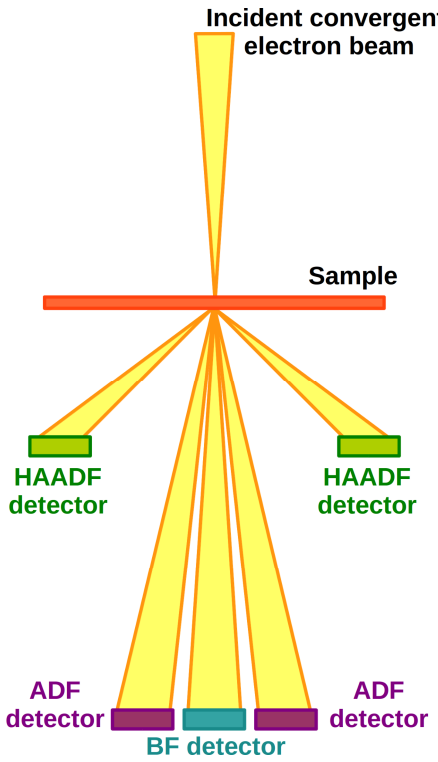

Figure 2.20.: Schematic outline of the arrangement of the various STEM detectors.

For this work, TEM analyses were performed by Rosa Ruggeri at the "Istituto per la Microelettronica e Microsistemi" (IMM) in Catania (Italy). Small and high angle annular dark field-scanning transmission electron microscopy (SAADF and HAADF STEM) and energy filtered TEM (EFTEM) analyses were performed using a JEOL JEM 2010F transmission electron microscope with a Schottky field emission gun operating at an acceleration voltage of 200 kV. The instrument is equipped with a GIF. The energy slit used to acquire energy-filtered images had a 4 eV width. Electron transparent samples were prepared by conventional mechanical polishing and argon-ion thinning.

2.3.2 Electrical characterizations

To perform electrical characterizations, coplanar ohmic contacts were made evaporating aluminum as shown in Figure 2.21, where h is the height of the contacts, L the thickness of the layer and l the inter-electrodes spacing.

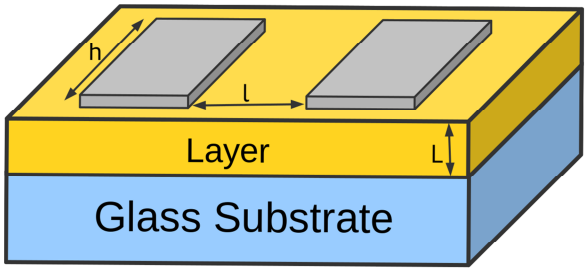

Figure 2.21.: Schematic representation of the coplanar configuration used to perform electrical measurements.

Dark Current & Steady State PhotoCurrent

The goal of *dark current* (DC) and *steady state photocurrent* (SSPC) measurements, is to deduce transport properties of the materials. Assuming a model of transport of free carriers above the mobility edge, the dark conductivity σ_{dark} can be written as

$$\sigma_{dark} = q\mu_n n_0 + q\mu_p p_0 \tag{2.10}$$

where q is the electron charge, μ_n and μ_p are respectively the mobilities of electrons and holes and n_0 and p_0 are the concentrations of free electrons and holes in the dark, respectively. For the studied materials it can be assumed that electrons are the majority carriers, with a mobility larger than that of holes, then $\mu_n n_0 \gg \mu_p p_0$ and the second term in Equation 2.10 can be neglected. Remembering that the density of free carrier can be written as

$$n(T) = \int_{E_c}^{+\infty} D_c(E) \cdot f(E,T) dE \tag{2.11}$$

where T is the temperature, E_c the conduction band (CB) edge, $D_c(E)$ the density of states (DOS) in the CB and $f(E,T)$ the Fermi function. Then, Equation 2.10 becomes

$$\sigma_{dark}(T) = \sigma_0 \cdot \exp\left\{-\frac{E_c - E_f}{kT}\right\}, \tag{2.12}$$

where $\sigma_0 = q\mu_n N_c$ represents the conductivity at the mobility edge, E_f the Fermi level and k the Boltzmann constant. N_c is the effective DOS in the CB and can be expressed as

$$N_c = 2\left(\frac{2\pi m_n^*}{h^2}\right)^{3/2}(kT)^{3/2} \tag{2.13}$$

where m_n^* is the electron effective mass.

Spear et al. showed that the quantity $E_c - E_f$ can exhibit small variations with the temperature (Spear, Allan, et al., 1980). Moreover, they proved that for temperatures above 300 K, this evolution is linear and can be written as

$$(E_c - E_f)(T) = (E_c - E_f)|_{T=0K} - \zeta kT \tag{2.14}$$

where ζ is a coefficient. Therefore, Equation 2.12 becomes

$$\sigma_{dark}(T) = \sigma_{00} \cdot \exp\left\{-\frac{E_a}{kT}\right\} \tag{2.15}$$

where $E_a = (E_c - E_f)|_{T=0K}$ is the activation energy (giving the position of the Fermi level at 0 K) and $\sigma_{00} = \sigma_0 \cdot \exp\left\{\frac{\zeta}{k}\right\}$ is the pre-exponential factor (that represents the average conductivity in the extended states). Thus, an Arrhenius plot of the dark conductivity allow one to determine the activation energy E_a.

If now the sample is illuminated with a continuous monochromatic photon flux F_{DC}, with an energy greater than the band gap of the material, steady state photocurrent (SSPC) measurements can be performed. The photoconductivity σ_{ph} at a depth z from the surface of the sample, can be written as

$$\sigma_{ph}(z) = q\mu_n \Delta n(z) + q\mu_p \Delta p(z) \tag{2.16}$$

where $\Delta n(z)$ and $\Delta p(z)$ are the excess electrons and holes and can be expressed as

$$\begin{aligned} \Delta n(z) &= n(z) - n_0 \\ \Delta p(z) &= p(z) - p_0 \end{aligned} \tag{2.17}$$

where n_0 and p_0 represent respectively the concentrations of electrons and holes in the dark.

In presence of a monochromatic continuous photon flux F_{DC} the electron-hole pairs generation rate at a depth z from the surface, can be written as

$$G(z) = \eta\alpha F_{DC}(1 - R)\exp\{-\alpha z\} \tag{2.18}$$

where η is the quantum efficiency of the electron-hole generation, R is the reflectance of the sample and α the absorption coefficient. Thus, $n(z)$ and $p(z)$ can be expressed as

$$\begin{aligned} n(z) &= G(z)\tau_n(z) \\ p(z) &= G(z)\tau_p(z) \end{aligned} \tag{2.19}$$

where $\tau_n(z)$ and $\tau_p(z)$ are respectively the free electrons and holes lifetimes. Supposing that $n(z) \gg n_0$ and $p(z) \gg p_0$, then Equation 2.16 becomes

$$\sigma_{ph}(z) = qG(z)\big(\mu_n\tau_n(z) + \mu_p\tau_p(z)\big). \tag{2.20}$$

The photocurrent dI that is flowing through a surface element $h\,dz$, can be written as

$$dI = \sigma_{ph}(z)\xi h\,dz, \tag{2.21}$$

where $\xi = V/e$ is the applied electric field, V being the bias applied between the electrodes, and h and e the parameters defined in Figure 2.21. Then, for a sample with a thickness L, the photocurrent is given by

$$\begin{aligned}\Delta I = I_{ph} - I_d &= h\xi \int_0^L \sigma_{ph}(z)dz \\ &= h\xi q\eta F_{DC}(1-R)\int_0^L \alpha e^{-\alpha z}\Big(\mu_n\tau_n(z) + \mu_p\tau_p(z)\Big)dz\end{aligned} \tag{2.22}$$

where I_{ph} and I_d are the photo and dark currents, respectively. Assuming that $\tau_n(z)$ and $\tau_p(z)$ are constant through the whole thickness of the sample, then Equation 2.22 becomes

$$\Delta I = h\xi q\eta F_{DC}(1-R)\mu\tau\Big(1-\exp\big(-\alpha L\big)\Big) \tag{2.23}$$

where $\mu\tau = \mu_n\tau_n + \mu_p\tau_p$. For the studied materials $\mu\tau \approx \mu_n\tau_n$, thus

$$\eta\mu_n\tau_n = \frac{\Delta I}{q h\xi F_{DC}(1-R)\Big(1-\exp\big(-\alpha L\big)\Big)}. \tag{2.24}$$

In Figure 2.22 a schematic representation of the equipment used to DC and SSPC measurements is presented. The sample is mounted in a cryostat that is kept under vacuum ($\sim 10^{-4}$ Pa) and where the temperature is carefully controlled via a proportional-integral-derivative (PID) controller. To perform the measurement, a constant bias is applied, to the sample, in its ohmic regime. To generate the photocurrent, a monochromatic photon flux (10^{12}-10^{15} cm^{-2} s^{-1}) emitted from a LED system is used. Three different wavelengths are available: 450 nm, 660 nm and 750 nm. Dark and photocurrents are measured via a picoammeter Keithley 617 and the dark and photo conductivities at a given temperature can then be calculated as

$$\sigma_{dark}(T) = \frac{I_d}{hL\xi} \qquad \sigma_{ph}(T) = \frac{I_{ph} - I_d}{hL\xi} \tag{2.25}$$

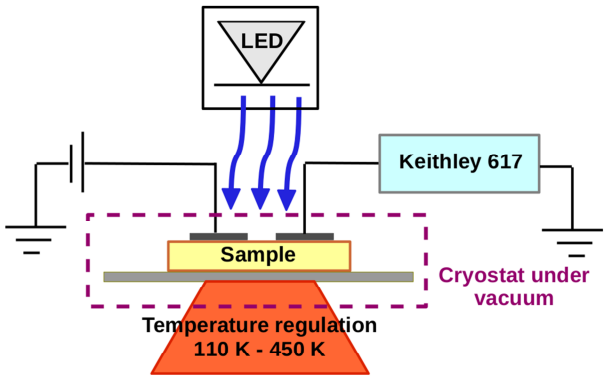

Figure 2.22.: Schematic representation of the equipment used to perform DC and SSPC measurements.

Steady State Photocarrier Grating

In contrast to the majority-carrier properties, which can be determined rather straightforwardly by stationary photocurrent measurements, the minority-carrier properties can only be revealed by more sophisticated methods. In this respect, the steady state photocarrier grating (SSPG) that was first develop by Ritter, Zeldov and Weiser in 1986 (Ritter, Zeldov, et al., 1986; Ritter, Weiser, et al., 1987), has had a significant impact.

This method is based on the carrier diffusion under the presence of a spatial sinusoidal modulation in the photogeneration rate G, which induces a so-called photocarrier grating. From photocurrent measurements at different grating periods Λ, the *ambipolar diffusion length* L_d can be determined by an analysis that assumes ambipolar transport and charge neutrality.

In general in a SSPG equipment, such as the one presented in Figure 2.23, a laser beam is divided into two components (B_1 and B_2) which are focused onto the surface of the sample, with a DC voltage applied between its electrodes. While the B_1 beam is directly focused on the sample, the B_2 beam is attenuated using a filter, then modulated by a chopper and finally focused on the sample. In this way B_2 represents only a small perturbation to the uniform illumination generated by B_1. The sample is thus illuminated by two coherent beams having respectively I_1 and I_2 intensity, with $I_1 \gg I_2$.

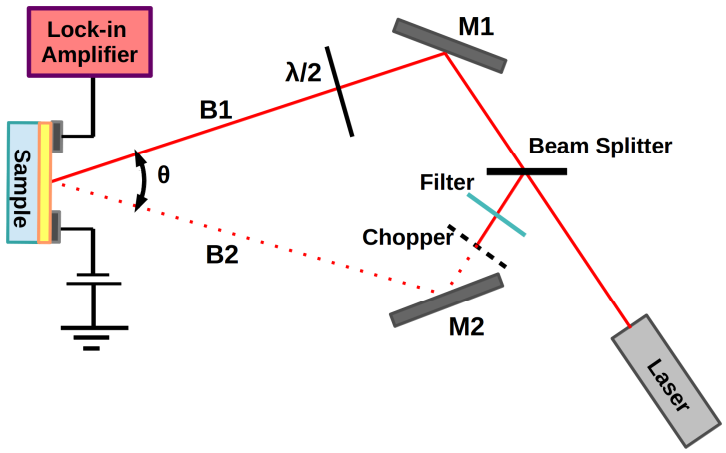

Figure 2.23.: Schematic representation of a generic equipment used to perform SSPG measurements.

If the two beams have the same polarization, interference fringes will be created and a succession of light (constructive interferences) and dark fringes (destructive interferences) will appear. The spatial grating of such fringes can be written as

$$\Lambda = \frac{\lambda}{2\sin\left(\frac{\theta}{2}\right)} \tag{2.26}$$

where λ is the laser wavelength and θ the angle between the two beams (see Figure 2.24). These light and dark areas correspond to zones with high and low carriers creation, respectively. Those generated in the illuminated areas will diffuse towards the dark ones in order to balance the gradient of carriers and will also drift due to the presence of the electric field. If $\Lambda < L_d$, carriers diffusion will lead to an effective homogenization of their concentration between the two electrodes. On the other hand, if $\Lambda > L_d$, carriers will not be homogeneously distributed and the collected current

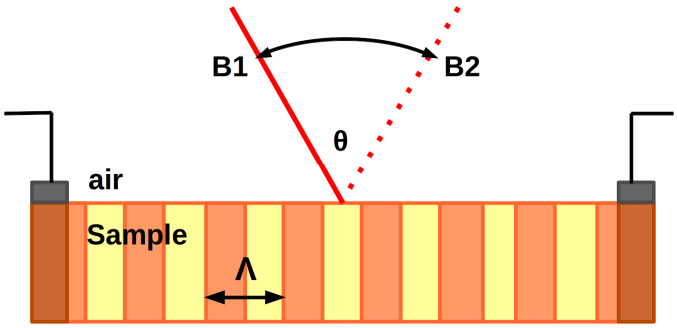

Figure 2.24.: Schematic representation of the interference fringes between coplanar electrodes.

will vary. If now the polarization of the B_1 beam is changed by 90° by using a $\lambda/2$ plate, the two beams will not interfere anymore.

In order to connect the diffusion length to the photocurrent, Ritter, Zeldov and Weiser defined the parameter β as

$$\beta = \frac{U_{coh}}{U_{incoh}}, \tag{2.27}$$

for a specific angle θ (thus, for a specific grating period Λ). U_{coh} and U_{incoh} denote the lock-in amplifier signals under coherent and incoherent beam conditions.

The link between the experimentally determined β and the diffusion length L_d is adjusted by an approximation of the current densities with the assumed (and also typically observed) power-law dependence of the photocurrent density $j_{ph} \propto G^{\gamma}$. Solving the transport equations under the assumption of ambipolar transport (so that only one carrier type is analyzed) and charge neutrality, leads then to

$$\beta = 1 - \frac{2\Phi}{\left(1 + \left(\frac{2\pi L_d}{\Lambda}\right)^2\right)^2} \tag{2.28}$$

where $\Phi = \gamma\gamma_0^2$, with γ_0 being the "grating quality factor" ($0 \leqslant \gamma_0 \leqslant 1$) introduced by Ritter, Zeldov and Weiser in order to account for a nonideal grating because of optical scattering, nonideal coherence or mechanical vibrations. The assumption in this formula is that the light is uniformly absorbed in the whole thickness of the sample and that no surface recombination takes place. These two phenomena would result in a gradient perpendicular to the film surface.

Equation 2.28 is the central equation of the SSPG analysis. The data sets of the measured β values at different positions Λ can be analyzed with this fit function, in order to calculate the diffusion length L_d and the parameter Φ, from the evaluation of which, together with the separate experimental determination of γ, the grating quality factor γ_0 can be determined (Brüggemann, 2011).

Balberg et al. (Balberg et al., 1988) suggested rearranging the data into a linear form as

$$\frac{1}{\Lambda^2} = \frac{\sqrt{\Phi}}{2\pi L_d^2}\sqrt{\frac{2}{1-\beta}} - \frac{1}{(2\pi L_d)^2} \tag{2.29}$$

with the ordinate values $1/\Lambda^2$ and the abscissa values $\sqrt{2/(1-\beta)}$. The diffusion length L_d can be determined from the fit parameters for the straight

line. The advantage of any linear plot is that a disagreement from the theoretical expectation may be more easily identified. Moreover, ambipolarity is not obeyed by charge separation under high electric fields, which can also be identified from a concave instead of a linear shape of the graph according to Equation 2.29 (Brüggemann, 2011).

In this work, measurements on a-$Si_{1-x}C_x$:H and μc-$Si_{1-x}C_x$:H were done at room temperature using an helium-neon laser ($\lambda = 633$ nm) with a photon flux of 10^{17} cm^{-2} s^{-1}. In Figure 2.25 an example of the two methods used to represent the evolution of β as a function of the grating period Λ is given for two a-$Si_{1-x}C_x$:H samples having different carbon contents.

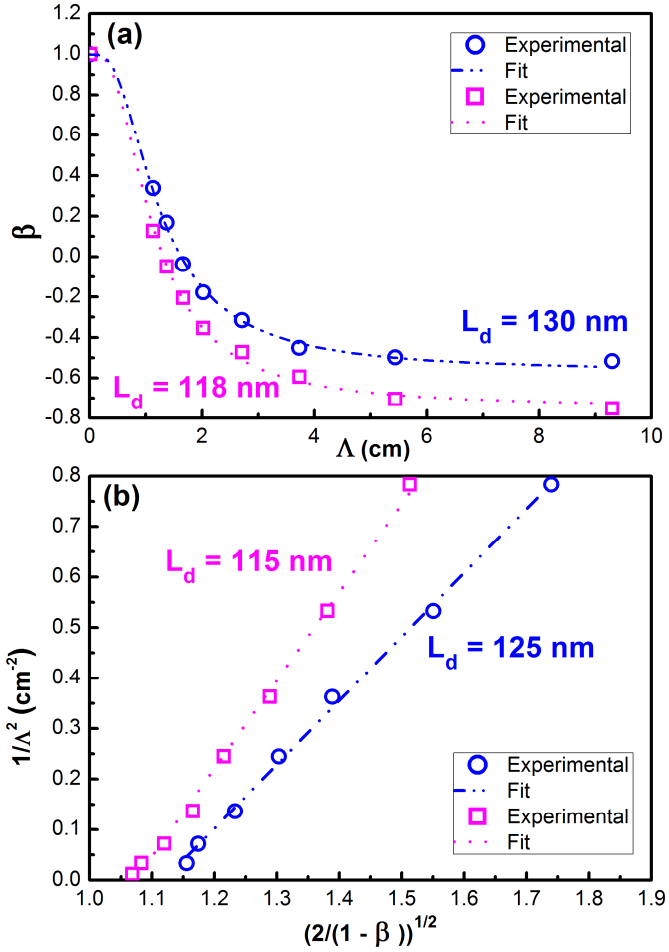

Figure 2.25.: Example of (a) the evolution of β as a function of the grating period Λ and (b) the analogous *Balberg* plot, showing the linear trend. The symbols represent the experimental data while the dashed and dotted lines represent the fit obtained from the theoretical equations.

It is important to remember that the application of SSPG to microcrystalline materials presents some obstacles due to the typically higher σ_d and to some possible effect of surface roughness, which reduces γ_0. Moreover, there are indications that transport is inhomogeneous in μc-Si:H for transport paths parallel or perpendicular to the film-growth direction (Švrček et al., 2001).

Modulated PhotoCurrent

The modulated photocurrent (MPC) technique is a powerful tool to study the density of defects in the band gap of a material. In 1981 Oheda showed that from the analysis of photocurrent measurements one could infer the energetic distribution of the defects in the band gap (Oheda, 1981). In 1990 Brüggemann et al. proposed a simpler analysis, compared to Oheda's (Brüggemann et al., 1990). They showed that at a given energy in the band gap, the DOS can be directly linked to the absolute value and the phase shift of the AC part of the photocurrent. Finally, the most complete work about this technique was developed by Longeaud and Kleider (Kleider, Longeaud, and Glodt, 1991; Longeaud and Kleider, 1992). In their work they generalized the calculation of the DOS underlying the existence of two different regimes:

- the *high frequency regime* (HF-MPC), for which the photocurrent is controlled by the process of trapping-and-release of carriers;
- the *low frequency regime* (LF-MPC), for which the photocurrent is linked to the recombination of carriers.

In this work it was decided to characterized both μc-$Si_{1-x}C_x$:H and a-$Si_{1-x}C_x$:H alloys performing MPC measurements only in the HF regime, which is the most common one.

The basic idea of the MPC technique is to shine a modulated monochromatic excitation light onto the sample. Thus, the photon flux is made of two contributions: a direct part (F_{DC}) and an alternating one (F_{AC}). As a consequence, the photocurrent is also made of a constant component and an alternating one, which has a phase shift φ compared to the excitation light. This phase shift is created by the interaction of the photo-generated carriers with the localized states in the band gap. Thus, the absolute value and the phase of the alternating component of the photocurrent are directly related to the trapping-and-release process or the recombination of the photo-generated carriers.

The theory of the MPC technique is based on the continuity equations of the free carriers and the Schockley-Read statistics (Shockley et al., 1952), in which it is assumed that traps can exchange electrons and holes via the conduction and valence band, respectively. The gap states are considered like monovalent states and are characterized by

- *capture rates*,

$$\begin{aligned} \overline{n} &= v_n \sigma_n n = c_n n \\ \overline{p} &= v_p \sigma_p p = c_p p, \end{aligned} \tag{2.30}$$

  v_n and v_p being the thermal velocities, σ_n and σ_p the capture cross sections, c_n and c_p the corresponding capture coefficients for electrons and holes, respectively, and n and p the concentrations of holes and electrons in the extended states;

- *emission rates*, e_n and e_p of electrons and holes, respectively.

In Figure 2.26 the possible transitions between the conduction and valence band states and a monovalent state at a given energy E in the band gap, are presented. According to the Schockley-Read statistics applied to a continuous distribution of states in the band gap, at a fixed temperature T and

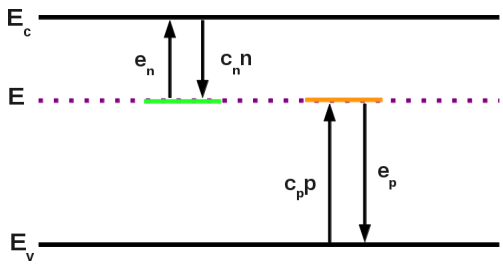

Figure 2.26.: Schematic representation of the possible transitions between the band states and a monovalent state in the band gap.

under illumination, the recombination zone is delimited by the quasi-Fermi levels E_{tn} and E_{tp} of trapped carriers. These energy levels are defined by

$$e_n(E_{tn}) = e_p(E_{tp}) = \overline{n} + \overline{p} \tag{2.31}$$

When a small AC signal is added to the photon flux, two energy levels $E_{\omega n}$ and $E_{\omega p}$ can be defined as

$$e_n(E_{\omega n}) = e_p(E_{\omega p}) = \omega, \tag{2.32}$$

where ω is the frequency of the excitation. Depending on the position of $E_{\omega n}$ and $E_{\omega p}$ with respect to the quasi-Fermi levels, two cases can be considered. If $\overline{n_{DC}}$ and $\overline{p_{DC}}$ are respectively the capture rates of free electrons and holes generated by the direct component of the excitation light (all the quantities, except the emission rates and $N(E)$, can be separated in two components indexed DC for the steady-state component and AC for the alternating one), then:

1. if $\omega \gg \overline{n_{DC}} + \overline{p_{DC}}$, the photocurrent is dominated by the trapping-and-release process and the MPC measurement is performed in the high frequency regime.
2. if $\omega \ll \overline{n_{DC}} + \overline{p_{DC}}$, the photocurrent is dominated by the the recombination of the free carriers and the MPC measurement is performed in the low frequency regime.

When $\omega \gg \overline{n_{DC}} + \overline{p_{DC}}$, $E_{\omega n}$ and $E_{\omega p}$ are located between the respective band-edge and the quasi-Fermi level (Figure 2.27). If states above (below) $E_{\omega n}$ ($E_{\omega p}$) are considered, their response is too fast compared to the characteristic period of the excitation. Similarly, states below (above) $E_{\omega n}$ ($E_{\omega p}$) are characterized by a response that is too slow. Therefore, the phase-shift between the excitation and the measured AC current is only related to the response of states at $E_{\omega n}$ and $E_{\omega p}$.

For a specific temperature T and frequency ω, Brüggemann et al. (Brüggemann et al., 1990) have shown that it is possible to reconstruct the DOS from the following relations:

$$\begin{aligned} N(E_{\omega n}) &= \frac{2N(E_c)}{\pi \nu_n}\left(Sq\xi\mu_n G_{AC}\frac{\sin\varphi}{|I_{AC}|} - \omega\right), \quad \text{for electrons} \\ N(E_{\omega p}) &= \frac{2N(E_v)}{\pi \nu_p}\left(Sq\xi\mu_p G_{AC}\frac{\sin\varphi}{|I_{AC}|} - \omega\right), \quad \text{for holes} \end{aligned} \tag{2.33}$$

where $E_{\omega n}$ and $E_{\omega p}$ are defined as

$$\begin{aligned} E_c - E_{\omega n} &= kT\ln\left(\frac{\nu_n}{\omega}\right) \\ E_{\omega p} - E_v &= kT\ln\left(\frac{\nu_p}{\omega}\right), \end{aligned} \tag{2.34}$$

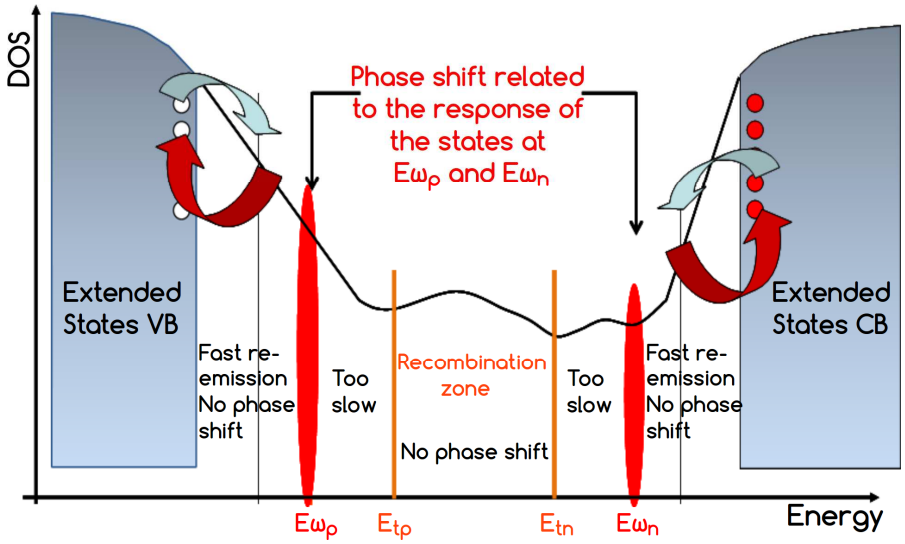

Figure 2.27.: Example of the the position of the quasi-Fermi levels of a trap state, at a given temperature T. The recombination zone is delimited by E_{tn} and E_{tp} (Gueunier-Farret, JNPV 2013).

and $N(E_c)$ and $N(E_v)$ are the DOS at the mobility edges, μ_n and μ_p the mobility in the extended states for electrons and holes, respectively, ξ is the applied electric field, G_{AC} the alternating component of the generation rate, S the surface through which the photocurrent is flowing and q the electron charge. Finally, $\nu_n = c_n kTN(E_c)$ and $\nu_p = c_p kTN(E_v)$ are the attempt-to-escape frequencies.

As frequency ω is negligible compared to the first term in the brackets, and taking into account the expressions for the attempt-to-escape frequencies, it is possible to rewrite Equations 2.33 as:

$$\begin{aligned} \frac{N(E_{\omega n})c_n}{\mu_n} &= \frac{2}{\pi kT}\left(Sq\xi G_{AC}\frac{\sin\varphi}{|I_{AC}|}\right), \quad \text{for electrons} \\ \frac{N(E_{\omega p})c_p}{\mu_p} &= \frac{2}{\pi kT}\left(Sq\xi G_{AC}\frac{\sin\varphi}{|I_{AC}|}\right), \quad \text{for holes} \end{aligned} \tag{2.35}$$

It should be noted that both expressions are valid only in presence of only one type of carriers and that they define the MPC-DOS (the Nc/μ ratio), which is determined by quantities that can be directly measured.

In Figure 2.28 a schematic representation of the equipment used to perform HF-MPC measurements is presented. Samples in coplanar configuration are introduced in a cryostat which is kept under vacuum.

The temperature is varied from 450 K to 110 K, and as in the SSPC setup, it is controlled through a PID controller. The illumination of the sample is obtained via a system of LED biased using a function generator. The driving voltage can be written as $V_{DC} + V_{AC}\cos(\omega t)$, where the frequency ω can be varied from 12 Hz to 40 kHz, in the high frequency regime. The frequency modulation is done using a geometric progression: $\omega_n = \omega_0 \cdot 1.5^n$. As a consequence, the photon flux is composed of a direct component (F_{DC}) and an alternating one (F_{AC}) and can be written as $F_{DC} + F_{AC}\exp(i\omega t)$.

The direct photon flux can be varied in the $10^{12} - 10^{15}$ $cm^{-2}s^{-1}$ range. As the theoretical analysis of the MPC technique is done for small signals, the alternating component of the photon flux (F_{AC}) is fixed so that it is small enough, but still measurable, and such that the ratio F_{DC}/F_{AC} is large enough to be in the "small signals" regime. Thus F_{AC} is taken to be

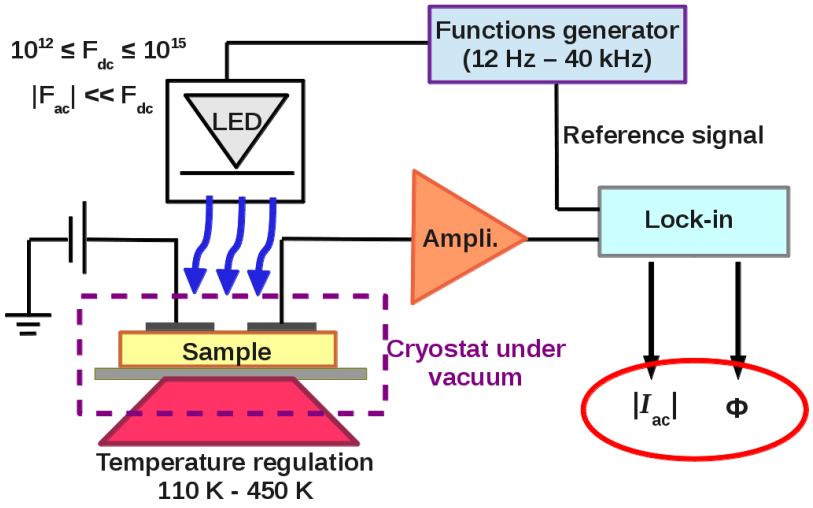

Figure 2.28.: Schematic representation of the equipment used to perform MPC measurements.

2.5 times lower that F_{DC}. The wavelength of the excitation light is chosen in oder to be close to the band gap of the material. Three systems of LEDs with emission at 660 nm, 450 nm and 750 nm, respectively, are available. The sample, with a DC bias applied between its electrodes in its ohmic regime, delivers a photocurrent which can be written as $I_{DC} + I_{AC} \exp(i\omega t)$, with $I_{AC} = |I_{AC}| \exp(i\varphi)$. The current is amplified through a current-to-voltage amplifier, with a gain of 10^7 V/A and finally the alternating part of the obtained voltage ($V_{DC} + V_{AC} \exp(i\omega t)$ where $V_{AC} = |V_{AC}| \exp(i\varphi)$) is analyzed by the Lock-In, taking as a reference the function applied to the LEDs. Thus, through the Lock-In it is possible to obtain directly the absolute value $|V_{AC}|$ and the phase shift φ.

To conclude, in the HF regime both types of carriers contribute to the photocurrent, thus the obtained MPC-DOS is representative of electron-traps or hole-traps. The probed states are those for which the Nc/μ ratio is the smallest. As a consequence, if only one type of carrier is contributing predominantly for all the frequencies and temperatures, then this kind of defect spectroscopy allows one to obtain *relative* values of the density of states, by fixing c and μ. One of the main interests in the application of the HF-MPC, is that it allows the direct comparison of different materials (by comparing the Nc/μ ratios). If one wants to reconstruct the DOS, then reasonable values for c and μ have to be fixed, in order to get the best overlap of the curves at different temperatures.

In Figure 2.29 a spectrum of an a-$Si_{1-x}C_x$:H sample is shown. In the HF regime, the MPC-DOS is obtained by the high frequency envelope (the continuous purple line) resulting from the overlap of data reconstructed at consecutive temperatures, the best overlap being obtained, in this case, for $c = 4 \times 10^{-9}$ cm^3 s^{-1}.

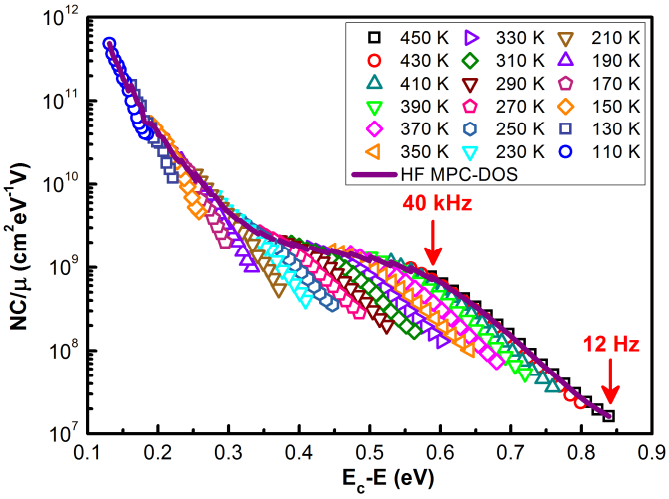

Figure 2.29.: Reconstructed MPC-DOS, obtained from the HF-MPC measurements. The different curves correspond to the measurements obtained at a fixed temperature, but varying the frequency from 12 Hz to 40 kHz. The full line represents the envelope of the measurements obtained varying the temperature and indicates the shape of the HF-DOS.

Light Soaking

As it has been said, one of the goals of the CANASTA project is to develop a material with electrical properties similar to a-Si:H, but not affected by the Staebler-Wronski degradation. For this reason, the behavior of the materials after the exposure to intense light for several hours had to be tested.

The influence of the Staebler-Wronski effect on the electrical properties of a material can be quantified by monitoring the evolution of the photo-current as a function of the elapsed time (Longeaud, Roy, et al., 2002). Longeaud et al. have shown that the evolution of the photo-current in a-Si:H during the light-soaking, cannot be fitted with a single stretched exponential (Longeaud, Roy, et al., 2002). They proposed that the evolution of the photo-current to be written as

$$\frac{I}{I_0} = \frac{I}{I_0}\bigg|_0 + \frac{I}{I_0}\bigg|_1 \cdot \exp\left\{-\left(\frac{t}{\tau_1}\right)^{\beta_1}\right\} + \frac{I}{I_0}\bigg|_2 \cdot \exp\left\{-\left(\frac{t}{\tau_2}\right)^{\beta_2}\right\} \tag{2.36}$$

where I_0 is the current measured in the initial state.

In Figure 2.30 the evolution of the normalized photocurrent (open circles) and its fit with one (dashed-dotted green line) or two (continuous red line) stretched exponentials are plotted as a function of the light soaking time.

Yang et al. provided convincing evidence that defect generation and annealing in a-Si:H are controlled by defect states of different characteristics and therefore two stretched exponentials should be used to fit the light-soaking kinetics (L. Yang et al., 1993). According to Longeaud et al. (Longeaud, Roy, et al., 2002), these states seem to be:

1. the *deep states*, the density of which modifies rapidly;

2. the *band tail states*, the density of which increases only after a given amount of time.

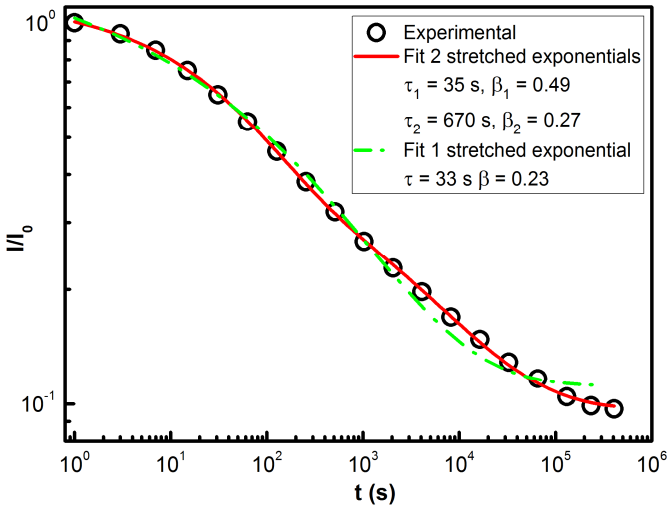

Figure 2.30.: Evolution of the normalized photocurrent as a function of the light soaking time, for a generic a-Si:H sample deposited by standard RF-PECVD. Experimental data are represented by O, the dashed-dotted curve (— · —) corresponds to the fit performed using only one stretched exponential (the obtained parameters τ and β are given in the legend), while the full line (—) corresponds to the fit performed using two stretched exponential (the fitting parameters τ_1, τ_2, β_1 and β_2 are given in the legend).

The only drawback is whether one can assume that the evolutions of these two distributions are independent, and thus it is possible to use two stretched exponential distributions to fit the kinetics, or not.

In this work, the light soaking of some selected samples was performed at room temperature, using a LED system delivering a white photon flux of nearly 4 suns.

2.4 DEVICE CHARACTERIZATION TECHNIQUES

2.4.1 Characterization methods

Hydrogenated microcrystalline silicon-carbon alloys were applied as an absorber layer in n-i-p/p-i-n photodiodes. These devices were studied using standard characterization techniques such as dark and light J(V) measurements and the external quantum efficiency (EQE). In the following, a short description of these techniques will be presented.

Dark & Light J(V) characteristics

A solar cell can be represented by an equivalent circuit composed by a current source (representing the photocurrent), in parallel with a diode, a series resistance and a shunt one (see Figure 2.31). While the series resistance is the resultant from the resistance of the contacts, of the different layers and of the interfaces, the shunt one is due to the leakage current.

The ideal diode equation is given by

$$J(V) = J_0\left[\exp\left(\frac{qV}{nkT}\right) - 1\right] \tag{2.37}$$

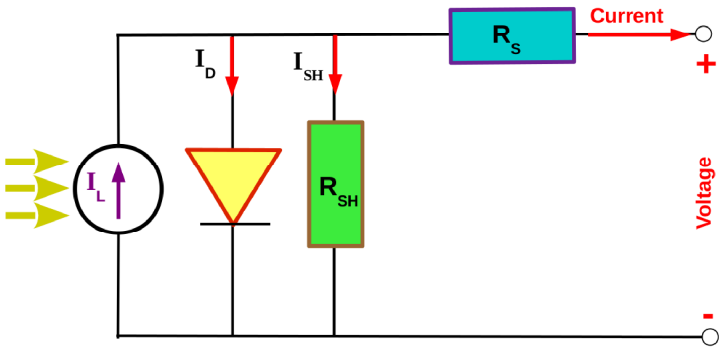

Figure 2.31.: Equivalent circuit of a solar cell. An ideal solar cell is modeled by a current source in parallel with a diode; in practice no solar cell is ideal, thus shunt and series resistances are added.

where q is the electron charge, k the Boltzmann constant, J_0 the dark saturation density of current and n the ideality factor of the diode. Ideally, the semi-log plot of the current density versus the voltage of the diode, should show a linear proportionality in the forward bias region. Extrapolating the linear region down to $V = 0$ gives the value of J_0, while from the slope it is possible to determine the ideality factor.

Once the solar cell is illuminated, the $J(V)$ characteristic can be approximated by the superposition of the $J(V)$ curve of the diode in the dark and the photocurrent under illumination:

$$J(V) = J_{ph} - J_0\left[\exp\left(\frac{qV}{nkT}\right) - 1\right]. \tag{2.38}$$

However, in presence of both *series* and *shunt* resistances, the $J(V)$ curve is given by

$$J(V) = J_{ph} - J_0\left[\exp\left(\frac{q(V - JR_s)}{nkT}\right) - 1\right] - \frac{V - JR_s}{R_{sh}} \tag{2.39}$$

Actually, amorphous silicon solar cells are p-i-n diodes, in which the main part of the photovoltaic generation occurs in the intrinsic i-layer. For these cells the recombination is relatively intense because of the presence of dangling bonds that act as recombination centers. Therefore, it is possible to describe a-Si:H solar cells by introducing an additional recombination loss term into the equivalent circuit, a term which is symbolized by the current sink (dashed lines) in Figure 2.32 (Merten et al., 1998).

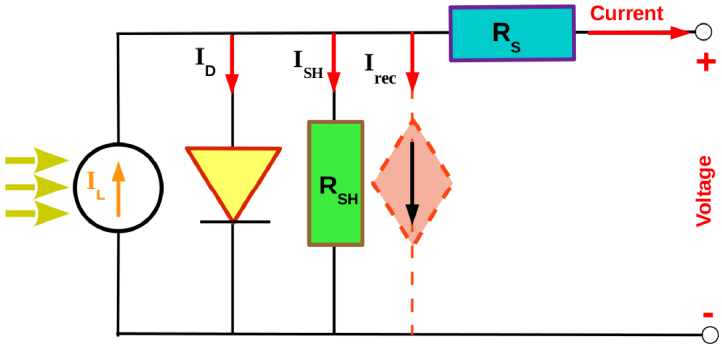

Figure 2.32.: Equivalent circuit for a photovoltaic solar cell, taking into account the current losses due to recombination in the i-layer of the device.

From these characteristics four parameters can be inferred to determine the quality of the device:

- the *short-circuit current* J_{sc}, that is the current for $V = 0$;
- the *open-circuit voltage* V_{oc}, that is the voltage for $J = 0$;
- the *fill factor* FF, which is a measure of the charge collection efficiency;
- the *efficiency* η.

The fill factor FF is defined as

$$FF = \frac{JV|_{max}}{J_{sc}V_{oc}}, \tag{2.40}$$

where the product JV corresponds to the power density delivered by the solar cell and $JV|_{max}$ is its maximum. The efficiency η is defined by

$$\eta = \frac{JV|_{max}}{P_i} \tag{2.41}$$

with P_i being the power of the incident light.

In Figure 2.33 an example of dark and light $J(V)$ curves of a monocrystalline silicon solar cell is given.

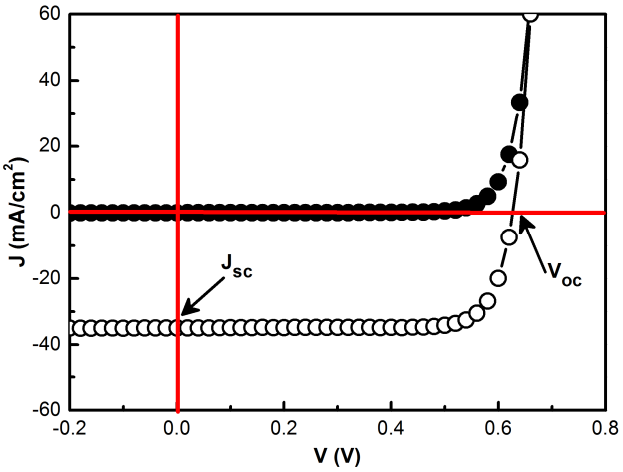

Figure 2.33.: Dark (●) and light (○) $J(V)$ curves for a monocrystalline silicon solar cells. The red continuous lines indicate the axes crossing at (V, J) = (0,0), highlighting J_{sc} and V_{oc}.

In this work, light $J(V)$ measurements were performed under a solar simulator, the spectrum of which correspond to the A. M. 1.5 solar spectrum, associated to an incident power of 100 mW/cm^{2}at 25° C.

External Quantum Efficiency

The "quantum efficiency" (QE) is the ratio of the number of carriers collected by the solar cell to the number of photons of a given energy incident on the solar cell. There are two types of QE:

- **Internal Quantum Efficiency** (IQE), which is the ratio of the number of charge carriers collected by the solar cell to the number of photons of the incident flux at a given energy, that are absorbed by the cell;

- **External Quantum Efficiency** (EQE), which is the ratio of the number of charge carriers collected by the solar cell to the number of photons of the incident flux, at a given energy.

In this work only EQE was measured. This parameter takes into account the collection and the recombination of the photogenerated carriers in the device and it includes the effect of optical losses such as transmission and reflection. Once a photon has been absorbed and has generated an electron-hole pair, the charges must be collected at the junction. In a device-quality material charge recombination has to be limited, as it causes a drop in the external quantum efficiency. Finally, the ideal EQE is limited at long wavelengths by the inability of the semiconductor to absorb photons with energies below its band gap.

Part II.

Material study

3 STRUCTURAL PROPERTIES AND GROWTH MECHANISMS

3.1 INTRODUCTION

The exploratory nature of this doctoral work required an investigation on the possibility of growing μc-$Si_{1-x}C_x$:H alloys applying different deposition techniques. In order to define optimal deposition conditions leading to materials with device-quality opto-electronic performance, the effect of several parameters (such as CH_4 flow rate, RF-power density, etc..), had to be tested. All the investigated inter-relations that were subjected to an analysis are shown in Figure 3.1.

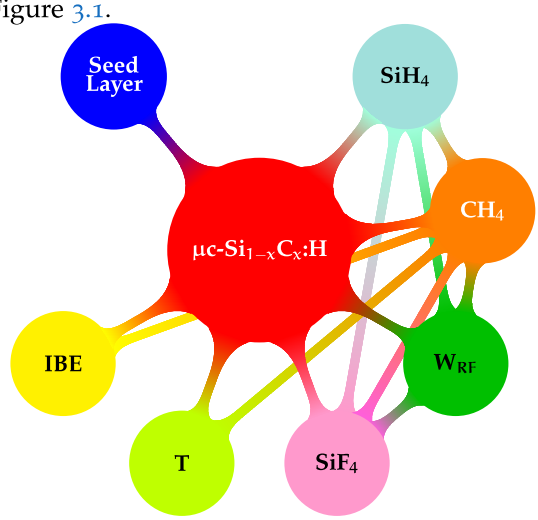

Figure 3.1.: Mindmap representing the investigated parameters (SiH_4, CH_4 and SiF_4 flow rate, RF-power density - w_{RF}, temperature - T and ion bombardment energy - IBE) and their inter-relations.

The absence of a stable sub-stoichiometric crystalline phase actually makes these alloys a very complex new class of materials for which complications in growth dynamics and material properties had to be faced. Nevertheless, the extensive structural characterizations led finally to the development of a growth model taking into account the different experimental results.

All samples were deposited fixing the pressure and the inter-electrode distance at 310 Pa and 1.2 cm, respectively. Materials were grown from a SiH_4 and CH_4 gas mixture highly diluted in H_2. For all depositions the H_2 flow rate was fixed at 500 sccm. The other deposition conditions were varied one parameter at a time, resulting in a wide number of sets of samples (20 sets, for a total of 100 samples). Only sets with useful data will be presented. The different series and their deposition conditions are listed in Table 3.1. The sets of samples are divided by deposition techniques and investigated parameter. The studied deposition parameter is marked in red (and sometimes it does not correspond to the varied parameter, i.e. effect of substrate temperature, but CH_4 flow rate varied). In each section a reference to this table will be made.

Table 3.1.: Summary of all the sets of samples that will be discussed in this work and their deposition conditions. For each set the single studied parameter is marked in red. The symbol † is used to identify those sets of samples for which UV-VIS transmission and electrical measurements were performed.

		SERIES		T (°)	W_{RF} (W)	w_{RF} (mW/cm^2)	SiH_4 (sccm)	CH_4 (sccm)	SiF_4 (sccm)	t (min)	ANALYSES
STANDARD RF	**Role of Seed Layer**	SET_{seed1}	seed layer	285	16	90	5	0	–	0 → 16	Ellipsometry, Raman, AFM, XRD, TEM
			main layer		40	226		1		30	
		SET_{seed2}	seed layer		16	90	13	0	–	0	Ellipsometry, Raman, XRD
			main layer		40	226		1		5 → 40	
		SET_{seed3}	seed layer		16	90	13	0	–	2	
			main layer		40	226		1		5 → 40	
	Effect of SiH_4	SET_{SiH_4}	seed layer	285	16	90	5	0	–	10	Ellipsometry, Raman, RF-GD-OES
			main layer		40	226	5 → 9	1		30	
	Effect of CH_4	$SET_{CH_4 1}$	seed layer	285	16	90	5	0	–	10	Ellipsometry, Raman, XRD, TEM, RF-GD-OES, FTIR
			main layer		40	226		1 → 2.5		30	
		†$SET_{CH_4 2}$	seed layer		16	90	6.5	0	–	10	
			main layer		40	226		1 → 1.8		75	
		†$SET_{CH_4 3}$	seed layer		16	90	13	0	–	2	
			main layer		40	226		1.1 → 1.4		40	
	Effect of W_{RF}	†$SET_{w_{RF}1}$	seed layer	285	16	90	6.5	0	–	10	Ellipsometry, Raman, XRD, TEM, RF-GD-OES, FTIR
			main layer		20 → 100	113 → 565		1.2		90 → 50	
		†$SET_{w_{RF}2}$	seed layer		16	90	13	0	–	2	
			main layer		20	113		1.2 → 5		60	
	Effect of SiF_4	†$SET_{SiF_4 1}$	seed layer	285	16	90	6.5	0	0	10	Ellipsometry, Raman, XRD, TEM, RF-GD-OES, FTIR
			main layer		40	226		1	0 → 1	75	
		†$SET_{SiF_4 2}$	seed layer		16	90	6.5	0	0	10	
			main layer		40	226		1.2	0 → 1	75	
		†$SET_{SiF_4 3}$	seed layer		16	90	13	0	0	2	
			main layer		20	113		1.4	0 → 1.5	70	
	Effect of T	SET_{T1}	seed layer	175	16	90	13	0	–	2	Raman, XRD, RF-GD-OES, FTIR
			main layer		20	113		1 → 1.6		90	
		SET_{T2}	seed layer		16	90	13	0	–	2	
			main layer		40	226		1.2 → 1.8		60	
TVW	Effect of CH_4	†SET_{peaks}	seed layer	285	20	113	13	0	–	2	Ellipsometry, Raman, XRD, RF-GD-OES
			main layer					1.1 → 1.4		60	
		$SET_{valleys}$	seed layer		20	113	13	0	–	2	
			main layer					1.1 → 1.4		60	

3.2 ROLE OF THE SEED LAYER

3.2.1 Seed layer deposition time

Initial attempts at growing thin μc-$Si_{1-x}C_x$:H layers (< 100 nm) by RF-PECVD had resulted in fully amorphous samples. This was attributed to the presence of CH_4 at the beginning of the deposition interfering with nucleation. It was therefore decided to investigate the effect of the addition of a seed layer deposited using a SiH_4 and H_2 gas mixture, for which the deposition time was varied from 0 to 16 minutes resulting in a seed layer with a thickness < 10 nm (SET_{seed1} in Table 3.1). The deposition of the seed layer was followed by a 30 minute deposition of the *main layer* for which CH_4 was added to the gas mixture.

In Figure 3.2 the imaginary part of the pseudodielectric function $<\epsilon_i>$ and Raman spectra of the samples are presented. Due to the low thickness of the layers, Raman measurements were performed using a blue laser (473 nm). It can be noted that a transition from an amorphous to a crystalline phase takes place as soon as the seed layer is added. Indeed, in the case of no seed layer, $<\epsilon_i>$ is characterized by a broad peak and the Raman spectrum is dominated by a broad component located around 480 cm^{-1}. This feature is typical of an amorphous material. On the other hand, with the introduction of the seed layer, signatures typical of μc-Si:H arise. The Raman spectra exhibit the appearance of the Si—Si Transversal Optical (TO) mode at 520 cm^{-1} which grows with increasing seed layer deposition time, and the ellipsometry spectra are characterized by the presence of two structures at about 3.5 eV and 4.2 eV, typical of μc-Si:H.

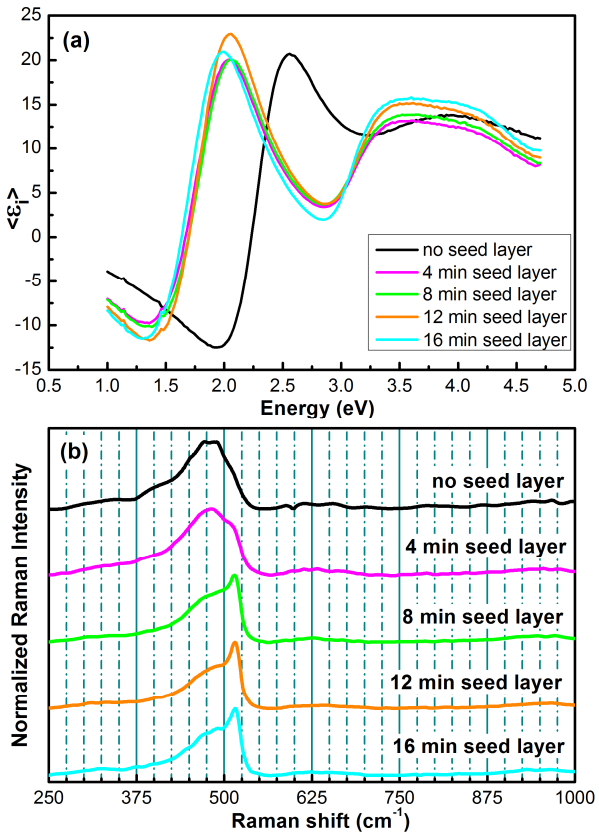

Figure 3.2.: (a) Experimental ellipsometry spectra and (b) Raman spectra of samples from SET_{seed1}, deposited varying the seed layer deposition time.

Considering that no SiC-related modes can be detected in the Raman spectra (they would be visible in the 800-900 cm^{-1} range), one can assume that these alloys are made of silicon crystallites and that the carbon incorporation happens only in the embedding matrix.

The thickness of the layers and their crystalline volume fraction were respectively determined from the ellipsometry modeling and from the deconvolution of the Raman spectra, as explained in section 2.3.1. Results are shown in Figure 3.3. Once the seed layer is added a phase transition is induced and the thickness of the alloy increases. It is noteworthy that when adjusting the seed layer deposition time the total thickness of the layer does not change, but it is possible to increase the crystalline content up to 35 % (for a $\sim$ 60 nm thick layer). The small variations induced in f_c^{Raman} for deposition times longer than 8 minutes can be linked to an homogenization of the material, as it will be shown in the following.

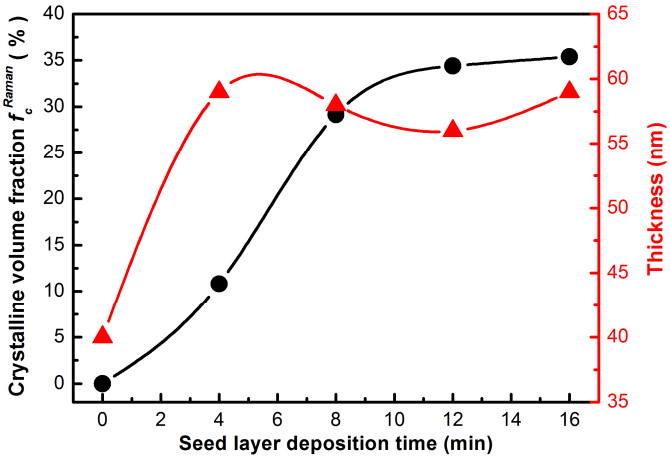

Figure 3.3.: Thickness (▲) and crystalline volume fraction (●) as a function of the seed layer deposition time.

The effect of the addition of the seed layer was also studied with the observation of the evolution of the surface structures, performing AFM measurements. In Figure 3.4 it can be seen that the sample is characterized by an extremely flat surface, when no seed layer is deposited; in contrast, with the introduction of the seed layer protrusions emerging from the surface start to appear. Although topography images allow one to estimate both lateral (xy) and height (z) dimensions, sometimes they do not really look like the studied object. The appearance of certain shapes is sometimes very different from the one that would be observed with an optical (or electron) microscope. Therefore, instead of creating a pseudo-3D image from the height data, it is possible to show the deflection (or amplitude) images, that are equivalent to a map of the slope of the sample and often display the shape of the surface structures more easily.

The amplitude image of the sample presented in Figure 3.4(b) is then shown in Figure 3.5 and was acquired using a higher magnification. The observed protrusions are consistent with aggregates (that will be called *grains* for simplicity) composed of nanometer sized subgrains elongated in the direction of growth (Fejfar, Mates, Certík, et al., 2004; Kočka et al., 2004). The dark zones shown in the topographic image correspond to amorphous areas between these aggregates.

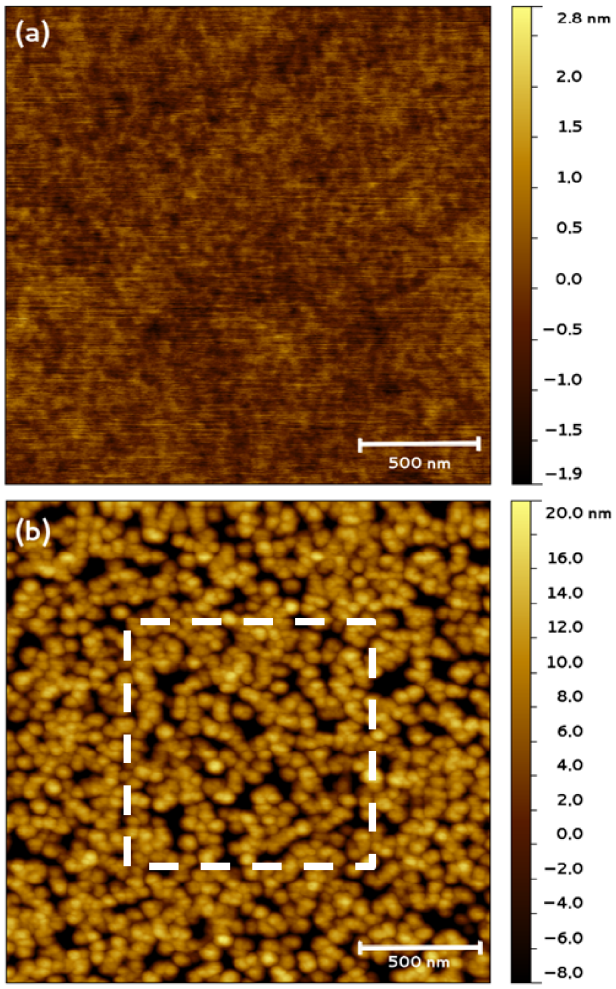

Figure 3.4.: AFM images of samples with (a) no seed layer and (b) a 4 minute deposition seed layer. The increase in the surface roughness is highlighted by the difference of the scale. In (b) the dark spots are amorphous zones between the aggregates and the dashed white line corresponds to the area where the AFM image in Figure 3.5 was taken.

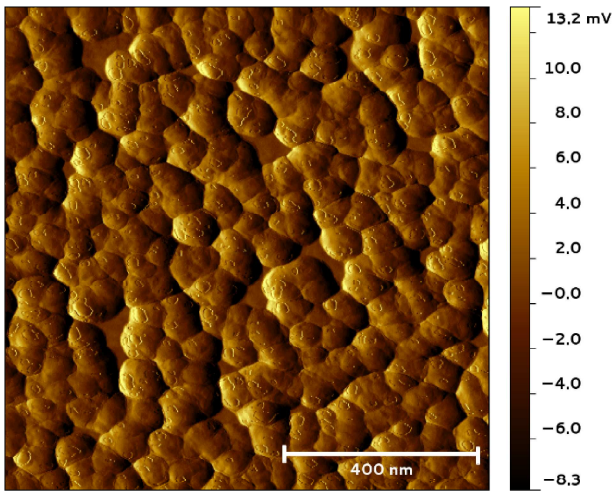

Figure 3.5.: Amplitude image of the sample deposited using a 4 minute deposition seed layer.

The appearance of the protrusions is translated in a root-mean-square (RMS) surface roughness (ρ_{RMS}) which increases with the introduction of the seed layer and remains constant after few minutes of seed layer deposition (Figure 3.6). Such evolution is consistent with the growth model suggested by Fejfar et al. (Fejfar, Mates, Koch, et al., 2001), where the μc-Si:H growth is modeled using a Voronoi network and it is assumed that the grains grow as spherically capped cones. The structure resulting from this kind of modeling can be characterized using common parameters such as the RMS roughness. Moreover, they also show that ρ_{RMS} reaches a maximum and then decreases again due to grain caps collisions.

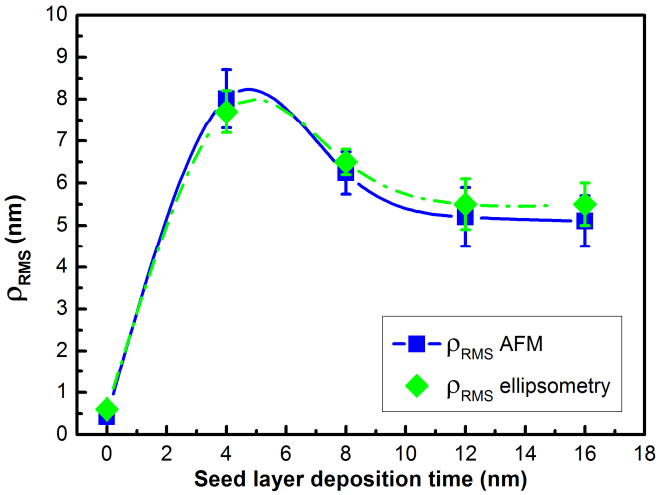

Figure 3.6.: RMS roughness ρ_{RMS} determined from AFM analyses (■) and ellipsometry modeling (◆) as a function of the seed layer deposition time.

One could argue that the protrusions observed in the AFM images and the relative dark areas could be respectively amorphous grains and empty spaces due to the lack of continuity in the thin film. Therefore, GIXRD and TEM analyses were carried out to study the microstructure of some of these layers and to confirm that carbon is only incorporated in the amorphous tissue surrounding the silicon crystallites.

As the layers are very thin (40-60 nm), to perform GIXRD measurements it has been necessary to reduce the incidence angle to $\theta_i = 0.23°$. However, the obtained patterns (Figure 3.7) still show the contribution from the substrate at $2\theta = 22°$. When no seed layer is added the diffraction pattern is characterized only by two broad humps located at $2\theta = 27.6°$ and 51°, which are due to short and medium range order and indicate the amorphous nature of the alloy (Williamson, 1999). On the other hand, with the addition of the seed layer, diffraction peaks characteristic of the cubic phase of crystalline silicon start to appear and are labeled in the figure. It is noteworthy that no crystalline silicon carbide or crystalline forms of carbon are present (they would appear at $2\theta = 35.67$, 41.43 - 3C-SiC, or $2\theta = 34.88$, 38.27, 43.43 - 4H-SiC, or $2\theta = 34.22$, 38.27, 45.46 - 6H-SiC, or $2\theta = 26.60$, 43.45, 46.33 - 3C-graphite). Therefore it can more confidentially be asserted that if carbon is incorporated in the alloy, it is trapped in the amorphous tissue surrounding the silicon crystallites.

From the Scherrer formula (Equation 2.9) the average size δ of the subgrains forming the aggregates can be determined and is shown in Figure 3.8. It seems that the seed layer deposition time does not have an influence

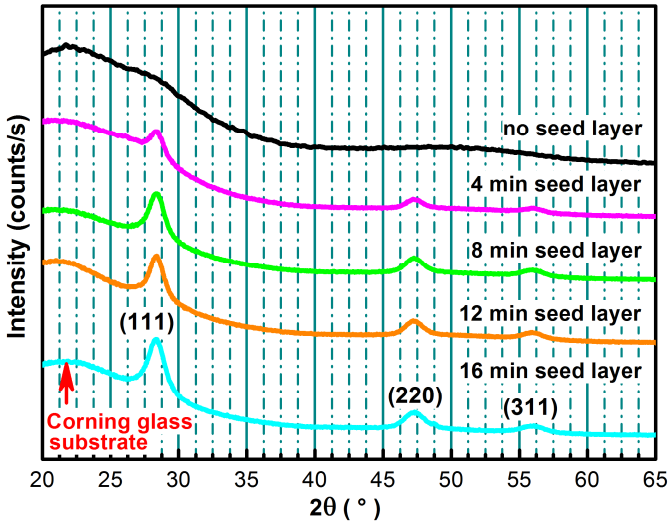

Figure 3.7.: GIXRD patterns of the samples from SET_{seed1}, deposited varying the seed layer deposition time. Lattice planes corresponding to c-Si diffraction peaks are labeled.

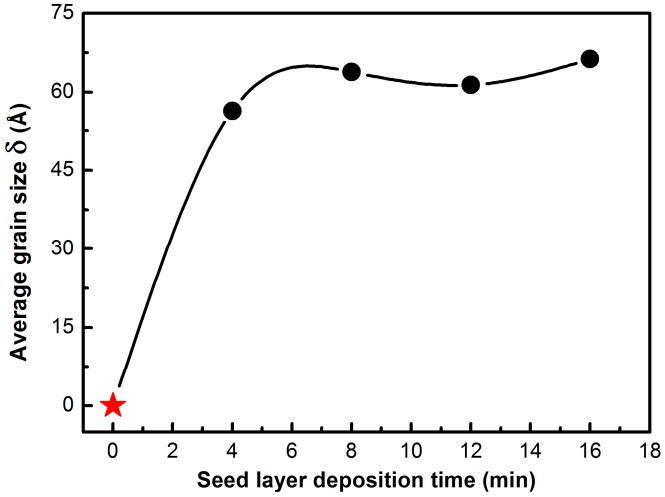

Figure 3.8.: Average grain size δ determined from the FWHM of the diffraction peaks in the GIXRD patterns. The ★ indicates the amorphous alloy, with no seed layer used for the deposition.

on δ which appears to be stable at (60 ± 5) Å. It is possible that, although the size of the domains (i.e. the grains) is different, the size of the subdomains is actually determined by the flux of carbon-based radicals that reach the surface and by the ion bombardment energy. Since the same RF-power and gas mixture are used, it can be assumed that for all samples the same amount of CH_4 molecules are broken and therefore that the flux of CH_x radicals arriving at the substrate is constant, leading to alloys with similar microstructural properties.

In Figure 3.9(a) the cross sectional TEM image of the sample deposited using a 8 minute seed layer is shown. The layer, 50 nm thick, is not homogeneous and is characterized by a particular morphology. The presence of 50 nm thick crystal grains, with a maximum diameter of 50 nm, embedded in a flat amorphous matrix ($\sim$ 25 nm thick) can be noted. It is then confirmed

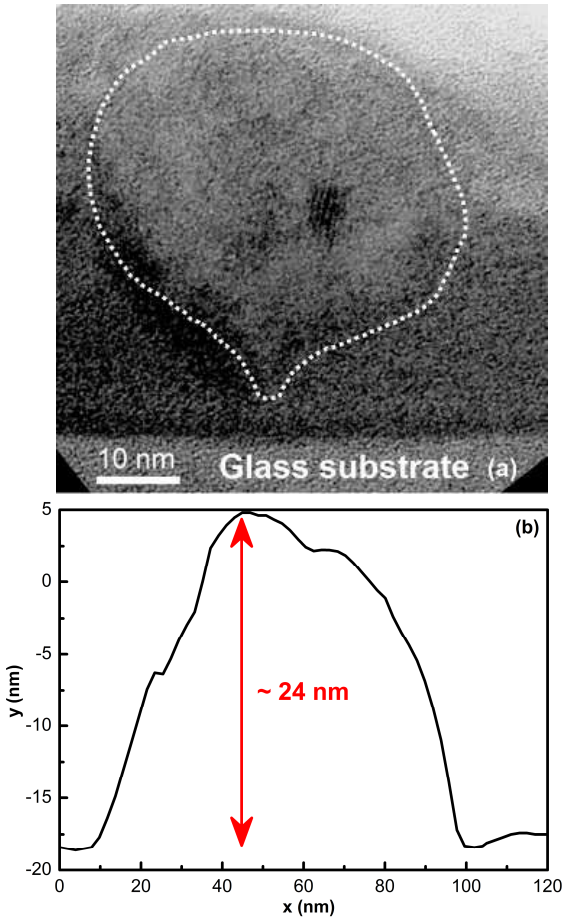

Figure 3.9.: (a) Cross sectional TEM micrograph of the sample deposited with a 8 minute seed layer and (b) AFM profile obtained on one isolated grain. Dotted lines in Figure (a) are used to clearly identify the presence of silicon crystals in the matrix.

that the humps observed with AFM analyses are silicon grains emerging from an amorphous matrix. The apparent disagreement between this image and the roughness calculated from AFM measurements can be linked to the different size of the areas probed by the two techniques and to the definition of ρ_{RMS} as the RMS average of the roughness profile ordinates. Therefore, where the growing grains are still isolated, the local roughness is 25 nm (as probed by TEM analyses), but once these grains start to collide, the ρ_{RMS} decreases due to a reconstruction of the surface (as probed by AFM). This is additionally confirmed by Figure 3.9(b), where the profile of an isolated grain is extracted from an AFM image, showing the same shape as reported in the TEM image. For longer seed layer deposition times, more uniform samples can be obtained. Indeed, in Figure 3.10 an area of the sample grown using a 16 minute seed layer is shown. The film, 60 nm thick with a 5 nm roughness, is clearly microcrystalline and shows the initial stages of a typical columnar growth, where the usual incubation layer is now reduced to a 5-10 nm region at the interface with the substrate.

As explained in section 2.3.1, energy filtered TEM images are obtained by collecting electrons that have lost a characteristic amount of energy when interacting with the sample. The energy difference between the silicon and the silicon carbide plasmonic peak should allow discrimination between the

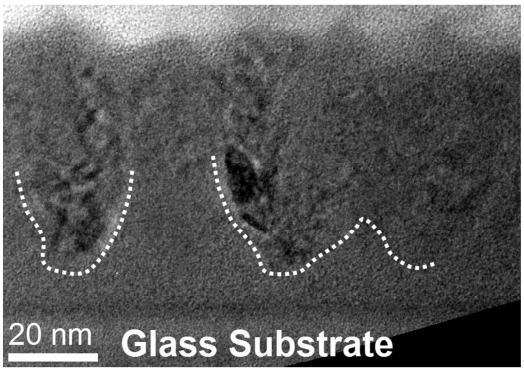

Figure 3.10.: Cross sectional TEM micrographs of the sample deposited with a 16 minute seed layer. The dotted lines underline the presence of grains in an amorphous matrix.

two different contributions. Therefore, it is possible to use this technique to confirm that despite the absence of carbon in any crystalline form, this element is actually incorporated in the layers, creating an a-$Si_{1-x}C_x$:H matrix embedding the silicon crystals. EFTEM images were acquired for the sample deposited with a 16 minute seed layer and are shown in Figure 3.11.

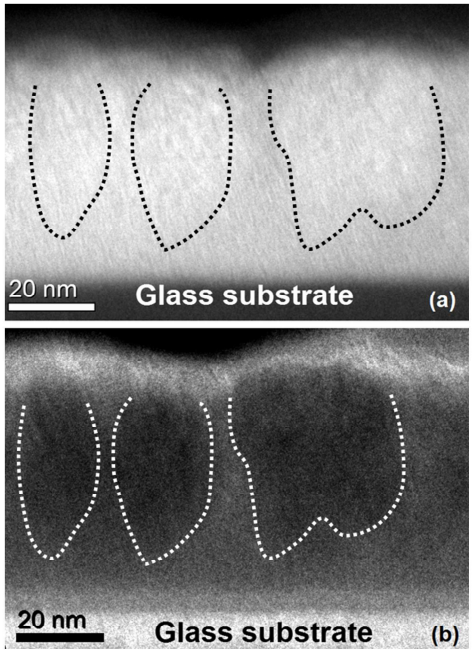

Figure 3.11.: Plasmonic images of the sample deposited with a 16 min seed layer. Images are acquired at (a) 16 eV and (b) 24 eV.

First an energy window (4 eV wide) is set at 16 eV, corresponding to the silicon plasmon loss, then to observe the presence of Si — C bonds, the well-known stoichiometric silicon carbide plasmonic excitation at 22 eV could be used. Actually, as the matrix in these layers is non-stoichiometric, a shift in the plasmonic peak can be expected (Egerton, 2009). Indeed, for an image acquired with an energy window centered at 24 eV, an increased brightness localized at the surface, at the interface with the substrate, and around the crystal grains can be observed. By comparing the image acquired at 16 eV (Figure 3.11(a)) with the one acquired at 24 eV (Figure 3.11(b)), it is once

again possible to confirm that crystals are composed primarily of silicon since they are brighter than the remaining part of the sample in the first image and vice-versa in the second one. It is thus clear that when using the RF-PECVD technique to deposit μc-$Si_{1-x}C_x$:H alloys, diphasic materials are obtained, characterized by a μc-Si:H phase, embedded in an a-$Si_{1-x}C_x$:H matrix.

3.2.2 Thickness series

Another way to study the influence of the seed layer is by depositing two sets of samples, one without and the other one with the seed layer, for which the main layer deposition time is changing (SET_{seed2} and SET_{seed3} in Table 3.1, respectively). For these two thickness series the main layer deposition was stopped after 5, 10, 15, 30 and 40 minutes.

Due to a shift in the opening threshold of the SiH_4 mass flow controller (MFC), the deposition conditions for these sets of samples had to be re-adjusted and the optimization of the seed layer deposition time had to be re-performed. In order to avoid this problem in the future, a careful calibration of partial pressures was done (and continuously checked before a set of depositions). In this way, despite a possible shift of the opening threshold of the MFC, identical working conditions can be reproduced from run to run.

In Figure 3.12 the evolution of the Raman spectra with the main layer deposition time is presented. It is clearly shown that the influence of the seed layer is fundamental in the very early stages of the growth of the alloy, with its beneficial effect being in fact more evident for samples deposited during 5 and 10 minutes.

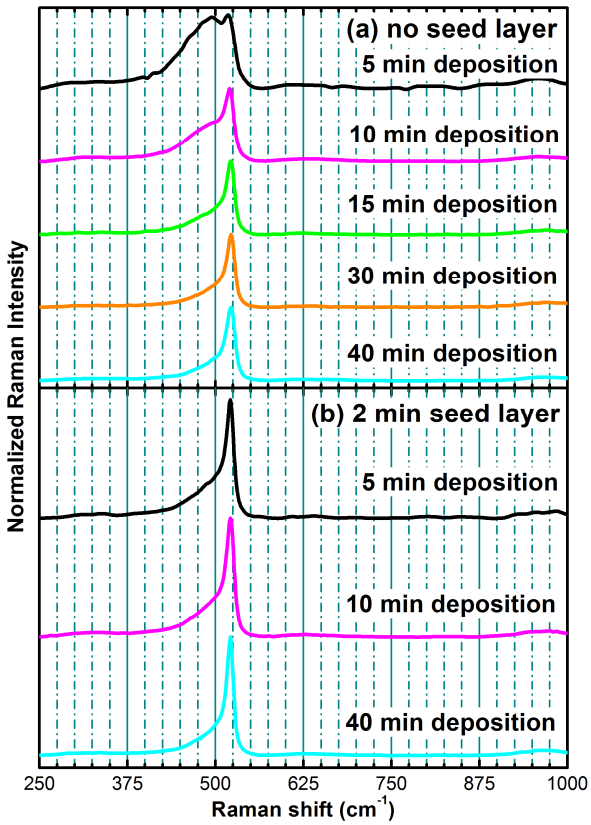

Figure 3.12.: Raman spectra of samples from (a) SET_{seed2} (no seed layer) and (b) SET_{seed3} (2 min seed layer), varying the main layer deposition time.

From the ellipsometry modeling, the thickness of the layers was determined and is plotted in Figure 3.13 as a function of the total deposition time. It can be seen that the presence of the seed layer does not affect the total thickness of the sample.

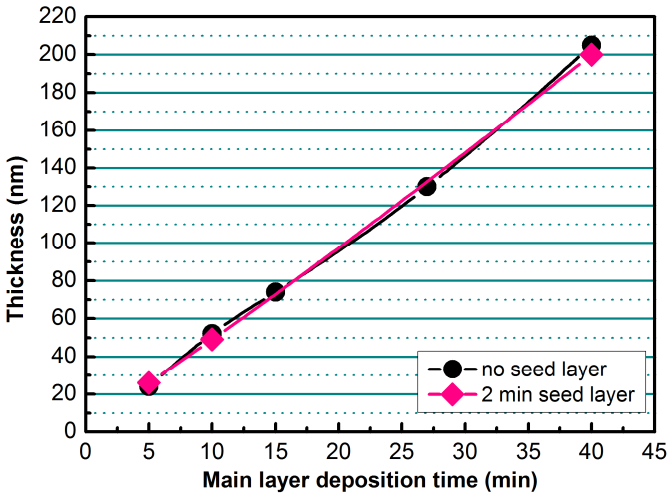

Figure 3.13.: Total thickness as a function of the total deposition time for samples deposited with no seed layer (SET_{seed2} - ●) and with a 2 min seed layer (SET_{seed3} - ◆).

With these new conditions, even without a seed layer, it is possible to obtain very thin layers (∼ 30-50 nm) showing some degree of crystallinity. Nevertheless, their Raman spectra are clearly dominated by the amorphous component located at 480 cm^{-1}. From the deconvolution of these spectra the crystalline volume fraction f_c^{Raman} was determined. The two trends are reported in Figure 3.14. Once the stationary growth is reached, the same crystalline fraction is obtained for both series of samples.

If one assumes that despite the presence of CH_4 in the gas mixture the growth of this kind of alloys is the same as for μc-Si:H (as shown in Fig-

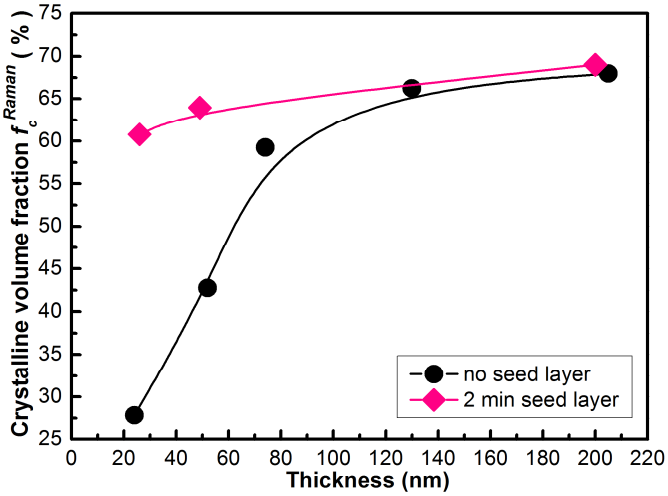

Figure 3.14.: Evolution of the crystalline volume fraction of samples deposited without (SET_{seed2} - ●) and with a 2 minute (SET_{seed3} - ◆) seed layer, as function of the total thickness.

ure 1.5), then it can be inferred that the absence of the seed layer leads to materials for which the incubation zone is mainly amorphous. Instead, its addition will lead to materials with incubation zones that are mainly microcrystalline.

GIXRD patterns were acquired for samples deposited for 5 and 10 minutes. For both deposition times, the thickness of the two layers is the same. Therefore, since GIXRD patterns were acquired keeping the same configuration with an incidence angle $\theta_i = 0.24°$, layers deposited with and without the seed layer can be directly compared, as the probed areas are the same. The obtained patterns are shown in Figure 3.15, where the diffraction peaks are labeled and correspond to the diffracting plane of the cubic phase of crystalline silicon.

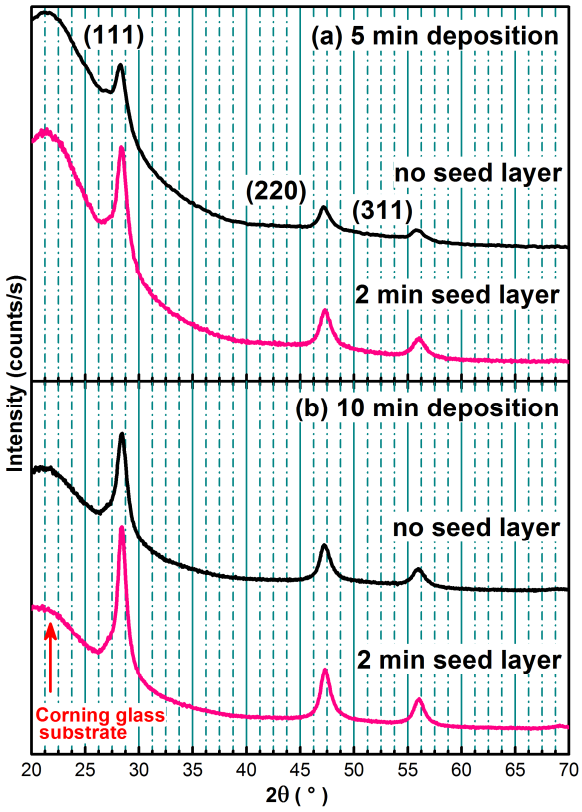

Figure 3.15.: XRD patterns acquired in grazing incidence mode for the samples deposited for (a) 5 minutes and (b) 10 minutes. Lattice planes corresponding to the different Si peaks are labeled.

Since the probed volumes are the same, in each figure the increase of the peaks intensity can be ascribed to an increased crystallinity due to the addition of the seed layer. On the other hand, the increased intensity observed in passing from 5 to 10 minutes, cannot only be related to the increased crystalline fraction, but also to the increased thickness, assuming a constant density of nano-grains per unit volume. Therefore Figure 3.15(a) and 3.15(b) cannot be directly compared. This is clearly underlined by the different intensity of the diffraction arising from the Corning glass substrate, at $2\theta = \sim 22°$. Since layers in Figure 3.15(b) are thicker than those deposited for 5 minutes, the X-rays penetrate less in the substrate, giving a less intense diffraction peak.

Finally, for both sets of depositions, the (111)/(220) and (220)/(311) ratios of the diffraction peak intensities are in good agreement with the powder standard of cubic silicon, proving that with or without seed layer there is no preferential orientation.

3.2.3 Role of the substrate

In this work all samples were deposited simultaneously on Corning "Eagle" glass, for structural and electrical characterizations, and <100> FZ c-Si, for FTIR measurements.

Preliminary analysis like ellipsometry and AFM measurements revealed some inconsistencies possibly linked to the different growth mechanisms happening on the different substrates. It is in fact known that the crystallinity of a μc-Si:H layer depends on the electrical and chemical properties of the substrate (Kondo, Toyoshima, et al., 1996). In Figure 3.16 the ellipsometry spectra of a sample co-deposited on Corning "Eagle" glass and FZ c-Si are shown.

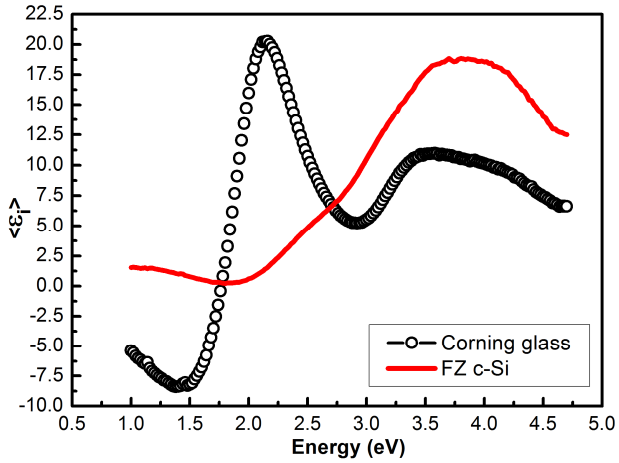

Figure 3.16.: Ellipsometry spectra of a μc-$Si_{1-x}C_x$:H sample simultaneously deposited on Corning glass (O) and FZ c-Si (—).

The difference in pseudodielectric function is possibly related to different structural properties due to the different nature of the substrate. To study the influence of the substrate on the growth of the material, TEM analyses were performed on the sample deposited on the FZ c-Si (Figure 3.17).

Three different areas can be distinguished. To understand the evolution of the layer, the Fast Fourier Transforms (FFTs) were generated from three chosen spots and are reported as insets in the figure. The red dotted FFT, centered on the c-Si substrate, corresponds to the diffraction pattern of a defect-less monocrystalline silicon. A second area (green dash-dotted) can be observed at the interface. The FFT shows the presence of an epitaxial re-growth characterized by a high density of stacking faults. The latter can be recognized by the broadening of the diffraction spots in the FFT, nearly forming lines. Finally, the dashed blue area shows the FFT typical of a polycrystalline material.

No dipping in hydrofluoric acid has been performed before loading the substrates in the reactor chamber, therefore the native oxide layer should be present at the interface with the growing layer. On the other hand, it is possible that the seed layer deposition, which is done using a SiH_4 highly

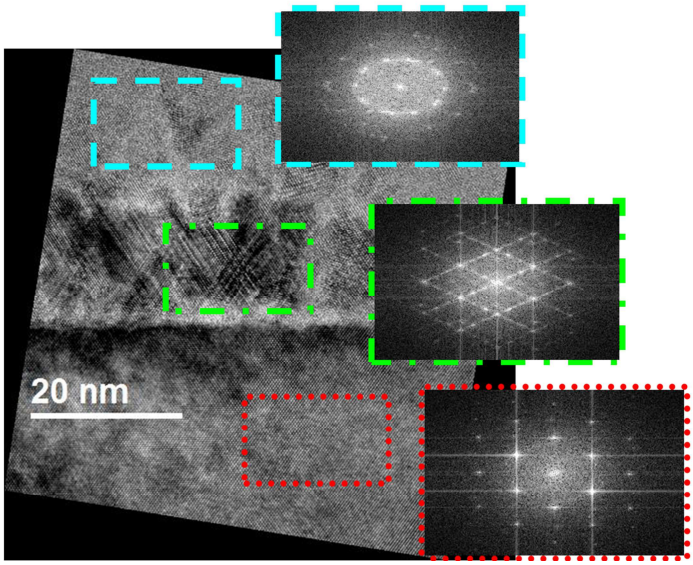

Figure 3.17.: Crossectional TEM image of a μc-$Si_{1-x}C_x$:H sample deposited on FZ c-Si. Three different areas are highlighted and their FFT are shown as insets.

diluted in H_2 gas mixture, breaks the native oxide. Where the oxide is broken an epitaxial re-growth takes place. The addition of CH_4 into the gas mixture disturbs the epitaxial growth, leading to a polycrystalline layer.

In order to avoid the problem of the epitaxial growth and of the resulting different growth of the μc-$Si_{1-x}C_x$:H alloys, it has been decided to deposit a $\sim$ 20 nm thick SiN_x layer on the FZ c-Si. This layer should not be etched by the H_2 plasma and therefore it should provide materials with properties similar to those obtained when growing on Corning glass. In Figure 3.18 the imaginary part of the pseudodielectric function of two alloys co-deposited on Corning "Eagle" glass and FZ c-Si with a SiN_x layer are shown.

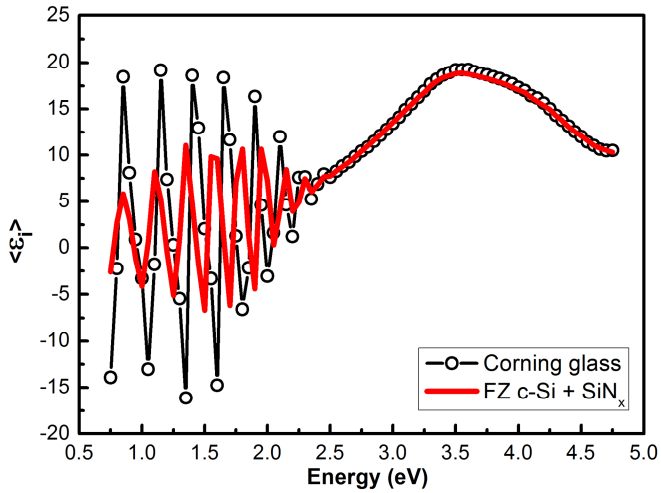

Figure 3.18.: Imaginary part of the pseudodielectric function of a μc-$Si_{1-x}C_x$:H sample simultaneously deposited on Corning glass (O) and FZ c-Si with a 22 nm SiN_x layer deposited on top to break the epitaxial re-growth (—).

With the addition of the SiN_x the two $<\epsilon_i>$ spectra correspond in the high energy region. To have additional informations about the growth, GIXRD analyses were performed on the alloys deposited on the two different substrates (Figure 3.19).

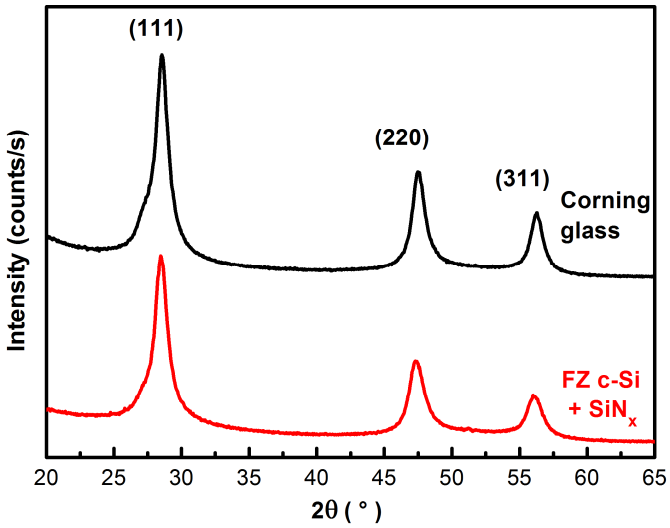

Figure 3.19.: GIXRD of a µc-$Si_{1-x}C_x$:H sample simultaneously deposited on Corning glass (—) and FZ c-Si with a 22 nm SiN_x layer deposited on top to break the epitaxial re-growth (—).

For both samples the FWHMs of the diffraction peaks match, giving an average grain size of 85 Å. An effective method to suppress the epitaxial re-growth and to obtain the same crystalline structure has been found and the information acquired from the FTIR spectra using FZ c-Si with the SiN_x layer can therefore be successfully applied to the material grown on Corning glass.

3.2.4 What is the seed layer?

The last important thing is then to understand *what the seed layer is*. For this reason, a seed layer was deposited on a Corning "Eagle" glass substrate, and then on a TEM grid.

In Figure 3.20 the AFM image of the surface of the seed layer deposited on Corning glass is shown. The presence of round features dispersed on a growth with a roughness $\rho_{RMS} = 0.36$ nm can be observed. Considering that conditions chosen for this seed layer are standard conditions used in the laboratory to obtain microcrystalline materials (15 nm thick, for longer deposition times), it can be assumed that the growth observed in the AFM image represents the very first stages of a microcrystalline growth.

When analyzing the seed layer deposited on the TEM grid, from the diffraction pattern it first appeared that whatever has been deposited on the grid is actually amorphous. Nevertheless, EFTEM images were acquired centering the energy window around 26 eV, which corresponds to the SiO_2 plasmonic energy. The result is shown in Figure 3.21.

The presence of some round structures can be observed, with an average diameter of 10 nm. It cannot be said if these structures were microcrystalline before the exposure to air. It is possible that some microcrystalline growth was started but that when exposed to air an amorphisation was induced by the oxidation, which also lead to an expansion of the volume.

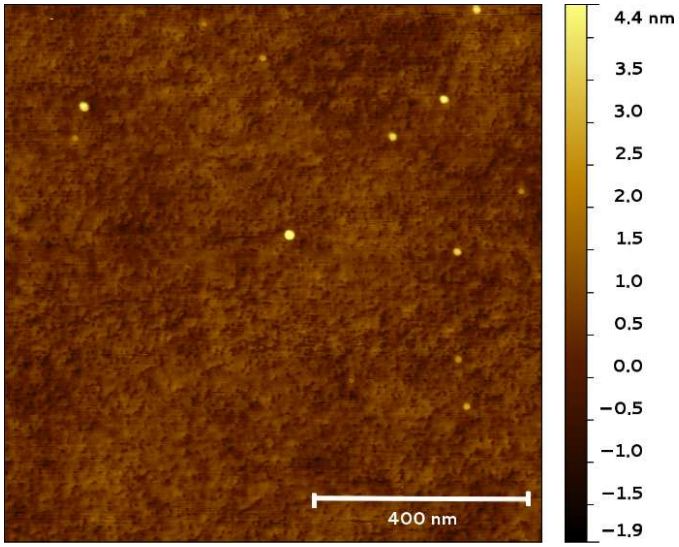

Figure 3.20.: AFM images of a 10 minute seed layer deposited on a Corning glass substrate.

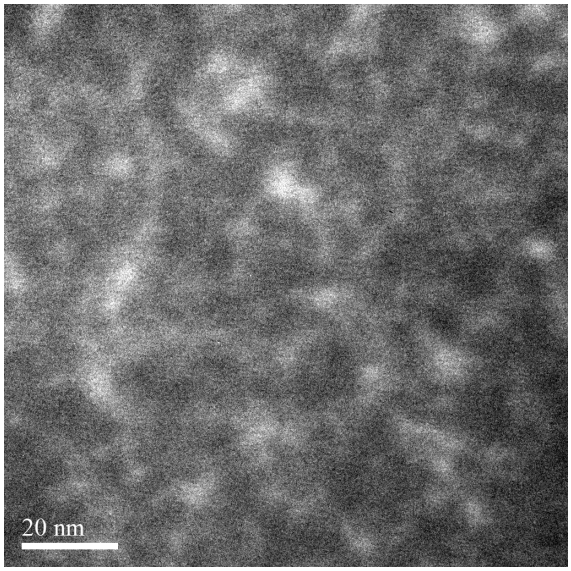

Figure 3.21.: EFTEM image of the seed layer deposited on the TEM grid, acquired centering the energy window at 26 eV.

Despite the difficulty of analyzing the seed layer by itself, it can be supposed that this first step of the deposition of μc-$Si_{1-x}C_x$:H alloys results in the very first stages of the microcrystalline nucleation. As it has been demonstrated in the previous sections, it can be expected that using this seed layer would lead to a lower chance of amorphization of the alloy, due to the presence of carbon based precursor into the plasma discharge.

3.3 GROWTH OF μC-SI$_{1-x}$C$_x$:H ALLOYS BY STANDARD RF-PECVD

The first technique that was used to investigate the growth of μc-Si$_{1-x}$C$_x$:H was standard RF-PECVD at 13.56 MHz. The growth of these materials was done from a highly H_2 diluted SiH_4 and CH_4 gas mixture, as the hydrogen dilution of the reactant gases produces an increased concentration of hydrogen radicals in the plasma which can favor the formation of microcrystals.

The novelty of this material requires the identification of the deposition parameters leading to alloys with interesting properties for photovoltaic application. Therefore, the impact of the variation of several deposition parameters on the structural properties of the alloys has been investigated.

3.3.1 Effect of SiH_4

The search for the most efficient conditions for the development of μc-Si$_{1-x}$C$_x$:H alloys started with the study of the role of SiH_4 flow rate at a constant CH_4 flow rate of 1 sccm (SET_{SiH_4} in Table 3.1). All samples were composed of an initial seed layer followed by a 30 minute deposition with the addition of CH_4 to the gas mixture. For this set of samples the SiH_4 flow rate was varied from 5 sccm to 9 sccm during the main layer deposition.

In Figure 3.22 the imaginary part of the pseudodielectric function and Raman spectra of the set of samples are reported.

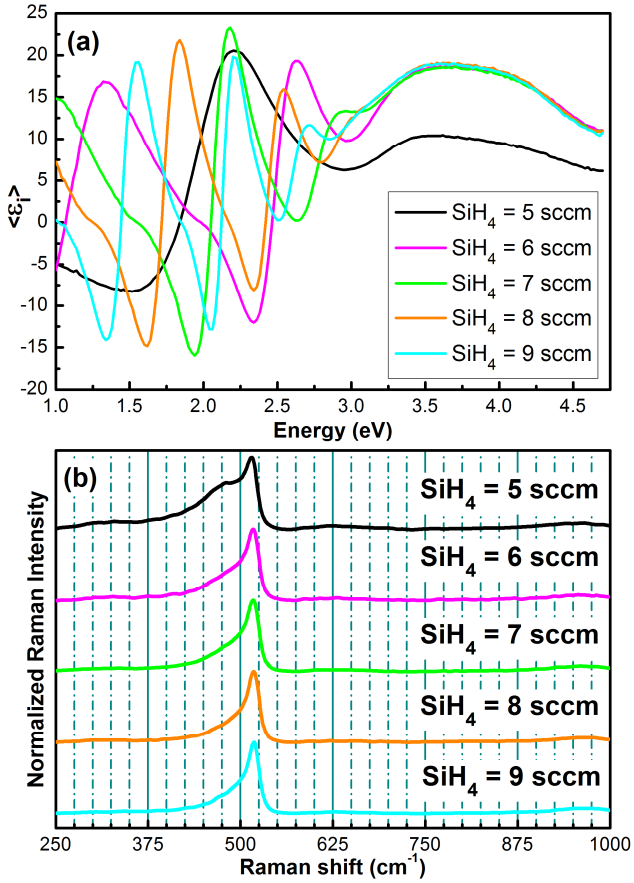

Figure 3.22.: (a) Experimental ellipsometry spectra and (b) Raman spectra of samples from SET_{SiH_4}, deposited varying the SiH_4 flow rate.

All samples show characteristics typical of microcrystalline materials, with $<\epsilon_i>$ exhibiting two defined features at 3.5 eV and 4.2 eV and Raman spectra dominated by the Si — Si TO mode at $\sim 520\ cm^{-1}$. This could be thought as a counter-intuitive result if compared to μc-Si:H growth as a function of the SiH_4 dilution. Indeed, it is known that when growing μc-Si:H, with increasing SiH_4 flow rate there is a transition to the amorphous phase. However for μc-$Si_{1-x}C_x$:H alloys it seems that the CH_4/SiH_4 ratio is more important than the SiH_4/H_2 one.

From the fitting of the ellipsometry spectra, an estimate of the thickness of the layers can be obtained, showing that the variation of the SiH_4 flow rate induces an increase of the deposition rate (Figure 3.23). One could argue that the evolution observed in the Raman spectra, where with increasing SiH_4 flow rate a decrease in the contribution arising from the amorphous phase ($\sim 480\ cm^{-1}$) can be observed, cannot be directly linked to an evolution of the structural properties of the material, as a comparison should be made only for samples having similar thicknesses or for systems that have reached the growth stability.

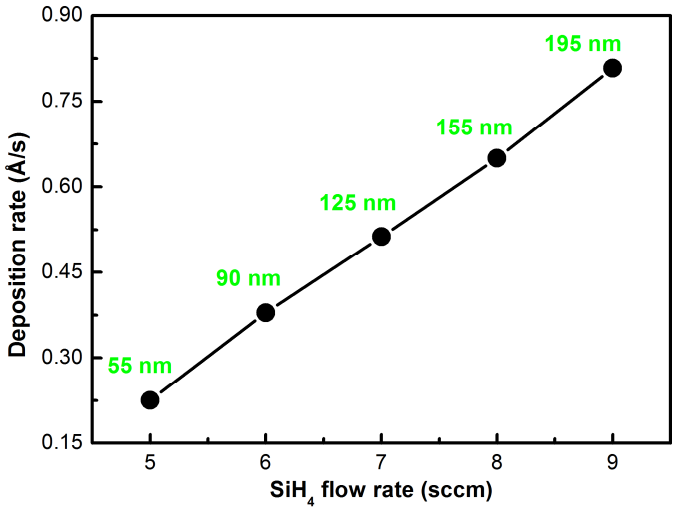

Figure 3.23.: Evolution of the deposition rate as a function of the SiH_4 flow rate. The obtained thickness after 40 minute deposition is marked in green in the figure.

In order to determine if the variation of the SiH_4 flow rate has an effect only on deposition rate or if it affects also the microstructural properties of the material, in Figure 3.24 the evolution of the crystalline volume fraction of these samples, calculated from the deconvolution of the Raman spectra, is compared to what has been obtained for the thickness series presented in Figure 3.14 (SET_{seed3} - ◆). These two series of samples were made using the same deposition conditions, but changing the SiH_4 flow rate (indicated in the figure). What can be observed is the fact that for a higher SiH_4 flow rate, even layers ~ 20 nm thick show a considerable crystalline volume fraction. Therefore, the SiH_4 flow rate not only determines an increase of the deposition rate, but also controls the crystallinity of the material.

Finally, in Figure 3.25 the evolution of the total carbon-silicon ratio R_C, as determined from RF-GD-OES measurements, is plotted as a function of the SiH_4 flow rate together with the amorphous fraction $f_a = 100 - f_c^{Raman}$. For a fixed CH_4 flow rate and RF-power, increasing the SiH_4 flow rate reduces the CH_4 percentage in the gas mixture. A higher flux of SiH_x radicals

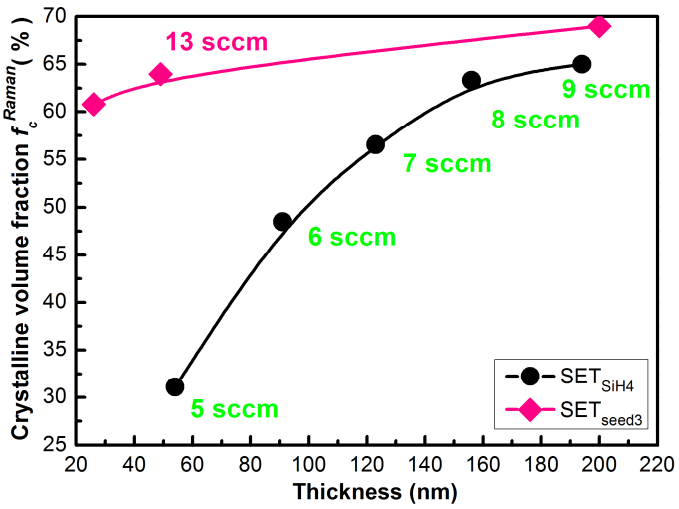

Figure 3.24.: Evolution of the crystalline volume fraction for samples deposited varying the SiH_4 flow rate (SET_{SiH_4} - ●) and for samples deposited varying the deposition time, presented in Figure 3.14 (SET_{seed3} - ◆). Values of the used SiH_4 flow rate are marked in green for the SiH_4 series and in pink for the thickness series.

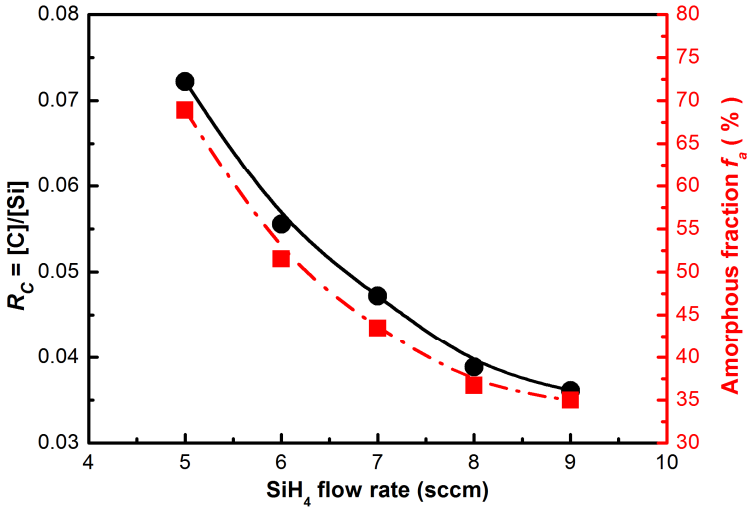

Figure 3.25.: Evolution of the total carbon-silicon ratio R_C (●) and of the amorphous phase f_a (■) as a function of the SiH_4 flow rate.

reaches the surface of the substrate, leading to a lower carbon incorporation. As carbon cannot be incorporated into the crystalline phase, the decrease of the amorphous fraction induces a decrease in the amount of carbon incorporated in the alloy.

3.3.2 Effect of CH_4

As the main goal of this work is to grow μc-Si$_{1-x}$C$_x$:H alloys from a SiH_4 and CH_4 gas mixture highly diluted in H_2, the role the CH_4 flow rate in the final properties of the material has to be understood. Indeed, it is known that the introduction of carbon containing gases into the silane discharge can be detrimental for the growth of μc-Si:H (Goldstein et al., 1988). However, it

was previously shown that the addition of the initial seed layer reduces the problems related to carbon incorporation in the first stages of the nucleation.

The $SET_{CH_4 2}$ (Table 3.1) was made varying the CH_4 flow rate from 1 sccm to 1.8 sccm during the main layer deposition. In Figure 3.26 the imaginary part of the pseudodielectric function and the Raman spectra of these samples are reported. In both cases, with an increasing CH_4 flow rate a transition from a microcrystalline to an amorphous phase is observed. Indeed, ellipsometric measurements show a transition from a dielectric function with two features at 3.5 eV and 4.2 eV, typical of μc-Si:H, to an amorphous material with a larger band gap, and in Raman measurements the $Si-Si$ TO mode at about 520 cm^{-1} decreases, leading to spectra that are characterized only by the broad peak of the amorphous phase. Moreover, Raman spectra show no signs of crystalline forms of SiC, the TO and LO phonons peaks of which should be around 800 cm^{-1} or 960 cm^{-1} (Finger et al., 2009).

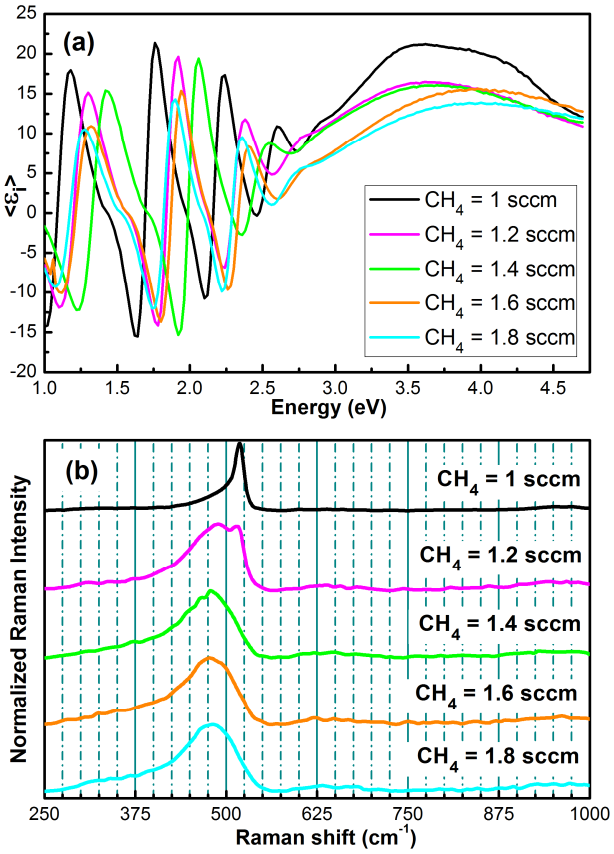

Figure 3.26.: (a) Experimental ellipsometry spectra and (b) Raman spectra of samples from $SET_{CH_4 2}$, deposited varying the CH_4 flow rate.

Using an incidence angle $\theta_i = 0.35°$, GIXRD analyses were performed to confirm the absence of any carbon-based crystalline phase, and to study the microstructural variations induced by the increase of CH_4 flow rate (Figure 3.27). As expected, the diffraction peaks, which are labeled in the figure, are characteristic only of the cubic phase of crystalline silicon. No crystalline forms of silicon carbide or crystalline forms of carbon are present. Therefore, all the carbon incorporated in the alloy composition must create an amorphous $Si_{1-x}C_x$ tissue embedding the growing silicon crystals. Moreover, exceeding a certain CH_4 threshold induces a structural variation and leads to completely amorphous materials, as demonstrated by the diffrac-

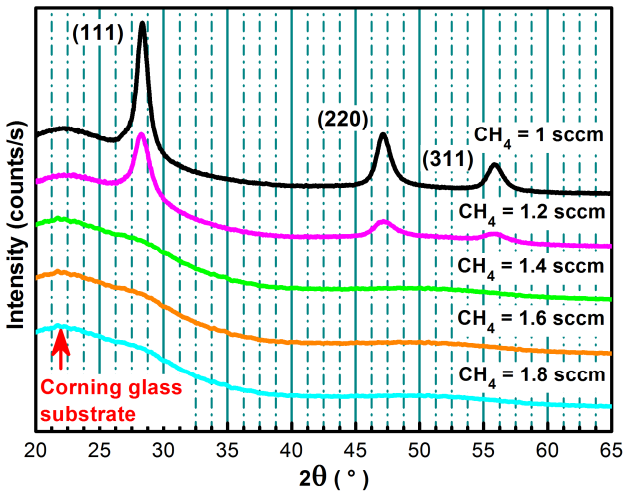

Figure 3.27.: GIXRD patterns for samples from SET$_{CH_4 2}$, deposited varying the CH_4 flow rate. Lattice planes corresponding to c-Si diffraction peaks are labeled.

tion patterns that exhibit only those signature characteristic of short and medium-range order (at $2\theta = 27.6°$ and $51°$).

SAADF STEM images were acquired for crystalline samples and are presented in Figure 3.28. The sample deposited with CH_4 = 1 sccm (Figure 3.28(a)), which is 230 nm thick, with a 5 nm roughness, is very microcrystalline, but is characterized by small grains. When the CH_4 flow rate is increased to 1.2 sccm, the layer, 240 nm thick with a 7 nm roughness, is clearly characterized by small crystallites dispersed in an amorphous matrix (Figure 3.28(b)). Attempts at acquiring Z contrast images, using the HAADF detector, led to images characterized by a very weak variation of contrast and that thus are not presented. This is possibly related to the very low amount of carbon incorporated in the alloys, which is barely reaching the detection limit.

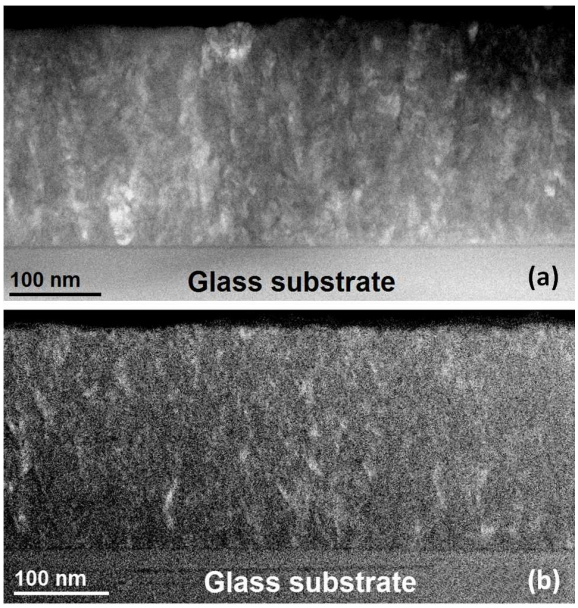

Figure 3.28.: SAADF-STEM images of sample deposited with (a) CH_4 = 1 sccm and (b) CH_4 = 1.2 sccm.

To obtain additional information about the chemical composition and distribution in the layer, an EFTEM study of the sample deposited with CH_4 = 1.2 sccm (which is on the microcrystalline-to-amorphous threshold) was performed. The energy window was first set at 17 eV, corresponding to the silicon bulk plasmon loss, and then centered at 24 eV, to observe the presence of a-$Si_{1-x}C_x$. Images of the interface between the sample and the glass substrate are shown in Figure 3.29. A direct comparison confirms that the crystalline phase in these alloys is made of silicon. The crystallites are indeed brighter than the remaining part of the sample in Figure 3.29(a) and become darker in Figure 3.29(b). In parallel, carbon-rich areas are bright in the image acquired selecting the 24 eV plasmonic energy and become dark in the 17 eV one. It is noteworthy that the material is characterized by a particular V structure typical of a columnar growth. Therefore, it can be inferred that the material is trying to grow with a classical columnar structure, typical of microcrystalline silicon, and that since carbon cannot crystallize in sub-stoichiometric alloys, it is incorporated in the amorphous grain boundaries, creating a thin interconnecting a-$Si_{1-x}C_x$:H tissue surrounding the silicon crystallites.

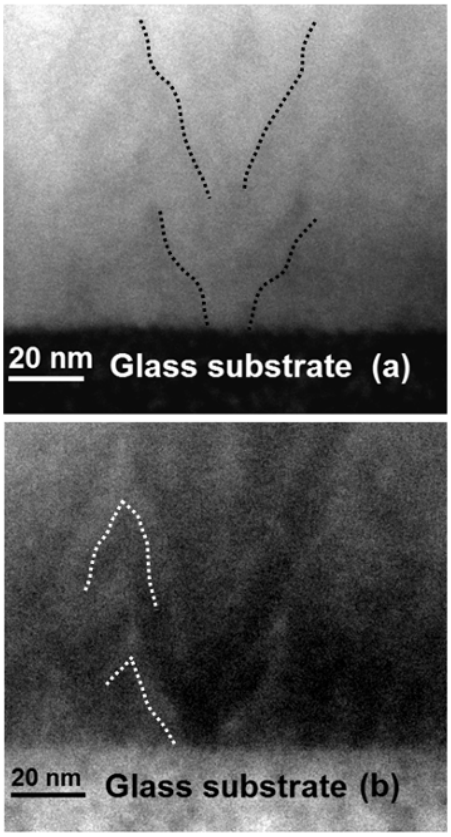

Figure 3.29.: Plasmonic images of the µc-$Si_{1-x}C_x$:H alloy made with a CH_4 flow rate of 1.2 sccm, acquired at different plasmonic excitation energies: (a) 17 eV, corresponding to Si bulk and (b) 24 eV corresponding to a-$Si_{1-x}C_x$. The dotted lines are used to underline zones with a contrast changing from bright to dark, depending on the chosen plasmonic excitation.

Additionally, the effect of CH_4 flow rate has been studied for other two sets of deposition conditions ($SET_{CH_4}1$ and $SET_{CH_4}3$ in Table 3.1), precisely for different SiH_4 flow rates (5 sccm and 13 sccm, respectively). As shown in the previous section, for a fixed CH_4 flow rate and RF-power the variation of the SiH_4 flow rate induces a variation of the CH_4 percentage in the gas mixture. Despite having the same flux of carbon-based radicals that reach the substrate surface, a variation of the SiH_4 flow rate induces an evolution of the flux of SiH_x radicals and this leads to a different carbon incorporation in the alloys, as can be seen in Figure 3.30. For all series, a linear relation can be observed with an offset in the incorporated carbon. It should be noted that the linearity of the CH_4 mass flow controller was verified over this entire range.

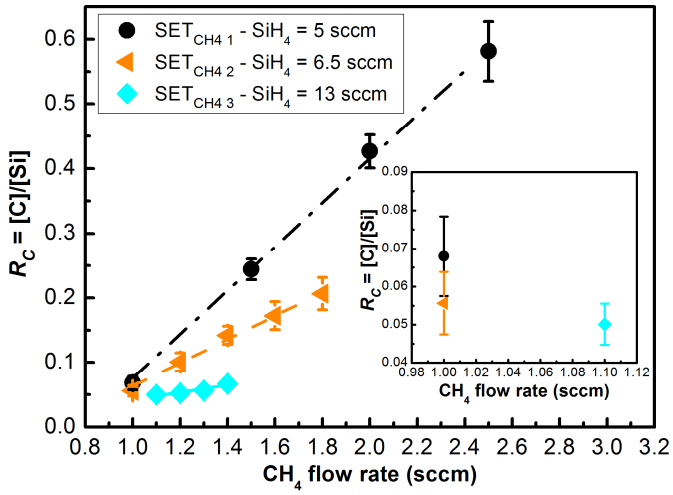

Figure 3.30.: Evolution of the total carbon-silicon ratio R_C as a function of the CH_4 flow rate, for samples deposited using 5 sccm ($SET_{CH_4}1$ - ●), 6.5 sccm ($SET_{CH_4}2$ - ◀) and 13 sccm ($SET_{CH_4}3$ - ◆) of SiH_4. In the inset a zoom on the low CH_4 flow rates is presented.

Despite the variation of the SiH_4 flow rate, increasing the CH_4 in the gas mixture leads always to a microcrystalline-to-amorphous transition, which is shifted to different thresholds according to the different SiH_4 flow rate. In Figure 3.31 the evolution of the crystalline volume fraction and of the average grain size is presented for the three sets of samples, as a function of the carbon incorporation. For these deposition conditions, small variations in the CH_4 flow rate are sufficient to induce a transition from highly crystalline materials ($f_c^{Raman} \sim 60$ %), to mainly amorphous ones ($f_c^{Raman} \sim 25$ %). Exceeding a CH_4 percentage that gives a carbon-silicon ratio above 0.1 results in alloys that are completely amorphous. Indeed, it is known that the addition of a carbon-based precursor into the plasma discharge induces the amorphization of the alloy, leading to a phase transition (Catherine, Turban, and Grolleau, 1981). For the deposition conditions used, an increase of the CH_4 flow rate in the gas mixture leads to an increased number of dissociated CH_4 molecules. The carbon incorporation, which cannot happen in the crystalline phase due to the metastability of sub-stoichiometric silicon-carbon alloys (Osten, 2000), leads to the distortion of bonds and angles in the lattice, creating an amorphous phase. The higher is R_C, the lower is the possibility for silicon crystallites grow. A growth model, taking into account these experimental results, will be presented in section 3.5.

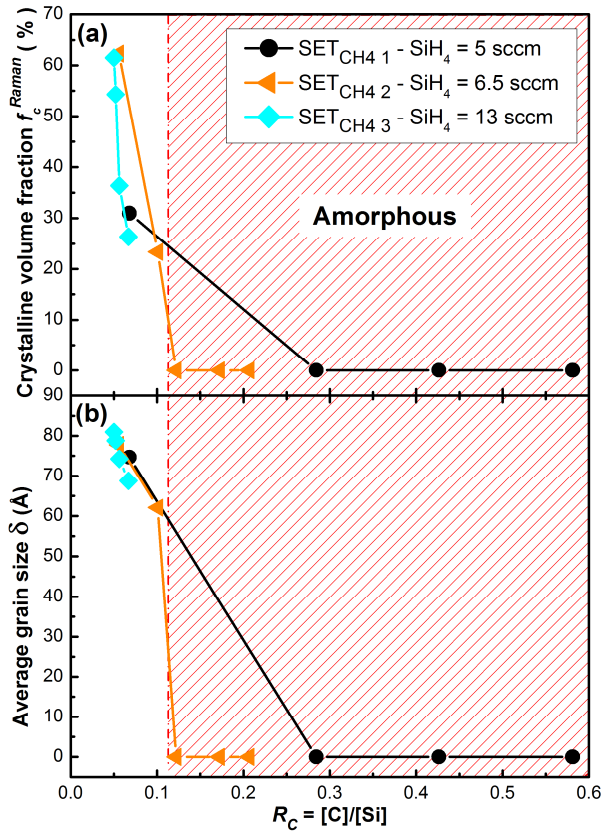

Figure 3.31.: Evolution of (a) crystalline volume fraction f_c^{Raman} and (b) average grain size δ as a function of the total carbon-silicon ratio R_C, for samples deposited using 5 sccm ($SET_{CH_4}1$ - ●), 6.5 sccm ($SET_{CH_4}2$ - ◀) and 13 sccm ($SET_{CH_4}3$ - ◆) of SiH_4.

With RF-GD-OES information about the total carbon incorporation are obtained. On the other hand, when using the FTIR technique the evolution of the chemical environment with the variation of the CH_4 flow rate can be studied. In Figure 3.32, FTIR spectra are reported only for $SET_{CH_4}2$ (samples deposited using SiH_4 = 6.5 sccm).

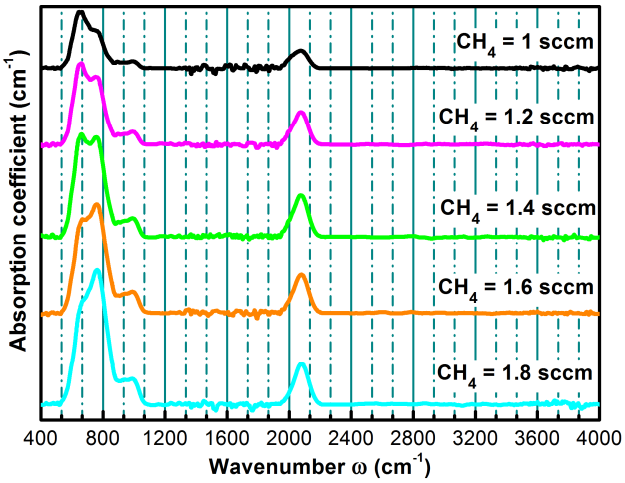

Figure 3.32.: IR spectra for samples from $SET_{CH_4}2$, deposited with different CH_4 flow rate.

For the other series of alloys a similar evolution can be observed. It can be noted that carbon is mainly bonded to silicon and that with increasing CH_4 flow rate the contribution of the Si — C stretching mode at ~ 760 cm^{-1} increases. From the deconvolution of the different bands the Si — C and Si — H bond concentrations N_{Si-C} and N_{Si-H} can be determined (Figure 3.33). At first glance, these results might seem at odds with those obtained by RF-GD-OES as a saturation in both Si — C and Si — H can be observed, whereas in Figure 3.30 a linear relation is presented. However, it is important to note that while RF-GD-OES measures the *total* carbon content, FTIR analyses enable the estimation of only the density of Si — C bonds, not taking into account any contribution arising from C — H and C — C bonds. For these sets of samples it has been impossible to determine the C — H bond density. Usually this is estimated from the deconvolution of the absorption region in the 2800-3000 cm^{-1} range as the 1000 cm^{-1} absorption band is considered to be not reliable. On the other hand, due to the low absorption strength of C — H bonds (when carbon is bonded to silicon), such determination has proved to be impossible for the materials under investigation. From the 1000 cm^{-1} band an increase of the C — H bond density is expected, especially since hydrogen is preferentially bonded to carbon (Bullot et al., 1987), but a quantitative determination was not achieved.

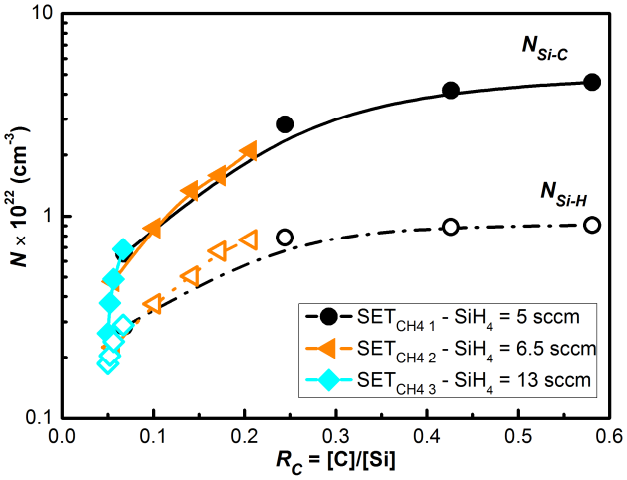

Figure 3.33.: Evolution of the Si-C and Si-H bond concentration (closed and open symbols, respectively), as a function of the total carbon-silicon ratio R_C, for samples deposited using 5 sccm ($SET_{CH_4}1$ - ●), 6.5 sccm ($SET_{CH_4}2$ - ◀) and 13 sccm ($SET_{CH_4}3$ - ◆) of SiH_4.

The carbon incorporation contributes also to the evolution of the 1900-2200 cm^{-1} absorption region, as shown in Figure 3.34 for samples deposited with SiH_4 = 6.5 sccm ($SET_{CH_4}2$). For low CH_4 values the presence of two bands can be distinguished, whereas with increasing CH_4 flow rate, one main contribution centered at about 2090 cm^{-1} seems to appear. Such behavior can be linked to the increased carbon incorporation. Indeed, it is known from the literature that the 2000 cm^{-1} Si — H stretching band can shift towards 2090 cm^{-1} due to carbon back-bonding (Bullot et al., 1987). In Figure 3.35 the shift $\Delta\omega$ of the Si — H stretching mode is plotted as a function of the total carbon-silicon ratio R_C, showing a linear relation. For values of $R_C > 0.3$, the peak shifts more than 90 cm^{-1}. At the present time, no significant explication for such a large shift can be found. This is still a matter for further investigation, which would require additional carbon-rich amorphous alloys to be deposited.

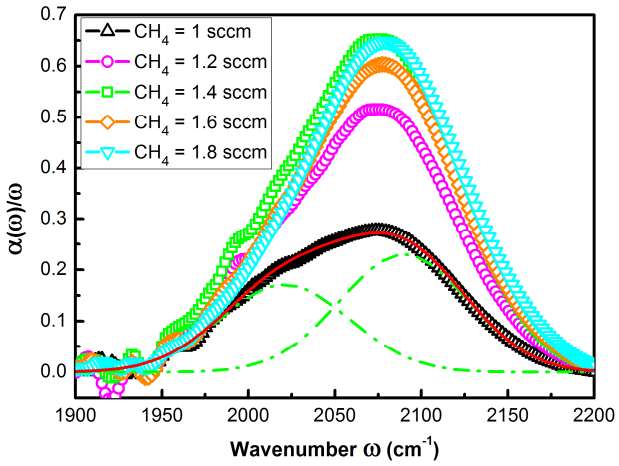

Figure 3.34.: Evolution of the 1900-2200 cm^{-1} band for the different samples presented in Figure 3.32. The $\alpha(\omega)/\omega$ ratio is plotted as a function of the wavenumber ω. As an example, for the sample deposited with CH_4 = 1 sccm (△) the dash-dotted green lines represent the fit of the two bands at 2000 cm^{-1} and 2090 cm^{-1}, and the continuous red line represents the total fit.

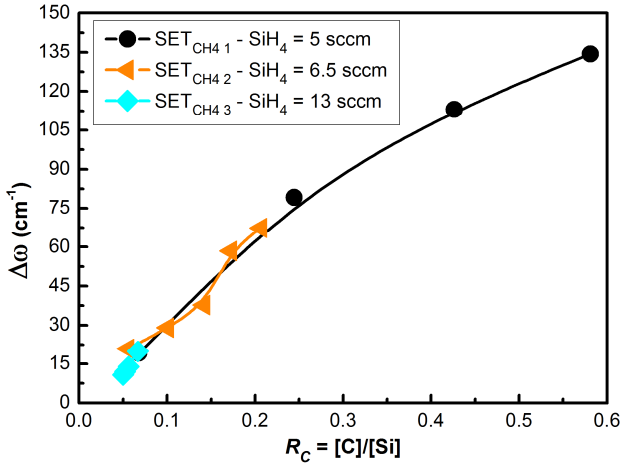

Figure 3.35.: Shift $\Delta\omega$ of the Si-H stretching mode, due to carbon back-bonding, for samples deposited using 5 sccm ($SET_{CH_4 1}$ - ●), 6.5 sccm ($SET_{CH_4 2}$ - ◀) and 13 sccm ($SET_{CH_4 3}$ - ◆) of SiH_4.

3.3.3 Effect of RF-power

It is known from the literature that the RF-power is one of the parameters that determines the quality and the crystalline content of μc-Si:H (Matsuda, 1999). To study its impact on the growth of μc-$Si_{1-x}C_x$:H, it was decided to start from deposition conditions giving a material with properties on the microcrystalline-to-amorphous threshold, and to vary the RF-power. The most appropriate conditions were found in the alloy deposited using CH_4 = 1.2 sccm from $SET_{CH_4 2}$ (Figure 3.26) and characterized by a $f_c^{Raman} \sim 25$ %. A new set of samples was deposited ($SET_{w_{RF}1}$ in Table 3.1) varying the RF-power density w_{RF} from 113 mW/cm^2 (20 W) to 565 mW/cm^2 (100 W), during the main layer deposition. To keep the total thickness of the layers in the 200-300 nm range, the deposition time was adjusted from 90 to 50 minutes with increasing RF-power (the deposition rate as a function of w_{RF} is plotted in Figure 3.36).

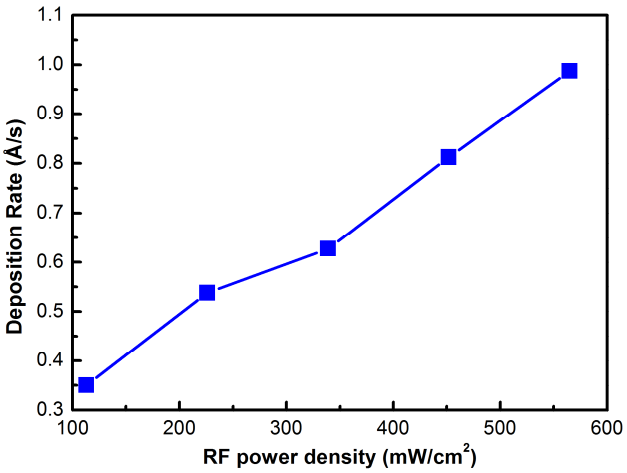

Figure 3.36.: Evolution of the deposition rate as a function of the RF-power density.

The imaginary part of the pseudodielectric function $<\epsilon_i>$ and the Raman spectra of this set of samples are shown in Figure 3.37. With increasing RF-power density a microcrystalline-to-amorphous transition is observed. For RF-power densities below 300 mW/cm^2 the alloys show the presence of a crystalline component, as evidenced by pseudodielectric functions characterized by two defined features at 3.5 eV and 4.2 eV and Raman spectra presenting the Si−Si TO mode at $\sim$ 520 cm^{-1}.

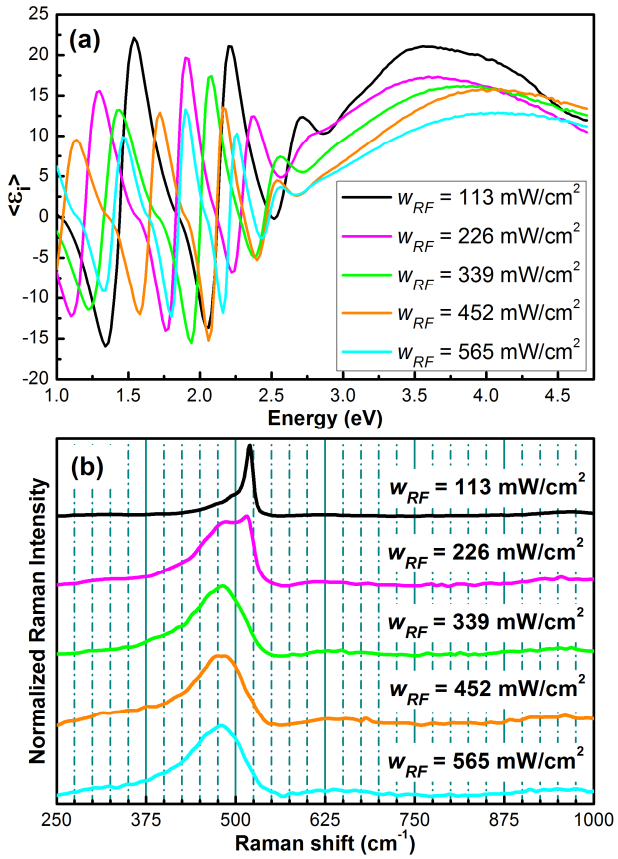

Figure 3.37.: (a) Experimental ellipsometry spectra and (b) Raman spectra of samples from SET$_{w_{RF}1}$, deposited varying the RF-power density w_{RF}.

However, higher RF-power densities result in completely amorphous alloys, and this nature is highlighted by a single broad peak in $<\epsilon_i>$ and Raman spectra dominated by the amorphous phase ($\sim$ 480 cm^{-1}). This evolution is also observed in the GIXRD patterns, which were acquired for $\theta_i = 0.35°$ (Figure 3.38). With increasing w_{RF} it is possible to pass from alloys exhibiting diffraction peaks corresponding to the cubic phase of crystalline silicon (w_{RF} < 300 mW/cm^2) to materials that are completely amorphous and for which only diffraction peaks of the short-medium range order are visible.

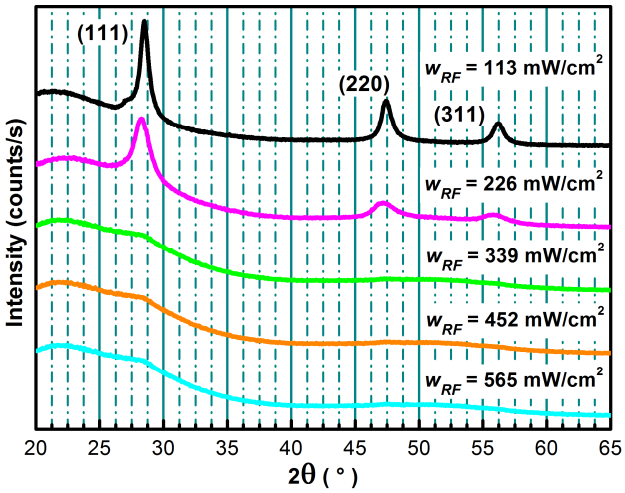

Figure 3.38.: GIXRD patterns for samples from $SET_{w_{RF}1}$, deposited varying the RF-power density w_{RF}. Lattice planes corresponding to c-Si diffraction peaks are labeled.

The phase transition can be linked to the increase of the carbon content incorporated in the material, as shown in Figure 3.39. Varying the RF-power density has a similar effect as the variation of the CH_4 flow rate, which was presented in the previous section. Indeed, the increase of w_{RF} induces the dissociation of a greater number of CH_4 molecules relative to the SiH_4 ones, leading to a higher flux of carbon-based radicals that reach the surface of the growing film. Therefore, in a similar way, the higher w_{RF}, the higher is the total carbon-silicon ratio R_C.

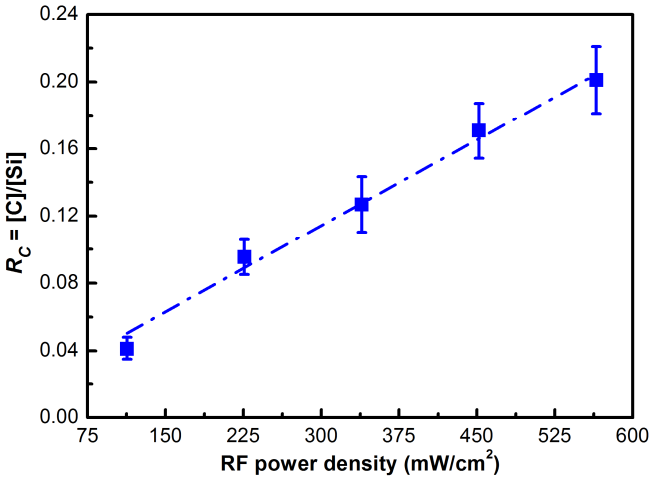

Figure 3.39.: Evolution of the total carbon-silicon ratio as a function of the RF-power density w_{RF}, as determined through RF-GD-OES measurements.

The evolution of the structural parameters (f_c^{Raman} and δ) is presented in Figure 3.40 as a function of the total carbon-silicon ratio. A deterioration of both crystalline volume fraction and grain size with increasing R_C is observed. For the chosen deposition technique the incorporation of carbon inhibits the growth of silicon crystallites (in the *low power regime*, $w_{RF} < 300$ mW/cm^2) or completely hinders their nucleation (in the *high power regime*, $w_{RF} > 300$ mW/cm^2). As a matter of fact, the variation of the RF-power density does not influence only the plasma chemistry, but also leads to a variation of the ion bombardment energy (IBE), which also contributes to the worsening of the crystallization process. A more detailed comparison between the effect induced by the variation of the different deposition parameter will be presented in section 3.3.6.

The FTIR technique was used to investigate the effect of the increase of w_{RF} on the chemical order (Figure 3.41). All the IR absorption spectra show the two distinctive bands arising from Si—H, Si—C and C—H vibrational modes (600-100 cm^{-1}) and Si—H and Si—H$_2$ (1900-2200 cm^{-1}). Carbon is

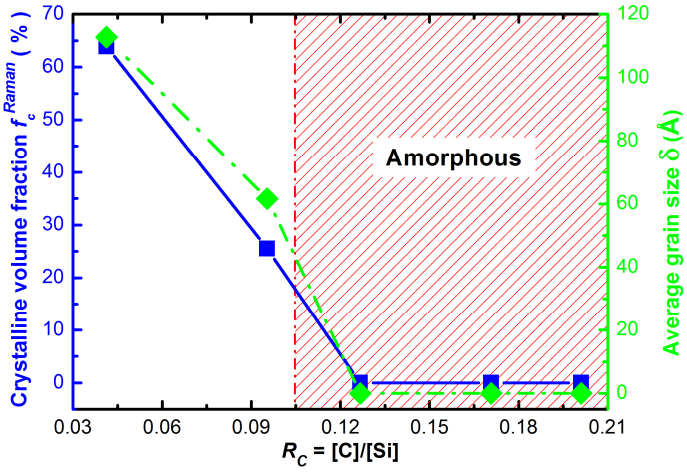

Figure 3.40.: Evolution of the crystalline volume fraction f_c^{Raman} (■) and of the average grain size δ (◆), as a function of the total carbon-silicon ratio.

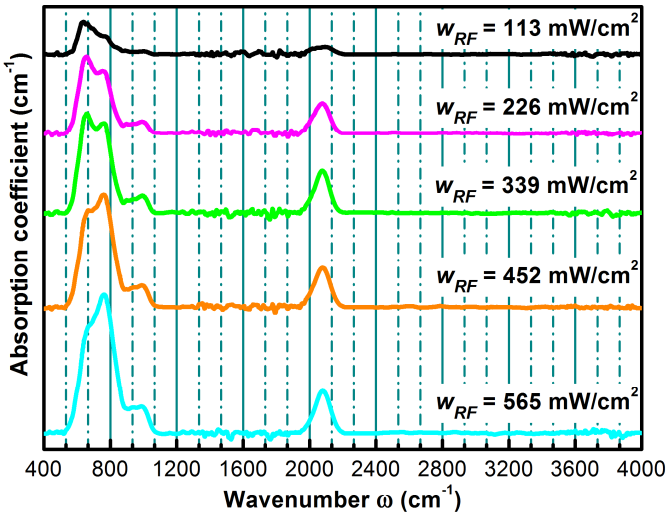

Figure 3.41.: IR spectra of samples from SET$_{w_{RF}1}$, deposited using different RF-power densities.

mainly bonded to silicon, and the intensity of the Si — C vibrational mode is observed to be increasing with increasing w_{RF}. From the deconvolution of the IR absorption bands, the Si — C and Si — H bond concentrations (N_{Si-C} and N_{Si-H}, respectively) were determined and are shown in Figure 3.42, as a function of the total carbon-silicon ratio R_C. The higher is the carbon content, the higher is the density of both Si — C and Si — H bonds.

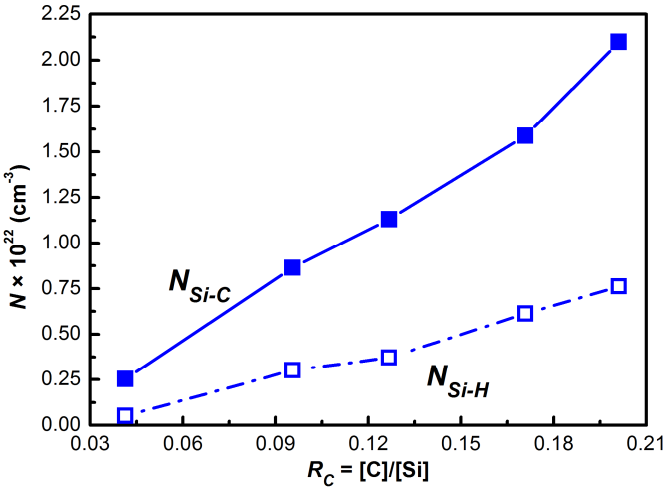

Figure 3.42.: Evolution of the Si-C and Si-H bond concentration (■ and □, respectively), as a function of the total carbon-silicon ratio R_C.

Also for this set of samples the effect of the variation of the chosen deposition parameter on the Si — H and Si — H_2 vibrational modes was investigated. The $\alpha(\omega)/\omega$ ratios for the 1900-2200 cm^{-1} absorption band are presented in Figure 3.43, as a function of the wavenumber ω. With increasing RF-power density a transition from a band clearly characterized by two distinct

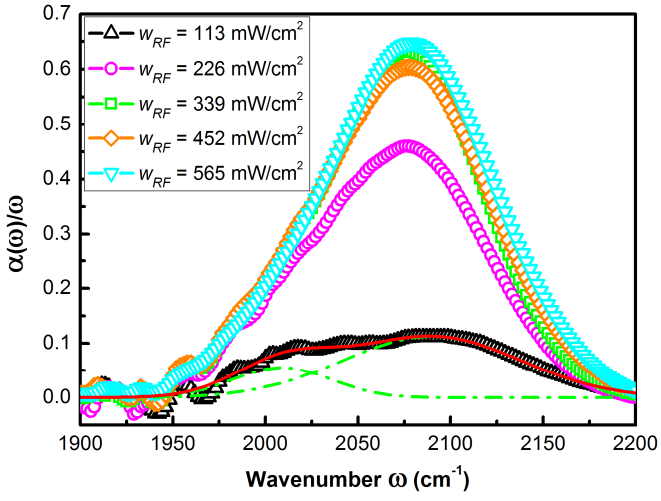

Figure 3.43.: Evolution of the 1900-2200 cm^{-1} IR absorption band for samples deposited varying the RF-power density. The $\alpha(\omega)/\omega$ ratio is plotted as a function of the wavenumber. As an example, for the sample deposited with w_{RF} = 113 mW/cm^2 (△) the dash-dotted green lines represent the fit of the two bands at 2000 cm^{-1} and 2090 cm^{-1}, and the continuous red line represents the total fit.

vibrational modes to a single contribution at ~ 2090 cm^{-1} can be observed. The fact that the peak is not symmetric still suggests the presence of two components. With increasing carbon incorporation the vibrational mode at lower wavenumber shifts towards 2090 cm^{-1}, due to carbon back-bonding of Si — H bonds. The shift of such band is presented in Figure 3.44, showing a linear relation.

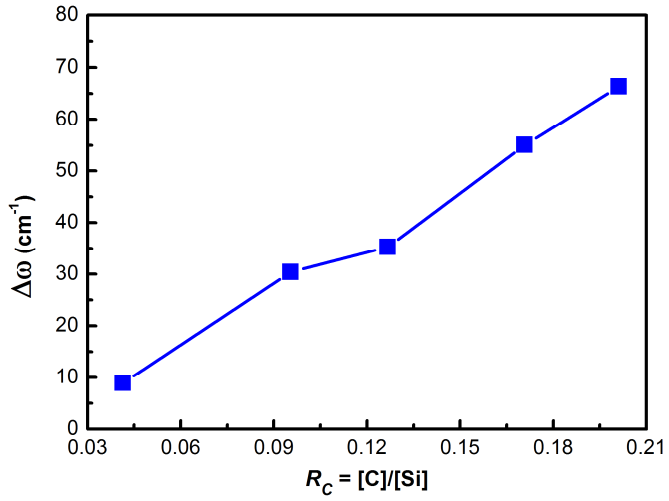

Figure 3.44.: Shift $\Delta\omega$ of the Si-H vibrational mode due to carbon back-bonding.

It is noteworthy that when w_{RF} is decreased to 113 mW/cm^2, an additional shoulder at $2\theta \sim 27^\circ$ appears in the GIXRD pattern. To clearly observe this additional diffraction peak, the intensity of the (111) diffraction plane of sample deposited using w_{RF} = 113 mW/cm^2 is shown in Figure 3.45, after the subtraction of the background.

Coscia et al. attributed the additional component to the presence of a small quantity of crystallized carbon in the graphitic form (U. Coscia, Ambrosone, Lettieri, Maddalena, Rava, et al., 2003). On the other hand

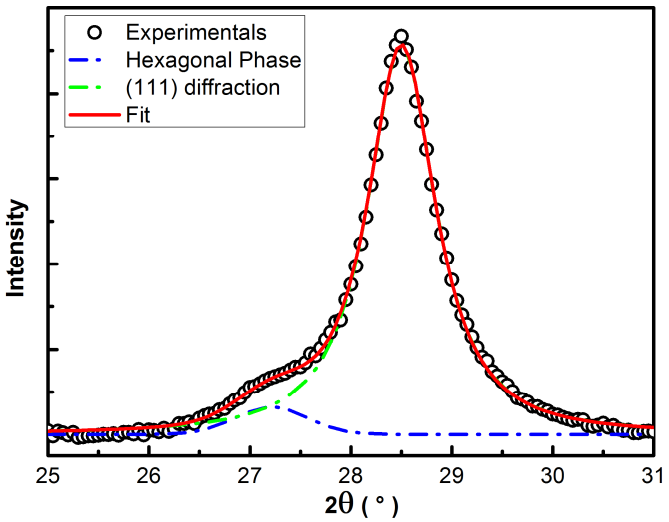

Figure 3.45.: Intensity of the (111) diffraction plane obtained in grazing incidence configuration for the sample deposited using w_{RF} = 113 mW/cm^2. The presence of an additional shoulder at $2\theta \sim 27^\circ$ is shown.

their TEM measurements did not show any crystalline form of carbon (Ambrosone, Barucca, et al., 2004). Moreover, the fact that this component appears only in highly crystalline alloys, having the lowest carbon content, makes it more reasonable to attribute its origin to structural defects and stacking faults. Indeed, it has been proved that a high density of stacking faults and/or twin planes gives rise to a new crystal structure. Moreover, various degrees of periodicity in their distribution underlie a *polytypic modification* (Hendriks et al., 1984). Polytypes are a special case of polymorphs where multiple close-packed crystal structures differ in one dimension only. Polytypes have identical close-packed planes, but differ in the stacking sequence in the third dimension perpendicular to these planes. As a consequence, the unit cell dimensions of polytypes are constant in two dimensions lying in the plane parallel to the stacked layers, but differ in the directions perpendicular to the layers. Normally, silicon crystallizes in a face-centered cubic structure, with an ABCABC stacking sequence of the (111) planes. On the other hand, stacking faults can occur in a way that the stacking order is locally changed to ABAB. Such a stacking sequence is characteristic of the hexagonal close-packed crystal structure (known as *"wurzite"*), which leads to the *hexagonal phase*. Depending on the periodicity, the polytypic modifications can result in different lattice spacings in the direction along the growth axis and therefore appear as diffraction peaks at different positions. More information on the cause of this additional peak, labeled *"hexagonal phase"* in the following, can be found in Hendriks et al., 1984 and were later supported in Luysberg et al., 1997.

Finally, SAADF-STEM analyses were performed on the sample deposited with w_{RF} = 113 mW/cm^2 (Figure 3.46). The sample, which is $\sim$ 180 nm thick, with a 6 nm roughness is characterized by a very well ordered columnar growth. Although some measurements suggest similar outcomes for materials when varying each parameter (similarly to the alloy presented in Figure 3.28(a), this sample is showing a $\sim$ 65 % crystalline volume fraction) SAADF-STEM analyses confirm the results obtained by means of XRD investigations, which show that the variation of CH_4 flow rate and w_{RF} actually result in very different microstructures. A more detailed comparison will be presented in section 3.3.6.

Analysis of the sample deposited with w_{RF} = 226 mW/cm^2 has already been presented in Figure 3.28(b).

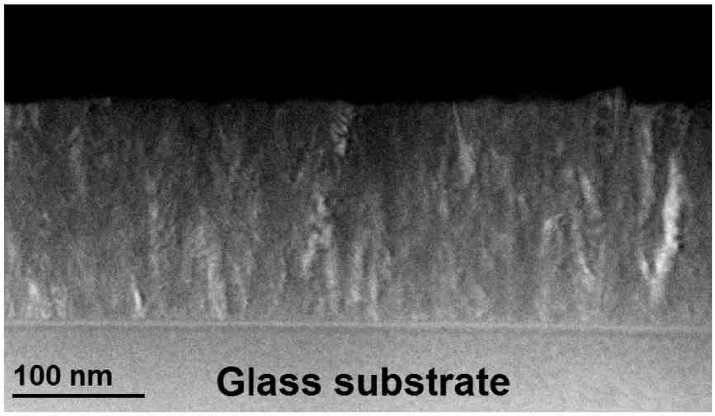

Figure 3.46.: SAADF-STEM image of the sample deposited with w_{RF} = 113 mW/cm^2.

Since the decrease in RF-power leads to materials showing better microstructural properties, a second set of μc-Si$_{1-x}$C$_x$:H alloys was deposited fixing w_{RF} = 133 mW/cm^2, SiH$_4$ = 13 sccm and varying the CH$_4$ flow rate (SET$_{w_{RF}2}$ in Table 3.1). Ellipsometry and Raman spectra are presented in Figure 3.47, showing a microcrystalline-to-amorphous transition. However, with a lower RF-power density a less number of CH$_4$ molecules is dissociated leading to a lower carbon incorporation, for a fixed CH$_4$ percentage in the gas phase (Figure 3.48). Using these deposition conditions, a higher CH$_4$ flow rate threshold has to be reached in order to induce the complete phase transition.

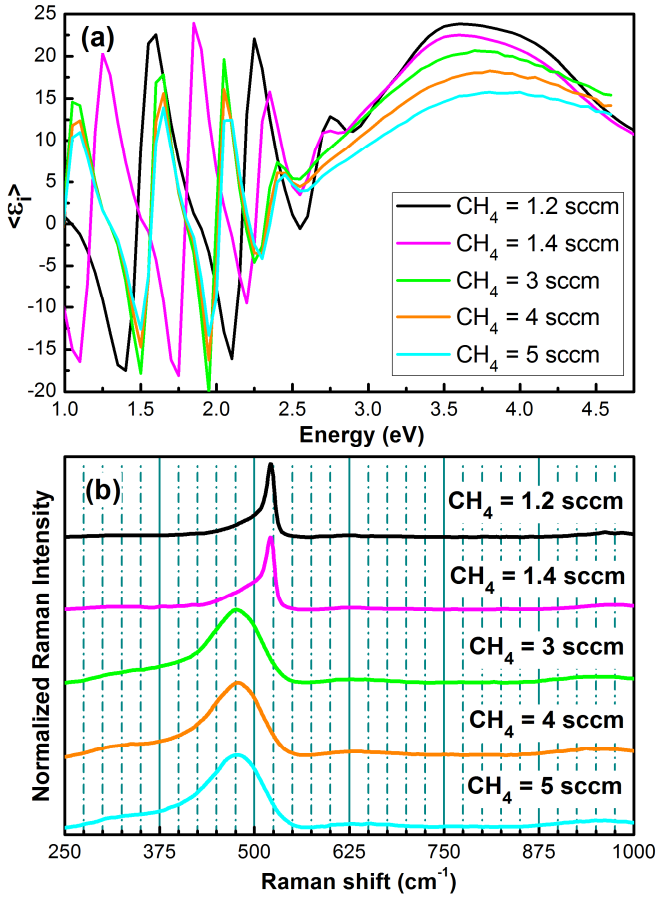

Figure 3.47.: (a) Experimental ellipsometry and (b) Raman spectra of samples from SET$_{w_{RF}2}$, deposited using w_{RF} = 113 mW/cm^2 and varying the CH$_4$ flow rate (SET$_{w_{RF}2}$).

The evolution of f_c^{Raman} and δ of samples from SET$_{w_{RF}2}$ is presented in Figure 3.49. Although the crystalline alloys show very good structural parameters, the increase in CH$_4$ flow rate is still responsible for the deterioration of both f_c^{Raman} and δ. To obtain materials with a significant crystalline fraction ($f_c^{Raman} > 50$ %), which is the basic requirement to maintain stability under light-soaking, a very small amount of carbon has to be incorporated. Once again, for $R_C > 0.1$ the full phase transition is attained.

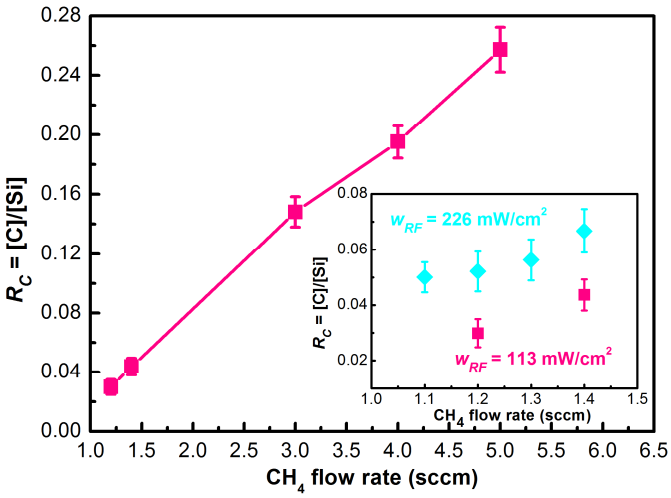

Figure 3.48.: Evolution of the total carbon-silicon ratio R_C for samples from $SET_{w_{RF}2}$, deposited varying the CH_4 flow rate. In the inset, alloys from $SET_{w_{RF}2}$ (w_{RF} = 113 mW/cm^2 - ■) are compared to alloys from SET_{CH_43} (w_{RF} = 226 mW/cm^2 - ◆).

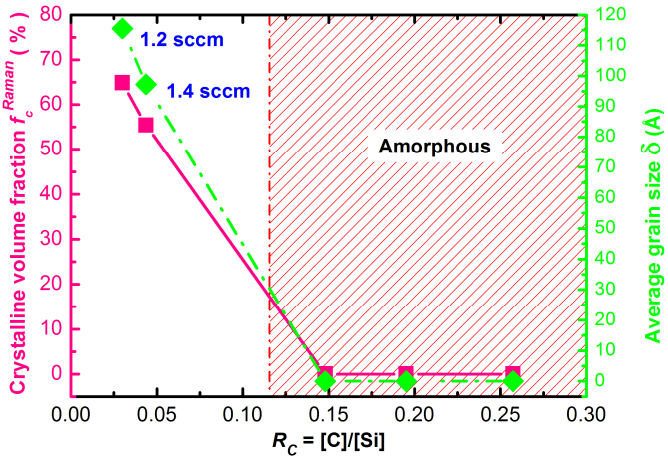

Figure 3.49.: Evolution of crystalline volume fraction f_c^{Raman} (■) and average grain size δ (◆) for samples from $SET_{w_{RF}2}$, deposited using w_{RF} = 113 mW/cm^2 and varying the CH_4 flow rate.

3.3.4 Effect of SiF_4

Another interesting deposition parameter to test is the addition of a small amount of SiF_4 to the gas mixture (few sccm, relative to SiH_4 and CH_4 flow rates). From the literature it is known that the presence of this precursor leads to μc-Si:H samples with a higher crystalline volume fraction and a lower oxygen content (Nakahata et al., 2000; Abramov et al., 2010), but its effect on the growth of μc-$Si_{1-x}C_x$:H has not been investigated yet.

Two sets of samples were deposited using CH_4 flow rates of 1 sccm and 1.2 sccm (respectively SET_{SiF_41} and SET_{SiF_42} in Table 3.1). For both sets, few sccm of SiF_4 were added to the gas mixture (ranging from 0 sccm to 1 sccm). When no SiF_4 is added, materials are the same as those from SET_{CH_42} presented in Figure 3.26.

The structural changes induced in the alloys with the variation of the SiF_4 flow rate have been studied using spectroscopic ellipsometry (Figure 3.50), Raman spectroscopy (Figure 3.51) and grazing incidence X-ray diffraction (Figure 3.52). All these techniques combined have proved to efficiently detect the structural changes induced by a phase transition.

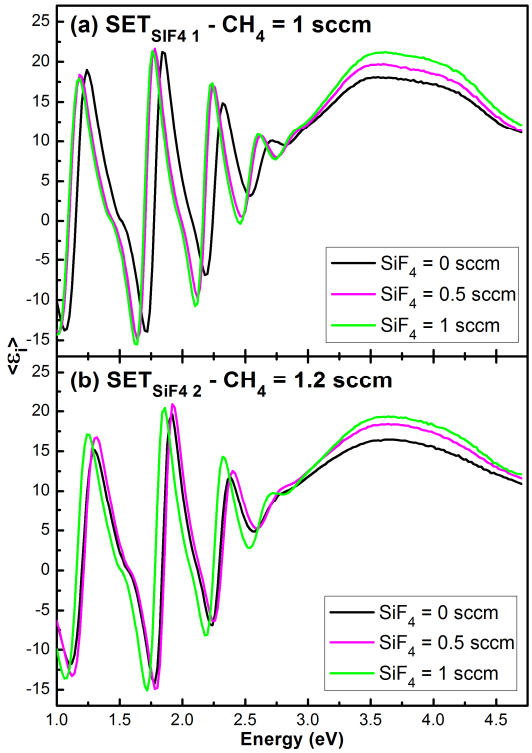

Figure 3.50.: Ellipsometry spectra of samples from (a) $SET_{SiF_4 1}$ and (b) $SET_{SiF_4 2}$, deposited varying the SiF_4 flow rate.

For both sets of samples the addition of SiF_4 to the gas mixture leads to an increase in crystallinity. However, while such evolution can be barely noted for samples from $SET_{SiF_4 1}$, the beneficial effects of the addition of just few sccm of this precursor are evident for samples from $SET_{SiF_4 2}$. For the latter, with the increase of the SiF_4 flow rate two features at 3.5 eV and 4.2 eV in the pseudodielectric function start to appear, indicating an enhancement of the microcrystalline silicon phase. This transition is highlighted in Raman spectra by the decreased intensity of the broad band at 480 cm^{-1} and by the appearance of the sharp Si—Si TO mode at $\sim$ 520 cm^{-1}, and in GIXRD patterns by the increased intensity of the diffraction peaks characteristic of the cubic phase of crystalline silicon (diffraction planes being at 2θ = 28.44°, 47.3° and 56.1°). It is noteworthy that in the diffraction patterns no crystalline silicon carbide or crystalline forms of carbon can be seen. Thus, the SiF_4 impacts only the μc-Si:H phase. Obviously, since carbon is incorporated only in the amorphous phase, the increase of the crystallinty of these samples is matched by the decrease in carbon incorporation, as presented in Figure 3.53.

The addition of SiF_4 to the silane discharge, has a more complicated effect compared to the CH_4 one. So far its role in a process using H_2 diluted SiH_4 and CH_4, has not been studied. Nevertheless, by referring to the impact of atomic fluorine during the growth of films from a SiF_4 and CH_4 gas mixture diluted in hydrogen, it is possible to infer its role when also SiH_4 is included.

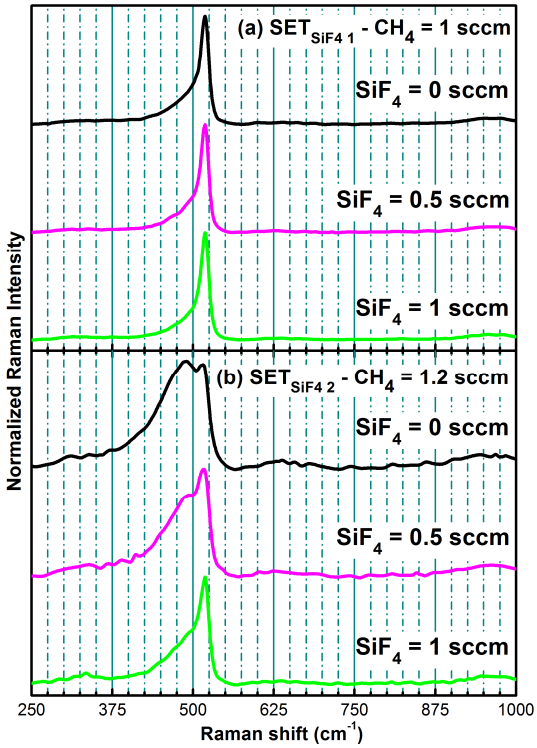

Figure 3.51.: Raman spectra of samples from (a) $SET_{SiF_4\,1}$ and (b) $SET_{SiF_4\,2}$, deposited varying the SiF_4 flow rate.

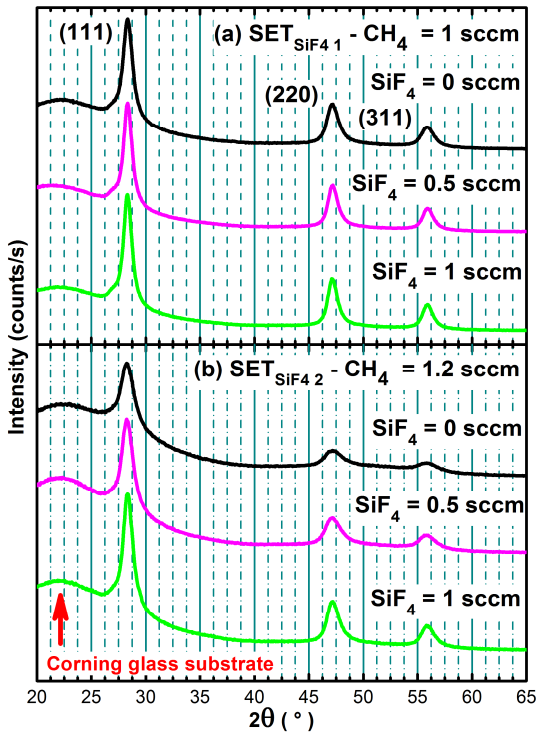

Figure 3.52.: GIXRD patterns of sample from (a) $SET_{SiF_4\,1}$ and (b) $SET_{SiF_4\,2}$, deposited varying the SiF_4 flow rate. Lattice planes corresponding to c-Si diffraction peaks are labeled in the figure.

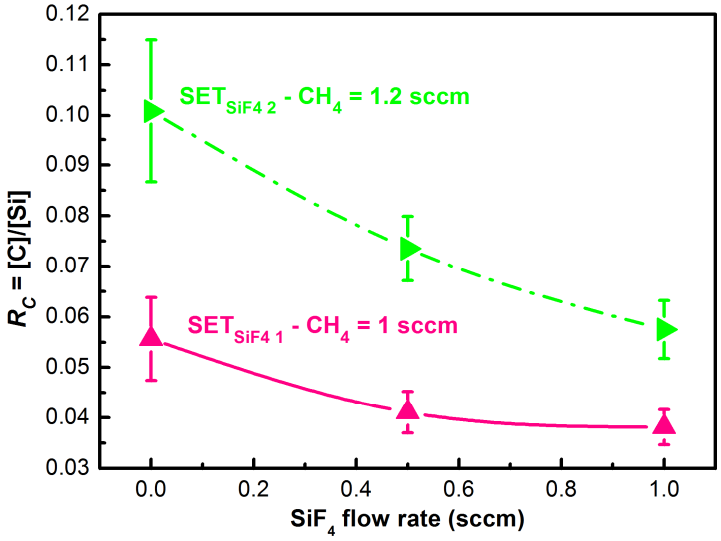

Figure 3.53.: Evolution of the total carbon-silicon ratio R_C, for samples from $SET_{SiF_4 1}$ (▲) and $SET_{SiF_4 2}$ (▶), as a function of the SiF_4 flow rate added to the gas mixture.

Cicala et al. have performed some experiments using fluorinated (SiF_4) and hydrogenated (CH_4) gases, as silicon and carbon sources, highlighting the role of F and H atoms in the growth etching/competition and, hence, in controlling the deposition kinetics and the film composition and structure (Cicala et al., 2001). They showed that hydrogen and fluorine determine two competitive etching mechanisms of both silicon and carbon atoms. But while hydrogen etches carbon in a more efficient way, fluorine does it for silicon. Therefore, the addition of SiF_4 to the gas mixture activates a second etching mechanism, which results in more crystalline films. More details on the growth model of μc-Si$_{1-x}$C$_x$:H will be given in section 3.5.

The evolution of the structural parameters (f_c^{Raman} and δ) is presented in Figure 3.54 as a function of the total carbon-silicon ratio R_C. For the two sets of samples, it can be seen that the addition of SiF_4 to the gas mixture has a beneficial effect for both crystallinity and average grain size. On the other hand, when alloys are already highly microcrystalline ($SET_{SiF_4 1}$ - CH_4 = 1 sccm presents $f_c^{Raman} \sim 60$ % already when no SiF_4 is added to the gas mixture), this precursor has a weak effect on the crystallinity and mainly acts on the quality/size of the grains. The addition of SiF_4 to the gas mixture induces only an increase in f_c^{Raman} of ∼ 10 % (passing from 60 % to 65 %) for samples of $SET_{SiF_4 1}$, whereas for samples of $SET_{SiF_4 2}$ f_c^{Raman} doubles with the addition of 1 sccm of SiF_4(passing from 25 % to 50 %). The effect exerted on the average grain size δ is, however, of a nearly 20 % increase for $SET_{SiF_4 1}$ samples and ∼ 35 % for $SET_{SiF_4 2}$.

SAADF-STEM analyses were performed on the sample from $SET_{SiF_4 2}$ deposited adding 1 sccm of SiF_4 to the gas mixture and are presented in Figure 3.55. The layer, which is ∼ 240 nm thick with a 5 nm roughness, is composed of small crystallites and shows a microstructure that is similar to that of the sample shown in Figure 3.28(a).

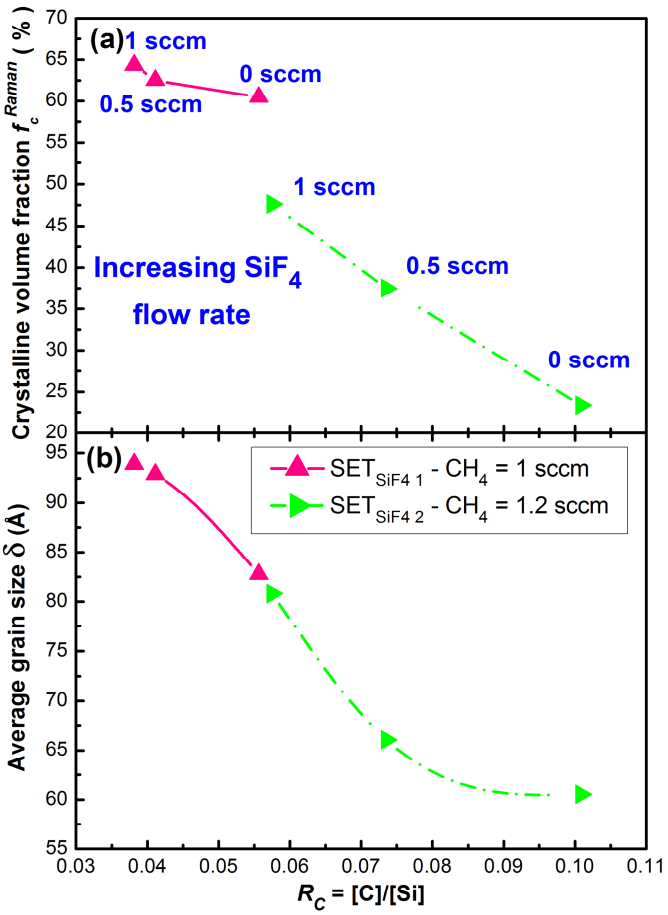

Figure 3.54.: Evolution of the (a) crystalline volume fraction f_c^{Raman} and (b) average grain size δ, for samples from $SET_{SiF_4 1}$ (▲) and $SET_{SiF_4 2}$ (▶), as a function of the total carbon-silicon ratio R_C.

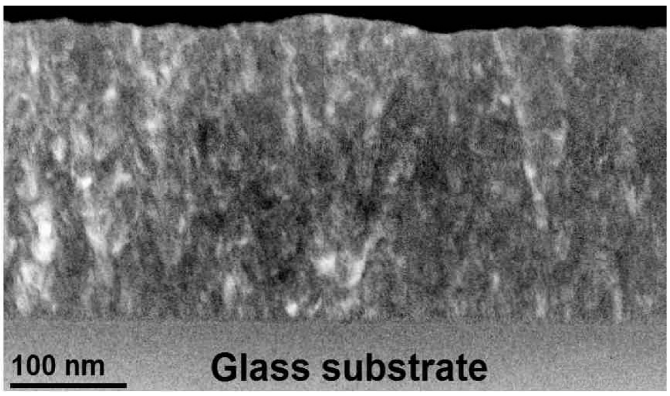

Figure 3.55.: SAADF-STEM image of the sample from $SET_{SiF_4 2}$, deposited with SiF_4 = 1 sccm.

The variation of crystallinity and carbon incorporation induced by the addition of SiF_4 has also an impact on the IR absorption spectra (Figure 3.56). They all present the two absorption regions at 500-1000 cm^{-1} and 1900-2200 cm^{-1}, which are the sum of different Si—H, Si—C and the C—H vibrational modes and Si—H and Si—H_2 stretching mode, respectively. Carbon is always mainly bonded to silicon and the addition of SiF_4 induces a decrease of the intensity of the Si—C band.

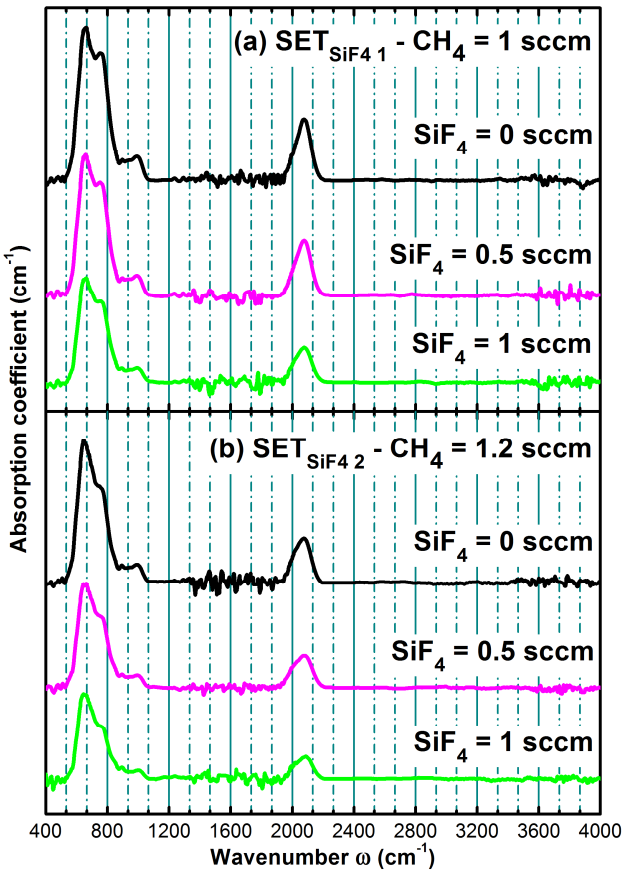

Figure 3.56.: IR absorption spectra of samples from (a) $SET_{SiF_4 1}$ and (b) $SET_{SiF_4 2}$, as a function of the SiF_4 flow rate.

From the deconvolution of these bands an estimation of the trend of the Si—C and Si—H bond concentration (N_{Si-C} and N_{Si-H}, respectively) can be obtained, showing that the increase in crystallinity, due to the addition of few sccm of SiF_4, results in material with lower carbon and hydrogen concentrations (Figure 3.57). SiF_4 plays also a role on the Si—H and Si—H_2 vibrational modes. The $\alpha(\omega)/\omega$ ratios for the 1900-2200 cm^{-1} absorption band are presented in Figure 3.58, as a function of the wavenumber ω. With increasing SiF_4 flow rate the shift of the Si—H stretching mode towards 2090 cm^{-1} which is due to carbon back-bonding of the Si—H bonds, is reduced as the carbon incorporation decreases. Therefore, a transition from a band characterized by a single contribution at $\sim$ 2090 cm^{-1} to a band clearly composed of two distinct vibrational modes can be observed. The presence of a second component is suggested by the fact that the peak is not symmetric. The shift $\Delta\omega$ of the band at $\sim$ 2000 cm^{-1} is plotted in Figure 3.59 as a function of the total carbon-silicon ratio R_C.

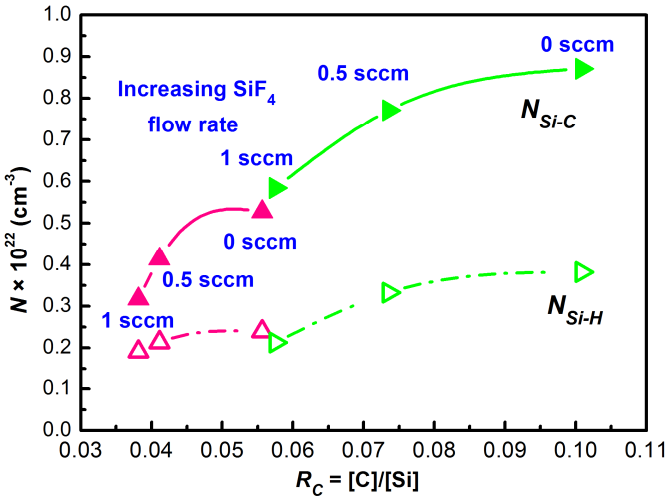

Figure 3.57.: Evolution of the Si−C (closed symbols) and Si−H (open symbols) bond concentration for samples from $SET_{SiF_4 1}$ (CH_4 = 1 sccm - ▲) and $SET_{SiF_4 2}$ (CH_4 = 1.2 sccm - ▶), as a function of the total carbon-silicon ratio R_C.

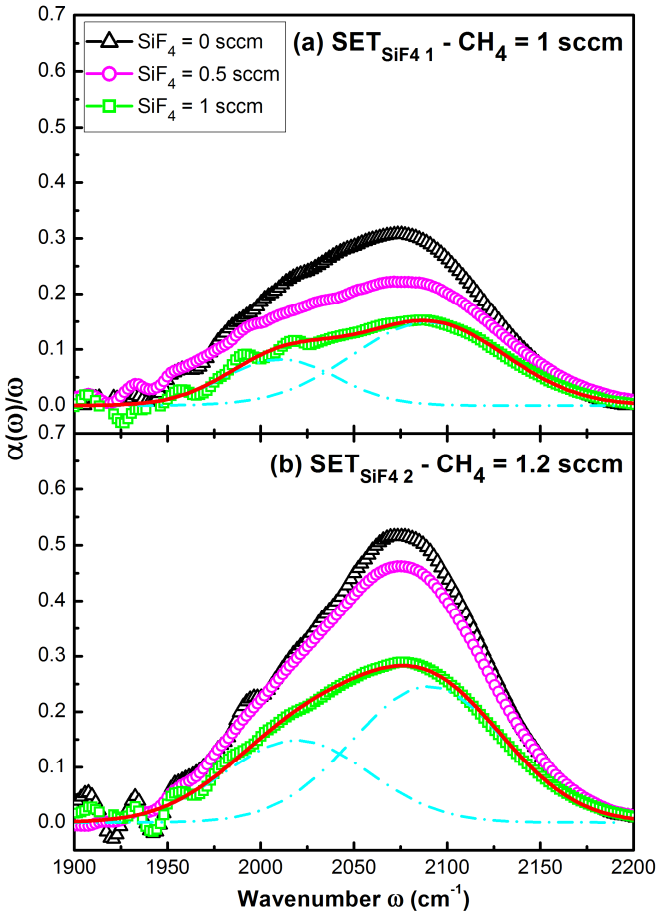

Figure 3.58.: Evolution of the 1900-2200 cm^{-1} band for samples deposited with (a) $SET_{SiF_4 1}$ and (b) $SET_{SiF_4 2}$, as a function of the SiF_4 flow rate. The $\alpha(\omega)/\omega$ ratio is plotted as a function of the wavenumber ω. As an example, for the samples deposited with SiF_4 = 1 sccm (□) the dash-dotted cyan lines represent the fit of the two bands at 2000 cm^{-1} and 2090 cm^{-1}, and the continuous red line represents the total fit.

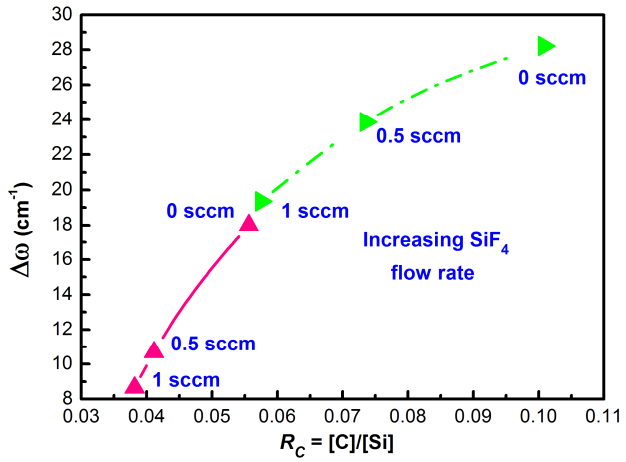

Figure 3.59.: Shift Δω of the Si-H vibrational mode due to carbon back-bonding, for samples from SET$_{SiF_4}$1 (CH_4 = 1 sccm - ▲) and SET$_{SiF_4}$2 (CH_4 = 1.2 sccm - ▶), as a function of the total carbon-silicon ratio R_C.

Finally, in the SET$_{SiF_4}$3 the combination of the low RF-power density (w_{RF} = 113 mW/cm^2) and the variation of SiF_4 flow rate was tested. In Figure 3.60 the Raman spectra and GIXRD patterns of these samples are presented. For this set, the incident angle used to perform GIXRD measurements is reduced to $\theta_i = 0.23°$, in order to avoid any contribution from the substrate.

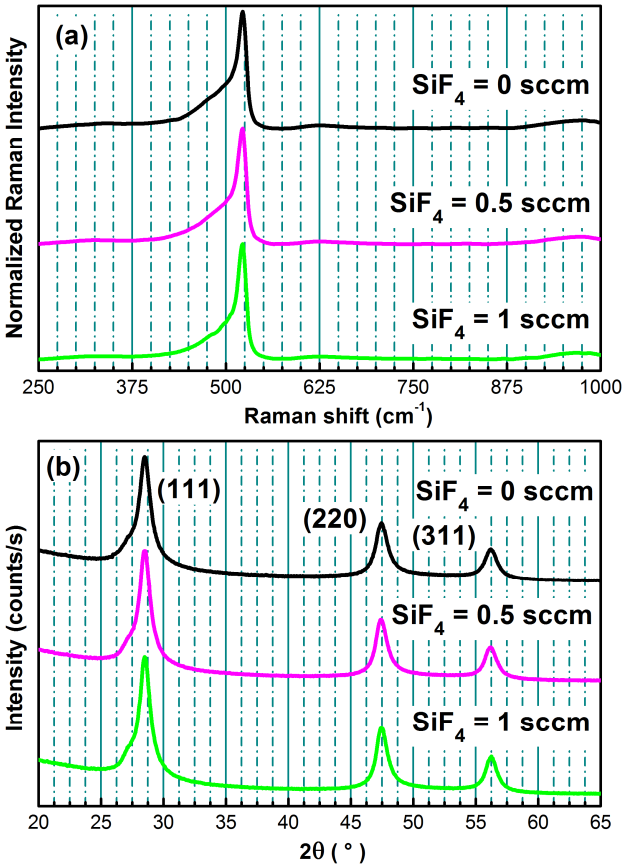

Figure 3.60.: (a) Raman spectra and (b) GIXRD patterns of samples from SET$_{SiF_4}$3, deposited using w_{RF} = 113 mW/cm^2 and varying the SiF_4 flow rate. Lattice planes corresponding to c-Si diffraction peaks are labeled.

As for the $SET_{SiF_4}1$, the effect of the addition of SiF_4 to the gas mixture is very weak as alloys are showing a crystalline volume fraction of $\sim$ 55 % already with no SiF_4 added. The total carbon-silicon ratio and the structural parameters for these three samples are listed in Table 3.2. As they have all a similar thickness, it is therefore possible to directly compare the evolution of the GIXRD patterns.

Table 3.2.: Total carbon-silicon ratio R_C and structural parameters (f_c^{Raman} and δ) for samples from $SET_{SiF_4}3$.

SiF_4 (sccm)	Thickness (nm)	R_C	f_c^{Raman} (%)	δ(Å)
0	235	0.045	55	90
0.5	230	0.040	60	92
1	233	0.030	65	93

In Figure 3.61 the normalized intensity of the diffraction peak corresponding to the (111) plane is presented, after the subtraction of the background. With increasing SiF_4 the shoulder linked to the so-called "hexagonal phase" increases indicating an enhancement of the structural defects in the material.

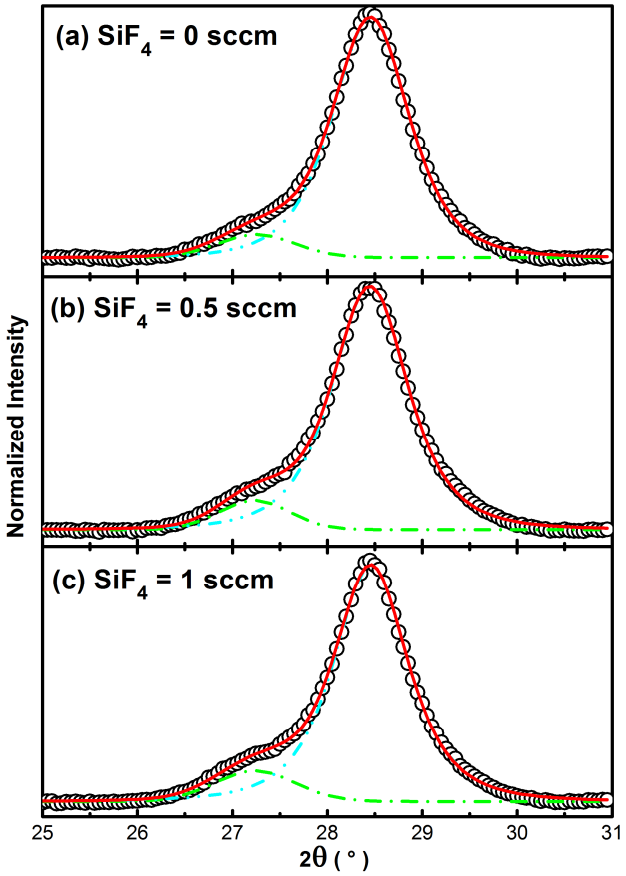

Figure 3.61.: Normalized intensity of the diffraction peak corresponding to the (111) planes, for samples from $SET_{SiF_4}3$, deposited using w_{RF} = 113 mW/cm^2 and (a) SiF_4 = 0 sccm, (b) SiF_4 = 0.5 sccm and (c) SiF_4 = 1 sccm.

3.3.5 Effect of substrate temperature

Finally, the last parameter that was investigated is the substrate temperature. At the beginning of this work the temperature was set at 285° C, which is the highest temperature that can be reached in the ARCAM reactor, because it was expected to help in some way the crystallization of a stoichiometric silicon carbide phase. However, such a high temperature imposes some constraints on the design of the devices in which μc-Si$_{1-x}$C$_x$:H alloys should be included as active layers. Especially, a high temperature can be detrimental for the p-layer, which has been proved to be extremely sensitive to this parameter (Nasuno et al., 2002). Having determined that with this PECVD system it is not possible to obtain stoichiometric SiC inclusions, it was decided to try to deposit alloys at a lower temperature, namely 175° C, at which a better device structure can be fabricated (see chapter 5) and for which it is possible to fully benefit from the LPICM know-how in terms of doped layers, transparent conductive oxides, etc..

For all these reasons, two new sets of samples were deposited at 175° C, changing the RF-power and the CH_4 flow rate (SET_{T1} and SET_{T2} in Table 3.1). Raman spectra and GIXRD patterns are shown in Figure 3.62 and Figure 3.63, respectively.

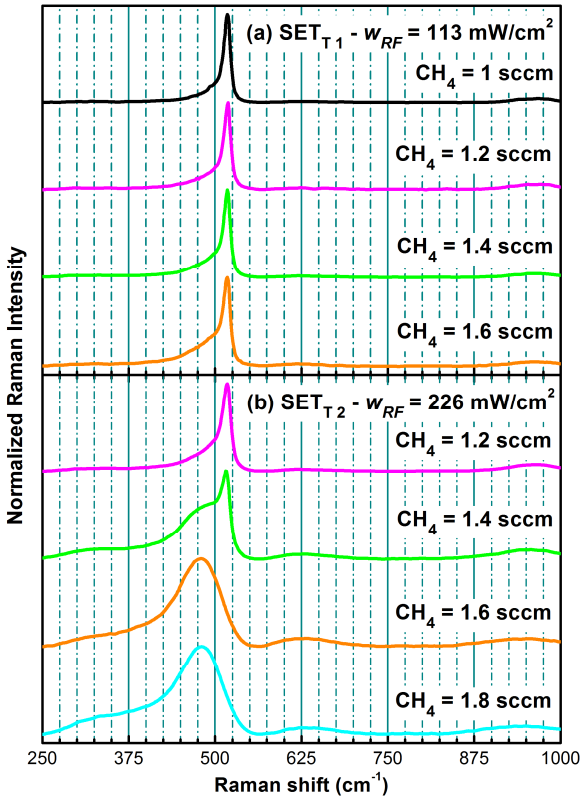

Figure 3.62.: Raman spectra of samples from (a) SET_{T1} (w_{RF} = 113 mW/cm^2) and (b) SET_{T2} (w_{RF} = 226 mW/cm^2), deposited at 175° C varying the CH_4 flow rate.

For w_{RF} = 113 mW/cm^2 (SET_{T1}) the studied range of CH_4 flow rates leads to Raman spectra that are all characterized by the Si—Si TO mode at 520 cm^{-1} and to GIXRD patterns that show all the diffraction peaks characteristic of the cubic phase of crystalline silicon (diffraction planes are at 2θ = 28.44°, 47.3° and 56.1°). Nevertheless, as already observed in section 3.3.2, the increase of the CH_4 flow rate induces a deterioration of the crystalline

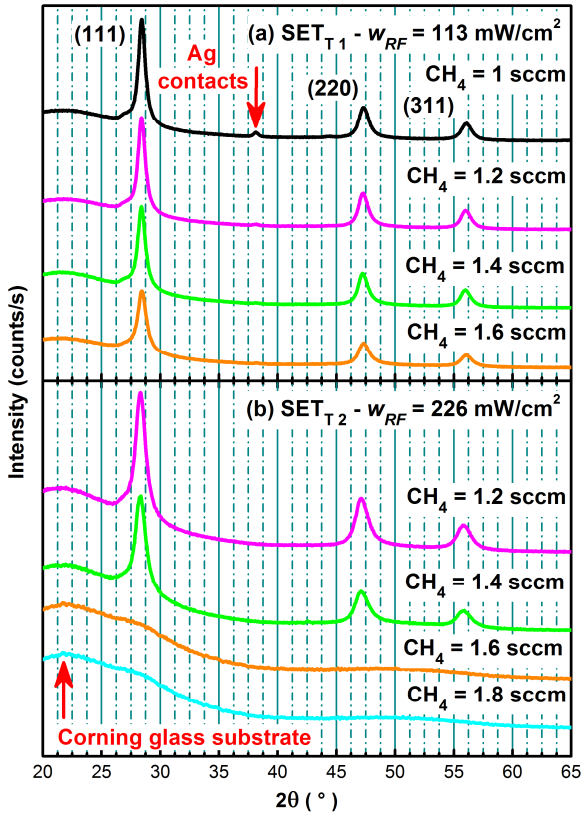

Figure 3.63.: GIXRD patterns of samples from (a) SET_{T1} (w_{RF} = 113 mW/cm^2) and (b) SET_{T2} (w_{RF} = 226 mW/cm^2), deposited at 175° C varying the CH_4 flow rate. Lattice planes corresponding to c-Si diffraction peaks are labeled.

quality of the alloys. On the other hand, for w_{RF} = 226 mW/cm^2 (SET_{T2}), such microcrystalline-to-amorphous transition is shifted at lower CH_4 flow rates. In this case, CH_4 flow rates above 1.4 sccm result in completely amorphous alloys. Raman spectra are in fact characterized only by the broad peak centered at 480 cm^{-1}, typical of an amorphous structure, and diffraction patterns show only the broad humps at 2θ = 27.6° and 51°, due to the short and medium range order in amorphous materials. Also at this substrate temperature, when alloys are microcrystalline, no crystalline silicon carbide or crystalline forms of carbon are present, as highlighted by the GIXRD measurements (U. Coscia, Ambrosone, Lettieri, Maddalena, and Ferrero, 2006). Moreover, for both series the ratios of the diffraction peaks intensities are in good agreement with the standard silicon powders, proving that these are randomly oriented polycrystalline layers (Schicho et al., 2012).

The phase transition observed with the increase of the CH_4 flow rate in the gas mixture (at a fixed RF-power density) is qualitatively consistent with what was already presented in section 3.3.2. However, the different threshold of the phase transition (depending on w_{RF}) is linked to the fact that the number of dissociated CH_4 molecules is linked to the RF-power density (as shown in section 3.3.3). In Figure 3.64 the evolution of the total carbon-silicon ratio R_C, as a function of the CH_4 flow rate is presented for the two sets of samples. A comparison with the high temperature series will be presented in the summary given in section 3.3.6.

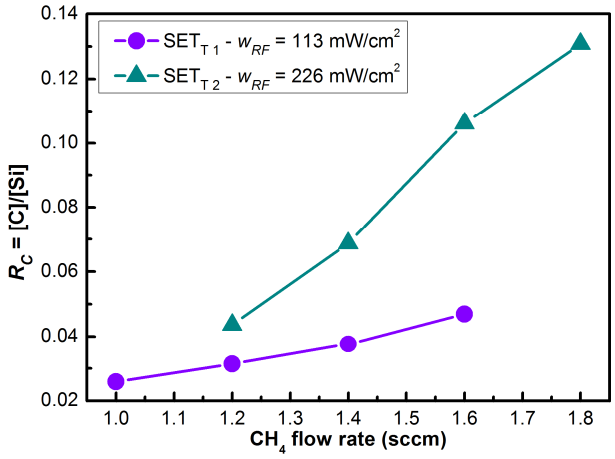

Figure 3.64.: Evolution of the total carbon-silicon ratio R_C for samples deposited at 175° C with w_{RF} = 113 mW/cm^2 (SET$_{T1}$ - ●) and w_{RF} = 226 mW/cm^2 (SET$_{T2}$ - ▲), as a function of R_C.

Using the Scherrer formula an estimation of the average grain size δ is obtained. Its evolution is shown in Figure 3.65(a) as a function of the total carbon-silicon ratio R_C, together with the crystalline volume fraction f_c^{Raman} (Figure 3.65(b)). Also at lower substrate temperature, the deterioration of the structural properties with increasing R_C is observed, and the increase in w_{RF} leads to a decrease of both average grain size and crystalline volume fraction due to a higher CH_4 dissociation rate and to the ion bombardment energy (Matsuda, 1999).

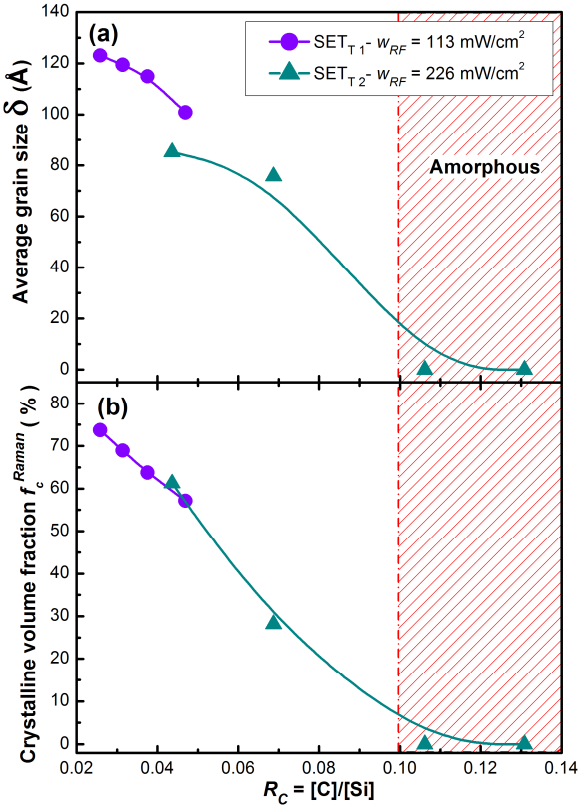

Figure 3.65.: Evolution of (a) average grain size δ and (b) crystalline fraction f_c^{Raman} for samples deposited at 175° C with w_{RF} = 113 mW/cm^2 (SET$_{T1}$ - ●) and w_{RF} = 226 mW/cm^2 (SET$_{T2}$ - ▲), as a function of R_C.

Finally, in Figure 3.66 the infrared spectra of the two sets of samples are presented. Consistently with results presented so far, carbon is mainly bonded to silicon and its incorporation increases with increasing CH_4 flow rate (increase of the Si — C band at 720-780 cm^{-1}).

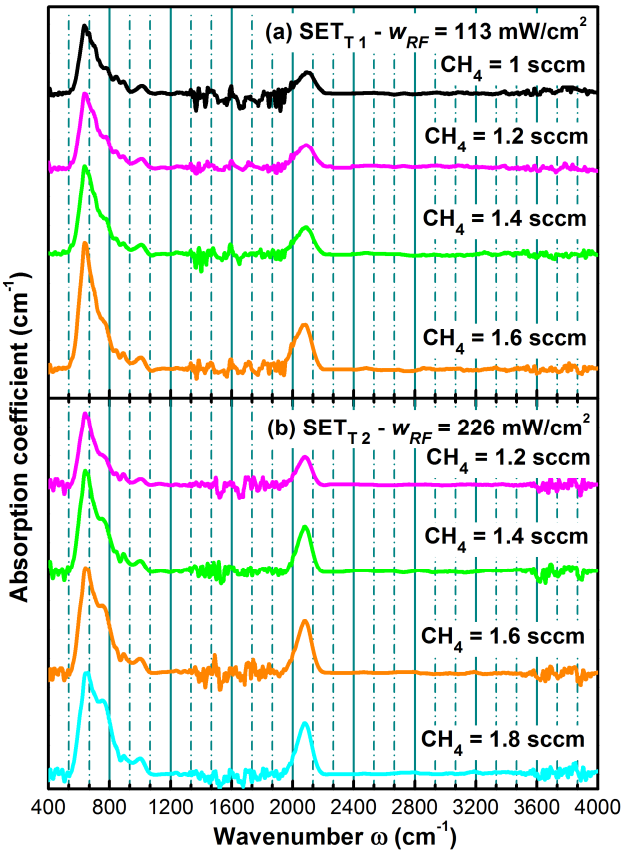

Figure 3.66.: IR absorption spectra of samples from (a) SET_{T1} (w_{RF} = 113 mW/cm^2) and (b) SET_{T2} (w_{RF} = 226 mW/cm^2), deposited at 175° C and varying the CH_4 flow rate.

The deconvolution of the different absorption bands allows the estimation of the concentration of Si — C and Si — H bonds (N_{Si-C} and N_{Si-H}, respectively) and the displacement $\Delta\omega$ of the Si — H stretching mode. The evolution of these quantities is shown in Figure 3.67 and Figure 3.68, as a function of the total carbon-silicon ratio in the alloy. For both sets of samples the increase in R_C is translated into an increased concentration of Si — C bonds. Moreover, consistently with previous results, the higher the carbon content, the greater is the shift $\Delta\omega$, due to the carbon back-bonding of the Si — H bonds.

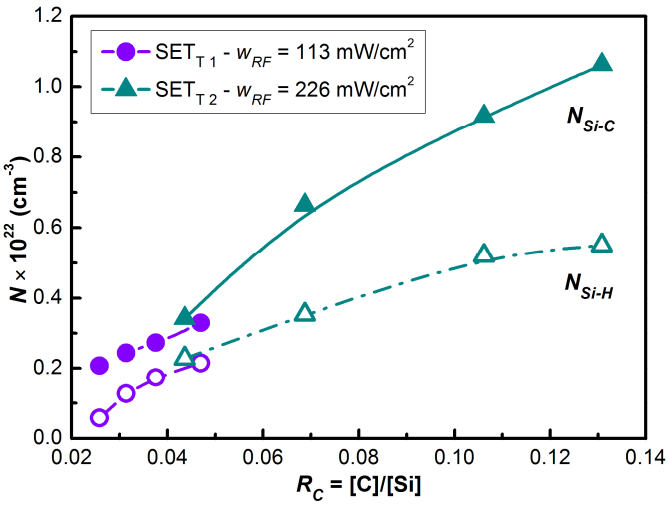

Figure 3.67.: Evolution of Si−C (closed symbol) and Si−H (open symbol) bond density, for samples deposited at 175° C with w_{RF} = 113 mW/cm^2 (SET$_{T1}$ - ●) and w_{RF} = 226 mW/cm^2 (SET$_{T2}$ - ▲), as a function of R_C.

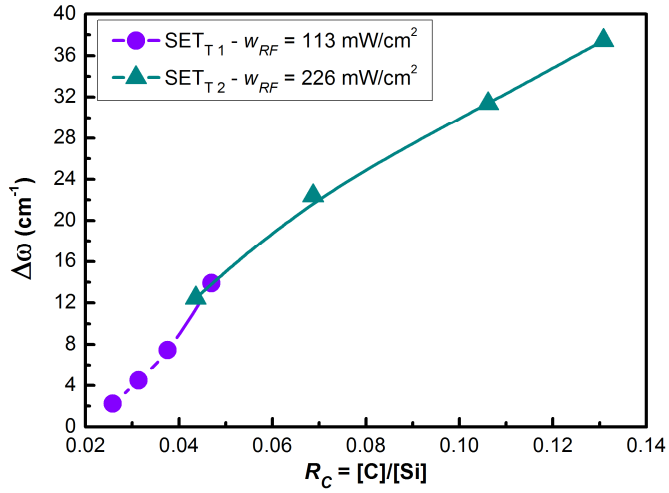

Figure 3.68.: Evolution of shift Δω of the Si−H stretching band, for samples deposited at 175° C with w_{RF} = 113 mW/cm^2 (SET$_{T1}$ - ●) and w_{RF} = 226 mW/cm^2 (SET$_{T2}$ - ▲), as a function of R_C.

3.3.6 Summary

In the previous sections details on the deposition of μc-Si$_{1-x}$C$_x$:H alloys from a silane and methane gas mixture, highly diluted in hydrogen, were presented. Different process parameters (SiH$_4$, CH$_4$ and SiF$_4$ flow rate, RF-power density and substrate temperature) were used to investigate the possibility of obtaining highly microcrystalline alloys (f_c^{Raman} ∼ 60-70 %). It was demonstrated that when alloys are deposited by RF-PECVD they are always composed of silicon crystallites embedded in an a-Si$_{1-x}$C$_x$:H matrix and that when carbon incorporation exceeds a certain threshold, materials are completely amorphous.

In this section a summary of the material properties and a comparison of the effects of the different deposition parameters will be presented, for some sets of samples. This is necessary in order to understand the mechanisms and to propose a model for the role of carbon during the growth

of μc-$Si_{1-x}C_x$:H thin films, providing important guidance as all structural properties may play a more important role on the electronic performance of the materials.

Using several characterization techniques such as Raman spectroscopy, spectroscopic ellipsometry, FTIR or RF-GD-OES, it was shown that different deposition parameters can be independently varied aiming always at materials with lower carbon content and hence higher crystalline volume fractions.

In Figure 3.69 the evolution of the total carbon-silicon ratio is presented as a function of the CH_4 flow rate. It is shown that the amount of carbon incorporated in the thin films can be controlled through different deposition parameters. Some act only on the amount of dissociated methane molecules (such as the increase of CH_4 flow rate or the increase in w_{RF}), others build on additional etching mechanisms (addition of SiF_4 to the gas mixture). The red dash-dotted line in the figure highlights the microcrystalline-to-amorphous threshold. No matter which parameter is changed, values of $R_C > 0.1$ lead to fully amorphous alloys.

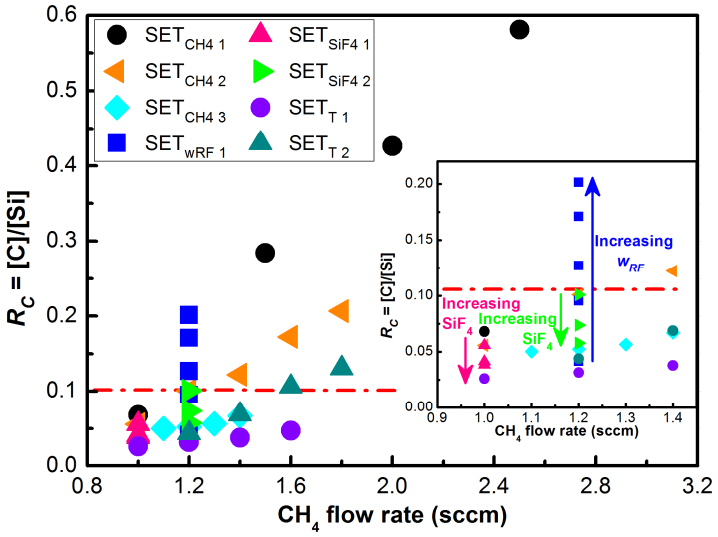

Figure 3.69.: Evolution of the total carbon-silicon ratio R_C as a function of the CH_4 flow rate for a selected ensemble of samples. The dashed-dotted red line highlights the microcrystalline-to-amorphous transition.

Carbon incorporation has a direct effect on the local order of the alloy as observed through IR measurements. For each parameter it was shown that two main absorption regions are present and that carbon incorporation acts on both of them. For the first one (500-1000 cm^{-1}) the increase in R_C induces an increased intensity of the Si—C band. For the second one (1900-2200 cm^{-1}), the effect of carbon is more subtle, as it acts on the shift of the Si—H stretching band towards 2090 cm^{-1}. Such shift is mainly due to inductive effects of carbon atoms on the Si—H bonds. The following configurations are assumed by Wieder, Cardona and Guarnieri to be responsible for the shift towards 2090 cm^{-1} (Wieder et al., 1979)

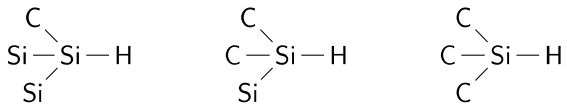

However, the authors say that they seem to be degenerate for carbon contents above 50 %, for which no modifications in the peaks shape have

been observed. From the deconvolution of these IR absorption regions, it has been possible to determine the Si—C and Si—H bond concentrations (N_{Si-C} and N_{Si-H}, respectively) and the shift $\Delta\omega$ of the Si—H stretching band. The variation of the different deposition parameters seems to have no effect on the chemical order of the amorphous matrix. They play a role on the amount of carbon incorporated in the films, but once this quantity is defined, all alloys exhibit the same trend for the Si—C and Si—H bond concentrations (Figure 3.70). Moreover, the different deposition conditions also do not act on the shift of the Si—H stretching band, which seems to be dominated only by the amount of carbon incorporated (Figure 3.71).

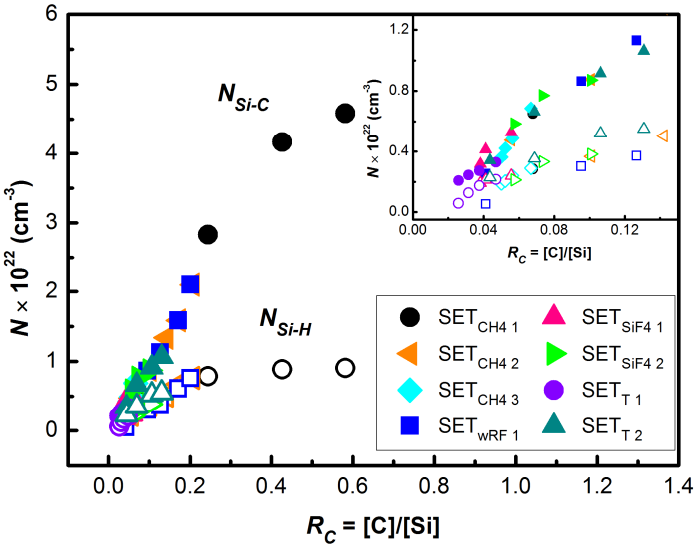

Figure 3.70.: Evolution of the Si—C (closed symbols) and Si—H (open symbols) bond concentrations as a function of the total carbon-silicon ratio R_C, for a selected ensemble of samples. In the inset, a zoom of the evolution for low R_C is presented.

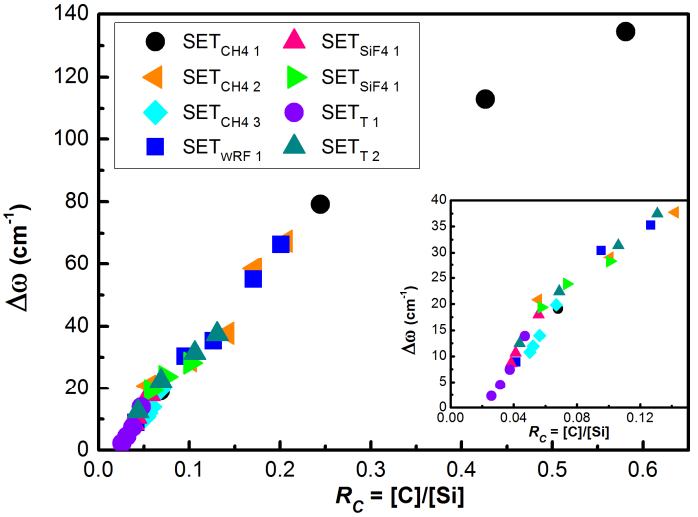

Figure 3.71.: Evolution of the shift $\Delta\omega$ as a function of the total carbon-silicon ratio for a selected ensemble of samples. In the inset, a zoom of the evolution for low R_C is presented.

Structural changes induced by the variation of the different deposition parameters have been investigated using several characterization techniques. First of all, from the deconvolution of the Raman spectra it has been possible to determine the crystalline volume fraction of the alloys. The evolution of this parameter is presented in Figure 3.72 as a function of the total carbon-silicon ratio R_C. With this technique, the increase of carbon incorporation can be directly linked to the amorphization of the material. Therefore, it has been found that there are several ways to tune the crystallinity of the alloys, but it is always connected to a variation of the amount of carbon incorporated in the film.

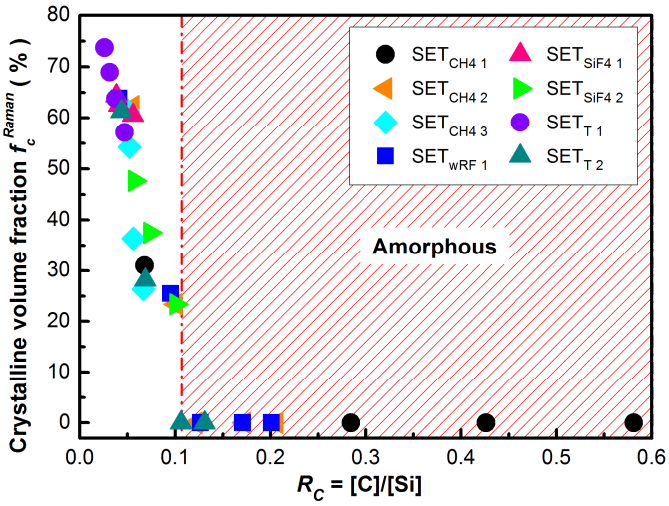

Figure 3.72.: Evolution of the crystalline volume fraction f_c^{Raman}, as a function of the total carbon-silicon ratio R_C.

Actually, as it was presented in section 3.3.3, the variation of the RF-power density does not affect simply the plasma chemistry, determining the amount of dissociated CH_4 molecules, but it also acts on the ion bombardment energy, which is itself detrimental for the crystalline quality of the material. Indeed, ionic species impinging on the surface of the growing film can disrupt the crystal formation, despite the loss of energy due to the collisions in the sheath (Kondo, Fukawa, et al., 2000; Matsuda, 2004). Techniques such as GIXRD and SAADF-STEM showed that the variation of the chosen parameters has an impact on the microstructual properties. In Figure 3.73, the evolution of the average grain size for the ensemble of samples is plotted as a function of the total carbon-silicon ratio R_C. Two different trends can clearly be defined, showing that the average crystallite size is most strongly controlled by the RF-power density. For similar carbon contents, samples deposited at lower RF-power exhibit a larger average grain size ($\sim$ 20 % more). This is consistent with the SAADF-STEM images where the sample deposited using w_{RF} = 113 mW/cm^2 (Figure 3.46) was presenting a better columnar growth, compared to materials deposited at higher RF-power (Figure 3.28(a)). Despite being deposited using different RF-power densities, the two alloys presented in the SAADF-STEM images have similar crystalline volume fractions ($\sim$ 60 %). This was achieved by changing the amount of CH_4 in the gas mixture. However, the highest w_{RF} results in a 30 % lower average grain size. This is also consistent with the values of δ obtained for samples deposited by adding SiF_4 to the gas mixture deposited using w_{RF} = 226 mW/cm^2 (Figure 3.55). Therefore one can assume that while

both RF-power and carbon incorporation contribute to defining the structural properties of the alloys, the former has the strongest influence on the crystalline phase due to the role of the ion bombardment energy, which also contributes to the deterioration of the crystallinity (Matsuda, 1999).

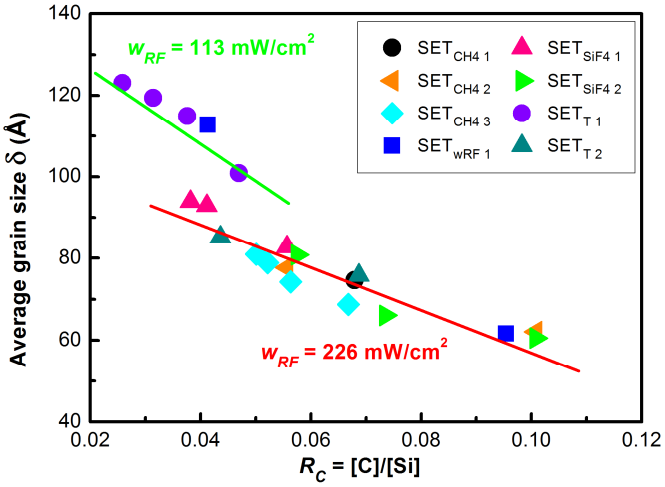

Figure 3.73.: Evolution of the average grain size δ as a function of the total carbon-silicon ratio. The green and red lines identify the *"low power"* and *"high power"* regime, respectively.

3.4 GROWTH OF μC-SI$_{1-x}$C$_x$:H ALLOYS BY TVW-PECVD

3.4.1 Introduction

The previous study highlighted the possibility of controlling the crystalline volume fraction of μc-Si$_{1-x}$C$_x$:H alloys using the RF-power density. Actually, the route through which this is achieved is unclear as w_{RF} has an influence on both the plasma chemistry and the ion bombardment energy (IBE).

The TVW technique, used to induce an electrical asymmetry in a plasma by applying non-sinusoidal voltage waveforms, allows the variation of the mean sheath potential at a selected electrode, while keeping a constant plasma density. This gives independent control over the IBE at the substrate surface, and thus control over either the enhancement or the suppression of nanocrystalline growth (Johnson, Verbeke, et al., 2010). Moreover, with this technique it was shown that the IBE influences μc-Si:H materials in more subtle ways, such as the Si—H bonding (Johnson, Pouliquen, et al., 2012). The TVW technique was therefore applied to separate the role of IBE from injected power when depositing μc-Si$_{1-x}$C$_x$:H, in order to study the effect of the IBE on the carbon incorporation.

3.4.2 Effect of CH_4

Two sets of samples (SET$_{peaks}$ and SET$_{valleys}$ in Table 3.1) were deposited changing the shape of the plasma excitation voltage waveform from *peaks* to *valleys*, which respectively minimize and maximize the IBE at constant RF-power. For these depositions the peak-to-peak voltage V_{pp} was fixed at 245 V. For the chosen conditions (number of harmonics, waveform ampli-

tude and DC bias), the maximum plasma potential is estimated to be equal to 22 V and 75 V for "peaks" and "valleys" voltage waveforms, respectively. Actually, to fully benefit from the variation of the IBE, depositions should be performed at relatively low pressure (3-10 Pa) in order to avoid the reduction of the IBE through gas phase collision (Johnson, Delattre, et al., 2012). Nevertheless, the necessity to compare these materials with those made by standard RF-PECVD, led to the decision of keeping a pressure of 310 Pa, as for the standard RF-PECVD depositions.

The evolution of the structural properties was studied by means of spectroscopic ellipsometry, Raman spectroscopy and GIXRD measurements, as a function of the variation of CH_4 flow rate. Results are respectively presented in Figure 3.74, 3.75 and 3.76.

It is evident that both conditions lead to materials showing a crystalline component. Ellipsometry spectra present the two structures at 3.5 and 4.2 eV, typical of microcrystalline silicon and Raman spectra are characterized by the presence of the sharp peak at 520 cm^{-1}, corresponding to the Si—Si TO mode. But while the low IBE conditions ("peaks") lead to materials for which with increasing CH_4 flow rate, no significant change is observed, the high IBE ones ("valleys") give materials characterized by the absence of a specific trend and for which the amorphous component (represented by the shoulder at 480 cm^{-1} in the Raman spectra) is dominant. At the same time, it is worth noting that samples deposited with a CH_4 flow rate of 1.1 sccm seem to exhibit a different FWHM for the Si—Si TO mode, indicating an

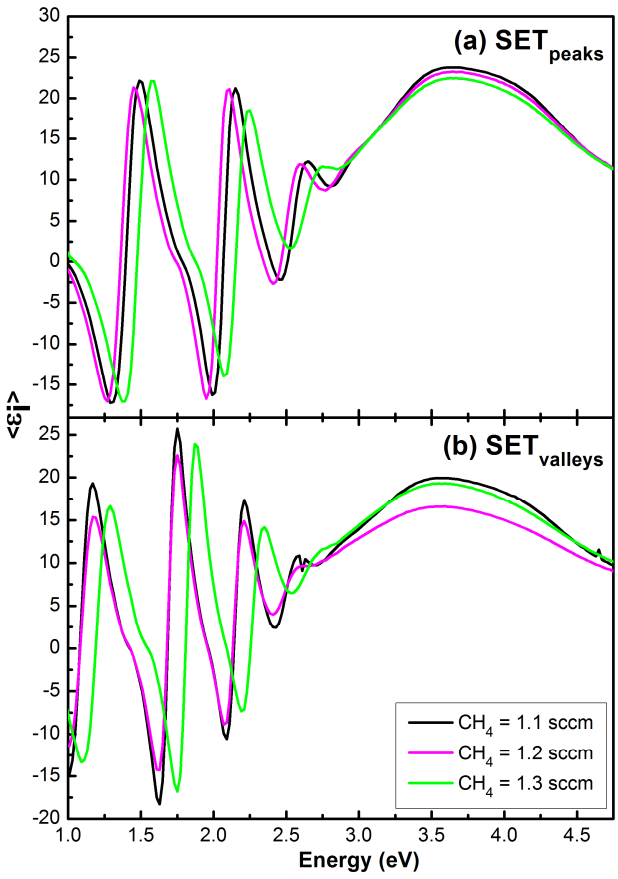

Figure 3.74.: Experimental ellipsometry spectra for samples from (a) SET_{peaks} and (b) $SET_{valleys}$.

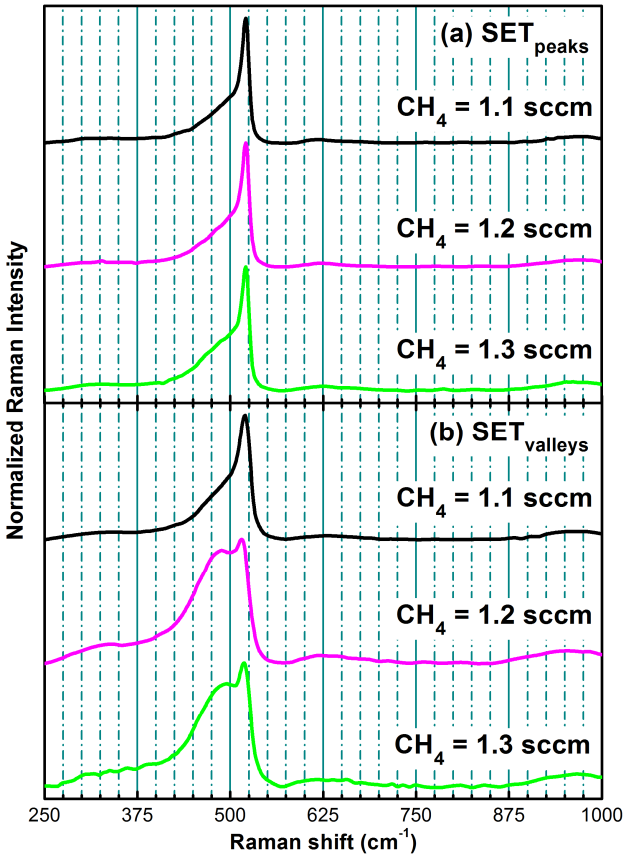

Figure 3.75.: Raman spectra for samples from (a) SET_{peaks} and (b) $SET_{valleys}$.

effect (even if weak) of the IBE on the structure of this complex diphasic alloy. GIXRD patterns, acquired with an incident angle $\theta_i = 0.35°$, show that even with this deposition technique, no crystalline silicon carbide or crystalline forms of carbon are present. Diffraction peaks are characteristic only of the cubic phase of crystalline silicon and the ratios of their intensities are in good agreement with the standard powder of crystalline silicon, proving that no preferential orientation is achieved. As all these layers have similar thicknesses, fixing the incident angle leads to similar analyzed areas. The increase/decrease of the intensity of the diffraction peaks can therefore be attributed to a variation of the crystalline degree of the alloy. Already by looking at the GIXRD patterns it is evident that samples from SET_{peaks} have all very similar crystalline contents, whereas those from $SET_{valleys}$ are more sensitive to the variation of CH_4 flow rate.

From RF-GD-OES measurements, significant differences in carbon incorporation between SET_{peaks} and $SET_{valleys}$ samples can be observed. In Figure 3.77 the evolution of the total carbon-silicon ratio R_C is presented as a function of the CH_4 flow rate. Despite the relatively high deposition pressure, the effect of the variation of the IBE can be observed. The carbon content of samples deposited using low IBE conditions (SET_{peaks}) doesn't seem to vary strongly with the CH_4 flow rate, and this is consistent with the structural observations. On the other hand, alloys obtained with the high IBE conditions ($SET_{valleys}$) show a much higher R_C, but also an erratic behavior of material properties, possibly linked to a high stress induced in the materials. These results are compared to microcrystalline alloys from $SET_{w_{RF}2}$

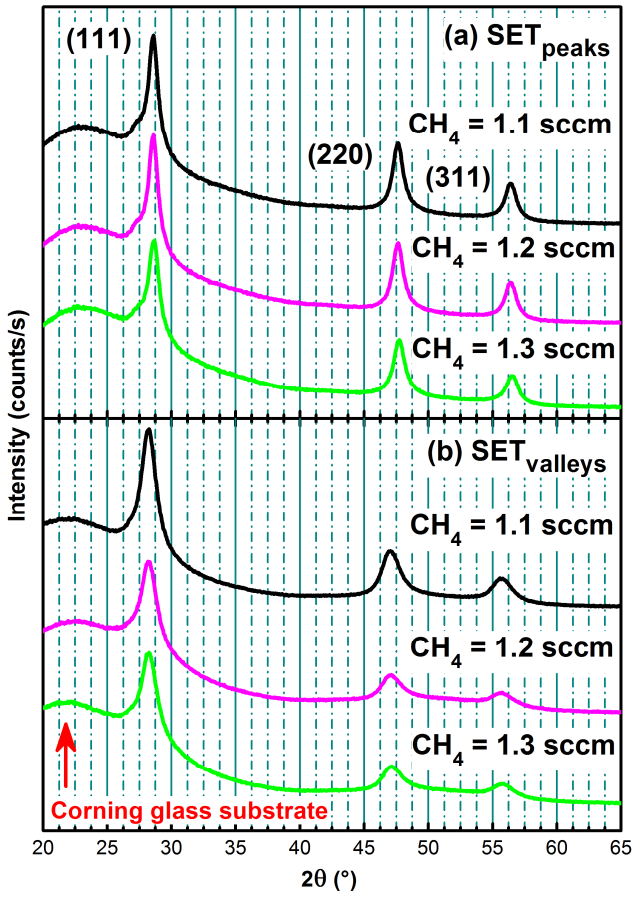

Figure 3.76.: GIXRD patterns for samples from (a) SET_{peaks} and (b) $SET_{valleys}$. The respective diffraction planes are labeled in the figure.

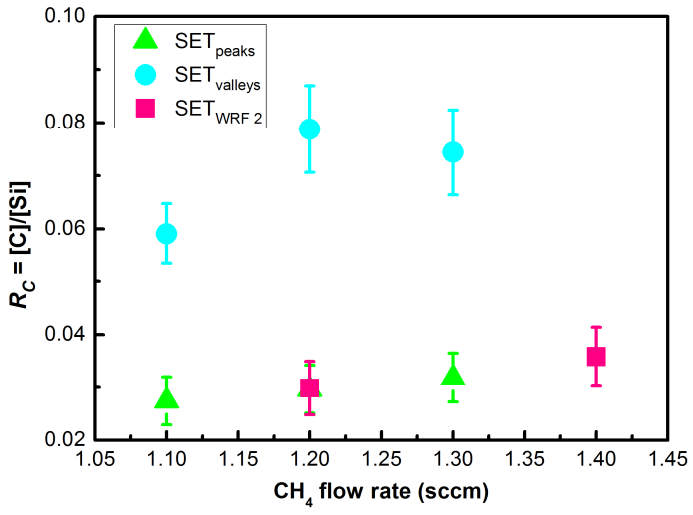

Figure 3.77.: Evolution of the total carbon-silicon ratio R_C for samples from SET_{peaks} (▲) and $SET_{valleys}$ (●) and for microcrystalline alloys from SET_{WRF2} (■), as a function of the CH_4 flow rate.

(■). This can be done as for all sets of samples the deposition rate was ∼ 0.5 Å/s, giving the same deposition rate as for an injected RF-power of about 20 W (113 mW/cm^2). As the deposition rate remains constant (as well as all other process parameters), no significant change in the plasma density or electron temperature should be expected, and so a similar flux of CH_x^+ ions should be incident on the surface. It appears that under these plasma conditions the low ion bombardment energy influences some surface process that limits carbon incorporation and, therefore, small flow rates changes are not sufficient to induce a large variation in the carbon incorporated in the material.

From the deconvolution of the Raman spectra and from the GIXRD patterns, it is possible to calculate the crystalline volume fraction f_c^{Raman} and the average grain size δ, respectively. Results are presented in Figure 3.78, as a function of the CH_4 flow rate.

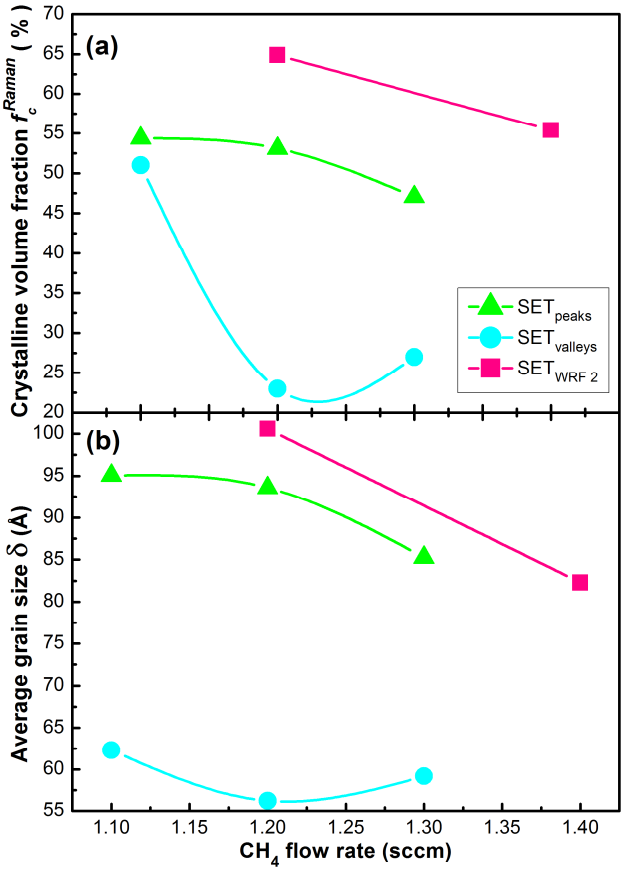

Figure 3.78.: Evolution of a) crystalline volume fraction f_c^{Raman} and b) average grain size δ for samples from SET$_{peaks}$ (▲) and SET$_{valleys}$ (●) and for microcrystalline alloys from SET$_{w_{RF}2}$ (■), as a function of the CH_4 flow rate.

For the chosen deposition conditions it can be assumed that also when using the TVW-PECVD technique an increase of the CH_4 flow rate leads to an increased number of dissociated CH_4 molecules, which induce the amorphization of the material. What is actually noteworthy is that, as already observed for carbon incorporation, the low IBE conditions do not induce any considerable variation in the material properties (f_c^{Raman} ∼ 50 %). Moreover, for materials having a similar value of R_C (CH_4 = 1.2 sccm), the samples from the SET$_{peaks}$ have actually a lower crystalline volume fraction. The

variation of the IBE could, in fact, be also responsible for a lower nucleation rate, leading to a higher amorphous fraction. On the other hand, samples deposited by TVW (both *peaks* and *valleys* voltage waveforms) with CH_4 = 1.1 sccm and by standard RF-PECVD with 1.4 sccm, seem to have similar values of f_c^{Raman}. This is possibly related only to the fact that the peak corresponding to the Si—Si TO mode is very narrow.

Another way to estimate the different impact of the IBE is by performing morphological analysis of the surface of the samples. Topographic images obtained for two materials deposited keeping the same precursors flow rates but using either "*peaks*" or "*valleys*" waveforms, are shown in Figure 3.79.

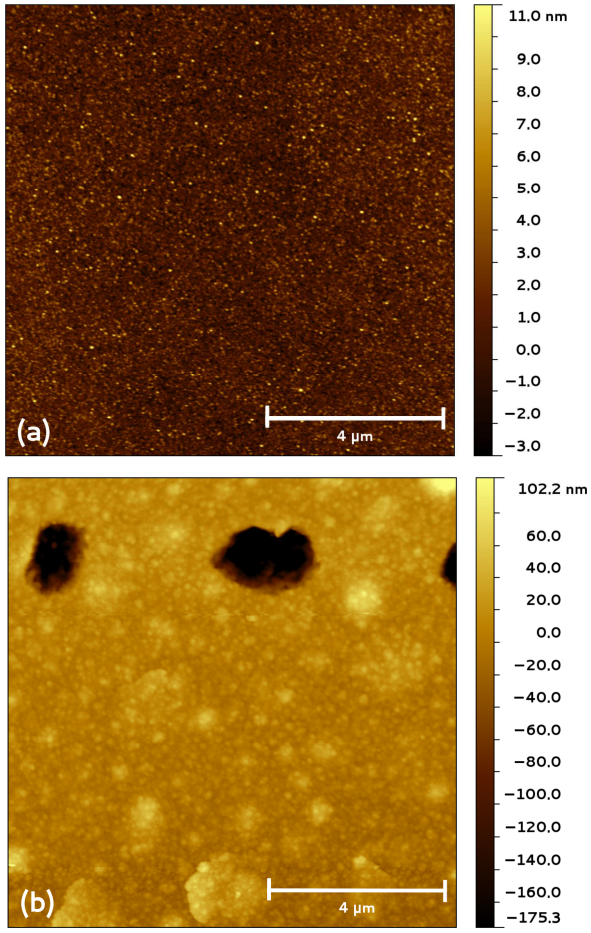

Figure 3.79.: Topographic images obtained by AFM measurements for samples deposited using (a) "peaks" and (b) "valleys" voltage waveforms. Both samples are deposited using CH_4 = 1.2 sccm during the main layer deposition.

The sample from SET_{peaks} exhibits a smooth surface characterized by a root-mean-square roughness ρ_{RMS} of 2.38 nm, whereas the one from $SET_{valleys}$ is rough and highly inhomogeneous (ρ_{RMS} = 37.5 nm). The difference among these alloys can be ascribed to a high IBE-induced stress. Indeed, the surfaces of all $SET_{valleys}$ samples show a "*milky*" aspect linked to the presence of craters (Figure 3.80(a)) that are nearly 250 nm deep (Figure 3.80(b)) and are consistent with flakes peeling off. Considering these observations, samples made using the valleys voltage waveforms are unsuitable for any application. The presence of craters that are as thick as the entire layer can be an additional source of shunts, once devices are fabricated.

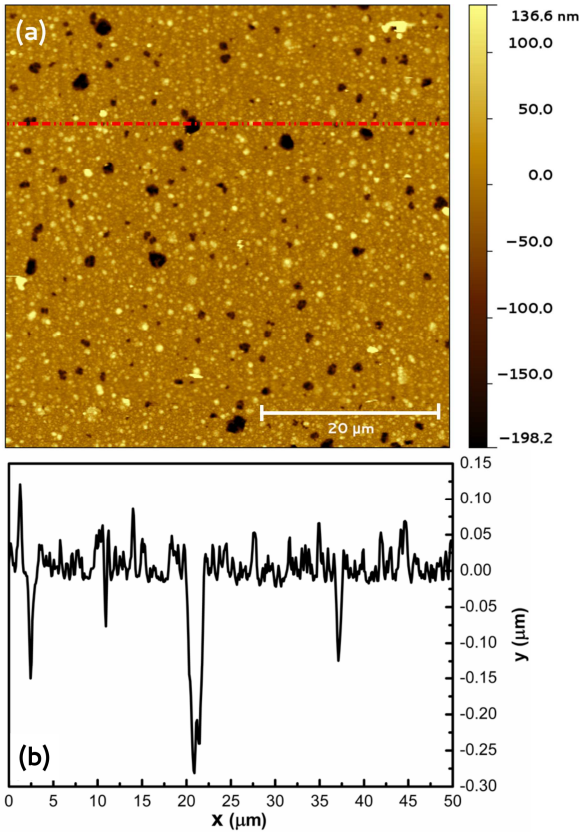

Figure 3.80.: (a) Topographic images obtained by AFM measurements for a sample deposited using "valleys" voltage waveforms. The red dashed line is representing the region of the sample where the profile in figure (b) was taken.

3.5 GROWTH MODEL

It has been shown that by playing with selected deposition parameter it is possible to induce an increased crystalline volume fraction. This behavior, as well as the complementary data presented so far, allows the proposition of a growth model for µc-$Si_{1-x}C_x$:H thin films, taking into account the role of carbon.

It has been demonstrated that virtually no carbon is incorporated into the microcrystalline phase of the material, as is known for large crystals (hence the lack of non-stoichiometric phases of c-SiC), but also seems to hold for nanometer-sized crystals at the growth temperatures under investigation. All of the carbon is therefore incorporated into an amorphous phase. However, it can be assumed that the flux of radicals from the plasma will be homogeneous over the surface (the nanocrystalline growth surfaces see the same flux as the amorphous regions), which raises the question of how the carbon interacts with the growing surface of the film.

As the instability of the non-stoichiometric c-SiC phase relies on the presence of a full three-dimensional crystal, carbon may remain in the few monolayers of growth at the microcrystalline silicon surface, before being eliminated. This is the key element of the proposed growth model (Figure 3.81). Even in the microcrystalline areas carbon is incorporated into the sub-surface growth zone in unstable sub-stoichiometric configurations. It

is the elimination of the carbon from these sub-stoichiometric phases that retards the growth of the nanocrystalline silicon areas, whereas the growth of the amorphous ones is not retarded by this effect as they can exist in sub-stoichiometric mixtures. The introduction of carbon into the silicon network will cause the alteration of bond lengths and the distortion of the bond angles, retarding the growth of the silicon crystallites or, when the CH_x flux is too high, completely hindering the formation of the crystalline lattice, leading to a crystalline-to-amorphous transition. This model is consistent with experimental data - it has been previously seen in this work and in the literature that the higher the carbon incorporation, the lower the possibility for silicon crystallites to nucleate and grow (U. Coscia et al., 2007).

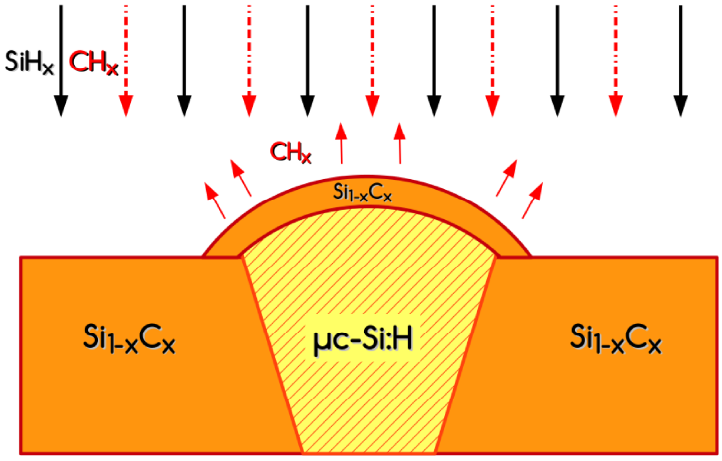

Figure 3.81.: Schematic representation of the proposed model for carbon incorporation during the growth of hydrogenated microcrystalline silicon-carbon alloys. The hashed cone correspond to the µc-Si:H columnar growth, whereas the full volumes corresponds to the a-$Si_{1-x}C_x$:H matrix (Gaiaschi, Ruggeri, Gueunier-Farret, et al., 2014).

With this growth model, the effect of CH_4 flow rate and RF-power density becomes clear. As the ionization energy threshold for CH_4 (12.6 eV) is greater than that of SiH_4 (11 eV), and depositions are done close to depletion conditions for SiH_4, increasing the RF-power density will result in a greater relative CH_x flux due to a greater incremental dissociation of this gas (Catherine, Turban, and Grolleau, 1981). In this way, lower RF-power densities and reduced CH_4 flow rates have both a similar effect: a reduced CH_x flux to the growth surface. Referring to this model, it means less carbon to be eliminated from the crystalline zones, faster growth of the crystalline areas (relative to the amorphous ones) and therefore a greater crystalline content in the material. However, the effect of the ion bombardment energy with the variation of the RF-power density has not been taken into account. A reduced RF-power density will decrease the IBE at the growing surface, leading to larger grains and hence a better microstructure.

Concerning the effect of the SiF_4 flow rate, as it was presented in section 3.3.4, this is not as trivial. To understand its role in the growth of these alloys from a silane and methane gas mixture, highly diluted in hydrogen, it is possible to rely on studies that have been performed on the role of atomic fluorine when µc-$Si_{1-x}C_x$:H alloys are grown from a SiF_4 and CH_4 gas mixture, diluted in H_2. In this case, the addition of hydrogen changes

the relative amounts of H and F atoms in the gas phase, which control the etching of carbon and silicon, according to the following reactions:

$$\begin{aligned} C(s) + H(g) &\xrightarrow{k^{C}_{HE}} CH_4 \uparrow (g) \\ Si(s) + H(g) &\xrightarrow{k^{Si}_{HE}} SiH_4 \uparrow (g) \end{aligned} \tag{3.1}$$

where $k^{C}_{HE} \gg k^{Si}_{HE}$, and

$$\begin{aligned} C(s) + F(g) &\xrightarrow{k^{C}_{FE}} CF_4 \uparrow (g) \\ Si(s) + F(g) &\xrightarrow{k^{Si}_{FE}} SiF_4 \uparrow (g) \end{aligned} \tag{3.2}$$

where $k^{Si}_{FE} \gg k^{C}_{FE}$. Si and C atoms are both etched by hydrogen, with carbon being etched faster (Saxena et al., 1989). However, the addition of atomic fluorine in the plasma (present due to the dissociation of SiF_4) induces a second etching mechanism. Atomic fluorine etches Si atoms faster than the carbon ones, but both elements more rapidly from the amorphous zones compared to the crystalline areas. While H_2 and CH_4 flow rates are fixed, leaving constant the hydrogen-related etching mechanism, the introduction of SiF_4 into the gas mixture induces an additional preferential etching of the amorphous areas, slightly shifting the advantage to the growth of the crystalline areas, and resulting in more crystalline films.

Finally, if one considers the schematic representation of the number of ions as a function of the ion bombardment energy for the three different types of excitation voltage waveforms (Figure 3.82), it is possible to understand the role of IBE.

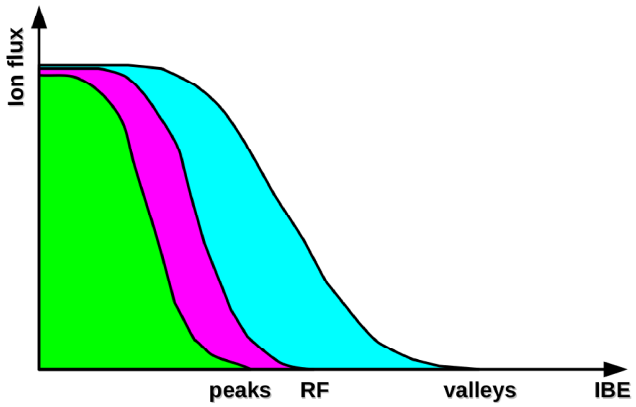

Figure 3.82.: Schematic representation of the ion flux as a function of the ion bombardment energy (IBE) for the different voltage waveforms.

It must be remembered that in this work samples were deposited at an average pressure of 310 Pa, therefore ion collisions in the sheaths cannot be neglected and the mean ion energy is much lower than the maximum IBE. Only a small percentage of the ions should arrive at the surface with an energy corresponding to the maximum IBE. Nevertheless, in the experimental section it was shown that the variation of the voltage waveform is sufficient to induce significant modifications of the material properties. Moreover, it has been shown in the literature that there are two different threshold for surface and bulk modifications (Bronneberg et al., 2012; Bruneau et al., 2014). It is possible that using the standard RF-PECVD conditions (with w_{RF} = 113 mW/cm^2) only a small number of ions reaches the substrate surface with a greater energy compared to TVW-PECVD with *peaks* voltage waveforms,

therefore the obtained structural properties are very similar. The reduced sensitivity to process conditions at low IBE indicates a strong dependence of surface reaction rates on the ion bombardment energy, but this point requires much further investigation to give quantitative results. On the other hand, using the TVW-PECVD deposition technique with the *valleys* voltage waveforms, it is possible that bulk modifications occur, inducing the stress that leads to the peeling of some areas of the samples. This drastic degradation in mechanical properties underlines the sensitivity to the IBE, but for both the high and low IBE conditions, the resulting films exhibited electronic behavior much as those deposited using standard RF-PECVD.

4 OPTO-ELECTRONIC PROPERTIES

4.1 INTRODUCTION

For μc-$Si_{1-x}C_x$:H alloys to be efficiently applied as active layers in photovoltaic devices, multiple material parameters must be present at the same time. Indeed, materials should simultaneously exhibit high photo-response ratio, acceptable values of the activation energy, high minority carrier diffusion length and the lowest MPC-DOS. This conclusion is logical as the coupling of all these properties can result in a well distributed internal electric field, good collection, and therefore a good photovoltaic device.

In the previous chapter it has been shown that selected deposition parameters can induce non-negligible structural evolutions in the thin films. It can be expected that these have some effect on both optical and electrical properties of the μc-$Si_{1-x}C_x$:H alloys, as they play an important role in the microstructure of the material.

In order to ascertain the relevance of the microstructure of the materials and therefore to understand the impact of each deposition parameter, transport and defect related properties have been investigated on a selection of samples († in Table 3.1). An estimate of the the band gap of these materials has been obtained through ellipsometry and UV/VIS transmission modeling.

4.2 BAND GAP

As demonstrated in chapter 3, hydrogenated microcrystalline silicon-carbon alloys are made of silicon crystallites embedded in an amorphous silicon-carbon matrix. For this kind of mixed-phase materials, the definition of optical band gap is not trivial.

In this work, two distinct definitions have been taken into account. First, from the fitting of ellipsometry spectra according to the Tauc's model (as presented in section 2.3.1), the optical band gap E_g was deduced. Despite the fact that the applicability of this model to materials composed by microcrystals embedded in an amorphous matrix is questionable, it can be considered as an average band gap, determined from the contribution of the two phases. A second definition can be obtained by considering the iso-absorption band gap E_{04}, that is the energy at which the absorption coefficient is equal to 1×10^4 cm^{-1}. These two definitions of "optical band gap" can be considered as a lower and upper limit, highlighting qualitative information about the degree of the films' transparency, but to be compared with their performance in devices (chapter 5). Indeed, if the effective electronic band gap were simply that of the μc-Si:H phase, then no effect on the open-circuit voltage (V_{oc}) of the solar cells should be expected, whereas in reality a correlation between the composition of the alloys and the V_{oc} of the devices will be presented in chapter 5.

In the following, the effect of the different deposition parameters on both E_g and E_{04} is shown, highlighting the absence of an influence of the microstructure (determined through TEM and GIXRD investigations) of the alloys on these properties.

For all sets of samples, the increase in carbon incorporation is translated into an increase of the average optical band gap. When materials are completely amorphous, E_g and E_{04} show the same evolution, due to the enlargement of the bad gap induced by the increasing carbon-silicon ratio (Bullot et al., 1987). On the other hand, for small carbon-silicon ratios, corresponding to the crystalline regime, the increase of E_g is not mirrored by an increase in E_{04}, which is stable around a mean value of 2 eV. This can be explained by the fact that for these materials E_{04} is the average of the iso-absorption band gap of the crystalline phase (E_{04c}) and that of the amorphous one (E_{04a}), weighted by their respective fractions. Therefore E_{04} can be written as:

$$E_{04} = E_{04c} \cdot \frac{f_c^{Raman}}{100} + E_{04a} \cdot \frac{f_a^{Raman}}{100}, \tag{4.1}$$

where $f_a^{Raman} = 100 - f_c^{Raman}$ is the amorphous fraction. With increasing total carbon-silicon ratio (and therefore decreasing crystalline fraction), in order for the average E_{04} to remain stable, the E_{04a} must decrease since the E_{04c} of the crystalline fraction remains constant. For E_{04a} to be decreasing with decreasing f_c^{Raman}, a decreasing carbon-silicon ratio in the amorphous phase should be expected. This could seem like a counter-intuitive result. However, if one considers the hydrogen and oxygen content to be small, relative to that of the silicon or carbon, the carbon-silicon ratio for the amorphous phase (R_{amorph}) can be determined. Knowing the percentage of the amorphous and crystalline phases, calculated from Raman scattering analysis, the relative carbon and silicon line intensities measured by RF-GD-OES, and the fact that no carbon is incorporated into the crystalline phase, R_{amorph} can be written as

$$R_{amorph} = \left(\frac{f_a}{100} \left(1 + \frac{1}{R_C} \right) - 1 \right)^{-1}. \tag{4.2}$$

In Figure 4.1, the relationship between R_{amorph} and f_c^{Raman} is shown for some selected microcrystalline samples. When presented in this way, the three sets of data show that higher crystalline volume fractions consistently result in greater carbon incorporation in the amorphous matrix.

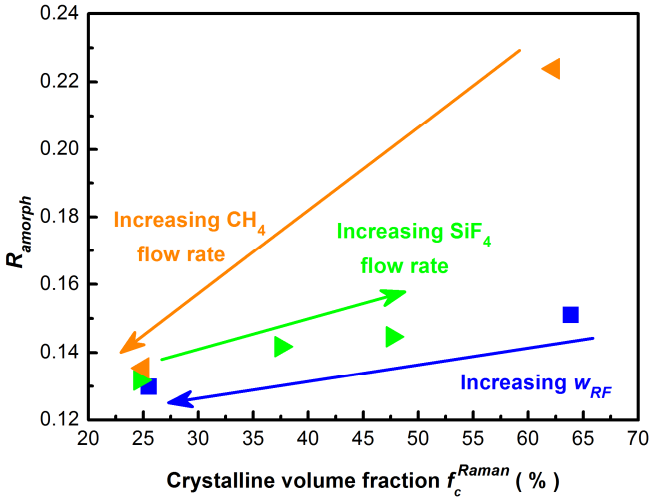

Figure 4.1.: Evolution of the carbon-silicon ratio in the amorphous phase R_{amorph} as a function of the crystalline volume fraction f_c^{Raman}, for samples from $SET_{CH_4 2}$ (◀), $SET_{w_{RF}1}$ (■) and $SET_{SiF_4 2}$ (▶).

EFFECT OF CH_4 FLOW RATE AND RF-POWER It has been shown that the increase in CH_4 flow rate and the increase in the RF-power have generally similar effects on the structural properties of μc-$Si_{1-x}C_x$:H alloys. In the previous chapter it was presented that the independent variation of these parameters induces a similar deterioration of the crystalline fraction (f_c^{Raman}) and an increase in the amount of carbon incorporated. On the other hand, the decrease in RF-power results in grains with a larger average grain size.

One could wonder if these two deposition parameters have a similar impact also on the optical band gap or if the optical properties are sensitive to the variation of the microstructure. For this reason, the evolution of E_g and E_{04} is studied as a function of the carbon-silicon ratio R_C. In Figure 4.2, results for CH_4 series (samples from $SET_{CH_4 2}$ and $SET_{CH_4 3}$) are presented, whereas the effect of w_{RF} is shown in Figure 4.3 (samples from $SET_{w_{RF}1}$).

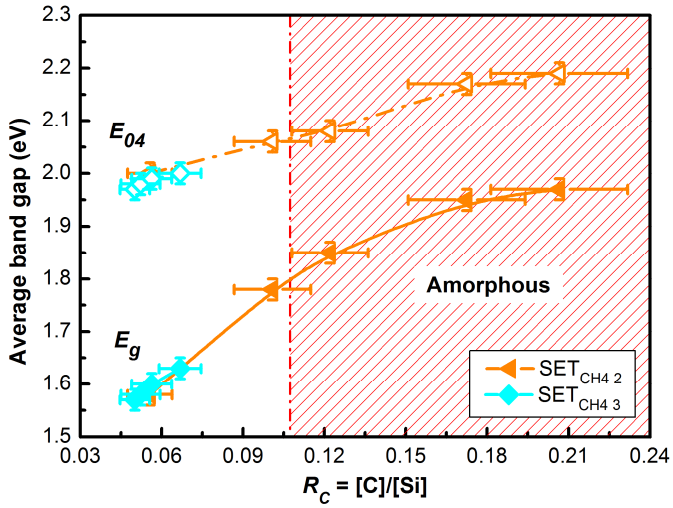

Figure 4.2.: Evolution of E_g and E_{04} (closed and open symbols, respectively) as a function of the total carbon-silicon ratio R_C, for samples from $SET_{CH_4 2}$ (◀) and $SET_{CH_4 3}$ (◆).

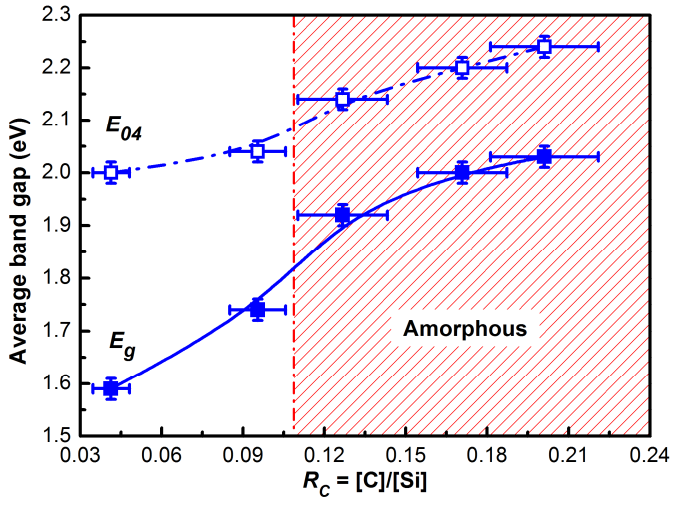

Figure 4.3.: Evolution of E_g and E_{04} (closed and open symbols, respectively) as a function of the total carbon-silicon ratio R_C, for samples from $SET_{w_{RF}1}$.

In both cases, for values of R_C lower than 0.12, E_g sharply increases from 1.55 eV to 1.80 eV, whereas values of E_{04} are stable around a mean value of 2 eV. Once the phase transition is reached, E_g and E_{04} evolve with similar trends. It seems to be impossible to distinguish between a low RF-power and a low CH_4 flow rate condition.

In order to study the impact of the improved microstructure, the evolution of E_g and E_{04} was investigated also for materials deposited at low RF-power, varying the CH_4 flow rate (w_{RF} = 113 mW/cm^2 - SET$_{w_{RF}2}$). Results are presented in Figure 4.4. Despite the fact that lower RF-power densities were shown to induce a better columnar growth, no influence of the microstructure on the optical band gap can be observed. Indeed, for similar values of R_C, E_g and E_{04} are in good agreement with what has been observed for the other sets of samples. Hence, E_g and E_{04} depend only on the carbon content.

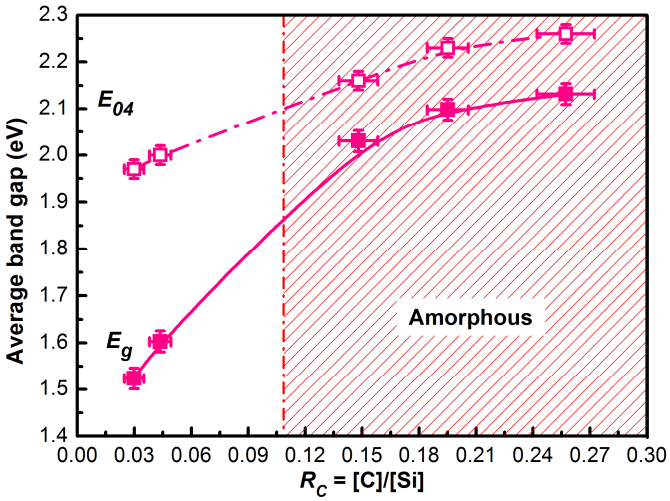

Figure 4.4.: Evolution of E_g and E_{04} (closed and open symbols, respectively) as a function of the total carbon-silicon ratio R_C, for samples from SET$_{w_{RF}2}$.

EFFECT OF SIF$_4$ FLOW RATE The addition of SiF_4 to the gas mixture was shown to have an impact on the crystalline component by introducing an additional etching mechanism which reduces the carbon incorporated in the thin film. If E_g and E_{04} are only controlled by R_C, the addition of SiF_4 should be matched by a decrease in the average band gap E_g with E_{04} being always stable as the microcrystalline-to-amorphous threshold is never crossed.

In Figure 4.5, the evolution of E_g and E_{04} for samples from SET$_{SiF_41}$ and SET$_{SiF_42}$ is presented as a function of the total carbon-silicon ratio. These materials are all in the microcrystalline region ($R_C < 0.12$). As expected, while E_g decrease with increasing SiF_4 flow rate (decreasing R_C), E_{04} is found nearly stable at $\sim$ 2 eV.

For materials deposited at w_{RF}= 113 mW/cm^2 with fixed CH_4 flow rate and addition of SiF_4 (SET$_{SiF_43}$), values of E_g and E_{04} are reported in Table 4.1. As previously observed, the improved microstructural properties (namely, the larger grain size due to the low RF-power) has no specific impact on the evolution of E_g and E_{04}, the values of which are only determined by the amount of carbon incorporated.

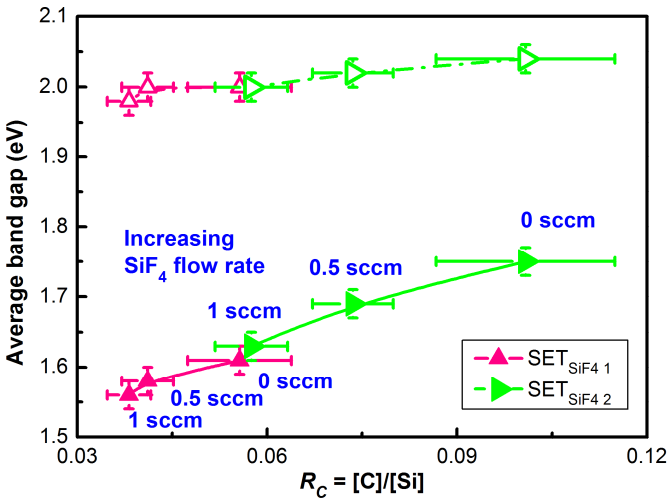

Figure 4.5.: Evolution of E_g and E_{04} (closed and open symbols, respectively) as a function of the total carbon-silicon ratio R_C, for samples from $SET_{SiF_4}1$ (▲) and $SET_{SiF_4}2$ (▶).

Table 4.1.: Evolution of E_g and E_{04}, as a function of the total carbon-silicon ratio R_C, for $SET_{SiF_4}3$ samples.

SiF_4 (sccm)	$R_C \pm 0.005$	$E_g \pm 0.02$ (eV)	$E_{04} \pm 0.02$ (eV)
0	0.045	1.56	1.97
0.5	0.040	1.54	1.97
1	0.030	1.52	1.97

EFFECT OF IBE Finally, the role of the IBE on E_g and E_{04} is presented in Table 4.2 for samples from SET_{peaks}, as a function of the carbon-silicon ratio R_C. As it was determined through the investigation of the structural properties, CH_4 flow rate variations that are sufficient to induce a phase transition at higher RF-powers (f_c^{Raman} going from $\sim$ 60 % to $\sim$ 20 % for $SET_{CH_4}3$), at low IBE are not enough to attain any significant modification in the alloys. Values of E_g and E_{04} are stable at 1.5 eV and 2 eV respectively, being in good agreement with other samples showing similar carbon incorporation ($R_C \sim 0.03$).

Table 4.2.: Evolution of E_g and E_{04} as a function of the total carbon-silicon ratio R_C, for SET_{peaks} samples.

CH_4 (sccm)	$R_C \pm 0.005$	$E_g \pm 0.02$ (eV)	$E_{04} \pm 0.02$ (eV)
1.1	0.027	1.50	2.00
1.2	0.030	1.50	2.00
1.3	0.032	1.50	2.00

4.3 TRANSPORT PROPERTIES

4.3.1 Room temperature dark and photo conductivity and activation energy

Temperature dependent dark and steady state photo-conductivity measurements (DC and SSPC, respectively) have been carried out as a function of the different deposition parameters. Measurements were performed in the 450-110 K temperature range, with a 10 K step. A 30 minute annealing under vacuum was made at 450 K, leading to the so called *"as-deposited"* state.

Due to the small thickness of the samples ($L < 300$ nm), it has been necessary to perform SSPC measurements using a monochromatic DC photon flux (1×10^{14} cm^{-2}s^{-1}) with $\lambda = 450$ nm. In this way, the light is not absorbed by the whole layer. Depending on the absorption coefficient α of the studied material at 450 nm, the carrier generation is reduced to an area of thickness $L_p = 1/\alpha_{450nm}$, close to the surface. Hence, it is possible to avoid any effect possibly related to the band-bending at the interface with the Corning glass substrate. For this reason, the photo-conductivity (σ_{ph}) was defined as:

$$\sigma_{ph} = \frac{(I_{ph}/L_p) - (I_{dark}/L)}{h\xi} \tag{4.3}$$

where I_{ph} and I_{dark} are the photo and dark currents, respectively, L_p is the penetration depth, deduced from the calculated absorption coefficient at 450 nm, L is the thickness of the sample, h the height of the metal contacts and ξ the applied electric field.

An example of the temperature dependence of σ_{dark} is given in Figure 4.6 for samples of $SET_{CH_4}2$. It can be seen that the semi-log plot of the dark conductivity exhibits a thermally activated behavior (in the 500-300 K temperature range) and therefore it is also possible to determine its activation energy E_a using Equation 2.15.

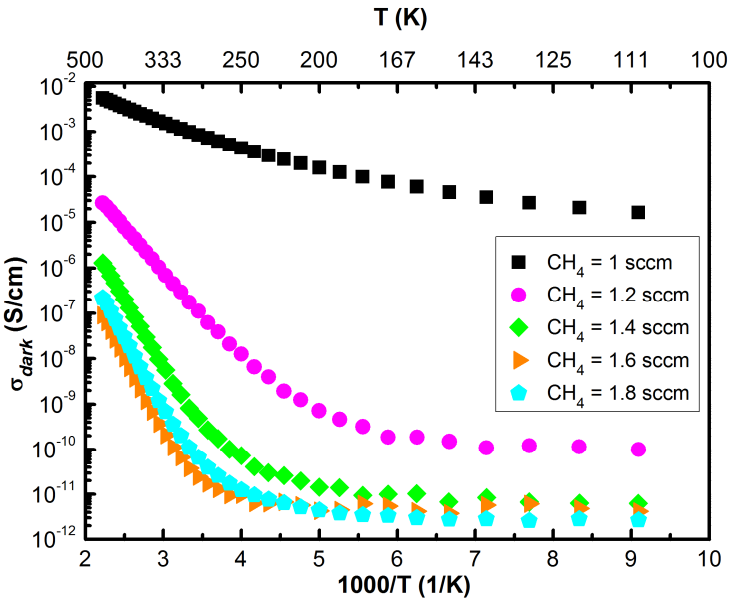

Figure 4.6.: Temperature dependent σ_{dark}, in the 450-110 K temperature range, for $SET_{CH_4}2$ samples deposited varying the CH_4 flow rate.

Actually, from an accurate study of the electrical dark conductivity as a function of temperature, important information regarding the transport mechanisms can be inferred. Several models have predicted the form of the dark conductivity temperature dependence for amorphous materials. However, for mixed-phase ones, the electrical conductivity over a wide range of temperatures can involve different mechanisms that depend on the microstructure of the samples, including also the chemical nature of the crystalline and amorphous phases.

Demichelis et al. performed a detailed analysis of the dark conductivity of μc-$Si_{1-x}C_x$:H alloys, in the 450-50 K temperature range, in order to define transport mechanism models for this kind of mixed-phase materials (Demichelis et al., 1994). They distinguished three regions:

1. *High temperatures* (450-200 K range), where the transport mechanism is highly dependent on the crystalline fraction of the material. It is possible to distinguish between:
   - **percolation through highly conductive regions**, for materials characterized by high values of f_c^{Raman};
   - **hopping between neighboring crystalline islands**, distributed in an amorphous matrix and **thermionic emission** from the crystalline areas to the amorphous ones, for materials with low values of f_c^{Raman}.

   In this range of temperatures, Demichelis et al. found that the slope of σ_{dark} decreases with increasing crystalline fraction and the corresponding activation energy varies from 0.9 eV (for completely amorphous alloys), to 0.2 eV (for highly microcrystalline ones). The pre-exponential factor is found to be varying slowly with the crystallinity of the material.

2. *Intermediate temperatures* (200-90 K range), where the predominant conduction path is assumed to be by **hopping in the tail states**. The broadening of the band tails arises from the disorder induced by the presence of the two phases, by fluctuations in the grain size and variation in the stoichiometry of the amorphous tissue. For this range of temperatures lower values of the activation energy ($\sim$ 0.1 eV) are found, and values of the pre-exponential factor are typically decreased by three orders of magnitude.

3. *Low temperatures* (90-50 K range), where the main conduction mechanism is assumed to be **hopping between localized states lying in a narrow band deep in the mobility gap**. Very low (and about constant) values of the activation energy and a large variation of pre-exponential factors are found.

In this work, for all samples the effect of the variation of the deposition parameters on the activation energy E_a and its prefactor σ_{00} has been investigated mostly for the high temperature region. In this range of temperatures, the transport mechanism strongly depend on the degree of crystallinity. As μc-$Si_{1-x}C_x$:H alloys are made of silicon crystallites embedded in an a-$Si_{1-x}C_x$:H matrix, the microcrystals can either be completely surrounded by the amorphous tissue, or can be interconnected, depending on the crystalline volume fraction.

For the intermediate temperature region (200-110 K), an estimation of E_a and σ_{00} has been obtained only for some alloys, as for most of them the

dark current at temperatures below 200 K reaches values of 0.1 pA, which are close to the detection limits of the Keithley.

Concerning the temperature range under investigation, for microcrystalline samples the dark conductivity can be written as:

$$\sigma_{dark}(T) = \sigma_{00H} \cdot \exp\left\{-\frac{E_{aH}}{kT}\right\} + \sigma_{00L} \cdot \exp\left\{-\frac{E_{aL}}{kT}\right\}, \tag{4.4}$$

where to distinguish between high-temperature region ($T > 200$ K) and intermediate-temperature region ($T < 200$ K), the activation energy and its prefactor are defined as E_{aH}, σ_{00H} and E_{aL}, σ_{00L}, respectively.

In addition, the impact on the transport properties has been studied also for the room temperature dark and photo conductivity (σ_{dark} and σ_{ph}, respectively) and of the photo-response Φ, which is defined as

$$\Phi = \frac{\sigma_{ph}}{\sigma_{dark}}. \tag{4.5}$$

EFFECT OF CH_4 FLOW RATE In Figure 4.7 the influence of the CH_4 flow rate is presented showing σ_{dark}, σ_{ph} and the photo-response Φ, as a function of the crystalline volume fraction, for samples from $SET_{CH_4 2}$ and $SET_{CH_4 3}$ (Table 3.1).

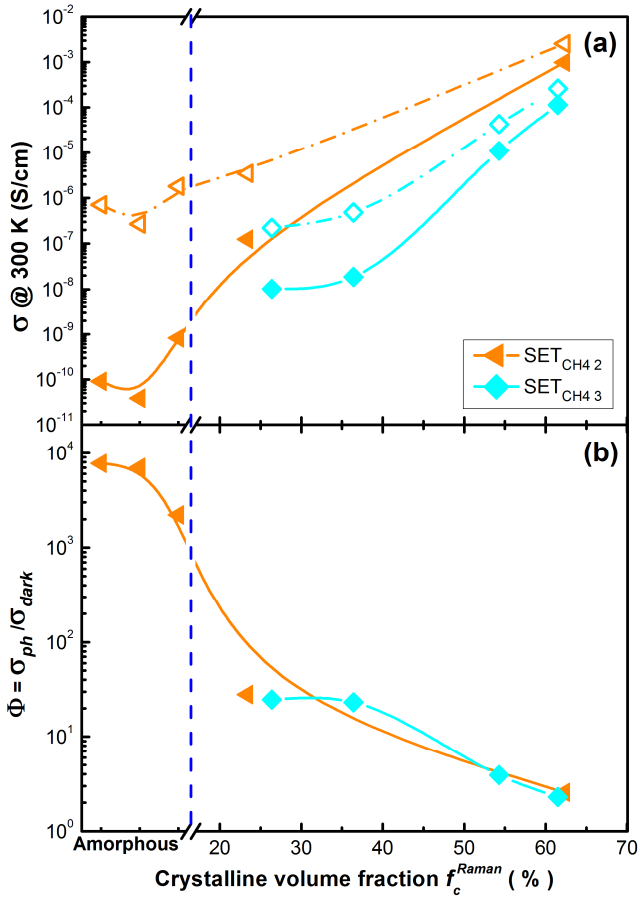

Figure 4.7.: Evolution of the room temperature (a) σ_{ph} (open symbols) and σ_{dark} (closed symbols) and (b) photo-response Φ as a function of the crystalline volume fraction f_c^{Raman}, for samples from $SET_{CH_4 2}$ (◀) and $SET_{CH_4 3}$ (◆).

The microcrystalline-to-amorphous transition induced by the increase of CH_4 flow rate, is reflected by a degradation of both σ_{dark} and σ_{ph} (Figure 4.7(a)). With decreasing crystalline volume fraction, σ_{dark} is decreased by nearly 8 orders of magnitude (passing from 1×10^{-3} to 1×10^{-11} S/cm) for $SET_{CH_4 2}$ and of nearly 4 for $SET_{CH_4 3}$ (passing from 1×10^{-4} to 1×10^{-8} S/cm). Such decrease is due to the amorphization of the material induced by the carbon incorporation. At the same time, as σ_{dark} decreases more rapidly than σ_{ph}, the photo-response Φ increases with the phase transition (Figure 4.7(b)), reaching values of $\sim 10^3/10^4$ which are typical for a-$Si_{1-x}C_x$:H alloys (Ambrosone, U. Coscia, Lettieri, et al., 2004).

It is worth noting that for similar crystalline volume fractions, the variation in SiH_4 flow rate (which is doubled going from $SET_{CH_4 2}$ to $SET_{CH_4 3}$), induces a deterioration of both σ_{dark} and σ_{ph}. This was also observed by Vetterl et al. for the deposition of μc-Si:H. They showed that the variation of the silane concentration does not affect only the structural properties of the material, but it also has an impact on the electrical ones, inducing a deterioration of both σ_{dark} and σ_{ph} (Vetterl et al., 2000). However, for these materials this "silane-induced" degradation seems to be similar for σ_{dark} and σ_{ph}, resulting in the same evolution of Φ.

In Table 4.3 the effect of the CH_4 flow rate on the activation energy is presented. In agreement with results presented by Demichelis et al., the decrease of the crystalline volume fraction induces an increase in the activation energy (Demichelis, Crovini, et al., 1994; Demichelis et al., 1994). For microcrystalline materials ($SET_{CH_4 2}$), a $\sim$ 60 % decrease in the crystalline volume fraction is translated into an increase of nearly 160 % in the high-temperature activation energy. Once the phase transition is completed, there is still an increase in E_{aH} with increasing amount of carbon incorporated in the material.

Table 4.3.: Evolution of activation energy and its prefactor as a function of the crystalline volume fraction f_c and the total carbon-silicon ratio R_C, for both high-temperature and low-temperature regions, for $SET_{CH_4 2}$ and $SET_{CH_4 3}$ samples.

	CH_4 (sccm)	f_c (%)	R_C	E_{aH} (meV)	σ_{00H} (S/cm)	E_{aL} (meV)	σ_{00L} (S/cm)
$SET_{CH_4 2}$	1.0	60	0.056	130	0.16	40	1.16×10^{-3}
	1.2	25	0.101	340	0.35	20	1.59×10^{-8}
	1.4	0	0.122	570	3.11	—	—
	1.6	0	0.172	630	0.96	—	—
	1.8	0	0.207	630	2.78	—	—
$SET_{CH_4 3}$	1.1	60	0.050	170	0.13	55	8.32×10^{-5}
	1.2	55	0.052	250	0.15	30	1.22×10^{-7}
	1.3	36	0.056	430	0.52	—	—
	1.4	25	0.067	490	2.57	—	—

EFFECT OF RF-POWER Since the variation of the RF-power density w_{RF} has a similar impact on the structural properties of μc-$Si_{1-x}C_x$:H alloys, as the increase of CH_4 in the gas mixture, one can expect to observe in the two cases a similar decrease of the electrical properties.

In Figure 4.8, the evolution of room temperature σ_{dark} and σ_{ph} and of the photo-response Φ is presented as a function of the RF-power density, for samples from $SET_{w_{RF}1}$.

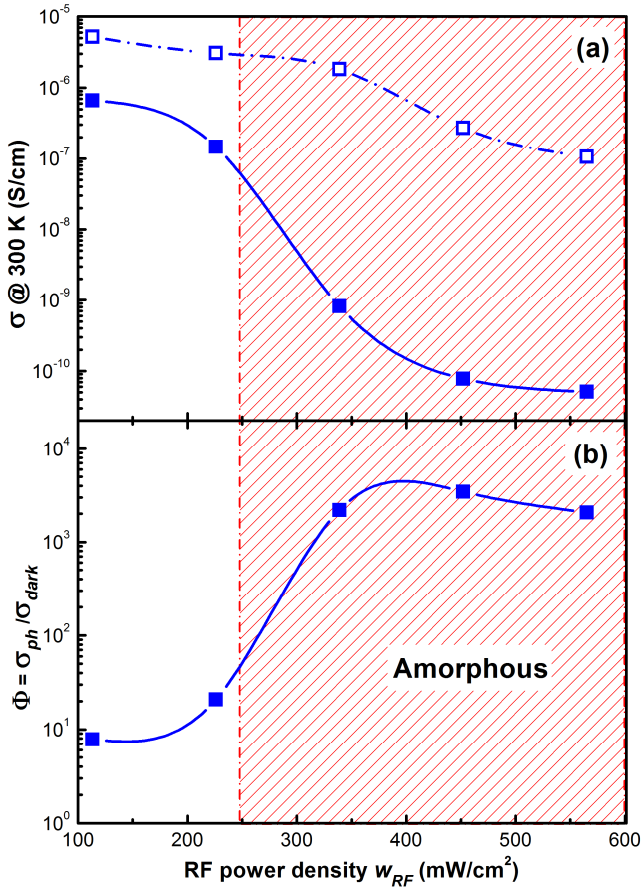

Figure 4.8.: Evolution of the room temperature (a) σ_{ph} (open symbols) and σ_{dark} (closed symbols) and (b) photo-response ratio Φ as a function of the RF-power density w_{RF}, for samples from $SET_{w_{RF}1}$.

With increasing w_{RF} both σ_{dark} and σ_{ph} decrease. While the first one decreases rapidly (nearly 4 orders of magnitude) going from 10^{-6} S/cm to 10^{-10} S/cm, the second one decreases more slowly (nearly 2 orders of magnitude), passing from 10^{-5} S/cm to 10^{-7} S/cm. Consistently with previous results, this deterioration is related to the carbon incorporation and the subsequent amorphization. The evolution of the photo-response Φ highlights directly the structural changes. Indeed, once the full phase transition is attained, a drastic increase in Φ is observed, reaching values that are typical of a-$Si_{1-x}C_x$:H alloys.

Similarly, in Table 4.4 the influence of the increase of the RF-power density on E_a is reported. The increase in RF-power, which induces a decrease of nearly 60 % in crystalline volume fraction, is translated into an increase of $\sim$ 15 % of the activation energy E_{aH}.

As the transport mechanisms depend on the crystalline degree of the material, it is safe to assume that they might also be influenced by the microstructural properties. Namely, it can be supposed that for similar values of f_c^{Raman}, a different average grain size can have an influence on the photo-response ratio. For this reason, the impact of the CH_4 flow rate on the transport properties has been studied also for materials deposited at low RF-power ($SET_{w_{RF}2}$).

Obviously, even if the low power conditions give a better microstructure, the carbon-induced amorphization linked to the increase of CH_4 flow rate

Table 4.4.: Evolution of E_a as a function of the crystalline volume fraction f_c and the total carbon-silicon ratio R_C, for $SET_{w_{RF}1}$ samples.

w_{RF} (mW/cm^2)	f_c (%)	R_C	E_{aH} (meV)	σ_{00H}(S/cm)	E_{aL} (meV)	σ_{00L} (S/cm)
113	65	0.040	420	15.60	—	—
226	25	0.095	360	0.35	20	1.59×10^{-8}
339	0	0.127	500	1.45	—	—
452	0	0.171	595	1.87	—	—
565	0	0.201	605	2.57	—	—

induces the degradation of both room temperature σ_{dark} and σ_{ph}. This evolution is presented in Figure 4.9 as a function of the crystalline volume fraction. It is worth noting that the sample from $SET_{w_{RF}2}$ deposited using CH_4 = 5 sccm ($R_C \sim 0.26$) is not conductive (it should be found in the dashed area in Figure 4.9).

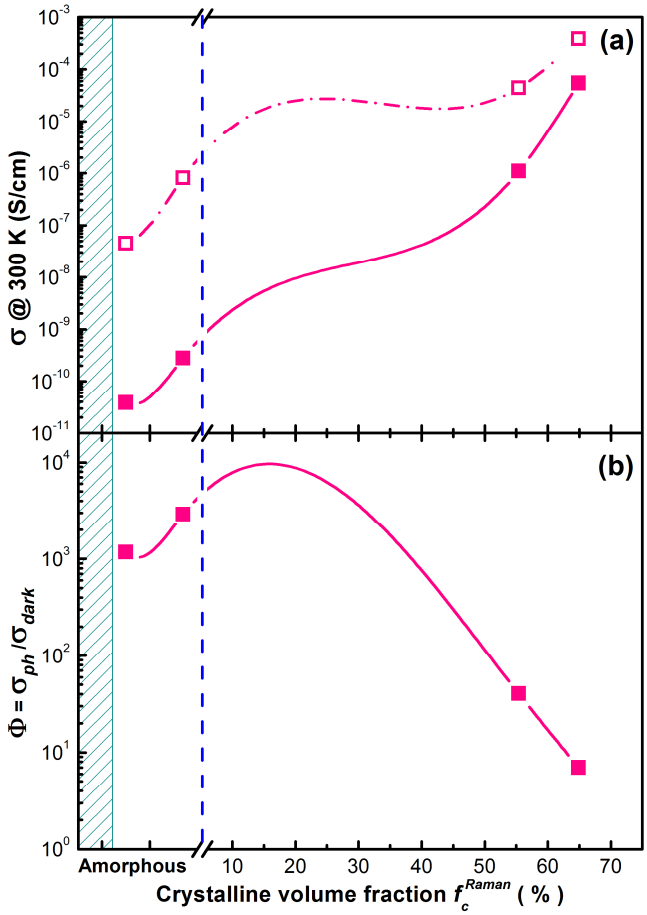

Figure 4.9.: Evolution of the room temperature (a) σ_{ph} (open symbols) and σ_{dark} (closed symbols) and (b) photo-response Φ as a function of the crystalline volume fraction f_c^{Raman}, for samples from $SET_{w_{RF}2}$. The dashed area highlights the region in which it should be expected to find the sample deposited using CH_4 = 5 sccm ($R_C \sim 0.26$), which is not conductive.

In Table 4.5 the evolution of the activation energy is presented, showing its increase due to the deterioration of the crystalline fraction. It is worth noting that compared to materials deposited at w_{RF} = 226 mW/cm^2, for similar values of f_c^{Raman} ($\sim$ 60 %), materials deposited at low RF-power exhibit values of E_a that are nearly 75 % higher. In section 4.3.3 a comparison of the impact on the electrical properties of the studied deposition parameters will be presented, stressing the role of the microstructure.

Table 4.5.: Evolution of E_a as a function of the crystalline volume fraction f_c and the total carbon-silicon ratio R_C, for $SET_{w_{RF}2}$ samples.

CH_4 (sccm)	f_c (%)	R_C	E_{aH} (meV)	σ_{00H}(S/cm)	E_{aL} (meV)	σ_{00L} (S/cm)
1.2	60	0.030	225	0.40	27	9.75×10^{-7}
1.4	55	0.044	410	4.75	—	—
3	0	0.150	670	50.67	—	—
4	0	0.195	695	8.05	—	—
5	0	0.257		Not conductive		

EFFECT OF SiF_4 FLOW RATE The impact of the addition of few sccm of SiF_4 to the gas mixture on the room temperature σ_{dark} and σ_{ph} and the photo-response ratio is presented in Figure 4.10.

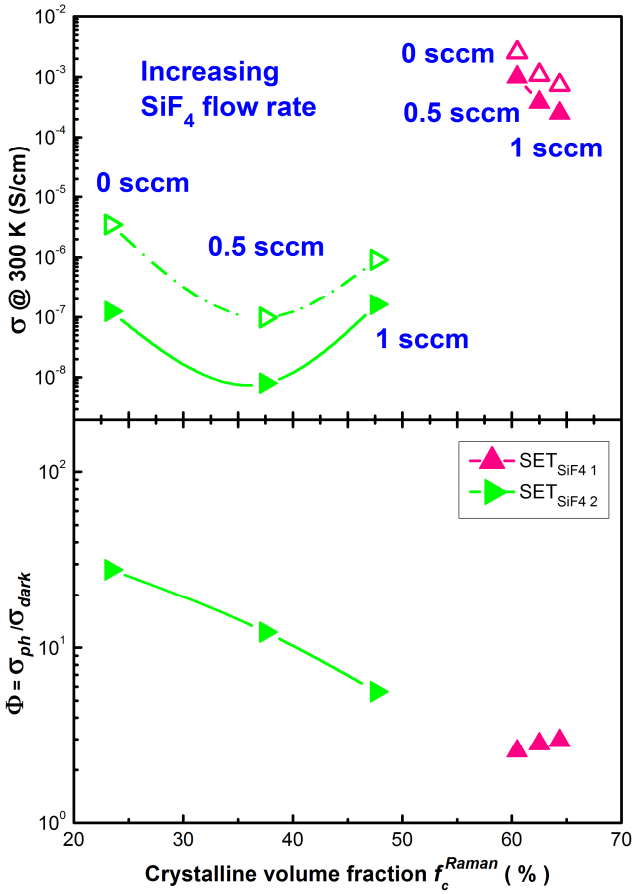

Figure 4.10.: Evolution of the room temperature (a) σ_{ph} (open symbols) and σ_{dark} (closed symbols) and (b) photo-response Φ as a function of the crystalline volume fraction f_c^{Raman}, for samples from $SET_{SiF_4 1}$ (CH_4 = 1 sccm - ▲) and $SET_{SiF_4 2}$ (CH_4 = 1.2 sccm - ▶).

When the starting material is already highly microcrystalline ($SET_{SiF_4 1}$ ▲) the addition of SiF_4 to the gas mixtures seems to induce a similar deterioration of both σ_{dark} and σ_{ph}, resulting in a stable value of Φ. Such degradation is possibly related to the increase of the defects density. On the other hand, when the starting material is on the threshold to the amorphous transition ($SET_{SiF_4 2}$ ▶) the increase in crystalline volume fraction induced by the addition of SiF_4 to the gas mixture induces a worsening mostly on σ_{ph}, leading to a decrease in the photo-response. This is consistent with the more significant phase evolution obtained with the addition of few sccm of SiF_4 (f_c^{Raman} is nearly doubled).

In Table 4.6 the effect of the addition of SiF_4 on the activation energy of these samples is presented. It is noteworthy that the increase of the crystalline volume fraction obtained with the addition of few sccm of this precursor is matched, in this case, by an increase of E_a, whereas it was previously shown that the higher f_c^{Raman}, the lower is E_a. For materials starting with a high crystalline volume fraction ($f_c^{Raman} \sim 60$ %) the effect of a low SiF_4 flow rate gives an increase in E_a of ~ 30 %. However, for materials characterized by relatively low starting values of f_c^{Raman} (~ 25 %) an increase of nearly 20 % in E_a is observed.

The fact that additional SiF_4 induces an increase in the activation energy (with increasing crystalline volume fraction), is possibly explained by the reduction of the level of oxygen contamination, as it was observed also by Abramov et al. (Abramov et al., 2010).

Table 4.6.: Evolution of E_a as a function of the crystalline volume fraction f_c and the total carbon-silicon ratio R_C, for $SET_{SiF_4 1}$ and $SET_{SiF_4 2}$ samples.

	SiF_4 (sccm)	f_c (%)	R_C	E_{aH} (meV)	σ_{00H} (S/cm)	E_{aL} (meV)	σ_{00L} (S/cm)
$SET_{SiF_4 1}$	0	60	0.056	130	0.16	40	1.16×10^{-3}
	0.5	62	0.040	165	0.22	50	4.67×10^{-4}
	1	65	0.038	175	0.23	60	3.34×10^{-4}
$SET_{SiF_4 2}$	0	23	0.100	355	0.35	20	1.59×10^{-8}
	0.5	37	0.075	495	0.98	—	—
	1	47	0.058	430	3.46	—	—

So far, looking at both structural and electrical properties, it seems that the impact of few sccm of SiF_4 is productive only when the starting material has a very low crystalline volume fraction. However, the possibility of combining the additional etching mechanism provided by the SiF_4 molecules, with the larger grain size yielded by the low RF-power conditions, seems to be a promising new alternative for the development of these materials. The effect of the addition of SiF_4 to the gas mixture has been investigated also for samples from $SET_{SiF_4 3}$, which were deposited at low RF-power (20 W = 113 mW/cm^2). The evolution of the electrical properties is reported in Table 4.7. With increasing crystalline volume fraction (~ 35 %), a decrease of σ_{dark}, σ_{ph} and Φ is observed.

Table 4.7.: Evolution of σ_{dark}, σ_{ph} and Φ, as a function of the crystalline volume fraction f_c^{Raman}, for $SET_{SiF_4 3}$ samples.

SiF_4 (sccm)	f_c^{Raman} (%)	$\sigma_{dark} \times 10^{-7}$ (S/cm)	$\sigma_{ph} \times 10^{-7}$ (S/cm)	Φ
0	55	10.9	441.4	40
0.5	60	0.5	8.5	16
1	65	0.7	11.7	17

In Table 4.8 values of the activation energy for samples from $SET_{SiF_4 3}$ are shown. For all these materials the activation energy in the intermediate temperature range couldn't be measured as I_{dark} was in the order of 0.1 pA. However, a 20 % increase in the crystalline volume fraction is matched by a $\sim$ 20 % increase of the activation energy E_{aH}. It is worth noting that for this set of samples all alloys are exhibiting a significant crystalline volume fraction. It is possible that the reduction of oxygen contamination, although competing with structural variations, is dominating and therefore is responsible for the increase in E_a. The direct comparison of the effect of all the deposition parameters will be presented in section 4.3.3.

Table 4.8.: Evolution of E_a as a function of the crystalline volume fraction f_c^{Raman} and the total carbon-silicon ratio R_C, for $SET_{SiF_4 3}$ samples.

SiF_4 (sccm)	f_c^{Raman} (%)	R_C	E_{aH} (meV)	σ_{00H}(S/cm)
0	55	0.045	410	4.75
0.5	60	0.040	455	9.35
1	65	0.030	480	17.34

EFFECT OF IBE Finally, the role of the ion bombardment energy (IBE) on electrical properties has been studied only for samples deposited using the *peaks* voltage waveforms.

In Table 4.9 values of σ_{dark}, σ_{ph} and Φ are reported. It can be clearly seen that the low IBE conditions, despite giving materials for which the variations in the CH_4 flow rate slightly change f_c^{Raman}, do not cause any notable evolution in the transport properties. Moreover, these materials are characterized by very low values of both σ_{dark} and σ_{ph}.

Table 4.9.: Evolution of σ_{dark}, σ_{ph} and Φ, as a function of the crystalline volume fraction f_c^{Raman}, for SET_{peaks} samples.

CH_4 (sccm)	f_c^{Raman} (%)	$\sigma_{dark} \times 10^{-8}$ (S/cm)	$\sigma_{ph} \times 10^{-8}$ (S/cm)	Φ
1.1	55	0.63	4.88	8
1.2	50	0.51	3.54	7
1.3	47	0.63	4.43	7

In Table 4.10 the effect of IBE on the activation energy E_a is presented. An estimation of the activation energy in the intermediate temperature range was meaningless, due to the low values of I_{dark}. For the high temperature range, a weak decrease in E_{aH} is observed, but actually values can be considered stable at about $\sim$ 500 meV. As all results have shown so far, at low IBE the considered variations in the CH_4 flow rate do not induce any notable evolution in the electrical and transport properties.

Table 4.10.: Evolution of E_a as a function of the crystalline volume fraction f_c^{Raman} and the total carbon-silicon ratio R_C, for SET_{peaks} samples.

CH_4 (sccm)	f_c^{Raman} (%)	R_C	E_{aH} (meV)	σ_{00H} (S/cm)
1.1	55	0.027	520	4.10
1.2	50	0.030	490	1.12
1.3	47	0.032	470	0.63

4.3.2 Minority carrier diffusion length

Steady state photo-carrier grating (SSPG) measurements were used to determine the minority carrier diffusion length L_d in μc-$Si_{1-x}C_x$:H and a-$Si_{1-x}C_x$:H. The evolution of this parameter, together with the previous ones, can help the identification of the most appropriate conditions for the development of these materials as active layers in photodiodes.

All the electrical properties studied so far were measured in a coplanar configuration, and it should be remembered that significant discrepancies between parallel and perpendicular transport properties can arise in materials like μc-Si:H, due to the columnar growth. Such structure is indeed characterized by the presence of (i) grain boundaries, (ii) high concentrations of defects in the column joints and (iii) the amorphous incubation layer at the interface with the substrate, which can be detrimental for in-plane transport properties. Hence, results from SSPG measurements can only give some hint on the performance of these alloys once integrated in devices.

EFFECT OF CH_4 FLOW RATE AND RF-POWER In Table 4.11 the effect of the increase of the CH_4 flow rate on the minority carrier diffusion length L_d is presented for samples from SET_{CH_43} (deposited at 226 mW/cm^2) and $SET_{w_{RF}2}$ (deposited at 113 mW/cm^2). With increasing CH_4 flow rate (decreasing f_c^{Raman}), values of L_d decrease in agreement with the evolution of room temperature σ_{dark} and σ_{ph}. The increase of disorder, induced by the amorphization of the material, is a possible explanation for the deterioration of this transport property. Despite the improved microstructural properties obtain thanks to a lower RF-power, values of L_d are similar for both sets of samples.

Table 4.11.: Evolution of L_d as a function of the crystalline volume fraction f_c^{Raman} and the total carbon-silicon ratio R_C, for samples from SET_{CH_43} and $SET_{w_{RF}2}$.

	CH_4 (sccm)	f_c^{Raman} (%)	R_C	L_d (nm)
SET_{CH_43}	1.1	65	0.050	140
	1.2	55	0.052	140
	1.3	36	0.056	135
	1.4	25	0.067	90
$SET_{w_{RF}2}$	1.2	65	0.030	140
	1.4	55	0.044	135
	3	0	0.150	60
	4	0	0.195	40
	5	0	0.257	**Not conductive**

EFFECT OF SiF_4 FLOW RATE The effect of the addition of few sccm of SiF_4 on L_d has been studied for samples deposited at low RF-power density (SET_{SiF_43}). In Table 4.12 results show that with the addition of SiF_4 values of L_d are stable at $\sim$ 135 nm.

Table 4.12.: Evolution of L_d as a function of the crystalline volume fraction f_c^{Raman} and the total carbon-silicon ratio R_C, for SET_{SiF_43} samples.

SiF_4 (sccm)	f_c^{Raman} (%)	R_C	L_d (nm)
0	55	0.044	135
0.5	59	0.039	130
1	65	0.031	140

EFFECT OF IBE Finally, the impact on the minority carrier diffusion length of the variation of CH_4 flow rate when low IBE conditions are applied, is presented in Table 4.13. As highlighted by all results presented so far, these conditions are not sufficient to induce a significant evolution in the transport properties of the alloys (L_d is stable at 95 nm). However, it is noteworthy that these materials exhibit very poor values of L_d.

Table 4.13.: Evolution of $E_a$as a function of the crystalline volume fraction f_c^{Raman} and the total carbon-silicon ratio R_C, for SET_{peaks} samples.

CH_4 (sccm)	f_c^{Raman} (%)	R_C	L_d (nm)
1.1	55	0.027	95
1.2	50	0.030	95
1.3	47	0.032	95

4.3.3 Summary

In the previous sections, details on the effect of the different deposition parameters on the electrical transport properties of μc-$Si_{1-x}C_x$:H alloys (grown from a silane and methane gas mixture, highly diluted in hydrogen), were presented. The complexity of this material system lies in its diphasic nature, made of silicon crystallites embedded in an amorphous silicon-carbon matrix the stoichiometry of which can be varied. Therefore, electrical properties may not only be affected by the crystalline volume fraction, but also by the chemical composition.

The analysis of the impact of the different deposition conditions on the average optical band gap, revealed that this parameter (either if one considers the Tauc band gap E_g or the iso-absorption band gap E_{04}) is not influenced by the microstructural properties (namely, the average grain size), but it seems to be controlled only by the crystalline volume fraction and the total amount of carbon incorporated R_C.

In Figure 4.11, values of E_g and E_{04} are plotted as a function of R_C for samples from SET_{CH_43}, $SET_{w_{RF}2}$, SET_{SiF_43} and SET_{peaks}. The variations of CH_4 or SiF_4 flow rate (for both standard RF-PECVD at high and low RF-powers and for TVW-PECVD), exert variations in the chemical composition of the alloy. Passing from R_C = 0.03 to R_C = 0.07 induces an increase in E_g of nearly 10 %, going from 1.5 eV to 1.7 eV. However, for this range of R_C values, materials are always microcrystalline and E_{04} remains stable at

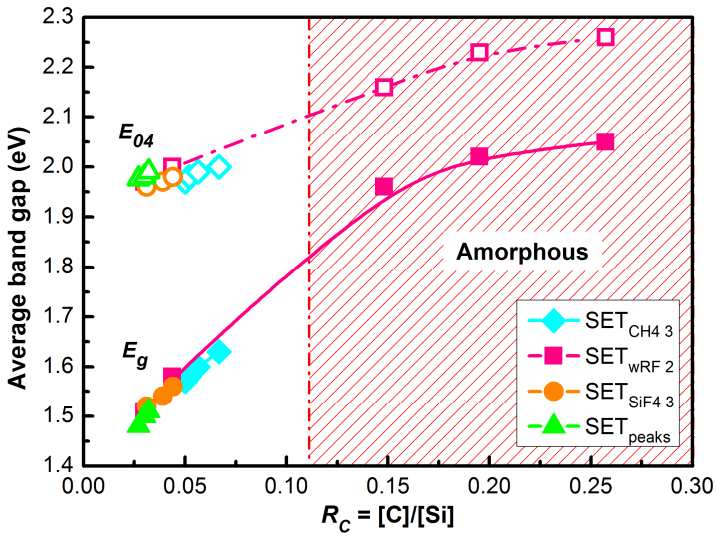

Figure 4.11.: Evolution of E_g and E_{04} (closed and open symbols, respectively) as a function of the total carbon-silicon ratio R_C, for samples from SET$_{CH_4 3}$ (◆), SET$_{wRF2}$ (■), SET$_{SiF_4 3}$ (●) and SET$_{peaks}$ (▲).

a mean value of 2 eV. For every set of samples a weak increase in E_{04} is observed, but it can be considered within the error bar.

Concerning room temperature σ_{dark} and σ_{ph}, and the photo-response Φ, it has been shown that no matter which parameter is varied, the microcrystalline-to-amorphous phase transition is accompanied by a deterioration of both σ_{dark} and σ_{ph}, and an increase in Φ (due to the weaker decrease of the photoconductivity, compared to the dark one). This result is in agreement with what can be found in literature. Demichelis et al. deposited μc-$Si_{1-x}C_x$:H alloys at $\sim$ 300 mW/cm^2 changing the crystalline volume fraction by varying the CH_4 flow rate. They established that the room temperature conductivity is strongly correlated to the crystallinity. They also showed that for high values of f_c^{Raman} there is a saturation of the dark conductivity, but they couldn't prove a relation between σ_{dark} and the chemical composition for very low amount of carbon content (Demichelis et al., 1994). However, results plotted in Figure 4.12, show that microstructural differences are not negligible.

Starting from samples deposited by standard RF-PECVD from a simple SiH_4 and CH_4 gas mixture highly diluted in H_2, films deposited at 226 mW/cm^2 (SET$_{CH_4 3}$) and at 113 mW/cm^2 (SET$_{wRF2}$) have comparable values of σ_{ph} for $f_c^{Raman} > 50$ % (Figure 4.12(a)), but the higher RF-power density leads to less photo-sensitive materials, σ_{dark} being twice higher. Indeed, these samples exhibit a photo-response that is nearly one order of magnitude lower, compared to that of samples deposited at 113 mW/cm^2 (Figure 4.12(b)). This can be related to a doped-type behavior, as it will be discussed further in this summary. When SiF_4 is added to the gas mixture, despite starting from an already highly microcrystalline material ($f_c^{Raman} \sim 55$ %), the electrical properties seem to be deteriorated. Both σ_{dark} and σ_{ph} decrease by nearly 95 %. This can be due to an increase of electrically active defects. In section 4.4 an analysis of *defect-related* properties will be presented, as a function of the different deposition parameters. It is noteworthy that for samples showing similar values of f_c^{Raman} ($\sim$ 50 %), the low IBE conditions achieved with the TVW-PECVD lead to materials characterized by values of

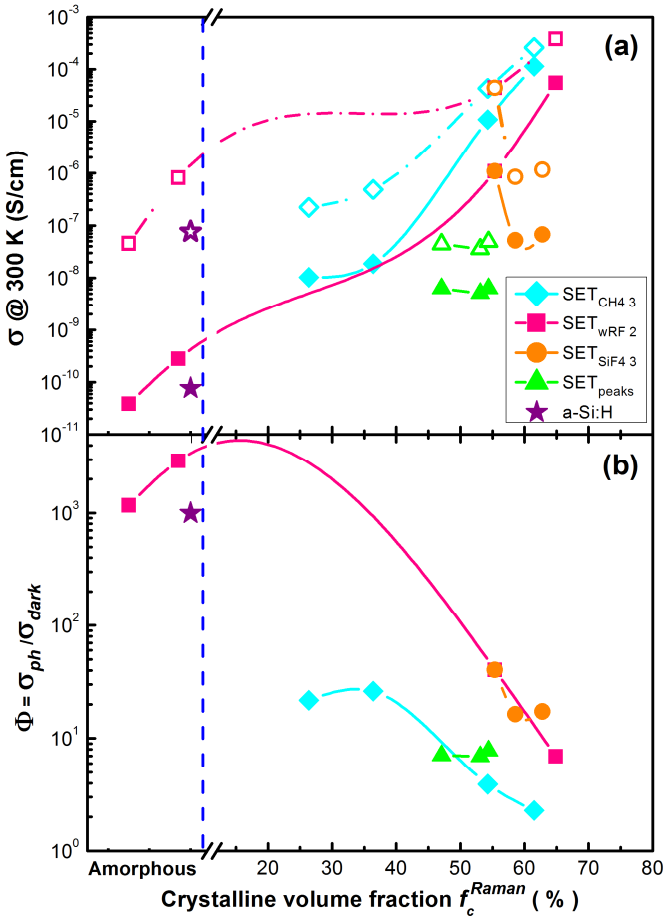

Figure 4.12.: Evolution of the room temperature (a) σ_{ph} (open symbols) and σ_{dark} (closed symbols) and (b) photo-response Φ as a function of the crystalline volume fraction f_c^{Raman}, for samples from SET_{CH_43} (◆), $SET_{w_{RF}2}$ (■), SET_{SiF_43} (●) and SET_{peaks} (▲). Results are compared to a device quality amorphous silicon sample deposited by standard RF-PECVD (★).

σ_{dark} and σ_{ph} that are drastically lower compared to samples from SET_{CH_43} ($\sigma_{dark} \sim 2000$ times higher) and $SET_{w_{RF}2}$ ($\sigma_{dark} \sim 200$ times higher). A possible reason for this dramatic decrease in conductivity can be related to the density of defects, as it will be addressed in the following (section 4.4).

Finally, in Figure 4.12 the performance of these materials is compared to that of a device quality a-Si:H reference sample deposited by standard RF-PECVD (★). Deposition conditions of this a-Si:H sample are presented in Longeaud, Roy, et al., 2002. It is interesting that whatever the crystalline volume fraction, μc-$Si_{1-x}C_x$:H alloys have comparable (or higher) values of σ_{ph} than that of the a-Si:H sample. Obviously, their photo-response Φ is at least 50 times lower than that of a-Si:H, due to the different structural phase. However, the a-$Si_{1-x}C_x$:H alloys presented in the figure and the a-Si:H sample, have comparable values of Φ. If these properties are matched by acceptable values of the activation energy and of the minority carrier diffusion length, it is possible for these materials to be efficiently applied into some kind of photovoltaic device. Nevertheless, their performance under light-soaking have still to be tested.

In Figure 4.13 Values of the activation energy E_a of the dark conductivity (in the 450-200 K temperature range) are presented as a function of the crystalline volume fraction, and are compared to those presented in Demichelis et al., 1994. For standard RF-PECVD films the increase in f_c^{Raman} leads to a decrease in E_a. The interesting thing is that such a decrease is more pronounced for samples deposited at higher RF-power density (SET_{CH_43} - w_{RF}= 226 mW/cm^2). In particular, for $f_c^{Raman} \sim 55$ %, samples deposited at w_{RF}= 113 mW/cm^2 exhibit an activation energy almost 65 % higher than for samples deposited at 226 mW/cm^2. This may be due to a lower density of defects in the material, directly related to better microstructure obtained with the lower RF-power conditions. Nevertheless, for materials having a crystalline volume fraction above 60 %, the discrepancy between high and low RF-power decreases and values of E_a differ only by $\sim$ 30%. Assuming that E_a gives the position of the Fermi level at 0 K with respect to the conduction band edge and considering the values of the optical band gap that were previously presented, these alloys are characterized by a doped-type behavior. Such low values of E_a are in agreement with what can be found in the literature (Demichelis, Crovini, et al., 1994; Demichelis et al., 1994). A possible explanation for this kind of doped-type behavior, could arise from the presence of different kinds of defects at the interface between the silicon crystallites and the surrounding a-$Si_{1-x}C_x$:H tissue, that place the Fermi level closer to the conduction band.

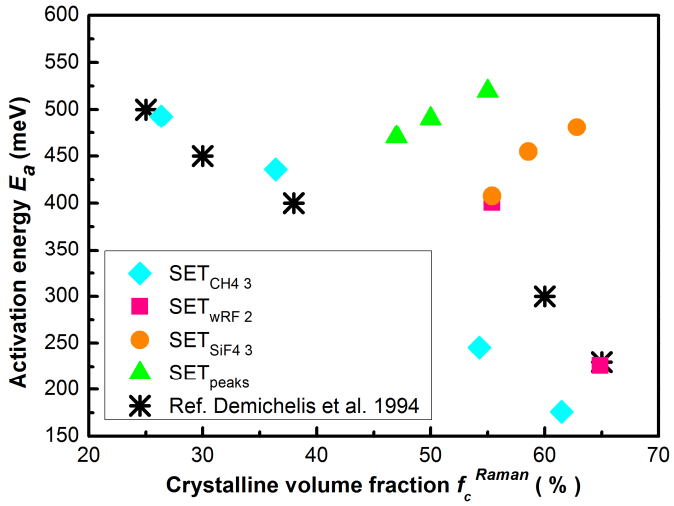

Figure 4.13.: Evolution of the activation energy E_a as a function of the crystalline volume fraction f_c^{Raman}, for samples from SET_{CH_43} (◆), $SET_{w_{RF}2}$ (■), SET_{SiF_43} (●) and SET_{peaks} (▲). Results from this work are compared to those presented in Demichelis et al., 1994 (✳).

Building on their experimental results on electrical properties, Demichelis et al. proposed a model for the band structure of μc-$Si_{1-x}C_x$:H (Figure 4.14). In Figure 4.14(a), the band diagram for interconnected silicon crystallites is shown, as for highly crystalline alloys the most probable transport mechanism is by percolation through interconnected silicon crystallites. With decreasing crystalline volume fraction the crystallites are more and more surrounded by the a-$Si_{1-x}C_x$:H tissue. In this case the conduction process is mostly controlled by c-Si/a-$Si_{1-x}C_x$:H interface and this case is presented in Figure 4.14(b). In both figures, the dashed lines close to the Fermi level and at the interfaces define some unoccupied defects due to disorder or

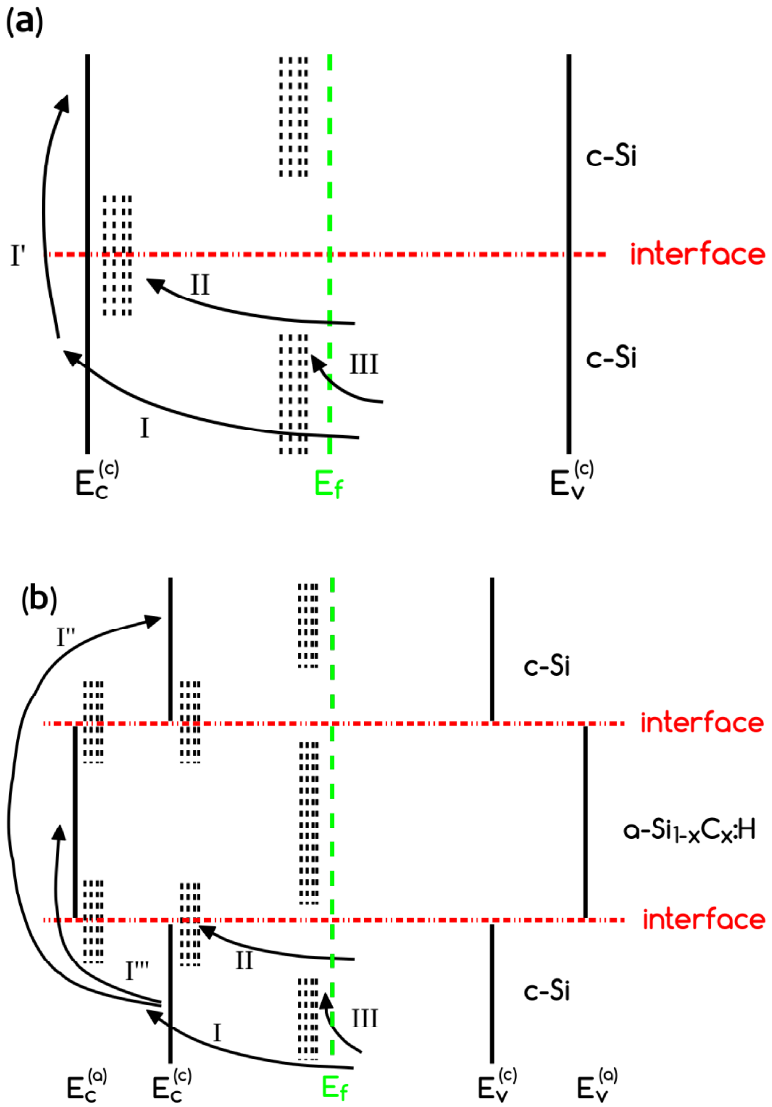

Figure 4.14.: Band diagram for a) interconnected silicon crystallites and b) silicon crystallites separated by a-$Si_{1-x}C_x$:H tissue (Demichelis et al., 1994.

interface mismatching. The arrows define the possible conduction paths, prevailing at different temperatures:

- *Transport in the high-temperature range* (**I**), 450-200 K. It can occur by thermionic emission between interconnected crystallites (**I'**), by hopping between crystalline "islands" (**I"**) and by thermionic emission between crystallites and amorphous tissue (**I"'**), depending on the sample crystalline fraction.
- *Transport in the intermediate-temperature range* (**II**) - 200-90 K. It can occur through hopping of carriers between localized tail states.
- *Transport in the low-temperature-range* (**III**) - 90-50 K. It can occur through hopping between localized states in the gap near the Fermi level.

A more detailed analysis on the density of defects depending on the deposition parameters and preliminary results concerning their simulations, will be presented in the following section.

Finally, the minority carrier diffusion length L_d was measured for samples from SET_{CH_43}, $SET_{w_{RF}2}$, SET_{SiF_43} and SET_{peaks}, by SSPG measurements. Results are presented in Figure 4.15. Moreover, these values are compared to what has been obtained for the device-quality a-Si:H reference sample.

Results presented in Figure 4.15 show that once f_c^{Raman} is above 40 %, the RF-power seems to have no influence on the minority carrier diffusion length, which takes values around 140 ± 5 nm. A decrease in f_c^{Raman} leads to a deterioration of L_d, due to the increase of the disorder related to the carbon incorporation. It is noteworthy that materials deposited by standard RF-PECVD conditions present values of L_d that are comparable to that of the device quality a-Si:H sample. Finally, as it was shown by all the characterization techniques used so far, the low IBE conditions results in materials characterized by modest material properties, with values of L_d that are nearly 35 % lower than those of alloys having similar crystalline volume fraction, but deposited by standard RF-PECVD. These values of L_d are equivalent to those obtained for alloys with a crystalline volume fraction of $\sim$ 25 %.

Due to the columnar growth of these materials, the obtained values of the minority carrier diffusion length, which were measured in coplanar configuration, can just be considered as a hint of the quality of the performance of this material in a photo-diode.

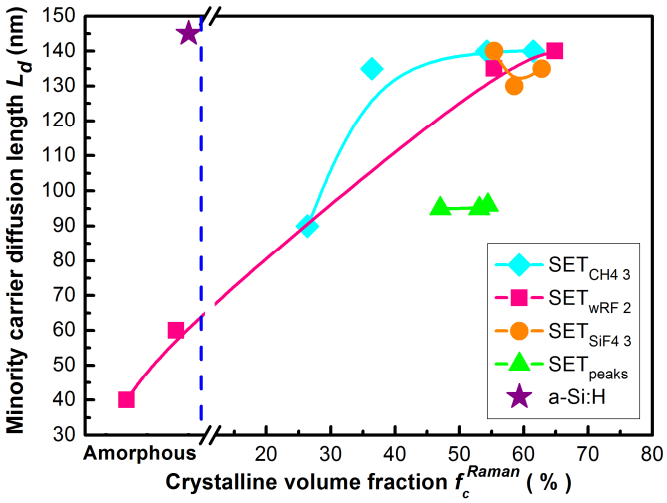

Figure 4.15.: Evolution of the minority carrier diffusion length L_d as a function of the crystalline volume fraction f_c^{Raman}, for samples from SET_{CH_43} (◆), $SET_{w_{RF}2}$ (■), SET_{SiF_43} (●) and SET_{peaks} (▲). Results are compared to a device quality amorphous silicon sample deposited by standard RF-PECVD (★).

4.4 DEFECT-RELATED PROPERTIES

A systematic characterization of the samples using the modulated photocurrent technique can lead to useful information concerning the effect of the selected deposition parameters on the density of states of the silicon-carbon alloys. This measurement consists of performing a temperature and frequency spectroscopy. For a selected temperature (in this work the measurements have been done in the 450-110 K temperature range) the AC component of the photo-current $|I_{AC}|$ and its phase shift φ, with respect to the monochromatic excitation light, are measured for frequencies ranging from 12 Hz to 40 kHz, that is the *high frequency* (HF) regime. In this way it is possible to reconstruct the DOS above the Fermi level.

This technique is sensitive to the Nc/μ ratio (called MPC-DOS), where N is the DOS, c the capture coefficient and μ the mobility in the extended states (see section 2.3.2). In chapter 2 it was shown that this ratio is completely composed of quantities that can be experimentally measured (Equation 2.35). However, the energy scale is determined by the choice of the capture coefficient c (Equation 2.34). For μc-$Si_{1-x}C_x$:H alloys no information on the capture coefficient can be found in the literature. Moreover, the variation not only of the crystalline fraction, but also of the chemical composition, could be responsible for c to vary for different samples. The choice of the correct value to be attributed to the capture coefficient is not straight forward. Usually, the most appropriate vales of c are those for which a good overlap of the curves measured at different temperatures is obtained.

In Figure 4.16 and 4.17 the MPC-DOS of a microcrystalline and an amorphous silicon-carbon sample are respectively shown. The effect of the variation of the capture coefficient on the energy scale, when reconstructing the MPC-DOS is presented. In the figures, each kind of symbol corresponds to a different temperature, and for a given temperature the 21 points correspond to the results obtained at different frequencies ranging from 12 Hz to 40 kHz.

In Figure 4.16(a) it can be seen that for a microcrystalline sample a capture coefficient $c = 4 \times 10^{-8}$ cm^3s^{-1}, typically used for a-Si:H, is too big and it is impossible to obtain a good overlap of the curves at the different temperatures. It is necessary to decrease the value of c to 1×10^{-10} cm^3s^{-1} (Figure 4.16(b)) in order to find a satisfying overlap. However, using this low capture coefficient for a completely amorphous sample (Figure 4.17(a)) leads to a reconstructed MPC-DOS which is not the proper one. Indeed, the curves corresponding to the different temperatures are all squeezed and contracted, and cross one another. A larger capture coefficient (Figure 4.17(b)) is needed in order to obtain an adequate overlap.

Finally, it is possible to judge the appropriateness of the chosen capture coefficient by remembering that with the MPC technique one obtains information on the DOS above the Fermi level. Therefore, choices of c that scale high temperature curves at values of $E_c - E$ greater than the activation energy have to be considered inappropriate.

In the following paragraphs all the reconstructed MPC-DOS have been plotted using the value of the capture coefficient leading to the best possible overlap. Only the envelops are shown. Moreover, due to the very low values of the activation energy of some samples, it has been impossible to successfully perform MPC measurements on samples having $E_a < 200$ meV.

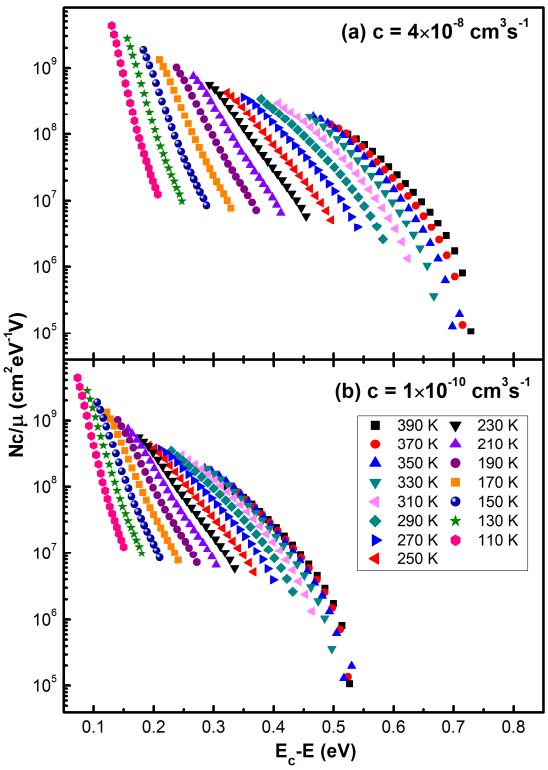

Figure 4.16.: The MPC-DOS (Nc/μ ratio) of a μc-$Si_{1-x}C_x$:H sample, reconstructed from the HF regime formulas using (a) $c = 4 \times 10^{-8}$ cm^3s^{-1} and (b) $c = 1 \times 10^{-10}$ cm^3s^{-1}.

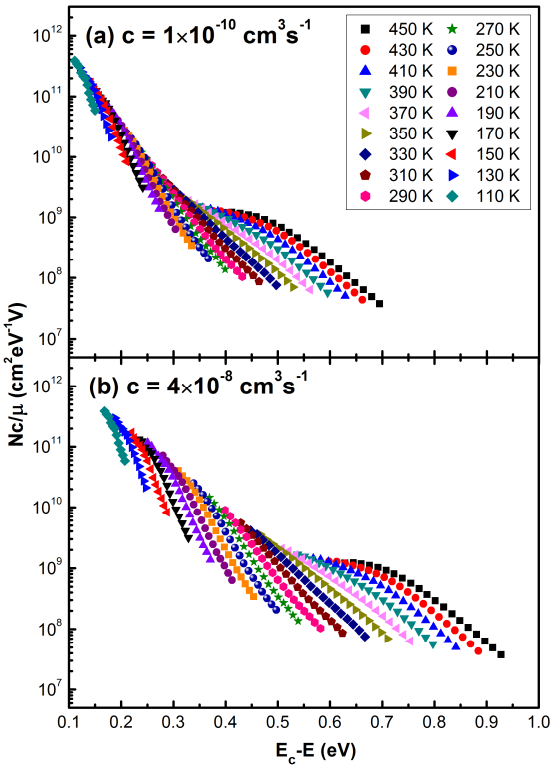

Figure 4.17.: The MPC-DOS (Nc/μ ratio) of a a-$Si_{1-x}C_x$:H sample, reconstructed from the HF regime formulas using (a) $c = 1 \times 10^{-10}$ cm^3s^{-1} and (b) $c = 4 \times 10^{-8}$ cm^3s^{-1}.

EFFECT OF CH_4 FLOW RATE AND RF-POWER The evolution of the MPC-DOS as a function of the CH_4 flow rate is presented in Figure 4.18, for samples from $SET_{CH_4 2}$ and $SET_{CH_4 3}$. The amorphization induced by the increase of the carbon-silicon ratio R_C leads to an increase in the disorder of the alloy.

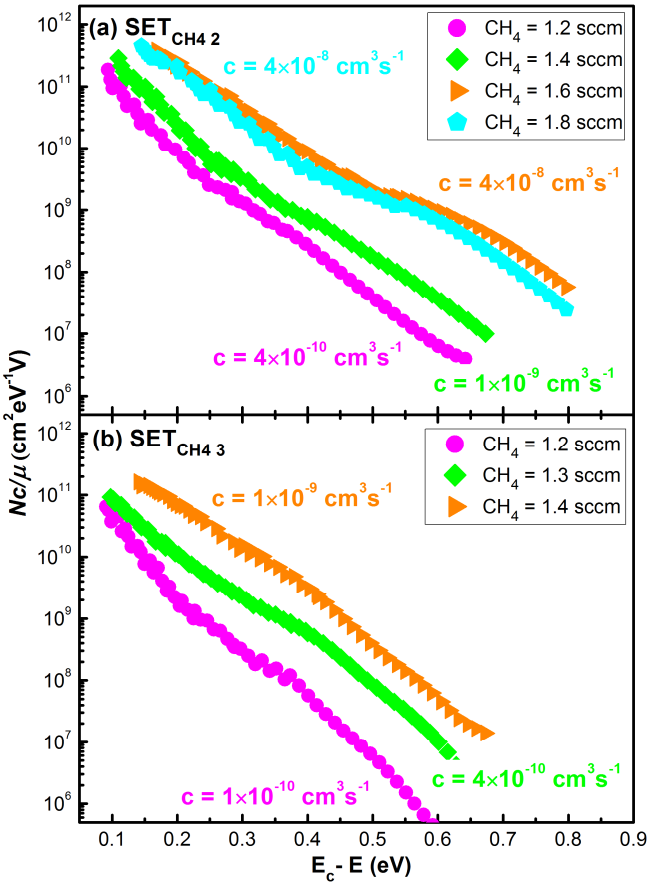

Figure 4.18.: MPC-DOS (Nc/μ ratio) of samples from (a) $SET_{CH_4 2}$ and (b) $SET_{CH_4 3}$ varying the CH_4 flow rate.

Indeed, all MPC-DOS are characterized by an exponential conduction band tail (CBT) and some deep defects linked to dangling bonds. However, the higher is the crystalline fraction of the μc-$Si_{1-x}C_x$:H samples, the lower is the MPC-DOS. Moreover, even for low crystalline fractions (for instance, the sample from $SET_{CH_4 2}$ deposited with CH_4 = 1.2 sccm) the obtained MPC-DOS is lower than that of the a-$Si_{1-x}C_x$:H samples. It is worth noting that with increasing CH_4 flow rate there is not only an increase of the deep defects, but also a broadening of the CBT. Moreover, the increasing amount of carbon incorporated is accompanied by an increase of the capture coefficient c, which acts on the energy scale (as explained in section 2.3.2, Equation 2.34). An increase in c of nearly two orders of magnitude ($SET_{CH_4 2}$) has an impact on the energy scale of nearly 4.5kT, which means 0.1 eV at room temperature.

The evolution of the MPC-DOS was also studied for samples deposited varying the RF-power density. Results are shown in Figure 4.19.

The increase of the RF-power density induces a phase transition which has an impact on the MPC-DOS, similar to the effect of the increasing CH_4 flow rate. Indeed, a broadening of the CBT and an increase in the deep

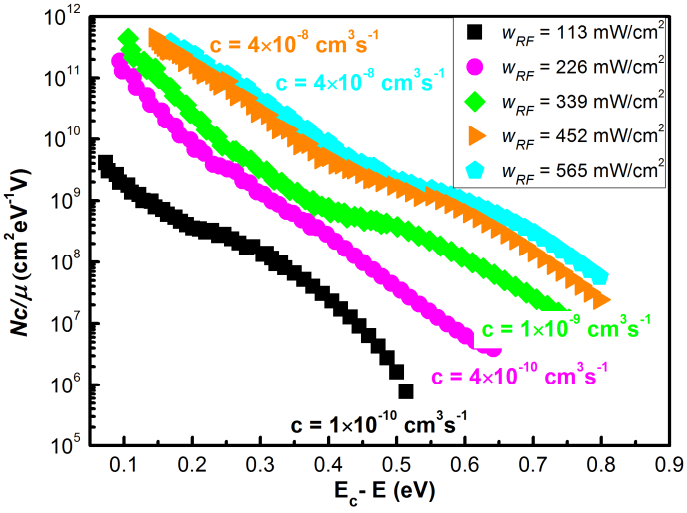

Figure 4.19.: MPC-DOS (Nc/μ ratio) of samples from SET$_{w_{RF}1}$ varying the RF-power density.

defects can be observed. Moreover, even for these samples the variation of the carbon content (microcrystalline-to-amorphous transition) is translated into an increase of the capture coefficient.

From SAADF-TEM analyses, it was highlighted that materials deposited at low RF-power have a better microstructure. One could wonder if such ordered columnar growth could be responsible for a lower degree of disorder. Indeed, the sample from SET$_{w_{RF}1}$ deposited using a RF-power density of 113 mW/cm^2 (■ in Figure 4.19) exhibits the lowest MPC-DOS. However, despite the relatively high crystalline volume fraction, both the CBT and deep defects can be observed.

Combining the low RF-power conditions with the variation of the CH_4 flow rate leads to identical results (Figure 4.20). The amorphization of the material induces an increase of the MPC-DOS, which are characterized by the broadening of the CBT, the increase of the deep defects and of the capture coefficient c.

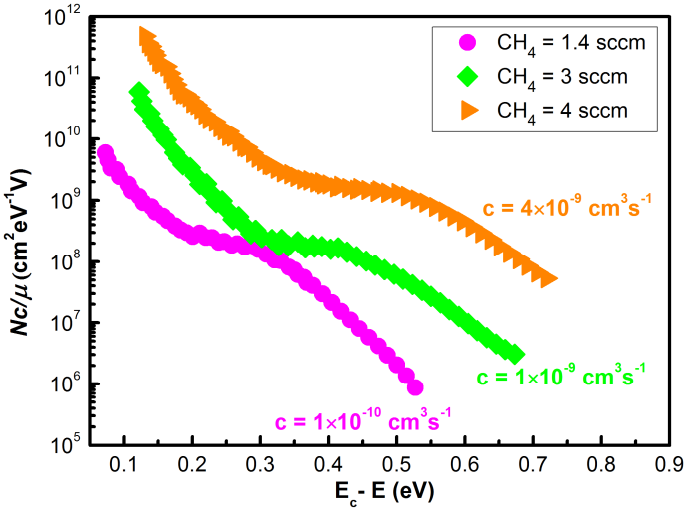

Figure 4.20.: MPC-DOS (Nc/μ ratio) of samples from SET$_{w_{RF}2}$, deposited at w_{RF} = 113 mW/cm^2 varying the CH_4 flow rate.

EFFECT OF SiF_4 FLOW RATE The effect of the SiF_4 flow rate on the MPC-DOS of the samples is presented in Figure 4.21 for samples from $SET_{SiF_4}2$. It has been impossible to perform this analysis on samples from $SET_{SiF_4}1$ due to their low values of the activation energy.

Despite the beneficial effect of the SiF_4 on the crystalline volume fraction, it is evident that the addition of this precursor has a slightly detrimental one on the MPC-DOS. Despite the starting sample being characterized by a low crystallinity (■ has $f_c^{Raman} \sim 25$ % in Figure 4.21), the increase in the crystalline component is not accompanied by a decrease of the deep defects. On the contrary, a larger CBT and a slight increase in the deep defects is observed. Moreover, to obtain a correct overlap, an increase in the capture coefficient has to be taken into account.

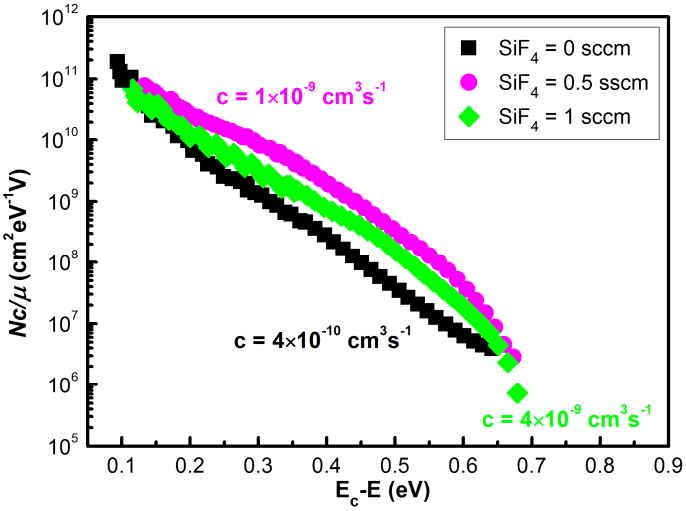

Figure 4.21.: MPC-DOS (Nc/μ ratio) of samples from $SET_{SiF_4}2$, deposited at 226 mW/cm^2 using a CH_4 flow rate of 1.2 sccm and varying the SiF_4 flow rate.

Is it possible that samples deposited using a combination of low RF-power conditions and addition of SiF_4 to the gas mixture to still be affected by an increase of the MPC-DOS? Indeed, if the low RF-power conditions are responsible for a more ordered growth (as observed with SAADF-STEM analyses), it could be possible for the MPC-DOS to be mildly affected by the addition of this precursor.

In Figure 4.22 results of the MPC measurements on samples from $SET_{SiF_4}3$ are presented. Even for these samples, an increase of the value of c has to be presumed to obtain a correct overlap of the curves at different temperatures. Moreover, even though the addition of SiF_4 to the gas mixture has a mild effect on the structural properties of these samples, it is translated into a broadening of the CBT and a drastic increase of the trap states.

EFFECT OF IBE Finally, the effect of the IBE on the MPC-DOS is presented in Figure 4.23. For these samples, the best overlap is obtained with $c = 4 \times 10^{-8}$ cm^{3}s^{-1}. It is noteworthy that all these materials are characterized by a very large MPC-DOS. These low IBE conditions, which have proved to give μc-Si:H and a-Si:H materials with good-enough properties for application in a photovoltaic device, when applied to the growth of μc-$Si_{1-x}C_x$:H result in materials affected by a disproportionately high MPC-DOS. This is in good agreement with what has been observed for transport properties: the high MPC-DOS is responsible for the low values of σ_{dark}, σ_{ph} and L_d.

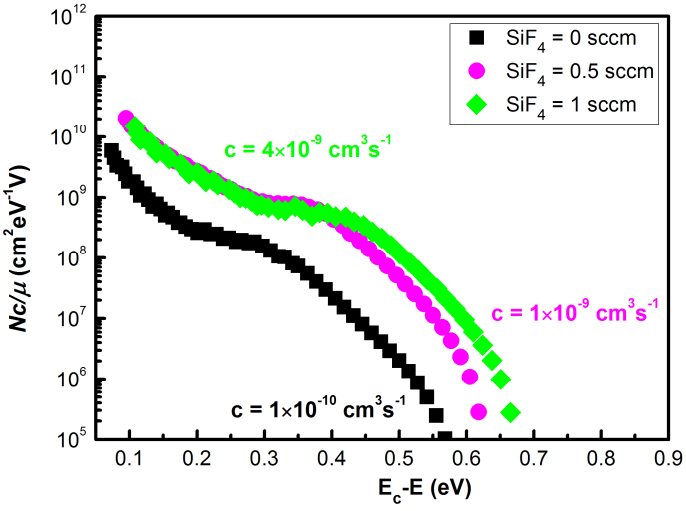

Figure 4.22.: MPC-DOS (Nc/μ ratio) of samples from $SET_{SiF_4 3}$, deposited at w_{RF} = 113 mW/cm^2 using a CH_4 flow rate of 1.4 sccm and varying the SiF_4 flow rate.

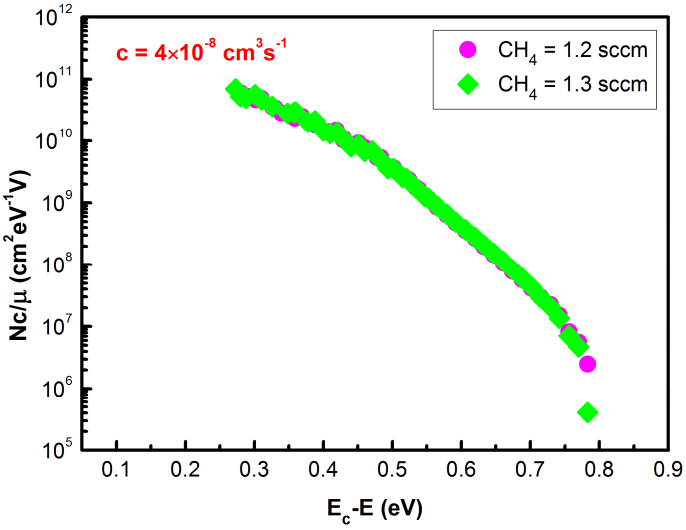

Figure 4.23.: MPC-DOS (Nc/μ ratio) of samples from SET_{peaks} varying the CH_4 flow rate.

4.4.1 Summary

In the previous paragraphs it was shown that no matter which parameter is varied, the microcrystalline-to-amorphous phase transition is translated into an increase of the DOS, reconstructed through the MPC measurements.

In Figure 4.24, the effect of the selected deposition parameters on the MPC-DOS of some chosen samples is presented. It was decided to compare only materials having a crystalline volume fraction of $\approx$ 60 %.

The MPC-DOS of these samples is compared to what was obtained for a device quality reference a-Si:H. For such sample the MPC-DOS is clearly characterized by an exponential conduction band tail (CBT) and some deep defects arising from the presence of Si dangling bonds. However, as it was previously pointed out, despite the relatively high crystalline volume fraction, both the CBT and deep defects can be observed also in the μc-

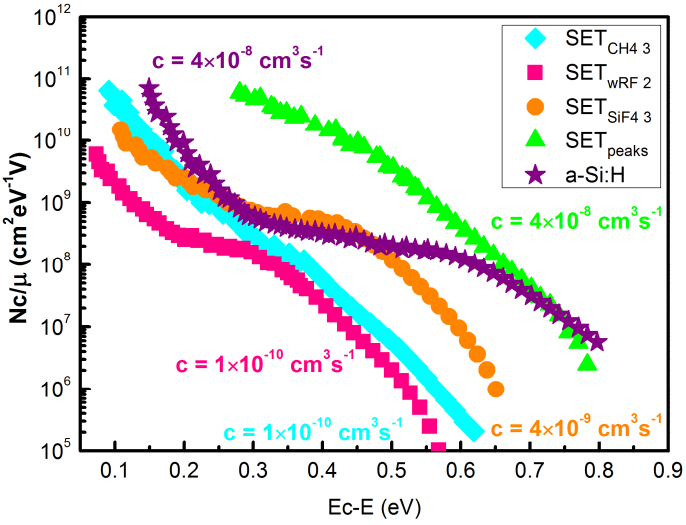

Figure 4.24.: MPC-DOS (Nc/μ ratio) of samples from $SET_{CH_4 3}$ (◆ - CH_4 = 1.2 sccm), $SET_{w_{RF} 2}$ (■ - CH_4 = 1.4 sccm), $SET_{SiF_4 3}$ (● - SiF_4 = 1 sccm) and SET_{peaks} (▲ - CH_4 = 1.2 sccm), having similar crystalline volume fraction ($f_c^{Raman} \approx 55 - 60$ %). These MPC-DOS are compared to what was obtained for the device quality reference a-Si:H (★).

$Si_{1-x}C_x$:H samples. Nevertheless, the MPC-DOS of these alloys is shown to be lower than that of the a-Si:H film. When comparing the effect of the different deposition parameters, it can be seen that the sample deposited using the TVW-PECVD technique (▲) is characterized by a very high MPC-DOS, consisting of an exponential tail decreasing from the conduction band edge E_c towards midgap, with the deep defect shoulder related to dangling bonds which does not clearly appear. Materials deposited by standard RF-PECVD confirm the structural results: using a high RF-power density (◆) leads to the characteristic energy of the CBT to be larger, compared to the one at 113 mW/cm^2 (■). Such differences in both the shape and the density of MPC-DOS between the two μc-$Si_{1-x}C_x$:H prove that growth mechanisms clearly differ from one deposition process to the other, leading to more promising electronic properties for samples deposited by RF-PECVD at 113 mW/cm^2.

4.5 LIGHT-SOAKING AND ANNEALING

Usually the term "microcrystalline" is often linked to the idea of a material being perfectly stable against light-soaking. One could easily think that finding conditions leading to the deposition of μc-$Si_{1-x}C_x$:H alloys having the highest crystalline volume fraction would make them technologically more interesting, as they should be less sensitive to the light-induced degradation. However, such statement may not hold if the material consists of a significant fraction of amorphous tissue (Ray et al., 2002).

In the last years it has been reported that when μc-Si:H is close to the microcrystalline-to-amorphous transition regime, the best solar cell performance is obtained (Vetterl et al., 2000; Okur et al., 2004). These cells are proved to be stable under light-soaking, despite the presence of a non negligible amorphous fraction. Since microcrystalline silicon is the major phase

in μc-$Si_{1-x}C_x$:H alloys, one could expect to observe the same tendency. On the other hand, it must be remembered that μc-Si:H is characterized by a heterogeneous nature which causes the presence of a high density of grain boundaries. When μc-Si:H is applied to solar cells, researchers have found that the grain boundary passivation can affect the open-circuit voltage (Werner et al., 2001). Therefore, if an electronically high grade material is wanted, their passivation is of extreme importance. Additionally, the presence of interconnected cracks getting oxidized during air-exposure becomes a crucial issues for the electronic properties of the films. Similarly, in μc-$Si_{1-x}C_x$:H alloys the a-$Si_{1-x}C_x$:H tissue at the grain boundaries may act as a passivation layer, but the presence of carbon can also introduce additional defects at the interface which can be detrimental for the stability under illumination. Therefore, it is important to study the behavior of μc-$Si_{1-x}C_x$:H alloys under light-soaking and to compare their degradation (if any) to standard a-Si:H.

The light-soaking effect on transport and defect-related properties was studied for four materials. A device quality a-Si:H sample deposited by standard RF-PECVD (introduced in section 4.3.3, Figure 4.12), one sample from $SET_{CH_4}2$, with a $f_c^{Raman} \sim 25$ % (CH_4 flow rate = 1.2 sccm) and two samples with $f_c^{Raman} > 50$ %: one from $SET_{w_{RF}}1$ (w_{RF} = 113 mW/cm^2) and one from $SET_{SiF_4}2$ (SiF_4 flow rate = 1 sccm). The possibility of restoring the electrical properties of these materials was studied by performing a high temperature annealing.

For all samples the same experimental procedure was followed. After measuring transport and defect-related properties in the *as deposited state* (**AD**), the *light-soaked state* (**LS**) of the samples was achieved as explained in section 2.3.2 and monitoring the light-soaking kinetics. Once this state was reached, transport and defect-related properties were estimated using DC, SSPC and MPC techniques, in the 390-110 K range. The temperature did not exceed 390 K, which is below the deposition temperature, in order to avoid any possible defect recovery, due to a high temperature annealing. Finally, the *annealed state* (**A**) was reached performing a thermal treatment under vacuum at 450 K for 12 hours. Transport and defect-related properties were also determined in the 450-110 K range.

4.5.1 Light-soaking kinetics

The effect of the Stabler-Wronski effect was quantified by monitoring the evolution of the photocurrent as a function of the elapsed time. In Figure 4.25 the evolution of the photocurrent (normalized to the value in the **AD** state) is presented.

It can be noted that while the degradation of the a-Si:H sample starts as soon as the light is turned on, for all μc-$Si_{1-x}C_x$:H samples the process is slow and is preceded by a plateau, independently of the crystalline volume fraction. Such a feature can be thought as a constant light-soaking and annealing step of the crystalline phase. However, the amorphous fraction in the studied alloys is not negligible ($\sim 40-50$ %) therefore, once a stable temperature is reached the degradation of the a-$Si_{1-x}C_x$:H tissue should take place. The peculiar behavior of μc-$Si_{1-x}C_x$:H alloys under light-soaking is still not understood and additional studies could help in identifying the origin of the initial stable phase. Finally, it is also noteworthy that materials with $f_c^{Raman} > 50$ % reach the saturation for values of I/I_0 that are higher than that of a-Si:H.

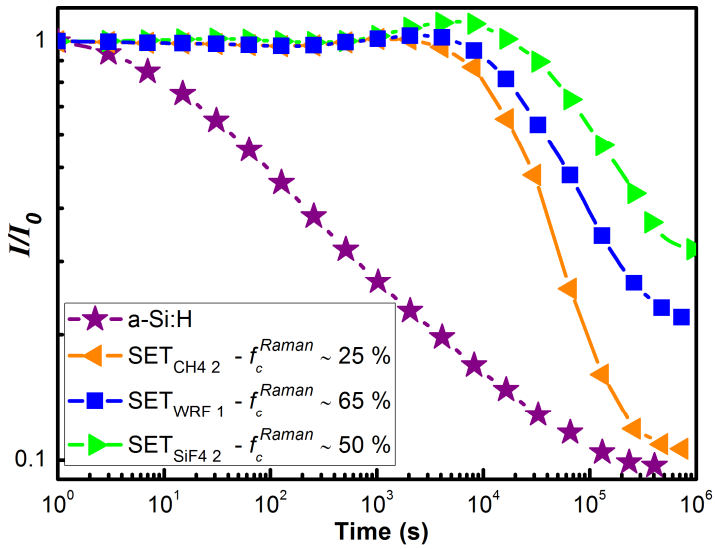

Figure 4.25.: Evolution of the photocurrent with time measured on samples from $SET_{CH_4\,2}$ (◀), $SET_{w_{RF}1}$ (■) and $SET_{SiF_4\,2}$ (▶) during light-soaking, normalized to the value measured in the **AD** state. Their light-soaking kinetics is compared to that of a device quality amorphous silicon sample deposited by standard RF-PECVD (★).

4.5.2 Evolution of transport properties

Transport properties in the **LS** and **A** state are presented in Table 4.14, and are compared to the **AD** state. First of all it can be seen that no matter which sample is considered, they all exhibit a deterioration of the transport properties. Moreover, the thermal treatment is demonstrated to be insufficient to restore the transport properties back to the **AD** state. However, it is interesting to observe the evolution of these parameters expressed as a percentage of the **AD** values.

Table 4.14.: Transport properties as calculated from DC and SSPC measurements for the samples from $SET_{CH_4\,2}$ (CH_4 = 1.2 sccm - ◀), $SET_{w_{RF}1}$ (w_{RF} = 113 mW/cm^2- ■), $SET_{SiF_4\,2}$ (SiF_4 = 1 sccm - ▶) and for device-grade a-Si:H (★). The evolution of the electrical properties is studied as a function of the state: as-deposited (**AD**), after light-soaking until saturation (**LS**) and after a 12 hour annealing (**A**).

Sample	f_c (%)	State	$\sigma_{dark} \times 10^{-9}$ (S/cm)	$\sigma_{ph} \times 10^{-9}$ (S/cm)	Φ	E_{aH} (meV)	σ_{00H} (S/cm)
		AD	0.04	100	2500	645	1.5
★	0	**LS**	0.01	5	500	650	0.6
		A	0.05	40	800	610	0.6
		AD	125	3490	28.0	340	0.35
◀	25	**LS**	0.6	8.4	14.0	430	0.4
		A	2	35	17.5	460	2.9
		AD	660	5200	8.0	420	15.6
■	65	**LS**	20	90	4.5	430	0.4
		A	60	315	5.5	455	2.9
		AD	160	910	6.0	430	3.5
▶	50	**LS**	5	20	4.0	460	0.3
		A	15	70	4.5	480	2.0

After the light-soaking step the device quality a-Si:H sample exhibits a photo-response Φ that is only the 20 % of the value measured in the **AD** state. With the annealing at 450 K for 12 hours the deterioration is only partially compensated and in fact the photo-response goes up to the 30 % of the initial value.

A similar behavior can be observed for the other samples. After the light-soaking step, the μc-$Si_{1-x}C_x$:H alloy with the lowest crystalline fraction (▶) is characterized by a Φ that is 50 % of the original value and after the thermal treatment it is restored to the 63 %. But what happens to materials having at least the double of the crystalline fraction?

Even though after the light-soaking both photo and dark conductivity values of the sample from $SET_{SiF_4}2$ (▶) are much lower than those of the sample from $SET_{w_{RF}1}$ (■), it can be seen that the photo-response of the latter seems to be less affected by the light induced degradation. After saturation, the photo-response Φ for the sample from $SET_{w_{RF}1}$ is the 49 % of the **AD** state, whereas for the sample from $SET_{SiF_4}2$ it is the 60 %. Moreover, after the annealing step the transport properties of both samples are only partially recovered and Φ for the sample from $SET_{w_{RF}1}$ increases to 65 % of the value in the **AD** state, while for the sample from $SET_{SiF_4}2$ it goes up to 77 %.

Finally, from the analysis of activation energy of the dark conductivity in the **LS** and **A** state, an increase of the activation energy, compared to the **AD** state, can be observed. This behavior is not yet completely understood. The possibility of the variation of the Meyer-Neldel (MNR) parameters after light-induced degradation, was considered as a possible reason for the increased values of E_a, and will be presented in section 4.6.

Despite being sensitive to the light-induced degradation, the presence of the crystalline component has an impact on the behavior of these alloys when exposed to intense light and their performance is anyway better compared to standard a-Si:H. These results are encouraging concerning the possible application of μc-$Si_{1-x}C_x$:H to photovoltaic devices.

4.5.3 Evolution of defect-related properties

Finally, the effect of the light-soaking and of the high temperature annealing on the MPC-DOS of the chosen samples are presented in Figure 4.26.

In the **AD** state (Figure 4.26(a)), the μc-$Si_{1-x}C_x$:H alloys are characterized by a DOS that is similar in shape to that of the a-Si:H, characterized by an exponential conduction band tail (CBT) and some deep defects. It is noteworthy that despite the different crystalline fraction, the sample from $SET_{CH_4}2$ (◀) and that from $SET_{SiF_4}2$ (▶) are very similar, showing no clear distinction between CBT and deep defects, due to a high density of the latter. On the other hand, the sample from $SET_{w_{RF}1}$ (■) is showing the lowest Nc/μ ratio, with a clear distinction between the CBT and the deep defects.

The **LS** step (Figure 4.26(b)) is more critical, revealing an interesting behavior of this diphasic material. In fact, no matter which is the crystalline volume fraction, these alloys are always sensitive to the light-induced degradation, showing an increase in both CBT and deep defects. Actually, an increase of the MPC-DOS can be related to an increase of the DOS or to an increase of the capture coefficient or both. For a-Si:H, it is believed that the increase of the deep states density might cause some modifications of the

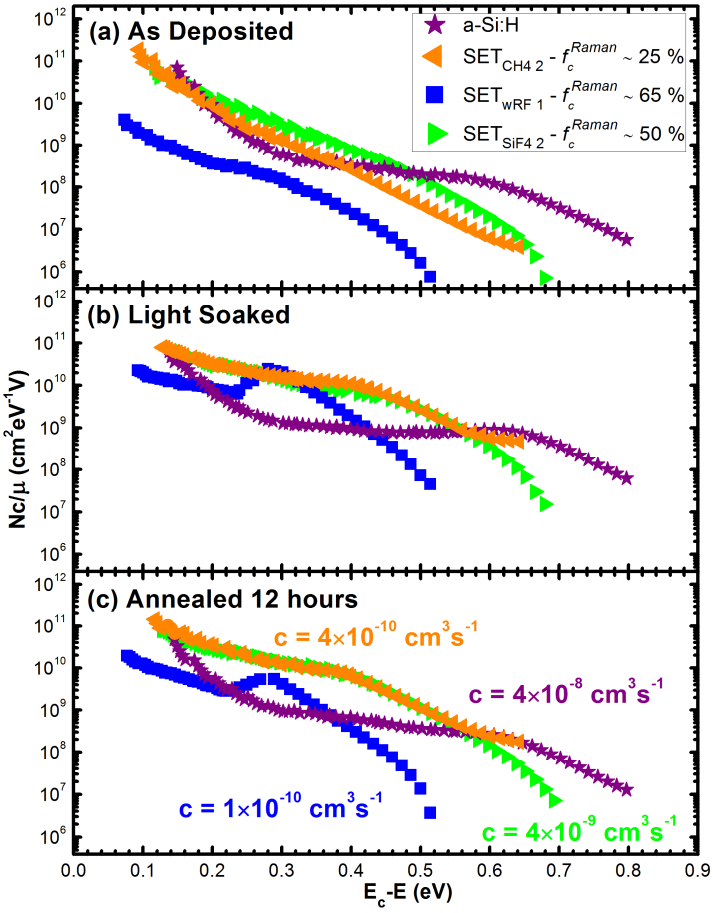

Figure 4.26.: MPC-DOS (Nc/μ ratio) of samples from $SET_{CH_4 2}$ (◀), $SET_{w_{RF}1}$ (■) and $SET_{SiF_4 2}$ (▶) in the (a) as deposited (**AD**), (b) light soaked (**LS**) and (c) annealed (**A**) state. Their MPC-DOS is compared to that of a device quality a-Si:H sample deposited by standard RF-PECVD (★). The capture coefficient c (marked in Figure (c)) is kept constant, independently of the state of the sample.

structure that eventually results in an increase of the CBT states (Longeaud, Roy, et al., 2002). In this work, the MPC-DOS are plotted using always the same value of c, independent of the state of the sample. The complexity of μc-$Si_{1-x}C_x$:H alloys lies also in presence of carbon altering the chemical order in the amorphous matrix, which could be an additional source of defects detrimental for the stability of the material. The sample from $SET_{CH_4 2}$ (◀) and that from $SET_{SiF_4 2}$ (▶) show a similar evolution, with an increase of the deep defects of nearly one order of magnitude, crossing the MPC-DOS of the a-Si:H sample (★). However, the most striking feature that can be observed appears in the DOS of the sample from $SET_{w_{RF}1}$ (■), where after the light soaking the sudden arise of a defect at 0.3 eV below the conduction band edge is seen. In the samples from $SET_{CH_4 2}$ (◀) and $SET_{SiF_4 2}$ (▶) its presence seems to be hidden by a larger CBT. Moreover, as the energy scale is controlled by the capture coefficient c, the position of the defect may be shifted to higher values of $E_c - E$, for higher values of c. However, the origin of such a defect could be carbon related but a more detailed study, focused on the evolution of the DOS for several a-$Si_{1-x}C_x$:H with increasing carbon content, is needed, and further completed by numerical simulations.

Finally, as far as annealing is concerned (Figure 4.26(c)), it is evident that this step is not sufficient to recover the MPC-DOS. For all μc-$Si_{1-x}C_x$:H samples there seem to be an irreversibility of the CBT. But while for samples from SET_{CH_42} (◀) and SET_{SiF_42} (▶) there is not much difference between the **LS** and **A** state, for the sample from $SET_{w_{RF}1}$ (■) a weak decrease of the defect at 0.3 eV below the conduction band edge can be observed, but always being clearly visible. The effectiveness of the annealing step might, therefore, depend on the microstructure of the material. However, for μc-$Si_{1-x}C_x$:H alloys the mechanisms might be complicated by the mixed-phase nature (structural and also chemical) of the materials.

4.6 THE MEYER–NELDEL RULE

After its discovery, the existence of a relationship between the conductivity prefactor and activation energy, the so-called Meyer-Neldel rule (MNR), has been observed in many materials, such as a-Si:H (Irsigler et al., 1983; Kirbs et al., 1990), μc-Si:H (Ram et al., 2008), but also chalcogenide glasses (Arora et al., 1991; Shimakawa et al., 1997) and fullerenes (Wang et al., 1998). Such ubiquity seems to be an interesting challenge for researchers in both experimental and theoretical physics (Yelon, Movaghar, and Crandall, 2006; Abtew et al., 2008). Such relation can be written as:

$$\sigma_{00} = \sigma_{MNR} \cdot \exp\left\{\frac{E_a}{E_{MNR}}\right\}, \tag{4.6}$$

where E_a is the activation energy of the dark conductivity, σ_{00} is its prefactor and σ_{MNR} and E_{MNR} are the Meyer-Neldel conductivity prefactor and the Meyer-Neldel energy, respectively.

Various theories have been developed to explain such relationship in a-Si:H, the most popular of which is based on a statistical shift of the Fermi level with temperature (Overhof and Beyer, 1983; Yelon, Movaghar, and Branz, 1992). However, the linear relation of the conductivity prefactor and the activation energy has been observed also in hydrogenated microcrystalline silicon, with MNR parameters similar to those obtained in a-Si:H. Despite the heterogeneous structural nature of μc-Si:H, with microcrystalline columns formed by the agglomeration of crystallites dispersed in an amorphous phase, the MNR dependence was explained in terms of the statistical shift model analogous to a-Si:H (Lucovsky et al., 1992). This led to the general belief that while the optical properties of μc-Si:H are governed by the crystalline component, the electrical transport is still controlled by the amorphous silicon phase.

In this work, the experiment was carried out as follows. Samples in their as deposited (**AD**) were annealed at 450 K for 1 hour and then cooled to 430 K with a 2 K step. Each 2 K, the DC conductivity was measured. Next, the samples were kept at 430 K for 1 hour, and conductivity measurements were then performed between 430 and 410 K, always with a 2 K step. The temperatures for the 1 h anneal were chosen to be 450 K, 430 K, 410 K, . . . , 290 K.

This analysis was performed only on two samples, in their **AD**, **LS** and **A** state, in order to test if the increase in the activation energy after the light-induced degradation and the recovering annealing was induced by a variation of the MNR parameters. The chosen samples were one from

SET_{CH_42}, deposited with CH_4 = 1.2 sccm and one from SET_{SiF_42}, deposited with SiF_4 = 1 sccm.

After having measured transport and defect related properties (DC, SSPC and MPC measurements) for the light-soaked state, samples were annealed at 390 K for 1 hour and then cooled to 370 K with a 2 K step. Each 2 K, the DC conductivity was measured. Next, the samples were kept at 370 K for 1 hour, and conductivity measurements were then performed between 370 and 350 K, always with a 2 K step. The temperatures for the 1 h anneal for the sample in the **LS** state, were chosen to be 390 K, 370 K, 350 K, . . . , 290 K. Then, samples were annealed at 450 K for 12 hours, to reach the **A** state. Once this annealing was performed, transport and defect-related properties were measured for this state and the Meyer-Neldel rule was verified between 450 K and 290 K, as it had been done for the **AD** state.

In Figure 4.27 the relation between the dark conductivity prefactor and the activation energy in the high temperature range is given for samples in all their states.

Not only they obey the Meyer-Neldel rule in their **AD** state, but such linear dependence in a semi-log scale is also conserved after the exposure to light-induced degradation and the subsequent recovering annealing. The values obtained from the linear fits are given in Table 4.15 and are in good agreement with what can be found in literature.

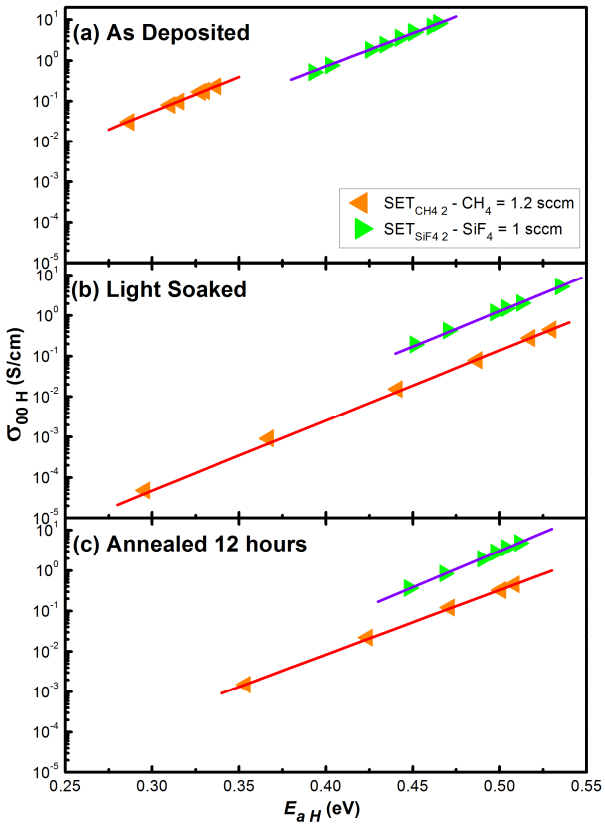

Figure 4.27.: Evolution of the dark conductivity prefactor σ_{00H} as a function of the activation energy E_{aH}, for the sample from SET_{CH_42} (◀ - CH_4 = 1.2 sccm), and for the sample from SET_{SiF_42} (▶ - SiF_4 = 1 sccm), in their (a) **AD**, (b) **LS** and (c) **A** state. The continuous lines represent the linear fits, proving that MNR applies. Values obtained from the fitting procedure are reported in Table 4.15.

Table 4.15.: Meyer-Neldel conductivity prefactor (σ_{MNR}) and Meyer-Neldel energy (E_{MNR}) obtained from the linear fits of data presented in Figure 4.27.

Sample	State	σ_{MNR} (S/cm)	E_{MNR} (meV)
$SET_{CH_4 2}$ -	**AD**	$(3.5 \pm 1.1) \times 10^{-7}$	25.0 ± 0.7
	LS	$(3.0 \pm 0.8) \times 10^{-10}$	25.1 ± 0.3
CH_4 = 1.2 sccm	**A**	$(3.4 \pm 0.4) \times 10^{-9}$	27.2 ± 1.5
$SET_{SiF_4 2}$ -	**AD**	$(2.2 \pm 0.8) \times 10^{-7}$	26.5 ± 0.5
	LS	$(2.3 \pm 0.7) \times 10^{-9}$	24.8 ± 0.3
SiF_4 = 1 sccm	**A**	$(3.2 \pm 1.7) \times 10^{-9}$	24.2 ± 0.6

When comparing the Meyer-Neldel conductivity prefactor and Meyer-Neldel energy for the samples in the different states, it can be seen that while σ_{MNR} decreases by at least 2 orders of magnitude, values of E_{MNR} remain stable. Moreover, once the sample is light-soaked till saturation, the thermal annealing at 450 K for 12 hours is not sufficient to restore the initial values of σ_{MNR}.

The influence of the duration of thermal treatment has also been studied for the sample from $SET_{SiF_4 2}$, deposited with SiF_4 = 1 sccm in its **AD** state. The MNR experiment was repeated performing a 2 hour annealing at the same temperatures and cooling down measuring the dark conductivity with a 2 K step. Results are shown in Figure 4.28, where it can be seen that the Meyer-Neldel parameters don't depend on the annealing time.

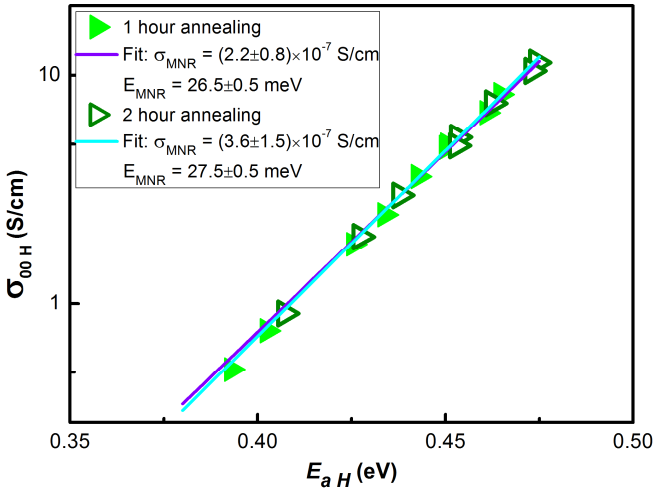

Figure 4.28.: Evolution of σ_{00H} as a function of E_{aH}, for the sample from $SET_{SiF_4 2}$, with a 1 hour (▶), and a 2 hour annealing (▷) each 20 K. The continuous lines represent the linear fit.

Finally, the effect of the repeated temperature annealing, necessary to verify the existence of the MNR, on room temperature σ_{dark}, σ_{ph} and E_a has been investigated. Results are reported in Table 4.16, showing that samples are stable enough for the thermal treatments to have no significant effect on the transport properties.

Table 4.16.: Effect of the different temperature annealing on room temperature σ_{dark}, σ_{ph} and E_a and its prefactor (for both high and intermediate temperature range).

Sample	State	$\sigma_{dark} \times 10^{-7}$ (S/cm)	$\sigma_{ph} \times 10^{-7}$ (S/cm)	E_{aH} (meV)	σ_{00H} (S/cm)
$SET_{CH_4 2}$ -	**AD**	1.25	34.9	340	0.35
CH_4 = 1.2 sccm	1 h MNR	1.34	35.2	330	0.30
$SET_{SiF_4 2}$ -	**AD**	1.62	9.1	430	3.45
	1 h MNR	1.74	10.7	410	1.45
SiF_4 = 1 sccm	2 h MNR	1.75	10.9	410	1.49

Part III.

Device study

5 DEVICE PROPERTIES

5.1 INTRODUCTION

In the previous chapters the detailed investigation of μc-$Si_{1-x}C_x$:H alloys showed that this new material system has structural and electrical properties that can be tuned varying accordingly the deposition parameters. Depending on the chosen deposition conditions, these materials can be extremely tempting for photovoltaic application (Matsumoto et al., 1990). For instance, the possibility of varying the effective band gap by changing the amount of carbon incorporated in the alloy, can lead to new interesting opportunities for the thin film technology. The idea of this doctoral work was not only to study this interesting diphasic material system, but also to test its application as the active layer in the top cell of a tandem solar cell, leading to the fabrication of the **CANASTA device** (Figure 5.1).

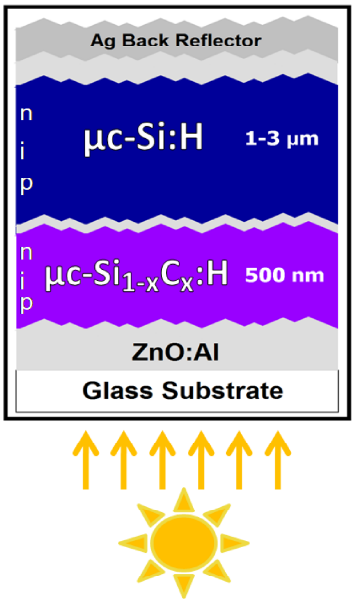

Figure 5.1.: Schematic representation of the CANASTA solar cell.

However, the production of tandem devices requires the knowledge of the strong points and the limitations of μc-$Si_{1-x}C_x$:H alloys, when applied to simple pin (nip) devices. Therefore, the first step is necessarily the fabrication of simple photo-diodes, to assess the quality of the performance of these alloys. In this way, it is possible to identify weaknesses and strengths of this new material system.

Above all, the most interesting thing to test, is the impact of the variation of the carbon-silicon ratio on the photovoltaic parameters. As μc-Si:H is the main component (for alloys with high crystalline fraction), it was verified if the effective electronic band-gap was simply that of the μc-Si:H phase, or if the addition of carbon in the alloys (even in low quantities) had any impact on the open-circuit voltage of the photo-diodes.

5.1.1 The structure

In this work, hydrogenated microcrystalline silicon carbon alloys are applied as the i-layer in p-i-n (n-i-p) structures in order to benefit from a drift-assisted collection and not only on the diffusion. Furthermore, devices are the only efficient way to test "out-of-plane" transport properties of this new material system. The order of the letters that define the device structure, refers to the order of deposition of the different layers:

N-I-P Usually called the *"substrate-type"* configuration, this kind of structure is built so that the cell stack is grown on the substrate on which the back contact has been sputtered. In Figure 5.2 a schematic representation of the structure used in this work is presented.

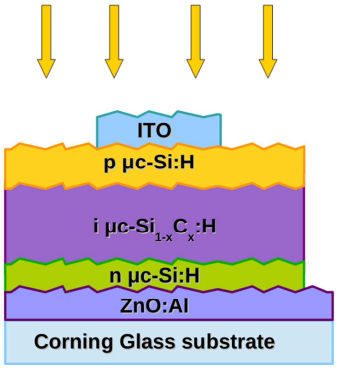

Figure 5.2.: Schematic representation of the n-i-p solar cell.

Once the stack is fully deposited, the p layer is covered by sputtered Indium Tin Oxide (ITO), in order for the stack to be illuminated through the p-side. The main disadvantage of this configuration lies in the fact that the highly conductive microcrystalline p-doped layer should be etched (by the Reactive Ion Etching technique) after the sputtering of the contacts, otherwise the cells can suffer from very low parallel resistances. Moreover, for technical reasons, no silver back reflector was used when fabricating this kind of devices. Attempts at using a chromium back-reflector were unsuccessful as all the devices were shunted.

P-I-N Usually referred as the *"superstrate-type"* solar cell, in this case the cell stack is deposited on the substrate, covered by a transparent conductive oxide (TCO), which will act as front contact. As shown in Figure 5.3, the device is then completed with the deposition of the back contact (usually ITO) and a back reflector (usually silver). Actually, for this kind of structure the impact of different back contacts was tested, using also simple ITO with no back reflector.

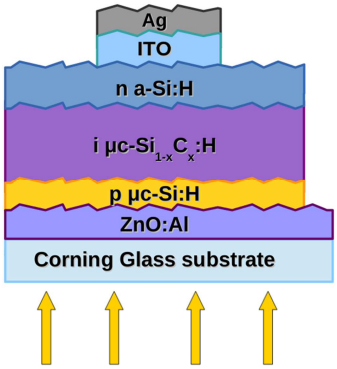

Figure 5.3.: Schematic representation of the p-i-n solar cell.

The temperature at which the deposition is done has a significant impact on the choice of the device structure. The use of a high temperature (285° C) for the deposition of μc-$Si_{1-x}C_x$:H alloys, introduces many limitations on the structure and the doped layers to be used, when photo-diodes are fabricated. Indeed, according to Nasuno et al., the p-layer is temperature sensitive (Nasuno et al., 2002). In their publication they investigated the origin of the difference in the optimum processing temperature of micro-crystalline silicon solar cells depending on the device structure, focusing on the comparison of a "superstrate-type" cell, and a "substrate-type" one. They found that the optimum temperature for the p-i-n cell is lower than that for the n-i-p one. Moreover, they showed that a significant degradation of the cell performance occurs during the deposition of the i-layer at higher temperatures. They attributed such degradation to the formation of defects at the p/i interface, due to the enhanced diffusion of the boron dopant from the underlying layer to the intrinsic one.

For this reason, first attempts at applying μc-$Si_{1-x}C_x$:H as active layers in photo-diodes, which were done at 285° C, required the use of a n-i-p structure, such as the one presented in Figure 5.2. In this way the p-layer is kept at high temperature for the least amount of time. On the other hand, for such a high temperature no optimized doped-layers have been developed in the LPICM laboratory. Transferring the deposition conditions to a lower temperature (175° C) led to the possibility of depositing p-i-n structures such as the one presented in Figure 5.3, that can fully benefit from the LPICM know-how.

5.1.2 The Transparent Conductive Oxide: Front and Back contacts

The transparent conductive oxide (TCO) is an important part of a photo-diode. In general, this layer has to be highly transparent (absorption below $6-7$ % over the range $400-1100$ nm), with a low resistivity (lower than $\sim 10\Omega$Sq). In addition, its surface texture has to be optimized to enhance the light scattering (typical $\rho_{RMS} \sim 50-150$ nm).

In this work, the TCO that was used as a back (front) contact in the n-i-p (p-i-n) structures was aluminum-doped zinc oxide (ZnO:Al). Indeed, it is not suitable to use the Indium Tin Oxide (ITO) for this kind of application as the exposure to the silane plasma, can cause the tin oxide (SnO_2) to be reduced by the hydrogen-rich plasma, especially at temperatures higher than 200° C (Hamma et al., 2001). As the sputtered ZnO:Al is flat, texturing is necessary and is obtained by chemical wet etching in a 0.5 %-diluted hydrochloric acid (HCl) bath for 30 seconds, resulting in a ρ_{RMS} in the $100-150$ nm range.

For n-i-p devices, the front contact is made by sputtering ITO, whereas for p-i-n devices, the back contact is made by sputtering ITO with (or without) a silver back reflector. Also aluminum could be used, but silver is a better reflector in the red, increasing the spectral response above 650 nm.

5.1.3 The doped layers

As presented in section 2.2.3, the ARCAM reactor is a multiplasma-monochamber system consisting of three separated plasma chambers located inside the same isothermal vacuum vessel. This structure allows the deposition of the entire device stack without breaking the vacuum.

The doped layers used in this work for the deposition of photo-diodes benefit from the specific know-how of the LPICM laboratory.

P-DOPED LAYERS The deposition of the p-doped layers is achieved by adding a small flow rate of tri-methyl-boron (TMB) to the usual SiH_4/H_2 mixture. Compared to the use of diborane as a doping gas, the dissociation of TMB leads to the incorporation of carbon atoms which induce the enlargement of the band gap of the p-doped layer (Kroely, 2010). Therefore, doping with TMB has the advantage of reducing the absorption inside this layer.

In this work, doped μc-Si:H was used as a p-layer (p:μc-Si:H) in both n-i-p and p-i-n devices. The activation energy of these layers can be below 50 meV and the conductivity, as high as $\sim 10^{-1}$ Scm^{-1} (Hamma et al., 2001). The thickness of the p μc-Si:H layer is fixed at around 15 nm.

Actually, for p-i-n devices deposited at 175° C, the application of different doped layers was investigated. Other sets of devices were made using p-doped a-Si:H (p:a-Si:H) or μc-SiO_x:H (p:μc-SiO_x:H). The latter is a mixed-phase material very similar to μc-$Si_{1-x}C_x$:H, although in this case, the microcrystalline silicon growth is embedded in an a-SiO_x:H matrix. According to Cuony et al., when used as a p-doped layer in μc-Si:H thin-film solar cells, it exhibits three main advantages, compared to p-doped hydrogenated microcrystalline silicon: lower absorption, lower refractive index, and tunable resistance (Cuony et al., 2010). Due to the presence of powders in the deposition chamber, all devices fabricated using p:a-Si:H were shunted and could not be studied.

N-DOPED LAYERS To obtain the n-doped layer, phosphine (PH_3) is added to the SiH_4/H_2 gas mixture, in order to incorporate phosphorous atoms in the matrix. In this work, for n-i-p devices, n-type μc-Si:H (n:μc-Si:H) was used (thickness fixed at around 15 nm), whereas for p-i-n devices n-type a-Si:H was used (n:a-Si:H), which should help to encapsulate the intrinsic microcrystalline layer and to avoid its post-oxidation.

5.1.4 The devices

In order to test the "out-of-plane" transport properties of μc-$Si_{1-x}C_x$:H alloys, several sets of devices were made. Due to lack of reactor time and to the slow deposition rate ($\sim$ 0.85 Å/s for w_{RF} = 226 mW/cm^2 and $\sim$ 0.5 Å/s for w_{RF} = 113 mW/cm^2), the number of sets of devices had to be considerably reduced compared to the material studies. However, different combinations have been tested to determine the performance of μc-Si:H alloys in generic devices (without any specific optimization). Furthermore, it is important to remember that when the materials are inserted into devices, additional problems may arise due to the choice of the doped layers, or the quality of the TCOs or the lack of general optimization.

In Table 5.1 the sets of devices studied in this work are presented. The different series are named after the set of materials used as the i-layer (see Table 3.1).

Table 5.1.: Summary of all the sets of diodes that will be discussed in this work. For each set the CH_4 flow rate is varied according to the deposition conditions presented in the material study. The name of different sets of devices is marked in blue and is consistent with the series of i-layer used, as marked in Table 3.1.

Structure	T (°)	Technique	SERIES	w_{RF} (mW/cm^2)	n-layer	p-layer	Back contact	Front contact	WORKING?
n-i-p	285	RF-PECVD	$\mathbf{SET_{CH_43}}$	226	n:μc-Si:H	p:μc-Si:H	ZnO:Al	ITO	✓
			$\mathbf{SET_{w_{RF}2}}$	113					✓
		TVW-PECVD	$\mathbf{SET_{peaks}}$	113					✓
p-i-n	175	RF-PECVD	$\mathbf{SET_{T1}}$	113	n:a-Si:H	p:μc-Si:H	ITO+Ag	ZnO:Al	✓
							ITO		✓
			$\mathbf{SET_{T2}}$	226		p:μc-Si:H	ITO+Ag		✓
							ITO		✓
						p:μc-SiO$_x$:H	ITO+Ag		✗
							ITO		✓
						p:a-Si:H	ITO+Ag		✗
							ITO		✗

5.2 DARK J(V) CHARACTERISTICS

Through dark J(V) characteristics the physical properties of the photo-diodes can be obtained. Thanks to these measurements information concerning the ideality factor and the dark saturation current (J_0) of the diodes can be determined, indicating the quality of the performance of the μc-$Si_{1-x}C_x$:H alloys, when applied into photovoltaic devices. Indeed, J_0 is a very important parameter, as it is a measure of the recombination in a device. A diode with a larger recombination will have a larger J_0 and inversely, low values of J_0 will lead to high values of the open-circuit voltage (V_{oc}). From the determination of J_0 it is possible to predict the expected open-circuit voltage using a simple formula:

$$V_{oc} = nkT \cdot \ln\left(\frac{J_{sc}}{J_0}\right) \tag{5.1}$$

where n is the ideality factor, k the Boltzmann constant, T the temperature and J_{sc} is the short-circuit photocurrent.

5.2.1 n-i-p devices at 285° C

As presented in Table 5.1, at 285° C three series of diodes were fabricated. For these sets, the i-layers were made using the same deposition conditions as for samples presented in the material study, namely: SET_{CH_43} (standard RF-PECVD at 226 mW/cm^2), $SET_{w_{RF}2}$ (standard RF-PECVD at 226 mW/cm^2) and SET_{peaks} (TVW-PECVD using "peaks" voltage waveforms). Therefore, the obtained i-layers are nearly 200-250 nm thick and have a crystalline volume fraction f_c^{Raman} that can be expected to be close to that presented in the material study.

In Figure 5.4, the semi-log plots of the dark J(V) curve at room temperature are shown, as obtained for the three sets of n-i-p photo-diodes. All devices show a rectifying behavior. Moreover, those made using the TVW-PECVD technique to deposit the i-layer show all the same dark J(V) characteristic. This is consistent with results presented in the material study: at the low IBE conditions the chosen CH_4 flow rates do not cause any significant evolution in the μc-$Si_{1-x}C_x$:H structural and electrical properties, and this is clearly translated into the devices. On the other hand, when standard RF-PECVD is used to deposit the i-layer, the variation of the CH_4 flow rate has a direct impact on the evolution of the diode characteristics.

In Figure 5.5 the values of J_0, obtained from the curves in Figure 5.4, are presented as a function of the f_c^{Raman} the i-layer. As expected, devices deposited by TVW-peaks have the same J_0, whereas when standard RF-PECVD is used, J_0 decreases with decreasing crystalline volume fraction, caused by the carbon-induced amorphization. It is noteworthy that for $f_c^{Raman} \sim 55$ % J_0 changes by almost an order of magnitude depending on the deposition technique, with the diode from $SET_{w_{RF}2}$ having the lowest value.

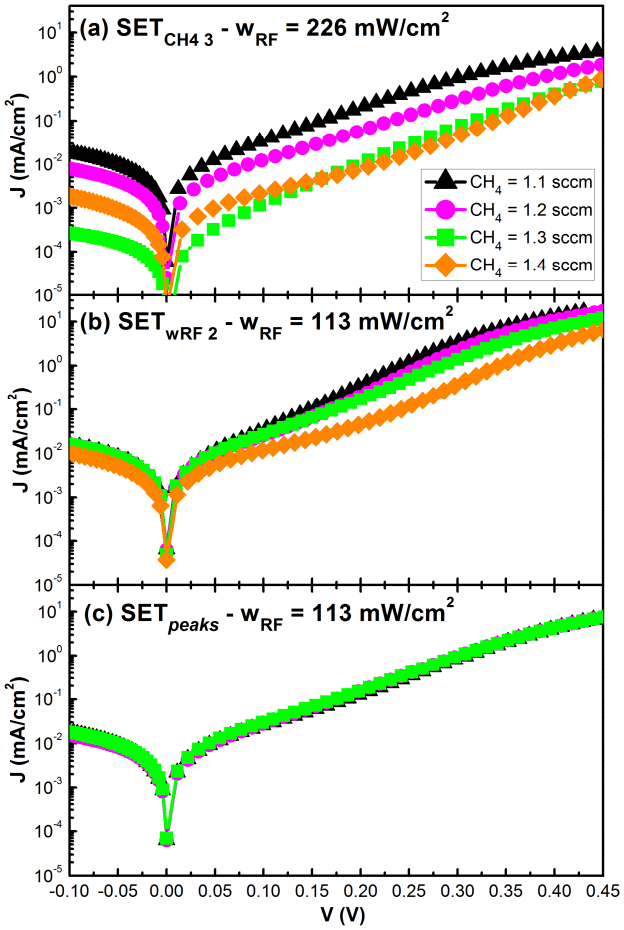

Figure 5.4.: Dark J(V) curves of n-i-p photo-diodes from (a) SET_{CH_43} (RF-PECVD at 226 mW/cm^2), (b) $SET_{w_{RF}2}$ (RF-PECVD at 113 mW/cm^2) and (c) SET_{peaks} (TVW-PECVD using "peaks" voltage waveforms).

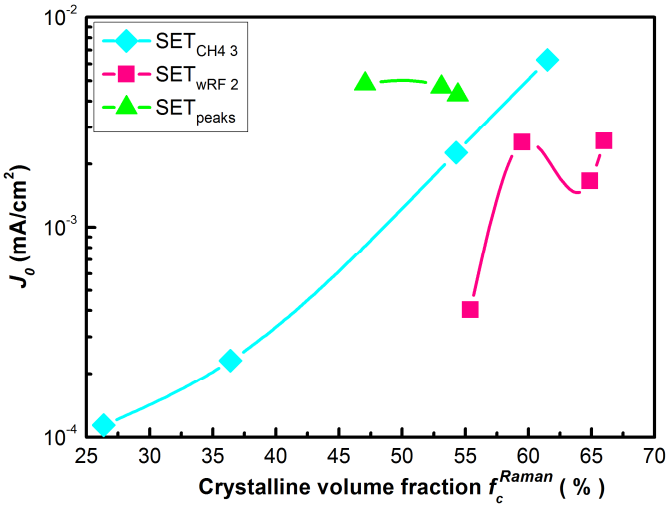

Figure 5.5.: Variation of J_0 as a function of the crystalline volume fraction f_c^{Raman} for n-i-p photo-diodes from SET_{CH_43} (RF-PECVD at 226 mW/cm^2 - ◆), $SET_{w_{RF}2}$ (RF-PECVD at 113 mW/cm^2 - ■) and SET_{peaks} (TVW-PECVD using "peaks" voltage waveforms - ▲).

5.2.2 p-i-n devices at 175° C

As the substrate temperature seems to have a negligible impact on the structural properties of the μc-$Si_{1-x}C_x$:H alloys, new sets of diodes have been fabricated using in this case a *superstrate* structure at 175° C. For these sets, materials deposited by standard RF-PECVD at 113 mW/cm^2 (SET_{T1}) and 226 mW/cm^2 (SET_{T2}) have been used as the i-layer (see Table 5.1). Therefore, also for these sets of diodes, the f_c^{Raman} of the i-layer can be expected to be close to that of the material study.

For such substrate temperature the impact of different doped layers on the diode performance was tested only for devices deposited using materials made by RF-PECVD at 226 mW/cm^2 as the i-layer.

p-doped μc-Si:H

In Figure 5.6, the semi-log plots of the dark J(V) curves at room temperature are shown for the two sets of p-i-n photo-diodes made using p:μc-Si:H and ITO/Ag as back contact.

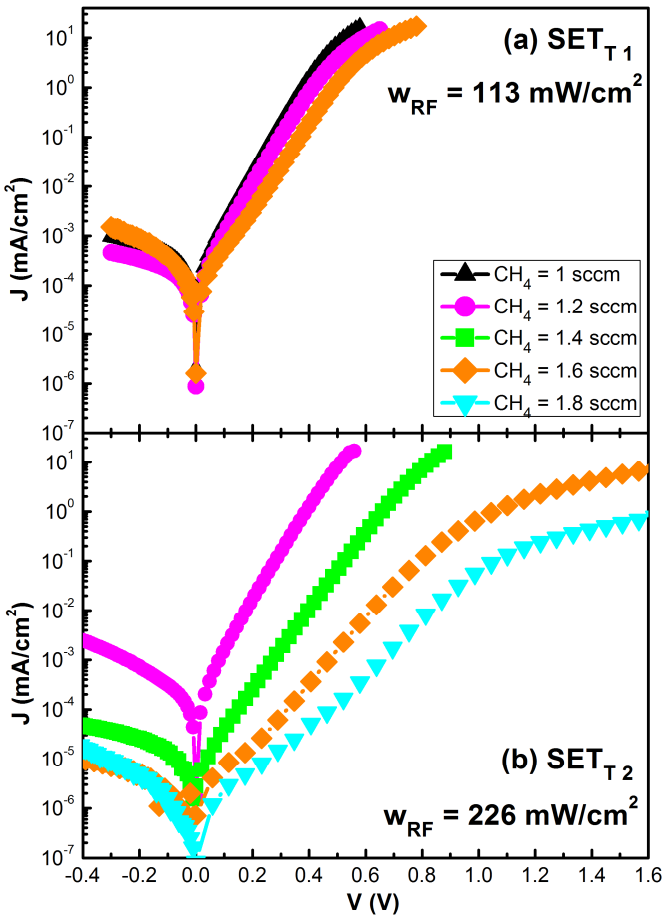

Figure 5.6.: Dark J(V) curves of p-i-n photo-diodes from (a) SET_{T1} (RF-PECVD at 113 mW/cm^2) and (b) SET_{T2} (RF-PECVD at 226 mW/cm^2).

All the devices show a rectifying behavior. Moreover, also for these conditions the variation of the CH_4 flow rate induces an evolution of the diode characteristics, due to the changes in the i-layer structural properties. From these curves the dark saturation current J_0 was extracted and is presented in Figure 5.7 (closed symbols), as a function of the crystalline volume fraction of the i-layer. With decreasing crystalline volume fraction, caused by the carbon incorporation, a decrease in J_0 is observed. Nevertheless, also for these devices the impact of the different microstructure on the device performance can be noted. Indeed, for $f_c^{Raman} \sim 60$ %, the diode from $SET_{w_{RF}2}$ presents a value of J_0 that is nearly 10 times lower than that of the diode from $SET_{CH_4}3$.

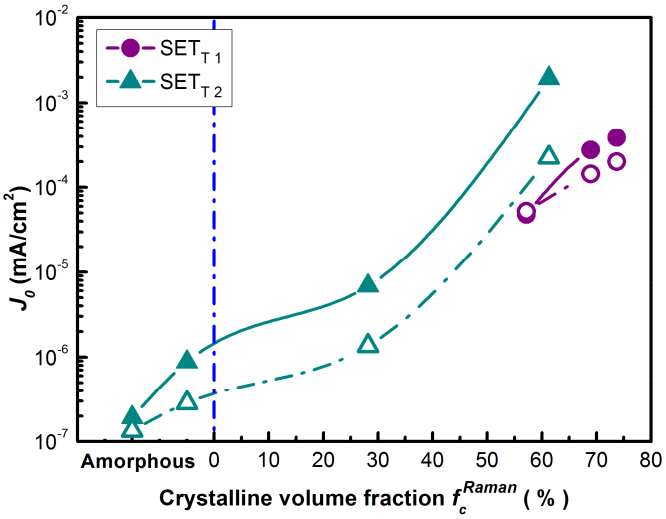

Figure 5.7.: Evolution of J_0 as a function of the i-layer crystalline volume fraction for p-i-n photo-diodes from SET_{T1} (RF-PECVD at 113 mW/cm^2 - ●) and SET_{T2} (RF-PECVD at 226 mW/cm^2 - ▲). The impact of the different back contact has been tested using ITO/Ag (closed symbols) and ITO (open symbols).

These devices have been co-deposited on a second ZnO:Al substrate. For this second set of devices a simple ITO back contact has been sputtered, with no back reflector. Values of J_0 obtained for these sets of devices are presented in Figure 5.6 (open symbols). While for SET_{T1} samples the difference in J_0 is minimal, for samples from SET_{T2} the difference from ITO/Ag and ITO is of nearly one order of magnitude. This is possibly related to the quality of the ITO. Indeed, during this period this TCO was found to be of fickle quality, due to some leakage in the oxygen line used for its sputtering. Despite frequent controls, the problem seems to be aleatory and is still under investigation. Nevertheless, such difference obtained by changing the back contact is surprising and is still a matter for further studies.

p-doped µc-SiO_x:H

It is possible that p:µc-Si:H is not the optimal doped layer to be used with µc-$Si_{1-x}C_x$:H alloys. As reported in Table 5.1, for p-i-n devices from SET_{T2} (standard RF-PECVD at w_{RF} = 226 mW/cm^2), the impact of p:µc-SiO_x:H was tested. For these devices an ITO back contact was used, as when trying to sputter ITO/Ag contacts devices were all shunted.

In Figure 5.8 the evolution of the dark J(V) curves are presented. Usually p:µc-SiO_x:H is efficiently integrated into devices using a-Si:H as the active layer, due to its higher band gap ($E_{04} \sim 2.5$ eV). Therefore, its application in devices integrating µc-$Si_{1-x}C_x$:H alloys, should be promising.

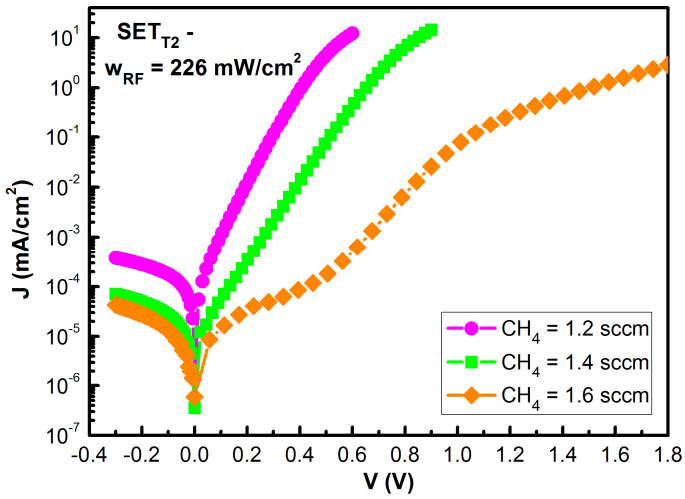

Figure 5.8.: Dark J(V) curves of p-i-n photo-diodes having µc-$Si_{1-x}C_x$:H as i-layers (SET_{T2}) and p:µc-SiO_x:H.

From these curves the value of the dark-saturation current has been determined, and in Figure 5.9 its evolution is presented as a function of the crystalline volume fraction of the i-layer. Usually, the integration of µc-SiO_x:H as a p-doped layer is beneficial, leading to an increase in the V_{oc}. However, already from the evolution of the dark saturation current it can be seen that for these p-i-n devices no particular improvement is obtained, compared to the use of p:µc-Si:H.

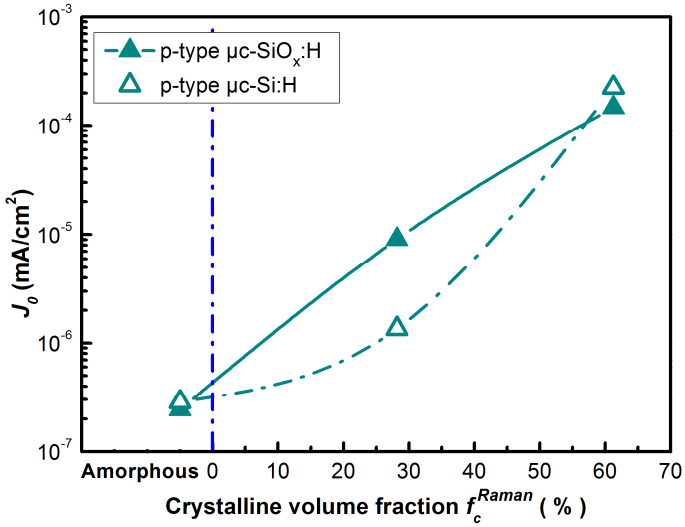

Figure 5.9.: Evolution of J_0 as a function of the i-layer crystalline volume fraction for p-i-n photo-diodes with p:µc-SiO_x:H (▲) and p:µc-Si:H (△).

5.3 LIGHT J(V) CHARACTERISTICS

The J(V) characteristics of the diodes were also measured under illumination through the p layer, using an AM 1.5 solar simulator. Results for series deposited at high and low temperature are presented in the following. In order to understand these results it is necessary to remember that two different light J(V) set up had to be used, depending on the structure of the devices. Indeed, while photovoltaic performance of n-i-p devices were measured using a solar simulator that has a high response in the blue, compared to the solar spectrum, p-i-n devices were measured using a halogen lamp, which has a higher response in the red. For these reasons in this section no efficiencies will be presented. They will be determined from external quantum efficiency measurements, that will be presented in the next section.

5.3.1 n-i-p devices at 285° C

In Figure 5.10, light J(V) curves of devices from $SET_{CH_4 3}$, $SET_{w_{RF}2}$ and SET_{peaks} (see Table 5.1) are presented. Different current-density scales are used for each set of diodes in order to easily compare the variation in device performance, due to changing CH_4 flow rate.

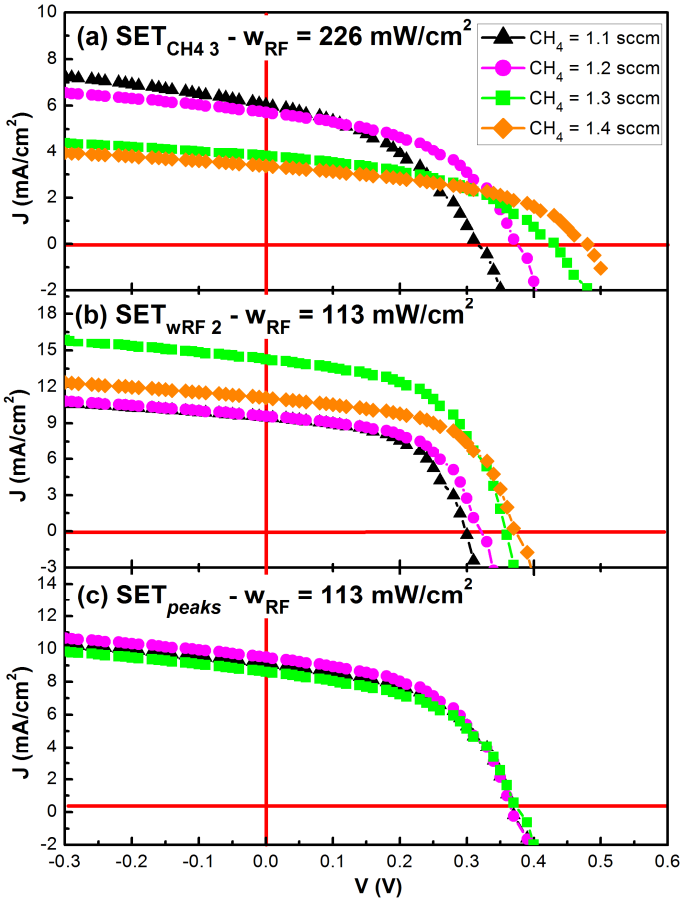

Figure 5.10.: Light J(V) curves for n-i-p photo-diodes from (a) $SET_{CH_4 3}$ (RF-PECVD at 226 mW/cm^2), (b) $SET_{w_{RF}2}$ (RF-PECVD at 113 mW/cm^2) and (c) SET_{peaks} (TVW-PECVD using "peaks" voltage waveforms). The red lines indicate the axes crossing at $(V, J) = (0, 0)$, highlighting J_{sc} and V_{oc}.

A good photoresponse is detected in all devices. It should be noted that these devices are only $\sim$ 250 nm thick and that the p:µc-Si:H layer outside the ITO contact was not removed, creating an increased collection area but through a more resistive path, giving the illusion of a low shunt resistance. Furthermore, the lack of a metallic back reflector in the structure limits the generated photocurrent. No matter which deposition process is considered, it is evident that these devices are limited by some degree of series resistance as well.

Another thing that it must be remembered is that for these devices no optimization was done, and no particular engineering of interfaces was introduced to reduce the series resistance. Nevertheless, some coherence with the material study previously presented can be noted. The TVW devices (SET_{peaks} in Figure 5.10(c)) show little variation with CH_4 flow rate, whereas those from SET_{CH_43} (w_{RF} = 226 mW/cm^2) in Figure 5.10(a) and $SET_{w_{RF}2}$ (w_{RF} = 113 mW/cm^2) in Figure 5.10(b) show a strong dependence. Devices deposited at low RF-power density ($SET_{w_{RF}2}$) show better performance in general than those made at w_{RF} = 226 mW/cm^2 (SET_{CH_43}). This is possibly due to the fact that multiple material parameters must be simultaneously present to give good devices. Indeed, these photo-diodes where made using as the i-layer materials with simultaneously acceptable E_a ($>$ 0.4 eV, Figure 4.13), high L_d (Figure 4.15), high photoresponse ratio (Figure 4.12), and the lowest defect density from MPC-DOS (Figure 4.24). This result is logical as the relatively low activation energy (these materials are characterized by an effective band gap E_g of $\sim$ 1.6 eV and an iso-absorption band gap E_{04} of $\sim$ 2 eV) may indicate the presence of defects blocking the Fermi level, and so must be coupled with both a good photoresponse, a low defect density, and a high L_d to result in a well distributed electric field, good collection, and a good photovoltaic device.

On the other hand, the only way to assess the out-of-plane electrical properties of a material is to integrate it into a device. However, while the contribution of interfaces is not at all accounted for in coplanar measurements, it adds an additional factor in devices. For example, it can be observed that n-i-p cells deposited by TVW exhibit comparable performance with those of RF-PECVD cells despite a lower material quality (shorter L_d, highest MPC-DOS, but acceptable E_a and photoconductivity ratio). This may be attributed to the effect of the lower IBE during the deposition which may be responsible for a better interface quality.

To compare these devices in a more quantitative way, Figure 5.11 presents the evolution of the devices parameters, (V_{oc}, J_{sc} and fill factor (FF)) as a function of the i-layer crystalline volume fraction.

Properties of devices made using standard RF-PECVD are strongly influenced by the variation of the crystalline volume fraction of the i-layer. With decreasing crystalline volume fraction an increase of the V_{oc} can be seen, possibly related to the microcrystalline-to-amorphous phase transition. Moreover, these results are in good agreement with what was previously observed by ellipsometry. Despite E_g being an average value of the optical band gap, determined from the presence of the amorphous and microcrystalline phases at the same time, this parameter correlates well with the crystalline fraction (Figure 4.11) and, consequently, with both J_0 and V_{oc} (Figure 5.11). The lack of optimization (series resistances, unetched p-layer and no back reflector) and the fact that these devices were made at 285° C, are likely responsible for the low absolute values of the V_{oc}, FF and J_{sc}. Furthermore, both doped layers are made using µc-Si:H, which may further limit the open

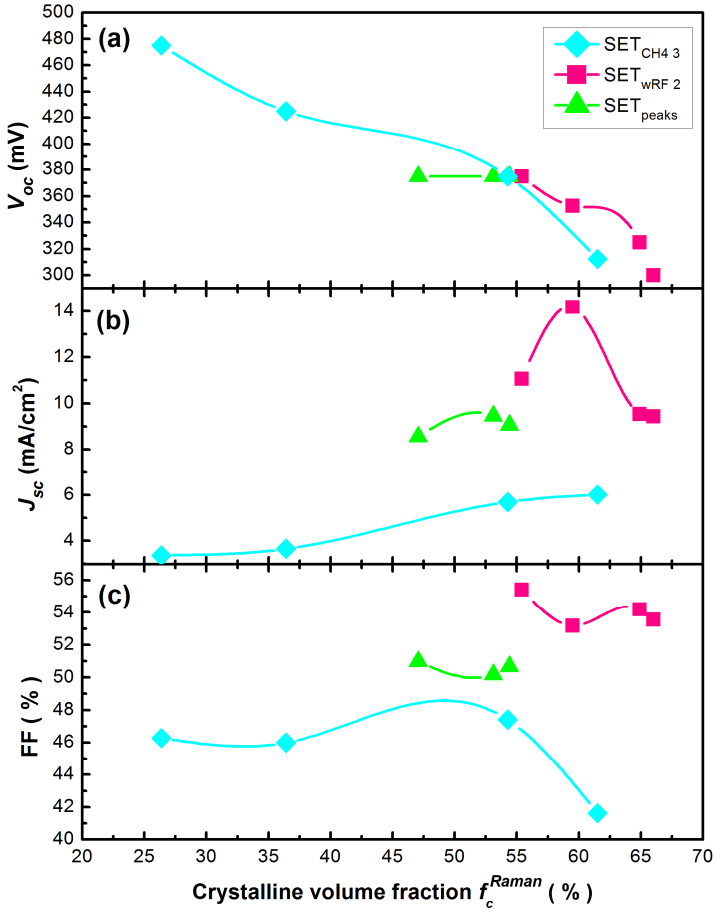

Figure 5.11.: Evolution of the device properties: (a) V_{oc}, (b) J_{sc} and (c) FF, as a function of the crystalline volume fraction of the i-layer, for devices from SET_{CH_43} (RF-PECVD at 226 mW/cm^2 - ◆), $SET_{w_{RF}2}$ (RF-PECVD at 113 mW/cm^2 - ■) and SET_{peaks} (TVW-PECVD using "peaks" voltage waveforms - ▲).

circuit voltage. The observed values for J_{sc} are coherent with the previously observed material properties. Diodes from $SET_{w_{RF}2}$ (standard RF-PECVD at 113 mW/cm^2) show the highest values of short-circuit current, whereas those from SET_{CH_43} (standard RF-PECVD at 226 mW/cm^2) show rather modest device properties. At the same time, no dependence on the CH_4 flow rate during deposition is seen, even upon illumination, in the properties of devices from SET_{peaks}. Finally, the best values of FF are obtained for diodes the i-layers of which were deposited by standard RF-PECVD at 113 mW/cm^2, although in these structures it is difficult to remove the parasitic effects (such as series resistance) that are not related to the i-layer quality, which is only 200-250 nm thick.

To conclude, of most interest to the main goal of this technology is the impact on V_{oc} provided by the use of CH_4 during the process. Although the absolute value is modest, due to the reasons listed above, it can be seen that an increase of almost 200 mV can be induced through modification of the growth by the addition of CH_4. Moreover, for devices from $SET_{w_{RF}2}$, the V_{oc} could be increased the most before the material quality began to break down at high CH_4 flow rates.

5.3.2 p-i-n devices at 175° C

In the previous section it was shown that first attempts at integrating μc-$Si_{1-x}C_x$:H alloys into the photovoltaic devices highlighted the existence of trends consistent with results presented in the material study (namely concerning the effect of the carbon-incorporation on J_0 and V_{oc}). However, limitations related to the high substrate temperature were identified, mostly related to the un-optimized doped layer and the need to use the "substrate-type" configuration. Therefore, new sets of diodes were fabricated at 175° C, using the p-i-n configuration and n:a-Si:H.

p-doped μc-Si:H

In Figure 5.12, light J(V) characteristics of p-i-n devices from SET_{T1} (standard RF-PECVD at 113 mW/cm^2 in Figure 5.12(a)) and SET_{T2} (standard RF-PECVD at 226 mW/cm^2 in Figure 5.12(b)) are presented.

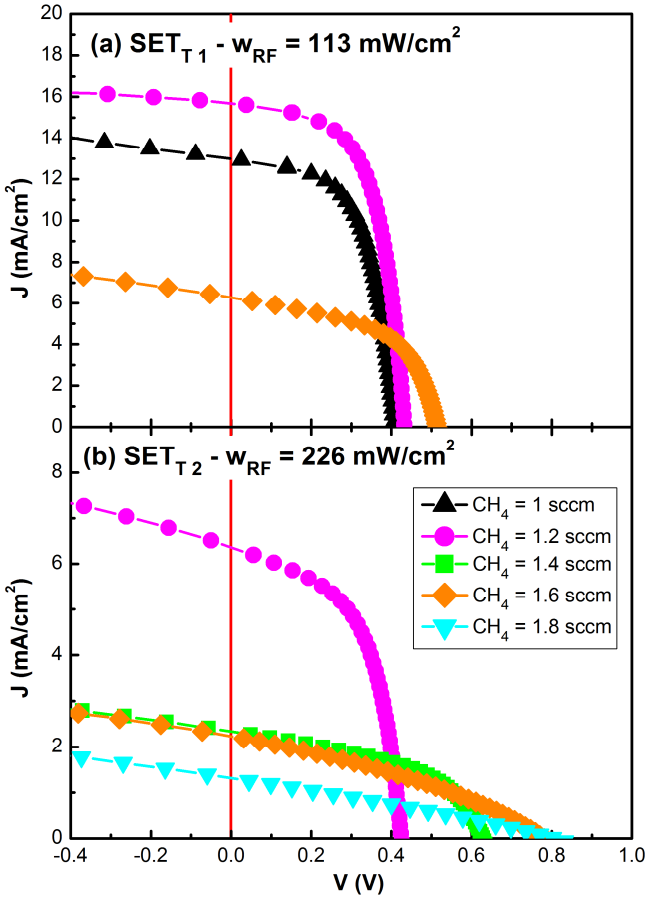

Figure 5.12.: Light J(V) curves for p-i-n photo-diodes from (a) SET_{T1} (w_{RF} = 113 mW/cm^2) and (b) SET_{T2} (w_{RF} = 226 mW/cm^2). The red line indicate the axis crossing at V = 0, highlighting J_{sc}).

The devices shown in the figure were nearly 200 − 250 nm thick and made using ITO/Ag as a back contact. It can be observed that when some degree of crystallinity is present, devices exhibit a good photoresponse. However, this is not the case for p-i-n diodes made with completely amorphous i-layer (a-$Si_{1-x}C_x$:H, obtained with CH_4 flow rates of 1.6 sccm and 1.8 sccm in SET_{T2}).

Despite the absence of optimization (no engineering of interfaces was introduced to reduce the series resistance), which can limit the device performance, some coherence with the material study is observed. Both devices from SET_{T1} (w_{RF} = 113 mW/cm^2) and SET_{T2} (w_{RF} = 226 mW/cm^2) show a strong dependence on the CH_4 flow rate. Furthermore, the former show in general better performance than the latter, for which the transition to a-$Si_{1-x}C_x$:H (CH_4 = 1.6 sccm and 1.8 sccm) leads to very poor properties. One should not be surprised by the presence of such strong influence of the i-layer crystalline volume fraction, also for devices deposited at 175° C. Indeed, in chapter 3 it was observed that the lower substrate temperature has a negligible impact on the structural properties of the materials. However, the decrease in substrate temperature has lead to much better performance, possibly related to improved doped layers and, in general, to the possibility of making p-i-n devices instead of n-i-p's.

In Figure 5.13 the evolution of the photovoltaic parameters is presented as a function of i-layer crystalline volume fraction. Results are shown for diodes made using ITO/Ag (closed symbols) and ITO (open symbols) as back contact. In both cases the light J(V) measurements were performed shining the light from the p-side. The difference in PV performance ob-

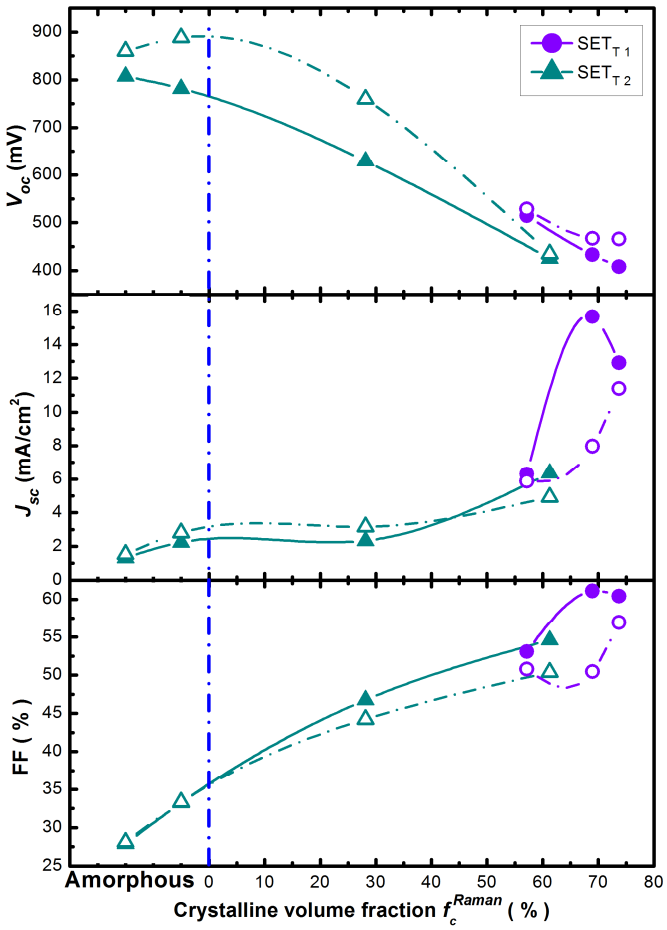

Figure 5.13.: Evolution of (a) V_{oc}, (b) J_{sc} and (c) FF, as a function of the i-layer crystalline volume fraction, for devices from SET_{T1} (w_{RF} = 113 mW/cm^2 - ●) and SET_{T2} (w_{RF} = 226 mW/cm^2 - ▲). Results are presented for ITO/Ag (closed symbols) and ITO (open symbols) back contacts.

served when changing from the ITO/Ag to the ITO back contact is still a matter of speculation.

For all sets of diodes, with decreasing crystalline volume fraction an increase of the V_{oc}, linked to the the phase transition and the carbon incorporation, can be observed. The impact of the RF-power density on J_{sc} is similar to what has been presented in the previous section for high temperature devices. Diodes from SET_{T1} show the highest values of short-circuit current, whereas those from SET_{T2} show modest performance that become very poor when the i-layer is completely amorphous. Finally, the best values of FF are also obtained for diodes the i-layer of which has been deposited by standard RF-PECVD at 113 mW/cm^2, although also for these structures it is difficult to take into account parasitic effects not related to the i-layer quality. A direct comparison of the properties of high and low temperature devices will be given in the summary in section 5.5.

p-doped μc-SiO$_x$:H

From dark J(V) measurements, p:μc-SiO$_x$:H seems to have no effect on the properties of the devices in the dark. In Figure 5.14 its impact on the light J(V) characteristics (acquired shining the light from the p-side) is presented.

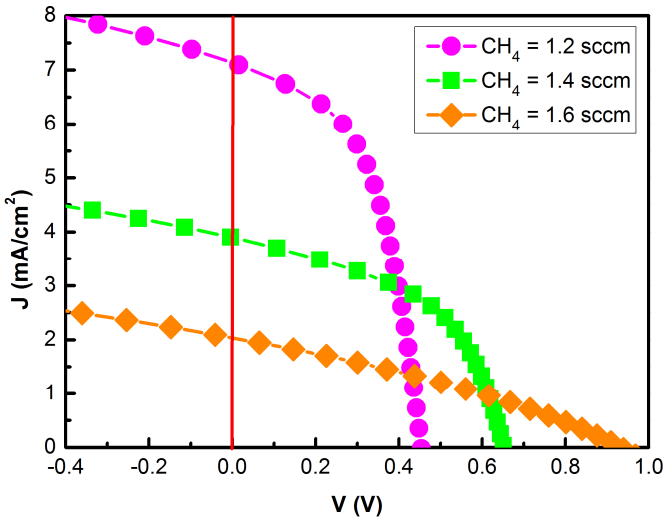

Figure 5.14.: Light J(V) curves for p-i-n photo-diodes from SET_{T2}, fabricated using p:μc-SiO$_x$:H. The red line indicate the axis crossing at V = 0, highlighting J_{sc}.

Also for these devices, when the i-layer is completely amorphous (CH_4 = 1.6 sccm) very poor performance is obtained. Therefore, the same considerations that arose from the analysis of devices made with p:μc-Si:H are valid when p:μc-SiO$_x$:H is used, proving the negligible impact of this doped layer on the p-i-n photo-diodes.

In Figure 5.15 the evolution of the photovoltaic properties of the devices is presented as a function of i-layer crystalline volume fraction. A comparison between PV parameters obtained for diodes with p:μc-Si:H (open symbols) and p:μc-SiO$_x$:H (closed symbols) is shown. The diodes performance are indeed very similar, despite the variation of the doped layer. Therefore, in section 5.5, high and low temperature devices will be compared only for p:μc-Si:H.

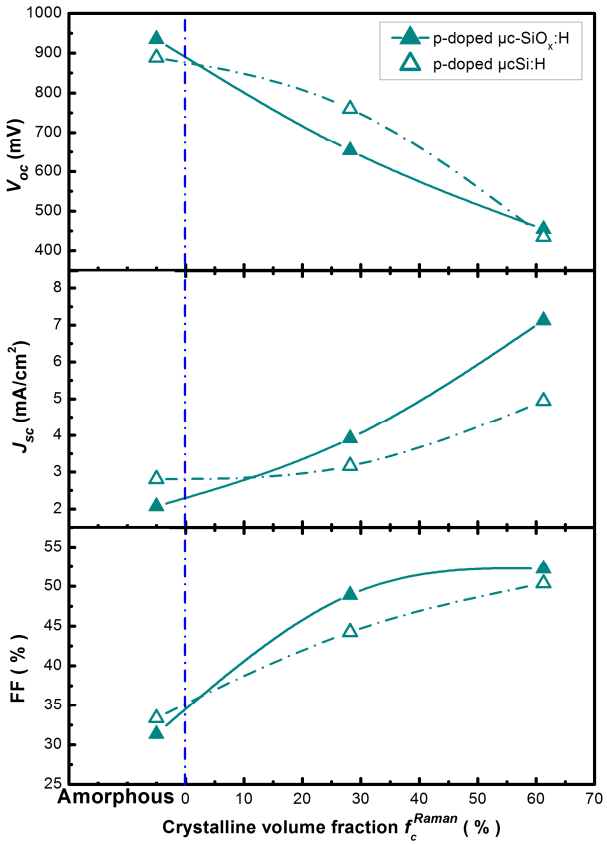

Figure 5.15.: Evolution of the PV parameters: (a) V_{oc}, (b) J_{sc} and (c) FF, as a function of the crystalline volume fraction of the i-layer, for devices from SET_{T2} using p:μc-SiO_x:H (▲) and p:μc-Si:H (△).

5.4 EXTERNAL QUANTUM EFFICIENCY

External quantum efficiencies (EQE) measurements are affected by the partial reflexion of the incoming photons due to the differences in optical indexes at the interfaces (air/glass, glass/TCO, TCO/cell) and by the absorption of the glass and TCO. However, they can provide useful information on the absorption of the material and the collection in the device.

For all sets of devices (at high and low temperature) EQE has been measured through illumination from the p-side. in addition, when looking at these results, one should remember that due to the low deposition rate ($\sim$ 0.85 Å/s for w_{RF} = 226 mW/cm^2, and $\sim$ 0.5 Å/s for w_{RF} = 113 mW/cm^2), and to the limited amount of reactor time available, devices are extremely thin ($\sim$ 250 nm).

5.4.1 n-i-p devices at 285° C

The evolution of the EQE for n-i-p devices deposited at 285° C is presented in Figure 5.16.

The first thing to be noted is the generally low value of the EQE but, as anticipated in the introduction to this section, it must be remembered that these devices are very thin ($\sim$ 200-250 nm). Additionally, for these n-i-p photo-diodes no back reflector was used. Moreover, the impact of the CH_4 flow rate on the material properties is mirrored by the evolution of the EQE.

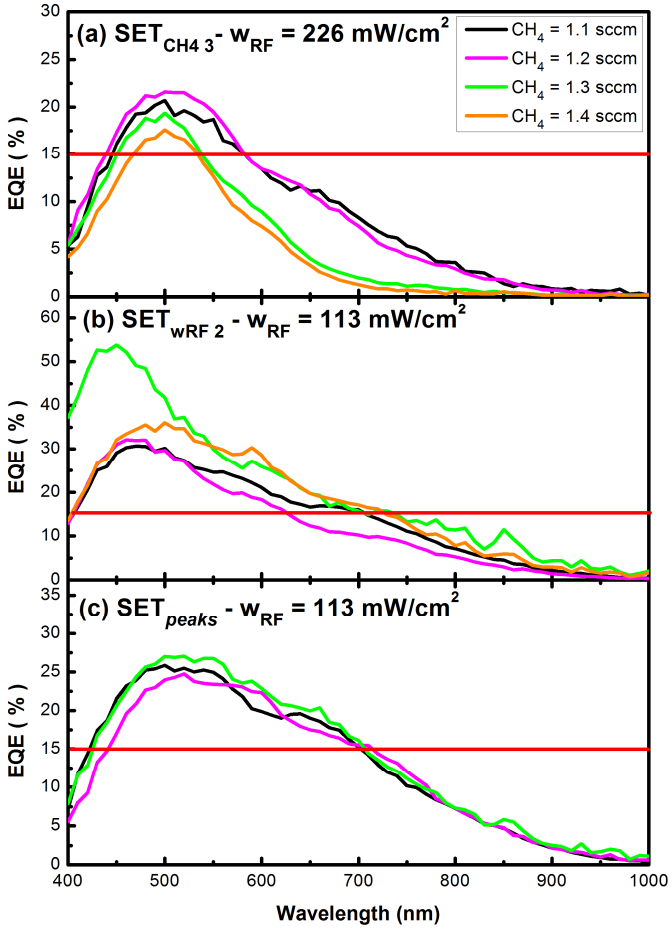

Figure 5.16.: Evolution of the EQE spectra for n-i-p devices from (a) $SET_{CH_4 3}$ (w_{RF} = 226 mW/cm^2), (b) $SET_{w_{RF}2}$ (w_{RF} = 113 mW/cm^2) and (c) SET_{peaks} (TVW-PECVD using the "peaks" voltage waveforms). The red horizontal line highlights EQE at 15 %.

At high RF-power density devices are more sensitive to the CH_4 flow rate variations. In Figure 5.16(a), it can be seen that with decreasing crystalline volume fraction (increasing CH_4 flow rate), the only contribution to the EQE comes from the low wavelength region ($\sim$ 450 nm). The amorphization of the material induces a decrease of the EQE at about 700 nm. On the other hand, for devices from $SET_{w_{RF}2}$ (Figure 5.16(b)), all the i-layers are characterized by a high crystalline volume fraction, and in fact the two components of the EQE are always present. However, the behavior of the sample deposited using a CH_4 flow rate of 1.3 sccm (— in Figure 5.16(b)) could seem at odds compared to the general trend. When this device was deposited, two main mistakes were made: first, a four times longer seed layer was used for the deposition of the i-layer, then the p:µc-Si:H layer was made by a 10 minute intrinsic µc-Si:H layer, followed by a 5 minute deposition with the addition of the doping gas (TMB). Usually, after the i-layer deposition, the p-layer was made by first depositing a 1 minute intrinsic µc-Si:H layer, to ensure microcrystallinity, followed by a 9 minute deposition adding TMB. From the study of this accidental device it should have been clear that all the other p-layers were too thick, causing a lower EQE in the low wavelengths range. Finally, as it was said, for devices made using

the TVW-PECVD technique to deposit the i-layer, no significant impact of the CH_4 flow ratio the EQE can be detected (Figure 5.16(c)). Furthermore, these last devices show EQEs that are similar to what is observed for devices from $SET_{w_{RF}2}$. This result is consistent with the crystalline volume fraction, which is found to be similar for the two sets of materials and in the case of deposition by TVW-PECVD, is found to be constant despite the increase in CH_4 flow rate.

From the EQE measurements it is possible to determine the short-circuit current J_{sc}, which can be compared to values obtained from light $J(V)$ measurements. In Figure 5.17 its evolution as a function of the the i-layer crystalline volume fraction is compared to values obtained from light $J(V)$ measurements. It can be seen that the J_{sc} calculated from the EQE spectra is $\sim$ 50 % lower that that measured from light $J(V)$. Such discrepancy can arise from the fact that (i) the solar simulator used to perform light $J(V)$ measurements has a higher response in the blue compared to the solar spectrum, and (ii) that for these n-i-p devices the p:µc-Si:H was not etched and therefore there is a collection over a larger area.

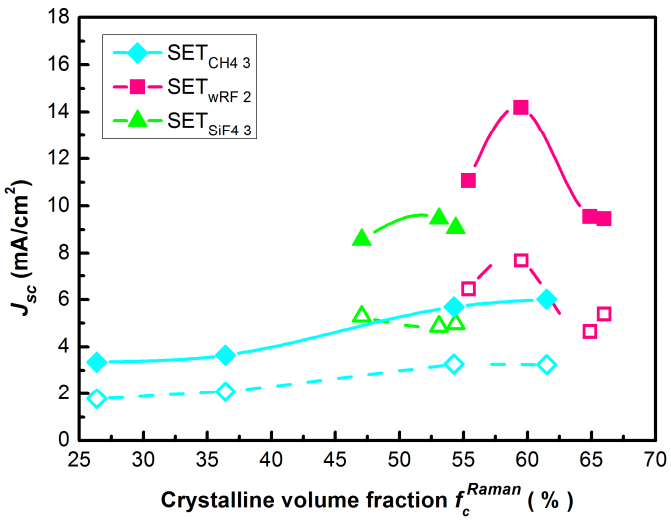

Figure 5.17.: Evolution of the short-circuit current J_{sc} as determined from EQE (open symbols) and light $J(V)$ (closed symbols) measurements, as a function of the crystalline volume fraction. Performance of n-i-p devices from $SET_{CH_4 3}$ (standard RF-PECVD at w_{RF} = 226 mW/cm^2 - ◆), $SET_{w_{RF}2}$ (standard RF-PECVD at w_{RF} = 113 mW/cm^2 ■) and SET_{peaks} (TVW-PECVD using "peaks" voltage waveforms - ▲).

5.4.2 p-i-n devices at 175° C

In the previous section it was shown that the external quantum efficiency of n-i-p devices made integrating µc-$Si_{1-x}C_x$:H alloys as the i-layer are characterized by very low values. One could wonder if the improvements achieved by switching to a p-i-n structure have a significant impact also on the EQE spectra.

p-doped μc-Si:H

In Figure 5.18 the evolution of the EQE is presented for diodes from SET_{T1} (w_{RF} = 113 mW/cm^2) and SET_{T2} (w_{RF} = 226 mW/cm^2), having p:μc-Si:H and ITO/Ag as back contact.

The first thing to be noted is that the decrease in substrate temperature has allowed to reach higher values of the EQE (∼ 60 % at 500 nm for devices from SET_{T1}). However, the deterioration of the performance with the decreasing crystalline volume fraction (increasing CH_4 flow rate) is still observed, showing a decrease of the EQE spectra in the 700 nm range. Moreover, the poor properties of devices having a fully a-$Si_{1-x}C_x$:H i-layer are evident also from EQE measurements, showing values of ∼ 10 % in the low wavelength region and no response at 700 nm. The improvement in the EQE may arise from a combination of better device design, more appropriate doped layers and the presence of the silver back reflector, especially since from the previous material study no impact of the lower substrate temperature was observed on the properties of μc-$Si_{1-x}C_x$:H alloys. Thus, if μc-$Si_{1-x}C_x$:H alloys want to be efficiently integrated into PV devices, it is necessary to continue investigating deposition in the low temperature regime.

Furthermore, the effect of the presence of the silver back-reflector can be easily observed when comparing these spectra with those presented in Figure 5.19, where only the ITO back contact was used. For devices from

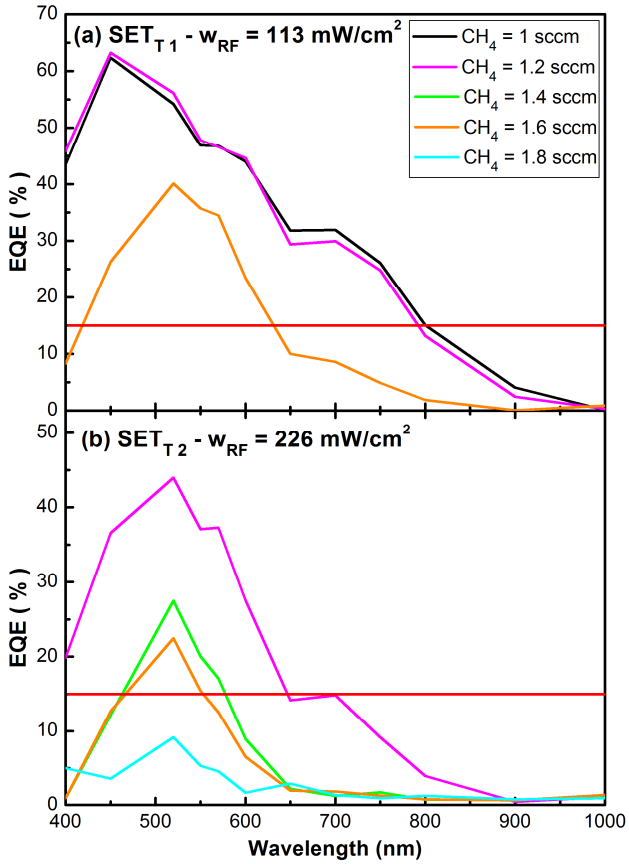

Figure 5.18.: Evolution of the EQE spectra for devices from (a) SET_{T1} (w_{RF} = 113 mW/cm^2) and (b) SET_{T2} (w_{RF} = 226 mW/cm^2), with ITO/Ag as back contact. The red horizontal line highlights EQE at 15 %.

SET_{T1} the presence of the silver back reflector induces a slight increase in the EQE, especially in the 700 nm region, where an increase of nearly 25 % (passing from an EQE of 24 % to an EQE of 30 %) can be seen. For devices fabricated at higher RF-power density, such an effect is more marked. Indeed, among the devices of SET_{T2} that with the highest crystalline fraction shows an increase of nearly 150 % (with the EQE passing from $\sim$ 6 % to $\sim$ 15 %). Therefore, the delivered current can not only be limited by the extreme thickness of these devices ($\sim$ 250 nm), but also by the absence of the back reflector.

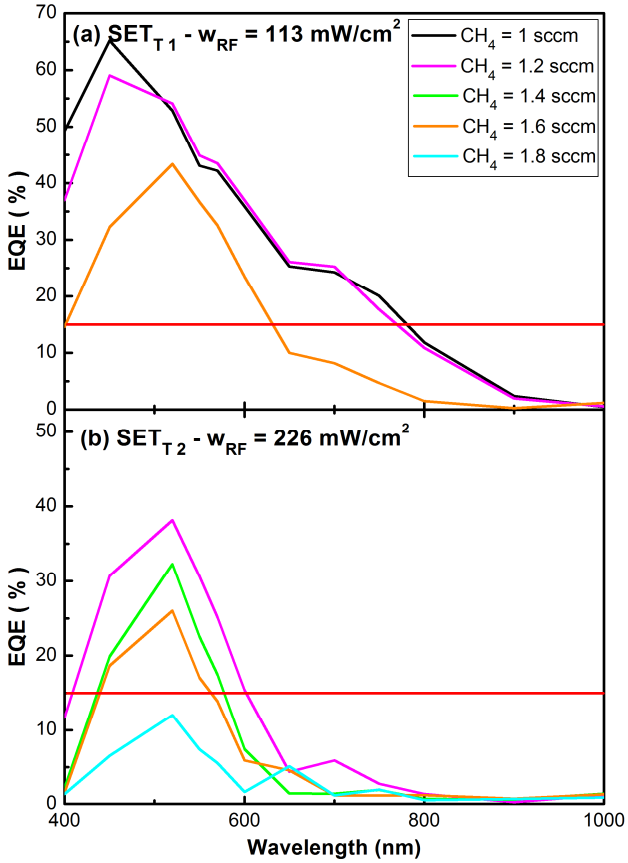

Figure 5.19.: Evolution of the EQE spectra for devices from (a) SET_{T1} (w_{RF} = 113 mW/cm^2) and (b) SET_{T2} (w_{RF} = 226 mW/cm^2), with the ITO back contact. The red horizontal line highlights EQE at 15 %.

Finally, an estimation of the short-circuit current was obtained and is compared to values measured through light J(V) measurements. These results are shown in Figure 5.20, where the evolution of J_{sc} is presented as a function of the crystalline volume fraction for devices from SET_{T1} and SET_{T2} using both ITO/Ag and ITO as back contact.

For both devices having ITO/Ag (Figure 5.20(a)) and ITO (5.20(b)) as back contact, a good correspondence between values of J_{sc} from EQE spectra and light J(V) measurements is achieved only for devices from SET_{T2} (w_{RF} = 226 mW/cm^2). For devices deposited at lower RF-power (SET_{T1} - w_{RF} = 113 mW/cm^2) a discrepancy between the two values is still observed, with light J(V) measurements overestimating the value of J_{sc}.

If one considers that the real value of J_{sc} is that determined through EQE measurements (open symbols), the impact of the addition of the silver back reflector on the delivered current can be studied. The red horizontal lines in Figure 5.20 can be used to observe the evolution of J_{sc}. For devices from

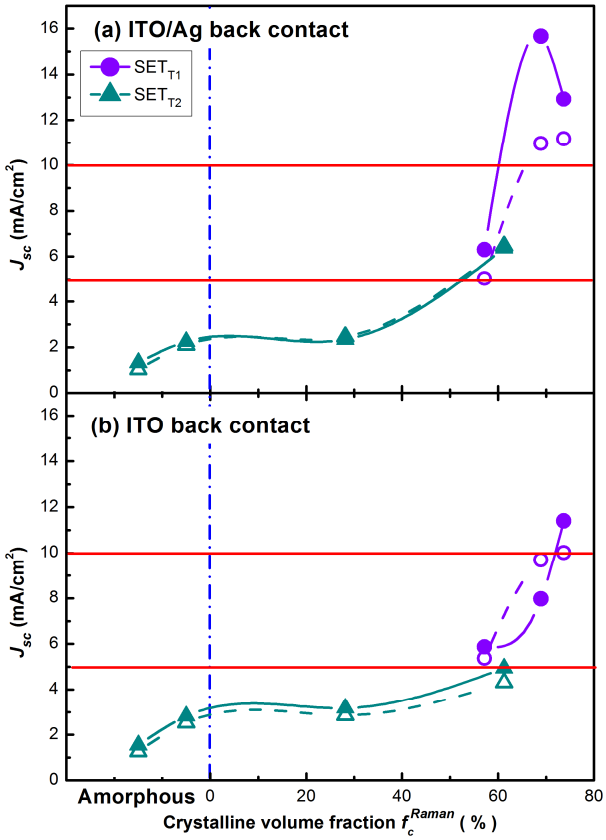

Figure 5.20.: Evolution of the short-circuit current J_{sc} as determined from EQE (open symbols) and light J(V) (closed symbols) measurements n-i-p devices from SET_{T1} (w_{RF} = 113 mW/cm^2 - ●) and SET_{T2} (w_{RF} = 226 mW/cm^2 - ▲). Results are presented for photo-diodes having (a) ITO/Ag and (b) ITO as the back contacts. Red horizontal lines highlight values of J_{sc} of 5 and 10 mA/cm^2.

SET_{T1} using the ITO/Ag back contact allows to reach values of J_{sc} around 11 mA/cm^2, whereas the simple ITO back contact leads to lower values of J_{sc}. A similar trend can be observed for devices from SET_{T2}. Despite values of J_{sc} being generally lower, compared to those of devices deposited at lower RF-power density (SET_{T1}), the presence of the Ag back reflector induces values of J_{sc} slightly higher for devices with $\sim$ 60 % crystalline volume fraction. It is worth noting that such improvement in $J_{sc}$is negligible for lower values of f_c^{Raman} and for devices integrating a-$Si_{1-x}C_x$:H alloys as i-layers.

p-doped μc-SiO_x:H

In Figure 5.21 the evolution of the EQE, measured shining through the p-side, as a function of the CH_4 flow rate is presented for devices fabricated with p:μc-Si:H (Figure 5.21(a)) and with p:μc-SiO_x:H (Figure 5.21(b)). It can be seen that the p:μc-SiO_x:H assures a better collection in the low wavelength region, but also in the 700 nm region, for the device made using the lowest CH_4 flow rate. For all the others, the amorphization of the i-layer, induced by the increased amount of carbon incorporated in the alloy, induces a general decrease in EQE, which is more dramatic in the 700 nm region.

If one compares the evolution of the values of J_{sc} as a function of the crystalline volume fraction, for devices fabricated with p:μc-SiO_x:H, once again

the overestimation of J_{sc} from light $J(V)$ measurements can be observed (Figure 5.22). Therefore, EQE is the only reliable technique to determine the delivered current and thus to have an estimation of the efficiency of these devices.

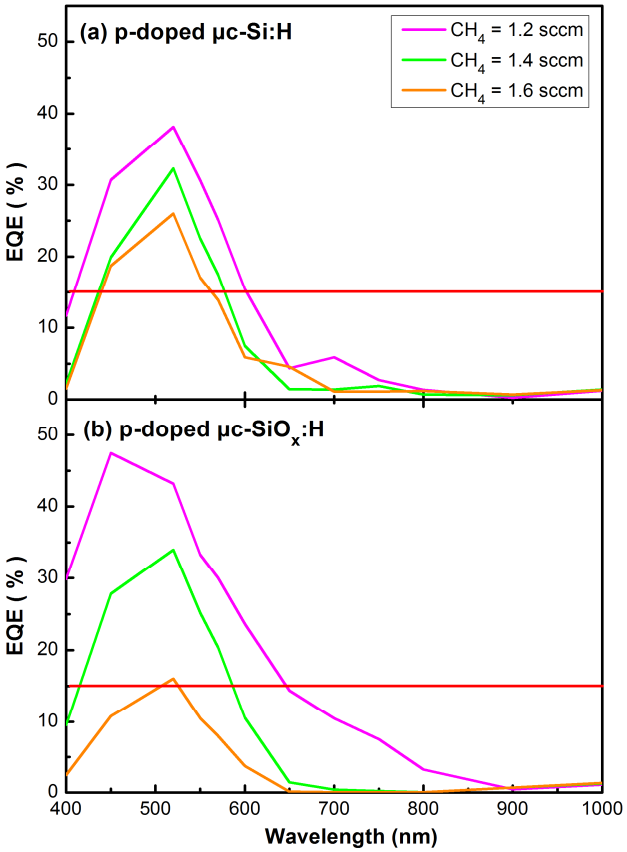

Figure 5.21.: Evolution of the EQE spectra for devices from SET_{T2} (w_{RF} = 226 mW/cm^2) using ITO back contact and (a) p:µc-Si:H and (b) p:µc-SiO_x:H. The red horizontal line highlights EQE at 15 %.

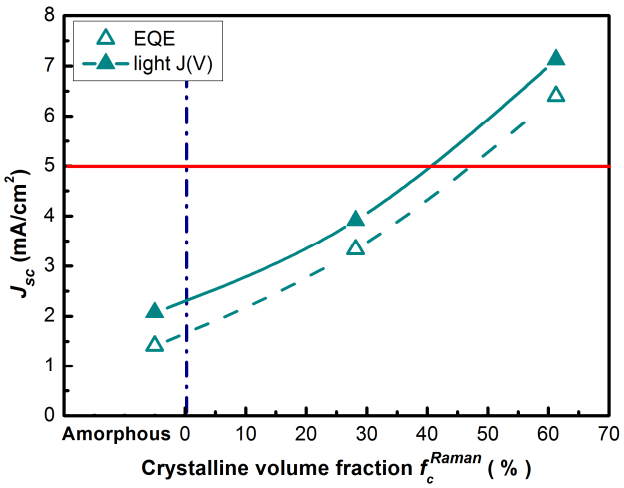

Figure 5.22.: Evolution of the short-circuit current J_{sc} as determined from EQE (△) and light J(V) (▲) measurements, for n-i-p devices from SET_{T2} (w_{RF} = 226 mW/cm^2), with p:µc-SiO_x:H and ITO back contact. The red horizontal line highlights the value of J_{sc} at 5 mA/cm^2.

5.5 SUMMARY

In the previous sections first attempts at integrating μc-$Si_{1-x}C_x$:H alloys in photovoltaic devices were presented showing that, so far, results are very modest. However, it must be taken into account that when out-of-plane properties of a material are tested through device fabrication, many complications can arise due to (i) the choice of the doped layers, (ii) the front and back contacts and (iii) the management of the interfaces. Therefore, it is possible that materials that look promising through a thorough material study, and behave poorly in photo-diodes, are just badly integrated. Due to lack of time and to the complexity of the material, additional tests on the devices should be performed. What is sure, is that their integration into solar cells would require a stronger effort from the whole scientific community.

In this last section a comparison between high temperature n-i-p and low temperature p-i-n devices will be presented. Results concerning devices from SET_{peaks} (TVW-PECVD using "peaks" voltage waveforms) will be omitted, as they have demonstrated that for a first basic understanding of μc-$Si_{1-x}C_x$:H alloys properties and their behavior in photo-diodes, this technique is not the most adapted one.

In Figure 5.23, the evolution of the dark saturation current is presented as a function of the crystalline fraction of the i-layer, for the two substrate temperatures. It can be seen that when passing from 285° C to 175° C, which allows the fabrication of a more adapted structure, a decrease in J_0 is induced for all the devices. Such a decrease is of nearly one order of magnitude for devices deposited by standard RF-PECVD at w_{RF} = 113 mW/cm^2, with a crystalline fraction of the i-layer of nearly 65 %.

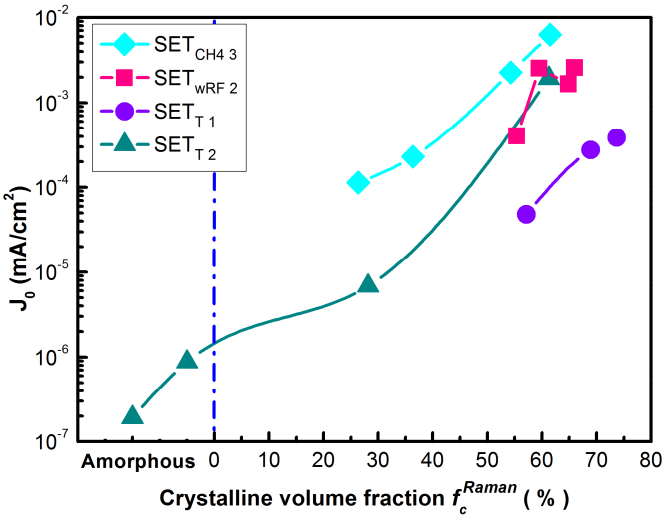

Figure 5.23.: Evolution of J_0, as a function of the crystalline volume fraction of the i-layer, for n-i-p devices made at 285° C (SET_{CH_43} - ◆, and $SET_{w_{RF}2}$ - ■), and for p-i-n devices made at 175° C (SET_{T1} - ●, and SET_{T2} - ▲).

The photovoltaic performance of the same diodes are reported in Figure 5.24. The improvement obtained with the fabrication of p-i-n devices is easily highlighted. For devices deposited using w_{RF} = 226 mW/cm^2 (SET_{CH_43} - 285° C and SET_{T2} - 175° C), the lower substrate temperature has an impact mainly on V_{oc}, with photo-diodes that are still affected by low values of J_{sc} and FF. On the other hand, when the i-layer is deposited by standard

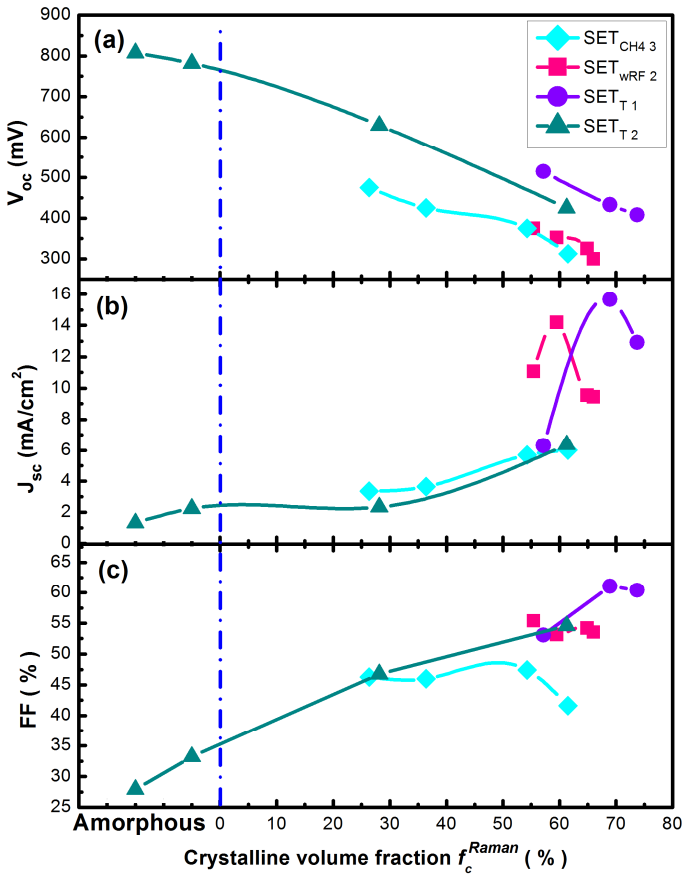

Figure 5.24.: Evolution of the device properties: (a) V_{oc}, (b) J_{sc} and (c) FF, as a function of the crystalline volume fraction of the i-layer, for n-i-p devices made at 285° C (SET_{CH_43} - ◆, and $SET_{w_{RF}2}$ - ■), and for p-i-n devices made at 175° C (SET_{T1} - ●, and SET_{T2} - ▲).

RF-PECVD with w_{RF} = 113 mW/cm^2 ($SET_{w_{RF}2}$ - 285° C and SET_{T1} - 175° C), passing from a n-i-p to a p-i-n structure, leads to higher values of V_{oc}, J_{sc} and also FF (especially for crystalline volume fraction of nearly 65 %). However, in the previous sections it has been demonstrated that due to the solar simulator and halogen lamp mis-calibration, values of J_{sc} as obtained from the light J(V) measurements are overestimated, compared to those calculated from the EQE spectra. Remembering that the efficiency η of a solar cell can be written as:

$$\eta = \frac{V_{oc} \cdot J_{sc} \cdot FF}{P_i}, \tag{5.2}$$

where P_i is the incident power (taken equal to 100 mW/cm^2), it is possible to determine the efficiency of the studied devices, knowing the short-circuit current from the EQE measurements.

The evolution of η is presented in Figure 5.25 as a function of V_{oc}. As expected, performance are modest, so far, but by changing the device structure it has been possible to improve the efficiency of the devices. Nevertheless, it becomes clear that even at 175° C, the most promising route to be investigated for the efficient integration of μc-$Si_{1-x}C_x$:H alloys into PV devices, is the use of low RF-power densities.

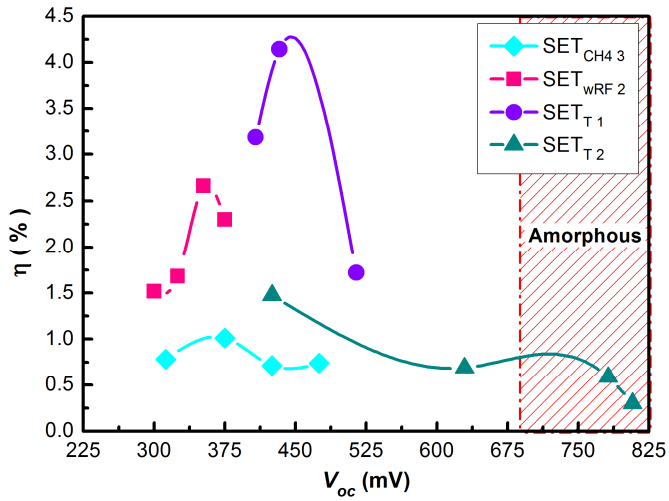

Figure 5.25.: Evolution of the efficiency η, as a function of V_{oc}, for n-i-p devices made at 285° C (SET_{CH_43} - ◆, and SET_{wRF2} - ■), and for p-i-n devices made at 175° C (SET_{T1} - ●, and SET_{T2} - ▲).

The study of the evolution of J_0 as a function of the crystalline volume faction cannot, however, highlight all the problems related to the quality of the materials. Therefore, the evolution of the measured V_{oc} (closed symbols) and the predicted one (open symbols), is presented in Figure 5.26 as a function of J_0. For the determination of the predicted V_{oc}, the expression 5.1 was applied, using the ideality factor n obtained from fitting the dark J(V) curves, and the J_{sc} determined through EQE measurements.

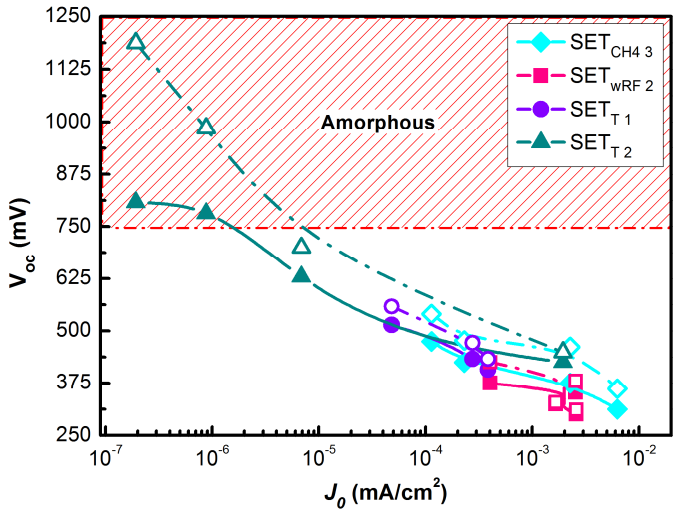

Figure 5.26.: Evolution of measured V_{oc} (closed symbols) and predicted V_{oc} (open symbols) as a function of J_0, for n-i-p devices made at 285° C (SET_{CH_43} - ◆, and SET_{wRF2} - ■), and for p-i-n devices made at 175° C (SET_{T1} - ●, and SET_{T2} - ▲).

It can be seen that the linear relation in the semi-log scale is scale is preserved. However when devices are fabricated using a-$Si_{1-x}C_x$:H alloys as the i-layer, a saturation in the measured V_{oc} is observed. In general, the discrepancy between the measured values of V_{oc} and the predicted ones, with the former being lower than the latter, can be ascribed to recombination. For

this reasons, additional efforts in the optimization of the devices could lead to even more promising performance.

The most important thing that can be inferred from these results is the fact that despite μc-$Si_{1-x}C_x$:H alloys being a complex diphasic material system, composed of two phases having different structure, composition and band gap, they can be efficiently described as a whole material having a varying effective band gap. Therefore, results from ellipsometry measurements, from which such an estimation of E_g was obtained, correlate well with the evolution of V_{oc}, proving that such modeling of this material system is not erroneous.

Finally, it has been stated that the analysis of the PV performance of both p-i-n and n-i-p devices, through light J(V) measurements, is tainted by the mis-calibration of the different lamps, compared to the real solar spectrum. However, in order to be able to directly compare all these devices, the concept of the collection voltage (V_{coll}) can be used. Indeed, V_{coll} is an important quantity for analyzing the performance of thin-film silicon solar cells and it can be defined as:

$$V_{coll} = R_{sc} \cdot J_{sc}, \tag{5.3}$$

where R_{sc} is the short-circuit resistance, and corresponds to the inverse of the slope of the J(V) curve at V = 0 (Shah, Sculati-Meillaud, et al., 2011). It has been proved that despite variation in the light intensity used to perform the light J(V) measurements, V_{coll} has a fixed value (Stückelberger et al., 2010).

In Figure 5.27 the evolution of this parameter is presented as a function of V_{oc}, assuming that shunt resistances can be neglected. Therefore, the slope at $V = 0$ can arise from recombination in both n-i-p and p-i-n devices and also extra collection, for n-i-p devices. These results are consistent with all the material study previously presented, proving that the low RF-power density route is the most promising one for the development of μc-$Si_{1-x}C_x$:H alloys as wide band gap materials for PV devices.

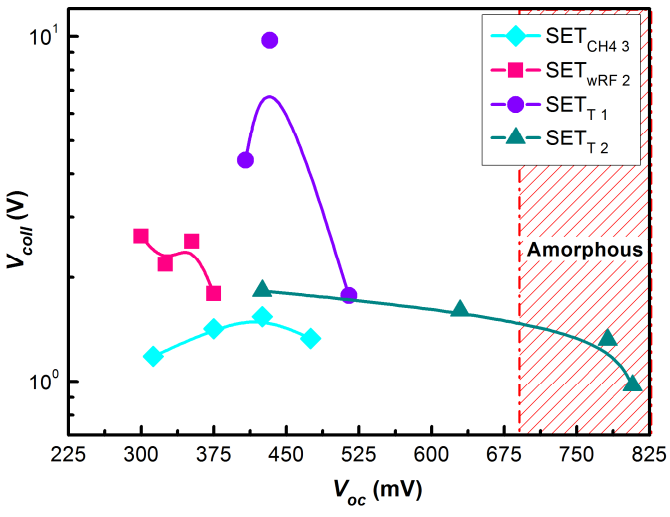

Figure 5.27.: Evolution of V_{coll} as a function of V_{oc}, for n-i-p devices made at 285° C (SET_{CH_43} - ◆, and SET_{wRF2} - ■), and for p-i-n devices made at 175° C (SET_{T1} - ●, and SET_{T2} - ▲).

To conclude, in this chapter it has been shown that with μc-$Si_{1-x}C_x$:H alloys one can have an additional control on the V_{oc}, by changing the amount of carbon incorporated in the alloy. It has been demonstrated that the decrease of the substrate temperature, which in the material study was determined to have a negligible impact on the structural properties of μc-$Si_{1-x}C_x$:H alloys, exerts however a considerable improvement on the device performance. This is possibly related to an improved device design, more appropriate doped layers and the possibility of introducing a back reflector. Nevertheless, it was also shown that the devices fabricated so far suffer from low FF and J_{sc}. Finally, it is true that compared to state-of-the art μc-Si:H solar cells, no matter which design one considers, values of J_{sc} are still low. Nevertheless, the improvements obtained transferring all deposition conditions to a lower temperature seem to have identified the most promising route to follow for the optimization of these materials, as active layers in photovoltaic devices.

CONCLUSIONS

The doctoral work described in this manuscript aimed to develop a new wide band gap microcrystalline material for application in thin film photovoltics. The motivation for such a challenging goal was to be able to provide a new kind of absorber layer, immune to the light-induced degradation that is currently limiting the "micromorph" technology (thanks to its microcrystalline structure) and leading to an increase in the open-circuit voltage of the top cell in tandem devices.

Hydrogenated microcrystalline silicon-carbon (μc-$Si_{1-x}C_x$:H) alloys were identified as such a promising material system, due to the possibility of tuning their average energy band gap by changing the amount of carbon in the alloy composition.

However, the first major disadvantage to overcome has been the absence of a stable sub-stoichiometric silicon-carbon crystalline phase. Indeed, no parallel with silicon-rich microcrystalline silicon-germanium alloys can be found, due to the low solubility of carbon in silicon. Thus, the alloying of these two elements leads to amorphous materials, for quantities of carbon below the stoichiometry. Actually, it is possible to grow sub-stoichiometric alloys using deposition techniques that work far away from thermodynamic equilibrium conditions, allowing a kinetic stabilization of metastable phases, but only below a critical thickness. Such alloys, however, were not observed, when using a standard technique, namely Radio Frequency Plasma Enhanced Chemical Vapor Deposition (RF-PECVD). The observed alloys were composed of a microcrystalline silicon phase, embedded in an amorphous silicon-carbon matrix the stoichiometry of which can be varied. The complexity of such diphasic materials lies not only in their structure, which combines ordered crystalline domains dispersed in an amorphous matrix, but also on the chemical inhomogeneity of these two phases. Indeed, the presence of different chemical species, with different bond lengths, induces an enhancement of the structural disorder.

Therefore, for the development of a successful device-quality material, it was first necessary to understand the impact of the different deposition parameters on the structural and opto-electronic properties of μc-$Si_{1-x}C_x$:H alloys, and then to test their integration as the absorber layers in photovoltaic devices.

The first phase of this project (chapter 3) has been the identification of the most interesting deposition parameters the impact of which could mostly affect the properties of μc-$Si_{1-x}C_x$:H alloys. Several tests have been performed using a substrate temperature of 285° C, leading to a wide number of series of samples. First of all, it has been demonstrated that the introduction of a *"seed layer"* is essential to obtain microcrystalline growth for very thin layers ($\sim$ 50 nm). In this way it is possible to reduce the amorphous incubation layer to a $5-10$ nm region, reducing the possibilities of carbon-induced amorphization in the very first stages of the growth (Gaiaschi, Ruggeri, Johnson, et al., 2014). Then, it has been shown that different deposition parameters, such as CH_4, SiH_4 and SiF_4 flow rate or RF-power density, can be independently varied aiming always at materials with lower carbon content and hence higher crystalline volume fractions. While some parameters act only on the amount of dissociated methane molecules (such

as the increase of CH_4 flow rate or the increase in w_{RF}), others build on additional etching mechanisms (addition of SiF_4 to the gas mixture), always leading to the same outcome: a higher crystalline volume fraction that thus can be tuned in several ways. No matter which parameter is changed, it has been demonstrated that values of the total carbon-silicon ratio > 0.1 lead to fully a-$Si_{1-x}C_x$:H samples. On the other hand, it is known that the variation of the RF-power does not affect simply the plasma chemistry, determining only the amount of dissociated CH_4 molecules. This deposition parameter, in fact, acts also on the ion bombardment energy (IBE), which is itself detrimental for the crystalline quality of the material. Techniques such as grazing incidence X-ray diffraction and small angle annular dark field scanning transmission electron microscopy (SAADF-STEM), have been proved very useful to determine that the microstructure and the average crystallite size are most strongly controlled by the RF-power density. Indeed, for similar carbon contents, samples deposited at low RF-power density (113 mW/cm^2, in this work) exhibit a 20 % larger average grain size compared to materials deposited using a RF-power density of 226 mW/cm^2. In addition, SAADF-STEM images showed that the low RF-power density conditions lead to a better columnar growth (Gaiaschi, Ruggeri, Gueunier-Farret, et al., 2014).

Due to the ambivalent effect of the RF-power density on both plasma chemistry and IBE, the route through which this parameter has a control on the structural quality of the materials is unclear. For this reason, in this work the possibility of applying the Tailored Voltage Waveform-PECVD technique to the growth of μc-$Si_{1-x}C_x$:H alloys was investigated. However, the application of this technique to such a complex material system has led to ambiguous results. On one hand, for the "low IBE conditions" no considerable variation in the material properties was induced by the variation of the CH_4 flow rate, a surprising result given the strong impact of similarly varying process parameters when using a RF waveform. On the other hand, all samples deposited using the "high IBE" conditions were characterized by a rough and highly inhomogeneous surface, possibly related to induced stress. All these materials exhibited a "*milky*" aspect due to the presence of craters nearly 250 nm deep and consistent with flakes peeling off. The striking change in the relationship between process conditions and film properties as a function of IBE raised more questions than it answered. However, in the end, the films deposited all fell within the same performance ranges as those using standard RF techniques.

Finally, the impact of the substrate temperature was tested by depositing sets of materials at 175° C, and comparing their structural properties with those of alloys deposited at 285° C (Gaiaschi, Gueunier-Farret, et al., 2014). From such a comparison (carbon content, crystalline fraction, average grain size, etc..) it was determined that the substrate temperature has a negligible impact of the structural quality of the materials, opening a broader range of possibilities for the integration of μc-$Si_{1-x}C_x$:H into photovoltaic devices.

Building on all the numerous experimental results it has been possible to propose a model for the growth of μc-$Si_{1-x}C_x$:H thin films, taking into account the role of carbon and the fact that the flux of radicals from the plasma can be assumed to be homogeneous over the whole growing surface. Carbon is assumed to remain in the few monolayers of growth at the microcrystalline silicon surface before being eliminated. Thus, even in the microcrystalline areas there is carbon incorporation, but only in unstable sub-stoichiometric configurations, the sub-surface growth. The elimination of carbon from these sub-stoichiometric phases retards the growth of the

nanocrystalline silicon areas, whereas the growth of the amorphous ones is not retarded. When the CH_x flux is too high the formation of the crystalline structure is completely hindered by the carbon incorporation into the silicon network, leading to a crystalline-to-amorphous transition.

In the second phase of the project, a correlation between the structural properties and the opto-electronic ones was investigated. Through ellipsometry and UV/VIS transmission measurements, an evaluation of the average optical band gap (E_g) and the iso-absorption band gap (E_{04}) were given, demonstrating that when samples are completely amorphous E_g and E_{04} show the same evolution, due to the enlargement of the band gap induced by the increasing carbon-silicon ratio. However, for small carbon-silicon ratios, corresponding to the crystalline regime, the increase of E_g is not mirrored by an increase in E_{04}, which is stable around a mean value of 2 eV.

Additionally, the microcrystalline-to-amorphous phase transition was demonstrated to be accompanied by a deterioration of all transport properties (σ_{dark}, $\sigma_{ph}$and minority carrier diffusion length L_d). These results are in good agreement with what can be found in literature. However, from this analysis, it can be proved that microstructural differences are not negligible. For samples with crystalline volume fraction $f_c^{Raman} > 50$ % the use of a lower RF-power density (113 mW/cm^2) leads to more photo-sensitive materials, compared to higher RF-power density conditions (namely 226 mW/cm^2). Moreover, from the determination of the activation energy from the Arrhenius plot of σ_{dark} in the high temperature range (450-200 K), it has been possible to show that samples deposited at w_{RF} = 113 mW/cm^2 exhibit an activation energy almost 65 % higher than for samples deposited at 226 mW/cm^2. This may be due to a lower density of defects in the material, directly related to better microstructure obtained with the lower RF-power conditions. Nevertheless, all alloys are affected by low values of the activation energy (considering values of E_g and E_{04}) which are indicative of a doped-type behavior, as it can be also found in the literature. In this work the possibility of a post-oxidation mechanism, linked to the porosity of the materials, was investigated. Indeed, unintentional oxygen contamination has also been suggested in the literature but the dependence of this behavior on other RF-power densities, as well as the presence of purifiers on the gas lines, led us to dismiss this possibility. The reason for the pronounced doped-type conductivity in some μc-$Si_{1-x}C_x$:H films remains not yet understood, but evidence suggests it is due to the presence of different kinds of defects at the interface between the silicon crystallites and the surrounding a-$Si_{1-x}C_x$:H tissue, that place the Fermi level closer to the conduction band.

First attempts at studying the defect-related properties of μc-$Si_{1-x}C_x$:H alloys were also presented. The Modulated PhotoCurrent technique was applied to obtain information about the density of states above the Fermi level. The obtained MPC-DOS was compared to what was obtained for a device quality reference a-Si:H. It was shown that μc-$Si_{1-x}C_x$:H alloys exhibit a lower MPC-DOS, compared to a-Si:H. However, despite the relatively high crystalline volume fraction, they are also characterized by the presence of both a conduction band tail (CBT) and deep defects. Nevertheless, the MPC-DOS of the μc-$Si_{1-x}C_x$:H sample deposited with the low RF-power density condition was shown to be lowest, proving that that growth mechanisms clearly differ from one deposition process to the other.

First tests on the behavior of μc-$Si_{1-x}C_x$:H alloys under light-soaking have been conducted, for materials having different crystalline volume frac-

tions. Usually the term "microcrystalline" is often linked to the idea of a material being perfectly stable against light-induced degradation. However, such statement may not hold if the material is mainly amorphous. The light-soaking kinetics of μc-$Si_{1-x}C_x$:H alloys was compared to that of a device quality a-Si:H, showing that while for the latter the degradation starts as soon as the light is turned on, for the former the process is slow and is preceded by a plateau, independent of the crystalline volume fraction. This behavior is still not understood and additional studies could help in identifying the source for the initial stable phase. The analysis of transport properties in the light-soaked state highlighted the increase of the activation energy, compared to the as-deposited state. The possibility of a variation of the Meyer-Neldel (MNR) parameters after light-induced degradation, was considered. However, no influence of this step was found on the MNR parameters. Therefore, the behavior of the activation energy in the light-soaked (and annealed) state is still a matter for further investigation. From the study of the defect related properties in the light-soaked state, it was identified that no matter which is the crystalline volume fraction, these alloys are always sensitive to the light-induced degradation, showing an increase in both CBT and deep defects. Actually, an increase of the MPC-DOS can be related to an increase of the DOS or an increase of the capture coefficient or both. For a-Si:H, it is believed that the increase of the deep states density might cause some modifications of the structure that eventually results in an increase of the CBT states. Additional studies on a-$Si_{1-x}C_x$:H alloys (in their as-deposited and light-soaked state) may help in the understanding of the role of carbon-induced defects. Through numerical simulations of multiple electrical measurements, thanks to a software developed by Christophe Longeaud of the LGEP, it may be possible to identify the presence of carbon-related defects, which could also help explaining the low values of the activation energy. This is a very interesting and promising outlook for the scientific understanding of transport mechanisms in such a complex material.

Finally, the last phase of the project involved the investigation of the possibility of successfully integrating μc-$Si_{1-x}C_x$:H alloys into photovoltaic (PV) devices. Results presented in this manuscript show that, so far, their performance is very modest. However, first it must be remembered that these are the very first devices fabricated using μc-$Si_{1-x}C_x$:H alloys as active layers, then it must be taken into account that device fabrication may induce the rising of several complications due to the choice of the doped layers, the front and back contacts and also the management of the interfaces. Therefore, it is possible that a non optimized integration of new materials into PV devices may lead to unsatisfying results.

Despite the modest performance, the most interesting result that was obtained is the possibility of varying the open-circuit voltage (V_{oc}) by changing the amount of carbon incorporated in the active layer. However, such control is achieved to the detriment of the crystalline volume fraction of the material. High values of V_{oc} can be reached, but the i-layers are completely amorphous and therefore any improvement in stability under light soaking can be assumed to be lost. It was demonstrated that at 175° C a p-i-n structure can be successfully deposited, and higher V_{oc} values can be obtained compared to the high temperature range. This was attributed to the improved quality of the doped layers. Nevertheless, all the investigated conditions led to devices that suffer from low values of J_{sc} and FF.

Margins of improvement can be identified in the mistakes that were highlighted in the manuscript, especially concerning the used p:μc-Si:H layer and the total thickness of the devices. Apart from additional material studies, an interesting perspective for devices employing these materials would involve the fabrication of low power devices using thinner p-doped layers and absorber layers that are at least twice as thick as those used in this work.

Hydrogenated microcrystalline silicon-carbon alloys are interesting materials not only for a possible photovoltaic application, but also from a scientific point of view. However, three years to perform an extensive study on a such a complex material system, with little literature available, have proved to be insufficient to solve all the challenges highlighted by such an ambitious exploratory project. Positive achievements on the understanding of these diphasic alloys have been achieved, however the road to successful integration into PV devices is still very long.

It should be noted that the diodes that were fabricated during this doctoral work were the very first ones integrating this new kind of alloys as an active layer. Therefore, even if modest, the performance achieved can be considered as a step ahead into the identification of the most promising routes to be followed for the development of μc-$Si_{1-x}C_x$:H alloys as photovoltaic materials.

Due to limited reactor time during these three years, and to the necessity of first understanding the material system, additional tests on the devices were left to be performed in order to completely identify the sources of limitations of these materials. Nevertheless, none of the investigated conditions led to an immediate improvement concerning the application of these alloys. Therefore, their successful integration into solar cells requires a stronger effort and collaboration with the whole scientific community.

As we've seen around the world
We won't go away
Cause we'll always feel this way
We're here to stay
And our impact will be felt
[..]Built to last

— Sick of it all

Appendices

A MATRIX DISTRIBUTED ELECTRON CYCLOTRON RESONANCE

A.1 INTRODUCTION

Another goal of the CANASTA project has been to investigate the effect of the application of high density plasma sources when trying to deposit μc-$Si_{1-x}C_x$:H, using the *Matrix Distributed Electron Cyclotron Resonance PECVD* (MDECR-PECVD). In the previous chapters it has been demonstrated that μc-$Si_{1-x}C_x$:H alloys can be efficiently deposited by standard RF-PECVD, but in order to obtain high quality materials, one is limited by the low deposition rate ($\sim$ 0.5 Å/s for w_{RF} = 113 mW/cm^2). However, as it was anticipated in Chapter 2, the use of the MDECR-PECVD technique for the development of μc-$Si_{1-x}C_x$:H alloys is extremely challenging due to the high deposition rates that can be achieved with this plasma technique. Indeed, this characteristic doesn't allow to efficiently implement the use of the *"seed layer"*, as materials always result in a stack of μc-Si:H and μc-$Si_{1-x}C_x$:H, as it will be shown in the following. Moreover, the mass flow controllers available on the LPICM MDECR-PECVD reactor, introduced additional constraints, due to the difficulty of reducing the CH_4 percentage in the gas mixture and therefore to obtain a microcrystalline growth.

A.2 FUNDAMENTALS

A.2.1 Matrix Distributed Electron Cyclotron Resonance Chemical Vapor Deposition

The basic principle of the electron cyclotron resonance (ECR) PECVD is based on the fact that an electron in a static and uniform magnetic field will move in a circle due to the Lorentz force. The result of this force is a helical trajectory around the magnetic lines with a frequency f_{Larmor} and a radius r_{Larmor} given by

$$f_{Larmor} = \frac{qB}{2\pi m} \tag{A.1}$$

$$r_{Larmor} = \frac{mv_{\perp}}{qB}, \tag{A.2}$$

where q is the electron charge, m the electron mass, B the magnetic field and $v_{\perp}$ the component of the electron velocity orthogonal to the magnetic field.

If a linearly polarized electric field with a frequency in the microwave range (f_{MW} = 2.45 GHz) is superimposed on the magnetic field and the electron gyration frequency matches the electric field frequency, then a resonant absorption can take place. The condition $f_{MW} = f_{Larmor}$ indicates that a specific value of the magnetic field ($\sim$ 875 Gauss) is required for the resonant absorption to happen. If all these conditions are met, then the electrons

are trapped in the magnetic field and acquire sufficiently high velocities to dissociate or ionize the precursors molecules. For this to be possible, the pressure in the reactor chamber has to be low enough, typically lower than $\sim$ 10 mTorr, so that the electron can be accelerated during a sufficient number of rotations and can pass several times in the ECR region before any collision. Thus, the mean free path of the electrons l_{eN} must be much larger than their Larmor radius

$$l_{eN} = \frac{1}{\sigma_{eN} N} \gg r_{Larmor} \tag{A.3}$$

where σ_{eN} is the total electron cross section and N is the total gas density.

In Figure A.1 a schematic representation of a MDECR-PECVD reactor is presented. The microwave power is brought to the antenna by a coaxial cable connected to it and injected inside the vacuum chamber via a coaxial feedthrough which ends with a permanent magnet. The matching of the impedance of each antenna has to be optimized manually for the used conditions. The axial magnetic field provides a magnetic confinement and the microwave power is absorbed in the resonant region where the electron cyclotron frequency matches the microwave frequency. The presence of a RF generator ensures the DC-biasing of the substrate (even an insulating one), which allows the control of the energy of the ions towards the substrate.

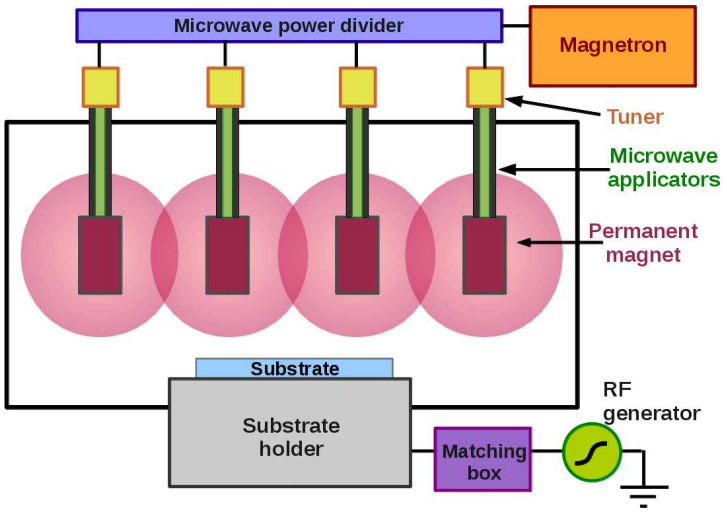

Figure A.1.: Schematic representation of a MDECR-PECVD reactor.

A.2.2 The ATOS reactor

MDECR-PECVD depositions were performed in the ATOS reactor, shown in Figure A.2. This system, built as part of Laurent Kroely's doctorate work, consists of a single "cross-shaped" vessel which, unlike the ARCAM, is also equipped with a load-lock that allows the main chamber not to be exposed to air. In this way a reduction of the oxygen content in the resulting films can be expected (Kroely, 2010). In the flange on the left (see Figure A.2) six microwave antennas are positioned on the edges of an hexagon, with a seventh placed in the center. The magnetic polarities of the antennas on the border are alternating (i.e. North-South-North etc..) in order to form a completely closed magnetic configuration, as can be seen in Figure A.3.

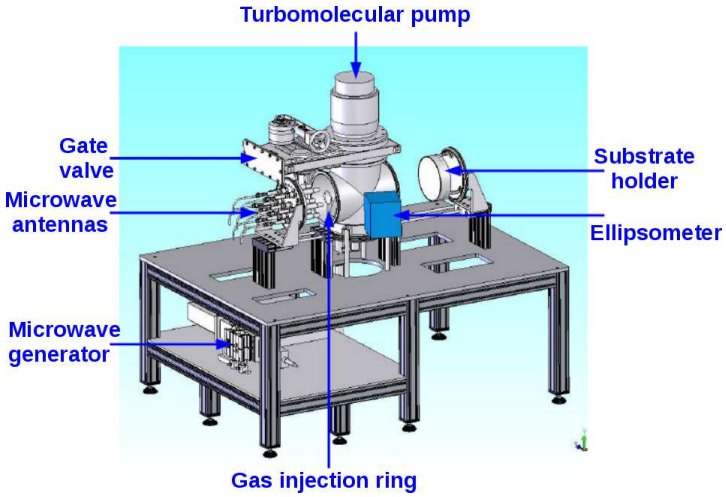

Figure A.2.: General view of the ATOS reactor (Kroely, 2010).

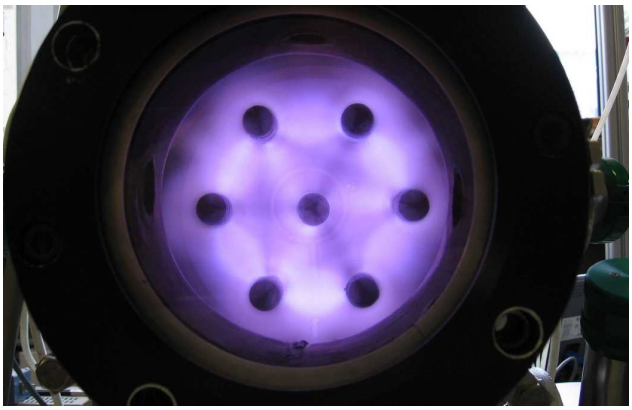

Figure A.3.: Magnetic structure (Kroely, 2010).

The total power generated by the magnetron (for a maximum of 2 kW) is split in eight using microwave power splitters (Pelletier et al., 1967). Coaxial cables are then used to connect these splitters and the microwave antennas. The connection is made using a circulator, a water-cooled load (in order to protect the microwave generator from the reflected power of the antennas and to dissipate it), and a coaxial impedance adapter, which has to be manually tuned for every deposition (in order to reduce the reflected power). In the ATOS reactor the substrate holder is heated using three lamps that allow it to reach a temperature of 250° C which is measured via a pyrometer located in the left flange. A thermocouple is also located just below the surface and a few millimeters away from the edge of the metallic frame holding the substrate.

A.3 HYDROGENATED MICROCRYSTALLINE SILICON–CARBON ALLOYS BY MDECR–PECVD

The use of the MDECR-PECVD technique to the growth of μc-Si$_{1-x}$C$_x$:H is rarely reported in the literature (Cheng et al., 1995). Some reports can be found concerning the application of this technique to the growth of amorphous silicon-carbon alloys (Conde et al., 1999; Racine et al., 2001)

The interest in trying to apply this technique to μc-$Si_{1-x}C_x$:H alloys, lies in the fact that the powder formation that usually happens in standard RF-PECVD plasma at high deposition rates can be avoided with the MDECR plasma technique due to low process pressures (Roca i Cabarrocas, Bulkin, et al., 2008). Therefore, the use of the MDECR-PECVD can hopefully lead to higher deposition rates compared to standard RF-PECVD. Moreover, its possibility to be scaled up to large size reactors gives an additional incentive for the application of this plasma technique.

The main disadvantage of this technique, however, lies mostly in the fact that the optimal conditions to obtain microcrystalline samples still need to be found, whereas for RF-PECVD they are known and only needed to be optimized to find the combination of parameters leading to the materials with the best structural and optoelectronic properties.

A.3.1 Determination of μc-Si:H growth conditions

As the addition of carbon-based precursors into the plasma discharge induces the degradation of the crystalline fraction (due to the absence of sub-stoichiometric crystalline phases), the first step of this work is inevitably the search for deposition conditions leading to μc-Si:H materials characterized by a relatively high crystalline volume fraction, before the addition of CH_4 to the gas mixture.

In Figure A.4 the evolution of the imaginary part of the pseudo-dielectric function is presented for samples deposited varying the SiH_4 flow rate. These materials were deposited on Corning "Eagle" glass at 250° C with a pressure of $\sim$ 9 mTorr, using a pure silane flow rate and a microwave power of 1 kW. It can be seen that a SiH_4 flow rate of 40 sccm leads to a material nearly $\sim$ 130 nm thick, that is completely amorphous (after a 2 minute deposition). Therefore, these conditions are not suitable for the development of μc-$Si_{1-x}C_x$:H alloys. However, by decreasing the SiH_4 flow rate, a transition to a microcrystalline phase occurs. In Figure A.5, the deposition rate as a function of the SiH_4 flow rate is presented and is compared to the deposition rate obtained by standard RF-PECVD using a RF-power density of 113 mW/cm^2 (★).

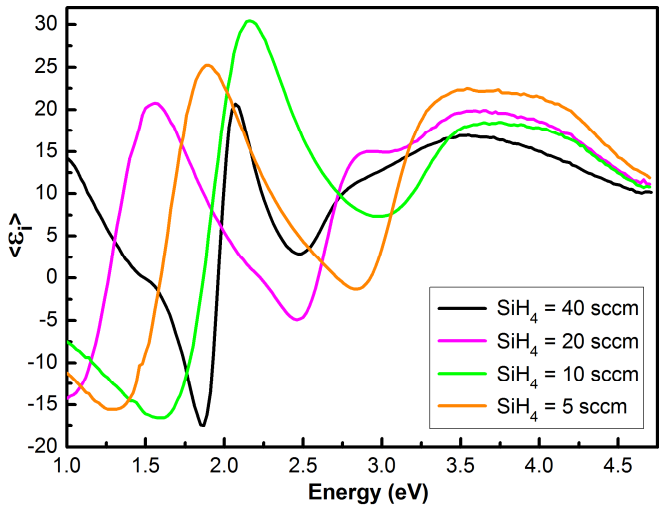

Figure A.4.: Evolution of the imaginary part of the pseudo-dielectric function for materials deposited varying the SiH_4 flow rate.

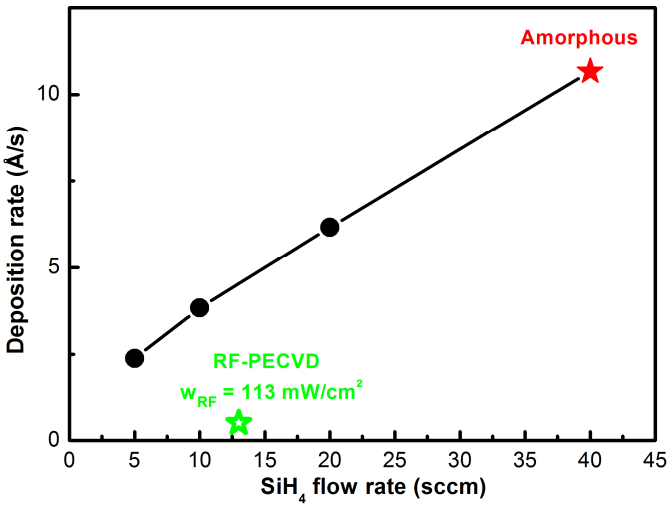

Figure A.5.: Deposition rate as a function of the SiH_4 flow rate, compared to what is obtained by standard RF-PECVD suing a RF-power density of 113 mW/cm^2 (★).

At this point, working at low SiH_4 flow rate seems to be the most promising route to follow. However, what happens when CH_4 is added to the gas mixture? A new sample was made: a 4 minute seed layer was deposited using a SiH_4 flow rate of 5 sccm, followed by a 4 minute deposition of the *"main layer"* adding 5 sccm of CH_4 to the gas mixture. The imaginary part of the pseudo-dielectric function of this sample is presented in Figure A.6.

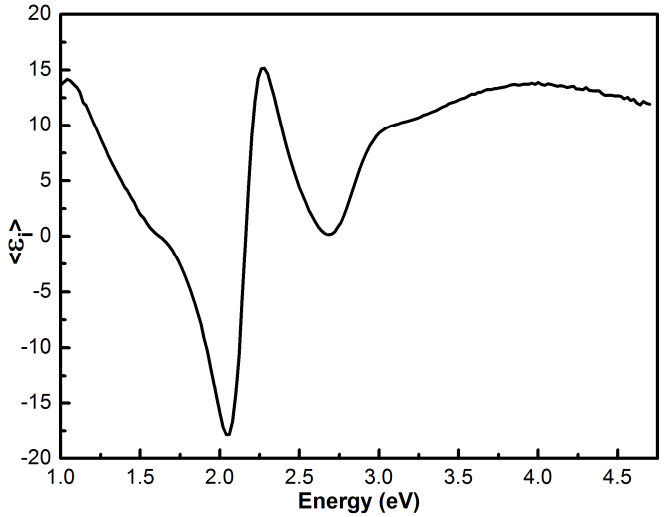

Figure A.6.: Imaginary part of the pseudo-dielectric function for a silicon carbon alloy deposited using SiH_4 = 5 sccm and CH_4 = 5 sccm.

Despite conditions to be sufficient at inducing the growth of μc-Si:H when no CH_4 is included in the gas phase, the addition of 5 sccm of this precursor induces the complete transition to an amorphous phase. As it was shown for RF-PECVD, it is possible that the CH_4/SiH_4 ratio is too high and the threshold of the CH_4 flow rate allowing still to deposit a microcrystalline sample has been crossed. In order to avoid the complete disruption of the microcrystalline growth, a lower CH_4/SiH_4 ratio has to be conserved.

A.3.2 Role of the seed layer

In the previous section it was shown that despite having conditions for the growth of μc-Si:H, the CH_4/SiH_4 ratio plays an important role in the growth of μc-$Si_{1-x}C_x$:H alloys. The lowest CH_4 flow rate allowed by the mass flow controller of the ATOS reactor corresponds to 3 sccm. Hence, in order to reduce the $CH_4/SiH_4/$ ratio, it is necessary to work with an increased SiH_4 flow rate. Previously it was also shown that when using a microwave power of 1 kW, a silane flow rate of 40 sccm results in the growth of a-Si:H for a 2 minute deposition (∼ 130 nm). In order to trigger the microcrystalline growth, the use of a seed layer could be critical.

Different tests concerning the application of a seed layer were made and their deposition conditions are summarized in Table A.1. Samples are grown fixing the temperature and the pressure at 250° C and 9 mTorr, respectively. As a seed layer, the material presented in Figure A.4 (the orange curve), deposited for 4 minutes with a SiH_4 flow rate of 5 sccm, was used.

Table A.1.: Deposition conditions of the μc-Si:H samples deposited by MDECR-PECVD to test the use of the seed layer.

Sample		P (kW)	SiH_4 (sccm)	t (min)	"Seed Layer" (nm)	L (nm)
No seed layer		1	40	2	—	130
Seed 1	seed	1	5	4	60	180
	main layer	1	40	2		
Seed 2	seed	1	5	4	60	195
	main layer	1.5	40	2		

In Figure A.7 the effect of the addition of the seed layer is shown. It can be seen that when using a microwave power of 1 kW, the addition of the seed layer is enough for the phase transition to happen. However, its effect is very weak and the material should still be optimized. On the other hand, when the microwave power during the main layer deposition is increased, a better material is obtained.

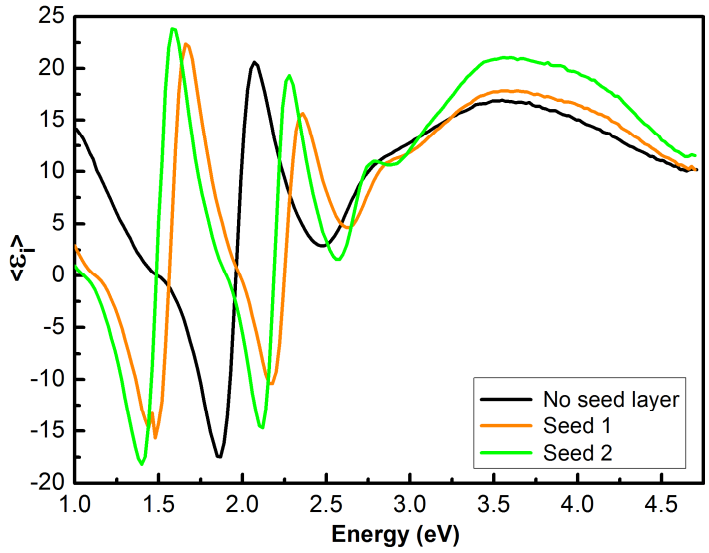

Figure A.7.: Imaginary part of the pseudo-dielectric function of μc-Si:H samples deposited using a seed layer.

The main disadvantage of this procedure is that when passing from the seed layer deposition to the main layer one, the manual adjustment of the gate valve in front of the turbo molecular pump, which is controlling the gas pressure, can take several minutes. The best approach would be to have no interruption between the seed layer growth and the silicon-carbon alloy one. Therefore, it is necessary to find conditions leading to μc-Si:H at higher SiH_4 flow rates.

The microwave power seems to play a non negligible role in the final structure of the material. In Figure A.8 the imaginary part of the pseudo-dielectric function of samples that could be used as seed layers are presented. With the increase in microwave power it is possible to deposit a μc-Si:H sample at SiH_4 flow rates $>$ 40 sccm. But what happens when CH_4 is added to the gas phase?

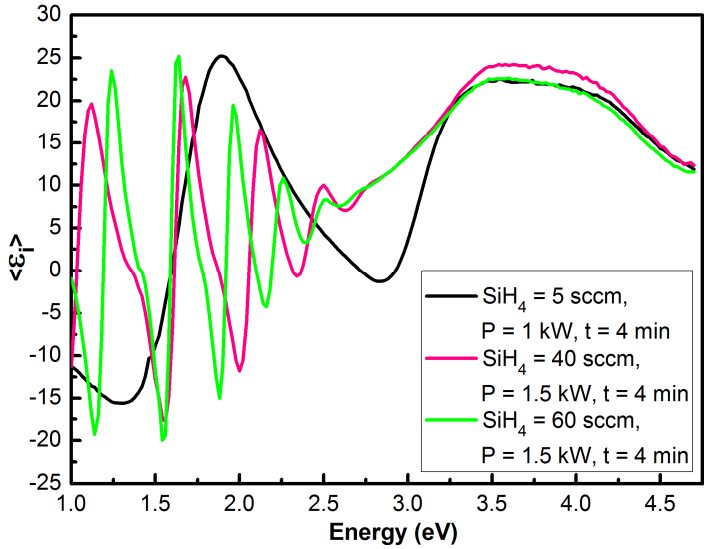

Figure A.8.: Imaginary part of the pseudo-dielectric function of μc-Si:H samples used as seed layers.

A.3.3 Hydrogenated microcrystalline silicon carbon alloys

Two sets of samples were deposited using different SiH_4 flow rates and varying the CH_4 one. Deposition conditions for these two sets of samples are presented in Table A.2. All samples are deposited fixing substrate temperature, microwave power and deposition time at 250°, 1.5 kW and 4 minutes, respectively, for both the seed layer and the main layer deposition. No interruption is made in passing from one layer to the other.

In Figure A.9 the imaginary part of the pseudo-dielectric function of these samples is shown. It can be seen that for both SiH_4 flow rates, with increasing CH_4 flow rate a transition from a microcrystalline to an amorphous phase occurs. Ellipsometric measurements show a transition from a dielectric function with two features (at 3.5 eV and 4.2 eV, typical of μc-Si:H), to an amorphous material.

Table A.2.: Deposition conditions of two set of samples deposited by MDECR-PECVD at different SiH_4 flow rate.

Sample		p (mTorr)	SiH_4 (sccm)	CH_4 (sccm)
SET_{40}	seed	9	40	0
	main layer	9.3	40	3
	seed	9	40	0
	main layer	9.5	40	5
SET_{60}	seed	9	60	0
	main layer	9.3	60	3
	seed	9	60	0
	main layer	9.5	60	5
	seed	9	60	0
	main layer	9.6	60	8

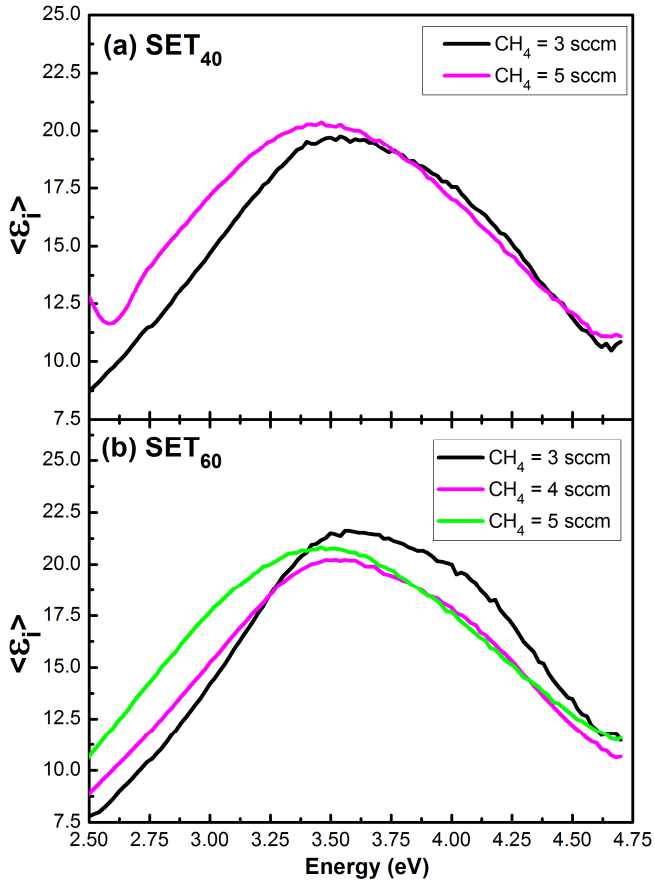

Figure A.9.: Imaginary part of the pseudo-dielectric function of μc-$Si_{1-x}C_x$:H samples deposited by MDECR-PECVD using (a) SiH_4 = 40 sccm (SET_{40}) and (b) SiH_4 = 60 sccm (SET_{60}), varying the CH_4 flow rate.

Similarly, Raman spectra presented in Figure A.10 show the same transition. The Si — Si TO mode at about 520 cm^{-1} decreases with increasing CH_4 flow rate, leading to spectra that are dominated only by the broad peak of the amorphous phase ($\sim$ 480 cm^{-1}). Moreover, no signs of crystalline forms of silicon carbide (TO and LO phonons peaks at $\sim$ 800 cm^{-1} or 960 cm^{-1}) can be seen.

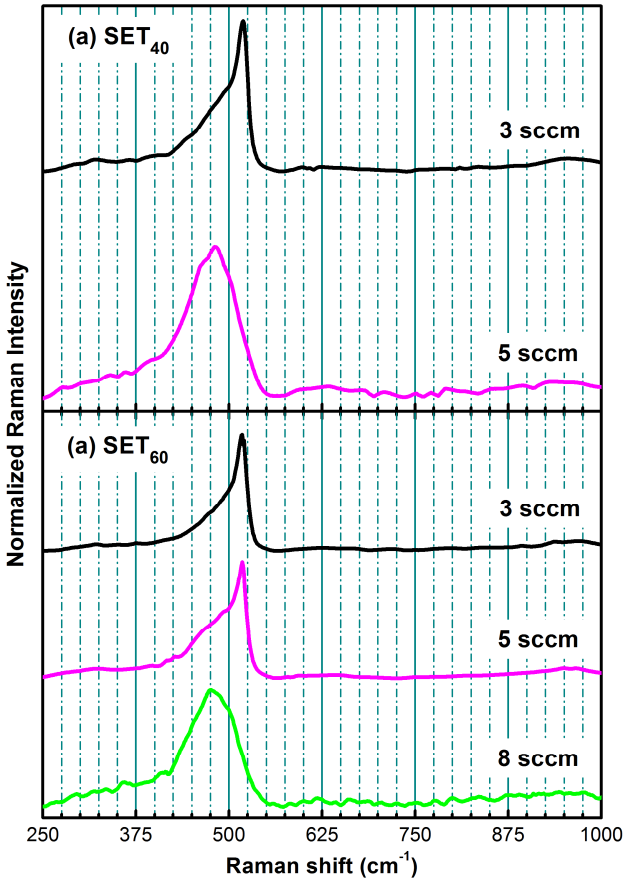

Figure A.10.: Raman spectra of μc-Si$_{1-x}$C$_x$:H samples deposited by MDECR-PECVD using (a) SiH_4 = 40 sccm and (b) SiH_4 = 60 sccm, varying the CH_4 flow rate.

For the sample from SET_{60} deposited using CH_4 = 3 sccm, the GIXRD pattern was acquired using an incident angle $\theta_i = 0.27°$ (penetration depth of nearly 190 nm). The pattern is shown in Figure A.11 and it can be noted that the diffraction peaks are only characteristic of the cubic form of crystalline silicon. No crystalline forms of carbon or silicon carbide can be detected. Moreover, the diffraction pattern (acquired from $2\theta = 25°$ to $2\theta = 100°$) shows all the peaks of the cubic silicon lattice, and the ratios of the peak intensities are those expected for a randomly oriented poly-layer. Finally, the average grain size was determined calculated from the FWHM of the peaks by using the Scherrer approach. The average diameter lies in the range of $6 - 9$ nm.

In Table A.3 the values of the carbon-silicon ratio R_C (obtained from RF-GD-OES measurements)) and of the crystalline volume fraction f_c^{Raman}, calculated from the deconvolution of the Raman spectra are presented.

Finally, in Figure A.12 the microcrystalline structure of the sample from SET_{60}, deposited with CH_4 = 3 sccm, can be observed. The layer is $\sim$ 800 nm thick, with a 4 nm roughness (Figure A.12(a)). It is noteworthy that near the interface with the substrate, a 50 nm thick region characterized by a lower crystalline degree can be observed. Using the Fresnel contrast it has been possible to reveal the presence of a high density of voids, which are homogeneously distributed, except in the first 50 nm (white lines in Figure A.12(b)).

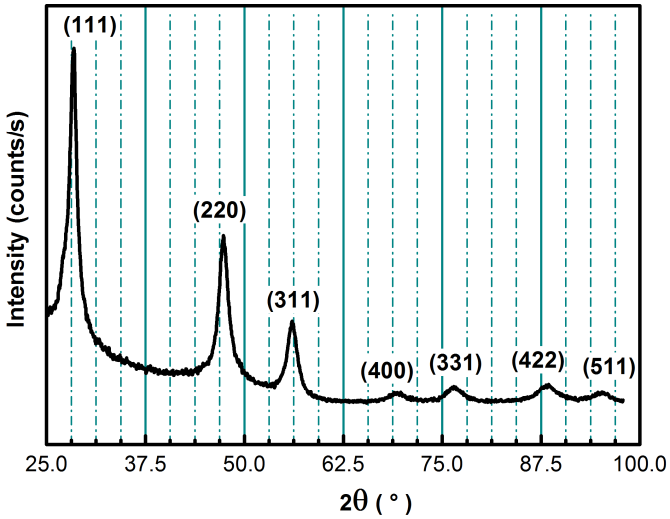

Figure A.11.: GIXRD pattern of the μc-$Si_{1-x}C_x$:H samples deposited by MDECR-PECVD using a SiH_4 flow rate of 60 sccm and a CH_4 flow rate of 3 sccm (SET_{60}). Diffraction planes are labeled in the figure.

Table A.3.: Values of the carbon-silicon ratio R_C and of the crystalline volume fraction f_c^{Raman} of samples deposited by MDECR-PECVD at different SiH_4 flow rate.

Sample	CH_4 (sccm)	L (nm)	R_C	f_c^{Raman} (%)
SET_{40}	3	530	0.028	50
	5	540	0.041	0
SET_{60}	3	720	0.024	55
	4	755	0.029	40
	5	730	0.044	0

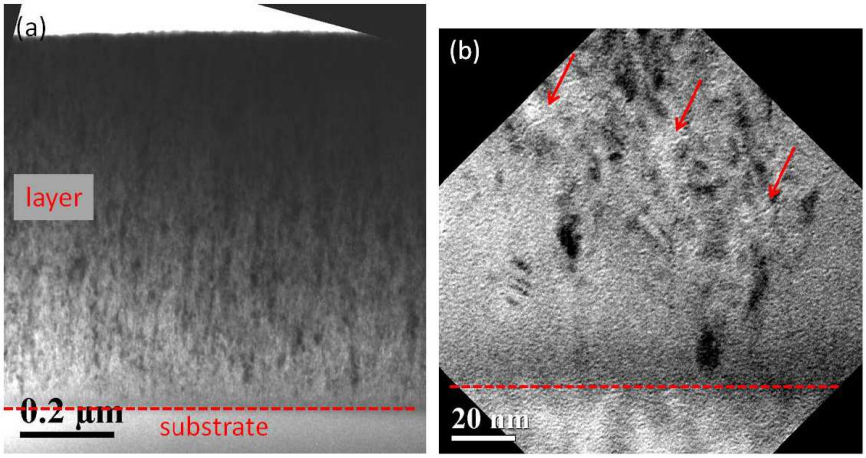

Figure A.12.: TEM micrographs of the μc-$Si_{1-x}C_x$:H samples deposited by MDECR-PECVD using a SiH_4 flow rate of 60 sccm and a CH_4 flow rate of 3 sccm (SET_{60}). In Figure (a) the whole layer is shown, whereas Figure (b) zooms on the interface with the substrate, highlighting a high density of voids.

BIBLIOGRAPHY

Abramov, A. and P. Roca i Cabarrocas (2010). "Addition of SiF_4 to standard SiH_4+H_2 plasma: an effective way to reduce oxygen contamination in µc-Si:H films". In: *physica status solidi (c)* 7, 529–532 (cit. on pp. 90, 129).

Abtew, T. A. et al. (2008). "Electrical conductivity and Meyer-Neldel rule: The role of localized states in hydrogenated amorphous silicon". In: *Journal of Non-Crystalline Solids* 354, 2909–2913 (cit. on p. 149).

Ahn, S.-W., S. E. Lee, and H. M. Lee (2012). "Toward commercialization of triple-junction thin- film silicon solar panel with $>$ 12 % efficiency." In: *27th European Photovoltaic Solar Energy Conference, Frankfurt, Germany* (cit. on p. 3).

Alvarez, F. and M. Sebastiani (1992). "Equilibrium density of defects in hydrogenated amorphous silicon carbon alloys". In: *Journal of Applied Physics* 71, 5969–5975 (cit. on p. 14).

Ambrosone, G., G. Barucca, et al. (2004). "Deposition of microcrystalline silicon-carbon alloys in low power regime". In: *Journal of Non-Crystalline Solids* 338, 163–167 (cit. on p. 88).

Ambrosone, G., U. Coscia, A. Cassinese, et al. (2007). "Low temperature electric transport properties in hydrogenated microcrystalline silicon films". In: *Thin Solid Films* 515, 7629–7633 (cit. on p. 11).

Ambrosone, G., U. Coscia, S. Lettieri, et al. (2004). "Deposition of microcrystalline silicon-carbon films by PECVD". In: *Thin Solid Films* 451, 274–279 (cit. on p. 125).

Arora, R. and A. Kumar (1991). "Electrical Conduction in Chalcogenide Glasses. Applicability of the Meyer-Neldel Rule". In: *physica status solidi (a)* 125, 273–278 (cit. on p. 149).

Bailat, J. et al. (2002). "Influence of substrate on the microstructure of microcrystalline silicon layers and cells". In: *Journal of Non-Crystalline Solids* 299, 1219–1223 (cit. on p. 8).

Balberg, I., A. E. Delahoy, and H. A. Weakliem (1988). "Self-consistency and self-sufficiency of the photocarrier grating technique". In: *Applied Physics Letters* 53, 992–994 (cit. on p. 44).

Basa, D. K. and F. W. Smith (1990). "Annealing and crystallization processes in a hydrogenated amorphous Si-C alloy film". In: *Thin Solid Films* 192, 121–133 (cit. on p. 28).

Benagli, S. et al. (2009). "High-Efficiency Amorphous Silicon Devices on LPCVD-ZnO TCO Prepared in Industrial KAI TM-M R&D Reactor". In: *24th European Photovoltaic Solar Energy Conference, 21-25 September 2009, Hamburg, Germany*, 2293–2298 (cit. on p. 3).

Beyer, W. (2003). "Diffusion and evolution of hydrogen in hydrogenated amorphous and microcrystalline silicon". In: *Solar Energy Materials & Solar Cells* 78, 235–267 (cit. on p. 8).

Birkholz, M. (2006). *Thin Film Analysis by X-Ray Scattering*. Wiley-VCH Verlag GmbH & Co. KGaA (cit. on pp. 34, 35).

Boulitrop, F. et al. (1985). "Disorder and density of defects in hydrogenated amorphous silicon-carbon". In: *Solid State Communications* 54, 107–110 (cit. on p. 14).

Breidthardt, A. (2011). *German government wants nuclear exit by 2022 at latest*. Ed. by Reuters. URL: http://uk.reuters.com/article/2011/05/30/us-germany-nuclear-idUKTRE74Q2P120110530 (cit. on p. xl).

Bronneberg, A. C. et al. (2012). "Ion-induced effects on grain boundaries and a-Si:H tissue quality in microcrystalline silicon films". In: *Journal of Vacuum Science & Technology A* 30, 061512 (cit. on p. 115).

Brüggemann, R. (2011). "Steady-State Photocarrier Grating Method". In: *Advanced Characterization Techniques for Thin Film Solar Cells*. Wiley-VCH Verlag GmbH & Co. KGaA, 177–202 (cit. on pp. 44, 45).

Brüggemann, R. et al. (1990). "An evaluation of phase-shift analysis of modulated photocurrents". In: *Philosophical Magazine Part B* 62, 29–45 (cit. on pp. 46, 47).

Bruneau, B. et al. (2014). "Growth mechanisms study of microcrystalline silicon deposited by SiH4/H2 plasma using tailored voltage waveforms". In: *Journal of Applied Physics* 115, 084901–084909 (cit. on p. 115).

Bullot, J. and M.P. Schmidt (1987). "Physics of Amorphous Silicon-Carbon Alloys". In: *physica status solidi (b)* 143, 345–418 (cit. on pp. 12, 14, 15, 27, 81, 118).

Bustarret, E., M. A. Hachicha, and M. Brunel (1988). "Experimental determination of the nanocrystalline volume fraction in silicon thin films from Raman spectroscopy". In: *Applied Physics Letters* 52, 1675–1677 (cit. on pp. 32, 33).

Cao, Y. et al. (2013). "Hydrogenated microcrystalline silicon germanium as bottom sub-cell absorber for triple junction solar cell". In: *Solar Energy Materials & Solar Cells* 114, 161–164 (cit. on p. xlii).

Cardona, M. (1983). "Vibrational Spectra of Hydrogen in Silicon and Germanium". In: *physica status solidi (b)* 118, 463–481 (cit. on p. 27).

Carius, R. et al. (1997). "Electronic Properties of Microcrystalline Silicon". In: *MRS Proceedings* 467 (cit. on p. 10).

Carlson, D. E. and C. R. Wronski (1976). "Amorphous silicon solar cell". In: *Applied Physics Letters* 28, 671–673 (cit. on p. 3).

Catherine, Y. and G. Turban (1979). "Reactive plasma deposited $Si_xC_yH_z$ films". In: *Thin Solid Films* 60, 193–200 (cit. on p. 13).

Catherine, Y., G. Turban, and B. Grolleau (1981). "Reaction mechanisms in plasma deposition of Si_xC_{1-x}:H films". In: *Thin Solid Films* 76, 23–34 (cit. on pp. 13, 14, 79, 114).

Chang, P. K. et al. (2011). "Development of high efficiency p-i-n amorphous silicon solar cells with the p-μc-Si:H/p-a-SiC:H double window layer". In: *Solar Energy Materials & Solar Cells* 95, 2659–2663 (cit. on p. 11).

Cheng, K. L. et al. (1995). "Microcrystalline SiC Films Grown by Electron Cyclotron Resonance Chemical Vapor Deposition at Low Temperatures". In: *Japanese Journal of Applied Physics* 34, 5527–5532 (cit. on p. 195).

Chittick, R. C., J. H. Alexander, and H. F. Sterling (1969). "The Preparation and Properties of Amorphous Silicon". In: *Journal of The Electrochemical Society* 116, 77–81 (cit. on p. 7).

Chopra, K. L., P. D. Paulson, and V. Dutta (2004). "Thin-film solar cells: an overview". In: *Progress in Photovoltaics: Research and Applications* 12, 69–92 (cit. on p. 7).

Cicala, G. et al. (2001). In: *Applied Surface Science* 184, 66 (cit. on p. 93).

Collins, R. W. et al. (2003). "Evolution of microstructure and phase in amorphous, protocrystalline, and microcrystalline silicon studied by real time spectroscopic ellipsometry". In: *Solar Energy Materials & Solar Cells* 78, 143–180 (cit. on p. 8).

Conde, J. P. et al. (1999). "Optoelectronic and structural properties of amorphous silicon-carbon alloys deposited by low-power electron-cyclotron resonance plasma-enhanced chemical-vapor deposition". In: *Journal of Applied Physics* 85, 3327–3338 (cit. on p. 195).

Coscia, U., G. Ambrosone, S. Lettieri, P. Maddalena, and S. Ferrero (2006). "Microcrystalline silicon-carbon films deposited by silane-methane mixture highly diluted in hydrogen". In: *Thin Solid Films* 511, 399–403 (cit. on p. 100).

Coscia, U., G. Ambrosone, S. Lettieri, P. Maddalena, P. Rava, et al. (2003). "Power density effects on the growth of microcrystalline silicon-carbon alloys by PECVD". In: *Thin Solid Films* 427, 284–288 (cit. on pp. 28, 87).

Coscia, U., G. Ambrosone, S. Lettieri, P. Maddalena, V. Rigato, et al. (2005). "Preparation of microcrystalline silicon-carbon films". In: *Solar Energy Materials & Solar Cells* 87, 433–444 (cit. on p. 16).

Coscia, U et al. (2007). "Carbon incorporation in silicon-carbon films grown at different substrate temperatures". In: *Thin Solid Films* 515, 7634–7638 (cit. on p. 114).

Cuony, P. et al. (2010). "Mixed-phase p-type silicon oxide containing silicon nanocrystals and its role in thin-film silicon solar cells". In: *Applied Physics Letters* 97, 213502 (cit. on p. 158).

Czarnetzki, U. et al. (2009). "The Electrical Asymmetry Effect - A novel and simple method for separate control of ion energy and flux in capacitively coupled RF discharges". In: *Journal of Physics: Conference series* 162, 012010 (cit. on p. 19).

Dasgupta, A. et al. (1999). "Substrate temperature: A critical parameter for the growth of microcrystalline silicon-carbon alloy thin films at low power". In: *Journal of Materials Research* 14, 2554–2559 (cit. on p. 16).

Delattre, P.-A. et al. (2013). "Radio-frequency capacitively coupled plasmas excited by tailored voltage waveforms: comparison of experiment and particle-in-cell simulations". In: *Journal of Physics D: Applied Physics* 46, 235201 (cit. on p. 20).

Demichelis, F., G. Crovini, et al. (1994). "Structural and optoelectronic properties of doped microcrystalline silicon carbide films". In: *Semiconductor Science and Technology* 9, 1543–1548 (cit. on pp. 125, 135).

Demichelis, F., F. Giorgis, and C. F. Pirri (1995). "Effects of hydrogen dilution of silane/methane gas mixtures on growth and structure of a-$Si_{1-x}C_x$:H alloys". In: *Solid State Communications* 96, 17–21 (cit. on pp. 3, 17).

Demichelis, F., C. F. Pirri, and E. Tresso (1992a). "Influence of doping on the structural and optoelectronic properties of amorphous and microcrystalline silicon carbide". In: *Journal of Applied Physics* 72, 1327–1333 (cit. on p. 15).

– (1992b). "Microcrystallization formation in silicon carbide thin films". In: *Philosophical Magazine Part B* 66, 135–146 (cit. on p. 16).

– (1994). "Electrical transport properties of diphasic amorphous-microcrystalline silicon carbon alloys". In: *International Journal of Modern Physics B* 8, 2059–2074 (cit. on pp. xxii, xxiv, 123, 125, 133, 135, 136).

Eaton, P. and P. West (2010). *Atomic force microscopy*. Oxford Univ. Press (cit. on p. 31).

Egerton, R.F. (2009). "Electron energy-loss spectroscopy in the TEM". In: *Reports on Progress in Physics* 72, 016502 (cit. on p. 65).

El Khakani, M. A. et al. (1994). "Hardness and Young's modulus of amorphous a-SiC thin films determined by nanoindentation and bulge tests". In: *Journal of Materials Research* 9, 96–103 (cit. on p. 11).

Escobar Galindo, R. et al. (2009). "Comparative depth-profiling analysis of nanometer-metal multilayers by ion-probing techniques". In: *TrAC Trends in Analytical Chemistry* 28, 494–505 (cit. on p. 26).

Fang, C. J. et al. (1980). "Bonding of fluorine in amorphous hydrogenated silicon". In: *Phys. Rev. B* 22, 6140–6148 (cit. on p. 28).

Fejfar, A., T. Mates, O. Certík, et al. (2004). "Model of electronic transport in microcrystalline silicon and its use for prediction of device performance". In: *Journal of Non-Crystalline Solids* 338, 303–309 (cit. on p. 60).

Fejfar, A., T. Mates, C. Koch, et al. (2001). "Microscopic Aspects Of Charge Transport In Hydrogenated Microcrystalline Silicon". In: *MRS Proceedings* 664, A16.1 (cit. on p. 62).

Finger, F. et al. (2009). "Microcrystalline silicon carbide alloys prepared with HWCVD as highly transparent and conductive window layers for thin film solar cells". In: *Thin Solid Films* 517, 3507–3512 (cit. on p. 76).

Franz, G. (2009). *Low pressure plasmas and microstructuring technology*. Springer (cit. on p. 18).

Fuhs, W., P. Kanschat, and K. Lips (2000). "Bandtails and defects in microcrystalline silicon (μc-Si:H)". In: *Journal of Vacuum Science & Technology B* 18, 1792–1795 (cit. on p. 11).

Gaiaschi, S., M.-E. Gueunier-Farret, and E. V. Johnson (2014). "Low temperature hydrogenated microcrystalline silicon-carbon alloys deposited by RF-PECVD". In: *Physica Status Solidi C (Accepted)* (cit. on pp. xvii, xliv, 186).

Gaiaschi, S., R. Ruggeri, M.-E. Gueunier-Farret, et al. (2014). "Use of radio frequency power, silicon tetrafluoride and methane as parameters to tune structural properties of hydrogenated microcrystalline silicon carbon alloys". In: *Journal of Physics D (Accepted)* (cit. on pp. xix, xliv, 114, 186).

Gaiaschi, S., R. Ruggeri, E. V. Johnson, et al. (2014). "Structural properties of hydrogenated microcrystalline silicon-carbon alloys deposited by Radio Frequency Plasma Enhanced Chemical Vapor Deposition: Effect of microcrystalline silicon seed layer and methane flow rate". In: *Thin Solid Films* 550, 312–318 (cit. on pp. xii, xliv, 185).

Giorgis, F. and C. F. Pirri (2001). "Chapter 5 - Growth, characterization, and physical properties of noncrystalline and nanostructured silicon-based alloys". In: *Silicon-Based Material and Devices*, 187–235 (cit. on p. 15).

Godet, C., B. Marchon, and M. P. Schmidt (1987). "Characterization of microcrystallinity in hydrogenated silicon thin films". In: *Thin Solid Films* 155, 227–242 (cit. on p. 36).

Goldstein, B. et al. (1988). "Properties of p^+ microcrystalline films of SiC:H deposited by conventional RF glow discharge". In: *Applied Physics Letters* 53, 2672 (cit. on p. 75).

Green, M. A. et al. (2014). "Solar cell efficiency tables (version 44)". In: *Progress in Photovoltaics: Research and Applications* 22, 701–710 (cit. on p. 3).

Grimm, W. (1967). *Glimmentladungsroehre*. German patent DE1589389 (cit. on p. 22).

Guha, S. et al. (1999). "Structural, defect, and device behavior of hydrogenated amorphous Si near and above the onset of microcrystallinity". In: *Applied Physics Letters* 74, 1860–1862 (cit. on p. 7).

Hamma, S. and P. Roca i Cabarrocas (2001). "Low-temperature growth of thick intrinsic and ultrathin phosphorous or boron-doped microcrystalline silicon films: Optimum crystalline fractions for solar cell applications". In: *Solar Energy Materials & Solar Cells* 69, 217–239 (cit. on pp. 157, 158).

Hattori, K. et al. (2003). "Photocarrier transport in undoped microcrystalline silicon studied by the modulated photocurrent technique". In: *Journal of Applied Physics* 94, 5071–5082 (cit. on p. 10).

Heil, B. G. et al. (2008). "On the possibility of making a geometrically symmetric RF-CCP discharge electrically asymmetric". In: *Journal of Physics D: Applied Physics* 41, 165202 (cit. on p. 19).

Hendriks, M. et al. (1984). "Additional X-ray and electron diffraction peaks of polycrystalline silicon films". In: *Thin Solid Films* 113, 59–72 (cit. on p. 88).

Houben, L., M. Luysberg, and R. Carius (2003). "Microtwinning in microcrystalline silicon and its effect on grain-size measurements". In: *Phys. Rev. B* 67, 045312 (cit. on pp. 8, 36).

Houben, L., M. Luysberg, P. Hapke, et al. (1998). "Structural properties of microcrystalline silicon in the transition from highly crystalline to amorphous growth". In: *Philosophical Magazine A* 77, 1447–1460 (cit. on p. 8).

Hourd, A. C., D. L. Melville, and W. E. Spear (1991). "Electronic properties of amorphous and microcrystalline silicon prepared in a microwave plasma from SiF_4". In: *Philosophical Magazine Part B* 64, 533–550 (cit. on p. 10).

Iacona, F. et al. (2004). "Formation and evolution of luminescent Si nanoclusters produced by thermal annealing of SiO_x films". In: *Journal of Applied Physics* 95, 3723–3732 (cit. on p. 39).

Iqbal, Z. et al. (1981). "Raman scattering from small particle size polycrystalline silicon". In: *Solid State Communications* 37, 993–996 (cit. on p. 32).

Irsigler, P., D. Wagner, and D. J. Dunstan (1983). "On the application of the Meyer-Neldel rule to a-Si:H". In: *Journal of Physics C: Solid State Physics* 16, 6605 (cit. on p. 149).

Itoh, T. et al. (2001). "Preparation of silicon-carbon alloy films by hot-wire CVD and their properties". In: *Thin Solid Films* 395, 240–243 (cit. on p. 15).

Jackson, W. B. et al. (1985). "Energy dependence of the optical matrix element in hydrogenated amorphous and crystalline silicon". In: *Phys. Rev. B* 31, 5187–5198 (cit. on p. 5).

Janz, S. (2006). "Amorphous Silicon Carbide for Photovoltaic Applications". PhD thesis. Fraunhofer institut for solar energy systems (cit. on p. 11).

Jellison, G. E. and F. A. Modine (1996). "Parameterization of the optical functions of amorphous materials in the interband region". In: *Applied Physics Letters* 69, 371–373 (cit. on p. 29).

Johnson, E. V., P.-A. Delattre, and J.-P. Booth (2012). "Microcrystalline silicon solar cells deposited using a plasma process excited by tailored voltage waveforms". In: *Applied Physics Letters* 100.133504 (cit. on p. 108).

Johnson, E. V., N. P. Kherani, and S. Zukotynski (2006). "Raman scattering characterization of SF-PECVD-grown hydrogenated microcrystalline silicon thin films using growth surface electrical bias". In: *Journal of Materials Science: Materials in Electronics* 17, 801–813 (cit. on p. 33).

Johnson, E. V., S. Pouliquen, et al. (2012). "Hydrogenated microcrystalline silicon thin films deposited by RF-PECVD under low ion bombardment energy using voltage waveform tailoring". In: *Journal of Non-Crystalline Solids* 358, 1974–1977 (cit. on p. 107).

Johnson, E. V., T. Verbeke, et al. (2010). "Nanocrystalline silicon film growth morphology control through RF waveform tailoring". In: *Journal of Physics D: Applied Physics* 43, 412001 (cit. on p. 107).

Kaneko, T. et al. (1994). "Change in crystalline morphologies of polycrystalline silicon films prepared by radio-frequency plasma-enhanced chem-

ical vapor deposition using SiF_4+H_2 gas mixture at 350 °C". In: *Applied Physics Letters* 64, 1865–1867 (cit. on p. 33).

Keppner, H. et al. (1997). "The "Micromorph" cell: a new way to high-efficiency-low-temperature crystalline silicon thin-film cell manufacturing?" In: *AIP Conference Proceedings* 394, 271–281 (cit. on p. xlii).

Kim, S. et al. (2013). "Remarkable progress in thin-film silicon solar cells using high-efficiency triple-junction technology". In: *Solar Energy Materials & Solar Cells* 119, 26–35 (cit. on p. xlii).

Kirbs, V., T. Drusedau, and H. Fiedler (1990). "Thermally induced metastability and the Meyer-Neldel rule in hydrogenated amorphous silicon". In: *Journal of Physics: Condensed Matter* 2, 7473 (cit. on p. 149).

Kirner, S. (2013). "Development of wide band gap materials for thin film silicon solar cells". PhD thesis. Technical University of Berlin (cit. on pp. 13, 15).

Kleider, J. P., C. Longeaud, R. Brüggemann, et al. (2001). "Electronic and topographic properties of amorphous and microcrystalline silicon thin films". In: *Thin Solid Films* 383, 57–60 (cit. on p. 11).

Kleider, J. P., C. Longeaud, and O. Glodt (1991). "Study of the density of states of hydrogenated amorphous silicon from time-of-flight and modulated photocurrent experiments". In: *Journal of Non-Crystalline Solids* 137, 447–450 (cit. on p. 46).

Klyui, N. I. et al. (2002). "Silicon solar cells with antireflection diamond-like carbon and silicon carbide films". In: *Solar Energy Materials & Solar Cells* 72, 597–603 (cit. on p. 11).

Kočka, J. et al. (2004). "The physics and technological aspects of the transition from amorphous to microcrystalline and polycrystalline silicon". In: *physica status solidi (c)* 1, 1097–1114 (cit. on pp. 8, 60).

Koh, J. et al. (1998). "Optimization of hydrogenated amorphous silicon p-i-n solar cells with two-step i layers guided by real-time spectroscopic ellipsometry". In: *Applied Physics Letters* 73, 1526–1528 (cit. on p. 8).

Kondo, M., M. Fukawa, et al. (2000). "High rate growth of microcrystalline silicon at low temperatures". In: *Journal of Non-Crystalline Solids* 266, 84–89 (cit. on p. 106).

Kondo, M., Y. Toyoshima, et al. (1996). "Substrate dependence of initial growth of microcrystalline silicon in plasma-enhanced chemical vapor deposition". In: *Journal of Applied Physics* 80, 6061–6063 (cit. on p. 69).

Kroely, L. (2010). "Process and material challenges in the high rate deposition of microcrystalline silicon thin films and solar cells by Matrix Distributed Electron Cyclotron Resonance plasma". PhD thesis. Ecole Polytechnique (cit. on pp. 158, 194, 195).

Ledoux, G. et al. (2001). "Crystalline silicon nanoparticles as carriers for the Extended Red Emission". In: *A&A* 377, 707–720 (cit. on p. 3).

Lee, W. Y. (1980). "X-ray photoelectron spectroscopy and Auger electron spectroscopy studies of glow discharge $Si_{1-x}C_x$:H films". In: *Journal of Applied Physics* 51, 3365–3372 (cit. on p. 14).

Lieberman, M. and A. J. Lichtenberg (2005). John Wiley and Sons, Inc. (cit. on p. 18).

Liu, H. and M. Xu (1986). "The Staebler-Wronski effect in microcrystalline silicon films". In: *Solid State Communications* 58, 601–603 (cit. on p. 11).

Longeaud, C. and J. P. Kleider (1992). "General analysis of the modulated-photocurrent experiment including the contributions of holes and electrons". In: *Phys. Rev. B* 45, 11672–11684 (cit. on p. 46).

Longeaud, C., J. P. Kleider, et al. (1998). "Properties of a new a-Si:H-like material: hydrogenated polymorphous silicon". In: *Journal of Non-Crystalline Solids* 227, 96–99 (cit. on p. 7).

Longeaud, C., D. Roy, and O. Saadane (2002). "Role of interstitial hydrogen and voids in light-induced metastable defect formation in hydrogenated amorphous silicon: A model". In: *Phys. Rev. B* 65, 085206 (cit. on pp. 50, 134, 148).

Lucovsky, G. et al. (1992). "Transport and Microstructure of Microcrystalline Silicon Alloys". In: *Symposium F - Microcrystalline Semiconductors-Materials Science and Devices*. Vol. 283 (cit. on p. 149).

Luysberg, M. et al. (1997). "Structure and growth of hydrogenated microcrystalline silicon: Investigation by transmission electron microscopy and Raman spectroscopy of films grown at different plasma excitation frequencies". In: *Philosophical Magazine A* 75, 31–47 (cit. on pp. 8, 88).

Matsuda, A. (1999). "Growth mechanism of microcrystalline silicon obtained from reactive plasmas". In: *Thin Solid Films* 337, 1–6 (cit. on pp. 9, 82, 101, 107).

– (2004). "Microcrystalline silicon.: Growth and device application". In: *Journal of Non-Crystalline Solids* 338, 1–12 (cit. on p. 106).

Matsuda, A. et al. (2003). "Control of plasma chemistry for preparing highly stabilized amorphous silicon at high growth rate". In: *Solar Energy Materials & Solar Cells* 78, 3–26 (cit. on p. 6).

Matsumoto, Y. et al. (1990). "A new type of high efficiency with a low-cost solar cell having the structure of a μc-SiC/polycrystalline silicon heterojunction". In: *Journal of Applied Physics* 67, 6538–6543 (cit. on p. 155).

McNally, J. R., G. R. Harrison, and E. Rowe (1947). "A hollow cathode source applicable to spectrographic analysis for the halogens and gases". In: *Journal of Optical Society of America* 37, 93–98 (cit. on p. 22).

Meier, J. et al. (1994). "Intrinsic microcrystalline silicon (μc-Si:H)-a promising new thin film solar cell material". In: *Photovoltaic Energy Conversion, 1994., Conference Record of the Twenty Fourth. IEEE Photovoltaic Specialists Conference - 1994, 1994 IEEE First World Conference on*. Vol. 1, 409–412 (cit. on p. xlii).

Meillaud, F. et al. (2005). "Light-induced degradation of thin film amorphous and microcrystalline silicon solar cells". In: *Photovoltaic Specialists Conference, 2005. Conference Record of the Thirty-first IEEE*, 1412–1415 (cit. on p. 11).

Merten, J. et al. (1998). "Improved equivalent circuit and analytical model for amorphous silicon solar cells and modules". In: *IEEE Transactions on Electron Devices* 45, 423–429 (cit. on p. 52).

Mishima, Y. et al. (1982). "Characterization of plasma-deposited microcrystalline silicon". In: *Philosophical Magazine Part B* 46, 1–12 (cit. on p. 33).

Morimoto, A. et al. (1982). "Defects in hydrogenated amorphous silicon-carbon alloy films prepared by glow discharge decomposition and sputtering". In: *Journal of Applied Physics* 53, 7299–7305 (cit. on p. 14).

Mott, N. (1987). "The mobility edge since 1967". In: *Journal of Physics C: Solid State Physics* 20, 3075 (cit. on p. 5).

Nakahata, K. et al. (2000). "Fabrication of Polycrystalline Silicon Films from $SiF_4/H_2/SiH_4$ Gas Mixture Using Very High Frequency Plasma Enhanced Chemical Vapor Deposition with *In Situ* Plasma Diagnostics and Their Structural Properties". In: *Japanese Journal of Applied Physics* 39, 3294–3301 (cit. on p. 90).

Nakamura, K. et al. (1995). "Roles of Atomic Hydrogen in Chemical Annealing". In: *Japanese Journal of Applied Physics* 34, 442 (cit. on p. 9).

Nasuno, Y. et al. (2002). "Formation of interface defects by enhanced impurity diffusion in microcrystalline silicon solar cells". In: *Applied Physics Letters* 81, 3155 (cit. on pp. 99, 157).

Nelis, T. and J. Pallosi (2006). "Glow Discharge as a Tool for Surface and Interface Analysis". In: *Applied Spectroscopy Reviews* 41, 227–258 (cit. on p. 22).

Nelis, T. and R. Payling (2003). "Glow Discharge Optical Emission Spectrometry". In: *Surface Analysis Methods in Materials Science*. Vol. 23. Springer Series in Surface Sciences, 553–559 (cit. on p. 23).

Noda, M. et al. (2003). "Large area thin film Si tandem module production using VHF plasma with a ladder-shaped electrode". In: *Photovoltaic Energy Conversion, 2003. Proceedings of 3rd World Conference on*. Vol. 2, 1849–1851 (cit. on p. xlii).

NREL - National center for photovoltaics (2013). *Research Cell Efficiency Records*. URL: http://www.nrel.gov/ncpv/ (cit. on p. xli).

Oheda, H. (1981). "Phase-shift analysis of modulated photocurrent: Its application to the determination of the energetic distribution of gap states". In: *Journal of Applied Physics* 52, 6693–6700 (cit. on p. 46).

Okada, T. et al. (1985). "Probing the Crystallinity of Evaporated Silicon Films by Raman Scattering". In: *Japanese Journal of Applied Physics* 24, 161–165 (cit. on p. 33).

Okur, S. et al. (2004). "Electronic transport properties of microcrystalline silicon thin films prepared by VHF-PECVD". In: *Journal of Materials Science: Materials in Electronics* 15, 187–191 (cit. on p. 144).

Osten, H. J. (1996). "Supersaturated carbon in silicon and silicon/germanium alloys". In: *Materials Science and Engineering: B* 36, 268–274 (cit. on p. 15).

– (2000). "MBE growth and properties of supersaturated, carbon-containing silicon/germanium alloys on Si(001)". In: *Thin Solid Films* 367, 101–111 (cit. on pp. 11, 79).

Overhof, H. (1998). "Fundamental concepts in the physics of amorphous semiconductors". In: *Journal of Non-Crystalline Solids* 227, 15–22 (cit. on p. 4).

Overhof, H. and W. Beyer (1983). "Electronic transport in hydrogenated amorphous silicon". In: *Philosophical Magazine Part B* 47, 377–392 (cit. on p. 149).

Patterson, M. M., H.-Y. Chu, and A. E. Wendt (2007). "Arbitrary substrate voltage wave forms for manipulating energy of bombarding ions during plasma processing". In: *Plasma Sources Science and Technology* 16, 257 (cit. on p. 21).

Pelletier, J. et al. (1967). U.S. Patent 6727656 (cit. on p. 195).

Pennycook, S. J. (1989). "Z-contrast stem for materials science". In: *Ultramicroscopy* 30, 58–69 (cit. on p. 39).

Pieters, B. E. (2008). "Characterization of Thin-film silicon materials and solar cells through numerical modeling". PhD thesis. Delft University of Technology (cit. on pp. 4, 5).

Pisonero, J. et al. (2006). "Glow-discharge spectrometry for direct analysis of thin and ultra-thin solid films". In: *TrAC Trends in Analytical Chemistry* 25, 11–18 (cit. on p. 22).

Powell, A. R. et al. (1993). "$Si_{1-x-y}Ge_xC_y$ growth and properties of the ternary system". In: *Journal of Crystal Growth* 127, 425–429 (cit. on p. 15).

Python, M. et al. (2010). "Microcrystalline silicon solar cells: effect of substrate temperature on cracks and their role in post-oxidation". In: *Progress in Photovoltaics: Research and Applications* 18, 491–499 (cit. on p. 8).

Racine, B. et al. (2001). "Properties of amorphous carbon-silicon alloys deposited by a high plasma density source". In: *Journal of Applied Physics* 90, 5002–5012 (cit. on p. 195).

Ram, S. K., S. Kumar, and P. Roca i Cabarrocas (2008). "Influence of the statistical shift of Fermi level on the conductivity behavior in microcrystalline silicon". In: *Phys. Rev. B* 77, 045212 (cit. on p. 149).

Ray, S. et al. (2002). "Transition from amorphous to microcrystalline Si:H: effects of substrate temperature and hydrogen dilution". In: *Journal of Non-Crystalline Solids* 299, 761–766 (cit. on p. 144).

Regolini, J. L. et al. (1993). "Growth and characterization of strain compensated Si_{1-x-y} epitaxial layers". In: *Materials Letters* 18, 57–60 (cit. on p. 15).

Ritter, D., K. Weiser, and E. Zeldov (1987). "Steady-state photocarrier grating technique for diffusion-length measurement in semiconductors: Theory and experimental results for amorphous silicon and semi-insulating GaAs". In: *Journal of Applied Physics* 62, 4563–4570 (cit. on p. 43).

Ritter, D., E. Zeldov, and K. Weiser (1986). "Steady-state photocarrier grating technique for diffusion length measurement in photoconductive insulators". In: *Applied Physics Letters* 49, 791–793 (cit. on p. 43).

Roca i Cabarrocas, P., P. Bulkin, et al. (2008). "Advances in the deposition of microcrystalline silicon at high rate by distributed electron cyclotron resonance". In: *Thin Solid Films* 516, 6834–6838 (cit. on p. 196).

Roca i Cabarrocas, P., J. B. Chévrier, et al. (1991). "A fully automated hot-wall multiplasma-monochamber reactor for thin film deposition". In: *Journal of Vacuum Science & Technology A* 9, 2331–2341 (cit. on p. 21).

Ruff, D. et al. (1998). "Charge transport in microcrystalline silicon films". In: *Journal of Non-Crystalline Solids* 227, 1011–1015 (cit. on p. 10).

Ruggeri, R. et al. (2012). "Luminescence properties of SiO_xN_y irradiated by IR laser 808 nm: The role of Si quantum dots and Si chemical environment". In: *Applied Physics Letters* 100, 042104 (cit. on p. 39).

Sanchez, P. et al. (2010). "Pulsed radiofrequency glow discharge optical emission spectrometry for the direct characterisation of photovoltaic thin film silicon solar cells". In: *J. Anal. At. Spectrom.* 25, 370–377 (cit. on p. 22).

Saxena, N., C. M. Fortmann, and T. W. F. Russell (1989). In: vol. 149. MRS Proceedings (cit. on p. 115).

Scher, H. and E. W. Montroll (1975). "Anomalous transit-time dispersion in amorphous solids". In: *Phys. Rev. B* 12, 2455–2477 (cit. on p. 11).

Schicho, S. et al. (2012). "The relationship of structural properties of microcrystalline silicon to solar cell performance". In: *Solar Energy Materials & Solar Cells* 98, 391–397 (cit. on pp. 36, 100).

Schiff, E. A., S. Hegedus, and X. Deng (2011). "Amorphous Silicon-Based Solar Cells". In: *Handbook of Photovoltaic Science and Engineering*. John Wiley & Sons, Ltd, 487–545 (cit. on p. 5).

Schmidt, M. P. et al. (1985). "Influence of carbon incorporation in amorphous hydrogenated silicon". In: *Philosophical Magazine Part B* 51, 581–589 (cit. on p. 14).

Seto, J. Y. W. (1975). "The electrical properties of polycrystalline silicon films". In: *Journal of Applied Physics* 46, 5247–5254 (cit. on p. 10).

Shah, A. V., J. Meier, et al. (2003). "Material and solar cell research in microcrystalline silicon". In: *Solar Energy Materials & Solar Cells* 78, 469–491 (cit. on p. 11).

Shah, A. V., F. Sculati-Meillaud, et al. (2011). "Diagnostics of thin-film silicon solar cells and solar panels/modules with variable intensity measurements (VIM)". In: *Solar Energy Materials & Solar Cells* 95, 398–403 (cit. on p. 182).

Shimakawa, K. and F. Abdel-Wahab (1997). "The Meyer-Neldel rule in chalcogenide glasses". In: *Applied Physics Letters* 70, 652–654 (cit. on p. 149).

Shockley, W. and W. T. Read (1952). "Statistics of the Recombinations of Holes and Electrons". In: *Phys. Rev.* 87, 835–842 (cit. on p. 46).

Smets, A. H. M., T. Matsui, and M. Kondo (2008). "Infrared analysis of the bulk silicon-hydrogen bonds as an optimization tool for high-rate deposition of microcrystalline silicon solar cells". In: *Applied Physics Letters* 92, 033506 (cit. on p. 8).

Smit, C. et al. (2003). "Determining the material structure of microcrystalline silicon from Raman spectra". In: *Journal of Applied Physics* 94, 3582–3588 (cit. on p. 32).

Spear, W. E., D. Allan, et al. (1980). "A new approach to the interpretation of transport results in a-Si". In: *Philosophical Magazine Part B* 41, 419–438 (cit. on p. 41).

Spear, W. E. and P. G. LeComber (1976). "Electronic properties of substitutionally doped amorphous Si and Ge". In: *Philosophical Magazine* 33, 935–949 (cit. on p. 12).

Staebler, D. L. and C. R. Wronski (1977). "Reversible conductivity changes in discharge-produced amorphous Si". In: *Applied Physics Letters* 31, 292–294 (cit. on p. 7).

Stewart, E. J. (2004). "Boron Segregation in $Si_{1-x-y}Ge_xC_y$ and $Si_{1-y}C_y$ Alloys and Application to P-Channel MOSFETs". PhD thesis. Princeton University (cit. on p. 15).

Stückelberger, M. et al. (2010). "Internal electric field and fill factor of amorphous silicon solar cells". In: *IEEE* 97, 1569 (cit. on p. 182).

Švrček, V. et al. (2001). "Transport anisotropy in microcrystalline silicon studied by measurement of ambipolar diffusion length". In: *Journal of Applied Physics* 89, 1800–1805 (cit. on p. 45).

Tsai, C. C. et al. (1989). "Control of silicon network structure in plasma deposition". In: *Journal of Non-Crystalline Solids* 114, 151–153 (cit. on p. 9).

Tsu, R. et al. (1982). "Critical volume fraction of crystallinity for conductivity percolation in phosphorus-doped Si:F:H alloys". In: *Applied Physics Letters* 40, 534–535 (cit. on p. 33).

Turban, G., Y. Catherine, and B. Grolleau (1979). "Reaction mechanisms of the radio frequency glow discharged deposition process in silane-helium". In: *Thin Solid Films* 60, 147–155 (cit. on p. 13).

Tzolov, M. et al. (1997). "Optical and transport studies on thin microcrystalline silicon films prepared by very high frequency glow discharge for solar cell applications". In: *Journal of Applied Physics* 81, 7376–7385 (cit. on p. 8).

Vallat-Sauvain, E. et al. (2000). "Evolution of the microstructure in microcrystalline silicon prepared by very high frequency glow-discharge using hydrogen dilution". In: *Journal of Applied Physics* 87, 3137–3142 (cit. on p. 8).

Vepřek, S. and V. Mareček (1968). "The preparation of thin layers of Ge and Si by chemical hydrogen plasma transport". In: *Solid-State Electronics* 11, 683–684 (cit. on p. 9).

Vepřek, S., F.-A. Sarott, and Z. Iqbal (1987). "Effect of grain boundaries on the Raman spectra, optical absorption, and elastic light scattering in nanometer-sized crystalline silicon". In: *Phys. Rev. B* 36, 3344–3350 (cit. on p. 32).

Vetterl, O. et al. (2000). "Intrinsic microcrystalline silicon: A new material for photovoltaics". In: *Solar Energy Materials & Solar Cells* 62, 97–108 (cit. on pp. 125, 144).

Viera, G., S. Huet, and L. Boufendi (2001). "Crystal size and temperature measurements in nanostructured silicon using Raman spectroscopy". In: *Journal of Applied Physics* 90, 4175–4183 (cit. on p. 32).

Wakagi, M. et al. (1993). "Crystallinity Analysis of Amorphous-Crystalline Mixed Phase Silicon Films Using EXAFS Method". In: *Japanese Journal of Applied Physics* 32S2, 646–648 (cit. on p. 33).

Wang, J. C. and Y. F. Chen (1998). "The Meyer-Neldel rule in fullerenes". In: *Applied Physics Letters* 73, 948–950 (cit. on p. 149).

Weis, T. et al. (2002). "Barrier-controlled carrier transport in microcrystalline semiconducting materials: Description within a unified model". In: *Journal of Applied Physics* 92, 1411–1418 (cit. on p. 10).

Werner, J. H. et al. (2001). "From polycrystalline to single crystalline silicon on glass". In: *Thin Solid Films* 383, 95–100 (cit. on p. 145).

Wieder, H., M. Cardona, and C. R. Guarnieri (1979). "Vibrational spectrum of hydrogenated amorphous Si-C films". In: *physica status solidi (b)* 92, 99–112 (cit. on pp. 27, 104).

Williams, D. B. and C. B. Carter (2009). *Transmission Electron Microscopy: A Textbook for Material Science*. Springer (cit. on p. 37).

Williamson, D.L. (1999). "Medium-range order in a-Si:H below and above the onset of microcrystallinity". In: *MRS Online Proceedings Library* 557 (cit. on p. 62).

Winchester, M. R. and R. Payling (2004). "Radio-frequency glow discharge spectrometry: A critical review". In: *Spectrochimica Acta Part B: Atomic Spectroscopy* 59, 607–666 (cit. on pp. 22, 23).

Wooten, F. (1972). *Optical Properties of Solids*. Academic Press (cit. on p. 6).

Yamamoto, K. et al. (2002). "Large area thin film Si module". In: *Solar Energy Materials & Solar Cells* 74, 449–455 (cit. on p. xlii).

Yang, J., A. Banerjee, and S. Guha (1997). "Triple-junction amorphous silicon alloy solar cell with 14.6 % initial and 13.0 % stable conversion efficiencies". In: *Applied Physics Letters* 70, 2975–2977 (cit. on p. xlii).

Yang, L. and L. Chen (1993). ""Fast" and "slow" metastable defects in hydrogenated amorphous silicon". In: *Applied Physics Letters* 63, 400–402 (cit. on p. 50).

Yelon, A., B. Movaghar, and H. M. Branz (1992). "Origin and consequences of the compensation (Meyer-Neldel) law". In: *Phys. Rev. B* 46, 12244–12250 (cit. on p. 149).

Yelon, A., B. Movaghar, and R. S. Crandall (2006). "Multi-excitation entropy: its role in thermodynamics and kinetics". In: *Reports on Progress in Physics* 69, 1145 (cit. on p. 149).

LIST OF PRESENTATIONS & POSTERS

ORAL PRESENTATIONS

26-30/04/2014 Low temperature hydrogenated microcrystalline silicon-carbon alloys deposited by RF-PECVD for photovoltaic application, **EMRS-European Material Research Society SPRING MEETING**, *Lille*

26-30/04/2014 Structural and electrical properties of hydrogenated microcrystalline silicon-carbon alloys deposited at low substrate temperature by RF-PECVD, **EMRS-European Material Research Society SPRING MEETING**, *Lille*

16-20/09/2013 μc-$Si_{1-x}C_x$:H by RF-PECVD: a novel material for photovoltaic applications, **EMRS-European Material Research Society FALL MEETING**, *Warsaw*

18-23/08/2013 Tailored Voltage Waveform Deposition of Hydrogenated Microcrystalline Silicon-Carbon alloys from Hydrogen-Diluted Silane and Methane gas mixture, **ICANS 25-International Conference on Amorphous and Nano-Crystalline Semiconductors**, *Toronto*

27-31/05/2013 Structural and electrical characterization of μc-$Si_{1-x}C_x$:H deposited by RF-PECVD, **EMRS-European Material Research Society SPRING MEETING**, *Strasbourg*

14-18/05/2012 Deposition of microcrystalline silicon-carbon alloys by RF-PECVD and MDECR, **EMRS-European Material Research Society SPRING MEETING**, *Strasbourg*

POSTERS

30/09-04/10/2013 RF power influence on structural and electrical properties of hydrogenated microcrystalline silicon-carbon alloys, **EU-PVSEC-European PV Solar Energy Conference**, *Paris*

11-14/12/2012 Caractérisations structurales et électriques de μc-$Si_{1-x}C_x$:H déposé par RF-PECVD, **JNPV-Journées Nationales PhotoVoltaique**, *Chantilly*

21/09/2012 Use of GD-OES for the rapid estimation of carbon content in microcrystalline $Si_{1-x}C_x$:H layer of thin film silicon solar cells, **6th International GD DAY**, *Paris*

18-28/07/2012 Microcrystalline silicon seed layer effect on growth of microcrystalline silicon-carbon alloys deposited by RF-PECVD and MDECR, **INTERNATIONAL SCHOOL: Materials for Renewable Energy**, *Erice*

LIST OF PUBLICATIONS

- S. Gaiaschi, R. Ruggeri, M.-E. Gueunier-Farret and E. V. Johnson (2014) "Use of radio frequency power, silicon tetrafluoride and methane as parameters to tune structural properties of hydrogenated microcrystalline silicon carbon alloys". In: *Journal of Physics D: Applied Physics* 47, 455102
- S. Gaiaschi, M.-E. Gueunier-Farret and E. V. Johnson (2014) "Low temperature hydrogenated microcrystalline silicon-carbon alloys deposited by RF-PECVD" In: *Physica Status Solidi C* 11, 1665
- S. Gaiaschi, R. Ruggeri, E. V. Johnson, P. Bulkin, P. Chapon, M.-E. Gueunier-Farret, G. Mannino, C. Longeaud, J.-P. Kleider (2014) "Structural properties of hydrogenated microcrystalline silicon-carbon alloys deposited by Radio Frequency Plasma Enhanced Chemical Vapor Deposition: Effect of microcrystalline silicon seed layer and methane flow rate". In: *Thin Solid Films* 550, 312-318

Phys. Status Solidi C 11, No. 11–12, 1665–1668 (2014) / DOI 10.1002/pssc.201400034

physica status solidi c
www.pss-c.com
current topics in solid state physics

Low temperature hydrogenated microcrystalline silicon-carbon alloys deposited by RF-PECVD

Sofia Gaiaschi[*,1,2], **Marie-Estelle Gueunier-Farret**[1], **and Erik V. Johnson**[2]

[1] LGEP-CNRS/SUPELEC, 11 rue Joliot Curie - Plateau de Moulon, 91192 Gif sur Yvette, France
[2] LPICM-CNRS, Ecole Polytechnique, 91128 Palaiseau, France

Received 28 April 2014, revised 22 September 2014, accepted 23 September 2014
Published online 9 October 2014

Keywords microcrystalline silicon-carbon alloys, RF-PECVD, low temperature, crystallinity

* Corresponding author: e-mail sofia.gaiaschi@lgep.supelec.fr, Phone: +33 169 851 680, Fax: +33 169 418 318

Two sets of hydrogenated microcrystalline silicon carbon alloys were deposited by standard radio frequency (RF) plasma enhanced chemical vapor deposition at a substrate temperature of 175 °C. The effect of the methane flow rate and of the RF-power were investigated. Samples were deposited from a silane and methane gas mixture, highly diluted in hydrogen. The increase in methane flow rates leads to a decrease of the crystalline volume fraction and an increase in carbon incorporation. On the other hand, decreasing the RF-power shifts the microcrystalline-to-amorphous transition at higher methane flow rates. Moreover, for similar amount of carbon incorporated, the decrease in RF-power leads to materials showing higher crystalline volume fraction and average grains sizes. Both ion bombardment energy and carbon incorporation contributes to the microstructural properties of the deposited alloys.

© 2014 WILEY-VCH Verlag GmbH & Co. KGaA, Weinheim

1 Introduction The light-induced degradation of hydrogenated amorphous silicon (a-Si:H) is still a limiting factor for the efficiency of "micromorph" solar cells, made by coupling a thin a-Si:H top cell and a thicker microcrystalline silicon bottom cell. Hydrogenated microcrystalline silicon carbon alloys (μc-$Si_{1-x}C_x$:H) are promising candidates to replace a-Si:H in this kind of devices [1]. By standard Radio Frequency Plasma Enhanced Chemical Vapour Deposition (RF-PECVD) it is possible to obtain μc-$Si_{1-x}C_x$:H alloys with an average energy gap similar to that of a-Si:H [2,3]. Nevertheless, the growth and the structure of these new alloys, made of silicon crystallites embedded in an amorphous silicon-carbon matrix, are complex and need to be fully investigated to find the best deposition conditions for photovoltaic applications. Moreover, the use of a low substrate temperature ($T < 200$ °C) for the solar cell deposition is necessary to prevent the substrate and the interfaces from damages [4]. Thus, μc-$Si_{1-x}C_x$:H alloys were deposited by RF-PECVD at 175 °C. The role of RF-power and of methane flow rate variation were studied in order to understand the evolution of carbon incorporation at this substrate temperature. Structural properties were investigated using several complementary techniques which confirmed that these materials consist of μc-Si grains embedded in an a-$Si_{1-x}C_x$:H tissue.

2 Experimental details Hydrogenated microcrystalline silicon-carbon alloys films were deposited by standard RF-PECVD at a substrate temperature of 175 °C. Films were grown from a silane (SiH_4) and methane (CH_4) gas mixture, highly diluted in hydrogen (H_2). The pressure and the inter-electrode distance were fixed at 307 Pa and 1.2 cm, respectively. All samples were deposited using a combination of a seed layer followed by the main layer deposition, with the addition of CH_4 [5]. For all samples, the H_2 and the SiH_4 flow rates were kept constant at 500 sccm and 13 sccm, respectively, during both the seed layer and the main layer depositions. For the different μc-$Si_{1-x}C_x$:H layer growths, the CH_4 flow rate was varied from 1 sccm to

© 2014 WILEY-VCH Verlag GmbH & Co. KGaA, Weinheim

1.8 sccm. The seed layer was always deposited by standard RF-PECVD, keeping the RF-power (W_{RF}) at 16 W (90 mW/cm^2). Two sets of samples were deposited changing the main layer deposition process. A first set (SET1) was made using W_{RF} = 40 W (226 mW/cm^2) and a second one (SET2) using W_{RF} = 20 W (113 mW/cm^2).

Samples were deposited simultaneously on two different substrates: a <100> float zone silicon substrate to perform infrared (IR) spectroscopy measurements and a Corning "Eagle" glass substrate for Raman spectroscopy, Grazing Incidence X-Ray Diffraction (GIXRD) and Radio Frequency Glow Discharge Optical Emission Spectroscopy (RF-GD-OES) measurements. IR absorption measurements between 400 and 4000 cm^{-1} were carried out using a Brüker Equinox 55 Fourier transform infrared spectrometer. Raman spectra were obtained in the 200-1100 cm^{-1} range using a LABRAM Aramis system, Confocal Raman Microscope by HORIBA Jobin Yvon, equipped with a 473 nm laser, providing a power density $w = 4\times10^6$ W/cm^2, when using a 100x objective. To avoid any crystallization induced by the heating of the laser, a $ND3$ optical filter was used, reducing the incident power density by a factor of 1000. The elemental composition and the depth profiles of carbon and silicon were determined by RF-GD-OES using a HORIBA Jobin Yvon GD-Profiler 2. With this spectrochemical technique it is possible to have a direct determination of major and trace elements in a sample, without the need for ultra high vacuum [6,7]. The total carbon incorporation was defined as R = [C]/[Si], where [C] and [Si] are respectively the line intensities for carbon and silicon, and was calibrated measuring this ratio in a reference monocrystalline silicon carbide sample. Diffraction patterns were acquired in grazing incident configuration using a Brüker D8 Discover-AXS diffractometer equipped with a k_α Cu source, Göbel mirror and Soller slits for thin films analyses. For all samples an incidence angle of 0.35° was used, allowing a $\sim$ 300 nm penetration depth in silicon.

3 Results and discussion Raman spectra and GIXRD patterns of μc-Si$_{1-x}$C$_x$:H deposited at 175 °C are shown in Fig. 1 and Fig. 2, respectively. For W_{RF} = 40 W, CH_4 flow rates above 1.4 sccm result in completely amorphous alloys. Indeed, Raman spectra are characterized by only a broad peak centered at 480 cm^{-1}, typical of an amorphous structure, and diffraction patterns show broad humps located at 27.6° and 51°, due to the short and medium range order in amorphous materials [8]. The decrease in CH_4 flow rate leads to an amorphous-to-microcrystalline transition. The enhancement of the microcrystalline silicon phase is highlighted in Raman spectra by the decreased intensity of the broad band at 480 cm^{-1} and the appearance of a sharp peak at around 520 cm^{-1}, corresponding to the Si-Si Transversal Optical (TO) mode. In the GIXRD patterns this transition is characterized by the appearance of diffraction peaks characteristic of the

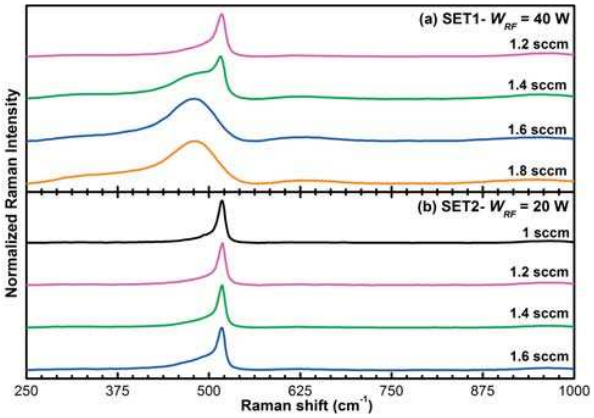

Figure 1 Raman spectra of samples deposited with (a) W_{RF} = 40 W and (b) W_{RF} = 20 W, varying CH_4 flow rate.

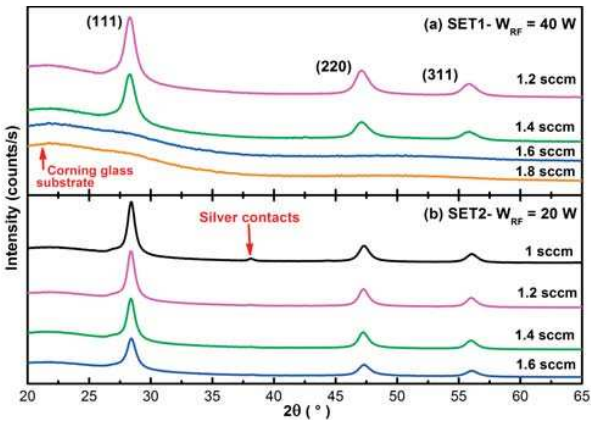

Figure 2 GIXRD patterns of samples deposited with (a) W_{RF} = 40 W and (b) W_{RF} = 20 W, varying CH_4 flow rate.

cubic phase of crystalline silicon (diffraction planes are at 2θ = 28.44°, 47.3° and 56.1° and are labeled in Fig. 2). On the other hand, for W_{RF} = 20 W, the amorphous to microcrystalline transition seems to be shifted at higher CH_4 flow rates and all materials are microcrystalline. In the studied range of CH_4 flow rates, Raman spectra are all characterized by the Si-Si TO mode at 520 cm^{-1} and GIXRD patterns show the diffraction peaks characteristic of the cubic phase of crystalline silicon. No crystalline silicon carbide or crystalline forms of carbon are present in these layers. Therefore, one can assume that these materials are made of silicon crystallites embedded in an amorphous Si$_{1-x}$C$_x$ matrix [9]. Moreover, for both series, the ratios of the diffraction peaks intensities are in good agreement with the standard silicon powders, proving that these are randomly oriented polycrystalline layer [10].

The phase transition is due to the amorphization of the alloy induced by the addition of a carbon-based precursor into the plasma discharge. For the used deposition

© 2014 WILEY-VCH Verlag GmbH & Co. KGaA, Weinheim

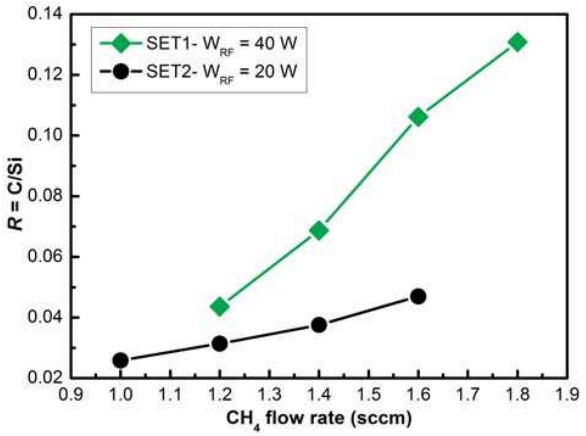

Figure 3 Evolution of the total carbon incorporation R for the two sets of samples, as a function of the CH_4 flow rate.

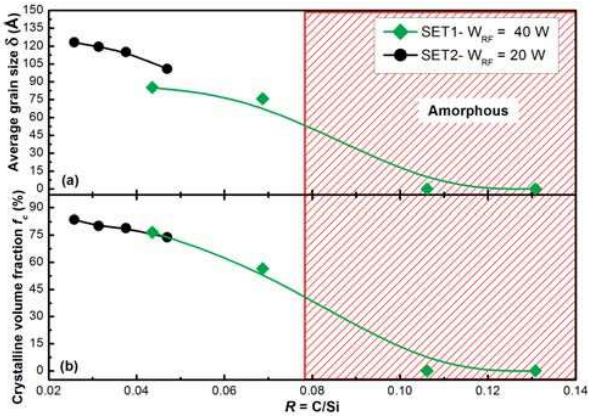

Figure 4 (a) Average grain size (δ) and (b) crystalline volume fraction (f_c) as a function of the total carbon incorporation R.

conditions it can be assumed that at a fixed W_{RF}, an increase of the CH_4 flow rate in the gas mixture leads to an increased number of dissociated CH_4 molecules. According to the binary Si-C phase diagram, the only stable compound is stoichiometric silicon carbide. Therefore, all alloys with smaller carbon content are thermodynamically metastable and the carbon incorporation R, which cannot happen in the crystalline phase [11], leads to the distortion of bonds and angles in the silicon lattice, creating an amorphous phase. The higher is R, the lower is the possibility for silicon crystallites to nucleate and grow [12]. At the same time, the different threshold of the phase transition according to W_{RF} is linked to the fact that the number of dissociated CH_4 molecules depends on the RF-power. The higher W_{RF}, the higher is the number of dissociated CH_4 molecules, leading to an increase of the amount of carbon incorporated in the alloy (Fig. 3) [13].

Using the Scherrer formula [14] it is possible to estimate the average grain size δ from the full width at half maximum (FWHM) of the diffraction peaks. Its evolution is shown in Fig. 4(a) as a function of the total carbon incorporation R. In Fig. 4(b) the crystalline volume fraction f_c is also plotted as a function of R. f_c was calculated from the deconvolution of the Raman spectra using the method explained in Ref. [15], where an a-Si:H spectrum is scaled and subtracted from the acquired spectra, leaving the Raman spectrum of the crystalline part of the microcrystalline films. Using the fitting thus done, f_c can be expressed as:

$$f_c = \frac{I_c}{I_c + 0.8 \cdot \eta \cdot I_a}, \tag{1}$$

where I_a and I_c are respectively the areas of the a-Si:H transversal optical (TO) mode (located at 480 cm^{-1}) and of the crystalline Si (c-Si) TO mode (at 520 cm^{-1}), η is the scaling factor and 0.8 is a coefficient that takes into account the lesser cross-section of the phonon interaction for c-Si, compared to that of a-Si:H [16–18]. For both sets of samples, the increase in R leads to a decrease in δ and f_c. It is noteworthy that samples made with the two different RF-powers and having $R = 0.05$ have different microstructures. The decrease in RF-power leads to an increase of both grain average size and crystalline volume fraction. Such a difference is not only due to a higher CH_4 dissociation rate with a higher RF-power, but also to a deterioration of the crystallinity because of the increase in the ion bombardment energy with a higher RF-power [19].

Finally, in Fig. 5 the infrared spectra of the two sets of samples are presented. They all exhibit two main absorption bands: 500-1000 cm^{-1} and 2000-2100 cm^{-1}. The band at 2800-3000 cm^{-1}, due to C-H stretching mode, is not detectable (it starts to appear for $R > 0.4$). The first absorption region is due to the superposition of four different bands: the Si-H wagging mode at 640 cm^{-1}, the Si-C stretching mode at 760-780 cm^{-1}, the Si-H bending mode at 800-900 cm^{-1} and the C-H wagging mode at 1000 cm^{-1}. The second absorption region arises from the superposition of the 2000 cm^{-1} and 2090 cm^{-1} bands, related to the Si-H and Si-H_2 groups, respectively [20]. The other two absorption regions at 1500-2000 cm^{-1} and 3500-4000 cm^{-1} are due to the absorption of residual atmospheric water in the measurement system and can be ignored. It can be seen that in both cases, carbon is mainly bonded to silicon and that with increasing CH_4 flow rate the shoulder at $\sim$ 780 cm^{-1} increases.

The Si-C bond concentrations N_{Si-C} can be calculated from the integrated area of the deconvoluted band at 780 cm^{-1}, using the following relation [2]:

$$N_{Si-C} = A_{Si-C} \cdot \int \frac{\alpha(\omega)}{\omega} d\omega \tag{2}$$

where $A_{Si-C} = 2.13 \times 10^{19}$ cm^{-2} is the inverse cross-section, $\alpha(\omega)$ is the absorption coefficient, which is a func-

© 2014 WILEY-VCH Verlag GmbH & Co. KGaA, Weinheim

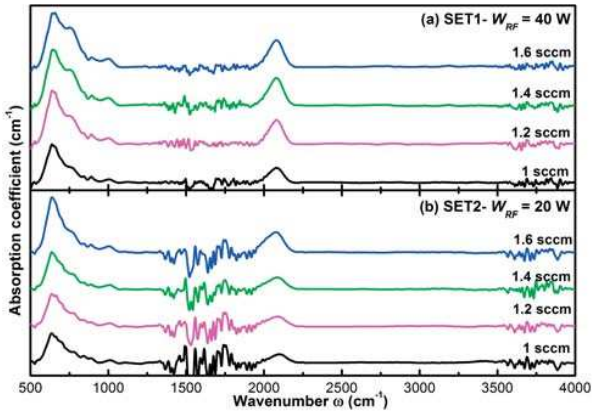

Figure 5 IR spectra for samples deposited with (a) W_{RF} = 40 W and (b) W_{RF} = 20 W, varying CH_4 flow rate.

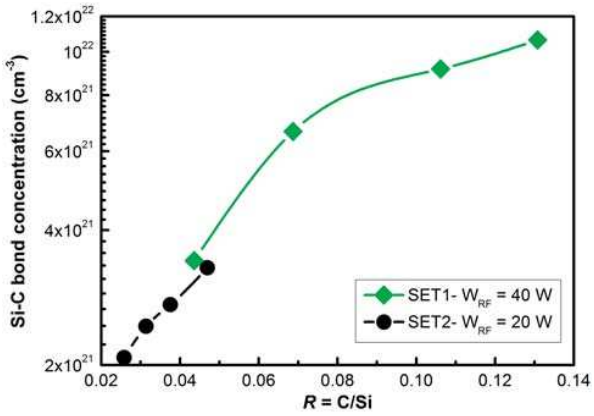

Figure 6 Si-C bond concentration N_{Si-C} as a function of the total carbon incorporation R.

tion of the wavenumber ω and the integration is done over the deconvoluted peak, after the subtraction of a baseline. The evolution of N_{Si-C} as a function of the total carbon incorporated in the alloy is shown in Fig. 6 for both sets of samples. It can be seen that in both cases the increase in carbon incorporation is translated into an increased density of Si-C bonds.

4 Conclusion Hydrogenated microcrystalline silicon-carbon alloys were deposited at 175 °C, from a highly hydrogen diluted silane and methane gas mixture. The effect of the RF-power and of the CH_4 flow rate were investigated. The increase of CH_4 flow rate leads to a decrease of the crystalline volume fraction, due to an increase in the carbon incorporation. The amorphization is related to the absence of stable substoichiometric silicon carbon alloys. The decrease of the RF-power leads to a shift in the microcrystalline-to-amorphous transition, due to a lower dissociation rate of CH_4 molecules. GIXRD measurements prove that no silicon carbide or crystalline forms of carbon are present, but that these alloys consist of silicon crystallites embedded in an amorphous silicon-carbon matrix. Finally, FTIR analyses proved the presence of carbon which is mainly bonded to silicon in the amorphous tissue.

Acknowledgements The authors would like to thank Patrick Chapon from Horiba Jobin-Yvon for the access to the RF-GD-OES measurements. This work has been supported by the French National Research Agency (ANR) through the "Habitat intelligent et solaire photovoltaïque" program (project CANASTA n° ANR-10-HABISOL-002).

References

[1] Y. Matsumoto, G. Hirata, H. Takakura, H. Okamoto, and Y. Hamakawa, J. Appl. Phys. **67**, 6538 (1990).
[2] F. Demichelis, F. Giorgis, and C. F. Pirri, Solid State Commun. **96**, 17 (1995).
[3] J. Bullot and M. Schmidt, Phys. Status Solidi B **143**, 345 (1987).
[4] Y. Nasuno, M. Kondo, A. Matsuda, H. Fukuhori, and Y. Kanemitsu, Appl. Phys. Lett. **81**, 3155 (2002).
[5] S. Gaiaschi, R. Ruggeri, E. Johnson, P. Bulkin, P. Chapon, M. E. Gueunier-Farret, G. Mannino, C. Longeaud, and J. P. Kleider, Thin Solid Films **550**, 312 (2014).
[6] J. Pisonero, B. Fernández, R. Pereiro, N. Bordel, and A. Sanz-Medel, TrAC Trends Analyt. Chem. **25**, 11 (2006).
[7] P. Sanchez, B. Fernandez, A. Menendez, R. Pereiro, and A. Sanz-Medel, J. Anal. At. Spectrom. **25**, 370 (2010).
[8] D. Williamson, MRS Proc. **557** (1999).
[9] U. Coscia, G. Ambrosone, S. Lettieri, P. Maddalena, and S. Ferrero, Thin Solid Films **511-512**, 399 (2006).
[10] S. Schicho, F. Köhler, R. Carius, and A. Gordijn, Sol. Energy Mater. Sol. Cells **98**, 391 (2012).
[11] H. Osten, Thin Solid Films **367**, 101 (2000).
[12] U. Coscia, G. Ambrosone, P. Maddalena, A. Setaro, A. Phani, and M. Passacantando, Thin Solid Films **515**, 7634 (2007).
[13] Y. Catherine, G. Turban, and B. Grolleau, Thin Solid Films **76**, 23 (1981).
[14] M. Birkholz, Thin Film Analysis by X-ray Scattering (Wiley-VCH Verlag GmbH & Co. KGaA, 2006).
[15] C. Smit, R. A. C. M. M. van Swaaij, H. Donker, A. M. H. N. Petit, W. M. M. Kessels, and M. C. M. van de Sanden, J. Appl. Phys. **94**, 3582 (2003).
[16] A. Gajović, D. Gracin, K. Juraić, J. Sancho-Parramon, and M. Čeh, Thin Solid Films **517**, 5453 (2009).
[17] P. L. Novikov, A. Le Donne, S. Cereda, L. Miglio, S. Pizzini, S. Binetti, M. Rondanini, C. Cavallotti, D. Chrastina, T. Moiseev, H. von Känel, G. Isella, and F. Montalenti, Appl. Phys. Lett. **94**, 051904 (2009).
[18] E. V. Johnson, L. Kroely, and P. Roca i Cabarrocas, Sol. Energy Mater. Sol. Cells **93**, 1904 (2009).
[19] A. Matsuda, Thin Solid Films **337**, 1 (1999).
[20] D. Basa and F. Smith, Thin Solid Films **192**, 121 (1990).

© 2014 WILEY-VCH Verlag GmbH & Co. KGaA, Weinheim

IOP Publishing Journal of Physics D: Applied Physics
J. Phys. D: Appl. Phys. 47 (2014) 455102 (10pp) doi:10.1088/0022-3727/47/45/455102

Use of radio frequency power, silicon tetrafluoride and methane as parameters to tune structural properties of hydrogenated microcrystalline silicon carbon alloys

S Gaiaschi[1,2], R Ruggeri[3], M-E Gueunier-Farret[1], E V Johnson[2]

[1] LGEP-CNRS/SUPELEC, 11 rue Joliot Curie—Plateau de Moulon, 91192 Gif sur Yvette, France
[2] LPICM-CNRS, Ecole Polytechnique, Route de Saclay, 91128 Palaiseau, France
[3] CNR-IMM, strada VIII n°5, zona industriale, 95121 Catania, Italy

E-mail: sofia.gaiaschi@supelec.fr

Received 24 June 2014, revised 24 August 2014
Accepted for publication 15 September 2014
Published 27 October 2014

Abstract
In the search for a material with electrical properties similar to those of amorphous silicon or amorphous silicon germanium, but stable under light soaking, hydrogenated microcrystalline silicon–carbon alloy (μc-$Si_{1-x}C_x$:H) thin films are a promising candidate. The interest in these materials lies in the possibility of varying the effective band gap by changing the amount of carbon in the alloy composition, while keeping a high crystalline fraction to maintain stability under light-soaking. In this study, μc-$Si_{1-x}C_x$:H thin films were deposited by radio frequency (RF) plasma enhanced chemical vapour deposition using a silane and methane gas mixture highly diluted in hydrogen. Three deposition parameters were investigated as a means to control the film crystallinity: the RF power density, the methane flow rate and the presence of a small amount of silicon tetrafluoride in the gas mixture. Although all three parameters can result in materials with a Raman crystalline volume fraction above 50%, it is shown that they result in very different microstructures, as evidenced by x-ray diffraction and scanning transmission electron microscopy analyses. A growth model is proposed to explain the influence of each of these parameters on the final film structure.

Keywords: silicon carbon alloys, RF power, silicon tetrafluoride, methane, crystallinity

(Some figures may appear in colour only in the online journal)

1. Introduction

After many years of research, thin film silicon multijunction solar cells are still limited by the light-induced degradation, known as the Staebler–Wronski effect, of the hydrogenated amorphous materials they employ (silicon, a-Si:H and silicon germanium, a-SiGe:H). Therefore, a material stable under light soaking and with electrical properties similar to those of a-Si:H or a-SiGe:H could be a breakthrough for devices using these material systems [1].

With this aim, hydrogenated microcrystalline silicon–carbon alloys (μc-$Si_{1-x}C_x$:H) are a very attractive new class of materials. By varying the carbon content in the alloy composition, it is possible to tune their effective energy gap [2]. However, deposition conditions have been proven to have a strong influence on the structure of the material, resulting in different transport and defect-related properties. Therefore, the effect of a selected range of deposition parameters has to be extensively studied in order to find the most promising conditions for the growth of highly crystalline alloys that could successfully be applied in photovoltaic devices.

The main disadvantage of this group of materials is the absence of a stable sub-stoichiometric crystalline phase [3]. When grown by standard Radio Frequency Plasma Enhanced Chemical Vapour Deposition (RF-PECVD), these materials are in fact composed of submicron-size silicon crystallites

 © 2014 IOP Publishing Ltd Printed in the UK

embedded in an amorphous silicon–carbon (a-$Si_{1-x}C_x$) matrix [4]. While the presence of the crystallites ensures a higher conductivity, compared to a-$Si_{1-x}C_x$ [5], the carbon incorporation leads to an effective energy gap larger than that of microcrystalline silicon [6, 7]. This complex nature motivates a more detailed study on the growth mechanisms and on the role of the carbon incorporation on the final structure of the alloy.

In this study, the variation of the RF power density, the variation of methane (CH_4) flow rate and the addition of a small amount of silicon tetrafluoride (SiF_4) to the gas mixture will be investigated as techniques to control the crystalline volume fractions of the alloys. Furthermore, their influence on other structural, optical and composition properties will be addressed.

2. Experimental details

The μc-$Si_{1-x}C_x$:H thin films were deposited by standard (13.56 MHz) RF-PECVD at a substrate temperature of 285 °C. Films were grown from a silane (SiH_4) and CH_4 gas mixture, highly diluted in hydrogen (H_2). The pressure and the inter-electrode distance were fixed at 307 Pa and 1.2 cm, respectively. All samples are composed of a thin initial seed layer (deposited at a RF-power of 16 W (90 mW cm^{-2})), followed by the main layer deposited with the addition of CH_4 [8]. For all samples, the H_2 and the SiH_4 flow rates were respectively kept constant at 500 sccm and 6.5 sccm during both the seed layer and the main layer depositions.

Three sets of samples were deposited and in each, one of the main layer deposition conditions was varied. The goal of the first set was to study the effect of the variation of the RF power density w_{RF} (SET_{RF} series), as it is known from the literature that the decrease of such parameter leads to an increase in the crystalline fraction [9]. Then, the addition of very few sccm of SiF_4 to the gas mixture (SET_{SiF_4} series) was investigated, as its presence leads to materials with a higher crystalline volume fraction [10, 11]. Finally, the variation of the CH_4 flow rate (SET_{CH_4} series) was studied as the introduction of carbon-based precursors in the gas phase can be detrimental for the microcrystallinity of the alloy [12]. More precisely, the deposition parameters used to make the main layer of these three sets of samples were adjusted in the following way:

- SET_{RF} series: w_{RF} was varied from 565 mW cm^{-2} to 113 mW cm^{-2} and the deposition time was increased from 60 min to 90 min, with decreasing w_{RF}, in order to keep the thickness of the layers in the 200–250 nm range. The CH_4 flow rate was fixed at 1.2 sccm;
- SET_{SiF_4} series: the SiF_4 flow rate was varied from 0 sccm to 1 sccm, while the RF power density, the deposition time and the CH_4 flow rate were kept constant at 226 mW cm^{-2}, 75 m and 1.2 sccm, respectively;
- SET_{CH_4} series: the CH_4 flow rate was varied from 1 sccm to 1.8 sccm, while the RF power density and the deposition time were fixed at 226 mW cm^{-2} and 75 m, respectively.

Samples were deposited simultaneously on <1 0 0 > float zone silicon for infrared (IR) measurements and on Corning Glass 'Eagle' for ellipsometry and Raman spectroscopy as well as optical transmission measurements, radio frequency glow discharge optical emission spectroscopy, x-ray diffraction and transmission electron microscopy analyses. Ellipsometry measurements were performed using a UVISEL spectroscopic ellipsometer from HORIBA Jobin Yvon in the spectral range from 1–4.7 eV. To analyse these spectra, a two Tauc–Lorentz dispersion formula [13] was used to model the dielectric function ϵ (E) = ϵ_r(E) + i·ϵ_i(E) as a function of the photon energy E, where ϵ_r(E) and ϵ_i(E) are the real and imaginary parts, respectively. From this model, the thickness and the average optical band gap of the samples were calculated. Optical transmission spectra were acquired using a PerkinElmer Lambda 950 UV/VIS Spectrometer, in the 250–2500 nm range in order to determine the absorption coefficient. Raman spectra were obtained in the 200–1100 cm^{-1} range using a LABRAM Aramis system and a Confocal Raman Microscope by HORIBA Jobin Yvon, equipped with a 473 nm laser. The elemental composition and the depth profiles of carbon and silicon were determined by Radio Frequency Glow Discharge Optical Emission Spectroscopy (RF-GD-OES) using a HORIBA Jobin Yvon GD-Profiler 2. This is a spectrochemical technique that allows direct determination of major and trace elements, without the need for ultra high vacuum [14, 15]. The instrument is equipped with a RF-generator, a standard HORIBA Jobin Yvon glow discharge source with a cylindrical anode of 4 mm internal diameter and two optical spectrometers (a polychromator and a monochromator). The sample, which serves as the negatively charged electrode, is mounted on an O-ring outside of the plasma chamber. High purity argon (99.999% minimum purity) from Air Liquide was employed as a discharge gas. When the RF-power is applied to the sample, a plasma is created in the tubular anode and its inner diameter defines the analyzed spot size, as the plasma is restricted to this area. When the discharge gas breaks down electrically, forming electrons and positively charged ions, the latter are accelerated towards the sample by the electric field and the ion bombardment of the surface of the sample causes the sputtering of the material to be analyzed. When entering the gas phase environment of the glow discharge, the sputtered atoms are excited by collisions with high energy electrons, metastable argon atoms and ions. De-excitation of the excited species causes the emission of photons characteristic of the material, which are collected using the optical spectrometers. As the sample is continuously sputtered, the collected light reflects the temporal evolution of the sputtered species [16, 17]. In this article the total carbon–silicon ratio has been defined as R = [C]/[Si], where [C] and [Si] are the line intensities for carbon and silicon, respectively. This ratio has been calibrated dividing the carbon–silicon ratio measured in the samples by that measured for a reference monocrystalline silicon carbide sample. IR absorption measurements between 400 and 4000 cm^{-1} were carried out using a Brüker Equinox 55 Fourier transform infrared spectrometer. Small Angle Annular Dark Field-Scanning Transmission Electron Microscopy (SAADF STEM) and Energy Filtered TEM (EFTEM) analyses were performed using a JEOL JEM

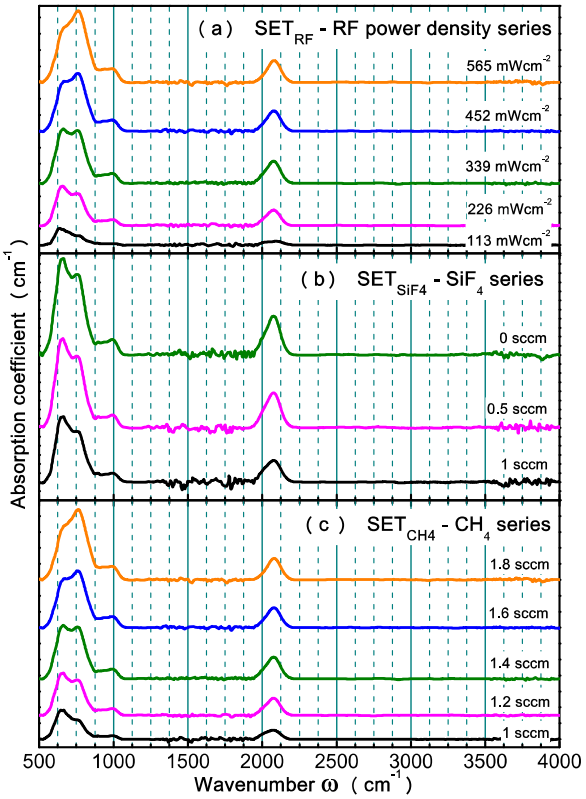

Figure 1. IR spectra of samples deposited varying (*a*) the RF power density, (*b*) the SiF_4 flow rate and (*c*) the CH_4 flow rate.

2010F transmission electron microscope with a Schottky field emission gun operating at an acceleration voltage of 200 kV. The instrument is equipped with a Gatan image filter. The EFTEM analyses were carried out collecting electrons that have lost a characteristic amount of energy when interacting with the sample, therefore obtaining a chemical mapping of all the desired elements [18]. The energy window was tuned in the range of low energy loss, to the value of the Si bulk plasmon (17 eV) and approximately to the value of SiC (24 eV). In both cases the energy slit used had a 4 eV width. TEM lamellas were prepared by conventional mechanical polishing and argon-ion thinning. X-ray diffraction (XRD) patterns were acquired in grazing incident (GI) mode using a Brüker D8 Discover—AXS diffractometer equipped with a k_αCu source, Goebel mirror and Soller slits for thin film analyses. For all sets of samples, GIXRD patterns were acquired keeping the same configuration with an incidence angle $\alpha_i = 0.35°$. In this case, the intensities of the signals from different layers with the same thickness can be directly compared, as the probed areas are the same.

3. Results and discussion

3.1. Vibrational spectroscopy and carbon incorporation

Hydrogenated microcrystalline silicon carbon alloys are a very complex new material system. As described above, three sets

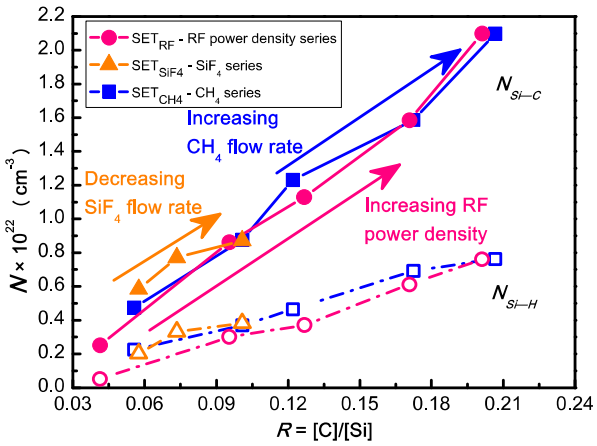

Figure 2. Si–C (closed symbols) and Si–H (open symbols) bond concentration for the three series of samples, as a function of the total carbon–silicon ratio R.

of samples (SET_{RF}, SET_{SiF_4} and SET_{CH_4}, each varying a single parameter) were deposited to study the evolution of the structural properties and the role of carbon incorporation. Within each set, one sample is deposited with common deposition conditions ($SET_{RF} - w_{RF} = 226$ mW cm^{-2}, $SET_{SiF_4} - SiF_4 = 0$ and $SET_{CH_4} - CH_4 = 1.2$ sccm). In order to quantify the bonding configurations of the Si, C and H in the films, IR absorption spectroscopy was applied to these three series of samples.

In figure 1 the IR spectra of the three series of samples are shown. They all present two main absorption regions at 500–1000 cm^{-1} and 1900–2200 cm^{-1}, which are the sum of different vibrational modes. The first zone arises from the superposition of the Si–H wagging mode at 640 cm^{-1}, the Si–C stretching mode at 740–780 cm^{-1}, the Si–H bending mode at 800–900 cm^{-1} and the C–H wagging mode at 1000 cm^{-1}. The second region is the superposition of the Si–H stretching mode at 2000 cm^{-1} and the Si–H_2 stretching mode at 2090 cm^{-1} [9]. The 2800–3000 cm^{-1} band, due to the C–H_n vibrational modes, is too weak to be seen. The other two absorption regions at 1500–2000 cm^{-1} and 3500–4000 cm^{-1} are related to the absorption of residual atmospheric water in the measurement system and can be ignored.

From the deconvolution of the IR absorption regions, the trend of the Si–C and Si–H bond concentration (N_{Si-C} and N_{Si-H}, respectively) can be determined. The bond concentrations were calculated from the integrated absorption of the deconvoluted stretching modes, following the relation

$$N = A \cdot \int \frac{\alpha(\omega)}{\omega} \mathrm{d}\omega \qquad (1)$$

where A is the inverse cross section and $\alpha(\omega)$ is the absorption coefficient, which is a function of the wavenumber ω and the integration is done over the deconvoluted peak, after the subtraction of a baseline. The values of A depend on the oscillator strength and the vibrational mode. The bond concentrations were determined using $A_{Si-C} = 2.13 \times 10^{19}$ cm^{-1} and $A_{Si-H} = 1.4 \times 10^{20}$ cm^{-1} [2, 19]. Figure 2 shows the evolution

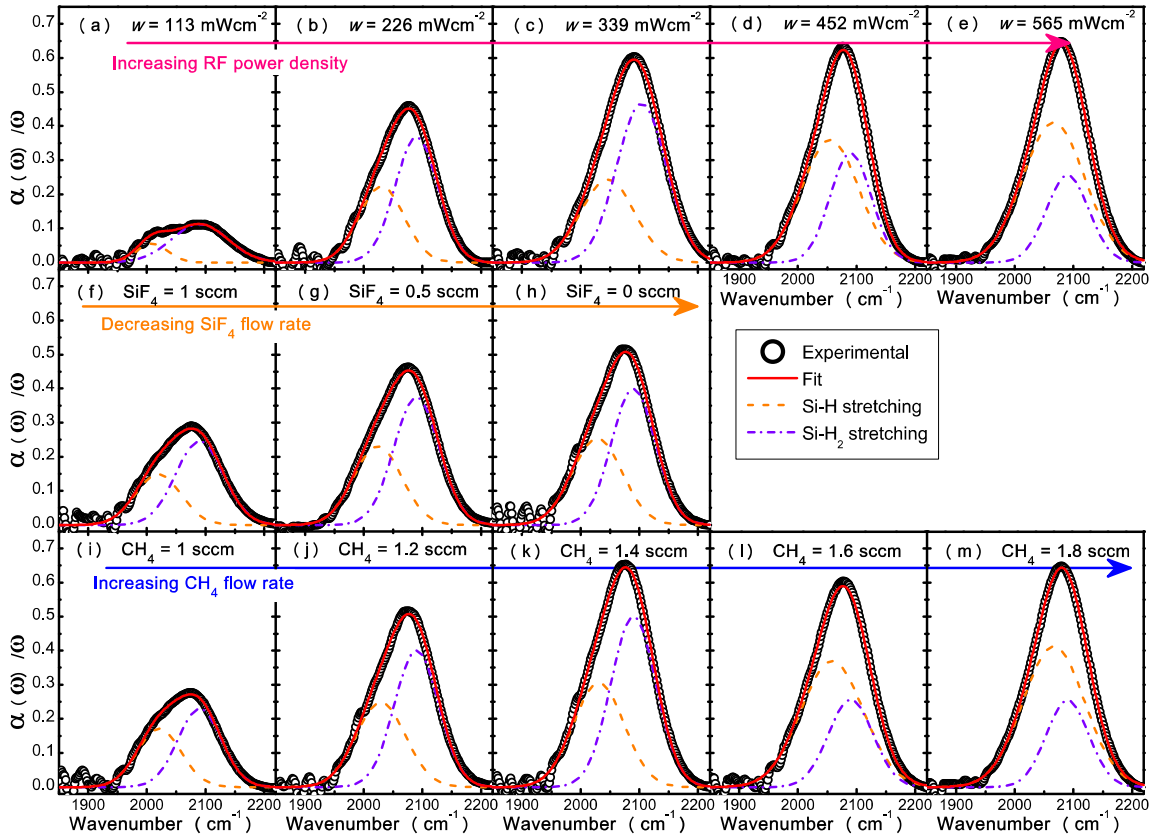

Figure 3. Si–H and Si–H_2 stretching band in the 1900–2200 cm^{-1} range for the different samples. The $\alpha(\omega)/\omega$ ratio is plotted as a function of the wavenumber ω. From (*a*) to (*e*) the effect of the increase of RF power density w_{RF} is shown. From (*f*) to (*h*) the effect of the addition of SiF_4 to the gas mixture is presented. Finally, from (*i*) to (*m*) the effect of the variation of the CH_4 flow rate is shown.

of N_{Si-C} and N_{Si-H} as a function of the total carbon–silicon ration *(R)* in the layers. For all samples, N_{Si-C} and N_{Si-H} increase with increasing value of *R*.

The evolution of the 1900–2200 cm^{-1} absorption region with the variation of the deposition parameters was studied and is shown in figure 3. For $w_{RF} < 226$ mW cm^{-2}, $SiF_4 = 1$ sccm and $CH_4 = 1$ sccm, the presence of two bands can be distinguished, whereas with increasing RF power density and CH_4 flow rate and with decreasing SiF_4 flow rate, one main contribution centred at about 2090 cm^{-1} seems to appear. Such behaviour can be attributed to an increase of carbon incorporation. Indeed, it is known from the literature that the 2000 cm^{-1} Si–H stretching band can shift towards 2090 cm^{-1} due to carbon back-bonding [20]. In figure 4 the shift $\Delta\omega$ of the Si–H stretching mode is plotted as a function of the total carbon–silicon ratio *R*, showing a linear relation.

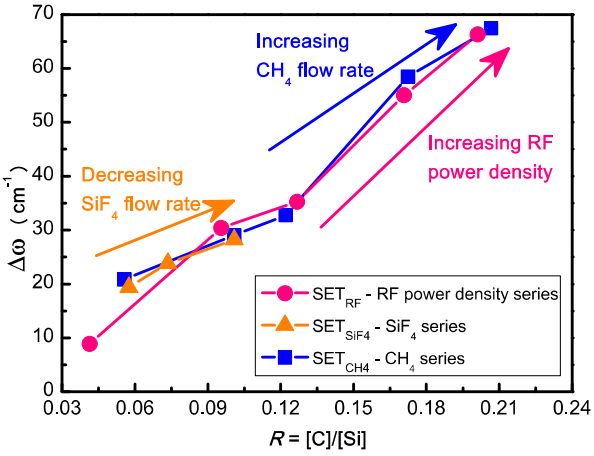

Figure 4. Shift $\Delta\omega$ of the Si–H stretching mode, due carbon back-bonding.

3.2. Amorphous to microcrystalline transition: influence of deposition parameters

The structural changes induced in the alloys with the variation of these deposition parameters have been studied using spectroscopic ellipsometry (figure 5), Raman spectroscopy (figure 6) and grazing incidence x-ray diffraction (figure 7) measurements. All these techniques can be used to highlight the transition between a-$Si_{1-x}C_x$:H and μc-$Si_{1-x}C_x$:H.

The typical ellipsometry spectra of an amorphous alloy is characterized by a single broad peak in the imaginary part of the pseudodielectric function ($<\epsilon_i>$). The amorphous nature

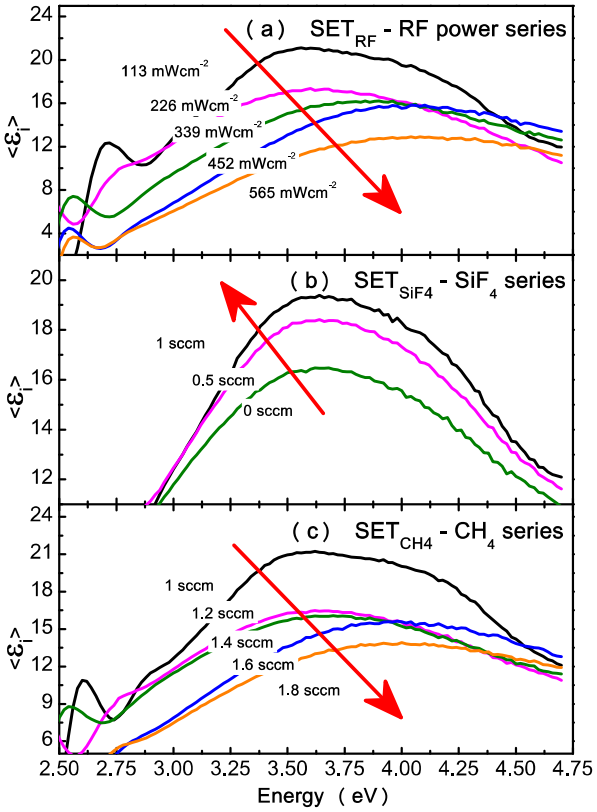

Figure 5. Experimental ellipsometry spectra of samples deposited varying (*a*) the RF power density, (*b*) the SiF_4 flow rate and (*c*) the CH_4 flow rate.

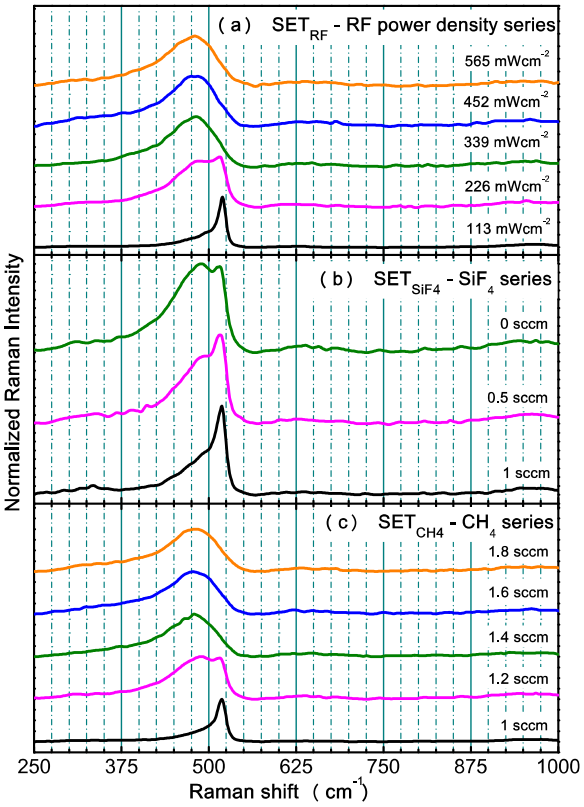

Figure 6. Raman spectra of samples deposited varying (*a*) the RF power density, (*b*) the SiF_4 flow rate and (*c*) the CH_4 flow rate.

of such materials can also be observed in Raman spectra, which show a broad peak centred at 480 cm^{-1}, as well as in x-ray diffraction patterns characterized only by broad humps located at 27.6° and 51°, due to the short and medium range order [21]. For the samples studied herein, such signatures are observed when alloys are deposited with $w_{RF} > 250$ mW cm^{-2}, when no SiF_4 is added to the gas mixture, or CH_4 flow rates are above 1.2 sccm. However, for $w_{RF} < 250$ mW cm^{-2}, few sccm of SiF_4 added to the gas phase or CH_4 flow rates below 1.2 sccm, ellipsometry spectra exhibit a pseudodielectric function clearly characterized by two features at 3.5 eV and 4.2 eV, typical of μc-Si:H. This transition, indicating an enhancement of the microcrystalline silicon phase, is highlighted in Raman spectra by the decreased intensity of the broad band at 480 cm^{-1} and the appearance of a sharp peak at around 520 cm^{-1}, corresponding to the Si–Si Transversal Optical (TO) mode and in GIXRD patterns by the appearance of diffraction peaks characteristic of the cubic phase of crystalline silicon (diffraction planes being at $2\theta = 28.44°$, 47.3° and 56.1° are labelled in figure 7). It is noteworthy that in the diffraction patterns, no crystalline silicon carbide or crystalline forms of carbon can be seen. Therefore, one can safely assert that all samples are made of silicon crystallites embedded in an amorphous $Si_{1-x}C_x$ matrix [22]. Moreover, for all sets of samples, the ratios of the GIXRD peaks intensities are in good agreement with the powder standard of cubic silicon, proving the absence of a preferential orientation. The diffraction patterns are thus characteristic of randomly oriented polycrystalline layers [23].

From the deconvolution of the Raman spectra, according to the method presented in [24], it is possible to calculate the crystalline volume fraction f_c, which is expressed as

$$f_c = \frac{I_{510} + I_{520}}{I_{480} + I_{510} + I_{520}} \qquad (2)$$

where I_{480}, I_{510} and I_{520} are the integrated areas of the peaks located at 480 cm^{-1}, 510 cm^{-1} and 520 cm^{-1}, respectively. Its evolution is shown in figure 8(*a*) as a function of the total carbon–silicon ratio *R*, together with the evolution of the average grain size δ (figure 8(*b*)), as determined from the full width at half maximum (FWHM) of the diffraction peaks, using the Scherrer approach [25].

As it has been previously observed, the variation of the selected deposition parameters leads to a phase transition. By decreasing the RF power density or the CH_4 flow rate, or by adding SiF_4 to the gas mixture, it is possible to obtain alloys with increasing f_c, which however exhibit very different microstructural properties. While the decrease in w_{RF} allows δ to nearly double, passing from ~60 Åto ~ 115 Å, the addition of SiF_4 and the decrease in CH_4 flow rate induce only a 25% increase of the average grain size (ranging from 60 to 80 Å). These results are additionally confirmed by

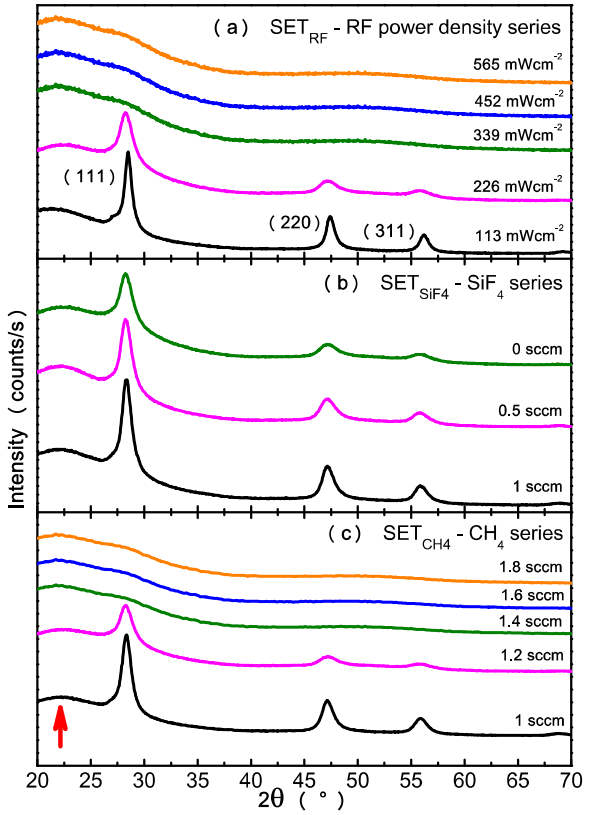

Figure 7. XRD patterns acquired in grazing incidence mode for samples deposited varying (*a*) the RF power density, (*b*) the SiF_4 flow rate and (*c*) the CH_4 flow rate. Diffraction peaks correspond to the cubic phase of crystalline silicon and the relative lattice planes are labelled. The broad shoulder at $2\theta = 22°$, indicated by the arrow, corresponds to the diffraction of the Corning glass substrate.

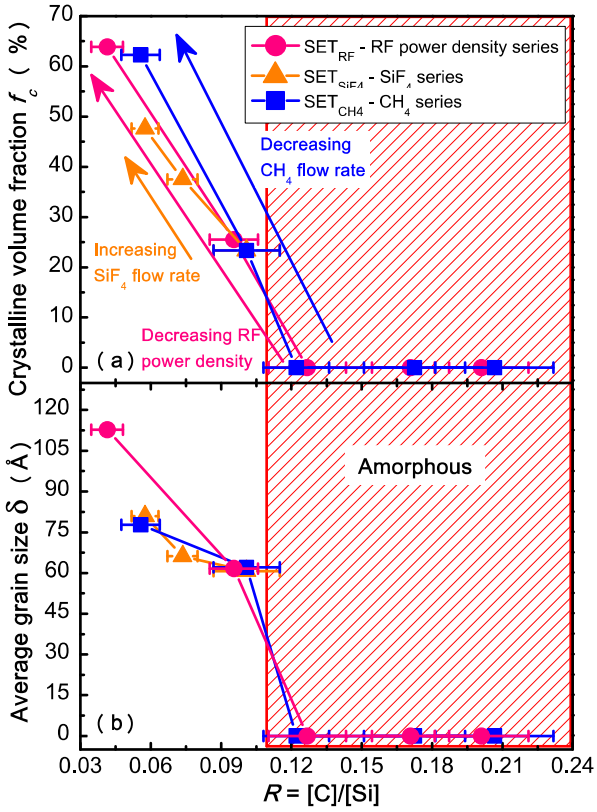

Figure 8. Evolution of (*a*) crystalline volume fraction f_c and (*b*) average grain size δ, as a function of the total carbon–silicon ratio R of samples deposited varying RF power density (•), SiF_4 flow rate (△) or CH_4 flow rate (□).

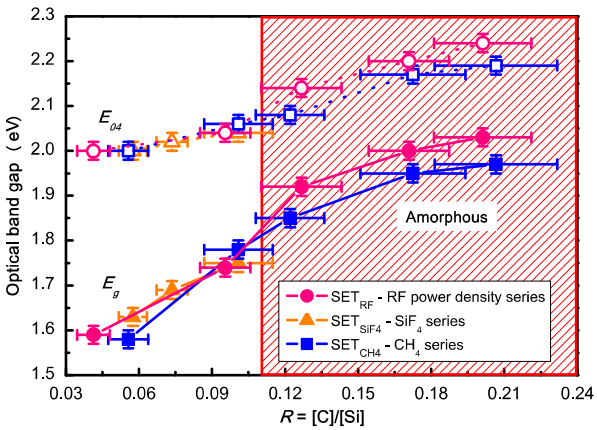

Figure 9. Evolution of the optical band gap of samples deposited varying RF power density (•), SiF_4 flow rate (△) or CH_4 flow rate (□), as a function of the total carbon–silicon ratio R. Open symbols correspond to the E_{04}, determined from transmission measurements and the closed ones to E_g, obtained from ellipsometry fitting.

TEM observations that will be presented in the following section.

Finally, the evolution of the average optical band gap, as determined by spectroscopic ellipsometry or transmission spectroscopy, is presented in figure 9 as a function of R. The definition of the optical band gap of this kind of mixed-phase material is not trivial. As previously shown, $\mu c\text{-}Si_{1-x}C_x{:}H$ alloys are made of silicon crystallites embedded in an amorphous silicon–carbon matrix. Therefore, the optical band gap E_g deduced from the ellipsometry fitting can be considered as an average band gap, determined from the contribution of the two phases. Another definition can be obtained by considering E_{04}, that is the energy at which we have an absorption coefficient equal to 1×10^4 cm^{-1}. These two definitions of 'optical band gap' in a mixed-phase material can be considered as a lower and upper limit, highlighting qualitative information about the degree of the films' transparency and how they may perform in electronic devices.

For all three sets of samples, the increase in R is translated into an increase of the average optical band gap E_g. Moreover, for $R < 0.12$, the increase of E_g is not mirrored by an increase in E_{04}, which is stable around a mean value of 2 eV. These values of R still correspond to the crystalline regime, although a gradual phase transition is taking place. As soon as the full phase transition is reached (red dashed area), E_g and E_{04} show the same evolution. This can be explained by the fact that the E_{04} of these materials is the average of the E_{04} of the crystalline phase and that of the

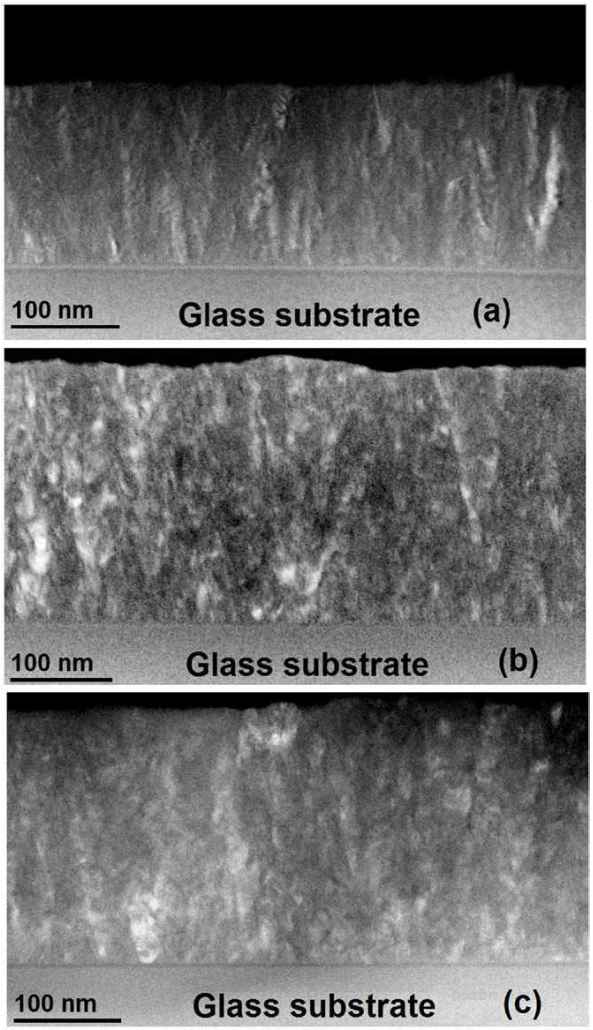

Figure 10. SAADF STEM images of sample from (*a*) SET_{RF} series, with $f_c \sim 65\%$ and $\delta \sim 115$ Å, (*b*) SET_{SiF_4} series with $f_c \sim 50\%$ and $\delta \sim 80$ Åand (*c*) SET_{CH_4} with $f_c \sim 65\%$ and $\delta \sim 80$ Å.

amorphous one, weighted by their respective percentages. With increasing total carbon–silicon ratio (and therefore decreasing crystalline fraction), in order for the average E_{04} to remain stable, the E_{04} of the amorphous phase must decrease since the E_{04} of the crystalline fraction remains constant. For the E_{04} of the amorphous tissue to be decreasing with decreasing crystalline fraction, a decreasing carbon–silicon ratio in the amorphous phase should be expected, which is a counter-intuitive result and one that will be tested in a later section of this paper. For $R > 0.12$, materials are completely amorphous and only the enlargement of the bad gap induced by the increasing carbon–silicon ratio plays a role, leading to the same trend for E_g and E_{04} [20].

3.3. Microstructural properties

SAADF STEM images were acquired for samples showing the highest crystalline volume fraction and are presented in figure 10. They confirm that the variation of each of the three deposition parameters leads to materials having very different microstructures, despite all resulting in a similar crystalline volume fraction. The layer deposited with $w_{RF} = 113$ mW cm^{-2} (figure 10(*a*)) is ~180 nm thick, with a 6 nm roughness and is characterized by a very well ordered columnar growth. On the other hand, the alloy made with the addition of 1 sccm of SiF_4 to the gas mixture, keeping $w_{RF} = 226$ mW cm^{-2}, is ~240 nm thick, with a 5 nm roughness and is composed of small crystallites (figure 10(*b*)). Finally, if the CH_4 flow rate is decreased, keeping always $w_{RF} = 226$ mW cm^{-2}, a layer nearly 230 nm thick, with a 5 nm roughness is obtained (figure 10(*c*)). It is noteworthy that the obtained microstructure is similar to that shown in figure 10(*b*).

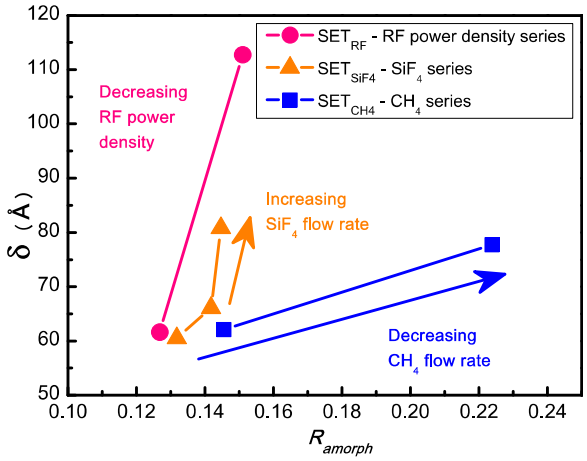

Figure 11. Average grain size δ as a function of the carbon–silicon ratio in the amorphous matrix (R_{amorph}).

It has already been demonstrated that the evolution of the structural properties of μc-$Si_{1-x}C_x$:H alloys can be linked to the carbon content [26]. If one considers the hydrogen and oxygen content to be small, relative to that of the silicon or carbon, the carbon–silicon ratio for the amorphous phase (R_{amorph}) can be derived. Indeed, knowing the percentage of the amorphous and crystalline phases, calculated from Raman scattering analysis, the relative carbon and silicon line intensities measured by RF-GD-OES and the fact that no carbon is incorporated into the crystalline phase, as shown by the absence of SiC diffraction peaks in figure 7, R_{amorph} can be written as

$$R_{amorph} = \frac{1}{\frac{f_a}{100}\left(1+\frac{1}{R}\right)-1} \quad (3)$$

where $f_a = 100 - f_c$ is the amorphous fraction.

In figure 11, the relationship between the average grain size, δ and R_{amorph} is shown. When presented in this way, the three sets of data show a counterintuitive set of results, as a greater carbon incorporation in the amorphous matrix generally results in larger crystallite sizes. However, these trends can be easily understood by seeing that when a process parameter is varied to lower R, the increasing crystalline fraction

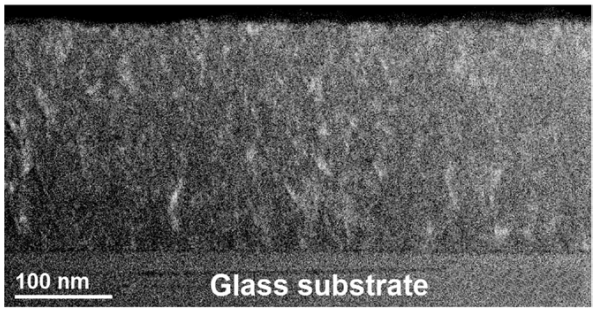

Figure 12. SAADF STEM image of the silicon–carbon alloy with $f_c \sim 25\%$ and $R = 0.09$, common to all series of samples.

(and the fact that carbon only goes into amorphous areas) leads to a greater R_{amorph}. More interestingly, the sensitivity of δ to R_{amorph} depends strongly on which of the three parameters was varied. It is seen that the average crystallite size is very sensitive to RF-power density (at constant C/Si) and less so to CH_4 and SiF_4 flow rate. This suggests that carbon incorporation in the amorphous parts of the film plays no fundamental role in the microcrystalline fraction of the film as a whole. Rather, this quantity is only a symptom of what is occurring for growth in the microcrystalline parts. This important point will be incorporated into the growth model, to be presented in section 3.4.

Finally, to directly observe the preferential incorporation of carbon in the amorphous regions, cross-sectional TEM images were obtained of the sample with the lowest crystalline volume fraction ($f_c \sim 25\%$), common to all sets of samples. Figure 12 shows the SAADF STEM image of the layer. The contrast is due to diffraction interference. The layer, 240 nm thick with a 7 nm roughness, is indeed characterized by crystallites embedded in an amorphous matrix.

To obtain additional information about the chemical composition and distribution in the layer, an EFTEM study of this sample was performed. The energy window (4 eV wide) was first set at 17 eV, corresponding to the silicon bulk plasmon loss and then centred at 24 eV, to observe the presence of a-$Si_{1-x}C_x$. As these layers are non-stoichiometric, a shift in the plasmonic peak can be expected, being the stoichiometric silicon carbide plasmonic excitation at 22 eV [27]. Images of the interface between the sample and the glass substrate are shown in figure 13. A direct comparison confirms that the crystalline phase in these alloys is made of silicon. The crystallites are indeed brighter than the remaining part of the sample in figure 13(*a*) and become darker in figure 13(*b*). In parallel, carbon-rich areas are bright in the image acquired selecting the 24 eV plasmonic energy and become dark in the 17 eV one. It is noteworthy that the material is characterized by a particular V structure, typical of a columnar growth. Therefore, it can be inferred that the material is trying to grow with a classical columnar structure, typical of microcrystalline silicon and that all the carbon is incorporated in the amorphous grain boundaries, creating a thin interconnecting a-$Si_{1-x}C_x$:H tissue surrounding the silicon crystallites.

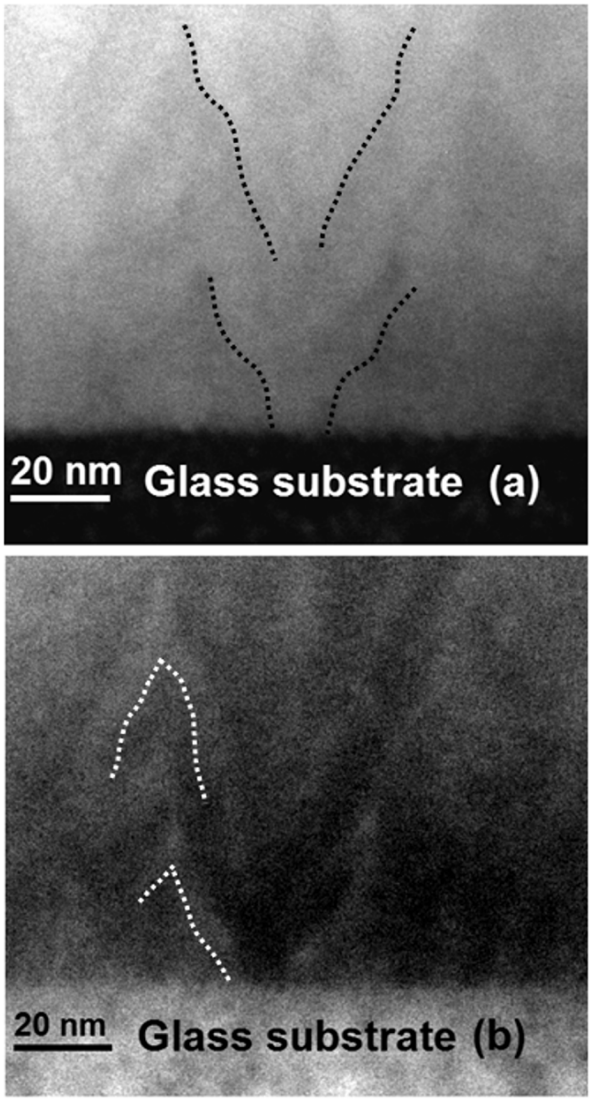

Figure 13. Plasmonic images of a silicon–carbon alloy with $f_c \sim 25\%$ and $R = 0.09$ acquired at different plasmonic excitation energies: (*a*) 17 eV, corresponding to Si bulk and (*b*) 24 eV corresponding to a-$Si_{1-x}C_x$. The dotted line is used to underline zones with a contrast changing from bright to dark, depending on the chosen plasmonic excitation.

3.4. Model for influence of carbon on thin-film growth

It has been shown in this work that a decrease in RF power density or in CH_4 flow rate, or the addition of SiF_4 to the gas mixture, all lead to alloys with an increased crystalline volume fraction. This behaviour, as well as the complementary data presented in this work, allows us to propose a model for the role of carbon during the growth of μc-$Si_{1-x}C_x$:H thin films.

It has been demonstrated that virtually no carbon is incorporated into the microcrystalline phase of the material, as is known for large crystals (hence the lack of non-stoichiometric phases of c-SiC), but also seems to hold for nanometer-sized crystals at the growth temperatures under investigation. All of

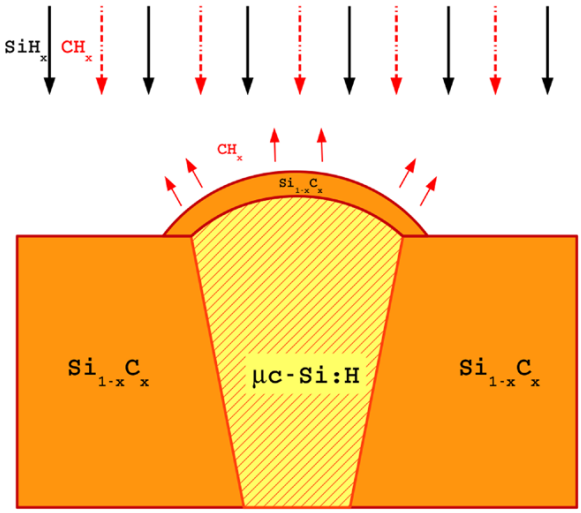

Figure 14. Schematic representation of the proposed model for carbon incorporation during the growth of μc-Si$_{1-x}$C$_x$:H. The hashed cone correspond to the μc-Si:H columnar growth, whereas the full volumes corresponds to the a-Si$_{1-x}$C$_x$:H matrix.

the carbon is therefore incorporated into an amorphous phase. However, it can be assumed that the flux of radicals from the plasma will be homogeneous over the surface—the nanocrystalline growth surfaces see the same flux as the amorphous regions, which raises the question of how the carbon interacts with the growing surface of the film.

As the instability of the non-stoichiometric c-SiC phase relies on the presence of a full 3D crystal, carbon may remain in the few monolayers of growth at the microcrystalline silicon surface before being eliminated. This is the key element of our growth model (figure 14): even in the microcrystalline areas, carbon is incorporated into the sub-surface growth zone in unstable sub-stoichiometric configurations. It is the elimination of the carbon from these sub-stoichiometric zones that retards the growth of the nanocrystalline silicon zones, whereas the growth of the amorphous zones are not retarded by this effect as they can exist in sub-stoichiometric mixtures. This model is consistent with experimental data—it has been previously seen in the literature that the higher the carbon incorporation, the lower the possibility for silicon crystallites to nucleate and grow [28].

With this growth model, the effect of the three parameters discussed in this paper becomes clear. As the ionisation energy threshold for CH_4 (12.6 eV) is greater than that of SiH_4 (11 eV) and we are operating close to depletion conditions for SiH_4, increasing the RF-power will result in a greater relative CH_x flux due to a greater incremental dissociation of this gas [29]. In this way, lower RF-power and reduced CH_4 flow rate both have a similar effect: a reduced CH_x flux to the growth surface (the effect of the ion bombardment energy with the variation of the RF power density is not taken into account). Referring to our model, this means less carbon to be eliminated from the crystalline zones, faster growth of the crystalline areas (relative to the amorphous ones) and therefore a greater crystalline content in the material.

The addition of SiF_4 to the gas mixture has a more complicated effect; it is known that the addition of a small amount of this gas to a process using H_2 diluted SiH_4 results in a negligible incorporation of fluorine in the silicon film, but a significantly reduced oxygen content [10]. However, its role when methane is included has not been studied. Nevertheless, the role of SiF_4 in this case can be discussed referring to the impact of atomic fluorine during the growth of films from a SiF_4 and CH_4 gas mixture diluted in hydrogen [30]. Si and C atoms are both etched by hydrogen, with carbon being etched faster [31], but the addition of atomic fluorine in the plasma (present due to the dissociation of SiF_4) induces a second etching mechanism. Indeed, atomic fluorine etches Si atoms faster than the carbon one, but both elements more rapidly from the amorphous zones compared to the crystalline areas. While the H_2 and CH_4 flow rates are fixed, leaving the etching mechanism due to atomic hydrogen constant, the introduction of SiF_4 into the gas mixture induces an additional preferential etching of the amorphous zones, slightly shifting the advantage to the growth of the crystalline areas and resulting in more crystalline films.

4. Conclusion

Details on the deposition of hydrogenated microcrystalline silicon–carbon (μc-Si$_{1-x}$C$_x$:H) alloys from a silane and methane gas mixture, highly diluted in hydrogen, using three different process parameters to change the crystalline volume fraction (decreased RF power density, addition of silicon tetrafluoride to the gas mixture, or variation of the CH_4 flow rate) were presented. With Raman spectroscopy, SAADF STEM, EF TEM and GIXRD analyses it was demonstrated that these alloys are composed of silicon crystallites embedded in an a-Si$_{1-x}$C$_x$:H matrix. Furthermore, although some measurements suggest similar outcomes for materials when varying each parameter (Spectroscopic Ellipsometry, Raman scattering, FTIR), they actually result in very different microstructures (as shown by GIXRD and TEM). The decrease of the RF-power leads to a well ordered columnar growth characterized by grains with a 115 Å average size, whereas the addition of SiF_4 or the decrease of the CH_4 flow rate induce a high crystalline fraction with an average size of ~80 Å. This provides important guidance, as the microstructure may play a more important role on the electronic performance of the materials and has been used to suggest a model for the role of carbon during the growth of microcrystalline films, wherein the presence of carbon in the sub-surface growth zone retards microcrystalline growth in favour of amorphous SiC regions which can exist in sub-stoichiometric ratios.

Acknowledgments

The authors would like to thank P Bulkin for the fruitful discussions and P Chapon from Horiba Jobin-Yvon for access to RF-GD-OES measurements. This work has been supported by the French National Research Agency (ANR) through the 'Habitat intelligent et solaire photovoltaïque' program (project CANASTA n°ANR-10-HABISOL-002)

References

[1] Matsumoto Y, Hirata G, Takakura H, Okamoto H and Hamakawa Y 1990 *J. Appl. Phys.* **67** 6538
[2] Demichelis F, Giorgis F and Pirri C F 1995 *Solid State Commun.* **96** 17
[3] Osten H J 2000 *Thin Solid Films* **367** 101
[4] Demichelis F, Pirri C F and Tresso E 1992 *J. Appl. Phys.* **72** 1327
[5] Dasgupta A, Saha S C, Ray S and Carius R 1999 *J. Mater. Res.* **14** 2554
[6] Coscia U, Ambrosone G, Lettieri S, Maddalena P, Rigato V, Restello S, Bobeico E and Tucci M 2005 *Sol. Energy Mater. Sol. Cells* **87** 433
[7] Demichelis F, Pirri C F and Tresso E 1992 *Phil. Mag.* **66** 135
[8] Gaiaschi S, Ruggeri R, Johnson E V, Bulkin P, Chapon P, Gueunier-Farret M E, Mannino G, Longeaud C and Kleider J P 2014 *Thin Solid Films* **550** 312
[9] Ambrosone G, Barucca G, Coscia U, Ferrero S, Lettieri S and Maddalena P 2004 *J. Non-Cryst. Solids* **338** 163
[10] Abramov A and Roca i Cabarrocas P 2010 *Phys. Status Solidi* **7** 529
[11] Nakahata K, Ro K, Suemasu A, Kamiya T, Fortmann C M and Shimizu I 2000 *Japan. J. Appl.* **39** 3294
[12] Goldstein B, Dickson C R, Campbell I H and Fauchet P M 1988 *Appl. Phys. Lett.* **53** 2672
[13] Jellison G E Jr and Modine F A 1996 *Appl. Phys. Lett.* **69** 371
[14] Pisonero J, Fernández B, Pereiro R, Bordel N and Sanz-Medel A 2006 *Trends Anal. Chem.* **25** 11
[15] Sanchez P, Fernandez B, Menendez A, Pereiro R and Sanz-Medel A 2010 *J. Anal. At. Spectrom.* **25** 370
[16] O'Connor J, Sexton B , Smart R S C 2003 Surface analysis methods in materials science *Springer Series in Surface Sciences* vol 23 (New York: Springer) p 553
[17] Winchester M R and Payling R 2004 *Spectrochim. Acta Part B: At. Spectrosc.* **59** 607
[18] Ruggeri R, Neri F, Sciuto A, Privitera V, Spinella C and Mannino G 2012 *Appl. Phys. Lett.* **100** 042104
[19] Basa D K and Smith F W 1990 *Thin Solid Films* **192** 121
[20] Bullot J and Schmidt M P 1987 *Phys. Status Solidi* **143** 345
[21] Williamson D L 1999 *MRS Online Proc. Library* **557** 251
[22] Coscia U, Ambrosone G, Lettieri S, Maddalena P and Ferrero S 2006 *Thin Solid Films* **511–2** 399
[23] Schicho S, Köhler F, Carius R and Gordijn A 2012 *Sol. Energy Mater. Sol. Cells* **98** 391
[24] Smit C, van Swaaij R A C M M, Donker H, Petit A M H N, Kessels W M M and van de Sanden M C M 2003 *J. Appl. Phys.* **94** 3582
[25] Birkholz M 2006 *Thin Film Analysis by X-ray Scattering* (New York: Wiley) 10.1002/3527607595
[26] Han W, Fan S and Gu B 1996 *Mater. Sci. Eng.* **41** 357
[27] Egerton R F 2009 *Rep. Prog. Phys.* **72** 016502
[28] Coscia U, Ambrosone G, Maddalena P, Setaro A, Phani A R and Passacantando M 2007 *Thin Solid Films* **515** 7634
[29] Catherine Y, Turban G and Grolleau B 1981 *Thin Solid Films* **76** 23
[30] Cicala G, Capezzuto P, Bruno G and Rossi M C 2001 *Appl. Surf. Sci.* **184** 66
[31] Saxena N, Fortmann C M and Russell T W F 1989 *MRS Proc.* **149** 99

Thin Solid Films 550 (2014) 312–318

Contents lists available at ScienceDirect

Thin Solid Films

journal homepage: www.elsevier.com/locate/tsf

Structural properties of hydrogenated microcrystalline silicon–carbon alloys deposited by Radio Frequency Plasma Enhanced Chemical Vapor Deposition: Effect of microcrystalline silicon seed layer and methane flow rate

S. Gaiaschi [a,b,*], R. Ruggeri [c], E.V. Johnson [b], P. Bulkin [b], P. Chapon [d], M.-E. Gueunier-Farret [a], G. Mannino [c], C. Longeaud [a], J.-P. Kleider [a]

[a] LGEP-CNRS/SUPELEC, 11 rue Joliot Curie, Plateau de Moulon, 91192 Gif sur Yvette, France
[b] LPICM-CNRS, Ecole Polytechnique, 91128 Palaiseau, France
[c] CNR-IMM, Strada VIII n 5, Zona Industriale, 95121 Catania, Italy
[d] HORIBA Jobin Yvon, 16-18, rue du Canal, 91165 Longjumeau Cedex, France

ARTICLE INFO

Article history:
Received 7 January 2013
Received in revised form 14 November 2013
Accepted 18 November 2013
Available online 25 November 2013

Keywords:
Hydrogenated silicon carbon
Microcrystalline silicon carbon
Radio Frequency Plasma Enhanced Chemical Vapor Deposition
Seed layer
Radio Frequency Glow Discharge Optical Emission Spectroscopy

ABSTRACT

Hydrogenated silicon–carbon thin films were deposited by Radio Frequency Plasma Enhanced Chemical Vapor Deposition using silane–methane gas mixtures highly diluted in hydrogen. The effects of the presence of a microcrystalline silicon seed layer and of the methane flow rate during deposition were investigated in order to find the optimal conditions for microcrystalline growth. The presence of a seed layer promotes the amorphous to microcrystalline transition at the interface with the substrate, reducing the incubation layer to a 5–10 nm thickness. At the same time, an excessive increase in the CH_4 flow rate suppresses crystalline growth, leading to extremely flat amorphous samples (root-mean-square surface roughness ρ_{RMS} ~ 0.5 nm), even with a seed layer. The total carbon content was measured by Radio Frequency Glow Discharge Optical Emission Spectroscopy. It was found that carbon is only incorporated in the amorphous tissue, and not in the crystalline phase. Thus, the increase of the crystalline fraction, directly linked to the increase of the seed layer deposition time, leads to a decrease of the carbon incorporation in the subsequent layer.

© 2013 Elsevier B.V. All rights reserved.

1. Introduction

A material stable to light soaking with an electronic band-gap similar to that of hydrogenated amorphous silicon (a-Si:H) holds great potential gains for thin film silicon-based photovoltaics [1].

Hydrogenated microcrystalline silicon–carbon alloys (μc - $Si_{1-x}C_x$:H) are potential candidates but possess complicated growth dynamics and material properties. Indeed, μc - $Si_{1-x}C_x$:H samples deposited by conventional Radio Frequency Plasma Enhanced Chemical Vapor Deposition (RF-PECVD), exhibit (i) a higher conductivity than their amorphous counterparts because of the presence of submicron-size silicon crystallites embedded in an amorphous silicon–carbon matrix [2,3], and (ii) a larger energy gap than that of microcrystalline silicon [4,5] due to carbon incorporation.

It is well known that the introduction of gasses containing carbon into the silane discharge can be detrimental to microcrystalline growth [6]; however, it is possible, by using a microcrystalline silicon seed layer (μc-Si:H), to eliminate the problem of carbon incorporation in the amorphous incubation layer (typical of all microcrystalline growth [7]), and to obtain thin micro-crystalline films of $Si_{1-x}C_x$:H(~50 nm).

In this paper, both the effects of the μc-Si:H seed layer and of the variation of the CH_4 flow during the subsequent growth were studied.

2. Experimental details

Hydrogenated silicon–carbon films were deposited by RF-PECVD at a substrate temperature of 275 °C. Films were grown from a mixture of silane (SiH_4) and methane (CH_4) highly diluted in hydrogen (H_2). The pressure and the inter-electrode distance were fixed at 240 Pa and 1.2 cm, respectively. All samples were deposited using a combination of a μc-Si:H seed layer, followed by a 30 minute deposition, with the addition of CH_4. Two sets of samples were deposited: in the first set (RF1) the effect of a μc-Si:H seed layer was investigated by varying its deposition time from 0 to 16 min (H_2, SiH_4 and CH_4 flow rates for the μc - $Si_{1-x}C_x$:H layer were kept constant at 500 sccm, 5 sccm, and 1 sccm, respectively). In the second set (RF2) the effect of the variation of the CH_4 flow rate (from 1 sccm to 2.5 sccm) during the μc - $Si_{1-x}C_x$:H layer deposition was studied. For both series, the H_2 flow rate was

* Corresponding author at: LGEP-CNRS/SUPELEC, 11 rue Joliot Curie, Plateau de Moulon, 91192 Gif sur Yvette, France.
E-mail address: sofia.gaiaschi@poly.polytechnique.edu (S. Gaiaschi).

0040-6090/$ – see front matter © 2013 Elsevier B.V. All rights reserved.
http://dx.doi.org/10.1016/j.tsf.2013.11.081

kept constant at 500 sccm. The SiH_4 flow rate was kept at 6 sccm during the μc-Si:H seed layer deposition and decreased to 5 sccm during the main layer deposition. Finally, the RF power was kept at 16 W during the seed layer deposition and increased to 40 W during the main layer deposition. The conditions used for the seed layer are known to result in highly microcrystalline samples when used to grow thicker films. Each sample was deposited simultaneously on two different substrates: <100> float zone silicon to perform infrared (IR) spectroscopy measurements and Corning "Eagle" glass to perform ellipsometry and Raman spectroscopy measurements as well as Atomic Force Microscopy (AFM) and Transmission Electron Microscopy (TEM) analyses.

Ellipsometry measurements were performed using a UVISEL spectroscopic ellipsometer from HORIBA Jobin Yvon in the spectral range 1–4.7 eV. To analyze these spectra, a two Tauc–Lorentz [8] dispersion formula for microcrystalline materials and a single Tauc–Lorentz dispersion formula for the amorphous ones were used to parametrize the dielectric function $\epsilon(E) = \epsilon_r(E) + i\epsilon_i(E)$ as a function of the photon energy E, where $\epsilon_r(E)$ and $\epsilon_i(E)$ are the real and imaginary parts respectively. The thickness of the samples was then determined using a single-layer with roughness model. Raman spectra were obtained in the 200–1500 cm^{-1} range using a LABRAM Aramis system, Confocal Raman Microscope by HORIBA Jobin Yvon, equipped with a 473 nm laser. IR absorption measurements between 400 and 4000 cm^{-1} were carried out using a Brüker Equinox 55 Fourier transform infrared spectrometer. Surface roughness was studied by means of a Dimension 5000 Atomic Force Microscope by Digital Instruments Inc. in air, operated in tapping mode. TEM and Energy Filtered-TEM (EF-TEM) analyses were performed using a JEOL TEM 2010 F electron microscope operating at an accelerating voltage of 200 kV and equipped with a Gatan electron energy loss image filtering. Plasmonic images were acquired using plasmonic excitation at 16 eV (Si – Si bond) and 24 eV (Si – C bond is at 22 eV). In both cases the energy slit used had a 4 eV width. Electron transparent samples were prepared by conventional mechanical polishing and argon-ion thinning. Finally, the elemental contents and the depth profiles of carbon and silicon were determined by Radio Frequency Glow Discharge Optical Emission Spectroscopy (RF-GD-OES) using a HORIBA Jobin Yvon GD-Profiler 2.

3. Results and discussion

3.1. Role of the seed layer

Initial attempts at growing thin μc - $Si_{1-x}C_x$:H layers (50–100 nm) by RF-PECVD for this study had resulted in fully amorphous samples. This was attributed to the presence of CH_4 at the beginning of the deposition interfering with nucleation. It was therefore decided to investigate the effect of a μc-Si:H seed layer, for which the deposition time was varied from 0 to 16 min.

Ellipsometry (only the imaginary part $<\epsilon_i>$ of the pseudodielectric function) and Raman spectra of the samples are presented in Fig. 1, while thickness and crystalline fraction, deduced from those measurements, are listed in Table 1. A transition from an amorphous to a crystalline phase can be observed as soon as a μc-Si:H seed layer is added. In the case of no seed layer, the ellipsometry spectrum results in a broad peak in the imaginary part $<\epsilon_i>$ of the pseudo-dielectric function, typical of an amorphous sample. The introduction of a seed layer, on the other hand, induces the presence of two structures, typical of μc-Si:H, at about 3.5 eV and 4.2 eV, meaning that a phase transition has taken place. Regarding the Raman spectra, the absence of the seed layer leads to a broad component located around 480 cm^{-1} which is characteristic of amorphous silicon. With an increase in the seed layer deposition time, the Si–Si Transversal Optical (TO) mode located at 520 cm^{-1} appears and grows with increasing the seed layer deposition time. Considering that no SiC-related mode can be detected in the Raman spectra, one can accept the dominant presence of silicon crystallites embedded in an amorphous $Si_{1-x}C_x$ matrix [9,10].

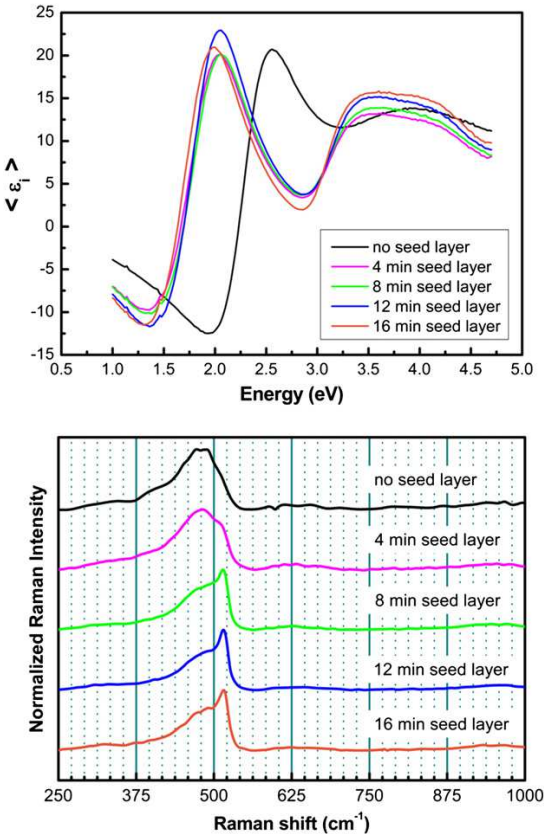

Fig. 1. Experimental ellipsometry spectra and Raman spectra of samples deposited varying the seed layer deposition time.

An estimation of the crystalline volume fraction, f_c, was obtained according to the relation

$$f_c = \frac{I_{510} + I_{520}}{I_{480} + I_{510} + I_{520}} \quad (1)$$

where I_{480}, I_{510} and I_{520} are the areas of the peaks located at 480 cm^{-1}, 510 cm^{-1} and 520 cm^{-1}, respectively [11]. So, while samples deposited without seed layer are completely amorphous ($f_c = 0\%$), with the introduction of such a layer it is possible to induce a phase transition. Moreover, increasing the seed layer deposition time leads to an increase of the crystalline content, up to 35%.

The importance of the seed layer can also be underlined by the surface structure, as shown in the topographic images obtained from AFM measurements in Fig. 2a) and b). When no seed layer is deposited, the sample exhibits an extremely flat surface; in contrast, the introduction of a thin μc-Si:H seed layer induces the presence of protrusions emerging from the surface, that are even more evident in Fig. 2c).

Table 1
Thickness and crystalline volume fraction f_c calculated from ellipsometry modeling and Raman spectroscopy fitting, respectively.

Sample	Seed layer time (min)	Thickness (nm)	f_c (%)
RF1(1)	0	40	0
RF1(2)	4	59	11
RF1(3)	8	58	29
RF1(4)	12	56	34
RF1(5)	16	59	35

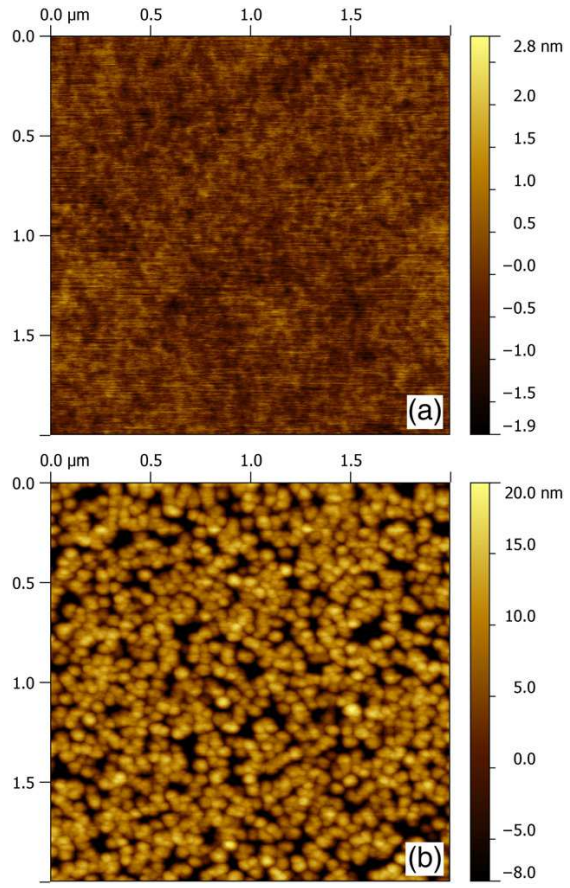

Fig. 2. AFM images of samples with a) no seed layer and b) four minute deposition seed layer. The increase in the surface roughness is highlighted by the difference of the scale. In b) the dark spots are amorphous areas between the aggregates.

These protrusions are consistent with aggregates composed of nanometer sized subgrains that are elongated in the direction of growth [12,13].

For this set of samples the root-mean-square (RMS) surface roughness ρ_{RMS} increases with the introduction of the seed layer and remains constant after a few minutes of seed layer deposition, as presented in Fig. 3. This is consistent with the growth model suggested by Fejfar et al. [14], where a Voronoi network is used to model the μc-Si:H growth, assuming that grains grow as spherically capped cones. The structure resulting from this kind of modeling can be characterized using common parameters such as the RMS roughness. They show that ρ_{RMS} reaches a maximum and then decreases again due to grain caps collisions.

TEM analyses were carried out to study the microstructure of some of these alloys. Fig. 4 shows an area of the sample RF1(5), grown using a 16 minute seed layer. The film, which is 60 nm thick with a 5 nm roughness, is clearly microcrystalline and shows the initial stages of a typical columnar growth, where the usual incubation layer is now reduced to a 5–10 nm region at the interface with the substrate.

To obtain some chemical information for such films, plasmonic images of the same sample were also acquired and are shown in Fig. 5. In EF-TEM mode, images are obtained by collecting electrons that have lost a characteristic amount of energy when interacting with the sample. Thus, chemical mappings of all the elements in the sample can be acquired, using an energy filter to select the desired plasmonic energy [15]. In our case, to map the presence of silicon crystals embedded in the matrix, we select an energy window (4 eV wide) at 16 eV,

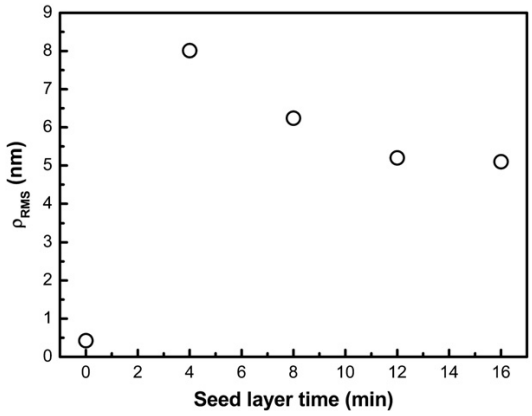

Fig. 3. RMS roughness ρ_{RMS} as a function of the seed layer deposition time.

corresponding to the silicon plasmon loss. The energy difference between the silicon and the silicon carbide plasmonic peak should allow discrimination between the two different contributions. To observe the presence of silicon–carbon bonds, one may use the well-known stoichiometric silicon–carbide plasmonic excitation at 22 eV, but as these layers are non-stoichiometric, a shift in the plasmonic peak can be expected [16]. In fact, for an image acquired with an energy window centered at 24 eV, an increased brightness localized at the surface, at the interface with the substrate, and around the crystal grains can be observed. Therefore, by comparing the image acquired at16 eV (Fig. 5a)) with the one acquired at 24 eV (Fig. 5b)), it is possible to confirm that crystals are composed primarily of silicon since they are brighter than the remaining part of the sample in the first image and vice-versa in the second one. It is thus clear that the analyzed sample is made of silicon crystals embedded in an amorphous silicon–carbon matrix.

3.2. Role of the CH_4 gas flow

Building on the previous results, a second set of samples was deposited with a ten minute deposition time seed layer and a CH_4 flow rate varying from 1 to 2.5 sccm.

The resulting ellipsometry and Raman scattering spectra are given in Fig. 6, while thickness and crystalline fraction are listed in Table 2. Both spectra show a transition from a microcrystalline to an amorphous phase with an increasing CH_4 flow rate.

The Raman spectra of all the samples exhibit a broad peak at 480 cm^{-1}, but a peak located at 520 cm^{-1} is also observed for the sample deposited with the lowest CH_4 flow rate. Moreover, ellipsometric measurements show a transition from a dielectric function with two

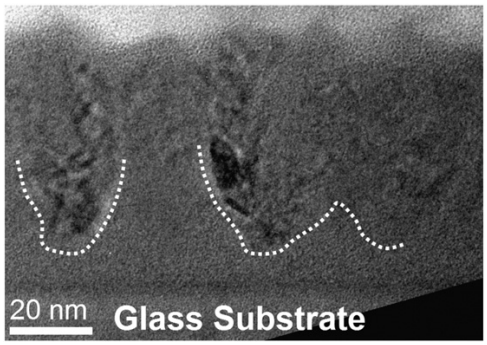

Fig. 4. Cross sectional TEM micrographs of RF1(5) sample deposited with a 16 minute seed layer. The dotted line underlines the presence of grains in an amorphous matrix.

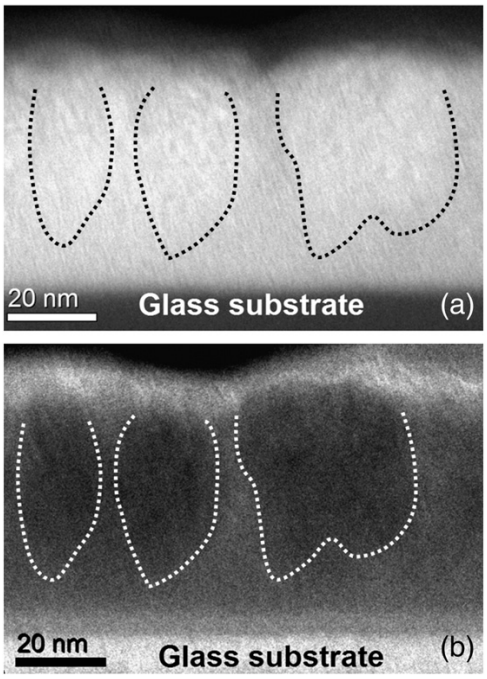

Fig. 5. Plasmonic images of RF1(5) sample deposited with a 16 min seed layer. Images are acquired at a) 16 eV and b) 24 eV.

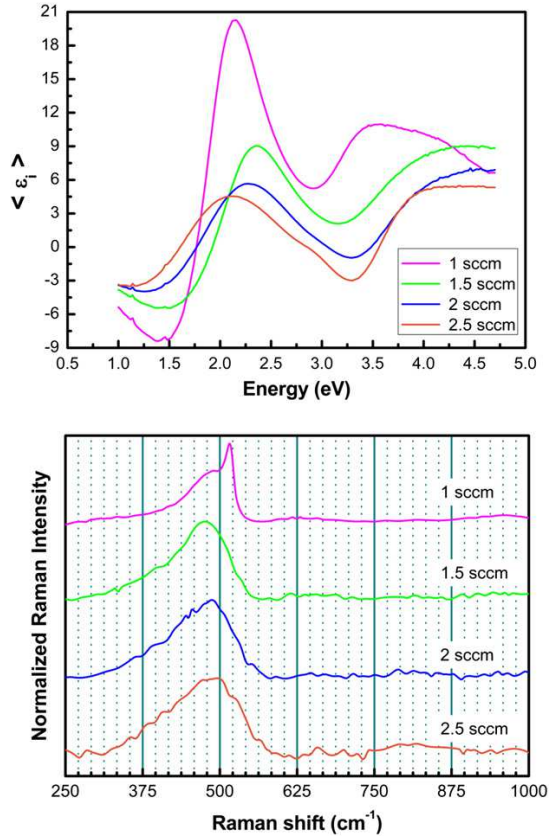

Fig. 6. Experimental ellipsometry and Raman spectra of samples deposited with various CH_4 flow rates.

Table 2
Thickness and crystalline volume fraction f_c calculated from ellipsometry modeling and Raman spectroscopy fitting, respectively.

Sample	CH_4 flow rate (sccm)	Thickness (nm)	f_c (%)
RF2(1)	1	56	31
RF2(2)	1.5	61	0
RF2(3)	2	72	0
RF2(4)	2.5	83	0

features at 3.5 eV and 4.2 eV, typical of μc-Si:H, to an amorphous material with a larger band gap.

It has been noted [17] that an increase in carbon content for such films leads to a decrease of crystalline volume fraction and/or size of silicon crystallites. Logically, for our deposition conditions, increasing the CH_4 flow rate leads to a greater number of dissociated CH_4 molecules, resulting in a rise of carbon incorporation in the films [18]. Moreover, the introduction of carbon atoms into the silicon network [6,17] causes altered bond lengths and distorted angles, which prevent the formation of silicon crystallites [19] leading to a crystalline–amorphous transition.

Considering that the Raman spectra have given no information about the presence of Si – C bonds (no signal at 800 cm^{-1} or 960 cm^{-1} [20]), the influence of the variation of CH_4 flow rate was also studied by FTIR spectroscopy.

In Fig. 7 the infrared spectra of RF2(1)–RF2(4) samples are compared. They all present two main absorption bands: 500–1000 cm^{-1} and 2000–2100 cm^{-1}. The band at 2800–3000 cm^{-1}, due to C – H stretching mode, is too weak to be visible at this scale. The first region can be considered as the superposition of four different bands: the Si–H wagging mode at 640 cm^{-1}, the Si – C stretching mode at 760–780 cm^{-1}, the Si – H bending mode at 800–900 cm^{-1} and the C – H wagging mode at 1000 cm^{-1}, while the second one is the superposition of the 2000 cm^{-1} and 2090 cm^{-1} bands, related to the Si–H and Si–H_2 groups, respectively [21]. The other two absorption regions at 1500–2000 cm^{-1} and 3500–4000 cm^{-1} are related to the absorption of residual atmospheric water in the measurement system and can be ignored.

The Si – C bond concentration N_{Si-C} was then calculated from the integrated area of the deconvoluted band at 780 cm^{-1}, using the following relation [22]:

$$N_{Si-C} = A_{Si-C} \cdot \int \frac{\alpha(\omega)}{\omega} d\omega \tag{2}$$

where $A_{Si-C} = 2.13 \cdot 10^{19}$ cm^{-2} is the inverse cross-section [23], $\alpha(\omega)$ is the absorption coefficient, which is a function of the wavenumber ω and the integration is done over the deconvoluted peak after the subtraction of a baseline. Fig. 8 shows that N_{Si-C} increases with

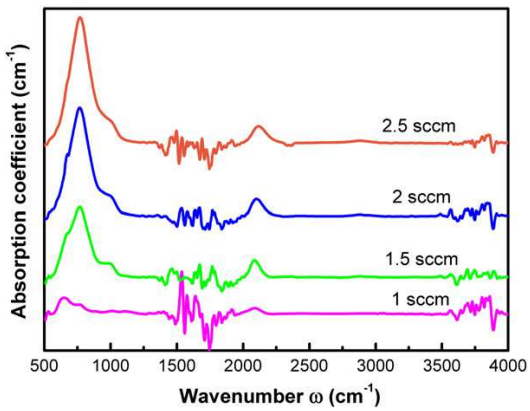

Fig. 7. IR spectra for samples deposited with different CH_4 flow rate.

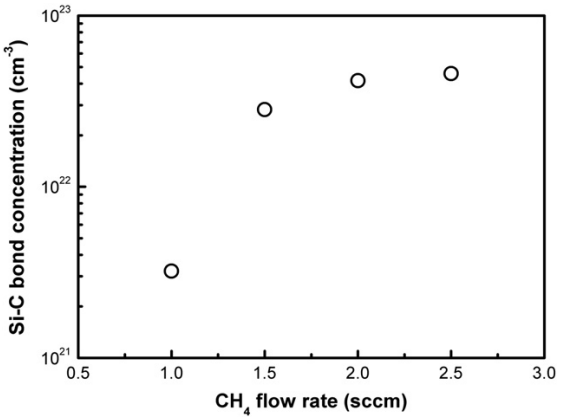

Fig. 8. Si – C bond concentration N_{Si-C} vs. CH_4 flow rate.

an increasing CH_4 flow rate. Therefore, an increase of the carbon incorporation in the matrix can be noted.

One of the most striking effects of the increase of the methane flow rate is in the surface roughness ρ_{RMS} values deduced from AFM measurements performed over a 4 μm^2 surface and given in Fig. 9. Exceeding a given methane threshold (>1 sccm) results in amorphous samples with extremely flat surfaces (ρ_{RMS} ~ 0.5 nm).

To confirm the hypothesis that the layers showing some crystalline character are in fact made up of silicon grains embedded in an amorphous $Si_{1-x}C_x$ matrix, cross sectional TEM micrographs of some samples were obtained.

In Fig. 10a) we see the cross sectional TEM image for the sample RF2(1). The layer, 50 nm thick, is not homogeneous and is characterized by a particular morphology. The presence of 50 nm thick crystal grains, with a maximum diameter of 50 nm, embedded in a flat amorphous matrix (~25 nm thick) can be noted. The apparent disagreement between this image and the roughness calculated from AFM measurements can be linked to the different size of the areas probed by the two different techniques and to the definition of ρ_{RMS} as the RMS average of the roughness profile ordinates. Furthermore, where the growing grains are still isolated, the local roughness is 25 nm (as probed by TEM analyses), but once these grains start to collide, the ρ_{RMS} decreases due to a reconstruction of the surface (as probed by AFM).

The plasmonic image of the same sample, acquired at 16 eV, is presented in Fig. 10b). It shows that the layer consists mainly of silicon but, as previously stated for the sample RF1(5), a clear difference exists in composition between the grains and the matrix, in terms of carbon incorporation.

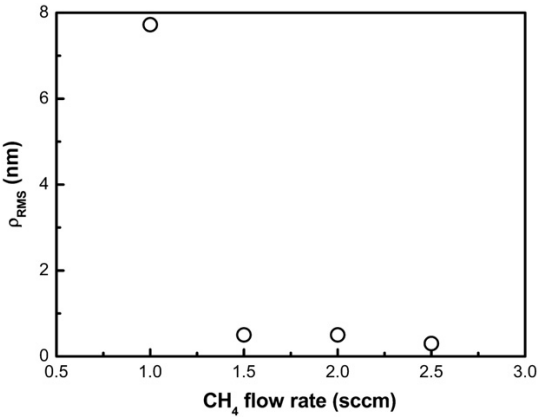

Fig. 9. RMS roughness ρ_{RMS} as a function of the CH_4 flow rate.

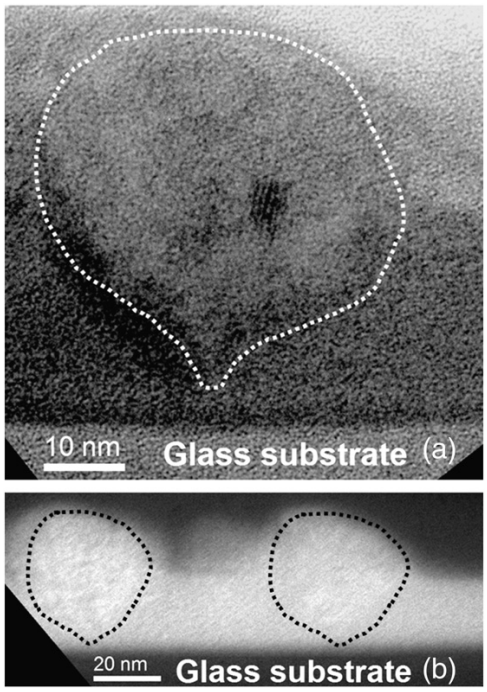

Fig. 10. Cross sectional TEM micrographs of the RF2(1) sample. a) Bright field image, and b) plasmonic image, acquired at 16 eV. Dotted lines are used to clearly identify the presence of silicon crystals in the matrix.

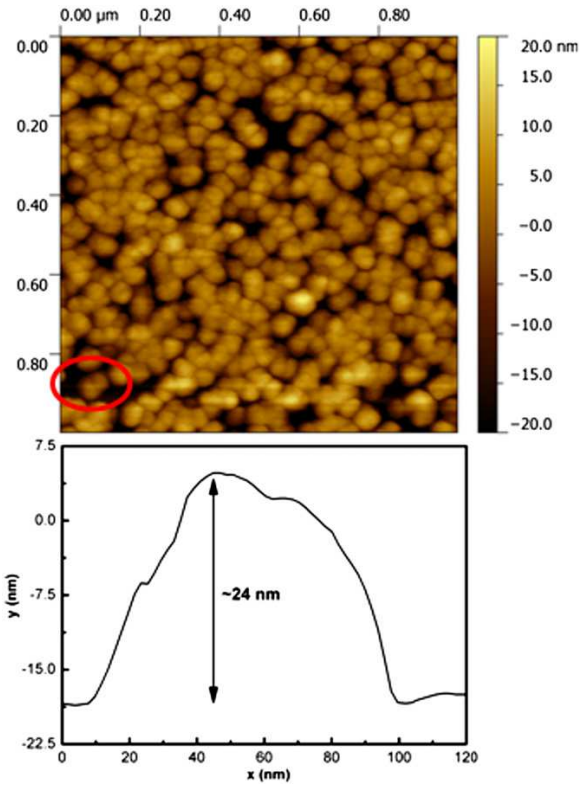

Fig. 11. AFM image of the sample with 1 sccm CH_4 flow rate and AFM profile obtained for the isolated grain highlighted by the red circle.

If one now looks at the surface of the RF2(1) sample (Fig. 11), the same type of protrusions can be observed, as were shown in the previous set of samples. The AFM profile obtained for one of these protrusions can be compared with the TEM micrograph, revealing the same type of structure.

On the other hand, the cross sectional TEM micrograph obtained for the sample RF2(2), shown in Fig. 12, clearly shows that exceeding a certain CH_4 threshold results in a completely amorphous sample. The bright field analysis (Fig. 12a)) shows that the 48 nm-thick layer is homogenous and flat. Furthermore, no sign of an initial crystalline growth can be seen; the excess in CH_4 completely suppresses any crystalline growth. Once again, the sample mainly consists of silicon (as shown in the plasmonic image, Fig. 12b)), but with the clear presence of carbon inside.

3.3. Carbon content by GDOES

The carbon content of each sample was measured by RF-GD-OES, which is a well-established spectrochemical approach for direct determination of major and trace elements. This technique offers several benefits such as high depth resolution, fast sputtering rate, multi-elemental capability and low limits of detection, with no need for ultra high vacuum [24,25].

The carbon–silicon ratio is defined as R = [C]/[Si], where [C] and [Si] are the line intensities for carbon and silicon respectively, and is calibrated by measuring this ratio in a reference monocrystalline silicon carbide sample.

In Fig. 13, the evolution of R in samples RF1(1)–RF1(5) and of the amorphous fraction, defined as $f_a = 100 - f_c$, as a function of the seed layer deposition time, is reported. As expected, despite the deposition gas mixture being kept constant, the variation in the seed layer deposition time is sufficient to alter the amount of carbon incorporated. As carbon is just going into the amorphous matrix, it becomes obvious that the higher the crystalline fraction of the layer (made possible by the thicker seed layer), the lower the total amount of carbon going into the film.

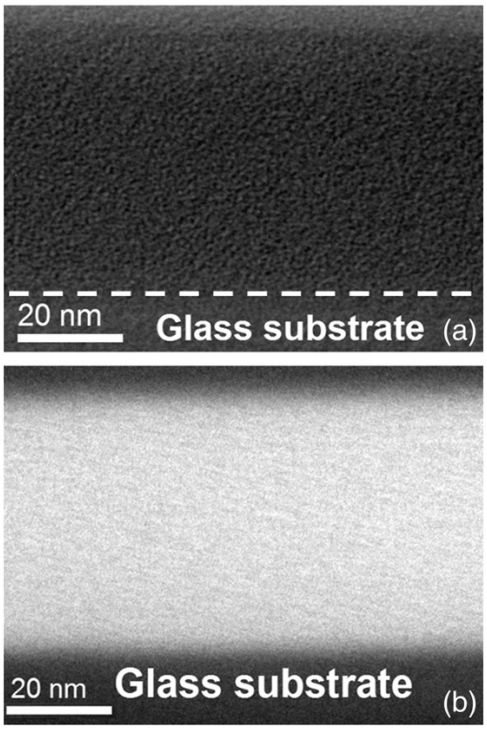

Fig. 12. Cross sectional TEM micrographs of the RF2(2) sample: a) bright field image where the dotted line highlights the interface with the substrate, and b) plasmonic image acquired at 16 eV.

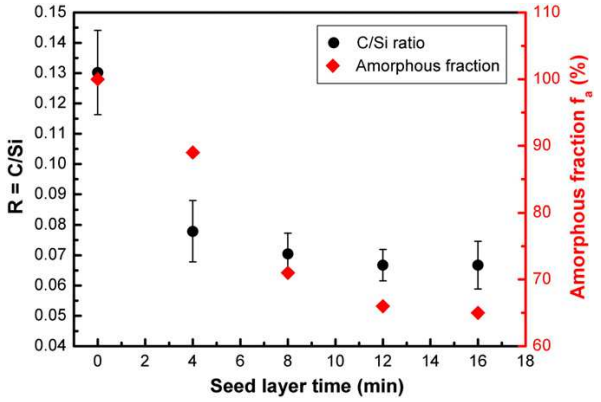

Fig. 13. C/Si ratio measured by RF-GD-OES for RF1(1)–RF1(5) and amorphous fraction $f_a = 100 - f_c$, as a function of seed layer deposition time.

Finally, for samples RF2(1)–RF2(4), the variation of R is reported in Fig. 14 as a function of the CH_4 flow rate during the deposition. A linear relation can be observed with an offset in the incorporated carbon. Furthermore, at low CH_4 flow rates, C is incorporated at disproportionately low rates, compared to higher flows. It should be noted that the linearity of the CH_4 mass-flow controller was verified over this entire range. At first glance, these results might seem at odds with those obtained by FTIR spectroscopy (Fig. 8). However, it is important to note that in Fig. 8, only the density of Si–C bonds is reported, not taking into account any contribution arising from C–H and C–C bonds, whereas by RF-GD-OES, one measures the total carbon content.

4. Conclusion

Hydrogenated microcrystalline silicon carbon (μc - $Si_{1-x}C_x$:H) samples have been deposited by standard RF-PECVD from a silane and methane gas mixture, highly diluted in hydrogen.

It has been shown that a microcrystalline silicon seed layer is needed to trigger microcrystalline growth, in layers thinner than 100 nm, and the well-known incubation layer is reduced to a 5–10 nm thickness; otherwise samples are completely amorphous. Furthermore, if the CH_4 flow rate is increased and a given threshold is exceeded, microcrystalline growth is suppressed and the transition to an extremely flat amorphous $SiSi_{1-x}C_x$:H phase takes place, giving a surface roughness (ρ_{RMS})

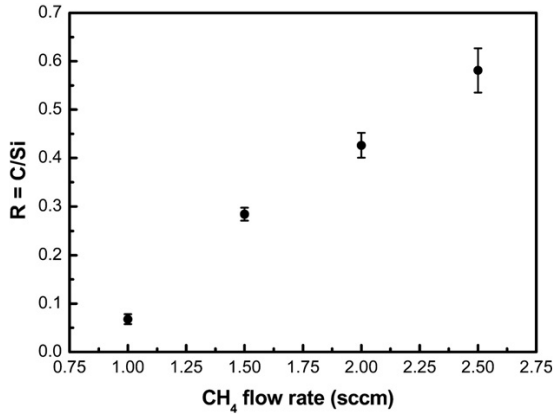

Fig. 14. Carbon content measured by RF-GD-OES for RF2(1)–RF2(4), as a function of CH_4 flow rate.

of around 0.5 nm. Properties of these films were characterized by several techniques (ellipsometry, Raman spectroscopy, AFM, FTIR spectroscopy, TEM, EF-TEM, RF-GD-OES). It has been demonstrated that crystalline samples present no crystalline SiC phase. They are made of silicon crystallites embedded in an a-$Si_{1-x}C_x$:H matrix. As carbon is going only in the amorphous tissue, it was shown that the increase in crystalline fraction, linked to the different seed layer deposition time, results in a lower carbon incorporation, despite the deposition gas mixture being kept constant. Further studies are required to investigate the effect of such parameters on electrical properties, so to identify optimal conditions for photovoltaic application.

Acknowledgments

This work has been supported by the French National Research Agency (ANR) through the "Habitat intelligent et solaire photovoltaïque" program (project CANASTA no. ANR-10-HABISOL-002).

References

[1] Y. Matsumoto, G. Hirata, H. Takakura, H. Okamoto, Y. Hamakawa, J. Appl. Phys. 67 (1990) 6538.
[2] F. Demichelis, C.F. Pirri, E. Tresso, J. Appl. Phys. 72 (1992) 1327.
[3] A. Dasgupta, S. Saha, S. Ray, R. Carius, J. Mater. Res. 14 (1999) 2554.
[4] U. Coscia, G. Ambrosone, S. Lettieri, P. Maddalena, V. Rigato, S. Restello, E. Bobeico, M. Tucci, Sol. Energy Mater. Sol. Cells 87 (2005) 433.
[5] F. Demichelis, C. Pirri, E. Tresso, Philos. Mag. B 66 (1992) 135.
[6] B. Goldstein, C. Dickson, I.H. Campbell, P. Fauchet, Appl. Phys. Lett. 53 (1988) 2672.
[7] M. Kondo, H. Fujiwara, A. Matsuda, Thin Solid Films 430 (2003) 130.
[8] J.G.E. Jellison, F.A. Modine, Appl. Phys. Lett. 69 (1996) 371.
[9] U. Coscia, G. Ambrosone, S. Lettieri, P. Maddalena, S. Ferrero, Thin Solid Films 511–512 (2006) 399.
[10] G. Ambrosone, U. Coscia, S. Lettieri, P. Maddalena, M.D. Noce, S. Ferrero, S. Restello, V. Rigato, M. Tucci, J. Non-Cryst. Solids 352 (2006) 1371.
[11] A. Abramov, Y. Djeridane, R. Vanderhaghen, P. Roca i Cabarrocas, J. Non-Cryst. Solids 352 (2006) 964.
[12] A. Fejfar, T. Mates, O. Certík, B. Rezek, J. Stuchlík, I. Pelant, J. Kočka, J. Non-Cryst. Solids 338–340 (2004) 303.
[13] J. Kočka, A. Fejfar, T. Mates, P. Fojtík, K. Dohnalová, K. Luterová, J. Stuchlík, H. Stuchlíková, I. Pelant, B. Rezek, A. Stemmer, M. Ito, Phys. Status Solidi C 1 (2004) 1097.
[14] A. Fejfar, T. Mates, C. Koch, B. Rezek, V. Švrček, P. Fojtík, H. Stuchlíková, J. Stuchlík, J. Kočka, MRS Proc. 664 (2001) A16.1.
[15] F. Iacona, C. Bongiorno, C. Spinella, S. Boninelli, F. Priolo, J. Appl. Phys. 95 (2004) 3723.
[16] R. Egerton, Rep. Prog. Phys. 72 (2009) 016502.
[17] W. Han, S. Fan, B. Gu, Mater. Sci. Eng. B 41 (1996) 357.
[18] Y. Catherine, G. Turban, B. Grolleau, Thin Solid Films 76 (1981) 23.
[19] U. Coscia, G. Ambrosone, P. Maddalena, A. Setaro, A. Phani, M. Passacantando, Thin Solid Films 515 (2007) 7634.
[20] F. Finger, O. Astakhov, T. Bronger, R. Carius, T. Chen, A. Dasgupta, A. Gordijn, L. Houben, Y. Huang, S. Klein, M. Luysberg, H. Wang, L. Xiao, Thin Solid Films 517 (2009) 3507.
[21] D. Basa, F. Smith, Thin Solid Films 192 (1990) 121.
[22] F. Demichelis, F. Giorgis, C. Pirri, Solid State Commun. 96 (1995) 17.
[23] U. Coscia, G. Ambrosone, S. Lettieri, P. Maddalena, P. Rava, C. Minarini, Thin Solid Films 427 (2003) 284.
[24] J. Pisonero, B. Fernández, R. Pereiro, N. Bordel, A. Sanz-Medel, TrAC Trends Anal. Chem. 25 (2006) 11.
[25] P. Sanchez, B. Fernandez, A. Menendez, R. Pereiro, A. Sanz-Medel, J. Anal. At. Spectrom. 25 (2010) 370.